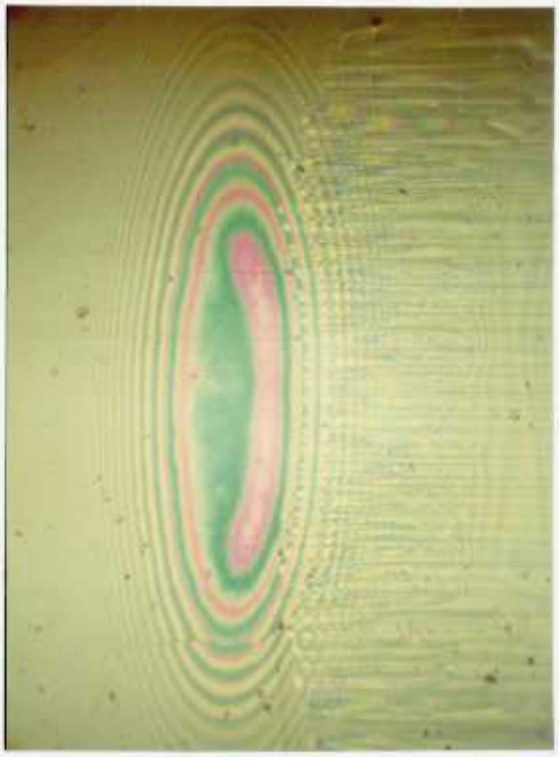


OIL FILM THICKNESS AND FRICTION IN ELLIPTICAL CONTACTS

by Neil Thorp

A thesis submitted for the degree of
DOCTOR OF PHILOSOPHY
of the University of London
and also for the
DIPLOMA OF IMPERIAL COLLEGE

October 1972

Lubrication Laboratory,
Department of Mechanical Engineering,
Imperial College of Science and Technology,
London S.W.7.

ABSTRACT

Optical interferometric measurements are reported of the thickness and shape of the oil film in the elliptical contact existing between a ball and a grooved raceway. Gyroscopic sliding is simulated by angling the ball shaft and it is shown that the most favourable condition for a thick oil film occurs when angling is absent. The transition from the elastohydrodynamic regime to the rigid piezo-viscous regime is evident from a change in gradient of film thickness against speed graphs. A numerical solution to the relevant equations for this latter regime is developed and gives good agreement with experiment. In the elastohydrodynamic regime existing elliptical contact theories are shown to be adequate for predicting film thicknesses under most conditions.

Results are also presented of friction measurements in circular and elliptical contacts. Conventional elastohydrodynamic theory is shown to give reasonable film thickness predictions in low modulus contacts, providing that oil property data is known. At the high pressures present in harder contacts, this theory is adequate only over a part of the load and speed range. Discrepances may be explained partly in terms of inaccurate temperature and pressure viscosity laws and partly in terms of non-Newtonian behaviour.

At high speeds there is a transition into the rigid piezo-viscous regime. Friction predictions based on the numerical solutions are developed and shown to agree with experiment in this region. The dependence of the predictions on the size of the contact meniscus indicates that starvation occurs more readily than under elastohydrodynamic conditions.

A brief investigation of film thicknesses in pure spinning shows that the film generating capacity is very low.

LIST OF CONTENTS

		Page number
Frontispiece		2
Title page		3
Abstract		4
List of contents		5
Preface		10
Acknowledgments		11
Nomenclature		12
Chapter 1.	INTRODUCTION	17
1.1	Exordium	17
1.2	A survey of theoretical work	18
1.2.1	Film thickness in line contacts	18
1.2.2	Film thickness in point contacts	21
1.2.3	Dimensional analysis	23
1.3	The development of film thickness measurement techniques	25
1.4	Ball spin	28
1.5	A review of sliding friction	30
1.5.1	Preamble	30
1.5.2	Rheological models	30
References for chapter 1.		33
Chapter 2.	EXPERIMENTAL APPARATUS	41
2.1	General description	41
2.2	Sliding friction measurement	41
2.3	Drive system	43
2.4	Speed measurement	44
2.5	Adaptations of the apparatus	44
2.6	Temperature measurement	45
2.7	Measurement of the groove radius	47

Page number

2.8 Improvements to the apparatus 48

References for chapter 2. 50

Chapter 3. THE OPTICAL SYSTEM AND ITS CALIBRATION 51

3.1 Introduction 51

3.2 Interferometric fundamentals 52

3.3 Choice of illumination system 54

3.4 Optical components 56

3.4.1 Viewing system 56

3.4.2 Ball 58

3.4.3 Raceways 58

3.5 Contact visibility 60

3.6 Calibration of fringes 64

3.7 Calculation of reduced modulus and phase change 67

3.8 Phase changes at the semi-reflecting layers 73

3.9 Refractive index in the contact 75

References for chapter 3. 78

Chapter 4. VARIATION OF VISCOSITY 80

4.1 Introduction 80

4.2 Experimental pressure-viscosity data 81

4.3 Pressure viscosity coefficient 83

4.3.1 Low shear rate 83

4.3.2 High shear rate 84

4.4 Limiting viscosity 86

4.5 Empirical formula 88

4.6 Viscosity variation with temperature 93

4.7 Discussion 95

References for chapter 4. 97

		Page number
Chapter 5.	FILM THICKNESS IN ELLIPTICAL CONTACTS	98
5.1	Introduction	98
5.2	Theory	99
5.2.1	Reynold's equation	99
5.2.2	Load taken	101
5.2.3	Boundary conditions	101
5.2.4	Non-dimensional groups	102
5.2.5	Previous solutions	104
5.3	Sliding contacts:theoretical & experimental	107
5.3.1	High speed photographs of the contact	107
5.3.2	Pressure distribution	113
5.3.3	Cavitation	114
5.3.4	Film profiles in sliding	122
5.3.5	Film thickness in sliding	123
5.4	Rolling contacts:theoretical & experimental	137
5.4.1	Resolved velocity in rolling	137
5.4.2	High speed photographs of the contact	139
5.4.3	Pressure distribution	143
5.4.4	Cavitation	143
5.4.5	Film profiles in rolling	145
5.4.6	Film thickness in rolling	159
References for chapter 5.		165
Chapter 6.	SLIDING FRICTION IN ELASTOHYDRODYNAMIC CONTACTS	167
6.1	Review	167
6.2	Theory	169
6.2.1	Introduction	169
6.2.2	Isothermal sliding friction	171
6.2.3	Sliding friction with heating (analytical)	173
6.2.4	Sliding friction with heating (numerical)	178
6.2.5	Non-dimensional groups	179

Page number

6.3 Experiment 180

6.3.1 Low modulus materials (Perspex) 180

6.3.2 Medium modulus materials (glass) 186

6.3.3 High modulus materials (sapphire) 197

6.4 Discussion of friction results 197

6.5 Viscometry 202

6.6 Conclusions 205

References for chapter 6. 206

Chapter 7. FRICTION IN UNDISTORTED CONTACTS 208

7.1 Review of previous work 208

7.2 Theory 209

7.2.1 Introduction 209

7.2.2 Rolling friction 210

7.2.3 Sliding friction 213

7.2.4 Sliding friction in the cavitated region 214

7.2.5 Direction of friction forces 215

7.3 Approximate analytic solutions 215

7.3.1 Introduction 215

7.3.2 Sliding friction in the cavitated region 215

7.3.3 Rolling friction 216

7.3.4 Sliding friction 217

7.4 Numerical solutions 218

7.4.1 Calculation procedure 218

7.4.2 Velocity correction 221

7.5 Region of friction 222

7.5.1 Experimental measurement 222

7.5.2 Dimensional analysis 225

7.6 Experimental and theoretical results 226

7.6.1 Experimental frictions 226

7.6.2 Theoretical frictions (elliptical contacts) 232

7.6.3 Theoretical frictions (circular contacts) 239

Page number

7.7 Discussion of results 243

References for chapter 7. 249

Chapter 8. FURTHER FILM THICKNESS INVESTIGATIONS 251

8.1 Film thicknesses under pure spinning 251

8.2 Film thickness in a high modulus point contact 258

References for chapter 8. 266

Chapter 9. CONCLUSIONS AND SUGGESTIONS FOR FUTURE WORK 267

9.1 Summary of main conclusions 267

9.2 A new thrust bearing rig 268

9.2.1 General description 268

9.2.2 Ball torque dynamometer 271

9.3 Suggestions for future work 273

References for chapter 9. 275

APPENDICES 276

Appendix 1. A program to calculate reduced modulus and phase change 277

Appendix 2. Computer prediction of pressure in a piezoviscous elliptical contact 280

Appendix 3. Adaptation of existing elliptical contact theories to plotted groups 296

Appendix 4. A program to give a numerical solution for the sliding friction with heating 298

Appendix 5. Program to derive α-value from friction measurements 304

Appendix 6. Subroutines to calculate friction in undistorted contacts. 308

Appendix 7. Summary of air bearing data 316

Appendix 8. Eddy current dynamometer design 319

PUBLICATIONS 324

PREFACE

The experimental work described in this thesis was performed using a ball and plate apparatus. The plate was grooved giving rise to an elliptical point contact which was studied using interferometry.

After chapter 1, which contains an introduction and a brief survey of relevant work, the apparatus is described in the second chapter. Chapter 3, a short description of the method of film thickness measurement, is followed by a detailed examination of the physical properties of the test lubricant. Chapter 5 contains the results of film thickness measurements for elliptical contacts with varying degrees of gyroscopic sliding, obtained by angling the ball drive shaft. Also contained in this chapter are the results of a numerical solution for the load carried in an undistorted contact. Elasto-hydrodynamic friction predictions are reported in chapter 6 using the information in the fourth chapter as a basis for a thermal-Newtonian approach. The predictions are compared with measurements made in a sliding point contact for a variety of materials. Given in chapter 7 are calculations of friction in undistorted contacts based on pressure distributions from the theory of chapter 5. These are compared with the point contact data of chapter 6 and also with further friction measurements made in elliptical contacts. Chapter 8 presents some further film thickness investigations (notably a short examination of film thickness in spinning) and, finally, chapter 9 contains a summary of the main conclusions and puts forward suggestions for future research.

ACKNOWLEDGEMENTS

The following people have aided and advised during the progress of the research reported in this thesis. Their assistance is gratefully acknowledged

Professor A. Cameron for providing funds to attend the 1971 ASLE - ASME Lubrication Conference.

Mr. R. Dobson for his encouragement and for advice on technical matters in the laboratory.

Dr. W. Pike of B.P. Sunbury Research Centre for supplying detailed information on the lubricant used during the work.

The Science Research Council for a research studentship and for the research grant which has supported the investigation.

Mr. D.G. Tatchell for his invaluable discussions especially on computational techniques.

Finally the greatest debt is owed to Dr. R. Gohar for suggesting the research topic and for providing such enthusiastic supervision over the three years which the work covered.

NOMENCLATURE

Where, to be consistent with normal usage, a symbol has another meaning, it is temporarily redefined in the text. Symbols used only once are also defined in the text.

$A = 1/(2R_x)$

a = radius of circular Hertzian contact (chapters 3 and 6)

$B = 1/(2R_y)$

a,b = normalising parameters

c = semi-axis of Hertzian contact ellipse in x-direction

d = semi-axis of Hertzian contact ellipse in y-direction

E_1, E_2 = elastic modulii of materials

$E' = 2\left[\frac{1-\sigma_1^2}{E_1} + \frac{1-\sigma_2^2}{E_2}\right]^{-1}$ = reduced modulus of elasticity

EHD = abbreviation for elastohydrodynamic

EHL = abbreviation for elastohydrodynamic lubrication

F_c = friction force due to cavitation streamers

F_{R_x}, F_{R_y} = friction force due to rolling in x and y-directions

F_s = friction force due to sliding

$G = (B/A)(b/a)^2$ = geometry group

$G^* = E'$ = materials parameter

$H_L^* = h_L/R$ = limiting film thickness parameter

$H_{min}^* = h_{min}/R$ = minimum film thickness parameter

$H_o^* = h_o/R$ = central film thickness parameter

h = film thickness at (x,y)

h_B = film thickness at $x = x_B$, $y = y_B$

h_c = film thickness at point of film rupture

h_L = limiting film thickness

h_{min} = minimum film thickness

h_o = central film thickness

$\bar{h} = h/h_o$ = non-dimensional film thickness

$\bar{h}_c = h_c/h_o$ = non-dimensional film thickness at rupture point

K = thermal conductivity of oil

K_o, K_1 = constants in modified exponential viscosity law(eq.4.3

$K^* = (K\eta_o\alpha^2)/(\beta R^2)$ = thermal conductivity parameter

k = constant in 'Kapitza' pressure distribution(see p 104)

L = length of line contact

m = film thickness where $\partial u/\partial z = (U_2 - U_1)/h$

N = fringe order

n = refractive index of lubricant

p = pressure at (x,y)

p_m = peak Hertz pressure

$\bar{p} = \alpha p$ = non-dimensional pressure

$\bar{p}_m = \alpha p_m$ = non-dimensional peak Hertz pressure

$q = (1 - e^{-\alpha p})/\alpha$ = reduced pressure at (x,y)

$\bar{q} = \alpha q = (1 - e^{-\bar{p}})$ = non-dimensional reduced pressure

R = ball radius

R_G = groove radius

R_x = principal radius of curvature in x-direction

R_y = principal radius of curvature in y-direction

r = polar co-ordinate

$\bar{r}$ = non-dimensional polar co-ordinate

$\bar{r}_B$ = non-dimensional radial boundary on friction integration

T = absolute temperature

t = temperature rise

[$U = (U_2 - U_1)/2$ = average surface speed (chapter 1 only)]

[$U^* = (\eta_o U/RE')$ = speed parameter (chapter 1 only)]

U_2, U_1 = velocity of upper and lower surfaces respectively

U_p = velocity of plate along groove axis

$U^* = (\eta_o \bar{V}/RE')$ = speed parameter

U, V = ball surface velocities in x and y-directions

u,v = velocities in x and y-directions at (x,y,z)

$\underline{V}$ = vector sum of U and V

V = modulus of $\underline{V}$

$\underline{V}_1$ = total rolling velocity vector

V_1 = modulus of $\underline{V}_1$

W = total load carried by point contact

W_L = total load carried by line contact

$\bar{W}$ = non-dimensional point contact load

$W^* = W/(E'R^2)$ = point contact load parameter

$W_L^* = W_L/(LE'R^2)$ = line contact load parameter

x,y,z = Cartesian co-ordinates along, across and normal to groove respectively

x_B,y_B = boundary of friction integral in x and y-directions

$\bar{x},\bar{y} = x/a,\ y/b$ = non-dimensional Cartesian co-ordinates

$\bar{x}_B,\bar{y}_B = x_B/a,\ y_B/b$ = non-dimensional boundary of friction integral in x and y directions

$x_B^* = x_B/R$ = inlet boundary parameter

α = pressure viscosity coefficient of lubricant

β = temperature coefficient of lubricant

β_o,β_p = β-values at atmospheric pressure and pressure p

$\delta^* = (U_2 - U_1)/(U_2 + U_1)$ = slide/roll ratio

η = viscosity at (r,ϕ, z)

η_m = viscosity at $(r,\phi,z=m)$

η_o = isoviscous viscosity or viscosity at atmospheric pressure

η_p = viscosity at pressure p

η_r = viscosity at $(r, \phi, z=0)$

η_s = viscosity at start of Hertz pressure curve

$\bar{\eta}_m = \eta_m/\eta_o$ = non-dimensional viscosity at $z = m$

Θ = oil temperature at (r, ϕ, z) (chapter 6)

Θ_c = maximum temperature rise (chapter 6)

Θ_s = oil temperature at inlet (chapter 6)

λ = wavelength of light

μ = coefficient of sliding friction (chapter 6)

μ_c = coefficient of cavitation sliding friction

μ_R = coefficient of rolling friction in sliding direction

μ_{R_x}, μ_{R_y} = coefficients of rolling friction in x and y-direction

μ_s = coefficient of sliding friction

$\xi = (6\eta_o \bar{v} \alpha)/(h_o^{3/2} A^{1/2})$ = independent program variable

ρ = density of lubricant

σ_1, σ_2 = Poisson's ratios of materials

τ = shear stress on element of fluid

τ_x = shear stress on plate in x-direction

$\oint$ = ellipticity factor (see equation 1.4, p 22)

$\oint_1, \oint_2$ etc. denote functional relationships

ϕ = polar co-ordinate

Ω = angular velocity of ball

Chapter 1 INTRODUCTION

1.1 Exordium

Elastohydrodynamic lubrication (EHL) has been defined by Dowson (1)* as the study of situations in which elastic deformation of the surrounding solids play a significant role in the hydrodynamic lubrication process. Although such situations can occur with soft materials, they are more usually generated in low conformity contacts such as exist in gears, cams and rolling bearings. The small size of such contacts gives rise to very high local pressures which may influence the properties of the lubricant. Viscosity, for instance, often increases dramatically with pressure. Although such a variation is not a necessary prerequisite for EHL, any solution of the Reynold's equation which ignores it, if it exists, is liable to be seriously in error.

As a field in the study of lubrication, EHL cannot really be regarded as new, since its beginnings may be traced back to the early 1950's. However, most of the important developments have taken place in the last few years, both theoretically and experimentally. Theoretically, the majority of effort has been concentrated on the line contact problem, because, as flow can be considered to be in one direction only, it is simpler to treat. No complete solution yet exists for the point contact situation because the problem is complicated by sideways flow of the lubricant.

Early experimental work also tended to concentrate on

---

* Numbers in brackets designate references at the end of the chapter.

line contacts, the disc machine proposed by Merritt (2), almost becoming a sine qua non of all lubrication laboratories. However, with the adaptation of optical interferometry to the study of EHL, circular point contacts have become quite popular, because of the ease with which film thickness can be measured. Recently, however, interferometry has been applied to line contacts by Wymer (3).

Line and point contacts having now been extensively investigated, it remains to extend the technique to the situation experienced in many real applications, namely to elliptical contacts. The experimental work presented in chapter 5 of this thesis, therefore, is an interferometric study of elliptical contact behaviour. The new information obtained will supplement the sparse experimental data already available on elliptical contacts, nearly all of which is due to Archard and co-workers (4,5) and hence should provide a means of checking those approximate point contact solutions which are general enough to be extended to the elliptical case.

1.2 A survey of theoretical work

1.2.1 Film thickness in line contacts

Because the film thickness determines the amount of metal-to-metal contact, the major effort in EHL theory has been directed towards its accurate prediction. That thicknesses greater than the surface roughnesses could exist, had been deduced from the lack of wear on gear teeth and cams, but Martin's attempt (6) to calculate the actual values gave answers which were far too small. His failure can be traced to the basic assumptions of the simple theory that he used, namely that the surfaces were rigid and the lubricant isoviscous.

Later workers improved marginally on his results by considering the effect of elastic deformation (7,8,9) and that of piezoviscosity (10 - 15) using various pressure viscosity relationships and cavitation boundary conditions.

However, the most significant work of this period was done by Ertel and published by Grubin (16) in 1949, who included the two effects simultaneously, thus obtaining the first realistic film thickness predictions. His basic assumption, later shown experimentally to be accurate, was that the shape of the bounding surfaces over most of the contact would be that calculated for dry contact by Hertz theory (17). He also discussed qualitatively the oil film pressure distribution in the contact zone, forecasting a basically Hertzian distribution with a very sharp second maximum near the exit to the contact. The film thickness predicted by this analysis can be expressed as:-

$$H_o^* = 1.95\ U^{*0.727}\ G^{*0.727}\ W_L^{*-0.091} \qquad -1.1$$

Petrousevich (18) confirmed Grubin's predictions when he obtained a simultaneous solution for the governing elastic and hydrodynamic equations at three different speeds. He showed, for the first time, the constant central film thickness and localised end closure characteristic of elastohydrodynamic contacts. Weber and Saalfeld (19) also obtained a solution to the equation, but since their investigations were restricted to small deformations, the features discussed by Grubin and Petrousevich did not appear.

In 1959 Dowson and Higginson (20) presented a new approach to the problem. Rather than solving for pressures directly, as Meldahl (9) had done, they described a procedure for solving

the inverse problem, first by assuming a pressure distribution and then finding the resultant film shape from the governing equations. Although initially they did not predict a pressure spike, later work for more severe conditions (21) did demonstrate its presence. The same authors (22) later derived a convenient formula for minimum film thickness:-

$$H^*_{min} = 1.6\ U^{*0.7}\ G^{*0.6}\ W_L^{*-0.13} \qquad -1.2$$

In 1967 Dowson (46) pointed out that this equation did not satisfy dimensional analysis and suggested that it would be better represented by:-

$$H^*_{min} = 2.65\ U^{*0.7}\ G^{*0.54}\ W_L^{*-0.13} \qquad -1.2(A)$$

Dowson, Higginson and Whitaker (23) included lubricant compressibility in the calculations and found that it resulted in the prediction of a slight increase in the film thickness just prior to the outlet constriction and also that the pressure spike was reduced in magnitude and moved downstream slightly.

Archard, Gair and Hirst (24) also employed the inverse solution procedure and were in overall agreement with the other workers. Their solutions, however, suffered a slight loss of accuracy resulting from separate treatment of the different regions of the contact. A direct solution was preferred by Osterle and Stephenson (25), but because of a lack of convergence, results had to be restricted to lightly loaded situations.

The complicated task of including thermal effects arising from viscous dissipation was tackled by Sternlicht, Lewis and Flynn (26). However, they assumed that all heat was removed by convection - the bounding surfaces being adiabatic - whereas

Dowson (1) has demonstrated that conduction outweighs convection under elastohydrodynamic conditions. The situation was remedied by Cheng and Sternlicht (27) who considered the conduction of heat to the bounding solids in their solution. They showed that the pressure spike persisted and that film thickness was little affected by the presence of sliding, thus confirming that Dowson and Higginson's formula (equation 1.2) was essentially correct.

Thus understanding of the line contact problem is well advanced; later efforts, therefore, have concentrated on extending the solutions to cover the whole range of conditions likely to be encountered. The most recent of these is by Baglin and Archard (28) who produced an analytic solution for film thickness in low modulus line contacts. The conditions here are such that the mechanism associated with pressure dependent viscosities does not operate. To provide for generation of the necessary pressures, therefore, the authors regarded the main load-bearing region as a tilted pad bearing. The solution they obtained gave similar values to the corresponding numerical calculations of Dowson and Swales (29) and of Herrebrugh (30).

1.2.2 Film thickness in point contact

Of more direct relevance to the work to be presented below are the theories concerned with point contacts. Their development has followed the same path as the line contact theories, but because of the extra complexity, has not reached the same stage and, as yet, there is no complete solution for point contacts. Indeed, until 1961 when Archard and Kirk (31) produced evidence to the contrary, it had been believed that only boundary lubrication could exist in lightly loaded point contacts. In the same paper, they presented the first Grubin-

type solution for the point contact problem. In terms of Dowson's groups (see section 1.2.3) this may be expressed as:-

$$H_o^* = 0.84\ U^{*0.741}\ W^{*-0.074}\ G^{*0.741} \qquad -1.3$$

Up to that time, point contact solutions such as those by Howlett (32), Kapitza (33) and Korovchinskii (34) had made the assumption that the surfaces were rigid. Kapitza, however, introduced the concept of pressure dependent viscosity into his solution and was able to derive a limiting film thickness. This solution and an extension of it due to Snidle and Archard (5) will be discussed further in section 5.2.5.

The line-contact solution was extended to elliptical contacts by Archard and Cowking (4) using an ellipticity factor defined as:-

$$\phi = \left[1 + \frac{2R_x}{3R_y}\right]^{-1} \qquad -1.4$$

to describe the effect of side leakage in a point contact. They also presented two semi-analytical solutions in the same paper, the first being similar to that of Kapitza, and the second a Grubin-type solution with the reduced pressure in the Hertzian region assumed constant at $1/\alpha$.

Cameron and Gohar (35) also made a Grubin-type assumption when they presented their numerical solution for circular point contacts. They had to use a hand relaxation technique, but later workers have had the benefit of high speed computers and consequently have been able to produce more refined solutions. Of these, Cheng's (36) can be applied to elliptical contacts, whilst that of Wedeven et al (37) deals only with circular contacts. Very recently, Petrousevitch et al (38) have given a solution for the non-stationary EHL problem at high pressures

in the contact zone. These authors report a film thickness equation of Kodnir which they say may be applied to elliptical contacts when the major axis is 5 - 10 times greater than the minor axis. This, however, is really a line contact solution and uses load in terms of 'capacity per cylinder length'. Also of interest in their paper are some results obtained by applying optical interferometry to an elliptical contact.

Although those point contact solutions which are applicable to the elliptical case are discussed further in section 5.2.5, it is instructive to compare all the solutions in terms of the constants K, a, b, c of equation 1.5:-

$$H^* = K\ U^{*a}\ W^{*b}\ G^{*c} \qquad -1.5$$

The table of figure 1.1 gives such a comparison. It is interesting to note that the differences between point and line contacts are not as great as was once thought.

1.2.3 Dimensional analysis

The equations presented so far have been expressed in terms of the dimensionless groups suggested by Dowson and Higginson (39). Namely:

dimensionless film thickness parameter $H^* = \frac{h}{R}$

dimensionless load parameter $W^* = \frac{W}{E'R^2}$

dimensionless speed parameter $U^* = \frac{U\eta_o}{E'R}$

dimensionless materials parameter $G^* = \alpha E'$

Although these can be obtained from the normal Buckingham or 'π' analysis (40), examination of the governing equations shows that the groups may be reduced to three,

AUTHOR	DATE			K	a	b	c
Ertel - Grubin	(1949)	Line contact	H_o^*	1.95	0.727	-0.091	0.727
Dowson & Higginson	(1961)	Line contact	H_{min}^*	1.6	0.70	-0.13	0.6
Dowson & Higginson	(1967)	Line contact	H_{min}^*	2.65	0.70	-0.13	0.54
Archard & Kirk	(1961)	Point contact	H_o^*	0.84	0.741	-0.074	0.741
Archard & Cowking	(1965)	Point contact	H_o^*	1.40	0.740	-0.074	0.74
Cameron & Gohar	(1966)	Point contact	H_o^*	3.0	1.0	-0.333	1.0
Cheng	(1969)	Point contact	H_o^*	1.69	0.725	-0.058	0.725
Wedeven et al.	(1970)	Point contact	H_o^*	1.73	0.714	-0.048	0.714

Fig. 1.1 Comparison of various film thickness theories (see equation 1.5)

without any loss of generality. Several three-parameter sets have been suggested (41 - 45), Dowson (46) pointing out that which is the most acceptable depends on whether physical appreciation or graphical convenience is the main objective, the two not necessarily yielding the same formulation.

Johnson (47) has reviewed the sets of groups proposed by other workers and has suggested a form of presentation of EHL data which reveals the different regimes of behaviour and gives a tentative idea of their boundaries. It is worth noting that these regimes can be classified as :- rigid-isoviscous, rigid-variable viscosity, elastic-isoviscous and elastic-variable viscosity. In describing these regimes, Johnson used the parameters proposed by Theyse (45), namely:

a viscosity parameter $$g_1 = \left[\frac{\alpha^2 W^3}{L^3 \eta_o U R^2}\right]^{\frac{1}{2}}$$

an elasticity parameter $$g_3 = \left[\frac{W^2}{L^2 \eta_o U E' R}\right]^{\frac{1}{2}}$$

and a dependent film thickness parameter $$\bar{h} = \left[\frac{h_o W}{L \eta_o U R}\right]$$

1.3 The development of film thickness measurement techniques

The existence of quite thick lubricant films in highly loaded contacts, deduced from the absence of wear, was confirmed as long ago as 1940(48). The technique employed was that of electrical resistance but, because the resistivity of the oil is highly dependent on temperature and moisture content, no qualitative measurement of film thickness could be obtained. The method was taken up by numerous other workers, notable amongst whom were Lane and Hughes (49) who demonstrated the presence of an oil film between gear teeth.

By increasing the voltage until the oil suffered dielectric breakdown, Brix (50) claimed to be able to make quantitative measurements, the film thickness then being proportional to the film breakdown voltage. The method was developed by Cameron and co-workers, for instance (51), and applied to gear teeth and the four ball machine. However, difficulties experienced with the technique and doubts as to the effect of the high currents involved (up to 5 amps) prompted Dyson (52) to examine its validity by comparison with the capacitance method which had by that time (1967) become firmly established. As a result of his comparisons the voltage discharge method fell into disrepute and disuse.

The electrical resistance method, however, still retains its validity and is a valuable tool in the field of partial EHL where there is an appreciable amount of metal-to-metal contact.

The feasibility of capacitance measurements for determining oil film thicknesses was first demonstrated by Lewicki (53) in 1955. In 1958, Crook (54) applied the method to his two-disc machine, measuring the capacitance between the discs and pads riding on the oil film adhering to them. He thus avoided the need to consider distortions when interpreting his results. In a later paper (55), he compared this arrangement with that of deducing the film thickness from the capacitance measured between the discs themselves, assuming in his calculations that the surfaces took on a Hertzian shape. Although he found good agreement, in a still later paper (56) the method of using pads was discarded altogether.

The results obtained by Crook were not in very good agreement with theory, giving as they did:

$$h_o \propto (U\, t_s)^{0.5} \qquad -1.6$$

t_s being the surface temperature of the discs. Archard and Kirk (31) also found disagreement with theory when they used the method for measuring film thicknesses in point contact. They found experimentally:-

$$h_o \propto (U)^{0.55} (\alpha \eta_o)^{0.57} R^{0.62} \qquad -1.7$$

but predicted theoretically that the relationship should be:-

$$h_o \propto (U)^{0.741} (\alpha \eta_o)^{0.741} R^{0.407} \qquad -1.8$$

When the procedure was extended to elliptical contacts (4), the dependence of film thickness on the ellipticity factor agreed well with theory, but no improvement in the speed dependence was reported. However, most later workers who employed the capacitance technique (57, 58, 5, 3) have found good agreement with theory. The last two have both made a comparison with the optical interference method for measuring film thickness, Snidle and Archard (5) using point contacts and Wymer (3) using line contacts. Although differing in detail, both concluded that there is broad agreement between the two methods and that the errors involved in capacitance measurements can be attributed to the necessary assumption of a parallel central oil film, whereas in fact it may be grossly distorted. If this be the case, then the capacitance technique can only give an average value of film thickness.

The optical technique used to establish the accuracy of the capacitance method forms the basis of the work to be presented and so is discussed in detail later (chapter 3, section 3.1). It is worth noting here, however, that it has become widely accepted as a method of measuring elastohydrodynamic film thickness, not only because of its accuracy, but

also because it gives a detailed plan of the deformations in the contact. It is not without its drawbacks however, the most serious of which is that one of the surfaces must be transparent. This immediately precludes its use at very high Hertz pressures unless sapphire or even diamond is used as the transparent member. The technique can also be difficult to apply in real situations where rough surfaces and external vibrations are usually experienced. In mitigation, however, it must be pointed out that only the qualitative electrical resistance method is readily adaptable to such cases, since the capacitance method also suffers from surface roughness effects (except at high film thicknesses) and external electrical noise.

Other techniques for film thickness measurement have been employed at various times; these deserve a brief mention. Sibley and Orcutt (59) have used measurements of the intensity of an X-ray beam transmitted through a disc machine contact as a basis for estimating minimum film thicknesses, R. Cameron (60) has used a magnetic reluctance technique, again in a disc machine, and Grafton (61) has measured the direct displacement to determine the film thickness in a real bearing.

1.4 Ball spin

Although much early work has been done on the effect of spin on the rolling motion of a sphere in dry contact (62, 63), only recently has the interest spread to the more important case of lubricated contacts. The main reason for this interest is a need to know the effect of a spin component on the tractive capacity of an EHL contact. In friction drives, where a high traction is required and roll and spin generally occur together, the spin component reduces the traction capacity (64).

In angular contact bearings, ball spin causes a torque about an axis normal to the contact area of the ball and race which is one of the major factors accounting for the frictional losses in such bearings (65).

Investigations into lubricated spin torque were performed by Reichenbach (66) under boundary lubricated conditions and, although he acknowledged that hydrodynamic forces may be important at higher speeds, he implied that this was not the case because the friction at such speeds was high. However, Parker et al (67) thought it probable that EHL prevailed and later (68) produced a theory for the spinning torque based on this assumption. Using a modified exponential pressure viscosity law (see figure 6.16) they obtained a correlation between the theory and experimental torque measurements, torque increasing with stress and speed and decreasing with per cent conformity.

The film thickness used in deriving the spinning torque was obtained by considering the contact as a series of elemental rollers and applying Dowson and Higginson's line contact equation to each element. Snidle and Archard (69) have also considered the problem of film thickness in spin. Assuming rigid surfaces and employing an approach similar to that of Kapitza (33) an expression for a limiting minimum film thickness was obtained. The thicknesses predicted are very small (typically 1×10^{-6}cm) and, although the authors pointed out that EHL might improve the film generation mechanism, the indications are that spinning motion has very little direct effect on the film thickness in rolling/spinning contacts.

A brief investigation into film generation by spinning, using optical interferometry, is described in chapter 8.

1.5 A review of sliding friction

1.5.1 Preamble

In elastohydrodynamic lubrication, traction is one of the most difficult variables to predict. The hopelessly high values given by Newtonian theory have led many workers to adopt complex mathematical models to describe oil behaviour in an attempt to obtain satisfactory comparisons with experiment. However, recent work by Ten Napel et al (70) has given good agreement with Newtonian theory. Such contradictions with previous work indicate that it is possible that, given adequate information about lubricant properties, Newtonian theory may not be as inadequate as believed. As chapter 6 represents an attempt to clarify this point, a review of previous work is best left until then. Therefore, only the mathematical models used by previous workers will be reviewed here.

1.5.2 Rheological models

The rheological model of Maxwell (71) predicts that the fluid behaves visco-elastically. The shear stress on an element of fluid can thus be expressed by superposition of the compliances of an elastic solid and of a viscous liquid. Hence

$$\tau = \eta\left(\frac{dU}{dz} - \frac{U}{G}\frac{d\tau}{dx}\right) \qquad -1.9$$

where G is a shear modulus.

Barlow and Lamb (72) have shown that such a model gives a fair representation of oil behaviour under low strains and at high frequencies. However, attempts to apply it to the traction problem have been only partially successful because the conditions in an EHL contact are of steady shear and large strains, under which conditions the Maxwell model gives poor predictions (73)

Dyson (73) has shown that visco-elastic effects are governed by the number

$$R_N = \text{relaxation time x shear rate} = \frac{\eta}{G}\left(\frac{\partial u}{\partial z}\right)$$

If R_N is much less than unity then the effects are not significant. When it is much greater than unity, visco-elastic effects are present and become evident in shear thinning of the oil.

The use of compliances in the Maxwell model is quite arbitrary. Barlow, Lamb et al (74) therefore suggested constructing a model from the addition of mechanical admittances instead; they then showed that many chemically defined liquids did in fact behave in this way. The model is also obeyed approximately by mineral oils (75). Dyson(73) applied the Barlow-Lamb model to the results of Johnson and Cameron (75), but only qualitative agreement was obtained.

An alternative approach to explaining lubricant rheology is to express the viscosity in terms of the molecular behaviour of the fluid. The most successful attempt has been that of Eyring et al (76) as applied by Bell (77). As with the Newtonian theory, the failure of the model stems from the need to assign values to the various parameters involved. These can only be determined with conventional apparatus and the results are not necessarily applicable under EHL conditions. Bell, nevertheless, found good qualitative agreement with the experimental data available.

In the region of extremely large relaxation number (R_N), many workers (73, 78, 79) have postulated a limiting shear stress which is independent of shear rate but dependent on pressure and temperature. They have pointed out that the

conditions inside an EHD contact are such that the lubricant can no longer be considered a liquid but should be treated more like a plastic solid.

Because it is easily understood, physically, such a model is extremely attractive and can give a good explanation for the traction peak (80). However, it implies that the traction curve peak represents a discontinuity in the physical properties of the lubricant. Dyson (73) has shown that there is evidence against such a discontinuity and is able to account for the peak in terms of his rheological model.

Recently Gentle (81) has attempted to explain the traction curve by analogy with the behaviour of powder beds under shear forces and found that such an analogy worked well. He explained the physical reality behind the assumption of granular behaviour in terms of freezing or glassing of the lubricant under the high pressure involved.

Unfortunately, the results to be presented in chapter 6 were obtained at pressures too low to display any limiting shear traction. They cannot, therefore, form a basis for examining the theories of limiting shear stress.

It was considered that, at these low pressures, it might still be possible to derive friction using Newtonian theory as had Ten Napel et al (70). As will be reported, the predictions are varied, being very good at low pressures (soft materials) but gradually worsening as pressures are increased (hard materials).

References for Chapter 1

1. Dowson D. 'Elastohoydrodynamic lubrication: an introduction and a review of theoretical studies' Proc. I.Mech.E.1965-66, Vol.180 Pt.3B, pp7-16.
2. Merritt H.E. 'Worm gear performance' Proc. I.Mech.E. 1935, Vol. 129, p 127.
3. Wymer D.G. 'Elastohydrodynamic lubrication of a rolling line contact' Ph.D. Thesis, University of London 1972.
4. Archard J.F. & Cowking E.W. 'Elastohydrodynamic lubrication at point contacts' Proc. I.Mech.E. 1965 - 6, Vol. 180 Pt.3B, pp 47 - 56.
5. Snidle R.W. & Archard J.F. 'Lubrication of elliptical contacts' Proc. I.Mech.E. 1968 - 9, Vol.183 Pt.3B, pp 140 -8.
6. Martin H.M. 'Lubrication of gear teeth' Engineering, London 1916 Vol. 102, p 199.
7. Peppler W. Maschinenelemente - Tagung, Aachen 1935, 42; V.D.I. Verlag, Berlin 1936.
8. Peppler W. V.D.I. - Forschungsheft 1938, p 391.
9. Meldahl A. 'Contribution to the theory of lubrication of gears and of the stressing of the lubricated flanks of gear teeth' Brown Boveri Review, 1941, Vol. 28 NO. 11, p 374.
10. Gatcombe E.K. 'Lubrication characteristics of involute spur-gears - a theoretical investigation' Trans. ASME, 1945, Vol. 67, p 177.
11. Hersey M.D. & Lowdenslager D.B. 'Film thickness between gear teeth. A graphical solution of Karlson's problem' Trans. ASME, 1950, Vol. 72, p 1035.
12. Blok H. 'Fundemental aspects of thin film lubrication' Ann. N.Y. Acad.Sci., 1950, Vol. 53, p 779.

13.McEwen E. 'The effect of variation with pressure on the load carrying capacity of oil films between gear teeth' Jour. Inst. Petroleum, 1952, Vol. 38, p 646.

14.Cameron A. 'Hydrodynamic theory in gear lubrication' Jour. Inst. Petroleum, 1952, Vol. 38, p 614.

15.Blok H. 'Discussion. Gear Lubrication Symposium Part 1, The lubrication of gears' Jour. Inst. Petroleum, 1952, Vol. 38, p 673.

16.Grubin A.N. 'Investigation of scientific and industrial research' Central Scientific Research Institute for Technology and Mechanical Engineering, Moscow, Bk. no.30, 1949, pp 115 - 6.

17.Hertz H. 'On the contact of elastic solids' and 'On the contact of rigid elastic solids and on hardness' reprinted in 'Miscellaneous Papers', translated by Jones D.E. & Schott G.A., Macmillan Co. Ltd., London, 1896, pp 146 - 162, 163 - 183.

18.Petrousevich 'Fundamental conclusions from the contact-hydrodynamic theory of lubrication' Izvestia Uzbekist Fil. Akad. Nauk SSSR (OTN), 1951, Vol.2, p 209. (M.O.D. Trans. no. 293).

19. Weber & Saalfeld Zeits. ang. Math. Mech., 1954, Vol. 34 (nos. 1,2), p 54.

20.Dowson D. & Higginson G.R. 'A numerical solution to the elastohydrodynamic problem' Jour. Mech. Eng. Sci., 1959, Vol.1, no.1, p 6.

21. Dowson D. & Higginson G.R. 'The effects of material properties on the lubrication of elastic rollers' Jour. Mech. Eng. Sci., 1960, Vol.2, no.3, p 188.

22.Dowson D. & Higginson G.R. 'New roller-bearing lubrication formula' Engineering, London, 1961, Vol.192, p 158.

23.Dowson D., Higginson G.R. & Whitaker A.V. 'Elastohydrodynamic lubrication - a survey of isothermal solutions' Jour. Mech. Eng. Sci., 1962, Vol.4, no.2, p 121.

24.Archard J.F., Gair F.C. & Hirst W. 'The elastohydrodynamic lubrication of rollers' Proc. Roy. Soc., 1961, Series A, Vol.262, p 51.

25.Osterle J.F. & Stephenson R.R. 'A direct solution of the elastohydrodynamic lubrication problem' Trans. ASLE, 1962, Vol.5, no.2, p 365.

26.Sternlicht B., Lewis P. & Flynn P. 'Theory of lubrication and failure of rolling contacts' Trans. ASME, 1961, Jour. of Basic Eng., Vol.83(D), no.2, p 213.

27.Cheng H.S. & Sternlicht B. 'A numerical solution for the pressure, temperature and film thickness between two infinitely long, lubricated rolling and sliding cylinders under heavy loads' Trans. ASME, 1965, Jour. of Basic Eng., Vol.87(D), pp 695-707.

28.Baglin K.P. & Archard J.F. 'An analytic solution of the elastohydrodynamic lubrication of materials of low elastic modulus' PaperC3/72, I.Mech.E., EHL Symposium, Leeds 1972.

29.Dowson D. & Swales P.D. 'The development of elastohydrodynamic conditions in a reciprocating seal' Proc. Third Int. Conf. Fluid Sealing, Cambridge 1967. (Br. Hydro. Res. Ass.).

30.Herrebrugh K. 'Solving the incompressible and isothermal problem in elastohydrodynamic lubrication through an integral equation' Trans. ASME, Jour. Lub. Tech., 1968, Vol.90(F) p 262.

31.Archard J.F. & Kirk M.T. 'Lubrication at point contacts' Proc. Roy. Soc., 1961, Series A, Vol.261, pp 532-550.

32.Howlett J. 'Film lubrication between spherical surfaces: with an application to the theory of the four-ball lubrucant testing instrument' Jour. of Applied Physics, 1946, Vol.17, no.3, pp 137-149.

33.Kapitza P.L. 'Hydrodynamic theory of lubrication during rolling' Zhurn. Tekh. Fiz., 1955, Vol.25, p 747.

34.Korovchinskii M.V. 'On the possible limit to the regime of hydrodynamic friction in the four-ball machine' Trenie i Iznos v machinax, Akad. Nauk., Moscow, 1958, Vol.12, pp 242-285.

35.Cameron A. & Gohar R. 'Theoretical and experimental studies of the oil film in lubricated point contacts' Proc. Roy. Soc., 1966, Series A, Vol.291, pp 520-536.

36.Cheng H.S. 'A numerical solution of the elastohydrodynamic film thickness in an elliptical contact' Jour. Lub. Tech. Trans. ASME, Series F, Vol.92, no.1, 1970, pp 155-162.

37.Wedeven L.D., Evan D, & Cameron A., 'Optical analysis of ball bearing starvation' Trans. ASME, 1971, Jour. Lub. Tech. Vol.93.

38.Petrousevitch A.I., Kodnir D.S., Salukvadze R.G., Bakashvili D.L. & Schwarzman V.Sh. 'The investigation of oil film thickness in lubricated ball-race rolling contact' Wear, Vol.19,1972, pp 369-389.

39.Dowson D. & Higginson G.R. 'Elastohydrodynamic lubrication' 1966, Pergamon Press.

40.Buckingham E. 'On physically similar systems; illustrations of the use of dimensional equations' Physical Review, 1914, Series 2, Vol.4, pp 345-376.

41.Blok H. 'Communication to ref.1' Proc. I.Mech.E., 1965-66, Vol.180, Pt.3B, p 237-8

42.Moes H. 'Communication to ref.1' Proc. I.Mech.E., 1965-66, Vol.180, Pt.3B, pp 244-5.

43.Archard J.F. 'Non-dimensional parameters in isothermal theories of elastohydrodynamic lubrication' Jour. Mech. Eng. Sci., 1968, Vol.10 no.2, pp 165-7.

44.Greenwood J.A. 'Presentation of elastohydrodynamic film thickness results' Jour. Mech. Eng. Sci., 1969, Vol.11 no.2, pp 128-132.

45.Theyse F.H. 'Some aspects of the influence of hydrodynamic film formation on the contact between rolling/sliding surfaces' Wear, 1966, Vol.9, pp 41-59.

46.Dowson D. 'Elastohydrodynamics' Paper 10, Convention on Lubrication and Wear - Fundamentals and Applications to design. Proc. I.Mech.E., 1967-68, Vol.182 Pt.3A.

47.Johnson K.L. 'Regimes of elastohydrodynamic lubrication' Jour. Mech. Eng. Sci., 1970. Vol.12, no.1, pp 9-16.

48.Beeck O., Givens J.W. & Smith A.E. 'On the mechanisms of boundary lubrication, 1: the action of long-chain polar compounds' Proc. Roy. Soc., 1940, Vol.177, Series A,p 90.

49.Lane T.B. & Hughes J.R. 'A study of the oil film formation in gears by electrical resistance measures' Brit. Jour. Appl. Phys., 1952, Vol. 3, pp 315-318.

50.Brix V.H., 'Electrical study of boundary lubrication' Aircraft Eng., 1947, Vol.19, pp 294-297.

51.McConochie I.O. & Cameron A.'The measurement of oil film thickness on gear teeth' Journal of Basic Eng., Trans. ASME 1960, Vol.82(D), p 29.

52.Dyson A. 'Investigation of the discharge-voltage method of measuring the thickness of oil films formed in a disc machine under conditions of elastohydrodynamic lubrication' Proc. I.Mech.E., 1966-7, Vol.181 Pt.1, pp 633-646.

53.Lewicki W. 'Some physical aspects of lubrication in rolling bearings and gears' Engineer, London, 1955, Vol.200, pp 176, 212.

54.Crook A.W. 'The lubrication of rollers' Phil. Trans. Roy. Soc., 1958, SeriesA, Vol.250, pp 387-409.

55.Crook A.W. 'The lubrication of rollers. II Film thickness with relation to viscosity and speed' Phil. Trans. Roy. Soc. 1961, Series A, Vol.254, p 223-236.

56.Crook A.W. 'The lubrication of rollers. IV Measurements of friction and effective viscosity' Phil. Trans. Roy. Soc. 1963, Series A, Vol.255, p 281-312.

57.Dyson A., Naylor H. & Wilson A.R. 'The measurement of oil film thickness in elastohydrodynamic lubrication' Proc. I.Mech.E., 1965-6, Vol.180 Pt.3B, p 119-134.

58.Vichard J.P. & Godet M.R. 'Simultaneous measurement of load, friction and film thickness in a cam-and-tappet system' Proc. I.Mech.E., 1967-68, Vol.182 Pt.3G, pp109-113.

59.Sibley L.B. & Orcutt F.K. 'Elastohydrodynamic lubrication of rolling contact surfaces' Trans. ASLE, 1961, Vol.4 no.2 pp 234-249.

60.Cameron R. 'Measurement of oil film thickness between rolling discs by a variable- magnetic-reluctance technique' Proc. I.Mech.E., 1967-68, Vol.182 Pt.3G, pp 59-61

61.Grafton M. 'Measurement of oil film thickness in a tapered roller thrust bearing' M.Sc. Thesis, University of Leeds, 1968

62. Johnson K.L. 'The effect of spin upon the rolling motion of an elastic sphere on a plane' Trans. ASME, 1958, Vol.25 no.3, pp 332-338.

63. Poon S.Y. 'An experimental study of the shear traction distribution in rolling with spin' Wear, 1967, Vol.10 pp 61-69.

64. Poon S.Y. 'Some calculations to assess the effect of spin on the tractive capacity of rolling contact drives' Report CUED/C-MECH/TR1 (1969), University of Cambridge, Engineering Department.

65. Dietrich M.W., Parker R.J., Zaretsky E.V. & Anderson W.J. 'Contact conformity effect on spinning torque and friction' Trans. ASME, 1969, Jour. Lub. Tech., Vol.91(F), pp 308-313.

66. Reichenbach G.S. 'The importance of spinning friction in thrust carrying ball bearings' Trans. ASME, 1960, Jour. Basic Eng. Vol.82(D) no.2, pp 295-301.

67. Parker R.J., Zaretsky E.V. & Anderson W.J. 'Spinning friction coefficients with three lubricants' Trans.ASME, 1968, Jour.Lub. Tech., Vol.90(F) no.1, pp330-332.

68. Allen C.W., Townsend D.P. & Zaretsky E.V., 'Elastohydrodynamic lubrication of a ball spinning in a non-conforming groove' Trans. ASME, 1970, Jour. Lub. Tech., Vol.92(F) no.1, pp 89-96.

69. Snidle R.W. & Archard J.F. 'Theory of hydrodynamic lubrication for a spinning sphere' Proc. I.Mech.E., 1969-70, Vol.184 Pt.1.

70. Ten Napel W.E., Moes H. & Bosma R. 'Traction in elastohydrodynamic lubrication at low sliding speeds' Tribology Convention 1971, I.Mech.E., London, Paper C82/71 pp 142-150.

71.Maxwell J.C. 'On the dynamic theory of gases' The London, Edinburgh and Dublin Philosophical Magazine and Journal of Science (series 4), 1868, Vol.35, pp 129, 185.

72.Barlow A.J. & Lamb J. 'Behaviour of lubricating oils under cyclic shearing stress' Proc. Roy. Soc., 1959., Vol.253, Series A, p 59.

73.Dyson A. 'Frictional traction and lubricant rheology in elastohydrodynamic lubrication' Phil. Trans. Roy. Soc., 1970, Vol.266, Series A 1170, pp 1-33.

74.Barlow A.J., Erginson A. & Lamb J. 'Visco-elastic relaxation of super-cooled liquids. II ' Proc. Roy. Soc., Series A Vol.298, 1967, p 481.

75.Hutton J.F. 'Visco-elastic relaxation spectra of lubricating oils and their component fractions' Proc. Roy. Soc., Series A, Vol.304, 1968, p 65.

76.Eyring H., Ree T. & Hirai N. 'Significant structures in the liquid state' Proc. Nat. Acad. Sci., Vol.44, 1958 p 683.

77.Bell J.C. 'Lubrication of rolling surfaces by a Ree-Eyring fluid' Trans.ASLE, 1962, Vol.5, p 160.

78.Smith F.W. 'Rolling contact lubrication. The application of elastohydrodynamic theory' Trans. ASME, 1965, Jour. Basic Eng., Vol.87(D), p 170.

79.Johnson K.L. & Cameron R. 'Shear behaviour of elastohydrodynamic oil films at high rolling contact pressures' Proc. I.Mech.E., 1967-68, Vol.182 Pt 1, p 307.

80.Plint M.A. 'Traction in elastohydrodynamic contacts' Proc. I.Mech.E., 1967-68, Vol.182 Pt 1, p 300.

81.Gentle C.R. 'Traction in elastohydrodynamic point contacts' Ph.D. Thesis, 1971, University of London.

Chapter 2 EXPERIMENTAL APPARATUS

2.1 General description

The basis of the apparatus was a one inch diameter rotating ball, supported in a P.T.F.E.-lined hemispherical cup, lubricated and loaded against a glass raceway with a groove machined in it.

Lubricant was supplied by gravity feed to the ball surface, the oil being carried up on the ball to the contact region. The cup was cut away in the meridian to reduce heating effects and the whole assembly was mounted on an air piston and loaded pneumatically onto the glass raceway, this being located above the ball (figure 2.1). The load applied at the contact was calculated from the air pressure in the loading cylinder, due allowance being made in the calculation for the weight of the ball and cup. A general view of the rig is shown in figure 2.2.

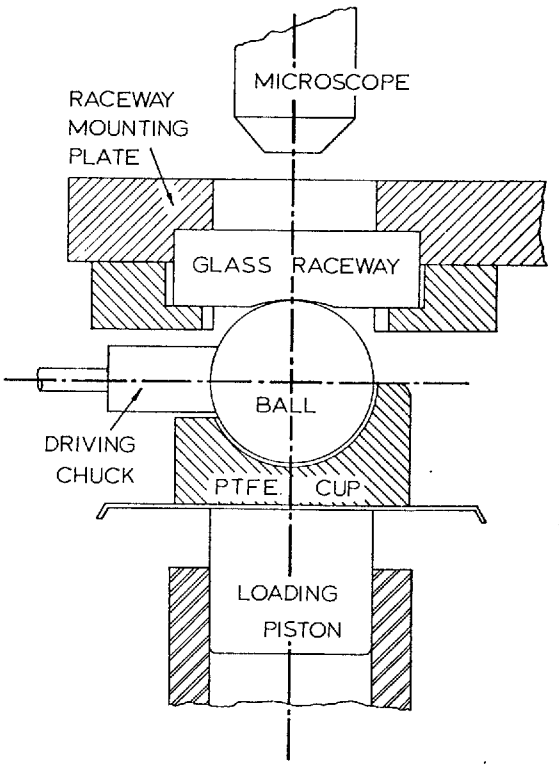


Fig. 2.1 Apparatus used in sliding experiments

2.2 Sliding friction measurement

The small raceway used in the sliding experiments was mounted on a steel plate(see figure 2.1), which was itself attached to a vertical axis, combined thrust and journal, air bearing as used by Foord (1). The traction transmitted across



Fig. 2.2 View of apparatus used for rolling film thickness measurements

the oil film produced a torque which tended to turn the bearing. Restraint was provided in the form of a small vertical spring balance, which acted via a length of nylon thread passing round the shaft of an air journal bearing. The balance suspension was adjustable, so that when an increase in traction caused an extension, the raceway could be returned to its original position. Although it was a spring mass system, no unstable vibrations were experienced, the damping of the oil film and of the air films in the bearings being sufficient to ensure stability.

This very simple system was capable of measuring tractive forces down to 0.025 lbf, the lower limit being imposed by stiction in the bearing system. The air bearings were theoretically frictionless at zero rotational speed, however, some dry friction was present in the balance itself. Also, dirt in the air supply (even though it was filtered) caused the friction in the air bearings to be finite (2).

2.3 Drive system

The ball was glued to a conical-faced steel chuck driven by a d.c. shunt motor via a reduction gearbox. The gearbox normally used provided a 20:1 reduction, which limited the ball surface speed to about llins/sec. It was however possible to provide a direct drive giving speeds up to 220 ins/sec. To give very fine control at low speeds, a 100:1 gearbox could be used.

In order to ensure good speed stability, the motor was controlled by a thyristor bridge speed controller (M.I. Sanders Type 5002) in conjunction with velocity feedback from a d.c. tacho-generator mounted on the rear of the motor shaft.

Feedback current was limited to a maximum of 3mA at full speed. Such a system was especially suitable for reducing speed variations resulting from changes in supply voltage, heating of the field windings and wide load variations. It was found that, for the system used, stability was better than 0.5% for motor speeds above 100 r.p.m.

2.4 Speed measurement

Ball speed was measured by means of a magnetic transducer positioned as close as possible to the teeth of a gear wheel mounted on the motor output shaft. The voltage pulses from the transducer were fed into a digital tachometer displaying to a maximum accuracy of 0.003%. At very low speeds of the motor, counting accuracy was reduced because the teeth passing the transducer produced only a small rate of change of magnetic reluctance. Consequently, the magnitude of the voltage pulse was too low to be counted consistently. This condition occurred when less than 6,000 teeth passed per minute (i.e. 100 r.p.m.). At speeds lower than this timing was performed using a stop-watch - a mean being obtained from a measurement over a large number of revolutions.

A stopwatch was also used to determine the rotational speed of the disc when measuring slip during rolling experiments. It was sufficiently accurate to time only one disc revolution as its speed was very low.

2.5 Adaptations of the apparatus

A primary requirement of the apparatus was for the ball drive to be angled relative to the groove. This posed no problems since it was possible to rotate the small sliding

raceway in its carrier to provide the desired amount of angling. When using the rolling raceway, the whole race and support bearing was moved relative to the ball until the required angle was obtained. The angle was set up initially using a protractor, the final adjustment being made whilst measuring the angle between the contact minor axis and the wake in sliding. Since the wake follows the resolved rolling velocity vector this gives a true reading.

Some preliminary tests were carried out to determine the effect of a vertical spin component on the film thickness. The apparatus was therefore modified in order to drive the ball in a spinning mode (see figure 2.3). In this arrangement the ball was attached to a short shaft projecting through the base of the cup. This shaft was driven from the motor by a light chain. The lubricant supply to the contact in pure spin was provided by covering both ball and race with oil just prior to a run. As the viscosity was high, the oil drained from the contact very slowly, thus permitting flooded conditions to be observed, followed by progressive starvation.

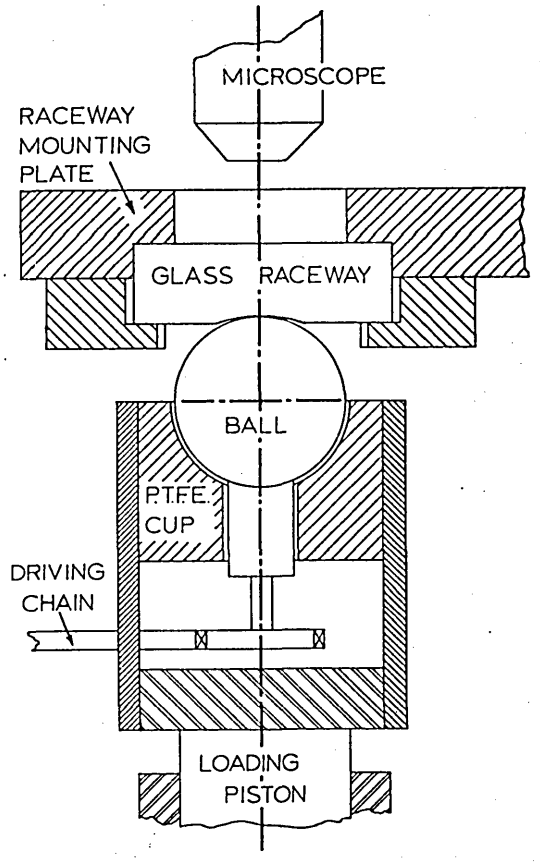


Fig. 2.3 Apparatus used in spinning experiments.

2.6 Temperature measurement

The oil temperature was measured by means of a trailing

Chromel/Alumel thermocouple resting on the ball at the entrance to the contact zone. Temperature readout was on an electronic thermometer (Comark typre BLS 1604) which measured directly the emf generated, eliminating the need for balancing the bridge. Full scale deflection was 10 centigrade degrees within the range $-60^{\circ}C$ to $+170^{\circ}C$. The scale could be read to $0.1^{\circ}C$, but the claimed accuracy was only $\pm 0.5^{\circ}C$. Calibration of the internal cold junction was made prior to each test run, using melting ice as a reference temperature.

The temperature recorded was taken as being that of the oil at inlet, rather than that of the ball's surface. Other workers (3,4) have found appreciable differences between these two quantities. In both quoted cases, surface temperatures were measured using embedded thermocouples and the results compared with the readings of trailing thermocouples. The conclusions were that differences resulted from the comparatively poor heat transfer characteristics of the thin film carried by the moving surfaces. In the present work, however, no great amount of heating was experienced. It was anticipated therefore that, if necessary, the recorded temperature could also be taken as a sufficiently accurate measure of surface as well as oil temperature.

The thermocouple junction was kept about 1.0 cm from the contact centre. Hence disruption of the oil flow was minimised and false readings due to inlet zone heating were avoided. Gohar (5) has examined this latter point in some detail. He found that temperature increased as the contact centre was approached and concluded that, if the junction were 0.2 cm from the centre, the temperature recorded would be that at inlet. However, as such a close approach could well cause

disruption of oil at the inlet, it was considered prudent to keep at least 1 cm from the contact centre, to give any wake behind the junction time to reform.

2.7 Measurement of the groove radius

To enable theoretical predictions to be made for conditions which were comparable to those used experimentally, it was necessary to measure the groove radius accurately. The problem was complicated because of the danger of damaging the semi-reflecting coating in the groove.

An initial attempt was made by sectioning a cast of the groove and measuring a segment on a shadow-graph. However, the technique finally employed was to derive the radius from measurements made on a photograph of a static contact ellipse.

The ratio of the axes of the Hertz contact ellipse depends solely on the contact geometry; by measuring this ratio, therefore, the groove radius may be derived, provided that the ball radius is known. Unfortunately, for reasons to be explained in the next chapter, it was not possible to be absolutely certain where the contact proper started. However, by measuring the gap profile outside the contact and extrapolating to zero thickness a check was obtained on the measured axis ratio. As the two methods gave almost the same answer, it was assumed that the errors were very small. The values obtained were a radius of 0.555 in for the sliding raceway and 0.572 in for the rolling raceway.

Recently, however, some results of McGrew (6) have cast doubts on the dimensions obtained. He produced a curve which described the gap shape for the geometry of the sliding race-way. When a comparison is made between this and an experimentally

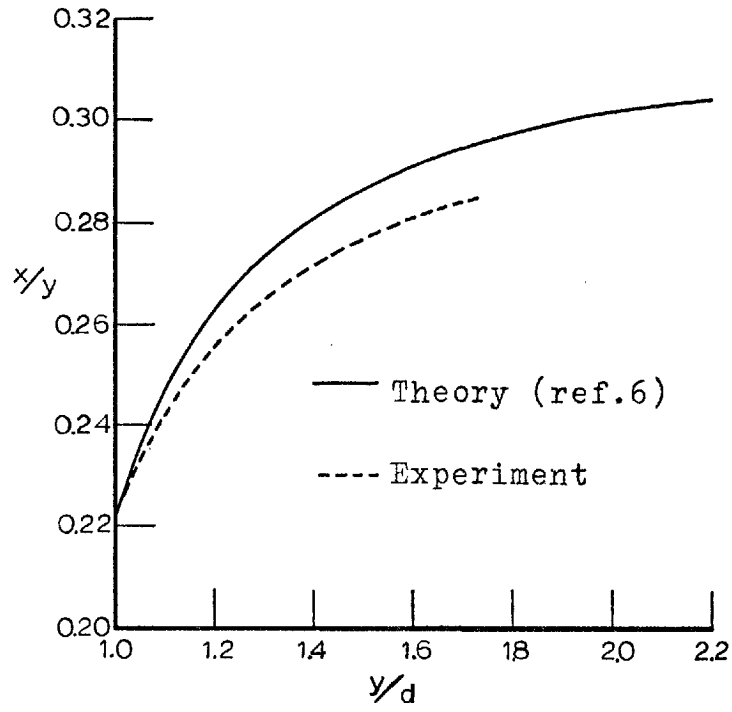


Fig. 2.4 Comparison of experimental and theoretical axis ratios for bands of constant thickness.

measured curve differences are observed (figure 2.4). These must be due either to an inaccuracy of the Hertz theory as used by McGrew, an error in measurement, or an error in the quoted groove radius. The last reason is the most probable, even though the radius was inferred from the Hertz contact axis-ratio, at which point the two curves agree. However, at this point there is an increase in gradient which could give rise to error when determining the intercept of the experimentally determined curve.

2.8 Improvements to the apparatus

The most serious restrictions on the apparatus used in the present work were that the load was limited and gave maximum Hertz pressures only up to 40,000 lbf/in^2 and that the ball was restrained by being supported in the cup and attached to the shaft. To overcome these deficiences, a new rig was

designed and manufactured, more closely resembling a real thrust bearing. It comprised an upper (glass) and lower (steel) raceway with three balls supporting the former and loading applied pneumatically to the upper raceway, rather than through the balls as at present.

The object of this new apparatus is to study the behaviour of a ball in a thrust bearing at high loads and speeds and to determine the effect of various cage designs on both the ball dynamics and the oil flow at the contact. The raceways may be driven directly or in counter-rotation via one of the balls. The behaviour of a free ball, restrained solely by the cage and raceways may then be investigated. Provision is also made for measuring the torque on the remaining ball in the system.

Unfortunately, because the upper plate air bearings did not initially meet the design requirements, it was not possible to use this apparatus in the present work. The details of the design are therefore included, more appropriately, under 'future work' in chapter 9.

References for Chapter 2

1. Foord C.A., Hammann W.C. & Cameron A. 'Evaluation of lubricants using optical elastohydrodynamics' Trans. ASLE, Vol.11, 1968, pp 31 -43.
2. Foord C.A. 'Pitting and film thickness in rolling contact' Ph.D. Thesis, 1968, University of London.
3. Leach E.F. & Kelley B.W. 'Temperature - the key to lubricant capacity' Trans. ASLE, Vol.8, 1965, pp 271-285.
4. O'Donoghue J.P. & Cameron A. 'Friction and temperature in rolling sliding contacts' Trans. ASLE, Vol.9, 1966, pp 186-194.
5. Gohar R. 'Oil films under elastohydrodynamic conditions' Ph.D. Thesis, 1965, University of London.
6. McGrew J.M. Discussion on 'Oil film thickness and shape for a ball sliding in a grooved raceway' by Thorp N. & Gohar R. ASME, Paper no. 71-Lub-18. Discussion to be published, 1972.

Chapter 3 THE OPTICAL SYSTEM AND ITS CALIBRATION

3.1 Introduction

The use of interferometry in lubrication experiments for the determination of surface roughnesses and curvatures has been quite common for some time, but only comparatively recently has the application been extended to dynamic contacts. They have been studied in this way for several years now and interferometry has become accepted as a powerful tool for investigating elastohydrodynamic oil films.

The technique, however, stretches back a long time. Newton (1), for instance, during his original experiments in interferometry, noticed cavitation patterns when he moved his lenses. So too, but much later (1902), did Skinner (2) who tried to relate what he saw to the lubrication of ball-bearings. Hardy (3) took the presence of coloured fringes as a qualitative measure of lubricant thickness, but it was not until 1963 that Archard and Kirk (4), following some initial work by the latter (5), put the technique to serious use in their study of the lubrication of Perspex.

Their fringe quality, however, was poor - a direct result of the closeness of the refractive indices of oil and Perspex. Cameron and Gohar (6) attempted to overcome this problem by using high refractive index glass. Fringe quality was improved and they obtained some now classic results. Since then the technique has been further refined by Foord (7) who used a semi-reflecting coating on the glass. This made the system independent of the refractive index, which was a double advantage since it enabled the transparent plate to be chosen for its mechanical properties, the coating being varied as necessary to give a consistent fringe

quality.

Several specialised systems are now available for particular applications (8). These include duochromatic fringes to give detailed measurements of thick films, multiple beam interferometry to give higher resolution and the use of spacer layers to give the facility for measuring ultra-thin films. In the present work a straight forward two beam interference system is used, employing monochromatic light (sodium or mercury) for most measurements and white light for detailing the film shape.

3.2 Interferometric Fundamentals

The principles of interferometry are explained in numerous text books one of the best being by Tolansky (9). Furthermore, the system used has been described in great detail by other workers in the field, so only the essentials will be considered here.

A collimated beam of light from the source (fig.3.1) is passed through the top surface of the glass disk, part of it being reflected by the semi-reflecting coating on the lower surface and part being transmitted. The transmitted rays are totally reflected from the polished surface of the ball and some pass through the coating again to recombine with the reflected rays. The other rays repeat the process, but subsequent reflections are too weak to be of any significance.

The recombined rays will interfere if they are in antiphase, or reinforce if they are in phase, producing the characteristic interference fringe pattern. The phase difference between the two rays is a function only

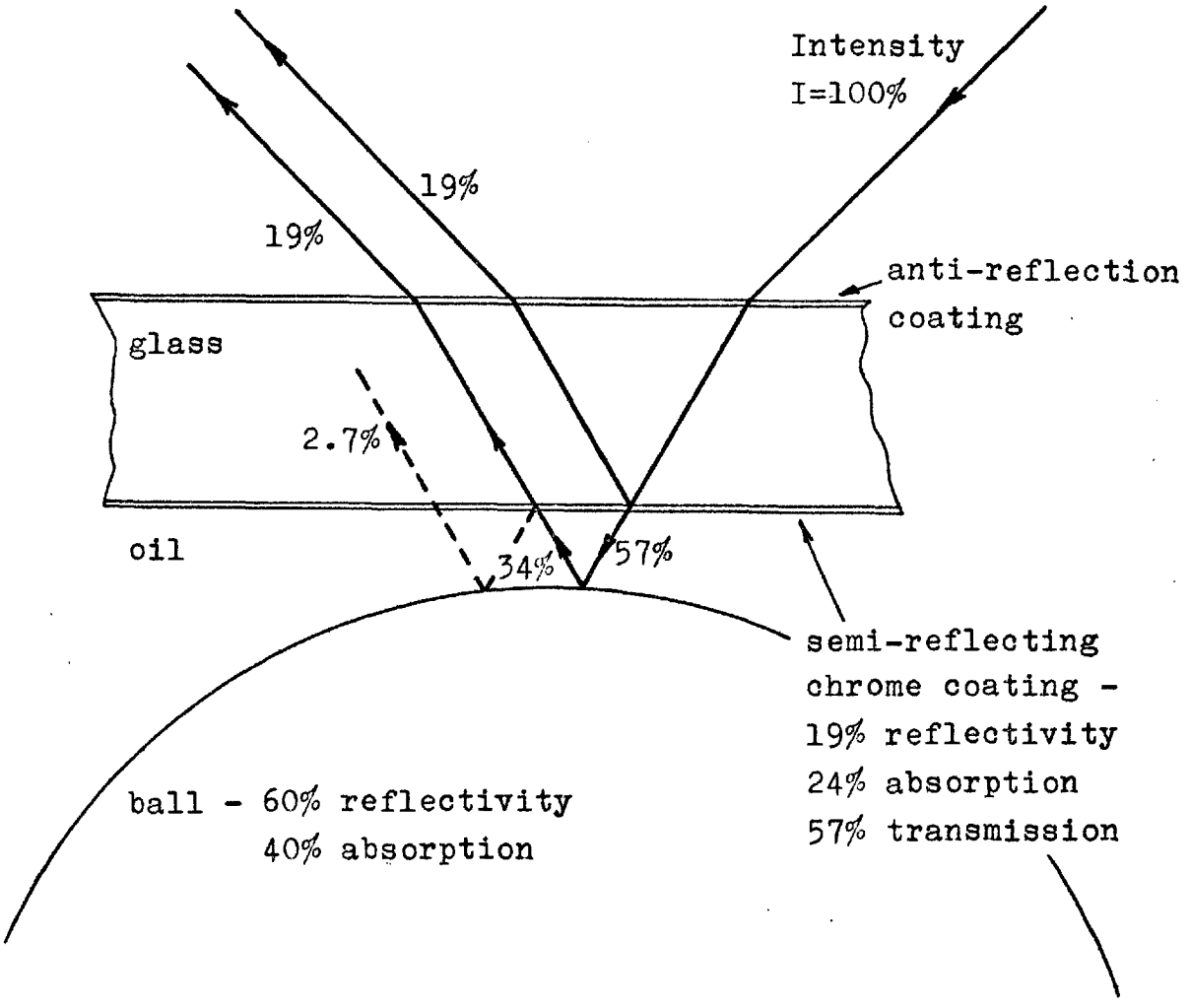


Fig. 3.1 Interference System

of their path difference and of the phase changes on reflection at the chrome layer and the ball, which are both constant. Thus, since the separation between the ball and glass is equal to half the path difference, the interference pattern will give the thickness of the oil film at any point in the field.

Good fringe visibility is ensured by making sure that the coating has a reflectivity such that the recombined rays have the same intensity. As the ball has a reflectivity in oil of approximately 60%, this entails a coating with approximately 20% reflectivity.(8)

3.3 Choice of Illumination System

For normally incident light with a wavelength of λ, in the medium, the beams reflected from the chrome layer and from the ball will reinforce each other if the path difference is $N\lambda$ (where N is an integer) and will cancel each other if the path difference is $(N+\frac{1}{2})\lambda$. Thus the difference between a bright fringe and an adjacent dark fringe represents a thickness of $\lambda/4$.

White light has no unique wavelength and although each individual wavelength interferes as described, the results are superimposed with a resulting pattern of bright fringes of which only a few distinct colours can be distinguished. These occur in a fixed sequence (1) and an increase of one in the 'order' (N) of the fringes involves them all instead of just one fringe as would be the case for a single wavelength. Thus measurements with white light give a more detailed picture than do those with monochromatic light. However, if the film becomes too thick, the coloured

fringes recur so close to each other that they reform white light and so can no longer be discerned.

The use of two or more discrete colours overcomes the disadvantages of white light whilst still giving better accuracy than monochromatic light (this system is described in ref. 8). However, in the present work it was decided to use just one colour in the majority of the measurements for the sake of simplicity and to reduce the cost of photography. White light was also used, but only when detailed knowledge of the deformed shape of the contact was required.

Two monochromatic light sources were employed: a sodium discharge lamp for ordinary observation and a xenon flash with mercury green line filter for photography. The former was preferable because, with its narrow spectral bandwidth, it gave excellent fringe visibility (10 p322), and was kinder to the eyes. The sodium source, however, was not sufficiently powerful to use for photography since short exposure times were required to 'freeze' the oil flow patterns in the outlet region. The xenon flash unit had an exposure time of about 1 millisecond with a flash energy of up to 1000 joules. This, in conjunction with the high speed film used (Ilford HP4), was ample. It also had the facility of being capable of providing continuous illumination (at reduced power) using an internal triggering system, which greatly aided setting-up. The unit is described in meticulous detail in ref. 11. This flash unit was also used without the filter, as the white light source, because it had a continuous spectrum similar to daylight.

3.4 Optical Components

3.4.1 Viewing System

The microscope used was a commercially available unit manufactured by Beck and fitted with a Beck 'Vertiphase' side illuminator shown diagramatically in fig. 3.2. This illuminator had two stops available, the field stop controlling the area illuminated and the aperture stop controlling the intensity and to some extent, the degree of collimation. This instrument did not produce perfectly collimated light but had a maximum deviation from normal of about 8°. Wedeven (11), who also used this type, has shown that this incidence still produces a fringe visibility better than 98% for mercury light, so the degree of collimation obtained was quite sufficient.

Photographs of the interference fringes were necessary when film shapes were being measured. To obtain these a 35 mm camera was mounted on the microscope tube. The latter was fitted with a X10 objective but the eyepiece was removed to improve picture quality and increase the field of view. For ordinary viewing of the fringes, as when measuring film thicknesses, it was found convenient to look at the contact through the microscope using closed circuit television (again with no eyepiece or camera lens). Although by no means necessary, this made prolonged measurements easier on the eyes and since the equipment was already available, placed no extra strain on the budget. An added advantage was the facility for adjusting the contrast of the fringes at will.

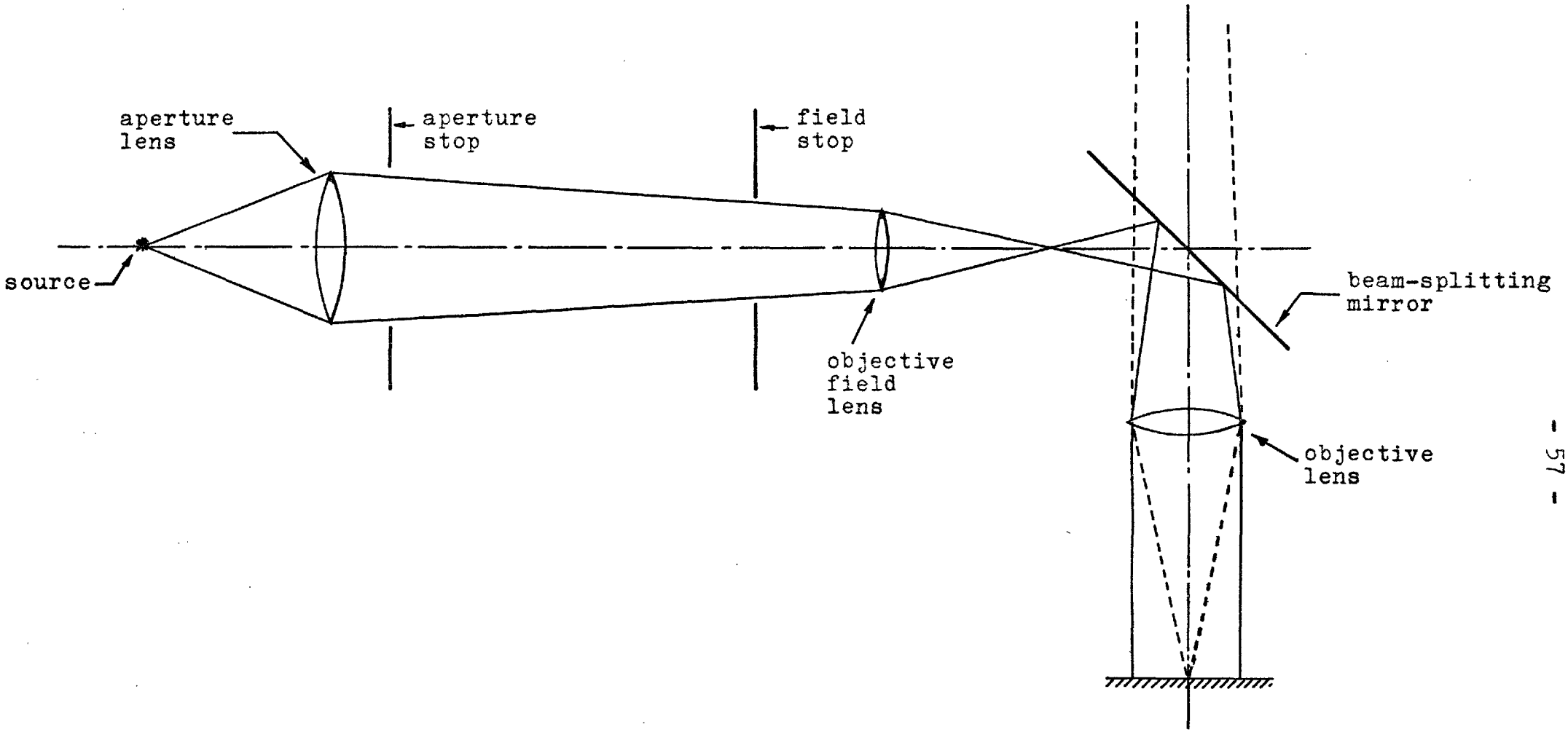


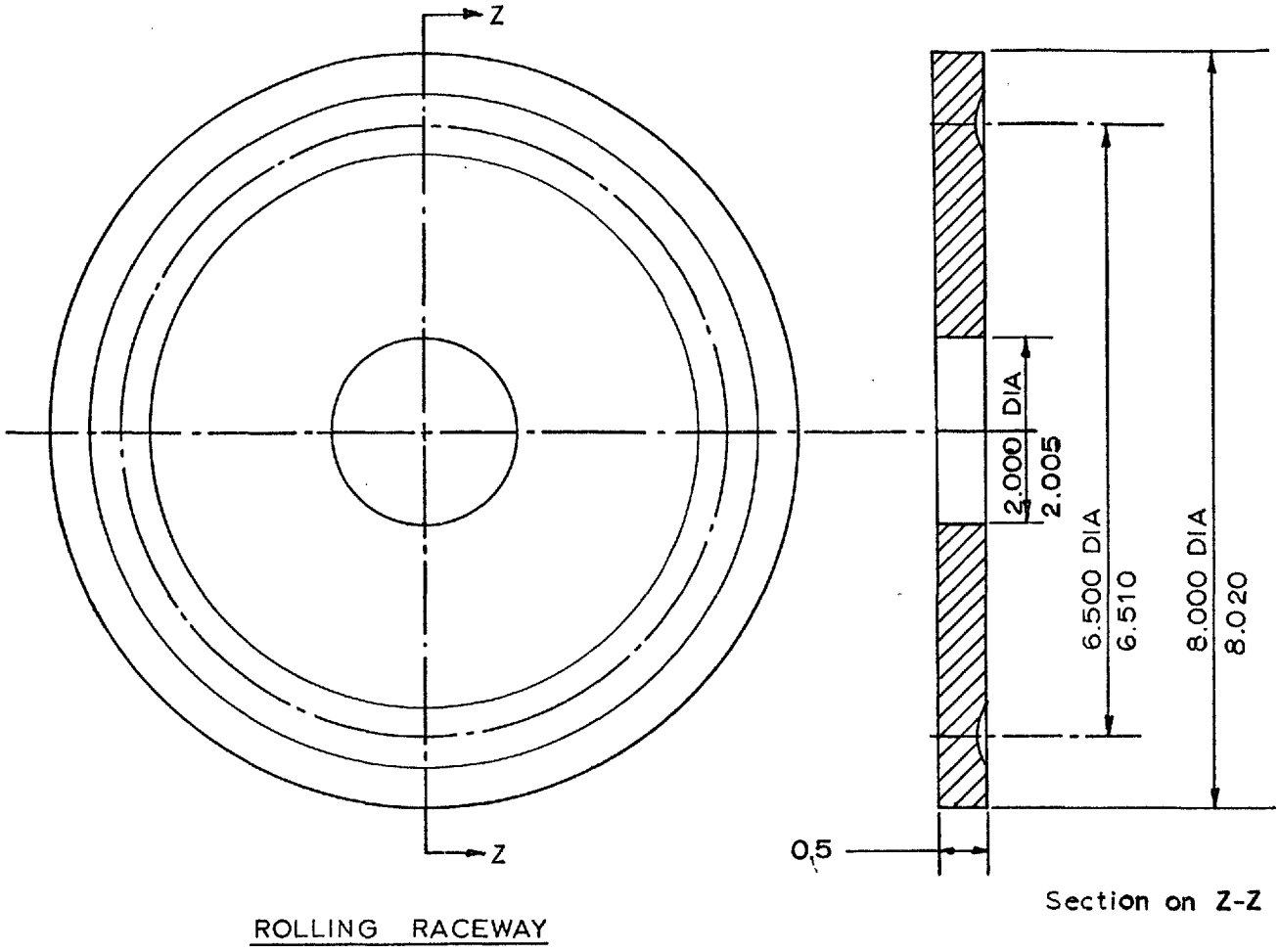
Fig. 3.2 Beck 'Vertiphase' Side-Illuminator

3.4.2 Ball

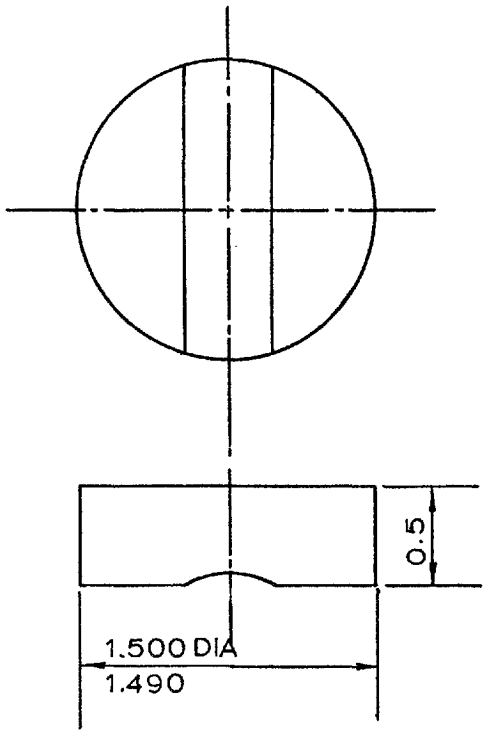
Throughout nearly all the tests described, only one ball was used. This was of highly polished tungsten carbide supplied by Insley Industrial Ltd. Previous workers have all used steel balls but tungsten carbide does have some advantages. Perhaps the most important is its durability - a steel ball was used in some early tests but was found to scratch fairly rapidly, presumably on debris which had become embedded in the P.T.F.E. cup which provided support. Replacement of the ball involved manufacture and attachment of another chuck which was tedious. The tungsten carbide ball, on the other hand, has yet to scratch. Another advantage is that with its high modulus of elasticity (approximately three times that of steel) it is easier to reach high Hertz pressures and the ball/glass race reduced modulus (E') more closely approaches that found in a real bearing. The advantages to be gained in this way are limited, however, since the softer material has a stronger influence on the value of E'.

3.4.3 Raceways

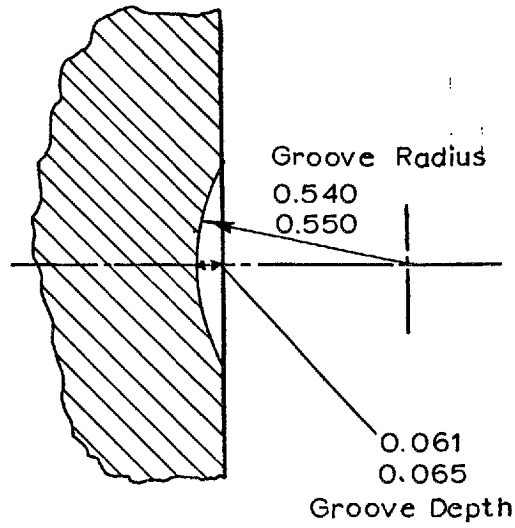
The glass raceways were made out of soda-lime plate glass and had a groove machined in them with a radius slightly larger than that of the ball. The sliding tests used a $1\frac{1}{2}$" dia. raceway with a straight groove and the rolling tests an 8" dia. disc with a circular groove of $6\frac{1}{2}$" dia.(see fig. 3.3). The groove geometry specified was designed to match the measurements of a commercial steel race. The surfaces were ground and polished, the groove geometry being held circular as evidenced by the elliptical shape of the static fringes (see fig. 3.4). The finish of



ROLLING RACEWAY



SLIDING RACEWAY



GROOVE DETAILS

Fig. 3.3 Raceway specifications (All Dimensions in Inches)

the smaller race was excellent, but that of the larger was marred slightly by pitting, which showed up as black dots on photographs. These pits were present only in the groove and were a result of the difficulties of machining such a shape in glass.

As described earlier, the lower surfaces of the plates were coated with a 20% reflecting chrome layer and the upper surfaces with an anti-reflection coating of magnesium fluoride.

The use of a grooved raceway presented a problem not experienced by previous workers who have used flat plates. This was that the groove necessarily restricted the experiments to one track only so that if bad scratching of the glass were to occur the raceway would become useless. With a flat plate, of course, a new track may be selected simply by moving the ball radially. The danger of scratching was reduced as much as possible by taking great care during start-up and loading, and also by restricting the investigations to viscous oils known to form thick films.

Some sliding experiments were also performed using small flat plates of glass, perspex and sapphire. These were all coated-with the exception of the perspex, which was thus restricted to measurements of friction, the fringes not being visible (except in the outlet region).

3.5 Contact Visibility

A difficulty encountered in the study of elliptical contacts is that of viewing the whole contact in detail. The reason is that the contact area is much larger, for a given load, than a corresponding point contact. This is

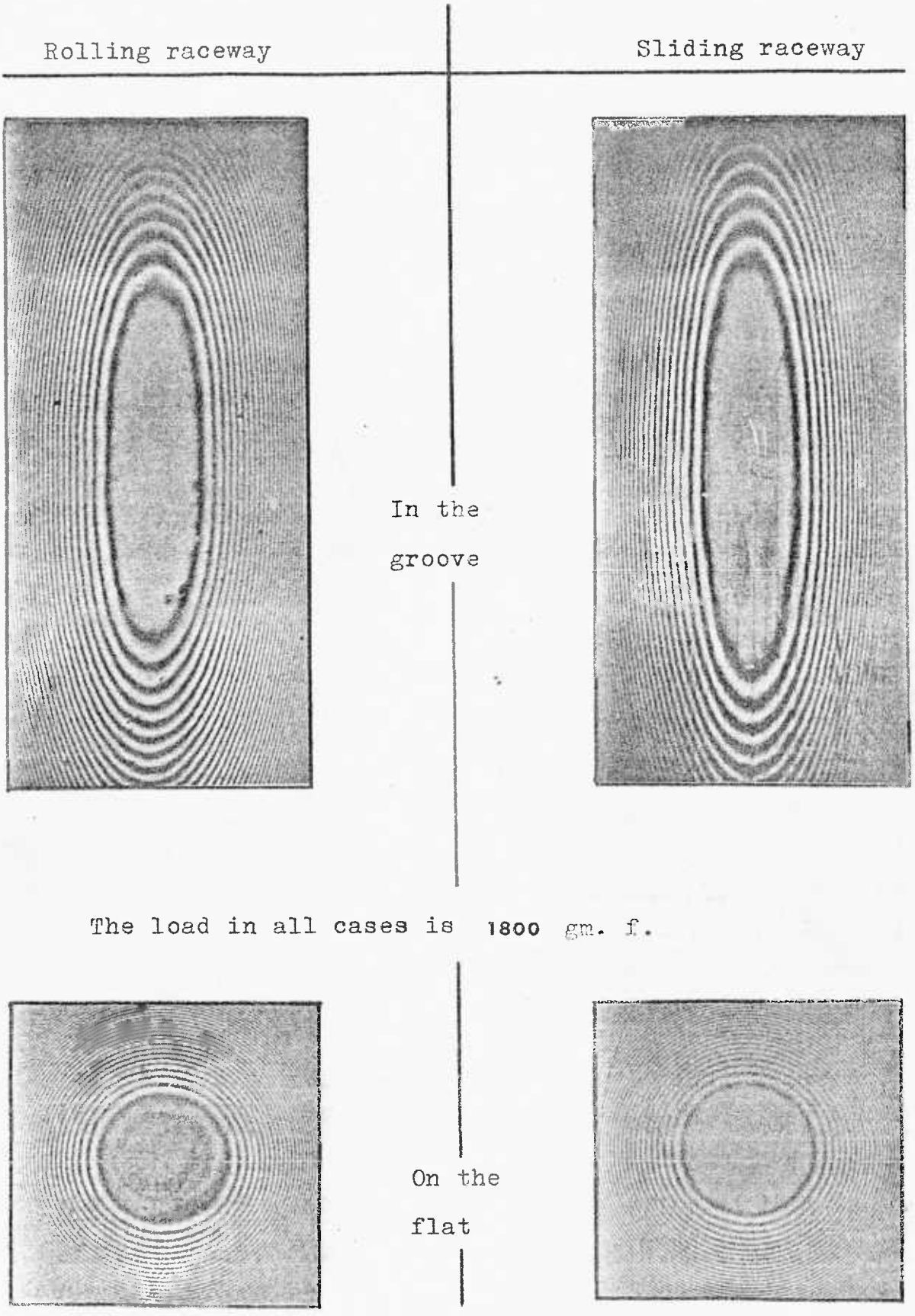


Fig. 3.4 Static fringe patterns at constant magnification

demonstrated by fig 3.4, where all the photographs are for the same load and have the same magnification. For the geometry chosen, the ellipse ratio was not large, so all the contact could be seen. However, a problem not anticipated was that the parts of the contact far out from the groove centre were in shadow. This effect has also been experienced by Westlake (12) in a similar situation.

It may be explained by noting that the silvered surface of the race acts as a plane diffusing source. This is justifiable since it is this plane on which the microscope has to be focused in order to see the fringes (ie. it is the only plane on which interference occurs). The intensity will drop if this plane is viewed obliquely as will be the case on the groove sides. The intensity drop is given by Lambert's (cosine) Law (10 pp181-2).

$$I(\alpha,\beta)=I_o \cos\theta \quad -3.1$$

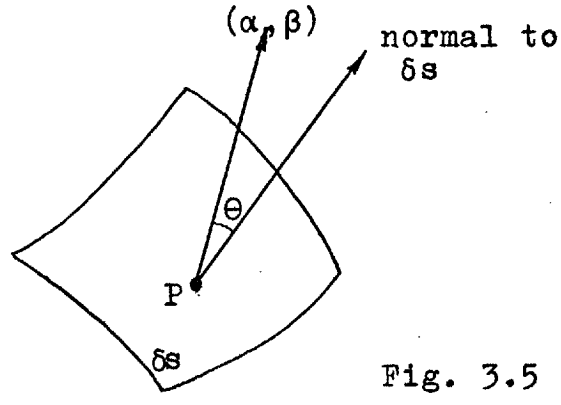


Fig. 3.5

where $I(\alpha,\beta)$ is the intensity of a typical point source (P) in the direction given by the polar angles (α,β), and I_o is the intensity of P in the direction normal to the element δs.

That visibility in the side regions is dependent solely on the incidence of viewing may be demonstrated by moving the ball away from the centre of the groove (fig. 3.6). Usually, with the ball at the top of the groove, regions A & B are in shadow. If the ball is moved to the left, the fringes in region A become visible, those in the centre moving into the shadow. The only difference between microscopes 1 & 2

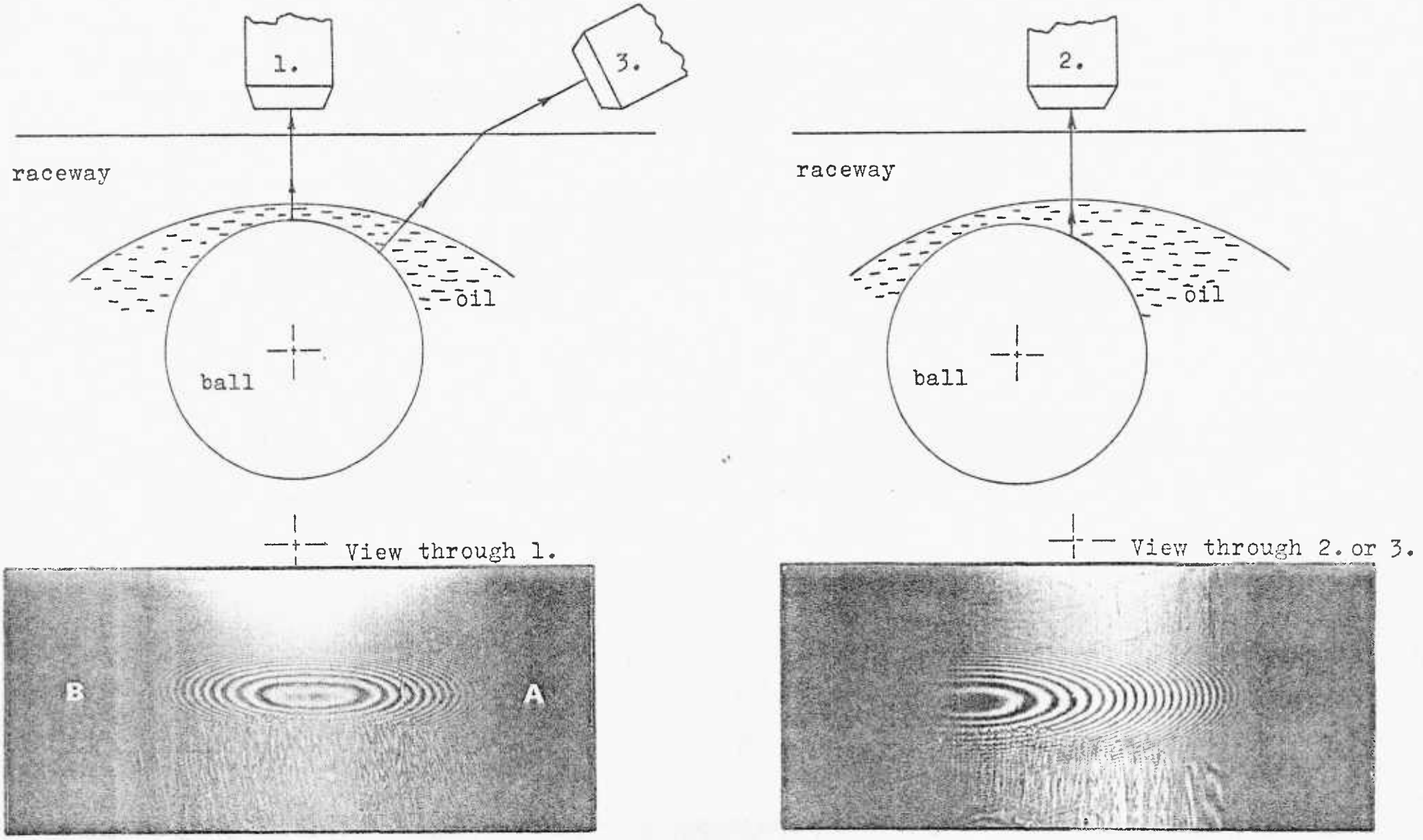


Fig. 3.6 Effect of Viewing Incidence

which makes region A visible is the viewing angle. Thus if 1 were moved to 3, (allowing for refraction at the top glass surface) fringes in region A would become visible with the ball at the top of the groove.

The visibility in the side regions could be improved without sacrificing that of the centre region, by using a microscope objective with a larger numerical aperture. A side-effect, however would be distortion of the image so the method was not used, visibility being just sufficient without. In any case, with very high loads or high conformities, the ellipse would become so long that it would approach a line contact, when only a discrete portion could be viewed at any one time.

3.6 Calibration of Fringes

Film thickness cannot be calculated directly from the fringe pattern without the latter first being calibrated in some way. This is because the film thickness is given by:

$$h=(\tfrac{1}{2}N\lambda + \beta\lambda/2) \quad \text{for a bright fringe}$$
$$h=(\tfrac{1}{2}N\lambda + \beta\lambda/2) + \lambda/4 \quad \text{for a dark fringe} \qquad -3.2$$

These equations involve two unknowns: λ and β. λ is the wavelength of light in oil, which is not known even for monochromatic light unless the refractive index of the oil is also known. β is the phase change associated with the reflections at the ball surface and at the chrome layer. At the former, the reflection is total and the phase change is very nearly π, at the latter, however, the change is not an exact multiple of π because the chrome layer is a very thin film. β has been found to vary from coating to coating even though they may all have been made to the same specification (see section 3.8). A direct

calibration removes the need to know these two quantities explicitly and is done by using the fringe pattern to measure a known geometry. Gohar (6) employed the gap between the ball and plate as his standard and calculated the thickness from the formula:-

$$h = r^2/2R \qquad -3.3$$

r being the fringe radius and R the ball radius. Foord (7) also used the above method but refined it by replacing the ball with a large radius spherical lens, thus increasing the fringe radii and hence the accuracy of the measurement. Both these workers loaded the contact until it 'just touched'. Wedeven (11) examined in detail this calibration method and pointed out that errors would be introduced by distortions if the contact had a finite load, or by separation due to surface roughness and dust particles if the load were vanishingly small. He also found that at these very light loads measurements were susceptible to external vibrations and so had to be made late at night.

Some alternative methods were suggested by him :-

a) Measure the radii for a series of loads approaching zero and extrapolate so that the fringe radius at zero load is constant, thus eliminating the errors of contact.

b) Measure the fringe radii for a deformed contact under a known load and use the gap formula of Hertz to obtain the thickness.

He concluded that the latter method was easier experimentally but relied upon a knowledge of the elastic properties, unlike the former. In the present work, the second method was used even though the elastic properties

were not always known. The technique used to remove this restriction on the method is described in the next section.

The Hertzian equation for the gap outside the main contact region in a circular contact is (ref. 13 p. 195):-

$$h = \frac{a.p_m}{E'}.\left\{-\left(2-\frac{r^2}{a^2}\right).\cos^{-1}\left(\frac{a}{r}\right) + \left(\frac{r^2}{a^2}-1\right)^{\frac{1}{2}}\right\} \quad - 3.4$$

where h is the film thickness, a the contact radius,
p_m the peak pressure, r the fringe radius,
E' the reduced modulus of elasticity.

The procedure followed during calibration was to press the ball against a flat portion of the plate with a known load and then to measure the resulting fringes using a travelling microscope with a filar eyepiece. Measurements were deliberately restricted to dark fringes since the position of their centres could be more accurately estimated than could those of bright fringes. The microscope had an extremely fine pitch thread and was accurate to 1/500 mm ($\simeq$80 μin.). The measurements were made with oil type BP 1065 between the ball and the plate. This oil was used in most of the experiments and at ambient pressure and temperature (22.5°C) it had a refractive index of 1.506, this value being determined using an Abbé Refractometer.

Most previous workers have performed their calibration in air, but it is equally valid with oil present and is particularly convenient if most of the work is done with this one oil. It also has the advantage that the fringes are more distinct so there is less chance of an error in the measurements. To use the calibrations with another lubricant it is necessary to allow for any change of

refractive index. This may be done using the equation :-

$$h_{actual} = \left(\frac{h_{optical}}{n}\right)_{\substack{calibration \\ fluid}} = \left(\frac{h_{optical}}{n}\right)_{\substack{test \\ fluid}} \qquad -3.5$$

To calibrate black and white fringes, the measured radii were substituted into eqn. 3.4 as described in the next section. The solution gave a value for the height of the first black fringe, this being a convenient manner in which to express the effect of the phase changes on reflection. When calibrating chromatic fringes, if E' was not known, it had first to be determined from measurements of black and white fringes. It was then possible to use eqn. 3.4 directly to calculate the height of any coloured fringe of known order. The film thicknesses corresponding to various colours are shown in the table of fig. 3.7. These are only a guide, since different people will tend to have differing colour vision. Fig. 3.8 shows the results of the calibration for the black and white fringes with the various plates used in the experiments.

3.7 Calculation of Reduced Modulus and Phase Change

If the reduced modulus of the material combination (E') is known, then the height of any fringe measured in the calibration experiments can be determined using eqn. 3.4. However, in several cases , E' was not certain, for instance, E for sapphire varies with the orientation of the crystal lattice and that of perspex with,amongst other things, the strain rate. Thus it was considered prudent not to assume the quoted values but to determine them experimentally.

The technique which immediately springs to mind is to use the Hertzian deformation as a measure of the modulus. If the

Fringe Order	Fringe Colour	Fringe Height (inches)
1st	yellow	0.94×10^{-5}
	red	1.11×10^{-5}
	blue	1.37×10^{-5}
	green	1.69×10^{-5}
2nd	yellow	1.94×10^{-5}
	red	2.20×10^{-5}
	blue	2.48×10^{-5}
	green	2.75×10^{-5}
3rd	yellow	2.96×10^{-5}
	red	3.35×10^{-5}
	blue	3.62×10^{-5}
	green	3.84×10^{-5}
4th	yellow	4.13×10^{-5}
	red	4.46×10^{-5}
	blue	4.75×10^{-5}
	green	5.02×10^{-5}

Fig. 3.7 Heights of chromatic fringes in air.

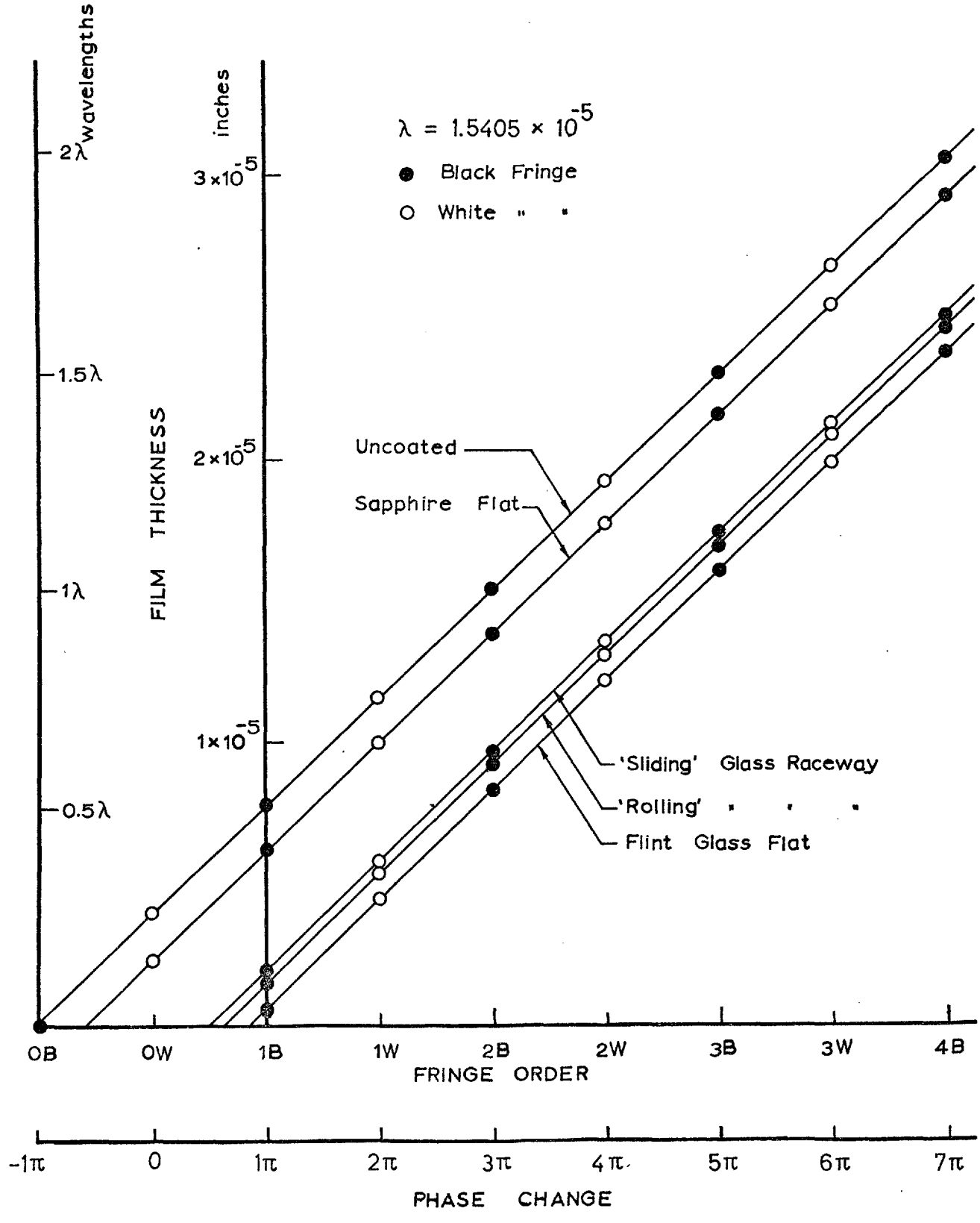


Fig. 3.8 Calibrations in Oil BP 1065 Using Sodium Light

radius of the contact is measured, then the modulus may be calculated from :-

$$a = 0.721 \sqrt[3]{\frac{2.W.D}{E'}} \qquad - 3.6$$

where W is the total load and D the ball diameter.

This method was used by Gohar (14) who checked the value he obtained by using it to calculate the gap shape then comparing with that measured experimentally. However, although he found satisfactory agreement, the method is not very accurate because it is not possible to measure the contact size with any degree of certainty. The first dark fringe is not at zero height and has a finite width, so the apparent contact areas of fig. 3.4 are in fact larger than the real ones.

An alternative method is to calculate the modulus directly from eqn. 3.4. Since this was also used for calibration there were two unknowns, h and E'. Taking data from two dark fringes with an order difference of N, two equations were obtained with three unknowns: E' and the fringe heights h_a & h_b. The necessary third equation involved the fringe spacing:-

$$h_a - h_b = (N\lambda/2n) \qquad -3.7$$

where λ is the (known) wavelength of light in air and n the refractive index of the oil. Eqn. 3.7 was used to reduce the unknowns to two: E' and the height of the first dark fringe (DEL); h_a and h_b were then expressed in terms of DEL.

The remaining equations were solved simultaneously using an iterative procedure. As an initial guess at the solution DEL was taken as $\lambda/2n$ and E' at the quoted value. In fact, the equations were found to converge even when the initial guesses were some way from the final solutions. These solutions

were deemed to have been achieved when the changes in both E' and DEL between sucessive iterations was less than 10^{-5}.

The calculations were repeated using most combinations of the measured fringes, thus reducing errors resulting from any inaccurate reading of a single fringe. This gave some thirty answers from each calibration experiment, the mean and variance of the group were calculated and these in turn, with statistical tables (15), were used to calculate a tolerance on the results. The flow chart and a listing of the computer program written to perform these calculations are given in appendix 1.

This procedure gives only a value for the reduced modulus which is all that was required in the work presented. The method could easily be extended to determine E for any transparent material by using a ball of known properties, the most convenient being steel. The real modulus could then be calculated from :-

$$\frac{1}{E'} = \tfrac{1}{2}\left\{\left(\frac{1-\sigma^2}{E}\right) + \left(\frac{1-\sigma^2}{E}\right)_{steel}\right\} \qquad -3.8$$

This presumes a knowledge of Poisson's ratio for the material under test, but a small error in this would not greatly affect the final value of E.

The results of the calculations for all the materials combinations tested are given in the table of fig. 3.9. Also shown are the individual modulii for the materials, assuming the manufacturer's data for the tungsten carbide ball, that is, $E = 98 \times 10^6$ p.s.i. and $\sigma = 0.26$.

Raceway material	Reduced Modulus (Experimental)		Raceway Modulus		Raceway Poissons Ratio
			measured‡	quoted	
	$lbf/in^2 \times 10^{-6}$	tol. 95% limits	$lbf/in^2 \times 10^{-6}$		
Heavy flint glass	19.09	± 1.26%	9.78	10.0** 8.0*	0.27*
Sapphire	65.40	± 7.74%	34.4	50-55	0.30
Plate glass sliding race	18.39	± 1.25%	10.55	11.0**	0.26**
Plate glass rolling race	18.61	± 0.86%	10.50	11.0**	0.26**
Perspex	0.89	± 3.31%	0.40	0.45" 0.89*'	0.328*

* Kaye & Laby 'Tables of physical & chemical constants' 13th Edition London 1966 Longmans.

** Manufacturer's data " Static value

' dynamic value @ 2.0 M.Hz.

‡ The values in this column were calculated using manufacturer data for the tungsten carbide ball ($E = 98 \times 10^6$ psi $\sigma = 0.26$) However, (*) quotes $E = 77.3 \times 10^6$ psi & $\sigma = 0.22$ but states that the value varies depending on the composition. The use of this lower value in calculations would increase the calculated values of E, the effect only being appreciable in the case of the sapphire.

Fig. 3.9 Raceway materials' elastic constants

3.8 Phase Changes at the Semi-Reflecting Layers

It was stated in section 3.6 that the phase change on reflection varied from coating to coating. This is demonstrated by fig. 3.8 which is a plot of film thickness against fringe order for the various coatings. Had the phase change been a constant the lines would all have been coincident.

The total relative phase change (ϕ) is given by the sum of the absolute phase changes at the reflecting surfaces. That is:-

$$\phi = \phi_{ball} + \phi_{coating} \qquad -3.9$$

If $\phi = 0$ then the contact area would be bright and if $\phi = \pi$, as would be the case if $\phi_{cr} = 0$, then it would be dark. In most cases the contact area was grey, with the first predominent fringe being black. The phase change may be calculated from the height of the first black fringe ($x\lambda$), this value being determined by the program as described. It follows that at a height $x\lambda$, $\phi = \pi$. Since a phase change of ϕ represents a thickness of $\lambda/4$, then a thickness of $x\lambda$ represents a phase change of $4\pi x$. Thus the total relative phase change at zero thickness is that at height $x\lambda$ minus the change represented by that height, that is :-

$$\phi = \pi - 4\pi x = \phi_{ball} + \phi_{coating}$$

If we assume that ϕ_{ball} is exactly π, to which it closely approximates, then

$$\phi_{coating} = - 4\pi x \qquad - 3.10$$

The phase changes for all the chrome coatings used were calculated in this manner and the results tabulated in fig. 3.10. As can be seen, there was a considerable variation

RACEWAY	PHASE CHANGE AT THE SEMI-REFLECTING COATING	HEIGHT OF THE FIRST DARK FRINGE	TOLERANCE - 95% INTERVAL
SODA-LIME PLATE GLASS (SLIDING)	-0.50π	0.125λ	$\pm$ 15.6%
SODA-LIME PLATE GLASS (ROLLING)	-0.39π	0.097λ	$\pm$ 13.8%
SAPPHIRE FLAT	-1.59π	0.397λ	$\pm$ 5.3%
FLINT GLASS FLAT	-0.17π	0.042λ	$\pm$ 16.8%

Fig. 3.10 Phase changes at the different coatings

from one to another even though they were all ostensibly made to the same specification. The wide confidence intervals reflect the difficulty in obtaining fringe measurements accurately enough to overcome the ill-conditioning of the equations. However, 15% on the first fringe represents less than 3% on the second and is negligible thereafter.

3.9 Refractive Index in the Contact

To calculate the thicknesses from the fringes observed during dynamic conditions, a knowledge of the refractive index (n) was essential. For the calibration tests the value obtained with the Abbé Refractometer at atmospheric pressure was used (n_o). However, at the pressures existing within a moving contact the refractive index has a different value (n_p) which was determined from the Lorentz-Lorenz equation

$$n_p = \left(\frac{1 + 2A}{1 - A}\right)^{\frac{1}{2}} \quad \text{where} \quad A = \frac{\rho_p}{\rho_o} \cdot \left(\frac{n_o^2 - 1}{n_o^2 + 2}\right) \qquad - 3.11$$

ρ_o and ρ_p are densities at atmospheric and contact pressures respectively.

The density ratio ρ_p/ρ_o was calculated from Hartung's empirical formula (16) :-

$$\frac{\rho_p}{\rho_o} = 1 + \frac{42.8 \times 10^{-6}}{(\eta_{100})^{0.0358}} \cdot p^{0.75} \qquad - 3.12$$

where η_{100} is the oil viscosity at 100°F in centistokes and p is the prevailing pressure (lbf/in^2).

Since most measurements of film thickness were made in the centre of the contact, the pressure used in calculations of the refractive index was the peak Hertz pressure.

However, for measurements of minimum film thickness the pressure used was 10% of the peak value and for measurements of overall film shape a mean pressure was used, equal to the load divided by the Hertz contact area. At the point of minimum film thickness the pressure is quite close to that assumed, but in film shape measurements the simplification of an overall value introduced some errors, the film thickness in the centre being slightly overestimated and that outside the contact being slightly underestimated. It was felt that the removal of these errors did not justify the extra complexity since they were small in size. For instance, in a circular contact with a peak Hertz stress of 1.5×10^5psi, the corresponding mean stress is 1.0×10^5psi. Under these conditions, the refractive index of BP 1065 oil varies from 1.506 at atmospheric pressure to 1.665 at the peak pressure, with values of 1.620 and 1.536 at the mean and 10% peak pressures respectively. The use of the mean value results in an overestimation of h by 2.8% at the centre and an underestimation at the point of minimum film thickness by 5.2%.

Recently, direct measurements have been made of refractive indices at the pressures encountered in an EHD contact (17). Thus, if maximum accuracy is required, it would be possible to determine the continuous variation of n throughout the contact and hence accurately calculate the film thickness. This presumes a knowledge of the pressure distribution, which is generally not known. For this reason, and because eqn 3.11 has been shown to be accurate to within about 0.6% for paraffinic mineral oils (18), the advantages to be gained in this way are of doubtful value.

For all calculations of refractive index, the contact

was assumed to be isothermal. Although not strictly true (especially for sliding contacts), this is a good enough approximation, because the oil density and hence the refractive index, does not vary much with temperature.

References for Chapter 3

1. Newton I. 'Optiks' Dover Publications 1952. Book Two part 1,Observation 11.
2. Skinner S. 'On the occurrence of cavitation in lubrication' Philosophical Magazine Vol. 7, 6th Series Jan-June 1904 pp 329-335
3. Hardy W. 'Collected Papers' Cambridge Univ. Press 1936 'On static friction' p 619
4. Archard J.F. & Kirk M.T. 'Influence of elastic modulus on the lubrication of point contacts' Paper 15 Lubrication and Wear Convention I. Mech E. pp 181-189
5. Kirk M.T. 'Hydrodynamic lubrication of Perspex' Nature No. 4832 June 9th 1962 Vol. 194 pp 965-6
6. Cameron A. & Gohar R. 'Theoretical and experimental studies of the oil film in lubricated point contact' Proc. Royal Soc. 1966 Vol. 291 Series A pp 520-536
7. Foord C.A.,Hammann W.C. & Cameron A. 'Evaluation of lubricants using optical elastohydrodynamics' A.S.L.E.Transactions Vol. 11 pp 31-43 1968
8. Foord C.A.,Wedeven L.D.;Westlake F.J.&Cameron A. 'Optical elastohydrodynamics' Proc. I.Mech.E. Vol.184 Pt. 1
9. Tolansky S. 'An introduction to interferometry' Longmans, London 1966
10. Born M. & Wolf E. 'Principles of optics' 3rd Ed., Pergamon Press 1965
11. Wedeven L.D. Ph.D. Thesis University of London, March 1970
12. Westlake F.J. Private Communication Imperial College
13. Cameron A. 'Principles of lubrication' Longmans,London 1966
14. Gohar R.,Ph.D. Thesis University of London 1965

15. Kreyszig E. 'Advanced engineering mathematics' 2nd Edition Wiley, New York 1967

16. Hartung H.A. 'Density-temperature-pressure relations for liquid lubricants' Trans. ASME July 1956 Vol. 78 No. 5

17. Paul G. Ph.D. Thesis, University of London 1971

18. Poulter, Ritchey & Benz 'The effect of pressure on the index of refraction of paraffin oil and glycerine' Physical Review Aug. 1st 1932 Vol. 41 pp 366-7

Chapter 4 VARIATION OF VISCOSITY

4.1 Introduction

The ability of lubricating oils to increase their viscosity under the influence of high pressures, such as encountered in point contacts, is extremely important since, without the existence of this phenomenon, it would be impossible to form an E.H.D. oil film.

Investigations into the laws relating pressure and viscosity have been quite frequent, most using as a basis the data contained in the A.S.M.E. report of 1953 (1). To enable predictions to be made of film thicknesses, frictions and the like, it is important to be able to quantify the viscosity change. To this end many laws have been postulated, those used in the present work are discussed in this chapter and compared with the available experimental data.

During nearly all the experimental work, only one oil was used, so it was possible to investigate its behaviour in detail. It was hoped that it would then be possible to make predictions with accuracy and hence ensure good agreement between theory and experiment. The oil was manufactured by British Petroleum, full details of composition etc., are given in the table below.

Cylinder Stock BG 1200/45 Sunbury Ref. L65/425			
Density at 15.6°C ($Kg./m^2$)	919.0	Viscosity Index	95
Kin. Vis. (cSt) @ 37.8°C	1189	Aromatic Rings (%)	8
@ 60.0°C	287.3	Naphthenic Rings (%)	29
@ 98.9°C	51.48	Paraffinic Rings (%)	63

Fig. 4.1 Specification of oil type BP 1065

4.2 Experimental pressure - viscosity data

Data on the variation of viscosity with pressure for the oil used was available from two sources (refs 2 & 3). It is shown graphically in fig. 4.2 but as can be seen, the two sources are not consistent with each other. There are several possible explanations for this difference, even assuming no errors of measurement. The two experimenters used the same oil (BP 1065) but different batches, Paul (2) used Sunbury ref. L62/1374 and Pywell (3) used L65/425, (the oil in the present work was from the latter batch). It is possible that the discrepancy is due to differences in refining or that Paul's oil, being three years older, contained oxidation products that affected his results.

It is, perhaps, more likely that the inconsistency springs from the different experimental techniques employed. Pywell's data at the lower pressures was obtained using a high pressure viscometer of the dropping ball type. He performed his tests at three temperatures and used the results to determine constants for use in an empirical equation relating all the variables (see section 4.5). It was this equation which was used to predict the values at 23°C shown on fig. 4.2. The equation gave excellent predictions at these low pressures. At a higher pressure, the sinker fall time became variable, indicating the development of a solid phase and since the oil could no longer be regarded as Newtonian, the tests were halted at this pressure. However, the appearance of the solid phase was found to take some minutes to occur which is a very long time compared with the transit time through an EHD contact.

Paul obtained the data at higher pressures by a new technique which involved optical measurements of the

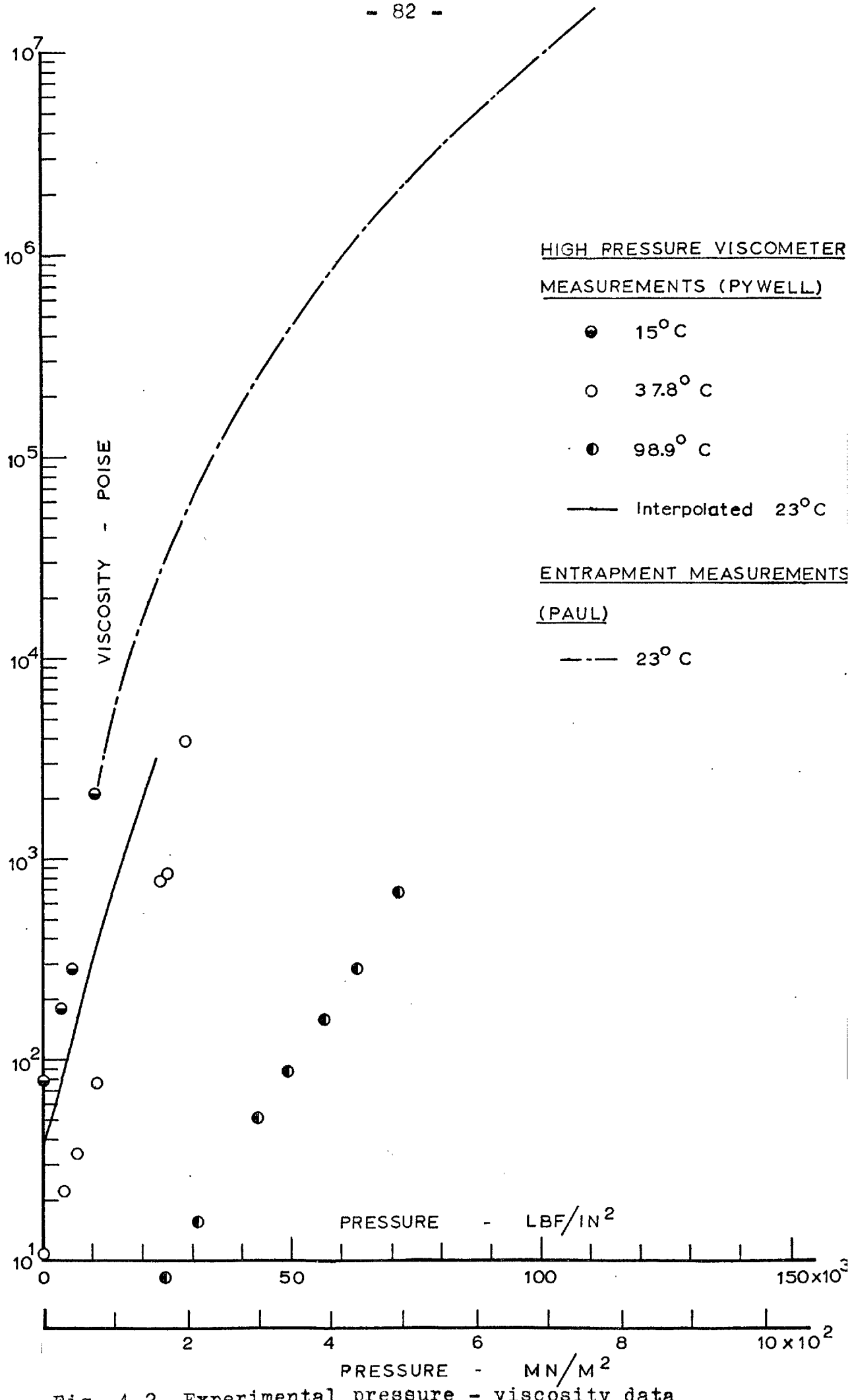


Fig. 4.2 Experimental pressure - viscosity data

entrapment of oil formed between a ball and glass plate during normal approach. The pressure inside the contact was then calculated from the elastic distortion of the surfaces. From this and the measurement of the refractive index, the change of density with pressure was found using the Lorentz-Lorenz relationship (eqn. 3.11). Reynolds' equation was then solved at discrete values of the radius of the contact and hence the variation of viscosity with pressure was determined. The total time involved for a complete set of measurements was about five seconds.

The physical condition of the lubricant in such a contact is not known, but at the lower end of the pressure range, it is likely to be fluid owing to the length of time which waxing takes to occur. It is probably this time difference which accounts for the differences between the two data sets.

The measurements of both Paul and Pywell were made at shear rates considerably lower than those experienced in an EHD contact. For instance, Paul quotes his range as 10^{-5} to 10^{-1} sec^{-1}, whereas that for a typical rolling point contact can exceed 10^{6} sec^{-1}.

4.3 Pressure viscosity coefficient

4.3.1 Low shear rate

The viscosity increase with pressure is usually described by quoting a constant pressure viscosity coefficient, α , for the oil. The viscosity, η_p at pressure p may then be related to the atmospheric viscosity η_o by the equation:-

$$\eta_p = \eta_o . \exp(\alpha . p) \qquad - 4.1$$

This relationship was originally suggested by Barus (4) as a result of measurements of the viscosity of marine glue. It

has the great advantage of computational simplicity, but its range of accuracy is severely limited, since α is not usually a constant but changes with both temperature and pressure. Chu and Cameron (5) have concluded that the law is adequate to describe the behaviour of naphthenic oils. However, even for other fluids, it is very conventient to be able to describe the behaviour, albeit approximately, by means of a single constant.

The value of this constant, α, was determined by substituting Pywell's experimental data in eqn. 4.1. The table of fig. 4.3 shows the results of these calculations together with the viscosity data used. As can be seen, α varies with both pressure and temperature. Representative values of 1.8×10^{-4} ins^2/lbf at 37.8^oC and 2.3×10^{-4} ins^2/lbf at 15^oC were taken and a value of 2.1×10^{-4} ins^2/lbf at 23^oC was obtained by interpolation It was considered that further accuracy was not justified.

4.3.2 High shear rate

For many fluids, particularly those containing polymer additives, the viscosity is often highly dependent on the prevailing shear rate. It is unlikely, therefore, that low shear rate measurements of the type just described will give meaningful α-values for fluids other than those of the highest shear stability.

A method of determining the pressure viscosity coefficient prevailing under conditions of high shear is to derive it from measurements of film thickness and speed made in a rolling contact ball and disc machine. When different lubricants are tested, the separation between plots of non-dimensional film thickness (H_o^*) and non-dimensional speed (U^*) for a given

Pressure		Viscosity	Coefficient
lbf/ins^2	kgf/cm^2	cP	ins^2/lbf
At 59^oF (15^oC) :-			
14.2	1	7625	
3,532	248.3	17896	2.43×10^{-4}
5,521	388.2	28020	2.36
10,290	723.2	221000*	3.28
At 100^oF (37.8^oC) :-			
14.2	1	1081	
3,982	280.0	2237	1.83×10^{-4}
6,400	450.0	3447	1.82
10,510	739.1	7674	1.87
23,830	1675.7	77400	1.79
24,540	1725.5	83900	1.77
28,730	2019.8	390700*	3.65
At 210^oF (98.9^oC) :-			
14.2	1	45.0	
4,193	294.8	81.9	1.43×10^{-4}
10,030	703.3	171.7	1.34
15,860	1115.3	338.8	1.27
24,250	1705.0	841	1.21
30,930	2174.6	1551	1.14
43,120	3031.7	5035	1.09
49,170	3457.2	8660	1.07
56,370	3963.2	15825	1.04
63,170	4441.3	27820	1.02
71,640	5037.2	65300*	1.02

* Abnormally high viscosity, probably due to separation of waxes.

Fig. 4 .3 Calculated pressure-viscosity coefficients for BP 1065 (L65/425)

dimensionless load (W^*), can, to a first order, be ascribed to differences in α(6). Hence α for a fluid under test can be obtained by comparison with a standard lubricant.

Westlake (7) has developed this method and correlated data obtained from a large number of fluids into the following empirical equation, thus eliminating the necessity of having a standard lubricant for comparison.

$$H_o^* = K_1.(U^*)^{a_1}.(W^*)^{b_1}.(G^*)^{c_1} \qquad - 4.2$$

where $K_1 = 62.0(U^*)^{-0.063}$

$a_1 = 1/90.\log_{10}W^* + 0.89$

$b_1 = 1/43.\log_{10}U^* + 0.30$

$c_1 = 0.550$

A test was run, using BP 1065, to determine the α-value from eqn. 4.2. The results are shown on fig. 4.4. W^* was chosen as 8.4×10^{-7} whilst H_o^* was taken from the plot at $U^* = 4.0\times10^{-11}$, these values being used to ensure consistency with Westlake's work. The results of the calculations gave α as 1.58×10^{-4} ins^2/lbf (cf. $\alpha = 2.1\times10^{-4}$ ins^2/lbf from Pywell's data). This reduction in the pressure viscosity coefficient is due mainly to the effect of pressure rather than of shear rate, since calculations at different values of U^* yielded the same answer.

4.4 Limiting viscosity

The entrapment measurements of Paul showed in several cases a limiting viscosity of the oil. There were indications too, that this would occur with BP 1065 had the pressures been increased. This ceiling viscosity was estimated to be in the

$W^* = 8.4 \times 10^{-7}$

$U^* = 4.0 \times 10^{-11}$

$H_o^* = 2.7 \times 10^{-5}$

$\alpha = 1.58 \times 10^{-4} \left(LBF/INS^2\right)^{-1}$

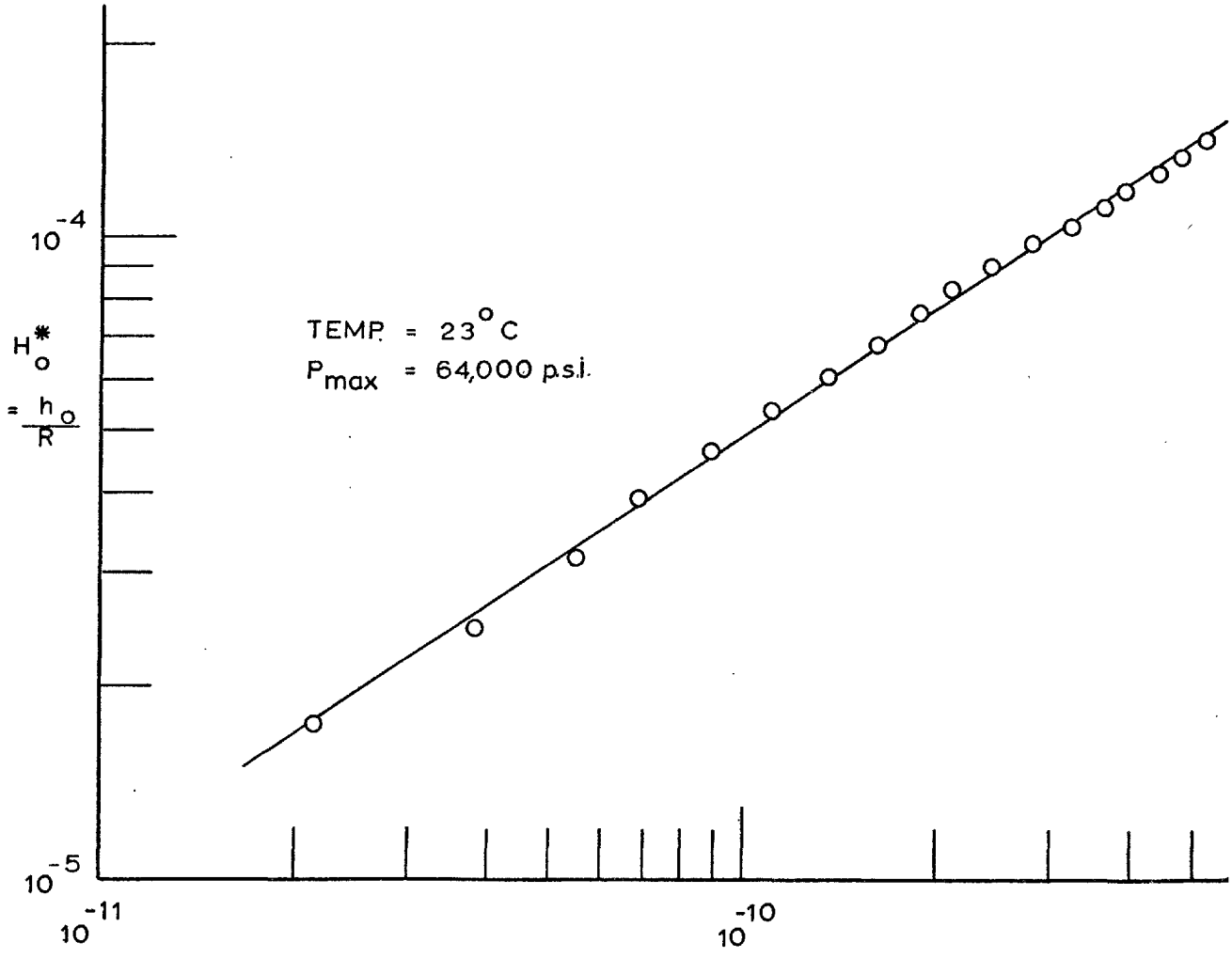


Fig. 4.4 Central film thickness vs. speed in a rolling point contact.

region of 10^{10} poise.

For this reason, an alternative expression to eqn.4.1 was investigated which incorporated a limiting viscosity and which therefore overcame one of the major failings of the simple exponential law. The expression has the form :-

$$\eta_p = \eta_o . \exp\left(\frac{K_o . p}{1 + K_1 . p} \right) \qquad -4.3$$

where K_o and K_1 are both constants. It is similar to that suggested to Dowson and Whitaker by Dyson (8), that is:-

$$\eta_p = \eta_o . \exp\left(\frac{G_o . \bar{p}}{1 + G_1 . \bar{p}} \right) \qquad -4.4$$

where $\bar{p} = p/E'$ and G_o & G_1 are constants which have to be 'selected for a given lubricant'. The implication is that G_o & G_1 vary with the material combination, it seems more reasonable, however, to fix K_o & K_1 for the lubricant since they are independent of E'.

The constants' values were obtained by fitting eqn. 4.3 to the experimental data of Paul. Fig. 4.5 shows, on a log.log plot, the fit obtained. Also shown are the measurements of Pywell and the more usual exponential law of eqn. 4.1 with α as the high shear value obtained from eqn. 4.2. As can be seen, at high pressures eqn. 4.1 predicts viscosities which are too high, (assuming the experiments to be correct), whereas eqn. 4.3 predicts realistic values.

4.5 Empirical formula

Pywell, at BP, has tested sixteen oils or oil blends in the high pressure viscometer and using the data obtained, has developed the following formula which can predict accurately the viscosity of these oils at any temperature and

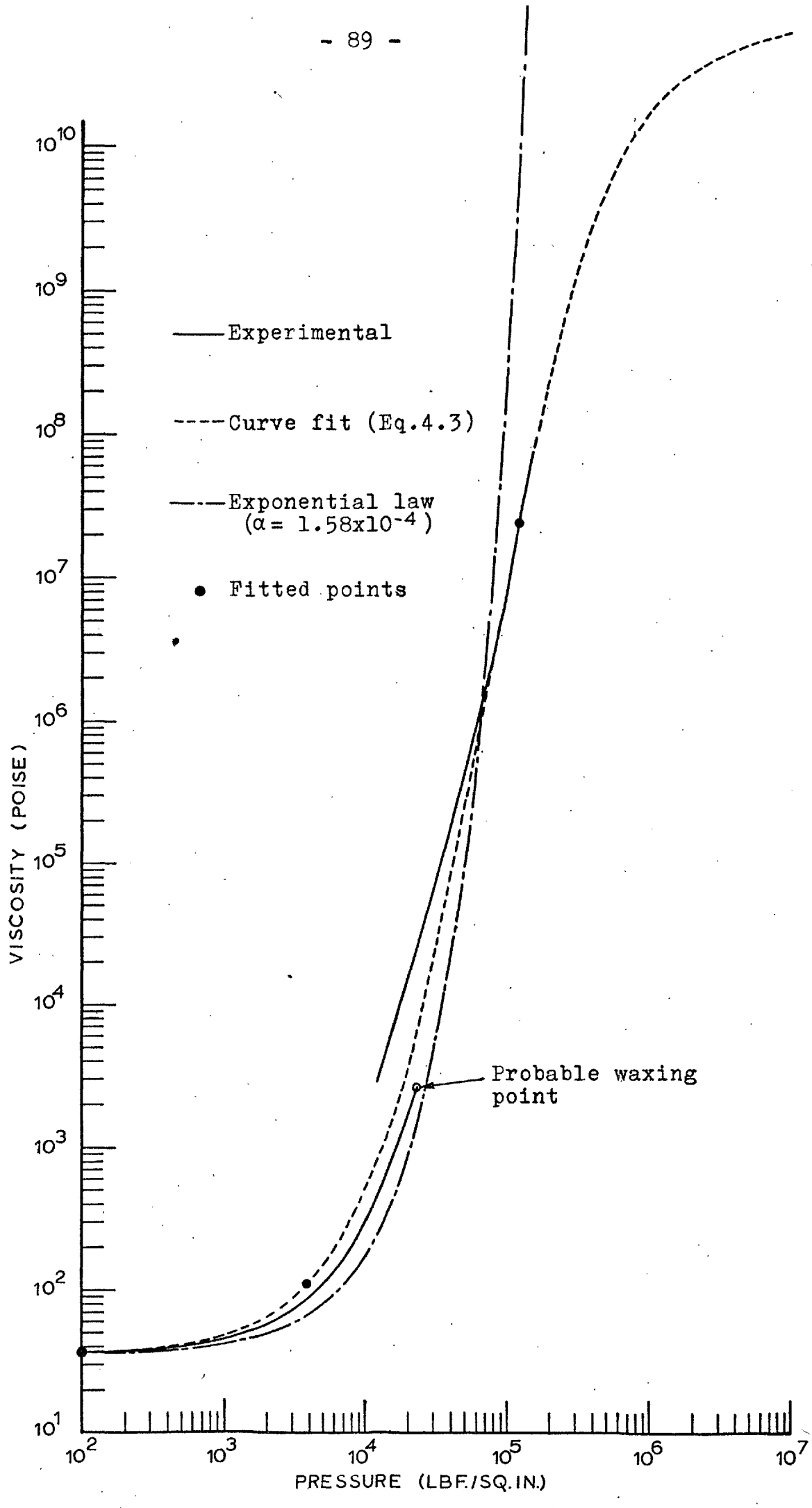


Fig. 4.5 Comparison of eq. 4.3 with experimental data

pressure within the range of his experiments.

$$\log(\eta+0.5)+D = ((p+p_o)/p_o)^Y((T/T_1)^B \log(\eta_1+0.5)+D)+10^{Y1}p^{Y2}T^{Y3} \quad -4.5$$

where η is the viscosity in centipoise

p is the pressure in MN/m^2

T is the temperature in ^oK

The values of the constants were adjusted for each oil; for BP 1065 they were found to be :-

Y1 = 9.2	B = -3.305
Y2 = 2.7	D = 2.70
Y3 = -7.4	$\log_{10}(\eta_1+0.5)$ = 3.018
Y = 0.553	p_o = 180 MN/m^2

As was mentioned above, this formula was used to predict the data at 23°C on fig. 4.2. However, at higher pressures, the predictions are similar to those of eqn. 4.1. This is demonstrated on fig. 4.6, where the formula has been extrapolated beyond the point at which waxing would have been expected. Eqn. 4.1 with the high shear rate α-value is again shown for comparison.

The family of curves shown in fig. 4.7 describes the overall behaviour of viscosity with temperature and pressure as predicted by the BP empirical formula. Within the experimental region shown, the forcasts are to within 5%, but outside, as has been demonstrated, the equation is no better than the much simpler exponential law. Further, the complexity of the equation makes it unsuitable for algebraic manipulation, so for these reasons it was not used in analytical work.

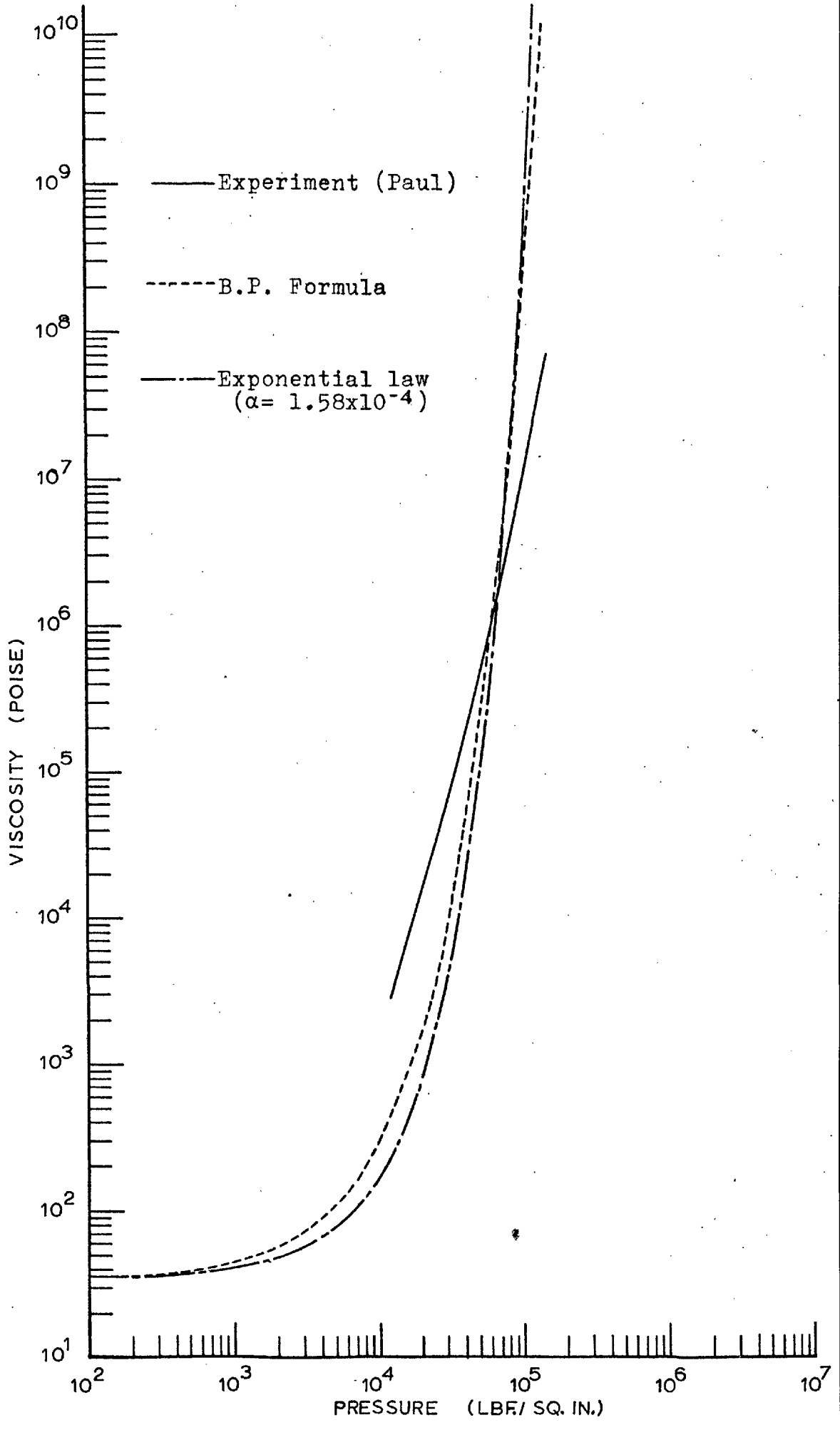


Fig. 4.6 Comparison of BP formula with exponential law

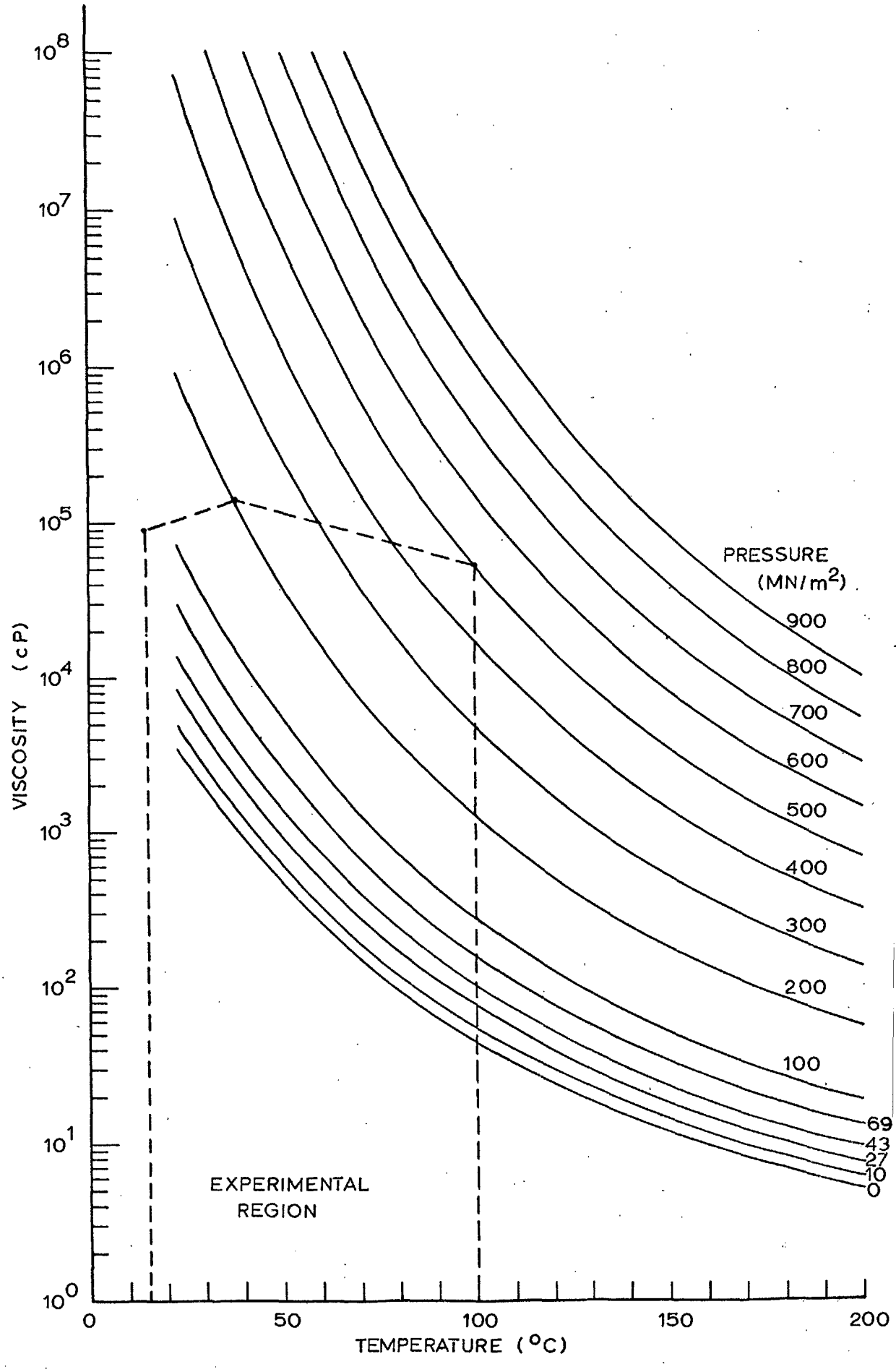


Fig. 4.7 Behaviour of BP 1065 (BP Empirical formula)

4.6 Viscosity variation with temperature

There are a multitude of equations which attempt to predict the variation of viscosity with temperature. A commonly used formula is the Walther - ASTM equation which forms the basis of the well-known viscosity chart (9):-

$$\log.\log.(\nu+0.6) = \text{const.} - \text{const.}\log(T) \qquad -4.6$$

where T is the absolute temperature

ν is the viscosity in centistokes

This formula was used,when analysing the experimental results for film thickness and friction, to allow for the change of inlet viscosity with the temperature measured by the trailing thermocouple (see section 2.6). Oil viscosity data provided by BP Ltd. at two temperatures was used to determine the two constants in the equation.

However, for analytical work, this expression was too complex and a much simpler, but less accurate, equation was used, namely :-

$$\eta = \eta_0.\exp(-\beta T) \qquad -4.7$$

This equation represents a straight line when plotted on the same base as fig. 4.7, hence it can be seen that it is only approximate. It is, however, suitable for use under inlet conditions where the pressure and temperature changes are relatively small.

In the nip, viscosity variations with temperature significantly affect the friction experienced. Since β itself varies with temperature and pressure, the errors introduced by using eqn. 4.7 are likely to be large. Thus, when possible, a more accurate equation was used, namely the Vogel equation.

The Vogel equation has the form:-

$$\eta = K.\exp\left[\frac{b}{t+\theta}\right] \qquad \therefore 4.8$$

where K,b and θ are constants and t the temperature rise. These constants have a recognisable significance. K is the 'thickness' of the oil and has units of viscosity. The constant b expresses the inherent viscosity temperature dependence of the oil and θ gives the temperature at which the oil has infinite viscosity, which is not necessarily related to its freezing point. Both b and θ have units of temperature.

Crouch and Cameron (10) pointed out that usually, values of θ lie between 50 & 150 and values of b between 500 & 2000, both on the centigrade scale. In an earlier paper (11), Cameron showed that θ for most conventional oils could be put equal to 95 (^{o}C). However, for BP 1065, the constants were calculated (from viscosity data at three temperatures) as θ= 144 and b = 1825, which are both at the top end of the range.

To apply the equation at high pressures, b & θ were initially assumed to remain constant - this was acceptable because of their physical meaning. K was assumed to vary as the oil thickened under the influence of pressure. Thus, taking the viscosity at pressure p and at zero temperature rise as η_p,

$$K = \eta_p.\exp(-b/\theta) \qquad - 4.9$$

Hence from 4.8 & 4.9, the Vogel equation becomes :-

$$\eta = \eta_p.\exp\left[\frac{-b.t}{\theta^2+\theta.t}\right] \qquad - 4.10$$

where η_p is given by the pressure viscosity relationship.

This modified Vogel equation may be considered as the general case of the Reynolds temperature viscosity equation (4.7)

with a β-value of $b/(\theta^2 + \theta.t)$ which is itself a function of temperature. However, in general, the β-value also varies with pressure.

An attempt was made to take this effect into account by modifying the value $b/(\theta^2 + \theta.t)$ by a factor dependent on pressure By plotting the β-values of equation 4.5 from figure 4.7, it was found that, to a first approximation, the variation with pressure over the pressure range likely to be encountered, could be expressed as:-

$$\beta_p = \beta_o.\exp(0.0015 \times p) \qquad - 4.11$$

where p is the pressure in MegaNewtons/square metre.

Thus equation 4.10 becomes:-

$$\eta = \eta_p.\exp\left[e^{.0015p}.\frac{-b.t}{\theta^2+\theta.t}\right] \qquad - 4.12$$

In practice, however, the effect of this pressure correction was very small and, except for very highly loaded contacts, could be neglected.

4.7 Discussion

The most convenient pressure viscosity equation to use is the simple exponential law of equation 4.1. It is suitable for analysis and describes the oil behaviour in terms of a single coefficient α. This coefficient is not constant, but it may be considered as such if the value is determined from measurements in a rolling contact at high shear rates. For BP 1065, the high and low shear rate values differed by 5.7% which demonstrates the high shear stability of the oil. These values, however, differed considerably (25%) from the low shear rate value determined at low pressures.

In most of the present work, the high pressure, high shear rate value of α was used in the formation of the non-dimensional group G^* ($=\alpha E'$). When considering the friction of soft surfaces, however, it was considered more appropriate to use the low pressure, low shear rate value.

For predictions of film thickness in an undeformed contact (described in a later chapter) equation 4.1 was found to be sufficiently accurate, since the pressures involved were low. The inaccuracies which were introduced at these low pressures were small and were tolerated for the sake of computational simplicity. Sliding friction, however, depends directly on the viscosity under high pressure in the contact zone. For accurate friction predictions, therefore, the ceiling viscosity implicit in equation 4.3 is particularly significant.

In a review of temperature viscosity laws, Crouch and Cameron (10) noted that the two constant Walther - ASTM formula (eqn.4.6) showed good correlation of results but was not reliable over extended ranges. They also noted that the most accurate of the formulae examined was the Vogel equation (eqn.4.8) which fitted results over a wide range of temperatures and was also simple mathematically.

Thus, in the present work, the Vogel equation was used in analytical work and the Walther equation restricted to the correction of experimental data where the range of temperature was very limited. In some cases, however, even the Vogel equation was too complex and use had to be made of the simple Reynolds law of equation 4.7.

References for Chapter 4

1. 'Viscosity and density of over 40 lubricants' Report of ASME Research Committee on Lubrication, ASME, New York 1953.
2. Paul G. Ph. D. Thesis, University of London 1971.
3. Pywell R.F. 'Viscosities and densities of oils at high pressure and their dependence on hydrocarbon type' 1970 Internal report 10,155, BP Research Centre, Sunbury, Middx.
4. Barus C. 'Isothermals, isopiestics and isometrics relative to viscosity' American Journal of Science(3),Vol 45 1893,pp 87 -96.
5. Chu P.S.Y. & Cameron A. 'Pressure viscosity characteristics of lubricating oils' Jour. Inst. Petroleum Vol.48, No. 461 May 1962, pp 147-155.
6. Foord C.A., Hammann W.C. & Cameron A. 'Evaluation of lubricants using optical elastohydrodynamics' A.S.L.E. Transactions Vol. 11 pp 31-43 1968
7. Westlake F.J. & Cameron A. 'Interferometric study of point contact lubrication' E.H.L. Symposium, Leeds 1972. I.Mech.E.
8. Dowson D. & Whitaker A.V. 'A numerical procedure for the E.H.D. problem of rolling and sliding contacts lubricated by a Newtonian fluid' I.Mech.E. Vol. 180 Pt. 3B pp 57-71
9. Walther C. Maschinenb., 1931, vol. 10, p. 671
10. Crouch R.F. & Cameron A. 'Viscosity temperature equations for lubricants' Jour. Inst. Petroleum Vol.47,No.453, Sept 1961 pp 307-313.
11. Cameron A. 'Determination of the pressure viscosity coefficien and molecular weight of lubricating oils' Jour. Inst. Petroleum Vol.31, 1945, pp 401-414.

Chapter 5 FILM THICKNESS IN ELLIPTICAL CONTACTS

5.1 Introduction

Over the past few years there has been a considerable amount of experimental work devoted to the study of the oil films in elastohydrodynamic nominal point and line contact. Point contact has been achieved by using a ball loaded against a plate (ref: 1,2,3). This arrangement has the advantage of simplicity, but it does not adequately simulate the geometry of a ball bearing. In order to do this, the experiments and theory described below use the arrangement of a ball loaded against a conforming groove. In common with previous experiments,(ref: 1,2,3) interferometry was used to measure the oil film. Advantage was taken of the quite low pressures that can be generated in such a contact. Thus, the oil film thickness and pressure distribution have been found theoretically under 'classical' conditions, that is, with the contiguous surfaces undistorted and only pressure viscosity effects significant (ref: 4). The effects of gyroscopic sliding have been included.

The procedure used in the calculations is outlined first. Measurements made in a sliding contact are then described and used as a basis for comparison with the theory. Rolling contact measurements are then described and also compared with the predictions. At higher loads,when elastohydrodynamic conditions obtain experimental results are compared with the theories of Archard and Cowking (5) and Cheng (6).

5.2 Theory

5.2.1 Reynold's Equation

The Reynold's equation in two dimensions, using Cartesian co-ordinates and assuming a sliding contact and constant density is:

$$\frac{\partial}{\partial x}\left[\frac{h^3}{6\eta}\cdot\frac{\partial p}{\partial x}\right] + \frac{\partial}{\partial y}\left[\frac{h^3}{6\eta}\cdot\frac{\partial p}{\partial y}\right] = \frac{\partial}{\partial x}(Uh) + \frac{\partial}{\partial y}(Vh) \qquad -5.1$$

U and V are the ball surface velocities in the x and y directions respectively (see figure 5.1). Allowance may readily be made for rolling (assuming no slip) by putting U = 2U in equation 5.1. If classical conditions obtain (ref:4), then elastic distortion is absent and oil viscosity is constant in the vicinity of the contact. Thus, for a constant viscosity η_o, let the pressure be denoted by a reduced pressure q. Equation 5.1 then reduces to:-

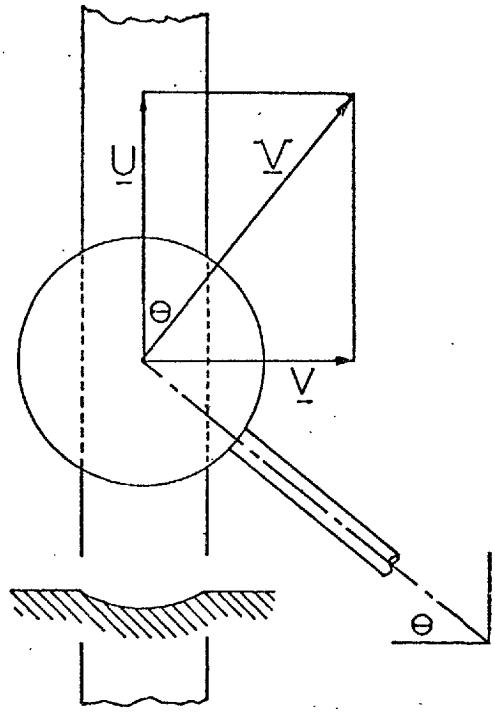


Fig.5.1 Schematic layout of ball and groove

$$\frac{\partial}{\partial x}\left[h^3\cdot\frac{\partial q}{\partial x}\right] + \frac{\partial}{\partial y}\left[h^3\cdot\frac{\partial q}{\partial y}\right] = 6\eta_o\left[U\cdot\frac{\partial h}{\partial x} + V\cdot\frac{\partial h}{\partial y}\right] \qquad -5.2$$

Equation 5.2 may be normalised by substituting:-

$$\bar{q} = \alpha q \quad \bar{h} = h/h_o \quad \bar{x} = x/a \quad \bar{y} = y/b \quad U = \nabla\cos\Theta$$

$$V = \nabla\sin\Theta$$

where 'a' is an arbitrary scaling factor governing the distance of the inlet boundary from the contact centre.

Let 'b' be related to 'a' by

$$\frac{b}{a} = \frac{d}{c} = \frac{\text{semiaxis of the Hertzian ellipse in the y direction}}{\text{semiaxis of the Hertzian ellipse in the x direction}}$$

The foregoing substitution transforms the region of calculation from an ellipse to a circle. In order to convert to polar co-ordinates, let

$$\bar{x} = \bar{r}\cos\phi$$

$$\bar{y} = \bar{r}\sin\phi$$

Equation 5.2 can now be written as:-

$$\left[\cos^2\phi + \sin^2\phi\left(\frac{a^2}{b^2}\right)\right].\left[3\bar{h}^2.\frac{\partial\bar{h}}{\partial\bar{r}}.\frac{\partial\bar{q}}{\partial\bar{r}} + \bar{h}^3.\frac{\partial^2\bar{q}}{\partial\bar{r}^2}\right]$$

$$+\left[\sin^2\phi + \cos^2\phi\left(\frac{a^2}{b^2}\right)\right].\left[\frac{\bar{h}^3}{\bar{r}}.\frac{\partial\bar{q}}{\partial\bar{r}} + \frac{\bar{h}^3}{\bar{r}^2}.\frac{\partial^2\bar{q}}{\partial\phi^2} + \frac{3\bar{h}^2}{\bar{r}^2}.\frac{\partial\bar{q}}{\partial\phi}.\frac{\partial\bar{h}}{\partial\phi}\right]$$

$$-\left[\sin\phi.\cos\phi\left(1 - \left(\frac{a^2}{b^2}\right)\right)\right].\left[\frac{2\bar{h}^3}{\bar{r}}.\frac{\partial^2\bar{q}}{\partial\bar{r}\partial\phi} + \frac{3\bar{h}^2}{\bar{r}}.\frac{\partial\bar{h}}{\partial\bar{r}}.\frac{\partial\bar{q}}{\partial\phi}\right.$$

$$\left.+\frac{3\bar{h}^2}{\bar{r}}.\frac{\partial\bar{q}}{\partial\bar{r}}.\frac{\partial\bar{h}}{\partial\phi} - \frac{2\bar{h}^3}{\bar{r}^2}.\frac{\partial\bar{q}}{\partial\phi}\right] = \frac{6\eta_o\bar{V}a\alpha}{h_o^2}.\left[\frac{1}{\bar{r}}.\frac{\partial\bar{h}}{\partial\phi}.\left(\left(\frac{a}{b}\right)\sin\theta.\cos\phi\right.\right.$$

$$\left.\left.-\cos\theta.\sin\phi\right) + \frac{\partial\bar{h}}{\partial\bar{r}}.\left(\left(\frac{a}{b}\right)\sin\phi.\sin\theta + \cos\phi.\cos\theta\right)\right] \quad -5.3$$

For no distortion of the contiguous surfaces, the film shape in the vicinity of the contact can be expressed, as in reference 4:-

$$h = h_o + Ax^2 + By^2 \quad -5.4$$

where the geometry is as shown in figure 5.2.

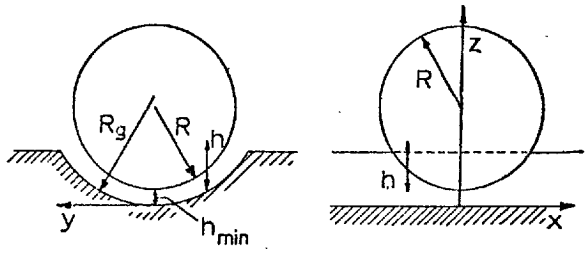


Fig.5.2 Geometry of contact

Normalising and expressing equation 5.4 in polar form,

gives equation 5.5:-

$$\bar{h} = 1 + \frac{Aa^2}{h_o}.\left[\left(\bar{r}\cos\phi\right)^2 + \frac{B}{A}\left(\frac{b}{a}\right)^2\left(\bar{r}\sin\phi\right)^2\right] \qquad -5.5$$

Equations 5.3 and 5.5 were solved for $\bar{q}$ over the whole region of contact using a finite difference method. Central differences were employed with a non-uniform grid in the radial direction and close spacing of grid lines near the contact centre. By this means, errors due to large gradients, in the region of high pressures, were minimised. Details of the program and the solution procedure are given in appendix 2. The boundary conditions employed are discussed below.

5.2.2 Load taken

The distribution of $\bar{q}$ obtained from equations 5.3 and 5.5 was modified to take into account the variation of viscosity with pressure. Since pressures were low, it was sufficiently accurate to assume an exponential pressure viscosity relationship (see section 4.3). The substitution $\bar{p} = -\ln\left(1 - \bar{q}\right)$ was made to give the actual non-dimensional pressure distribution. The resulting $\bar{p}$ distribution was then integrated over the grid (see appendix 2) to give the non-dimensional dependent load $\bar{W}$, where

$$\bar{W} = \iint \bar{p}.d\bar{x}\ d\bar{y} \qquad -5.6$$

which can be written as

$$\left(\frac{a}{b}\right).\left(\frac{\alpha}{a^2}\right)\iint p\ dx\ dy \qquad -5.7$$

that is

$$\bar{W} = \left(\frac{a}{b}\right)\left(\frac{W\alpha}{a^2}\right) \qquad -5.8$$

5.2.3 Boundary Conditions

Assuming that the cavitation causes rupture of the lubricating film on the exit side, then the Reynold's condition

$$q = \frac{\partial q}{\partial x} = \frac{\partial q}{\partial y} = 0$$

must be satisfied there (ref: 7). These conditions were obtained by making $\bar{q}$ zero round the boundary of the finite difference grid and also by putting $\bar{q}$ to zero whenever it was calculated as negative. In this manner, the shape and position of the outlet boundary are self-determining.

The extent of the grid in the radial direction is ideally infinite. It was found, however, that after a certain radius had been reached, further increase did not have any significant effect on the peak pressure or the load (see figure 5.3). This is the radius required to simulate fully flooded conditions, anything less being starved (ref: 8). In practice the inlet radius used was chosen to be slightly larger than the minimum, to coincide with a grid line. It was given by $\bar{r} = 23.25$, that is, at $x = 23.25\sqrt{(h_o/A)}$.

An iterative boundary condition was required at the grid centre because of a singularity caused by $\bar{r}$ being zero there. The singularity was avoided by ensuring continuity of pressure and pressure gradient at this point.

5.2.4 Non-dimensional Groups

The independent variables may be collected from equations 5.3 and5.5 to form non-dimensional groups

$$\frac{B}{A}, \quad \frac{Aa^2}{h_o}, \quad \frac{6\eta_o V a \alpha}{h_o^2}, \quad \theta$$

The ratio a/b is uniquely dependent on B/A (ref: 9). Also, since 'a' is arbitrary, it may be chosen to make one of the groups unity. Thus,'a' was chosen such that

$$a = (h_o/A)^{\frac{1}{2}} \qquad -5.9$$

The non-dimensional groups are now

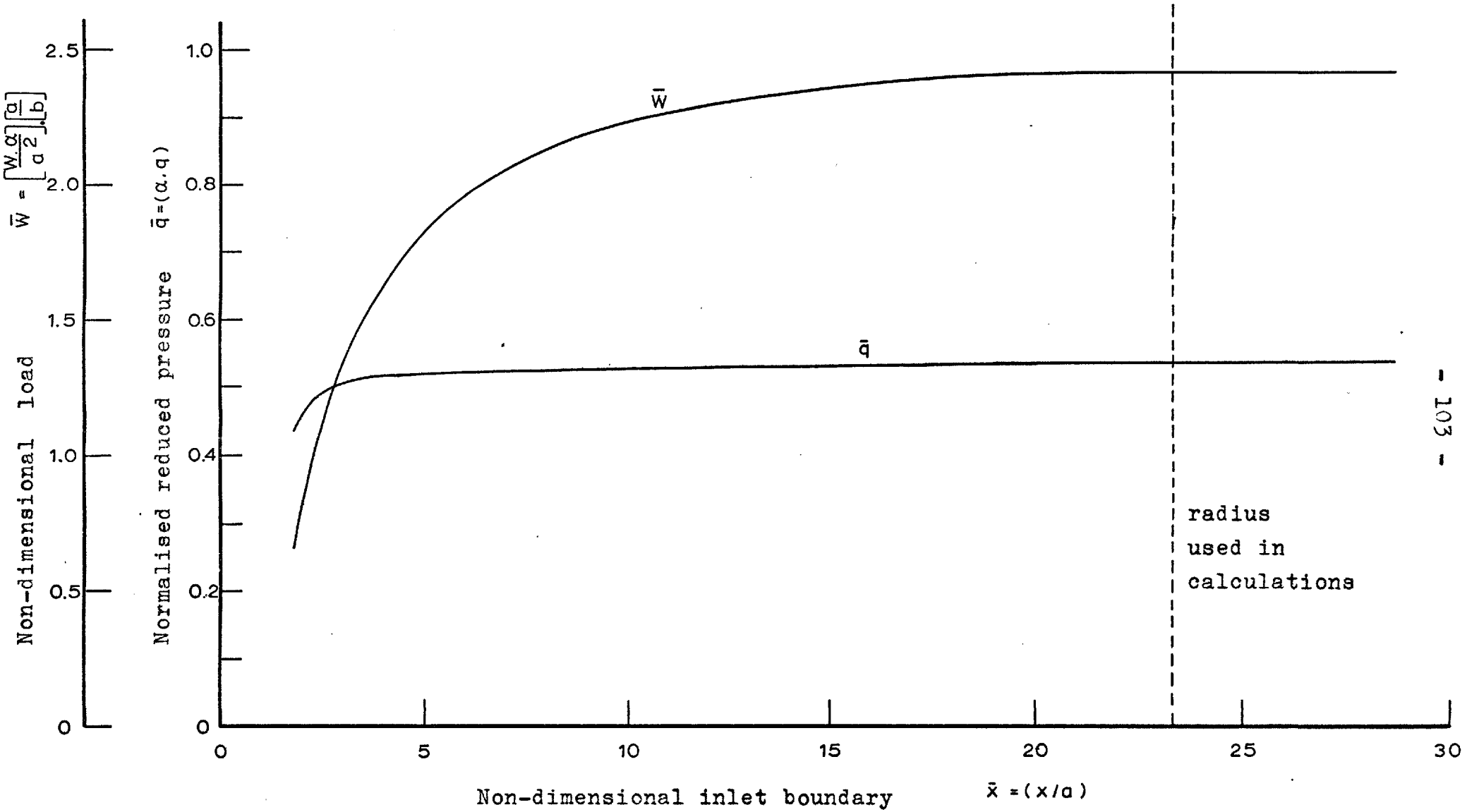


Fig.5.3 Effect of inlet boundary position on load and peak pressure.

$$\frac{B}{A}\ ,\quad \frac{6\eta_o V\alpha}{A^{1/2}h_o^{3/2}}\ ,\quad \frac{W\alpha A}{h_o},\quad \theta$$

where $A = 1/2Rx = 1/2R$ for a ball in a straight groove

If the parameters are put into the more familiar groups obtained for the point contact situation (ref: 3), namely

$$G^* = \alpha E',\quad U^* = \frac{\eta_o}{RE'},\quad W^* = \frac{W}{E'R^2},\quad H_o^* = \frac{h_o}{R}$$

after some slight manipulation, the following functional relationship is obtained

$$\frac{H_o^*}{W^*G^*} = \phi_1\left[\frac{U^*}{W^{*3/2}G^{*1/2}}\ ,\quad \frac{B}{A}\ ,\quad \theta\right] \qquad -5.10$$

for an undeformed contact.

As the geometry is invariable, B/A is constant and $H_o^*/(W^*\ G^*)$ may be plotted against $U^*/(W^{*3/2}\ G^{*1/2})$ for each value of θ. Now the pressure distributions $\bar{p}$, obtained from the expression $\bar{p} = -\ln(1 - \bar{q})$, are no longer valid when $\bar{q} > 1$, that is, when $q > 1/\alpha$. Kapitza (4) has called this the limiting pressure for pressure dependent viscosity. It seems reasonable to assume that by then deformation has become important. Inclusion of deformation should therefore add another group to equation 5.10.

5.2.5 Previous Solutions

Of the point contact film thickness solutions mentioned in the review(chapter 1), only a few are general enough to extend to elliptical contacts.

The preceeding analysis involved many of the assumptions of the solution due to Kapitza (4). His solution, however, was analytic since he realised that $q = kx/h^2$ was a particular solution of the isoviscous Reynold's equation. As noted earlier a 'reduced pressure' solution becomes mathematically invalid when $q = 1/\alpha$. Thereafter Kapitza postulated that the film

thickness would remain constant despite increasing load. Further restrictions on his solution are that the hydrodynamic velocity should be along an axis of symmetry of the contact ellipse and, more important, that a half-Sommerfeld boundary condition should be used. This implies that all pressures in the exit half of the contact must be zero.

In the paper by Snidle and Archard (10), the first of these restrictions has been removed, although the latter remains. They derived an expression for the limiting film thickness which in the present notation, can be expressed as:-

$$h_L = \left[1.95 \, \nabla \eta_o \alpha \right]^{\frac{2}{3}} \left[2R \right]^{\frac{1}{3}} \left[\frac{\cos^2\theta}{\left(3 + 2\left(\frac{B}{A}\right) \right)^2} + \frac{\sin^2\theta}{\left(\frac{B}{A}\right)\left(3 + 2\left(\frac{A}{B}\right) \right)^2} \right]^{\frac{1}{3}} \qquad -5.11$$

When $\theta = 0$, equation 5.11 reduces to Kapitza's solution. In terms of the groupings of equation 5.10, equation 5.11 becomes:-

$$\frac{H_L^*}{W^* G^*} = 1.97 \left[\frac{U^*}{W^{*3/2} G^{*1/2}} \right]^{\frac{2}{3}} \left[\frac{\cos^2\theta}{3 + 2\left(\frac{B}{A}\right)^2} + \frac{\sin^2\theta}{\left(\frac{B}{A}\right)\left(3 + 2\left(\frac{A}{B}\right) \right)^2} \right]^{\frac{1}{3}} \qquad -5.12$$

At present there is no complete numerical solution for elastohydrodynamic elliptical contacts. Cheng (6) has obtained the entry film thickness for an elliptical contact by means of a Grubin approximation (11), which forces a Hertzian shape onto the inlet part of the oil film. This assumption makes the indices of U^* and W^* the same, whereas a full numerical solution might not. For example, in the numerical solution of the line contact problem, there is a difference between these indices (ref: 12) and in point contact experiments the difference is quite significant (ref: 3). However, Grubin type solutions

have proved to be quite accurate at high loads and low speeds where experiments have shown the film shape to be similar to that assumed (ref: 8). Now, in order to compare with experiments, which ranged from undistorted surfaces through to elastohydrodynamic conditions, Cheng's numerical solution can be adjusted to form the same groups as those of equation 5.10. Cheng's result (see appendix 3) for an elliptical contact having the geometry used in the sliding experiments, reduces to:-

$$\frac{Ho^*}{W^*G^*} = 1.45 \left[\frac{U^*}{G^{*1/2}W^{*3/2}} \right]^{0.738} (W^*G^{*3})^{0.036} \qquad -5.13$$

for $\theta = 0^\circ$ and to:-

$$\frac{Ho^*}{W^*G^*} = 0.462 \left[\frac{U^*}{G^{*1/2}W^{*3/2}} \right]^{0.639} (W^*G^{*3})^{-0.014} \qquad -5.14$$

for $\theta = 90^\circ$.

There is therefore, as predicted, an additional group W^*G^{*3} caused by deformation effects. It should be noted, however that any solution is weakly dependent on this new group. For a one hundredfold change in W^*, the additional group alters only by a factor of 1.2 for $\theta = 0^\circ$ and 1.1 for $\theta = 90^\circ$.

Archard and Cowking (5) have also obtained an approximate solution for an elliptical contact. They found the entry film thickness by considering only the axis of symmetry of an elasohydrodynamic point contact. They then multiplied it by a side leakage factor which was obtained from a comparison of a Kapitza solution and a solution for an undistorted line contact.

Archard's solution (see appendix 3) can be expressed as:-

$$\frac{Ho^*}{W^*G^*} = 1.165 \left[\frac{U^*}{G^{*1/2}W^{*3/2}} \right]^{0.74} (W^*G^{*3})^{0.037} \qquad -5.15$$

for $\theta = 0^\circ$ and

$$\frac{H_o^*}{W^*G^*} = 0.269 \left[\frac{U^*}{G^{*1/2}W^{*3/2}} \right]^{0.74} (W^*G^*)^{0.037} \qquad -5.16$$

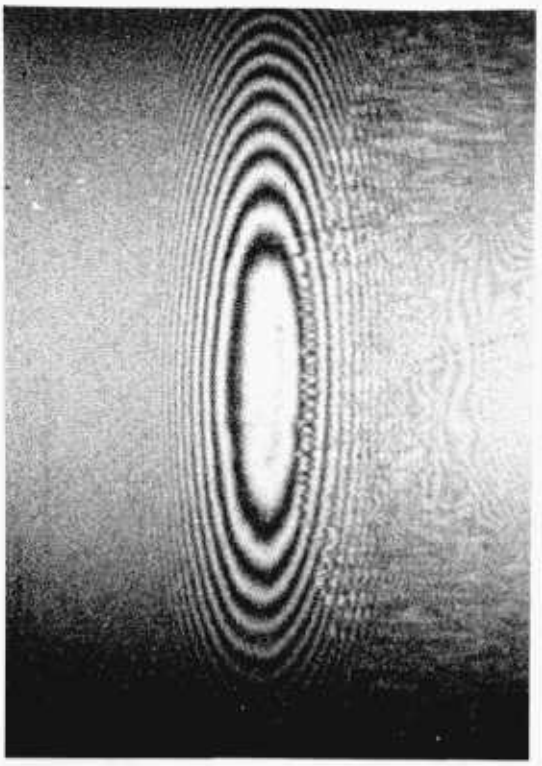
for $\theta = 90^\circ$.

5.3 Sliding Contacts: theoretical and experimental

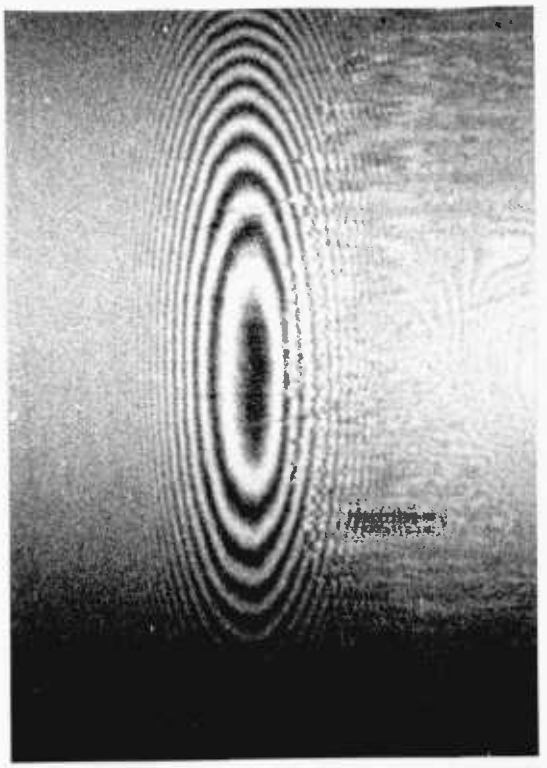
5.3.1 High-speed photographs of the contact

A series of black-and-white photographs of the contact were taken using monochromatic light. Three loads were used with corresponding peak Hertz stresses ranging from 20,000 psi to 38,000 psi. At each load, speeds were selected such that the minimum film thickness corresponded to a fringe of a known order ranging up to a maximum of the third black fringe for the lightest load and the eighth black fringe for the highest load. Such a set of photographs was obtained for each of the six drive angles employed, making a total of about one hundred and thirty. Of these, sixteen are presented (figures 5.4 to5.7) corresponding to the first and third dark fringe for the lightest load and to the first bright and sixth dark fringe for the highest load, for four of the six drive angles (0°,67°, 82°,90°).

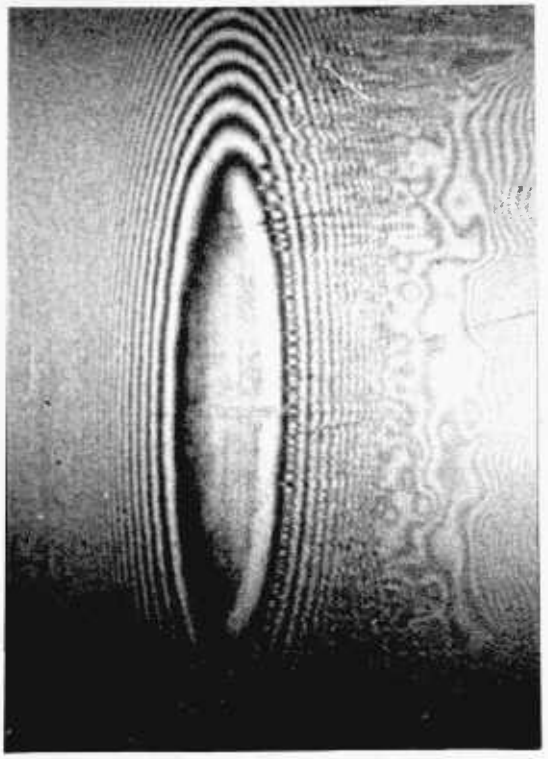
For the light load or high speed photographs (b and d) where distortions were not very significant, the minimum film thickness occurs at the centre of the contact. As load is increased or speed decreased (a and c) the pressure distribution modifies sufficiently to cause elastic deformation of the boundary surfaces. The minimum then moves to the trailing edge of the contact or, depending on the amount of angling, to one or both of the sides. In the 0° example of figure 5.4(c) there is a flat central region with a long end closure and limited



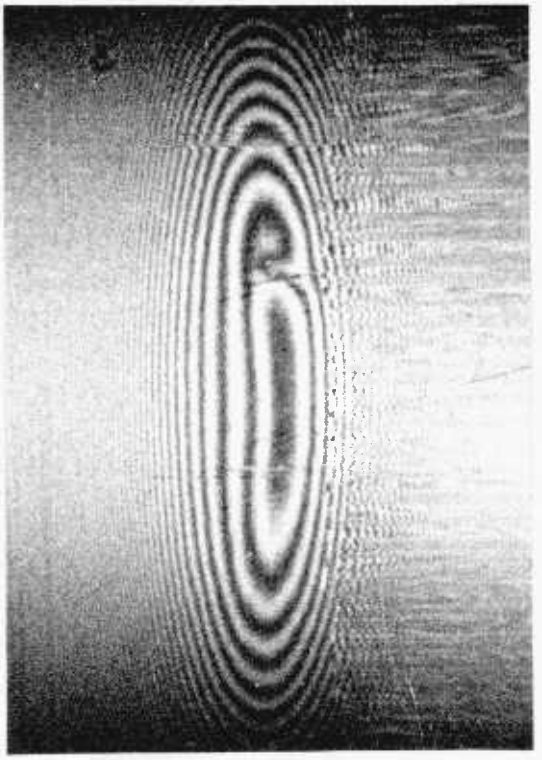
(a) 1st dark just visible
$W^* = 1.67 \times 10^{-7}$



(b) 3rd dark fringe
$W^* = 1.67 \times 10^{-7}$



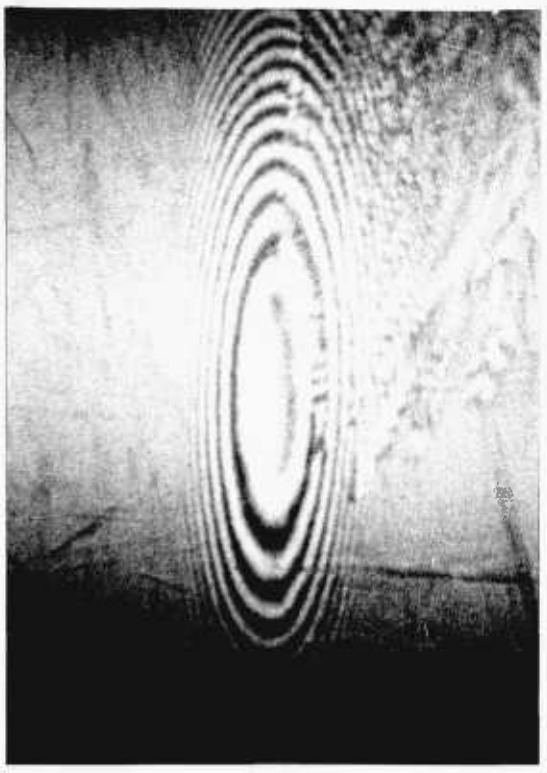
(c) 1st bright fringe
$W^* = 1.19 \times 10^{-6}$



(d) 6th dark fringe
$W^* = 1.19 \times 10^{-6}$

MAGNIFICATION X 70

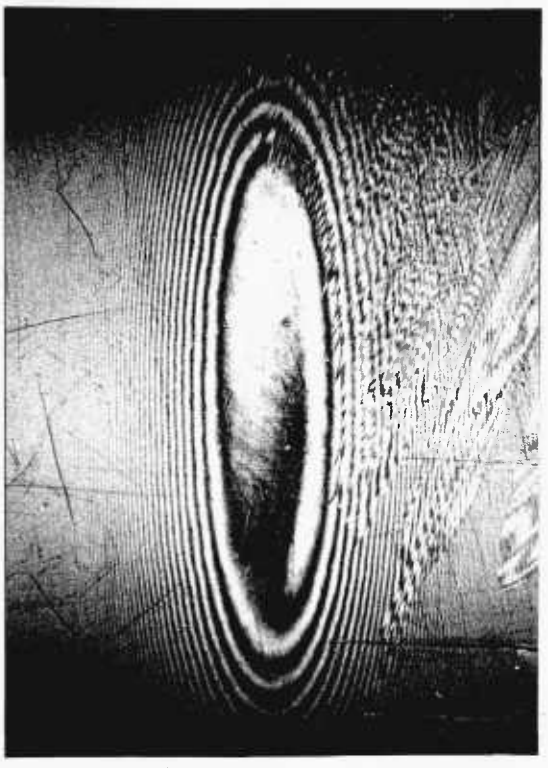
Fig. 5.4 Fringe patterns in a sliding contact - drive angle = 0°



(a) 1st dark fringe
$W^* = 1.67 \times 10^{-7}$



(b) 3rd dark fringe
$W^* = 1.67 \times 10^{-7}$



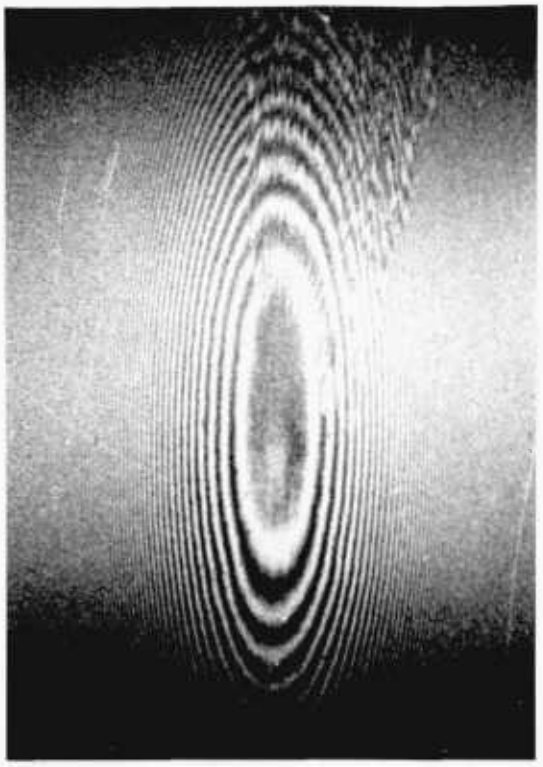
(c) 1st bright fringe
$W^* = 1.19 \times 10^{-6}$



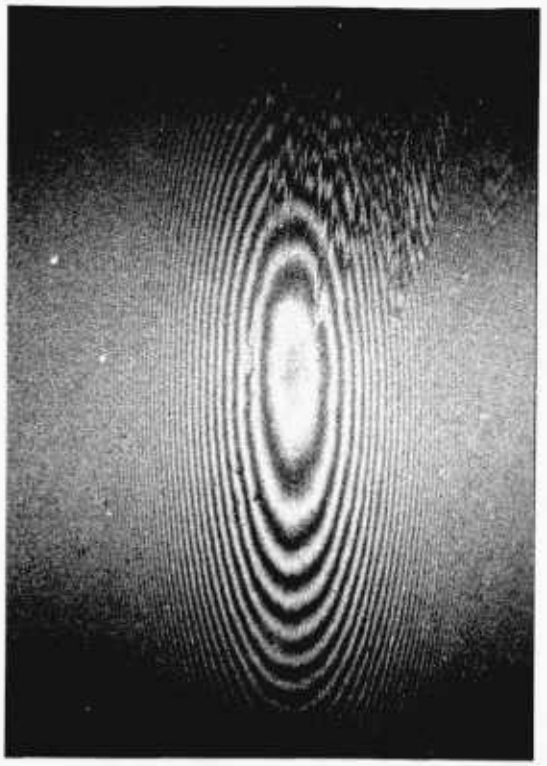
(d) 6th dark fringe
$W^* = 1.19 \times 10^{-6}$

MAGNIFICATION X 70

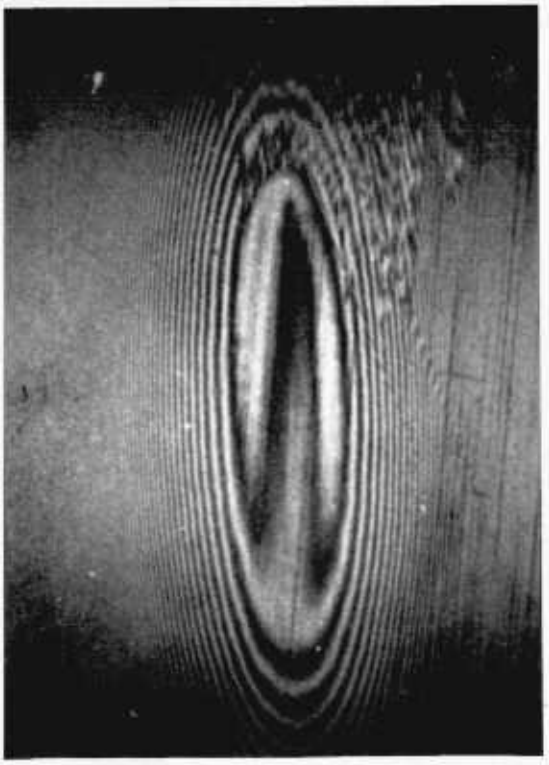
Fig. 5.5 Fringe patterns in a sliding contact - drive angle = 67°



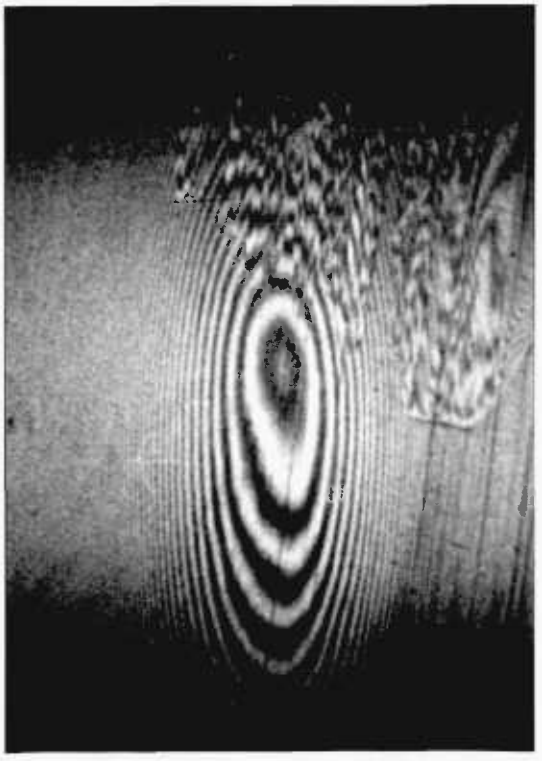
(a) 1st dark fringe
$W^* = 1.67 \times 10^{-7}$



(b) 3rd dark just visible
$W^* = 1.67 \times 10^{-7}$



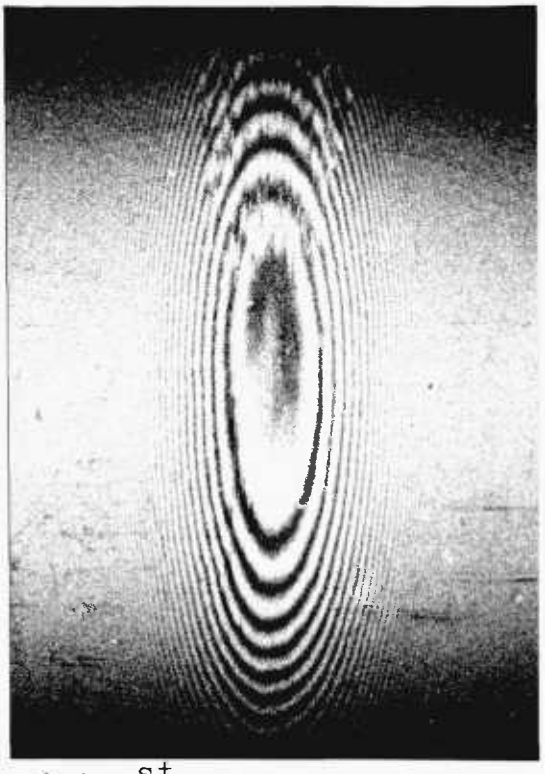
(c) 1st bright fringe
$W^* = 1.19 \times 10^{-6}$



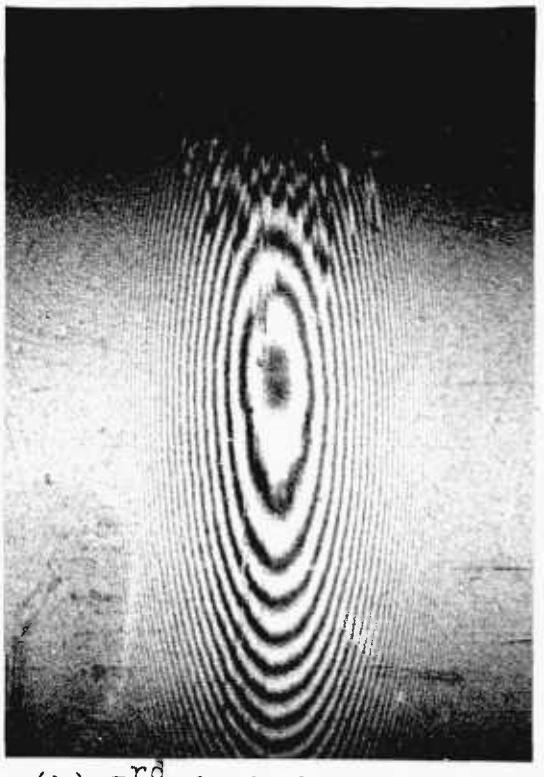
(d) 6th dark fringe
$W^* = 1.19 \times 10^{-6}$

MAGNIFICATION x 70

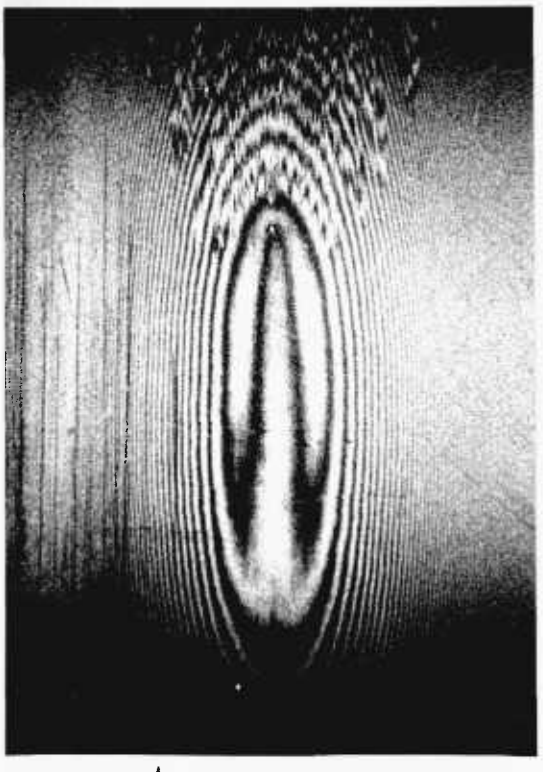
Fig. 5.6 Fringe patterns in a sliding contact - drive angle = 82°



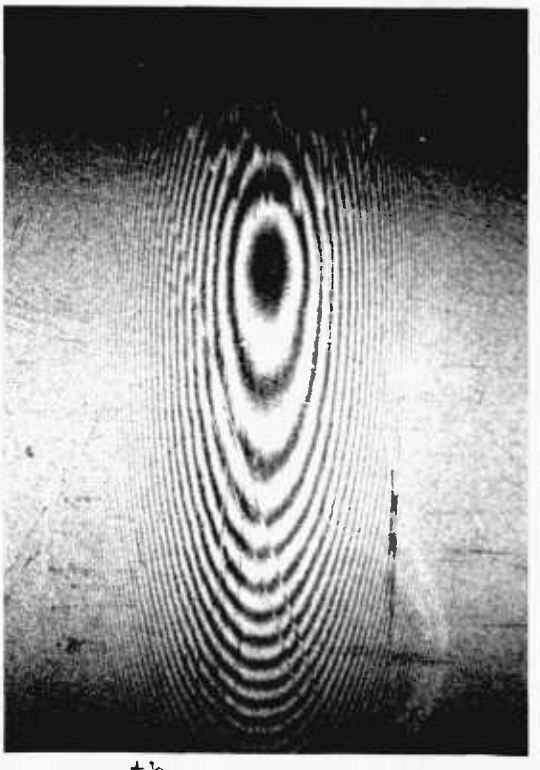
(a) 1st dark fringe
$W^* = 1.67 \times 10^{-7}$



(b) 3rd dark fringe
$W^* = 1.67 \times 10^{-7}$



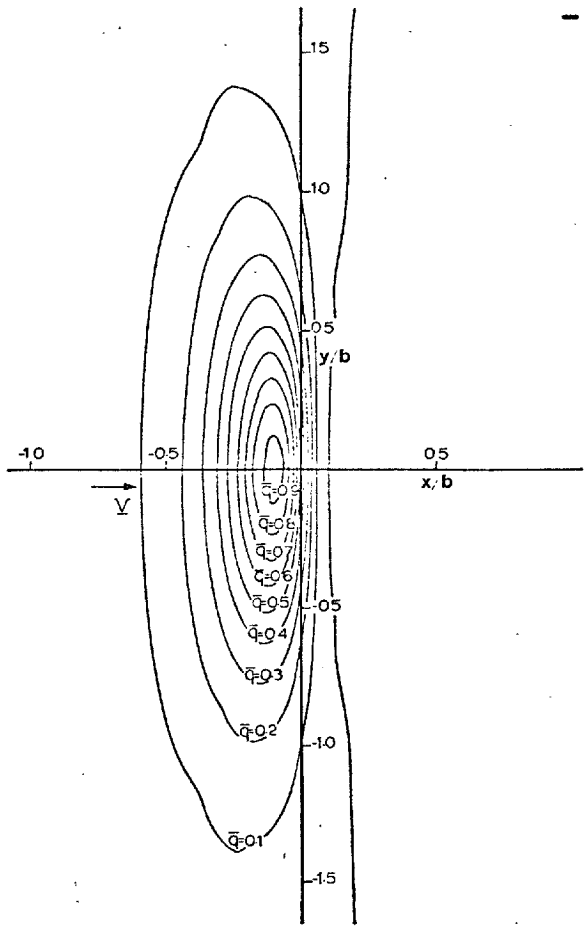
(c) 1st bright fringe
$W^* = 1.19 \times 10^{-6}$



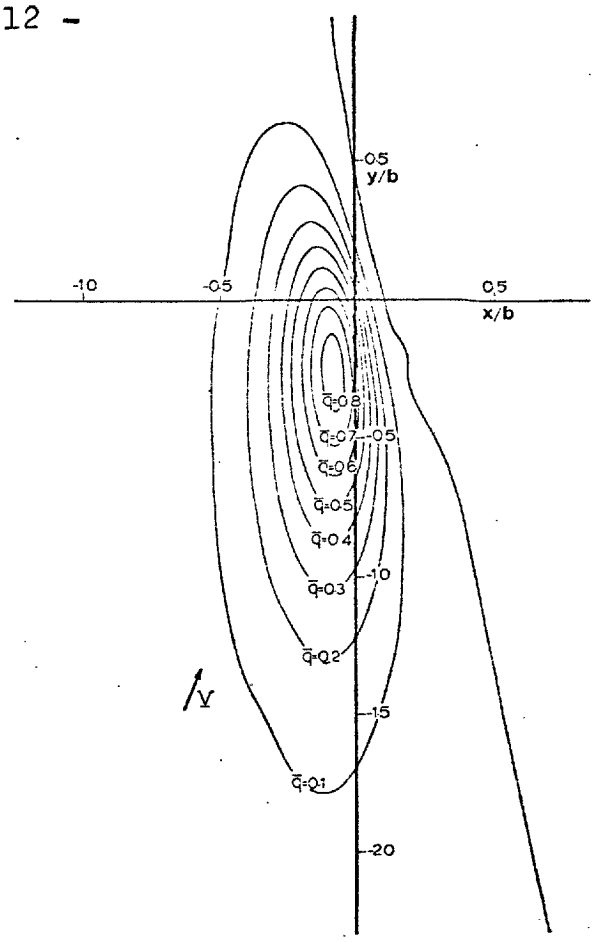
(d) 6th dark fringe
$W^* = 1.19 \times 10^{-6}$

MAGNIFICATION X 70

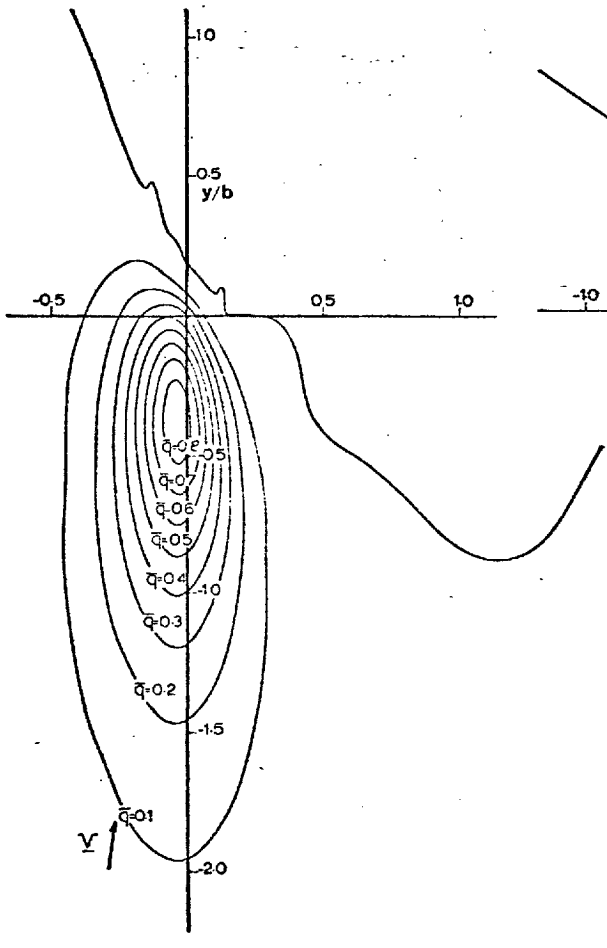
Fig. 5.7 Fringe patterns in a sliding contact - drive angle = 90°



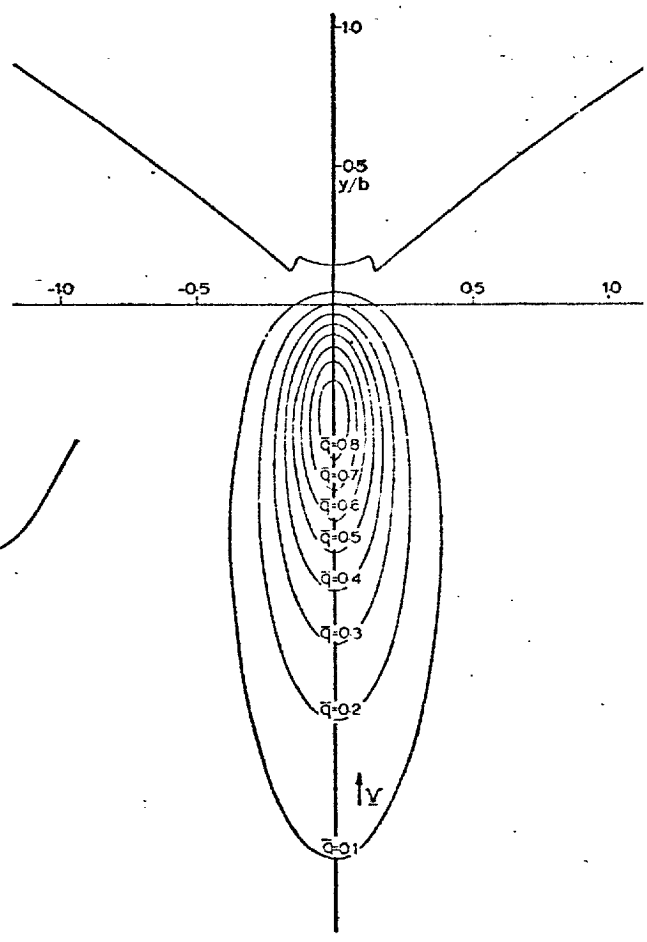
(a) $\theta = 0$ deg $H^*/W^*G^* = 3.1 \times 10^{-2}$
$\frac{U^*}{W^{*1.5}G^{*0.5}} = 5.0 \times 10^{-3}$



(b) $\theta = 67$ deg $H^*/W^*G^* = 3.5 \times 10^{-2}$
$\frac{U^*}{W^{*1.5}G^{*0.5}} = 1.1 \times 10^{-2}$



(c) $\theta = 82$ deg $H^*/W^*G^* = 3.5 \times 10^{-2}$
$\frac{U^*}{W^{*1.5}G^{*0.5}} = 1.4 \times 10^{-2}$



(d) $\theta = 90$ deg $H^*/W^*G^* = 3.5 \times 10^{-2}$
$\frac{U^*}{W^{*1.5}G^{*0.5}} = 1.5 \times 10^{-2}$

Fig. 5.8 Reduced pressure isobars from computer solution.

localised side closures. Over most of the contact the geometry is similar to that of a line contact. The shape suggests a pressure distribution which falls away quite gradually at the sides. On the other hand, when $\theta = 90^{\circ}$ (figure 5.7c) the minimum film wraps round the contact and the oil is entrained through a narrow passage in the centre. The pressure must climb up from a long inlet sweep, through a gradually changing geometry. At the sides, the fall away of pressure is more severe, causing the surfaces to spring out to form the characteristic side lobes seen in point contact (ref: 1).

At the intermediate angles of 67° (figure 5.5c) and 82° (figure 5.6c) the symmetry of the film shapes has been distorted by the modified pressure distribution. The bottom left has become an inlet and there is a localised uniform film thickness occurring near the centre. Towards the outlet, in the top right, end closure has occurred followed by the cavitation wake lined up with the velocity vector. Most of this film shape redistribution must be due to pressure rather than shear forces which are, at most, only 10% of the load under pure sliding (ref: 8).

5.3.2 Pressure distribution

Using the theory described in section 5.2, non-dimensional isobars have been produced for the various drive angles used experimentally (figure 5.8). It is instructive to compare the isobars with the fringe photographs for the corresponding angles and conditions. This does not necessarily imply very light loads for the film is practically undistorted in figures 5.4d to 5.7d where the load is high, but there is also a high value of ∇. When θ is large, as in figures 5.8 b and c, the direction of $\underline{V}$ causes side leakage to reduce in the lower part of the region and to increase in the upper part. Consequently, there

is more oil available to fill the gap in the lower part and cavitation occurs later. The shape of the boundary in the vicinity of the contact is similar to that in the corresponding fringe photographs. It is interesting to note that the pattern follows, quite faithfully, the direction of $\underline{V}$.

5.3.3 Cavitation

Considering, for simplicity, only the 0° case where sliding is along the groove, examination of figures 5.4a and 5.4b demonstrates the effect of speed on the cavitation boundary, since all other things being equal, a higher speed is required to reach a thick film. As the speed increases, the part of the cavitation boundary close to the contact centre moves out slightly. In this region the film shape causes side leakage to be low and the position of the boundary is governed by the locus of the x-direction local pressure maxima. These maxima move towards the inlet with the increase of U (V = 0). Then, in accordance with flow continuity requirements, cavitation occurs later.

The half-Sommerfeld boundary condition adopted by Kapitza(4) and Snidle (10) implies an increase of flow rate at x = 0 which is impossible. If the Reynold's condition is adopted, there is no difficulty about disposing of the excess oil flow because the oil can cavitate and break into streamers filling only a part of the gap (ref; 7)

For discs, Cameron (7) gives the position of film rupture as:

$$x / (2Rh_o)^{\frac{1}{2}} = 0.475 \qquad -5.17$$

If we assume no side leakage, then this condition can be extended to an elliptical contact, to give an approximate expression for the shape of the cavitation boundary. The minimum film at each position (h_o') is given by:

$$h_o' = h_o + By^2 \qquad -5.18$$

Substituting 5.18 in 5.17, and remembering that Aa^2/h_o has been chosen to be unity, this expression may be written as:-

$$\bar{x}^2 - \bar{y}^2\left[\frac{B}{A}\left(\frac{b}{a}\right)^2\right] = 0.226 \qquad -5.19$$

Figure 5.9 shows the form of equation 5.19 with the boundary of figure 5.8a. Comparison with an experimental boundary such as figure 5.4b shows that the actual shape of the boundary is modified further out by side leakage. This causes the wake angle to decrease with increase of speed (compare figures 5.4c and d).

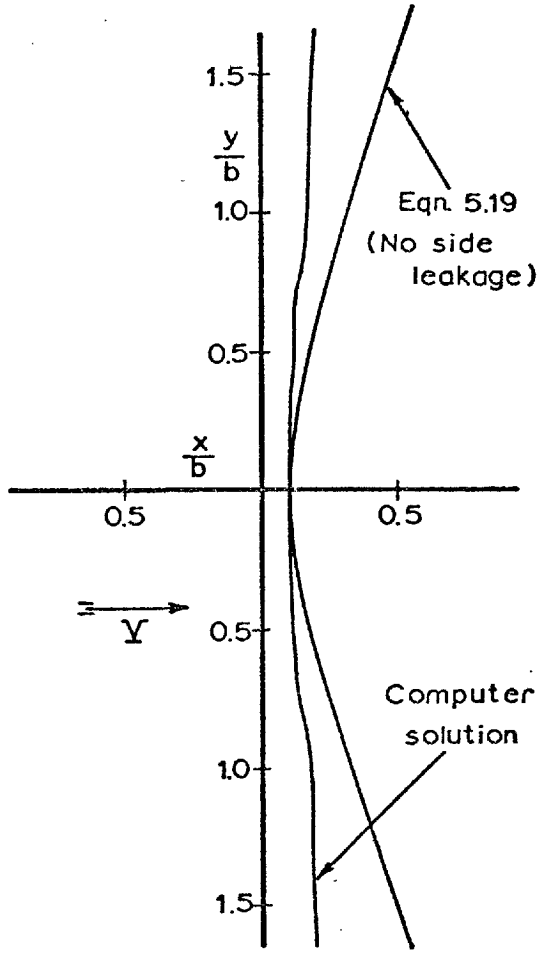
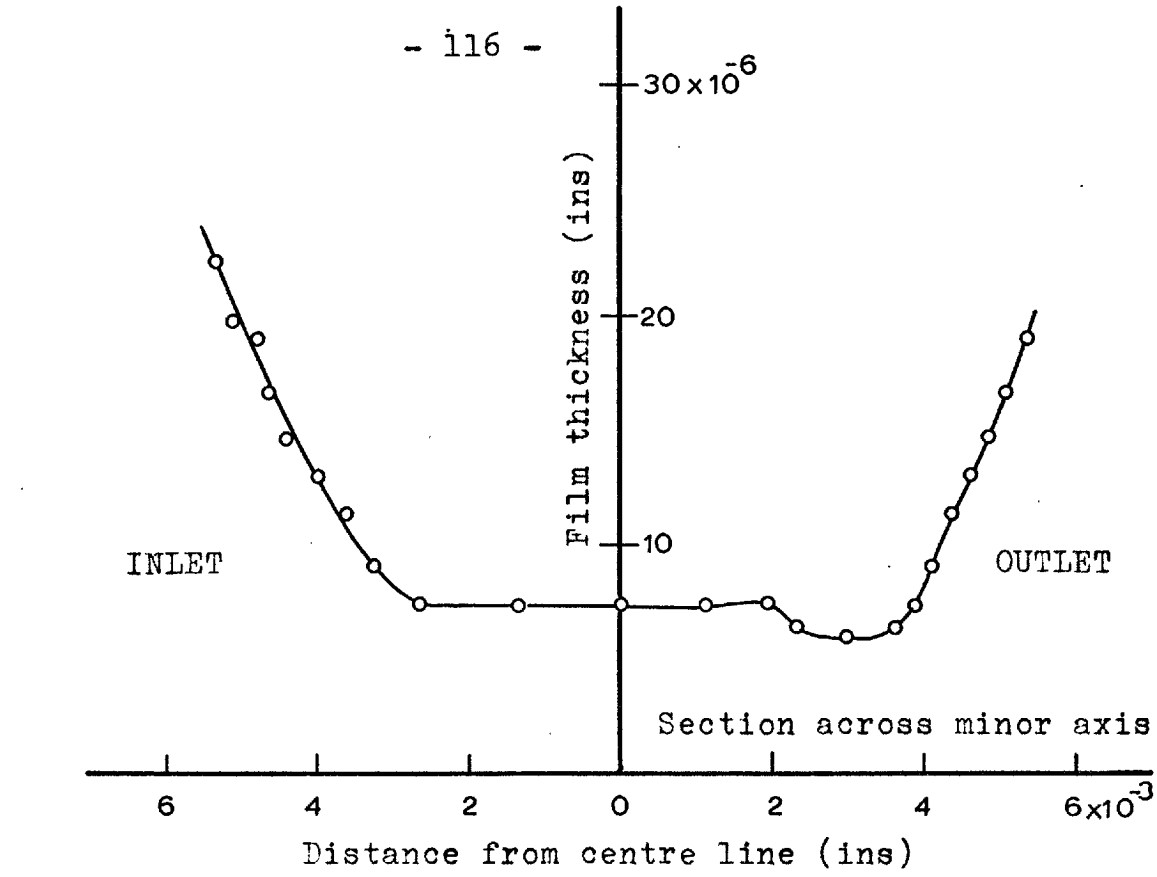


Fig. 5.9 Cavitation boundaries.

It is interesting to note that early cavitation can be caused by a scratch on one of the surfaces. In figure 5.7b, for instance, a single cavitation streamer starts almost in the centre of the contact. The scratch acts as a drain for lubricant and so reduces the pressure build-up, allowing cavitation to take place earlier in the exit region.

It is also of interest to note that although the blemish passing through the contact in figure 5.4d is severe enough to distort the fringe pattern, its effect has not been felt downstream, the position of the cavitation boundary being unaffected.



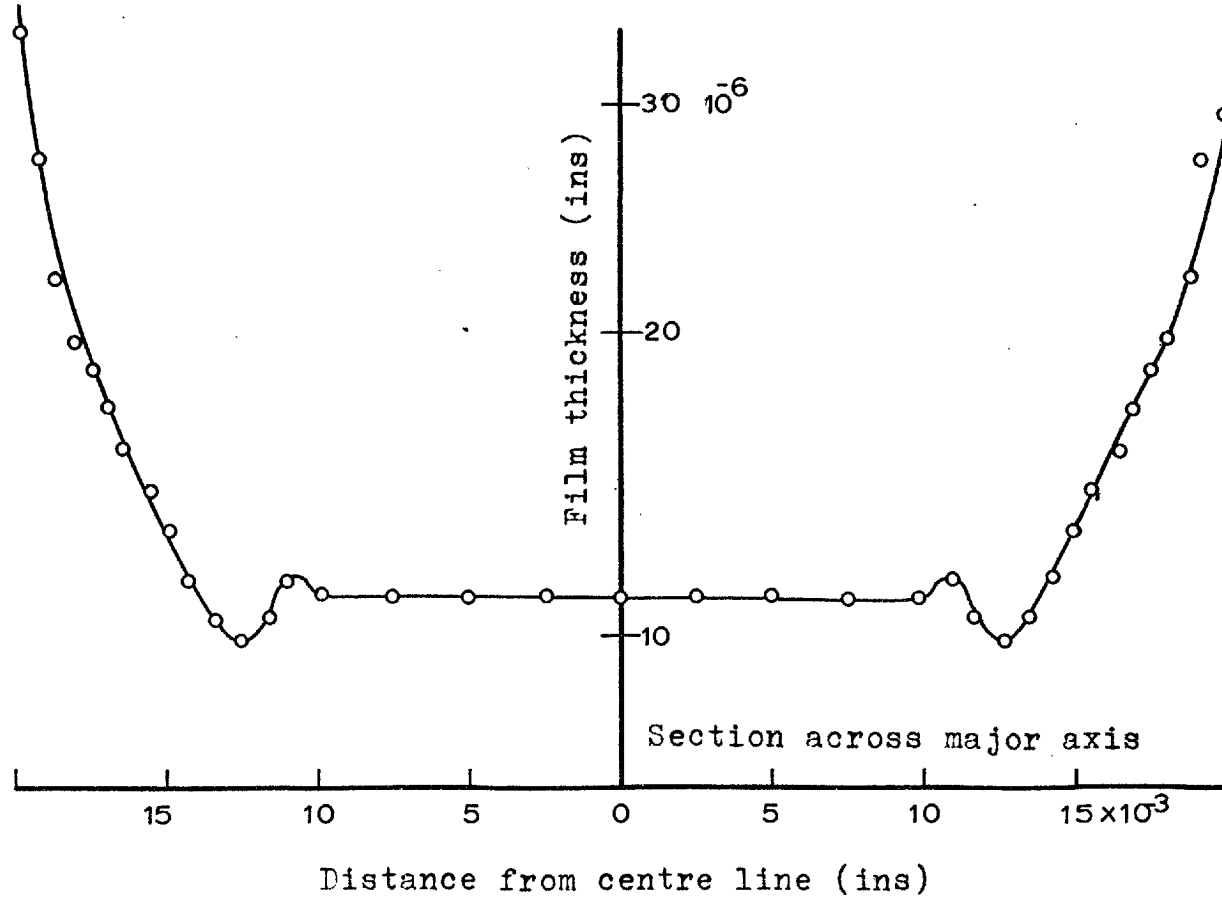
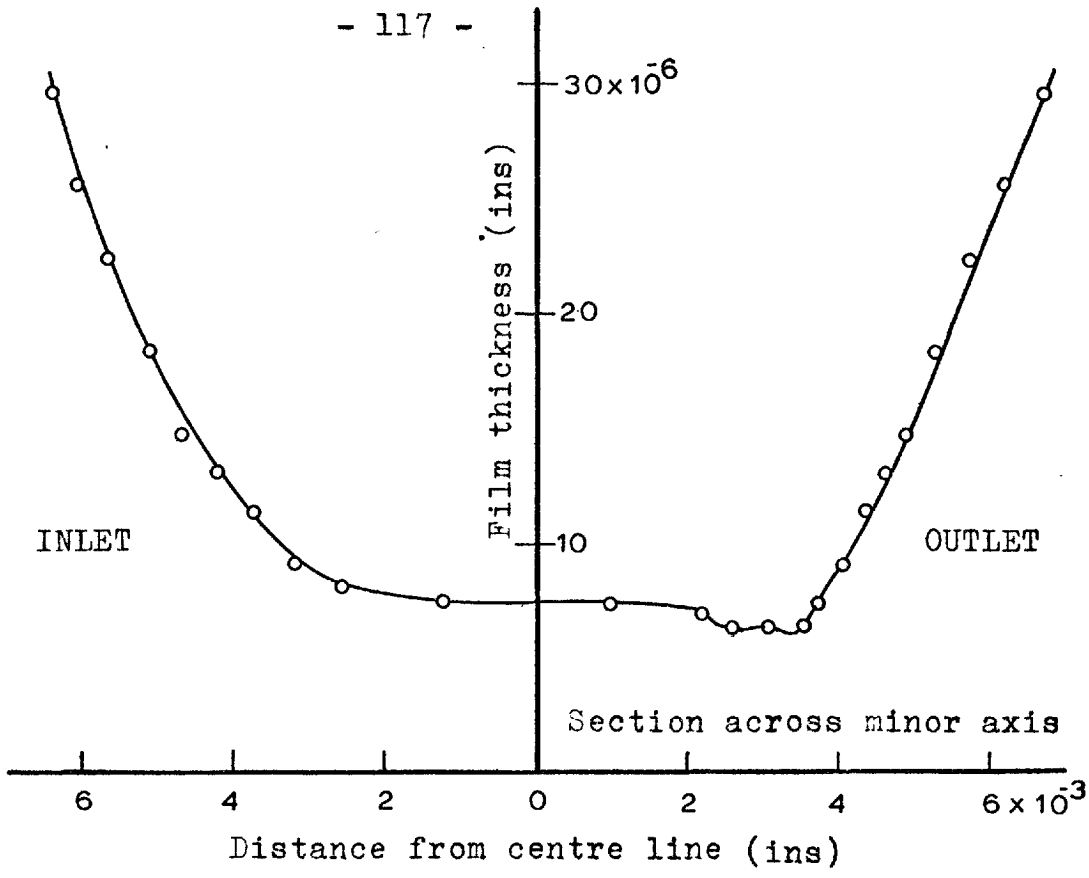


Fig. 5.10 Film profiles in sliding for drive angle of 0 deg.

$U^*=1.32\times10^{-11}$ $H_{min}^*= 1.23\times10^{-5}$ $W^*=8.5\times10^{-7}$



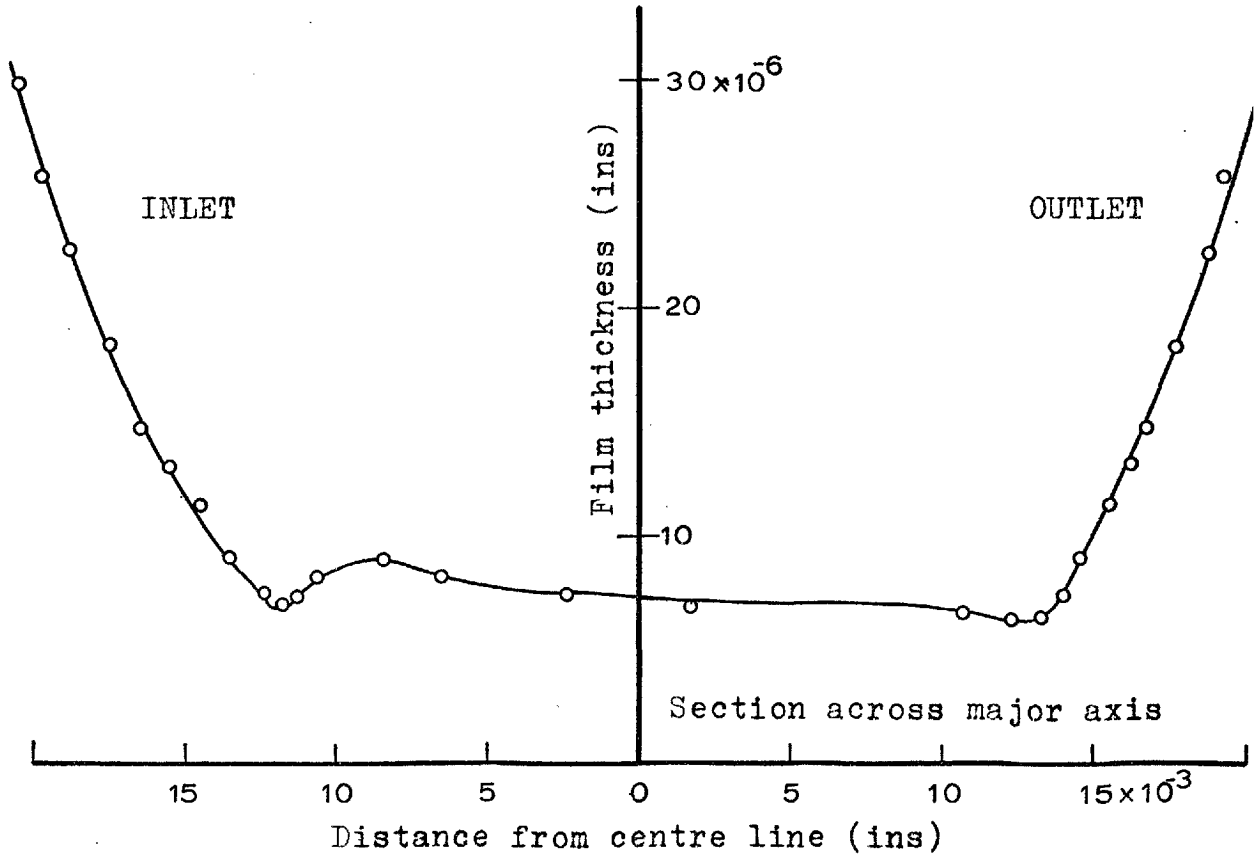
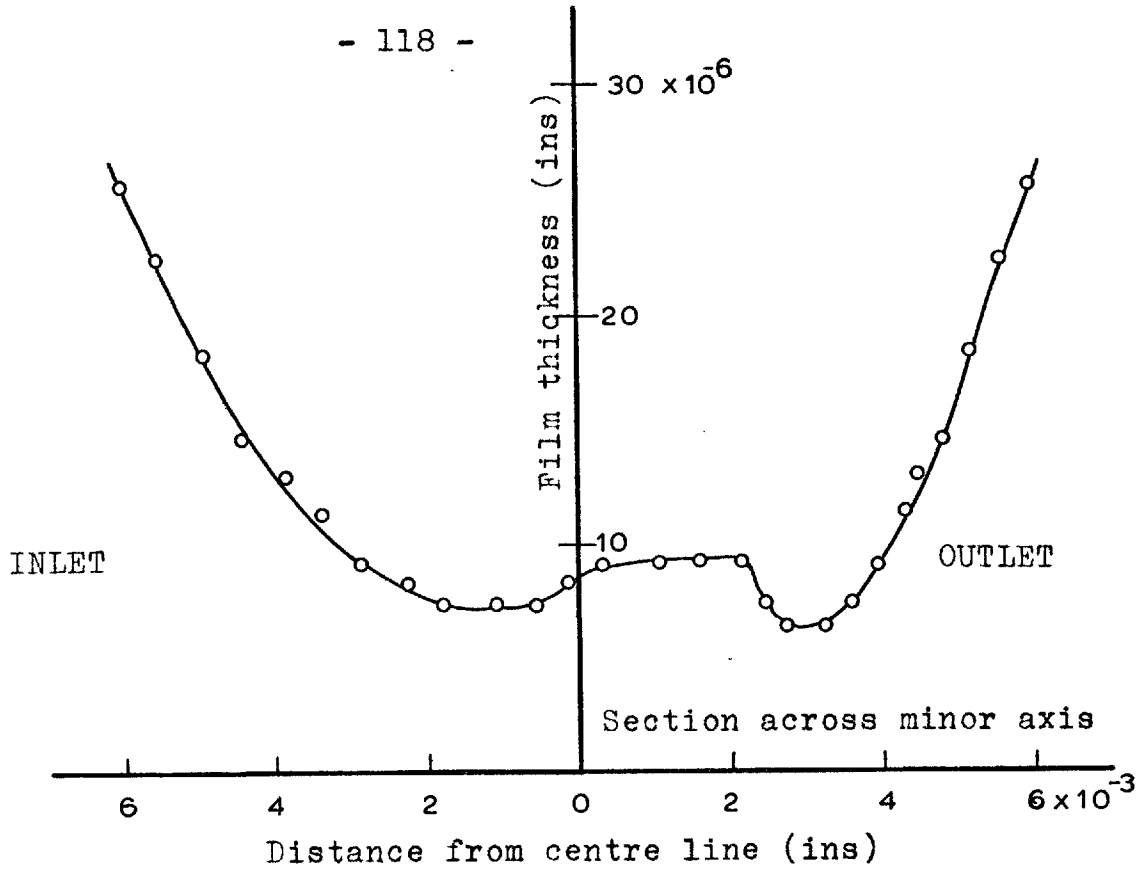


Fig. 5.11 Film profiles in sliding for drive angle of 38 deg.

$U^*=1.66\times10^{-11}$ $H_{min}^*=1.23\times10^{-5}$ $W^*=8.5\times10^{-7}$



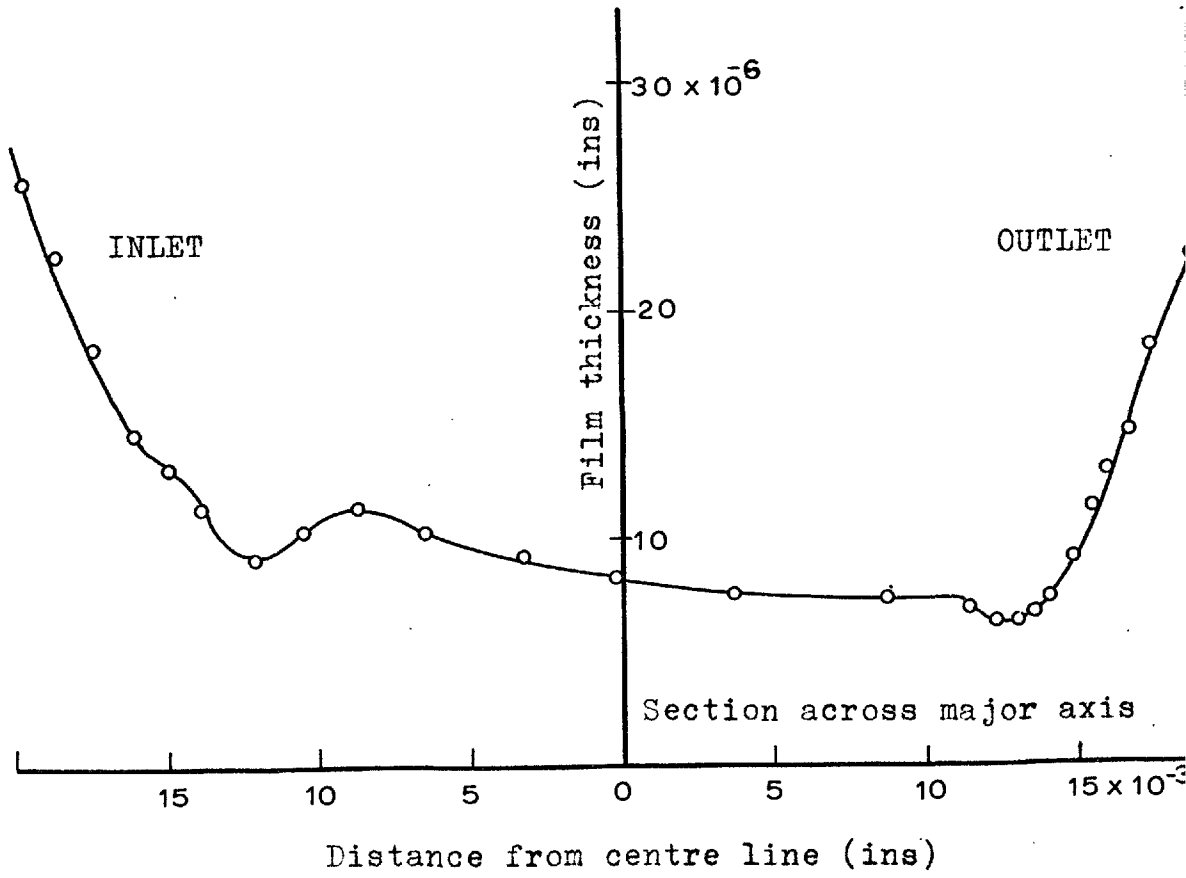
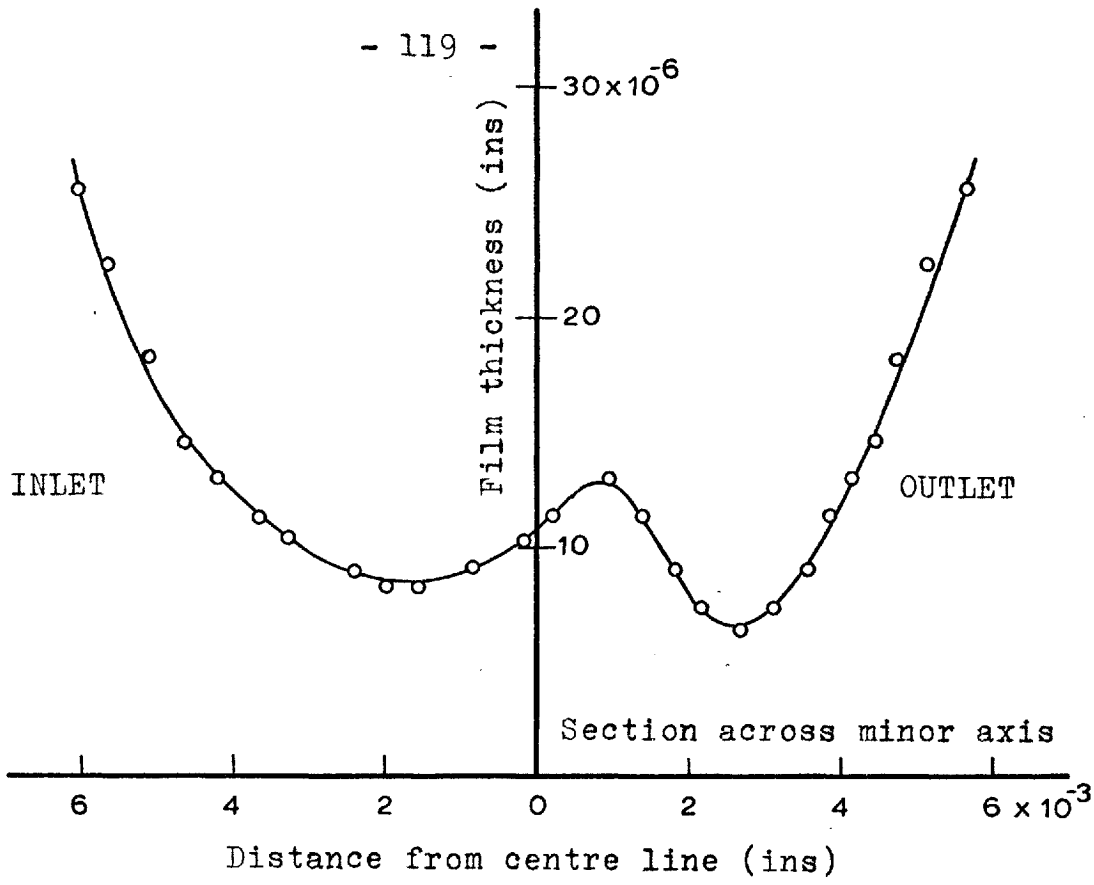


Fig. 5.12 Film profiles in sliding for drive angle of 54 deg.

$U^*=2.45\times10^{-11}$ $H_{min}^*=1.23\times10^{-5}$ $W^*=8.5\times10^{-7}$



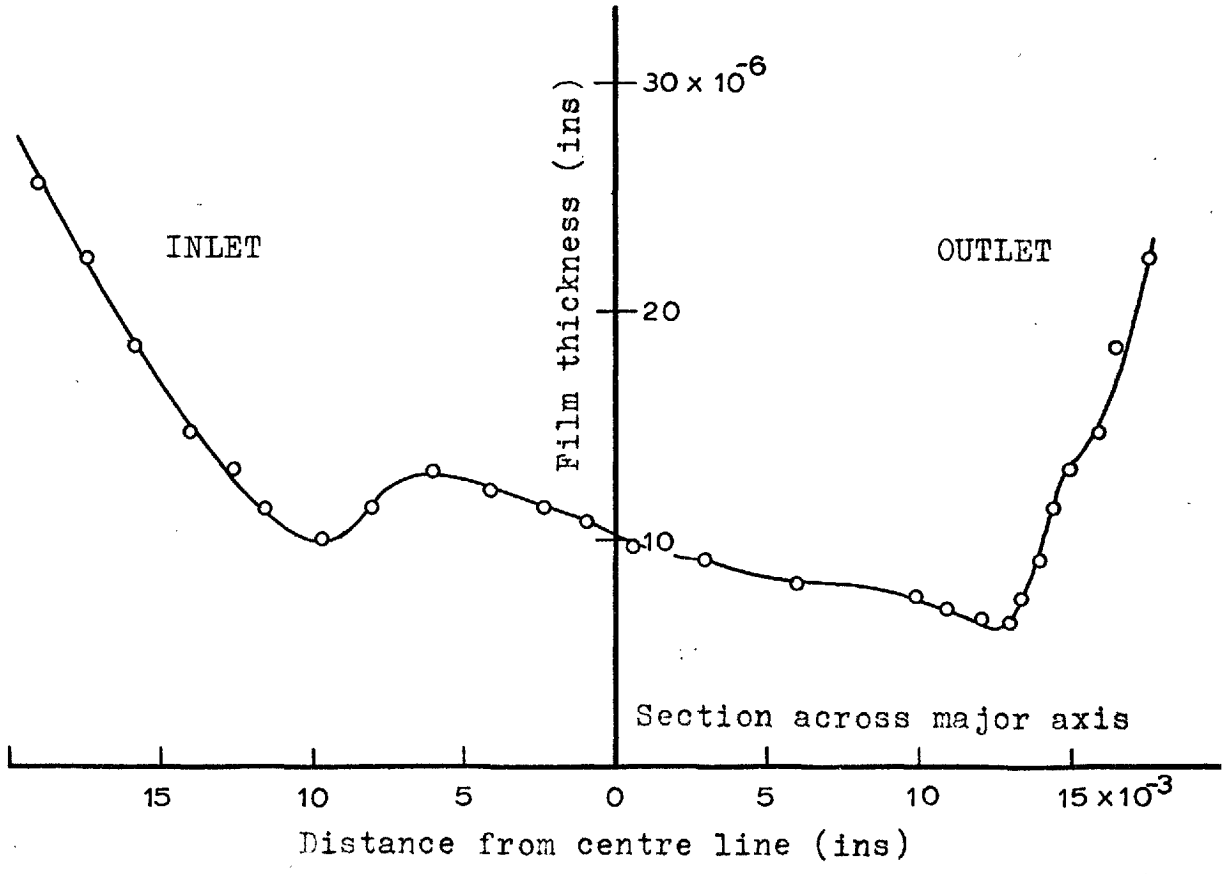
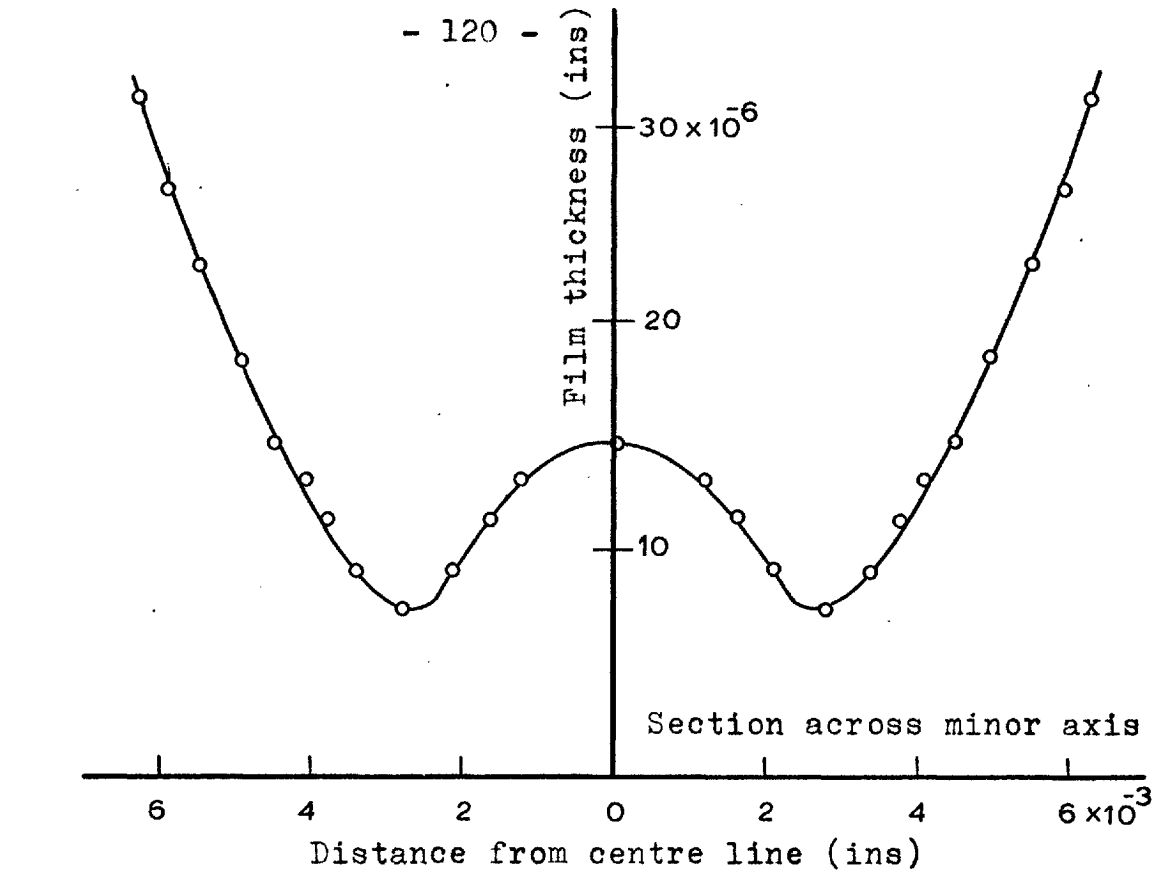


Fig. 5.13 Film profiles in sliding for drive angle of 75 deg.

$U^*=3.96\times10^{-11}$ $H_{min}^*=1.23\times10^{-5}$ $W^*=8.5\times10^{-7}$



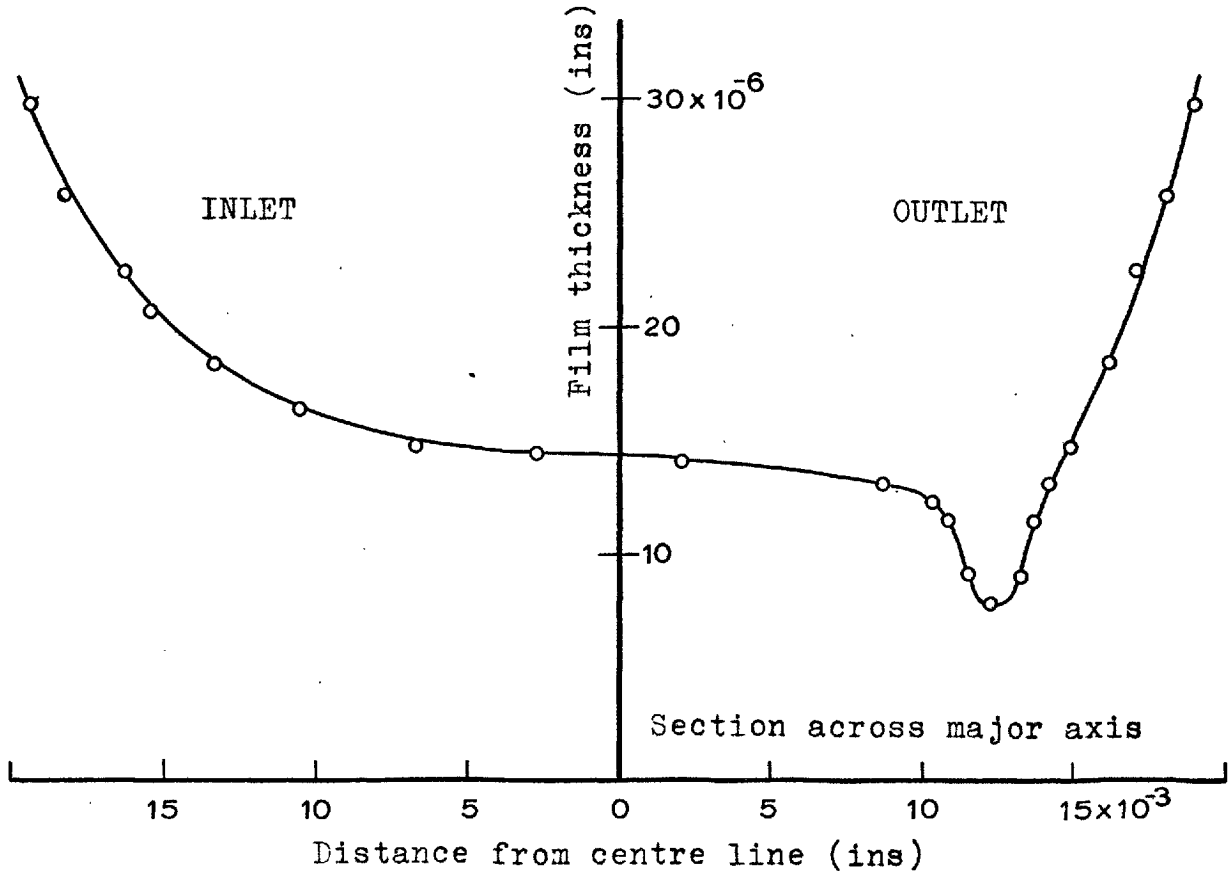
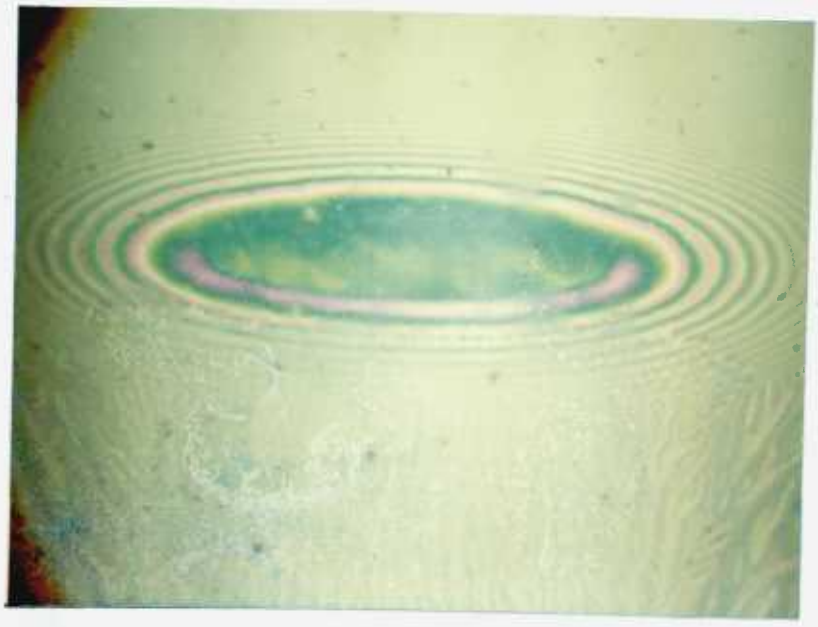


Fig. 5.14 Film profiles in sliding for drive angle of 90 deg.

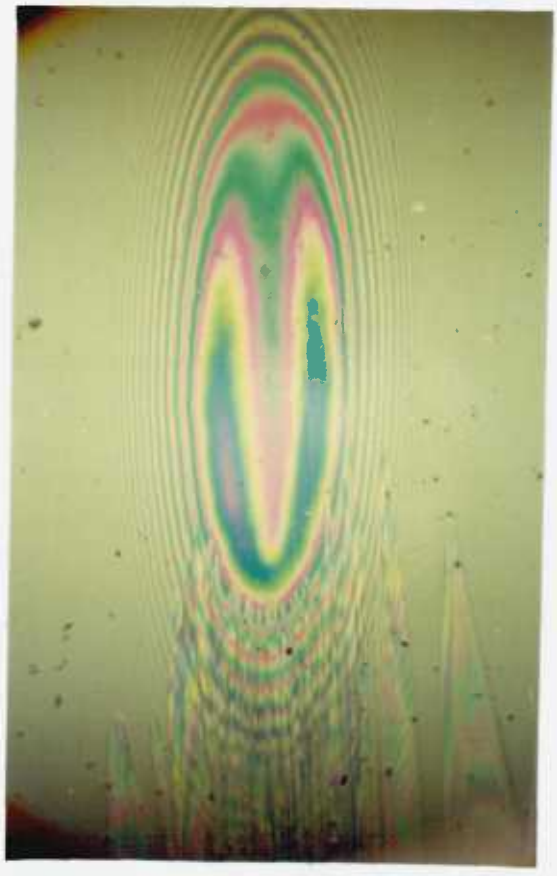
$U^*=6.28\times10^{-11}$ $H_{min}^*=1.23\times10^{-5}$ $W^*=8.5\times10^{-7}$



Direction of oil flow

a) Rolling contact $\theta = 0^{\circ}$

$U^* = 1.83 \times 10^{-11}$ $H_{min}^* = 1.47 \times 10^{-5}$ $W^* = 1.53 \times 10^{-6}$



b) Sliding contact $\theta = 90^{\circ}$

$U^* = 7.61 \times 10^{-11}$ $H_{min}^* = 1.47 \times 10^{-5}$ $W^* = 1.53 \times 10^{-6}$

Fig. 5.15 Fringe patterns at drive angles of 0° & 90°.

5.3.4 Film profiles in sliding

The shape of the film was plotted from measurements made on the photographs using a travelling microscope. The use of colour photographs for profile measurements was most accurate because of the close spacing of the fringes (described in chapter 3). However the loss of colour clarity at high film thicknesses places a restriction on their usefulness, since details of the inlet and outlet regions are thus hidden. Black and white photographs carry more information about the film shape in these regions, but are less accurate elsewhere. When measuring black and white photographs, therefore, both bright and dark fringes were used to increase accuracy.

As film profiles can be produced ad libitum, the number presented here has been deliberately restricted to those shown in figures 5.10 to 5.14, for five different drive angles. These profiles were taken from colour photographs obtained using the 'rolling' raceway in the sliding mode. Each of the figures shows a section along each axis of the contact ellipse. Together they demonstrate how the contact changes from the 0° to the 90° case. It should be noted that there is a change of lateral scale between the upper and lower profiles in each of the figures.

Note that the profiles have hardly changed at all between figures 5.10 and 5.11, although the angle is nearly 40°. When angling has reached 54°, however, the changes have become noticeable and by 75° the major axis profile has taken on the characteristic end closure and the minor axis profile already has side lobes. Further angling to the limit of 90° has the effect of making these closures far more pronounced.

The drastic change in shape resulting from a high degree of angling is best illustrated by the photographs of figure 5.15

Since these are in colour, the fringe spacing in the central regions is very close and reveals details otherwise hidden. The end closure in the 0° case is very clearly demonstrated and for the 90° case, it can be seen that the minimum film occurs at the side lobes - a fact not evident from examination of the corresponding black and white photograph of figure 5.7c.

5.3.5 Film thickness in sliding

In order to show how the oil film alters with changes in the external parameters, graphs have been plotted between the appropriate non-dimensional groups discussed in the theory. The two thicknesses of interest are the central film thickness h_o, and the minimum h_{min} wherever it occurs. Figures 5.16 to 5.21 show how the minimum film H^*_{min} varies with U^* and W^* for different θ, while figures 5.22 to 5.26 show how the central film H^*_o varies. Following the usual convention the plots are logarithmic so that a relation of the form $H^* \propto U^{*n}$ will appear as a straight line.

The following observations can be made.

1. For a given value of G^* (constant at 2,906) only two groups are necessary, despite the range of conditions. Gohar (3) has noted this effect for point contact. His experimental results can be expressed as:-

$$\frac{H_o^*}{W^*G^*} \simeq 1.28 \left[\frac{U^*}{W^{*3/2}G^{*1/2}} \right]^{0.7} \left(W^*G^{*3} \right)^{-0.05} \qquad -5.20$$

He concludes that changes in the group (W^*G^{*3}) hardly affect (H_o^* / W^*G^*).

2. In figures 5.16 to 5.21, for H^*_{min}, the slope changes from about 1.75 for undistorted contacts to about 0.78 when the conditions are full EHL. The theory described in the second section of this chapter is shown on these graphs and agrees

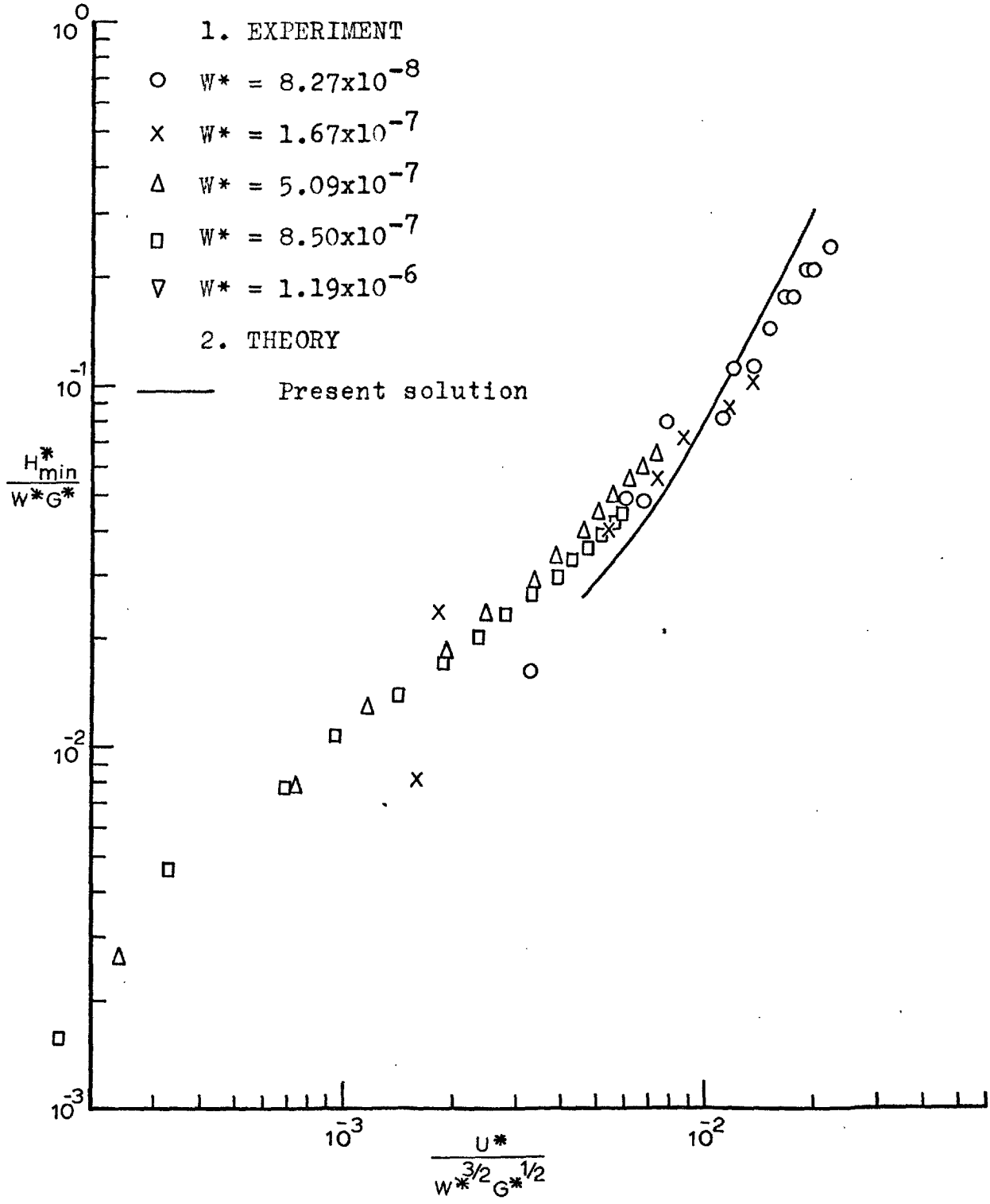


Fig. 5.16 Minimum film thickness group vs. speed group for drive angle of 0 deg.(Sliding contact)

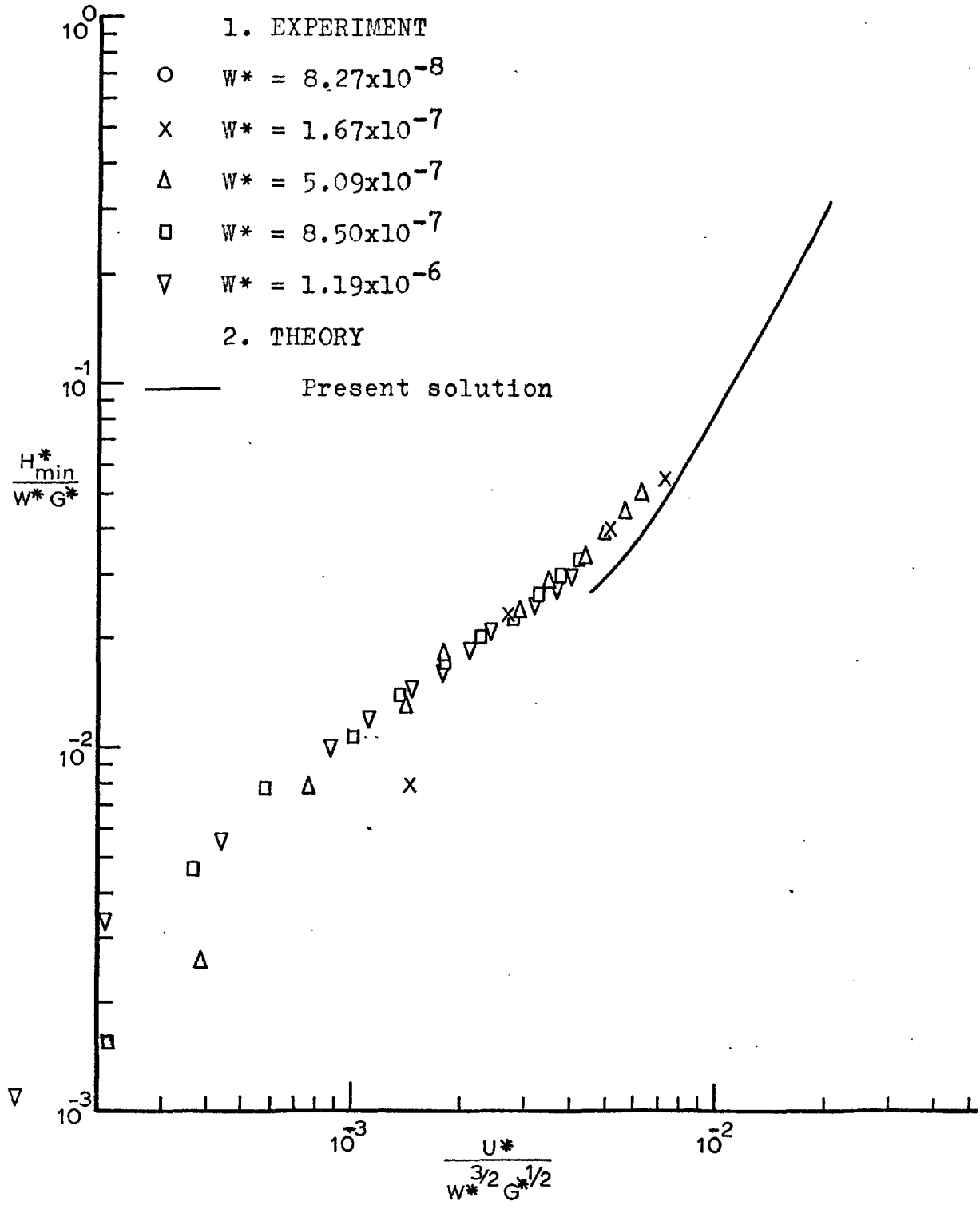


Fig. 5.17 Minimum film thickness group vs. speed group for drive angle of 10 deg. (Sliding contact)

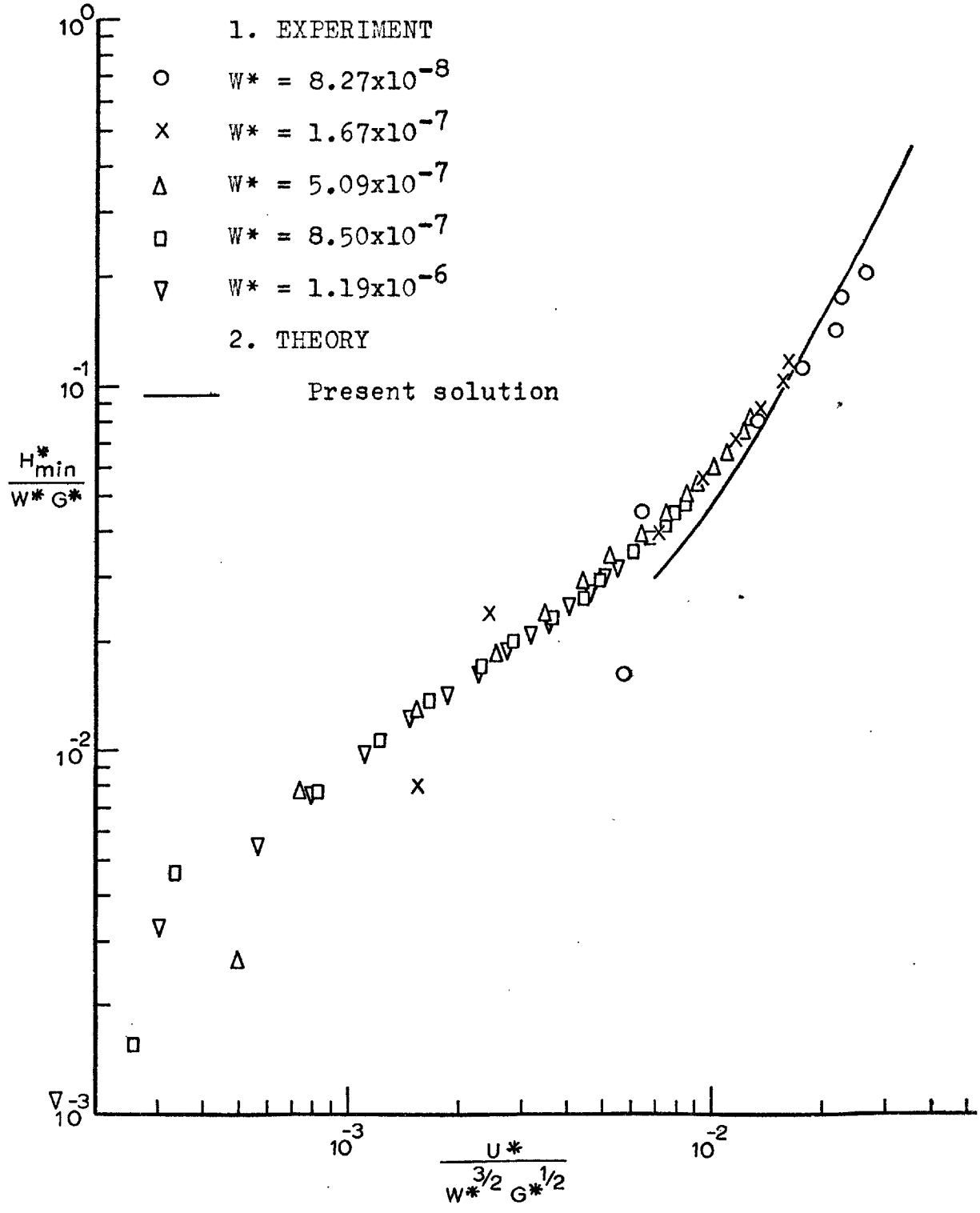


Fig. 5.18 Minimum film thickness group vs. speed group for drive angle of 50 deg. (Sliding contact)

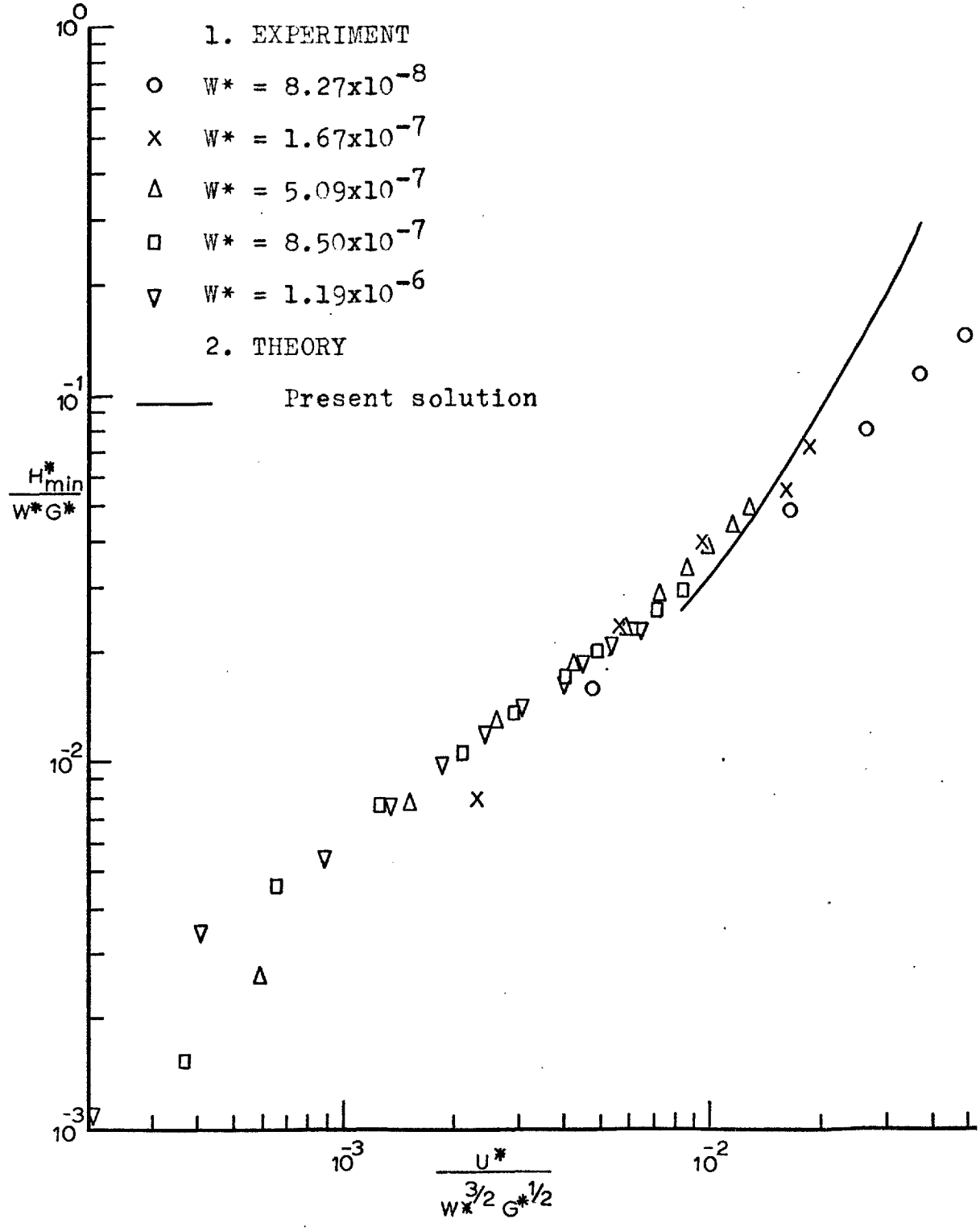


Fig. 5.19 Minimum film thickness group vs. speed group for drive angle of 67 deg. (Sliding contact)

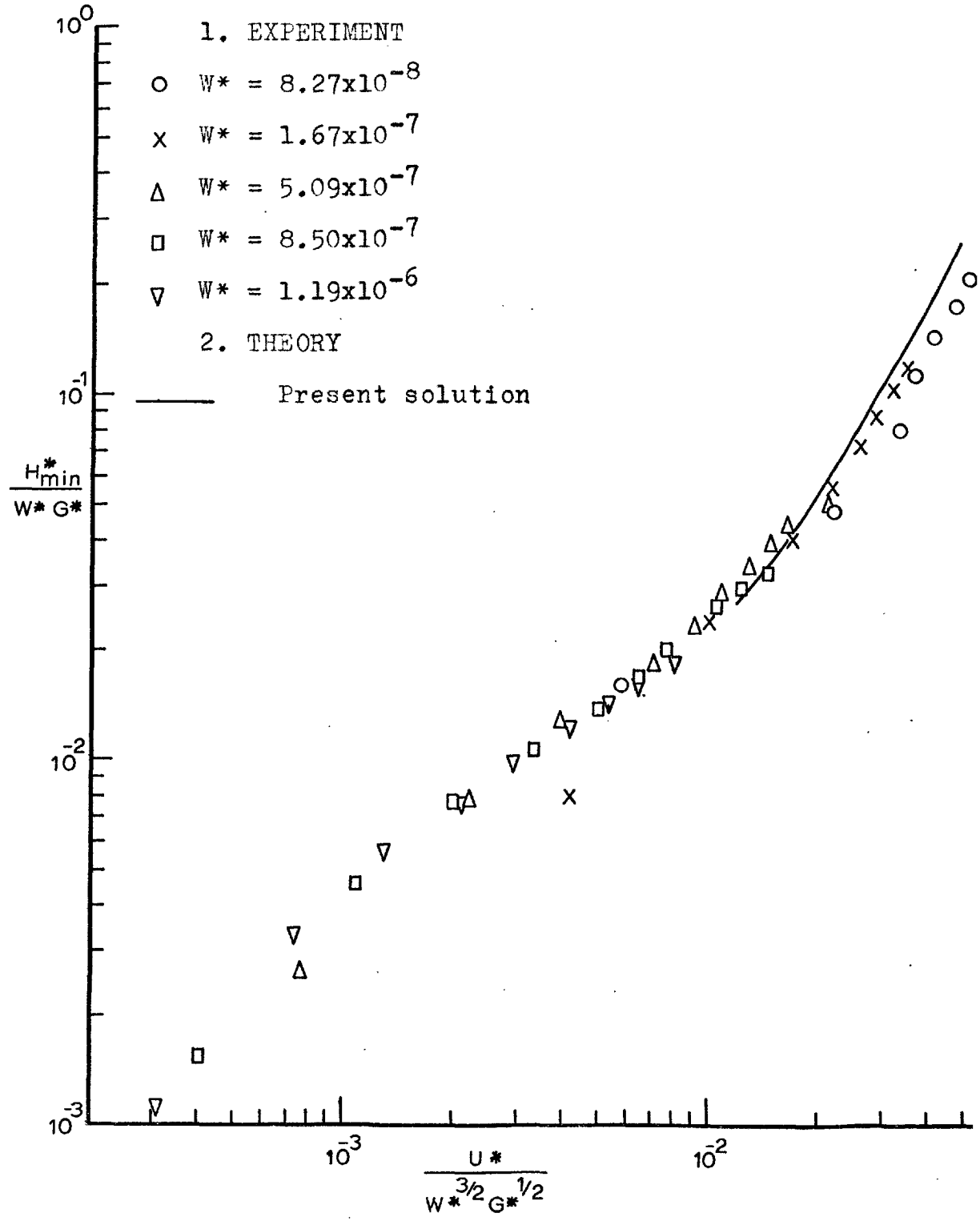


Fig. 5.20 Minimum film thickness group vs. speed group for drive angle of 82 deg. (Sliding contact)

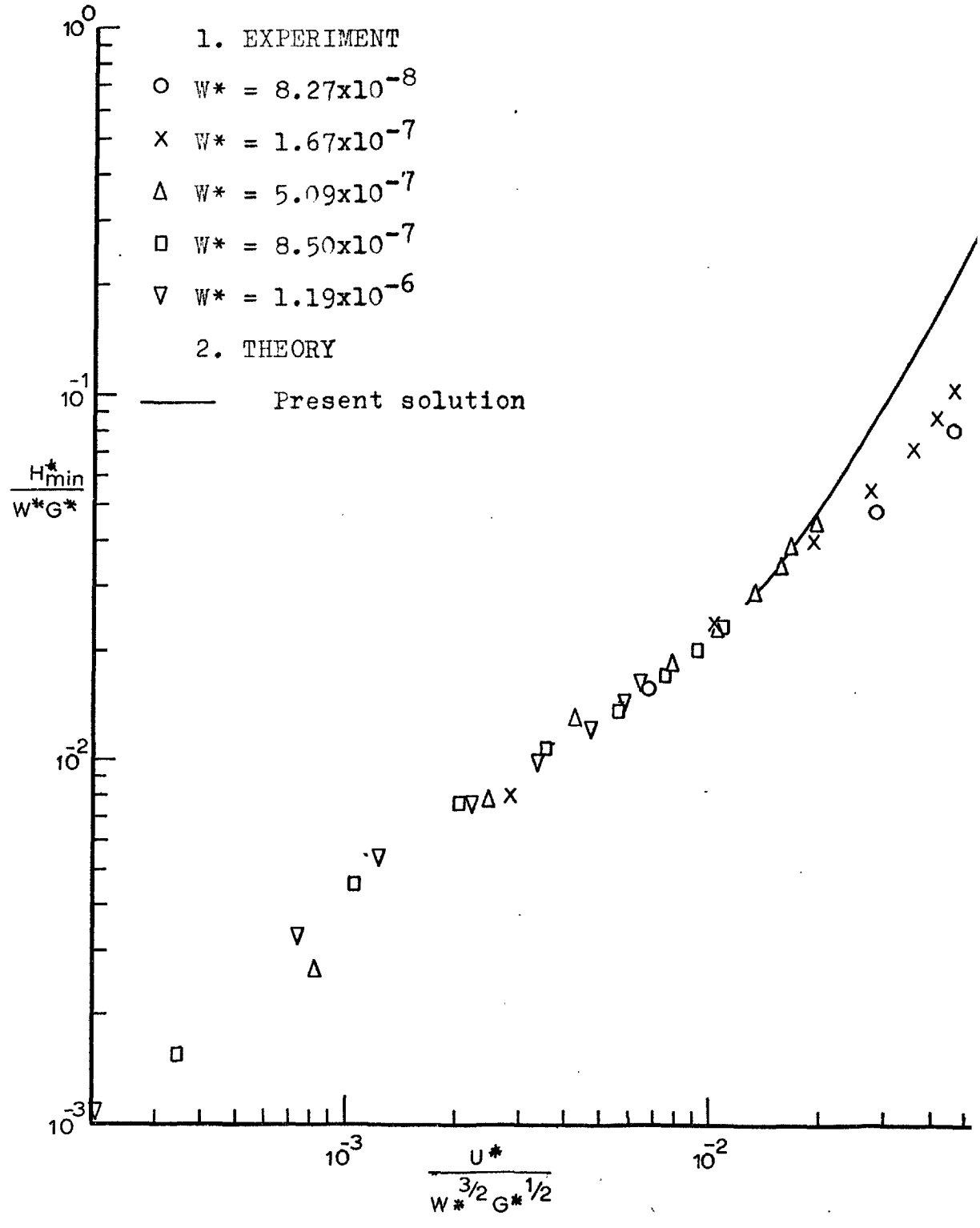


Fig. 5. 21 Minimum film thickness group vs. speed group for drive angle of 90 deg. (Sliding contact)

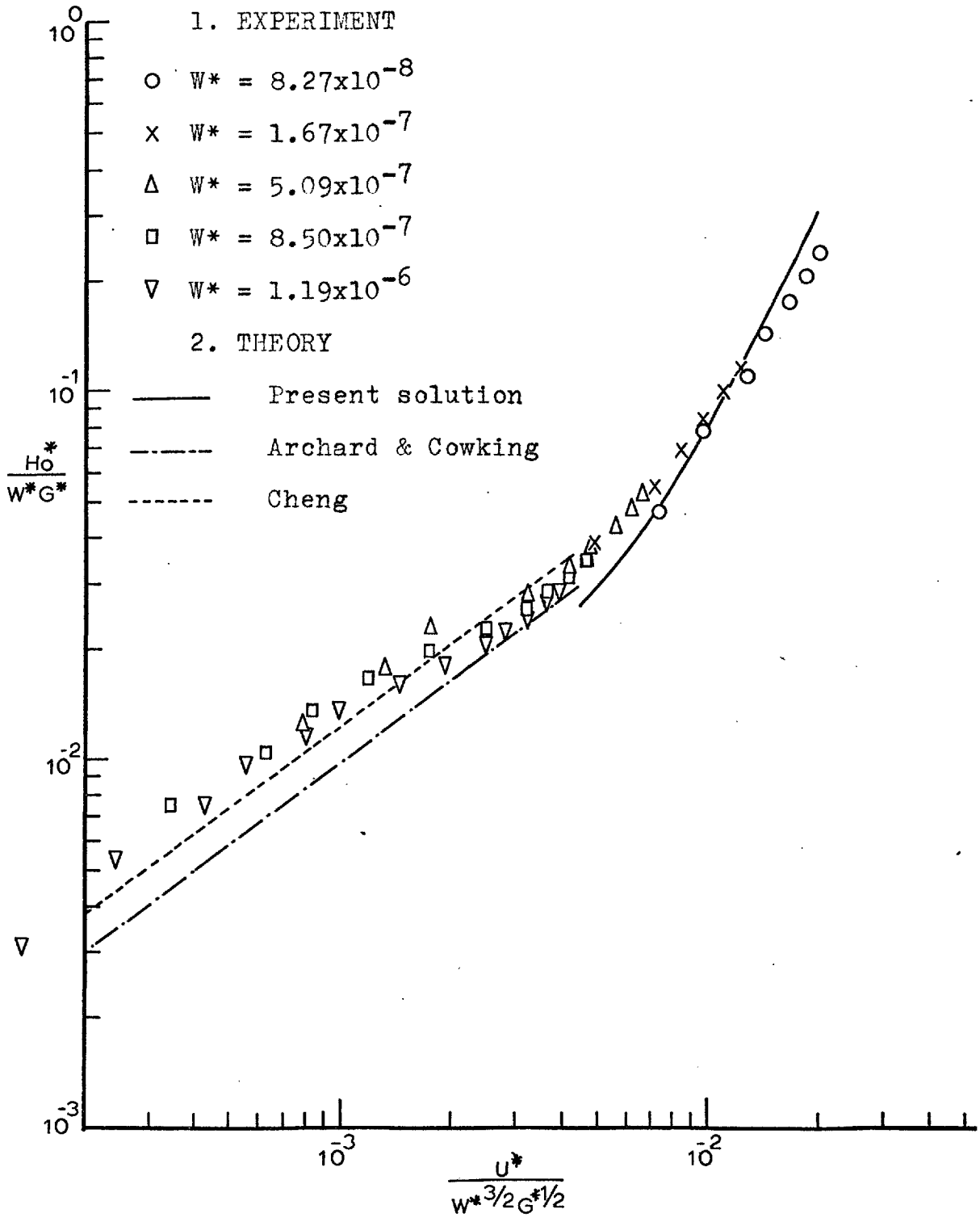


Fig. 5.22 Central film thickness group vs. speed group for drive angle of 0 deg.(Sliding contact)

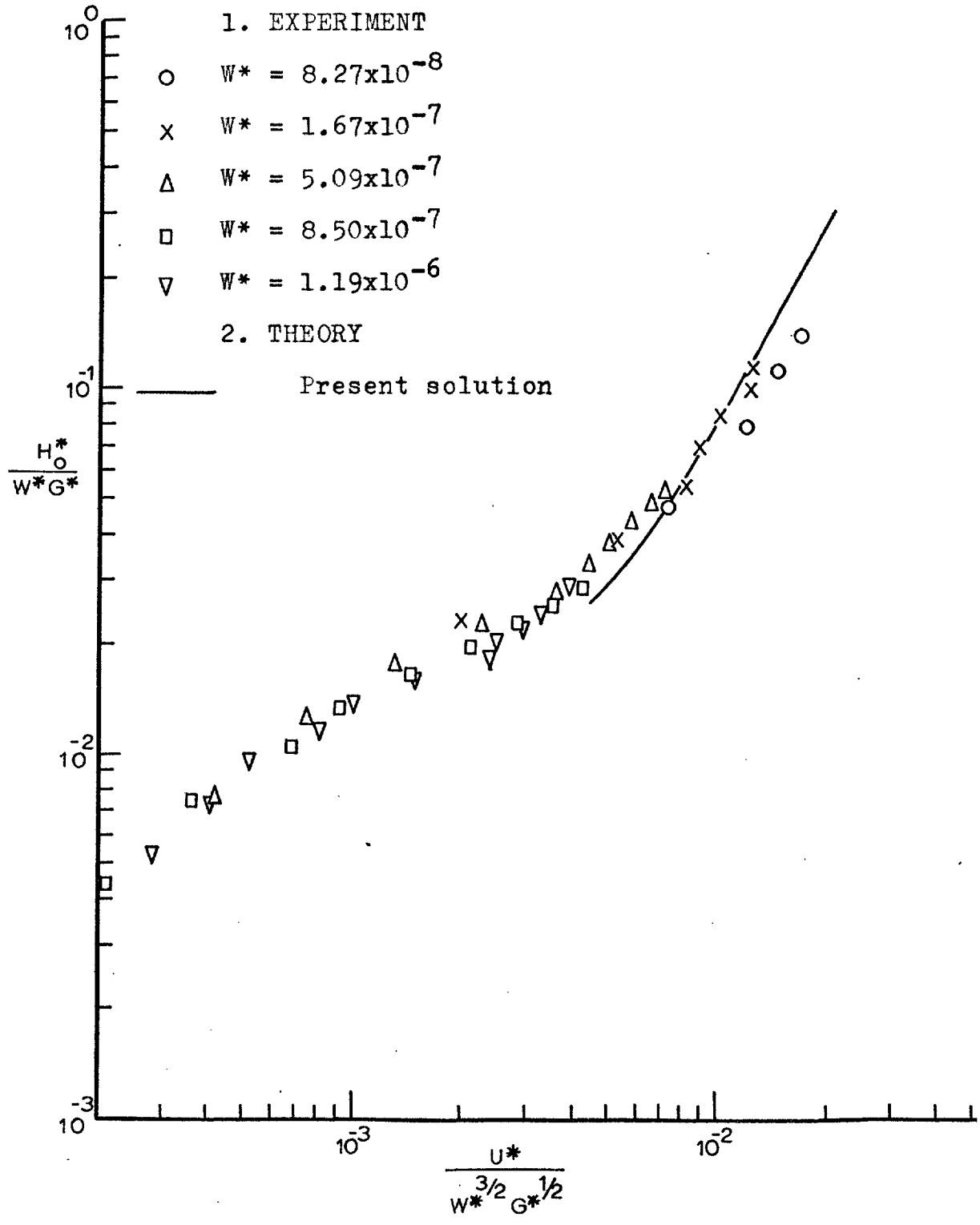


Fig. 5.23 Central film thickness group vs. speed group for drive angle of 10 deg. (Sliding contact)

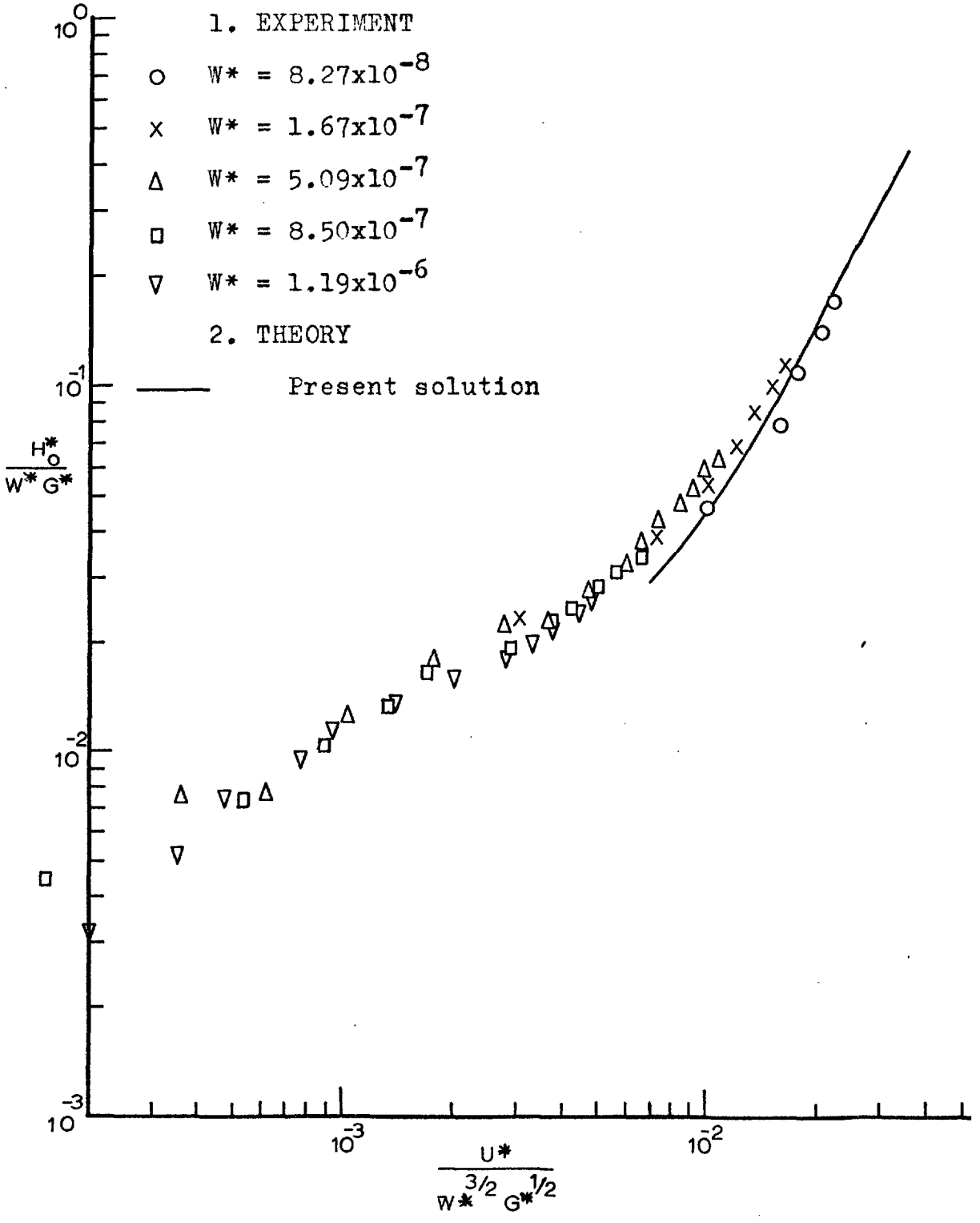


Fig. 5.24 Central film thickness group vs. speed group for drive angle of 50 deg. (Sliding contact)

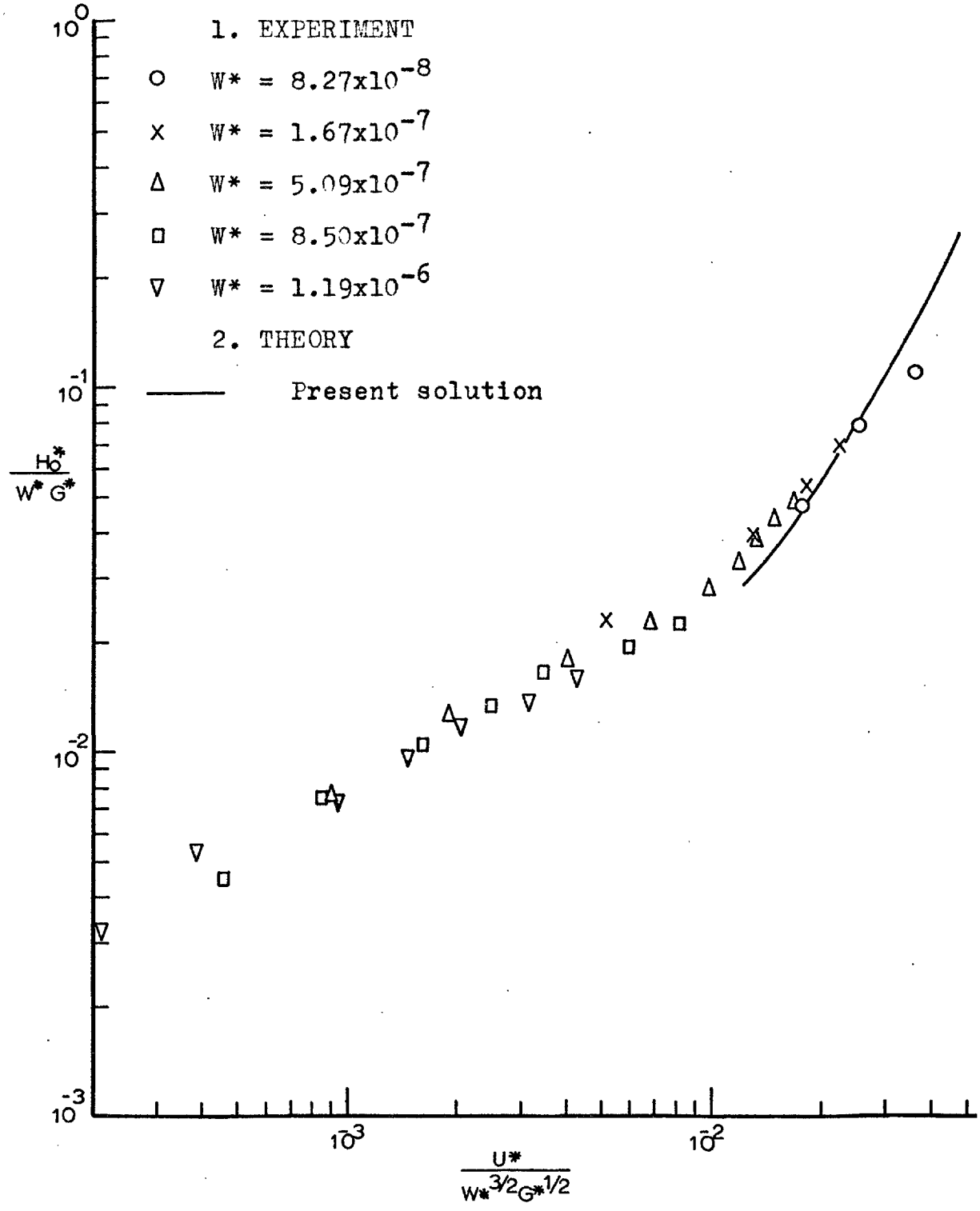


Fig. 5.25 Central film thickness group vs. speed group for drive angle of 82 deg. (Sliding contact)

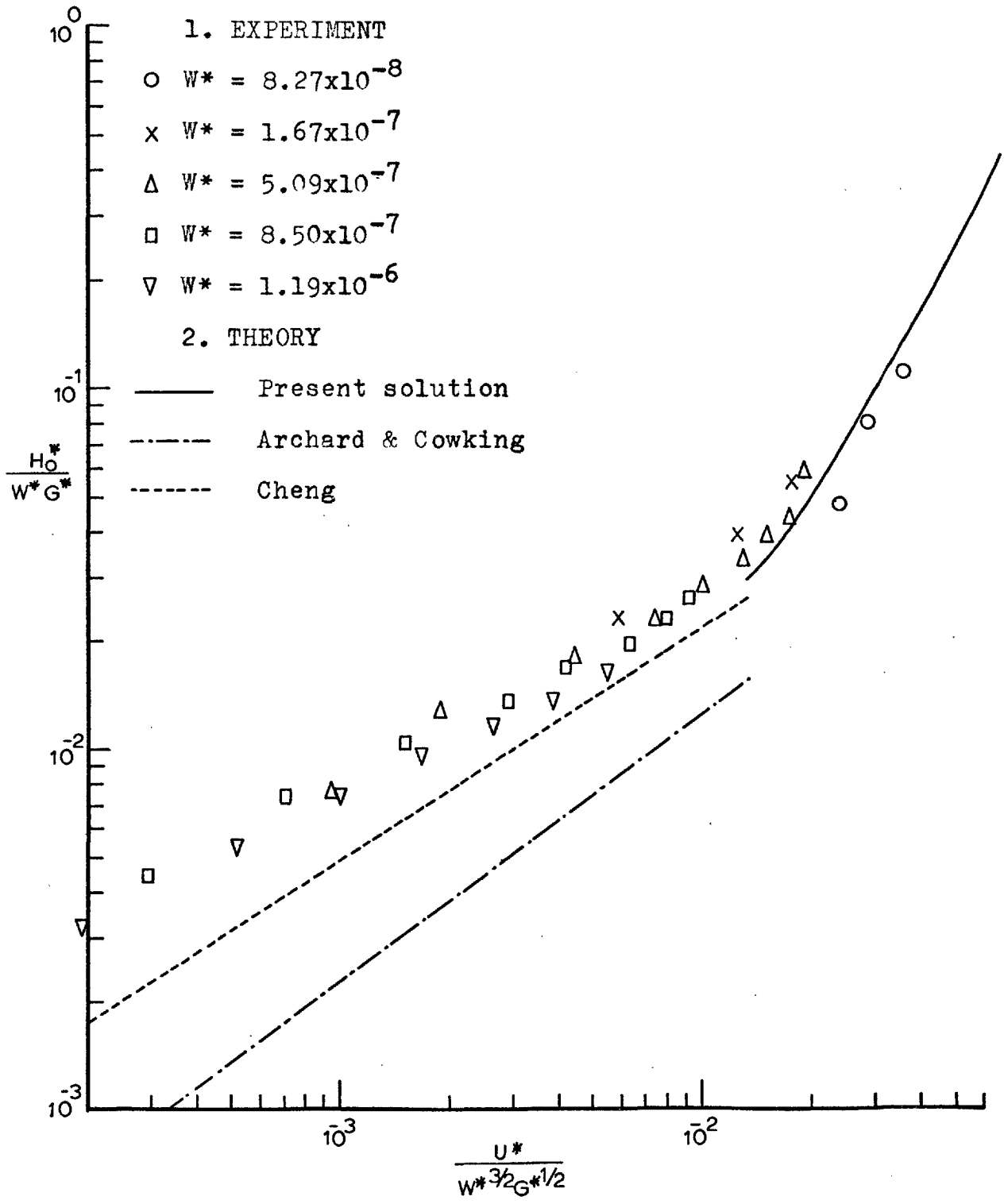


Fig. 5.26 Central film thickness group vs. speed group for drive angle of 90 deg. (Sliding contact)

quite closely with the experiments. At still higher speeds it is to be expected that the slope will increase, since a slope of 2 is obtained for undistorted, isoviscous point contact assuming half-Sommerfeld conditions (ref: 7). The slope of 0.78 for EHL agrees with that obtained by Gohar (3) in EHL point contact.

3. In figures 5.22 to 5.26, for H_o^*, the slope changes from about 1.75 for undistorted contacts, to 0.68 for $\theta = 0^\circ$ and 0.58 for $\theta = 90^\circ$, when the conditions are EHL. Once again, the theory of section 5.2 agrees quite closely with experiments. This is only to be expected however, since, when the contact is undistorted, there is no difference between H_o^* and H_{min}^*. Figures 5.22 and 5.26 also show Cheng's (6) and Archard and Cowking's (5) theories for H_o^*. The agreement, as can be seen, is very good, except for Archard's 90° result. It is gratifying to see that Cheng's predictions also show a reduction in slope at $\theta = 90^\circ$. The difference between theory and experiment must in part be due to the assumption that the main contact region at the inlet is flat, whereas in fact, it can be grossly distorted, especially when $\theta = 90^\circ$ (figure 5.15). Fortunately, this condition is never realised in real bearings. A value of $\theta = 10^\circ$ seems more likely, the component 'V' being caused by gyroscopic sliding.

4. The final observation to be made from the graphs is that the lower the value of θ, the higher the film thickness under given external conditions. Also, the lower θ, the lower the value of $U^* / (W^{*3/2} G^{*1/2})$ at which EHL commences.

It can be concluded, therefore, that $\theta = 0^\circ$ is the most favourable condition for the formation of a thick oil film. There may, however, be advantages derived from the other

velocity component 'V' caused by gyroscopic effects in a rolling bearing, namely the continual presentation of a fresh part of the ball surface to the groove. That EHL becomes important earlier at high values of θ is to be expected, because distortion is much more important when θ is high.

Snidle and Archard (10) have investigated the effect of changes in θ on the limiting film thickness which they predicted (equation 5.11). Figure 5.27 shows their predictions and also

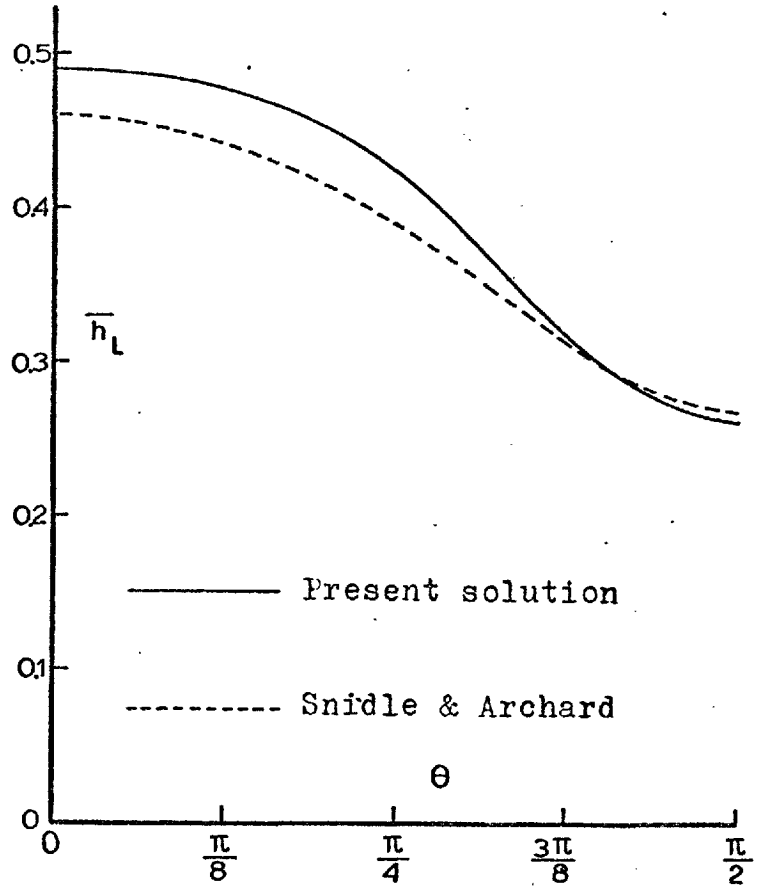


Fig. 5.27 Variation of non-dimensional film thickness with drive angle.

those of the present solution, both for the experimental geometry (A/B = 9.91). The ordinates are non-dimensional limiting film thickness $\bar{h}_L$ as defined by these authors. That is, in the present notation:-

$$\bar{h}_L = 0.5085 \left[\frac{H^*_L}{U^{*\frac{2}{3}} G^{*\frac{2}{3}}} \right] \qquad -5.21$$

As can be seen, the two predictions are very close. Snidle and Archard justified the use of the half-Sommerfeld boundary condition by arguing that, in the formulation of an approximate film thickness equation, the concern is with the maximum pressure generated, which is only weakly dependent on the choice of boundary conditions. Figure 5.27 confirms this argument, but it will be shown later, in chapter 7, that the choice of boundary conditions is of prime importance when predicting frictions. Because the boundary conditions used in the solution outlined earlier have been shown to be realistic, the pressure distributions obtained from this more complex procedure can be used in the prediction of friction.

5.4 Rolling Contacts: theoetical and experimental

The results presented in this section follow the same plan as those in the previous one. As most of the observations made earlier for sliding contacts also apply to rolling contacts, they will not be repeated. However, the differences that exist between the two situations will be pointed out.

5.4.1 Resolved velocity in rolling

The primary difference between rolling and sliding in the experimental situation lies in the velocity vector. The geometry permits rolling along the groove only, whilst across the groove only sliding can take place. The ball surface velocity, which is that measured, has components U and V along and across the groove respectively. If the race/ball contact is rolling, then the plate too has a velocity along the groove (U_p). Unless the plate is driven independently, some slip must occur at the

ball/race contact to provide the traction necessary to overcome the frictional losses in the support bearing. In general, therefore, $U_p < U$.

If the drive angle is θ and the ball surface speed V, then it can be seen from figure 5.28 that the resolved velocity V_1 is given by:-

$$V_1 = V\left(\left(\cos\theta + \frac{U_p}{V}\right)^2 + \sin^2\theta \right)^{\frac{1}{2}} \qquad -5.23$$

which, if there is no slip ($U_p = V\cos\theta$) becomes:-

$$V_1 = V\left(\sin^2\theta + 4\cos^2\theta \right)^{\frac{1}{2}} \qquad -5.24$$

and the effective drive angle θ_1 by:-

$$\theta_1 = \tan^{-1}\left[\frac{V\sin}{U_p + V\cos} \right] \qquad -5.25$$

which, if there is no slip, becomes:-

$$\theta_1 = \tan^{-1}\left[\frac{\tan\theta}{2} \right] \qquad -5.26$$

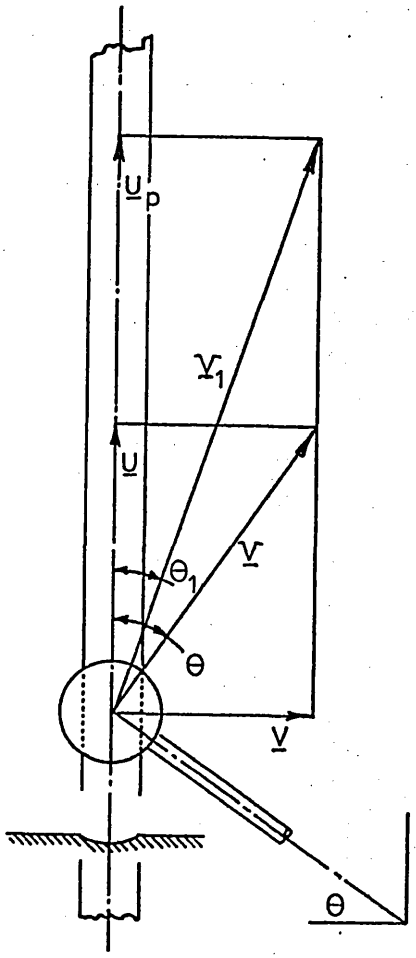


Fig. 5.28 Resolved velocity in rolling.

Since the support bearing was aerostatic, frictional losses were very small. It was assumed, therefore, that slip too would be very small and that the plate speed could be taken to be the same as that of the ball, thus eliminating the need for monitoring them both and permitting the use of equations 5.24 and 5.26 in preference to equations 5.23 and 5.25. The assumption was justified by measuring slip over the range of conditions employed. Over most, it was found to be sufficiently accurate, slip speed being less than 3% of roll speed. However, at light loads, the assumption did not apply, and slip occurred up to

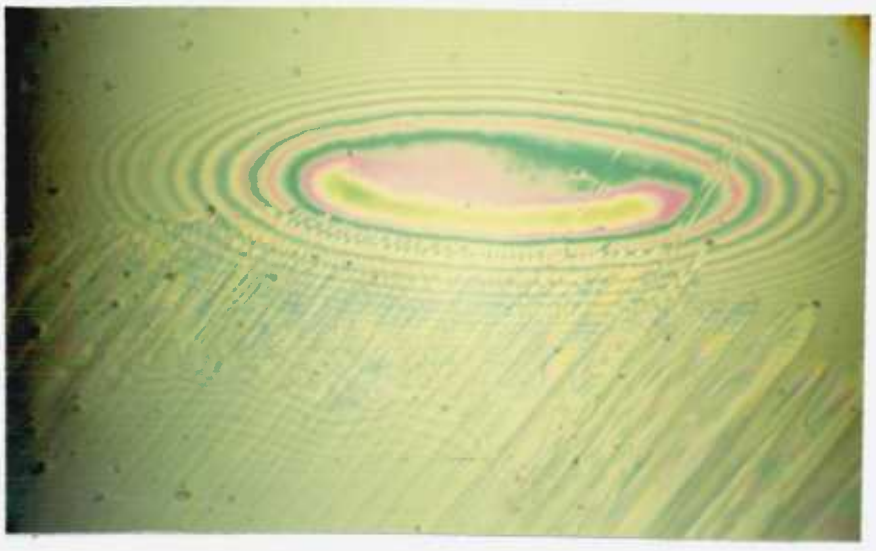
a maximum of 55% of rolling speed. As it could not be eliminated, or even reduced, this slippage was taken into account when appropriate, and corrections made to the calculated velocity vectors (see section 5.4.6).

5.4.2 High speed photographs of the contact

The fringe patterns observed in rolling are very similar to those experienced in sliding but, as would be expected, for a given drive angle, the asymmetry of the distortion is less under rolling conditions because, as equation 5.25 demonstrates, the total U component of velocity is more dominant and so the effective drive angle is less than under sliding conditions.

Figure 5.29 clearly demonstrates this effect. It shows two fringe patterns, both with the same drive angle, load and minimum film thickness, but one in sliding and one in rolling. The sensitivity of the colour fringes to changes in film thickness shows that, in the sliding example (a), the film on the left hand part of the central region is less than that on the right. In the rolling example (b) the film thickness over the whole central region is shown to be virtually constant.

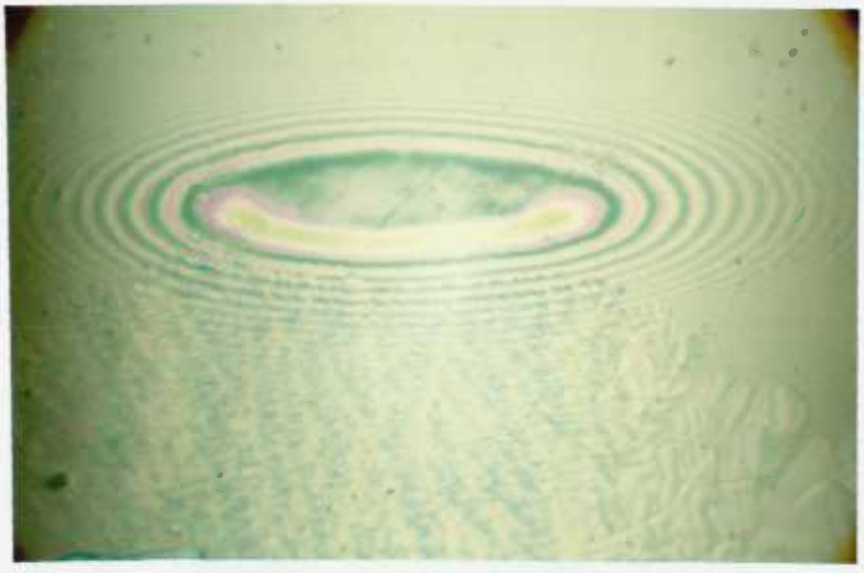
Although true in the full EHL regime, the opposite effect, that is, more distortion in the rolling case, is evident under less severe conditions. By considering the 0° case, the effect of angling can be eliminated. The overall similarity between the film shapes in rolling and sliding in the absence of angling is evident from a comparison of figures 5.30 (a) and (b) where, for both photographs, the minimum film thickness and load are the same. However, in the rolling example (b), the inlet region appears to be slightly more developed, the second black fringe being wider at this point. At higher loads, the effect is more noticeable and the contrast between rolling and



a) Sliding contact $\theta = 54^{\circ}$

$U^* = 4.45 \times 10^{-11}$ $H_{min}^* = 2.4 \times 10^{-5}$ $W^* = 8.50 \times 10^{-7}$

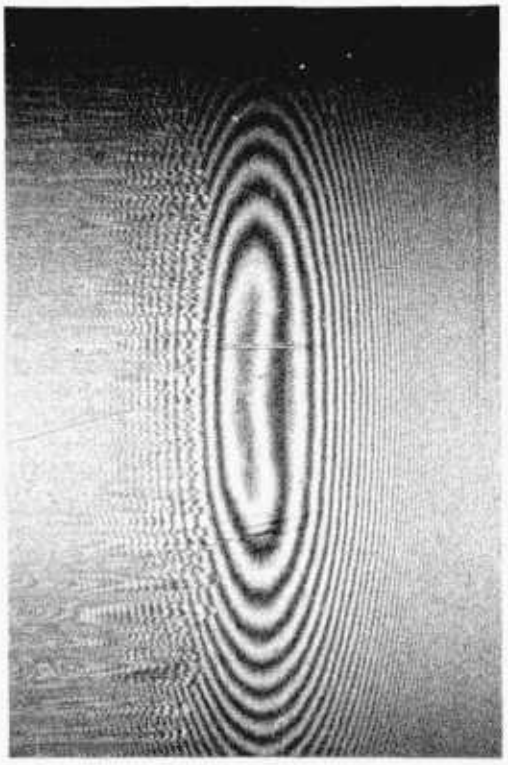
Direction of oil flow



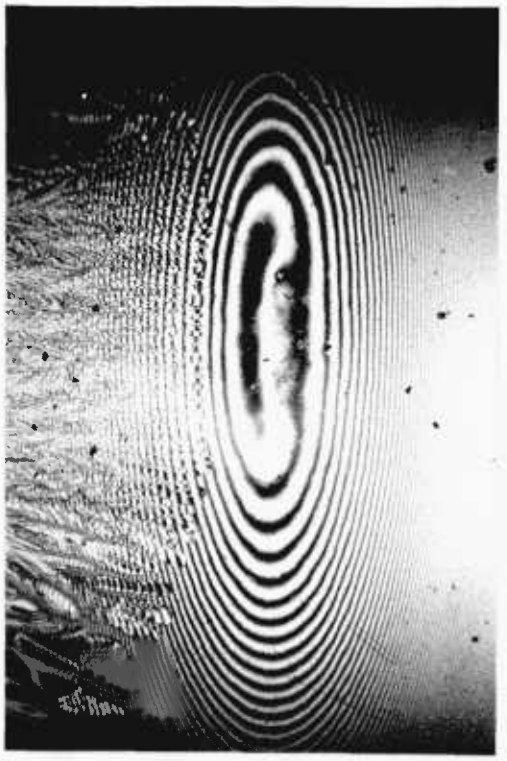
b) Rolling contact $\theta = 54^{\circ}$

$U^* = 4.24 \times 10^{-11}$ $H_{min}^* = 2.4 \times 10^{-5}$ $W^* = 8.50 \times 10^{-7}$

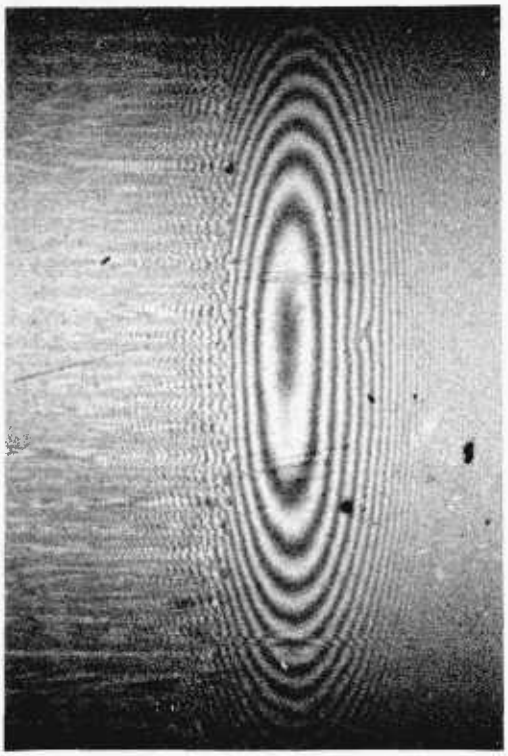
Fig. 5.29 Comparison of fringe patterns in sliding & rolling.



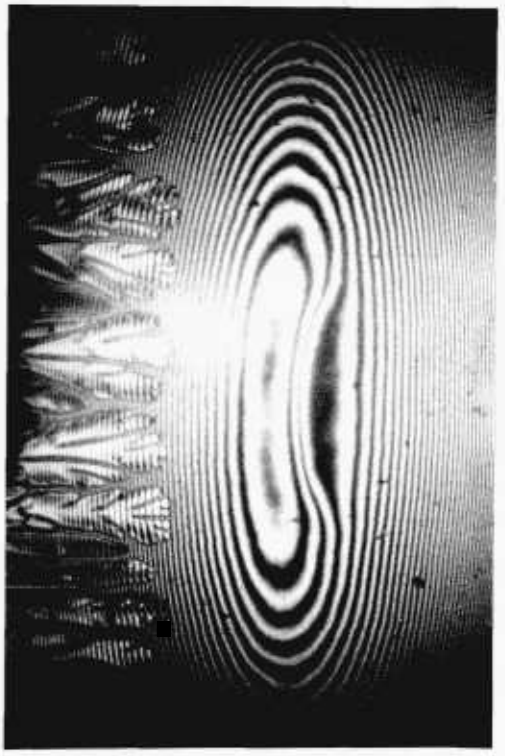
(a) $\frac{H^*}{W^*G^*} = 2.3\times10^{-2}$ Sliding



(b) $\frac{H^*}{W^*G^*} = 2.3\times10^{-2}$ Rolling



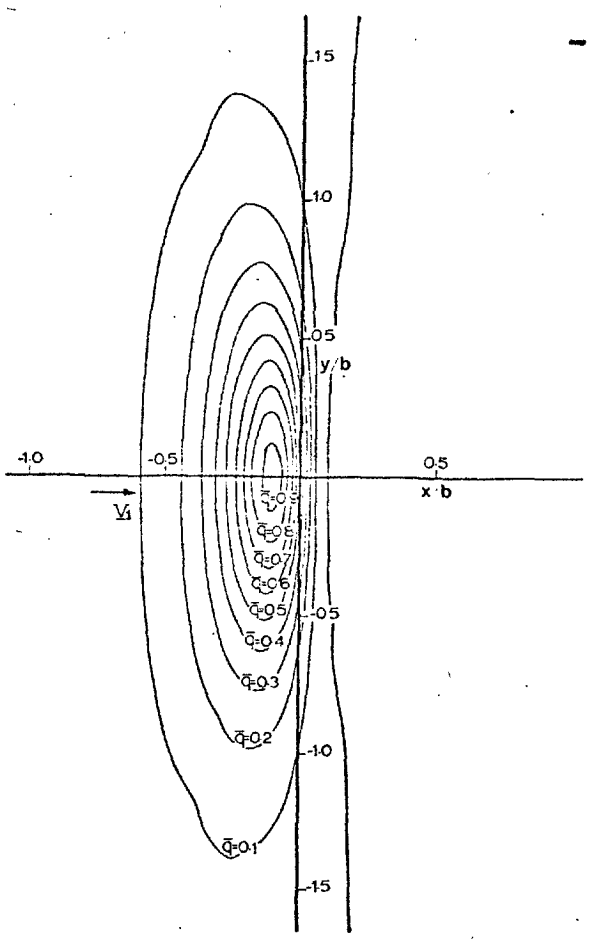
(c) $\frac{H^*}{W^*G^*} = 4.5\times10^{-2}$ Sliding



(d) $\frac{H^*}{W^*G^*} = 4.5\times10^{-2}$ Rolling

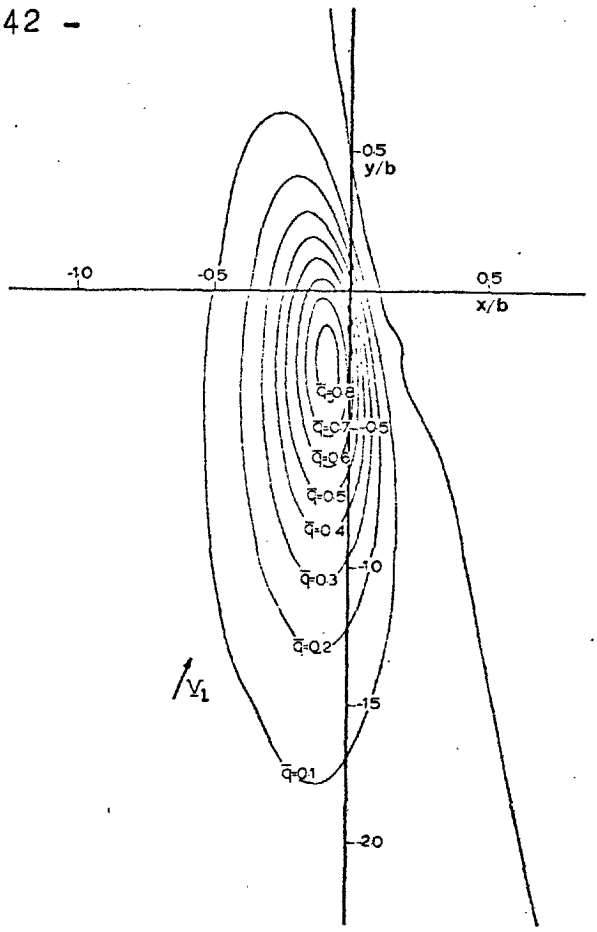
MAGNIFICATION X 70

Fig. 5.30 Comparison of rolling and sliding contacts (θ = 0deg.)



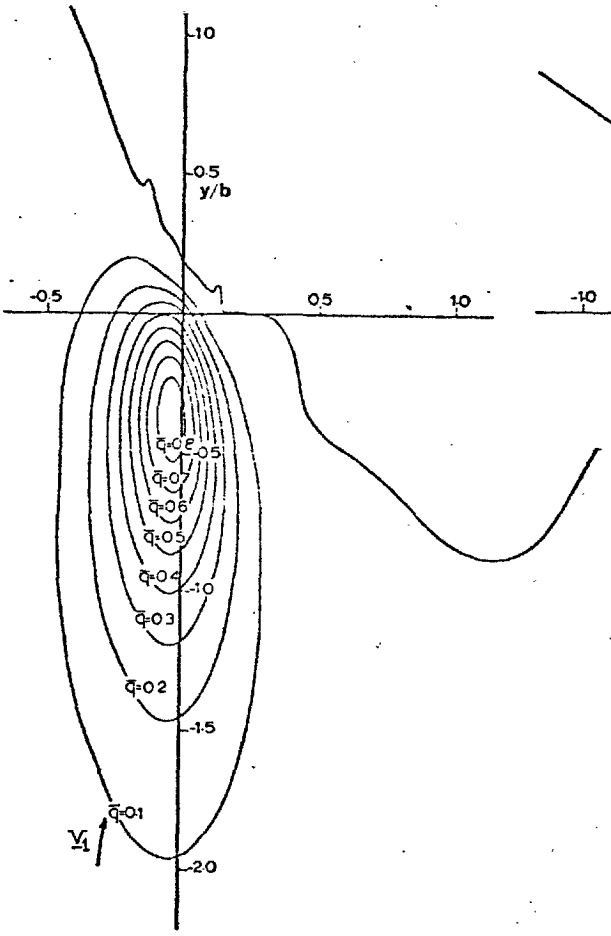
(a) $\theta = 0$ deg $H^*/W^*G^* = 3.1 \times 10^{-3}$

$\frac{U^*}{W^{*1.5}G^{*0.5}} = 5.0 \times 10^{-3}$



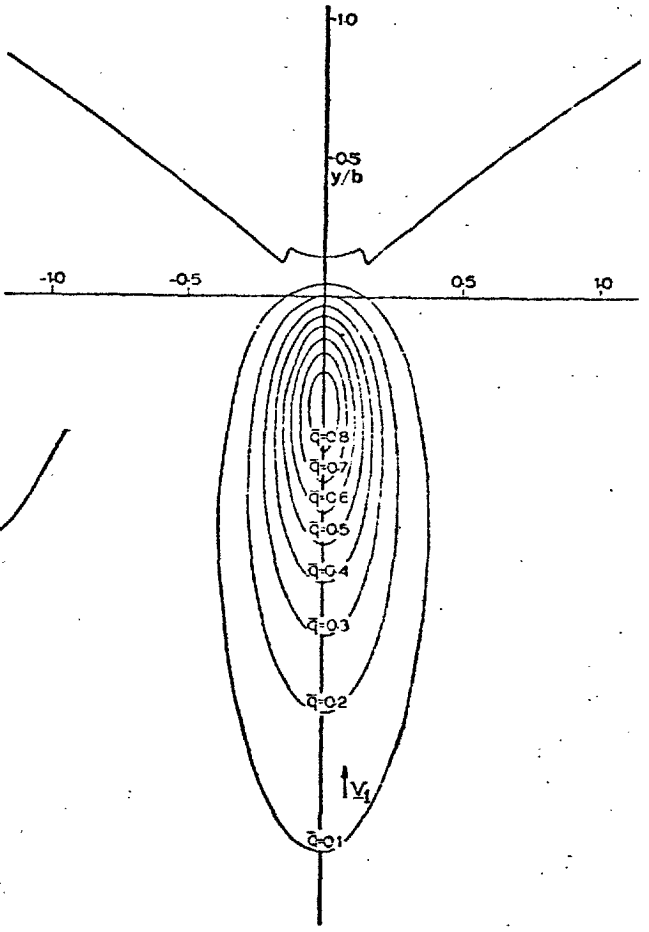
(b) $\theta = 78$ deg $H^*/W^*G^* = 3.5 \times 10^{-2}$

$\frac{U^*}{W^{*1.5}G^{*0.5}} = 1.1 \times 10^{-2}$



(c) $\theta = 86$ deg $H^*/W^*G^* = 3.5 \times 10^{-2}$

$\frac{U^*}{W^{*1.5}G^{*0.5}} = 1.4 \times 10^{-2}$



(d) $\theta = 90$ deg $H^*/W^*G^* = 3.5 \times 10^{-2}$

$\frac{U^*}{W^{*1.5}G^{*0.5}} = 1.5 \times 10^{-2}$

Fig. 5.31 Reduced pressure isobars in rolling.

sliding greater (compare figures 5.30 (c) and (d)). The rolling example (d) still shows a considerable degree of distortion even though the film is quite thick($\simeq 63\,\mu$ in minimum), whilst the sliding example (c) is close to being undistorted.

Foord (2) noticed similar contrasts between rolling and sliding in a circular point contact. Although his loads were too high to reach the transition zone between EHL and undistorted contacts, he did note that at high film thicknesses entry to the Hertzian flat was more gently curved in the sliding case. For a given film thickness the difference in the film shapes must be attributable to the surface tractions, which can be up to 5% of the normal load (see chapter 7) under sliding. These tractions act in different directions on the two bodies and consequently modify the distortion from those experienced in rolling, which are due solely to pressure forces.

5.4.3 Pressure distributions

The theory described in section 5.2 takes no account of any differences that exist between rolling and sliding, save those concerned with the size and direction of the velocity vector as discussed in section 5.4.1. Thus the distributions presented earlier (figure 5.8) are perfectly valid for rolling contacts, provided that they are suitably re-labelled to take into account these changes (figure 5.31).

5.4.4 Cavitation

One striking difference which exists between rolling and sliding contacts is the appearance of the cavitated region. The contrast is superficial rather than of real significance.

In sliding, the oil which has passed through the contact vents into a stagnant region until it is carried away from the contact on the balls surface. Such a region is visible in

figure 5.4(c) and is characterised by a random pattern of interference fringes. The oil streamers in the cavitated region are very well defined and run parallel to each other, being aligned with the direction of the velocity vector.

In a rolling contact, if a high degree of angling is present, well defined streamers are again visible. A streamer is formed under sliding action and then carried away on the raceway, another being formed to take its place. The bubbles so produced merge, though slowly, because of the retarding effects of viscosity and surface tension. In practice this may be a considerable disadvantage, because if the oil film has not reformed before it reaches the next rolling element, then starvation may result.

In rolling at lower angles, the wake patterns resemble those of figure 5.30 (b) and (d); discrete streamers are no longer visible, being replaced by feather-like patterns. Similar patterns have been observed by Wedeven in circular point contacts (8), but he made no attempt to explain their shape. One hypothesis is now advanced.

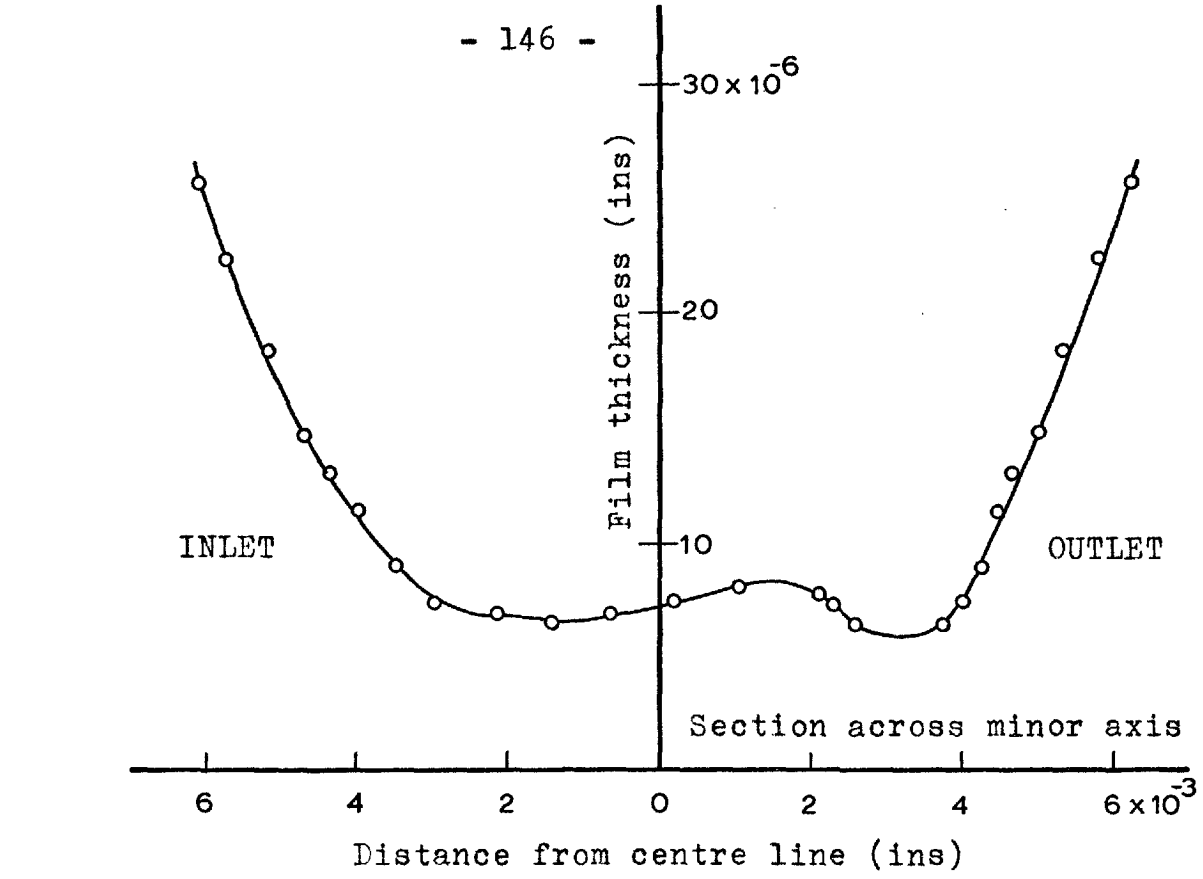
The flow is mainly one dimensional in separation, thus in the sliding case the air fingers tend to remain separate and, as has been remarked, follow the flow vector. Transfer of oil between streamers is non-existent in these circumstances. That such a situation can exist, is a consequence of the static oil build-up behind the contact, the oil streamers not being open to the atmosphere, except, possibly, at their extremities. Under rolling, no such build-up is possible because the disk carries away any excess oil. The oil streamers then exist with one side open to the air and consequently collapse. It is suggested, therefore, that this gives rise to the shapes observed, because, as the oil film tries to reform, there will

be transfer across the meniscus, giving the two dimensional flow pattern. Some confirmation is given by the fact that the bubbles were found (by Wedeven) to be much larger and more rounded if the surface tension of the fluid was high, and also by the fact that similar patterns are observed during reformation of the oil film should the ball be removed normally from static contact.

The situation is slightly more complex, because, as can be seen, the cavitation pattern differs between the region immediately behind the contact and that at the side. Under sliding, the air streamers in this central region are narrow and sharp-pointed in contrast to those at the sides, which are wide and round-nosed. In rolling too, the patterns in the centre are finer and sharper than those in the outer regions. Taylor (13) labels the two conditions as separation (large, rounded air fingers) and cavitation (narrow, pointed air fingers). Such a distinction is largely academic and indeed, at high film thicknesses, both regions appear as the sides appeared at lower film thicknesses. This suggests that the differences were due merely to the quantity of oil rather than to anything more fundamental.

5.4.5 Film profiles in rolling

Three further sets of film profiles taken from colour photographs are presented in figures 5.32 to 5.34. The loads, drive angles and minimum film thicknesses have been chosen so that a direct comparison may be made with the corresponding profiles obtained in sliding (figures 5.11 to 5.13). No profiles have been presented for the cases of rolling at 0° and 90°, the former because the shapes have been shown to be virtually the same as in sliding, and the latter because rolling at 90° is



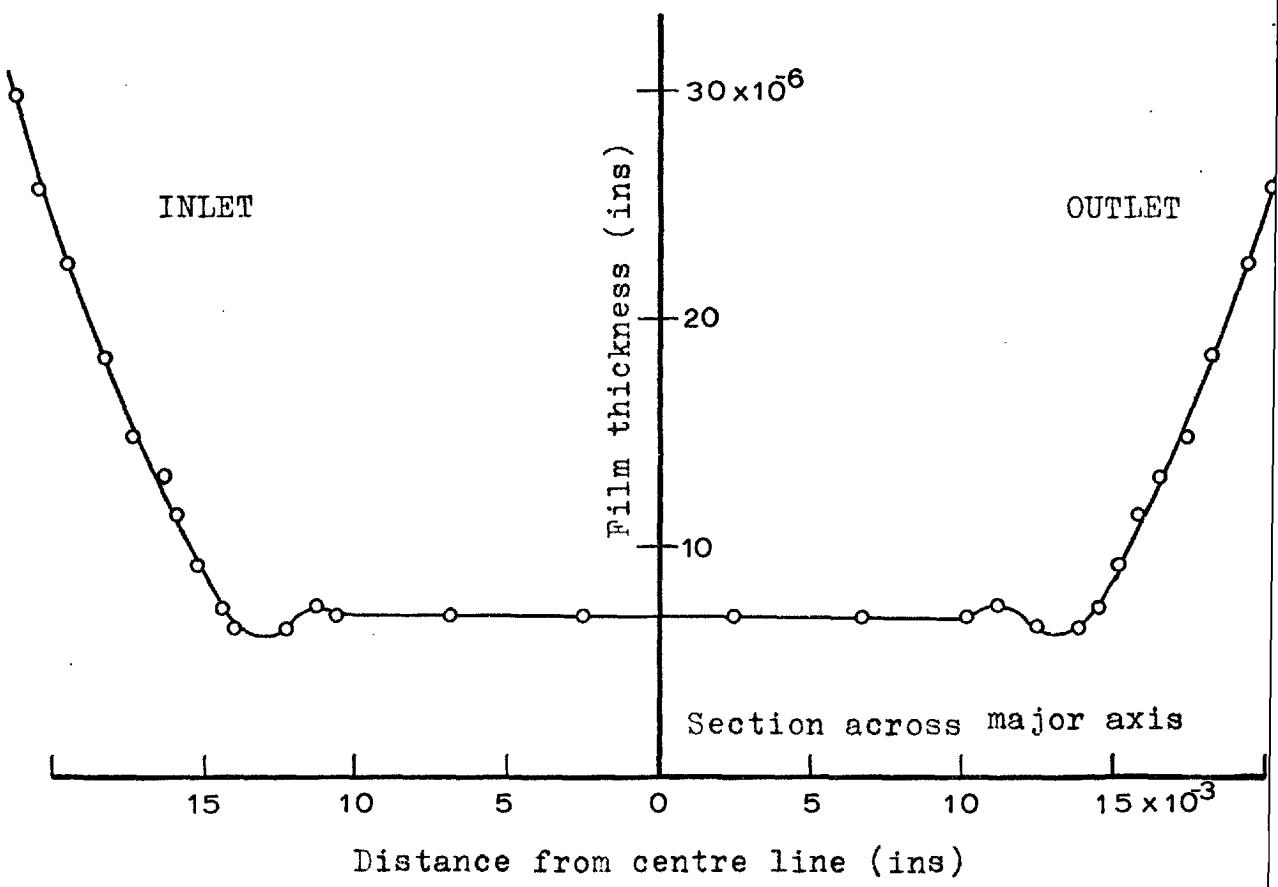
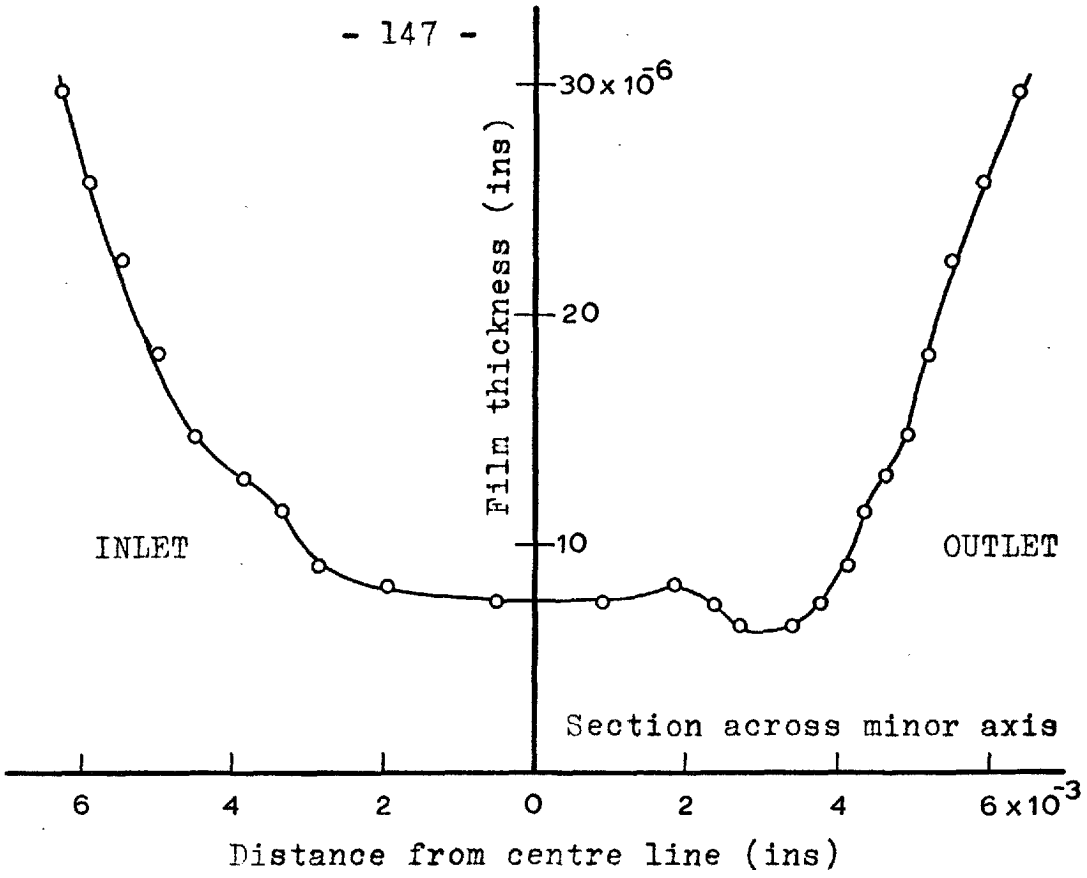


Fig. 5.32 Film profiles in rolling for drive angle of 38 deg.

$U^* = 1.41 \times 10^{-11}$ $H_{min}^* = 1.23 \times 10^{-5}$ $W^* = 8.5 \times 10^{-7}$



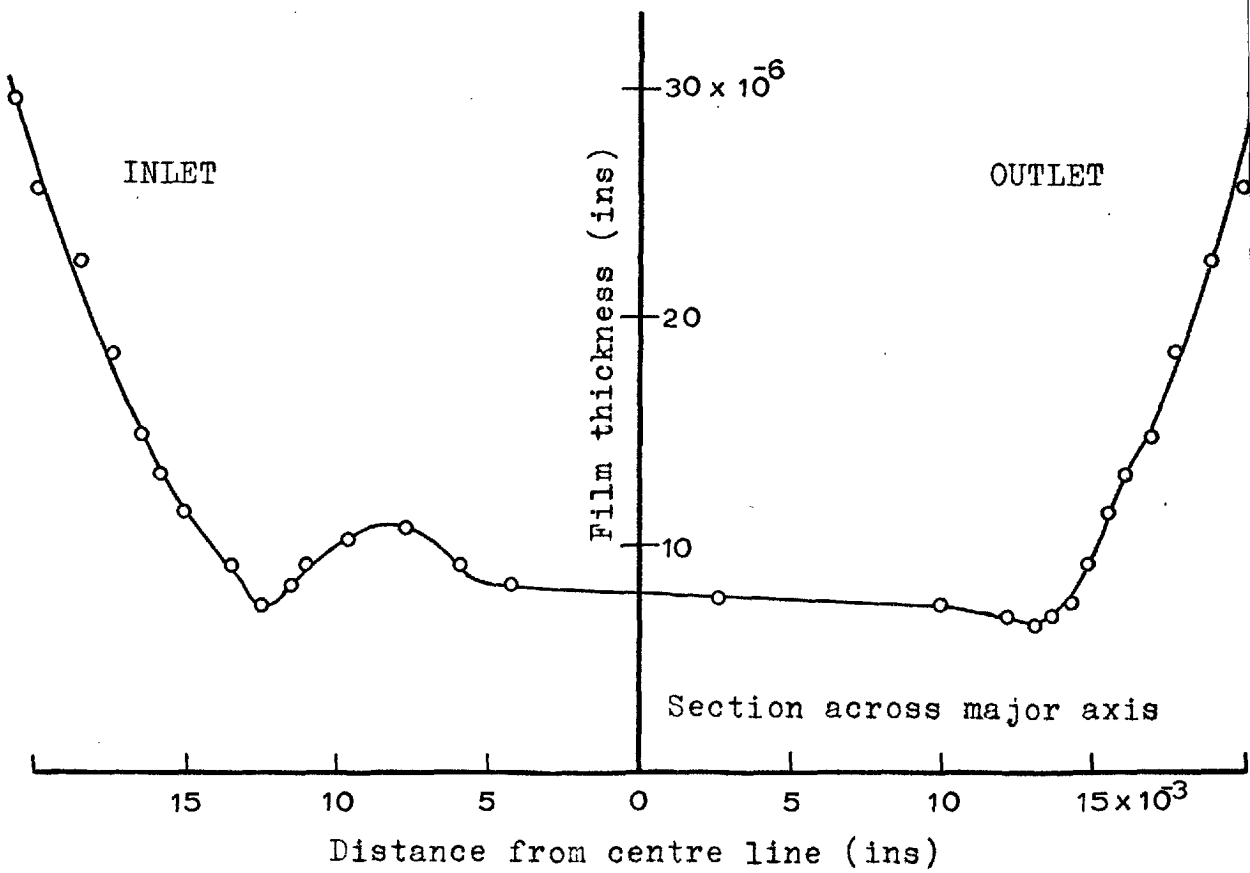
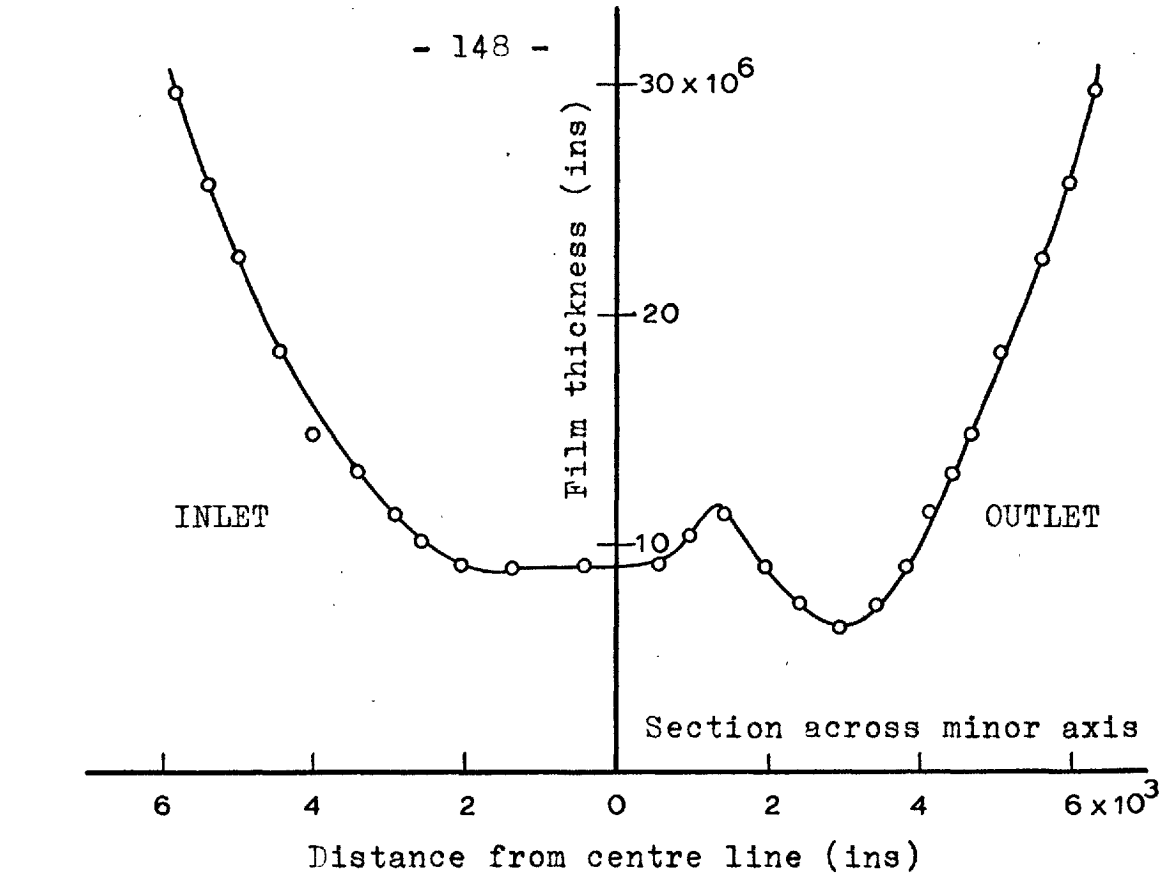


Fig. 5.33 Film profiles in rolling for drive angle of 54 deg.

$U^* = 1.9 \times 10^{-11}$ $H_{min}^* = 1.23 \times 10^{-5}$ $W^* = 8.5 \times 10^{-7}$



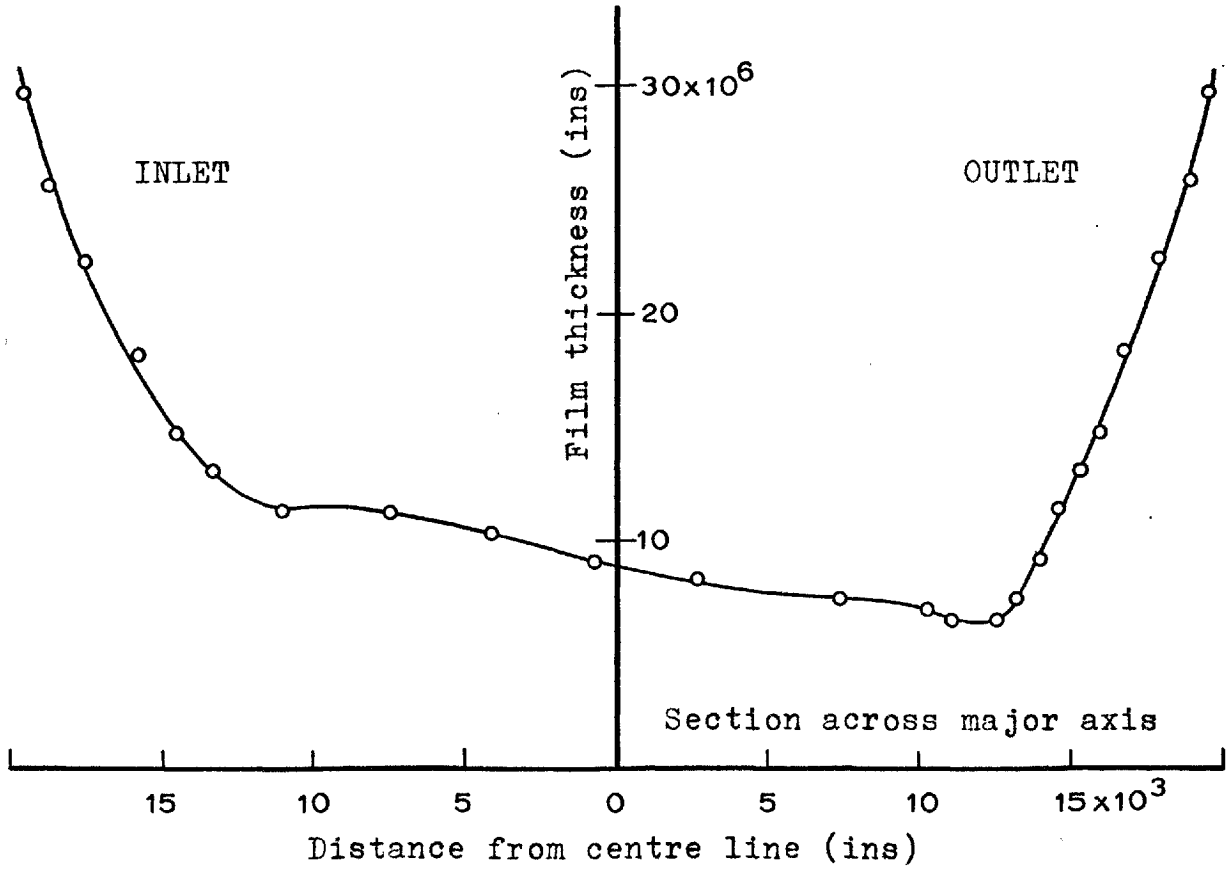


Fig. 5.34 Film profiles in rolling for drive angle of 75 deg.

$U^*=2.89\times10^{-11}$ $H_{min}^*=1.23\times10^{-5}$ $W^*=8.5\times10^{-7}$

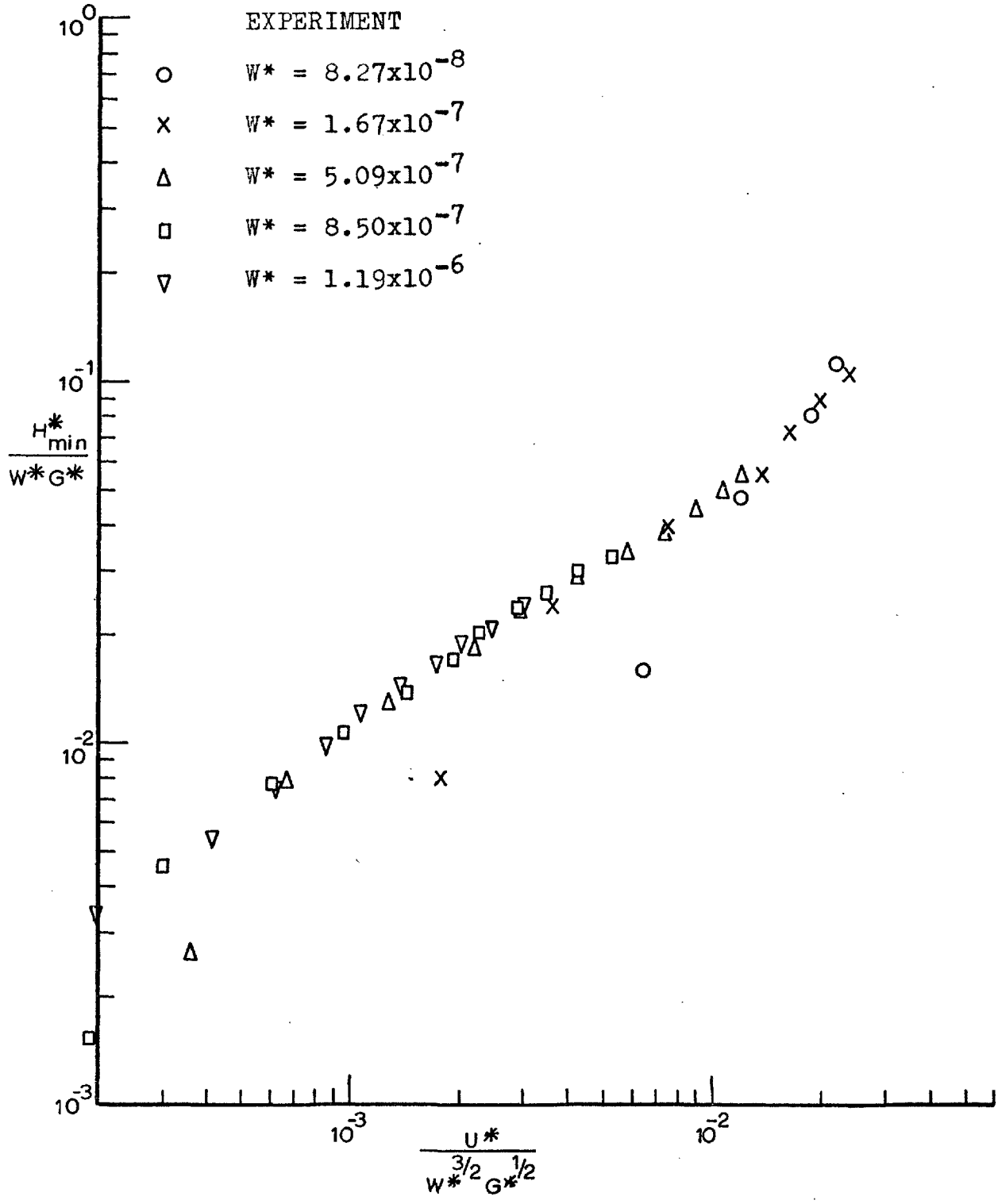


Fig. 5.35 Minimum film thickness group vs. speed group fro drive angle of 0 deg. (Rolling contact)

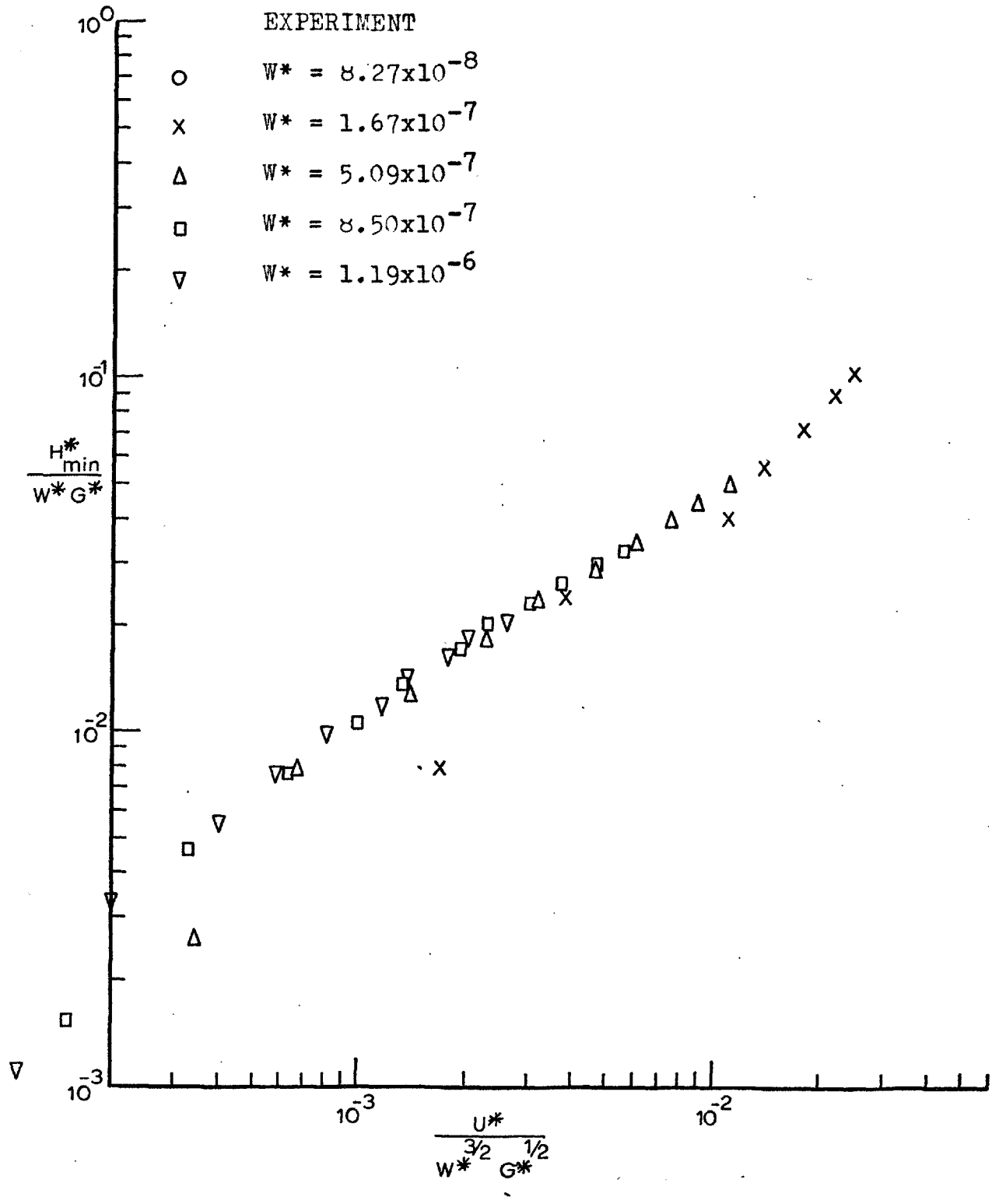


Fig. 5.36 Minimum film thickness group vs. speed group for drive angle of 20 deg. (Rolling contact)

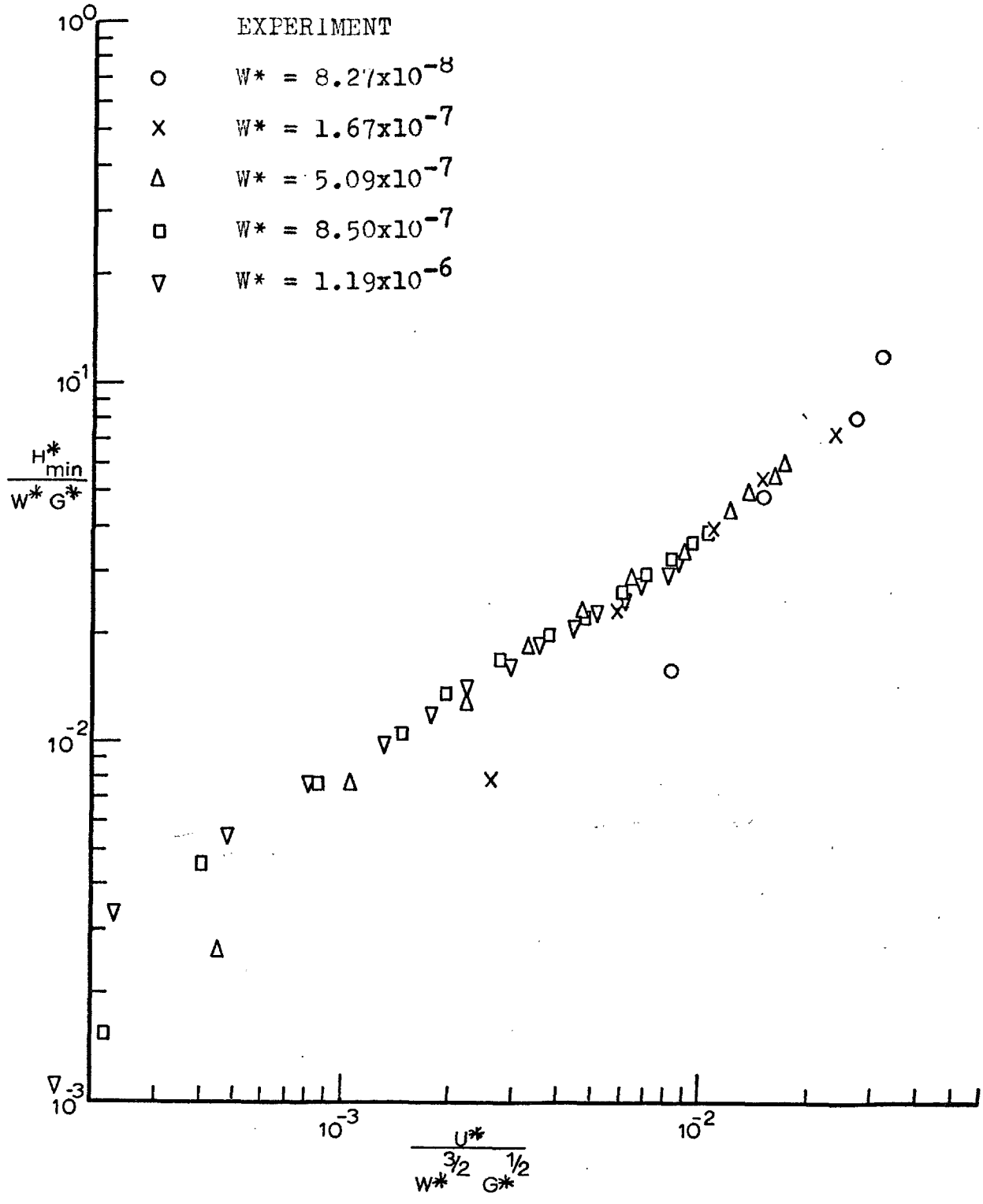


Fig. 5.37 Minimum film thickness group vs. speed group for drive angle of 67 deg. (Rolling contact)

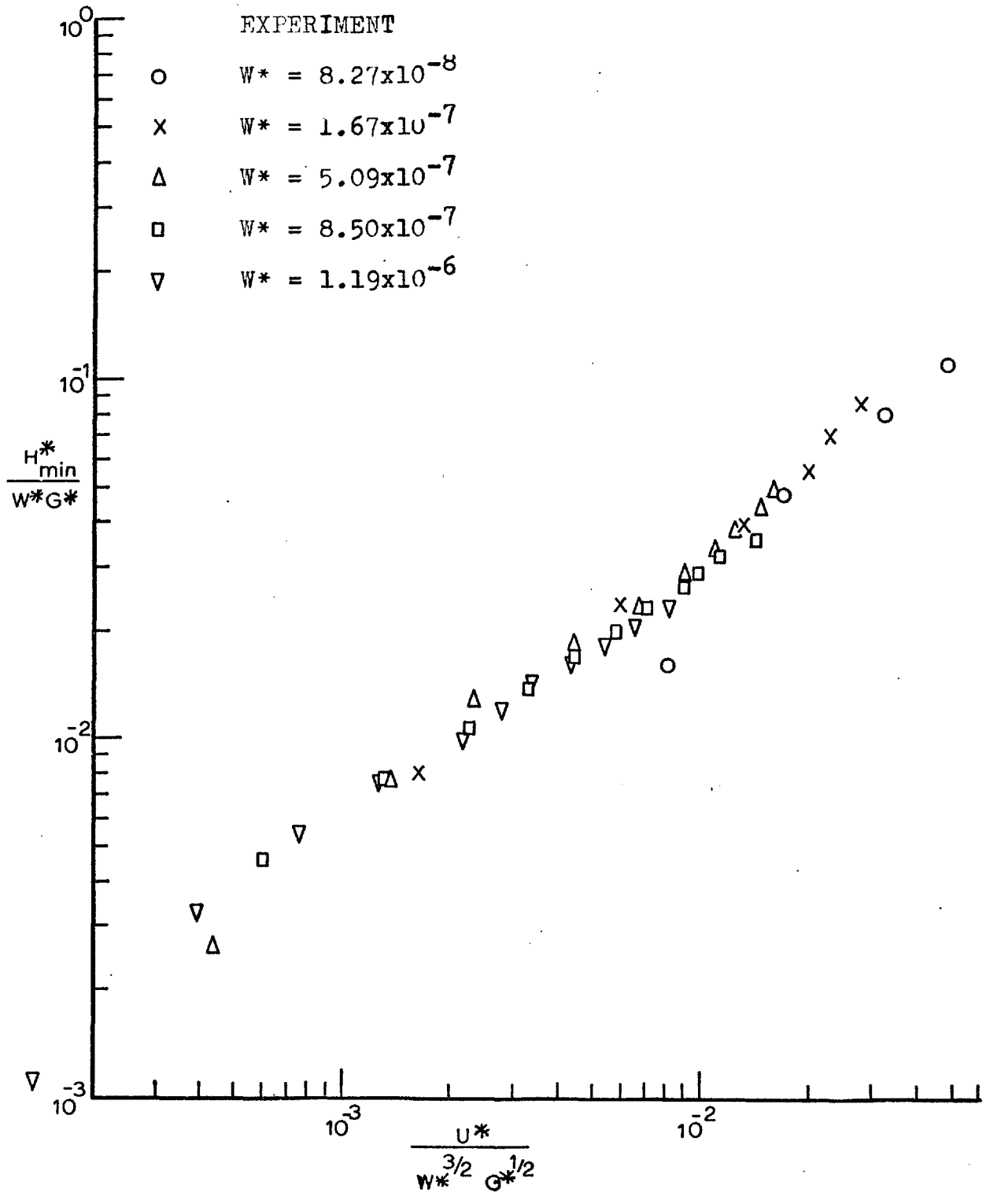


Fig. 5.38 Minimum film thickness group vs. speed group for drive angle of 78 deg. (Rolling contact)

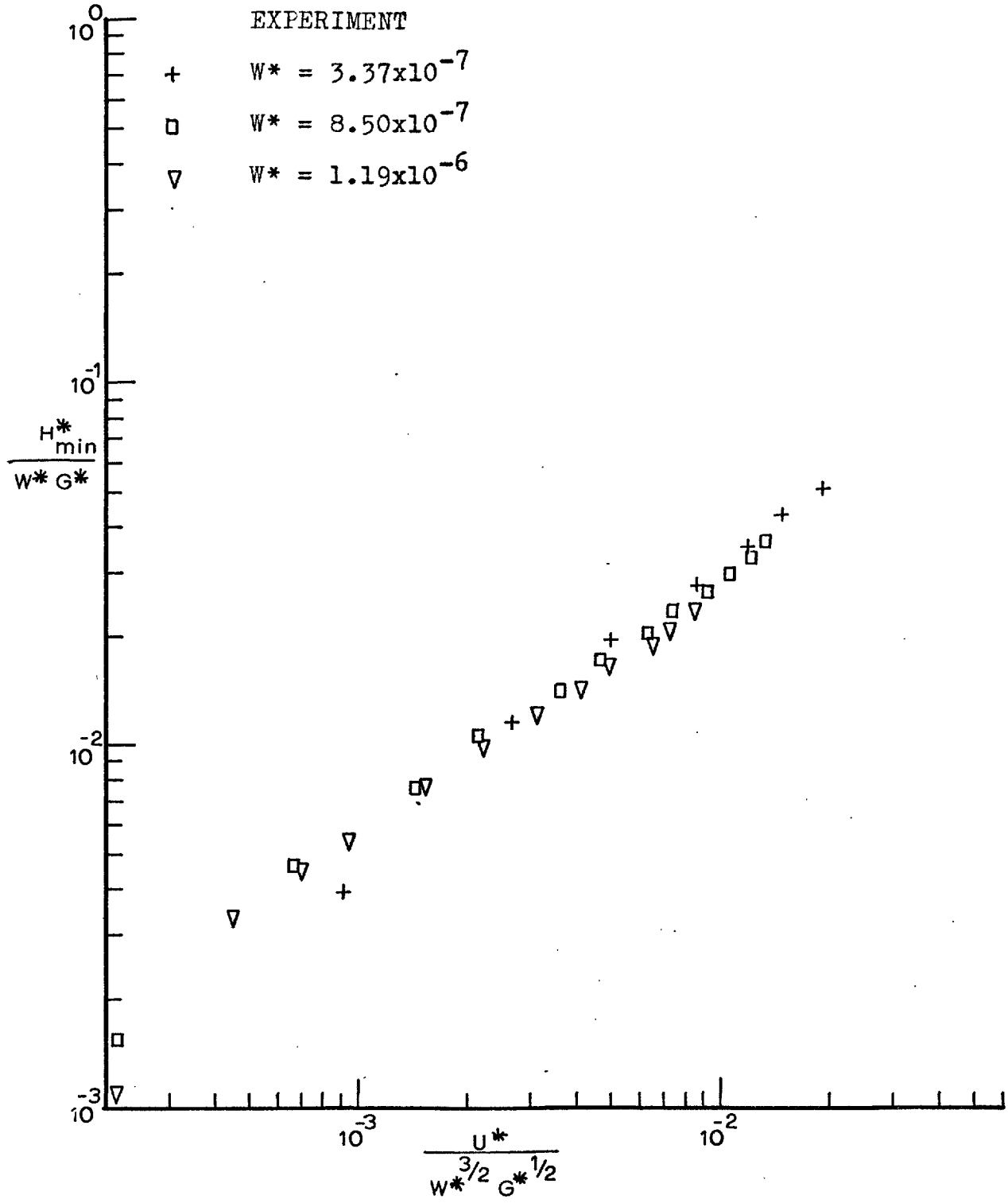


Fig. 5.39 Minimum film thickness group vs. speed group for drive angle of 82 deg. (Rolling contact)

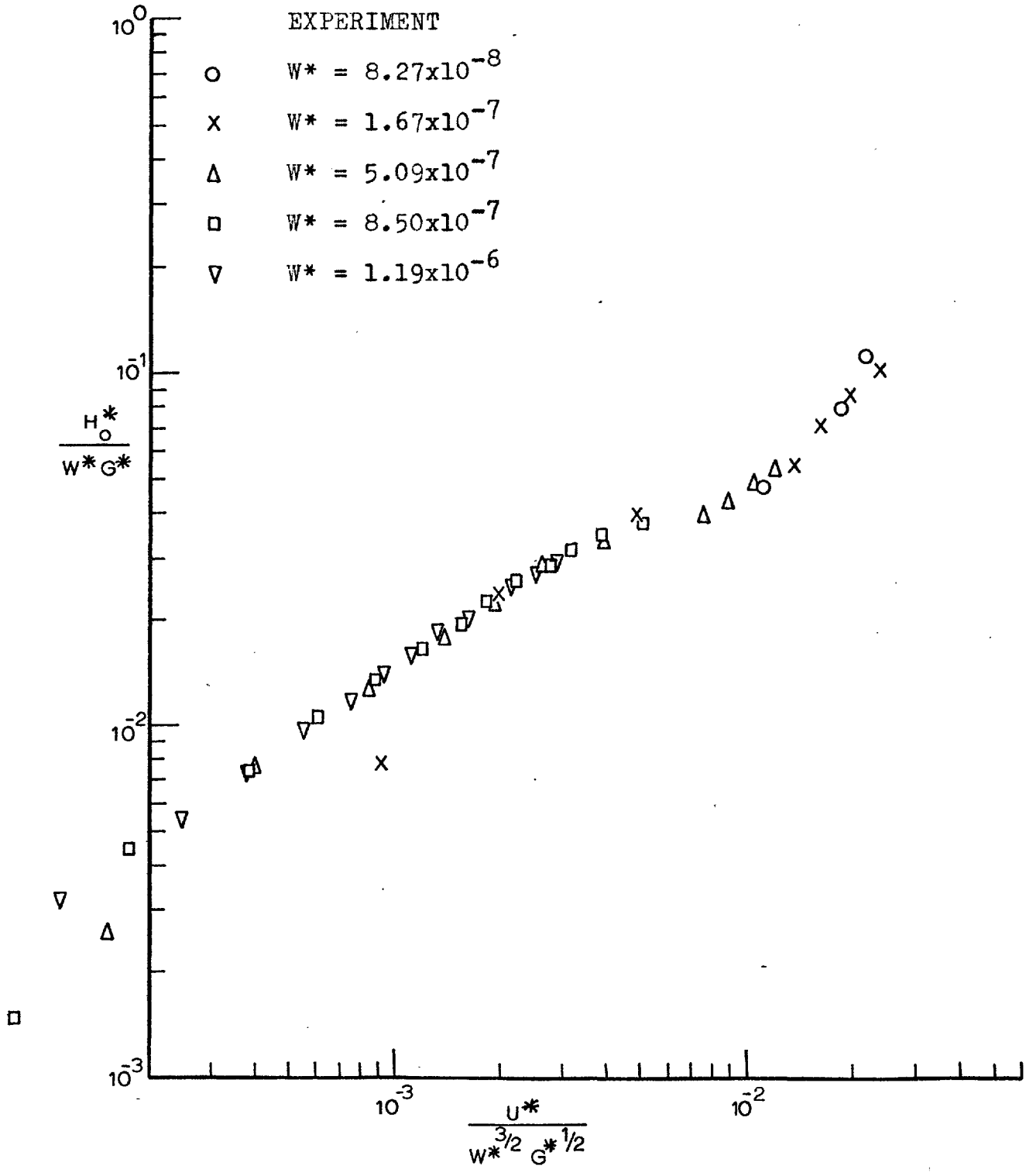


Fig. 5.40 Central film thickness group vs. speed group for drive angle of 0 deg. (Rolling contact)

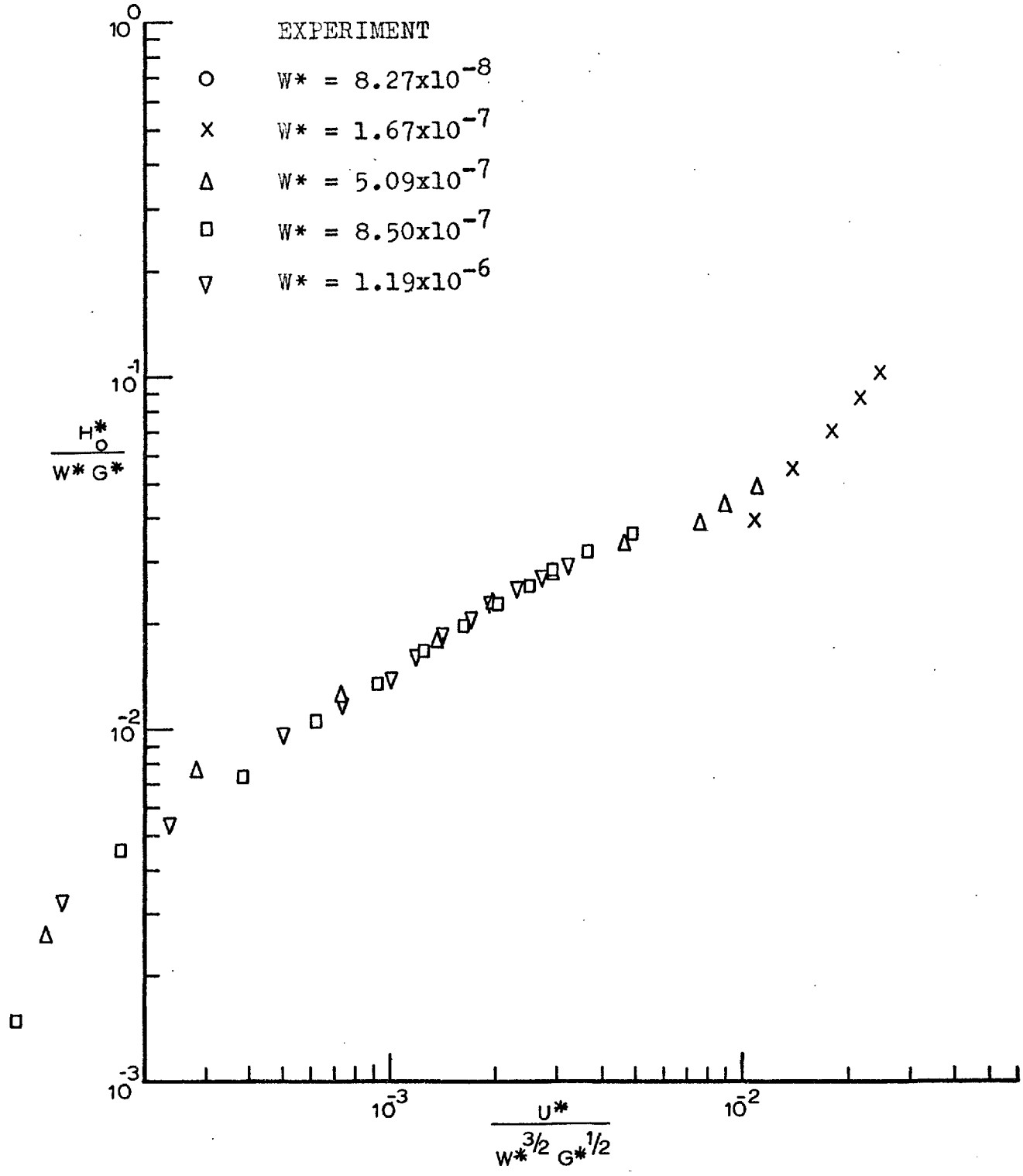


Fig. 5.41 Central film thickness group vs. speed group for drive angle of 20 deg. (Rolling contact)

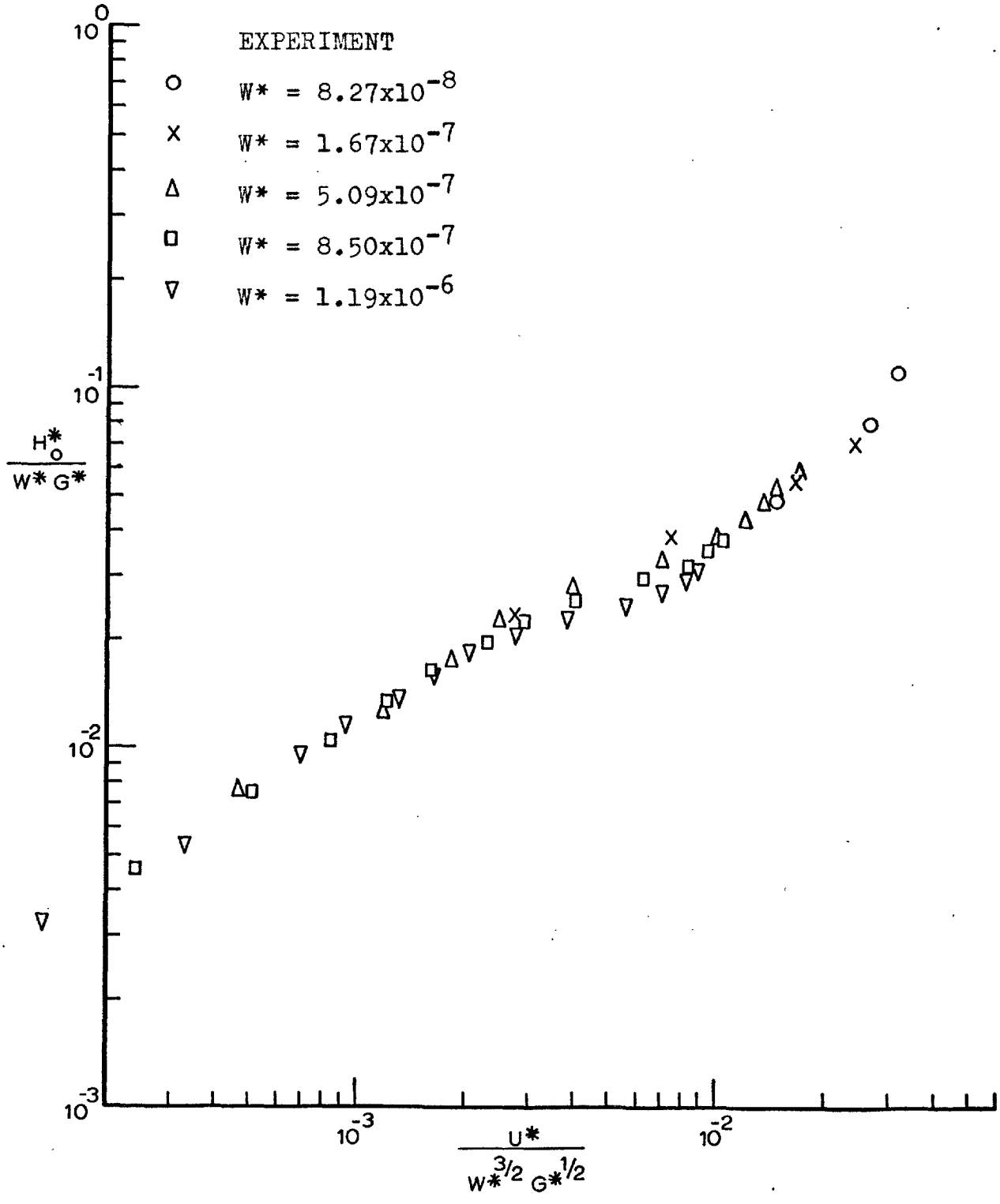


Fig. 5.42 Central film thickness group vs. speed group for drive angle of 67 deg. (Rolling contact)

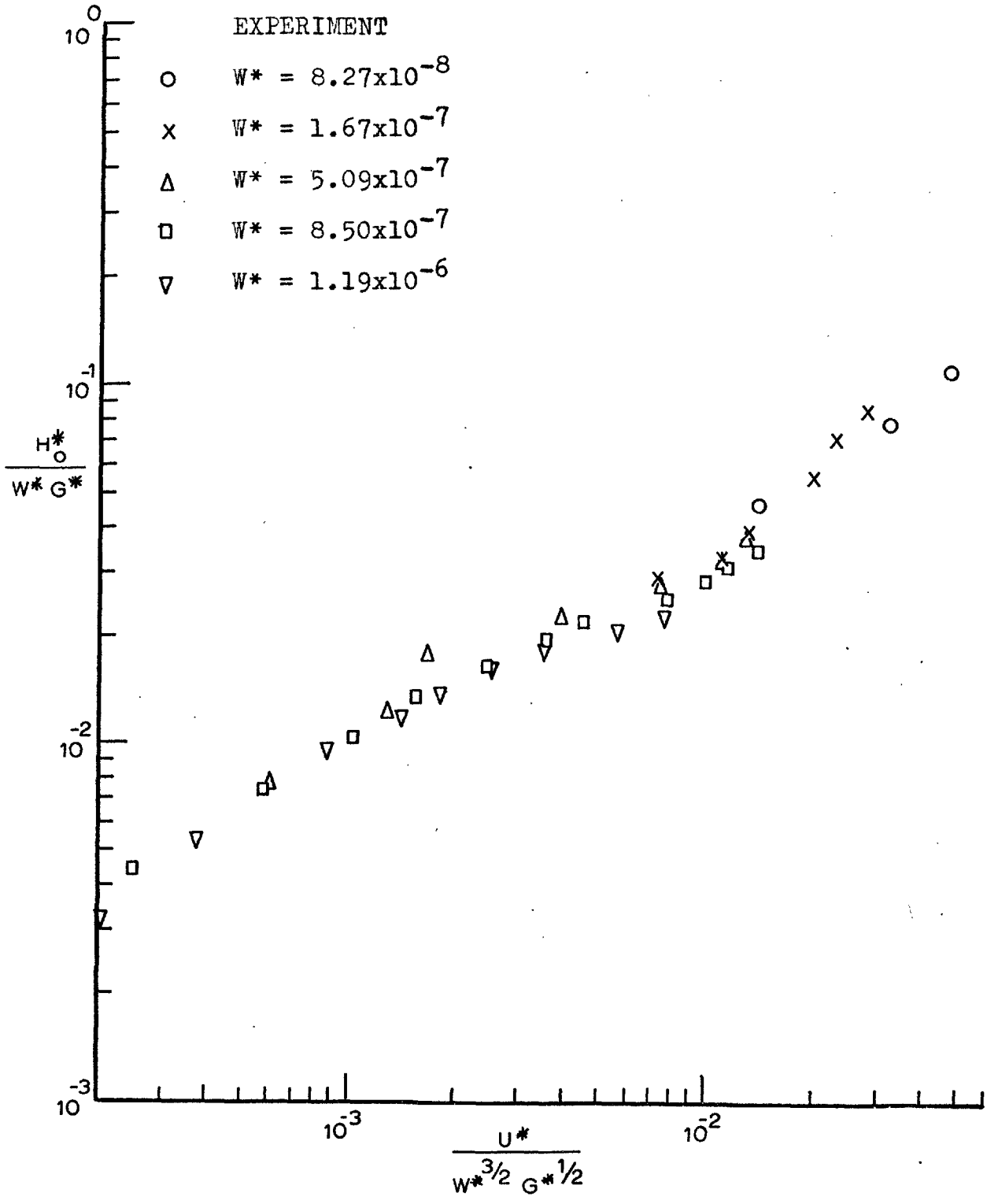


Fig. 5.43 Central film thickness group vs. speed group for drive angle of 78 deg. (Rolling contact)

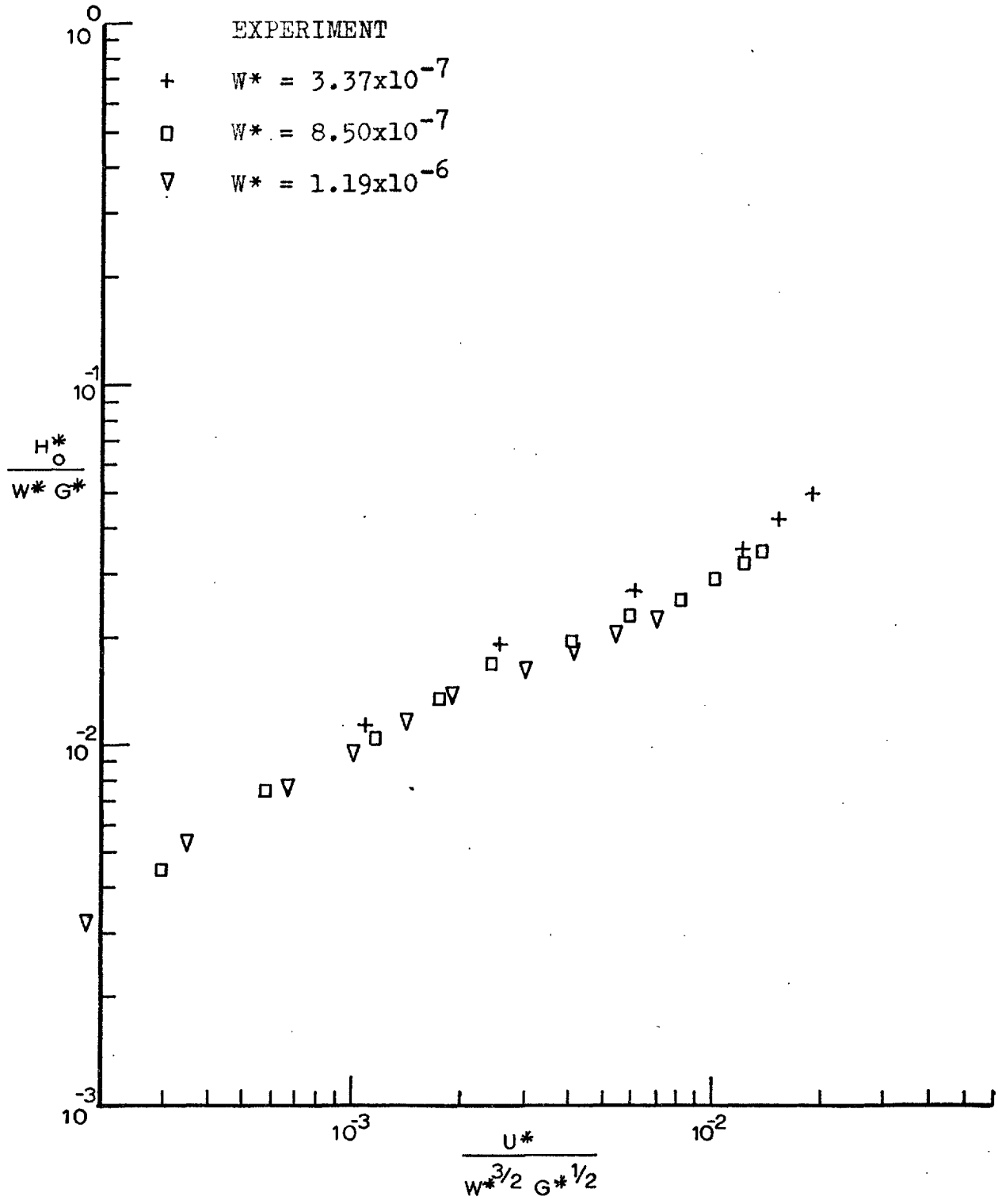


Fig. 5.44 Central film thickness group vs. speed group for drive angle of 82 deg. (Rolling contact)

not geometrically possible.

The three profiles demonstrate once again that the change in shape resulting from angling is less under rolling conditions than under sliding. Interesting points to note from all the profiles presented, both rolling and sliding, are the increase in film thickness just prior to the end closure and the inflexion that occurs in the early part of the rise from the minimum in the exit and at the sides.

The former effect has been predicted by Dowson et al (12). When they took the lubricant compressibility into account in their calculations, they found that the film shape was modified by a small increase prior to the rear constriction and also that the height of the pressure peak was reduced and moved downstream slightly.

The latter effect has been observed by other workers, but only Gohar (14) has attempted an explanation. He hypothesised that, since pressures were near atmospheric, the surfaces tended to relax towards their undeformed shapes. Ranger (15) has pointed out that, in the computation of pressures from film thickness measurements, an inflexion as observed is necessary to prevent the prediction of large negative pressures.

5.4.6 Film thickness in rolling

Figures 5.35 to 5.39 show how the rolling film thickness (H^*_{min}) varies with U^* and W^* for different Θ, and figures 5.40 to 5.44 show how the central film thickness ($H_o{}^*$) varies. The drive angles have been chosen so that, for no slip, the effective drive angles predicted by equation 5.26 are comparable with the angles used in the sliding experiments. Thus 20° rolling may be compared with 10° sliding, 67° rolling with 50° sliding and 78° rolling with 67° sliding.

Figure 5.45 shows such a comparison for both H^*_{min} and $H_o{}^*$

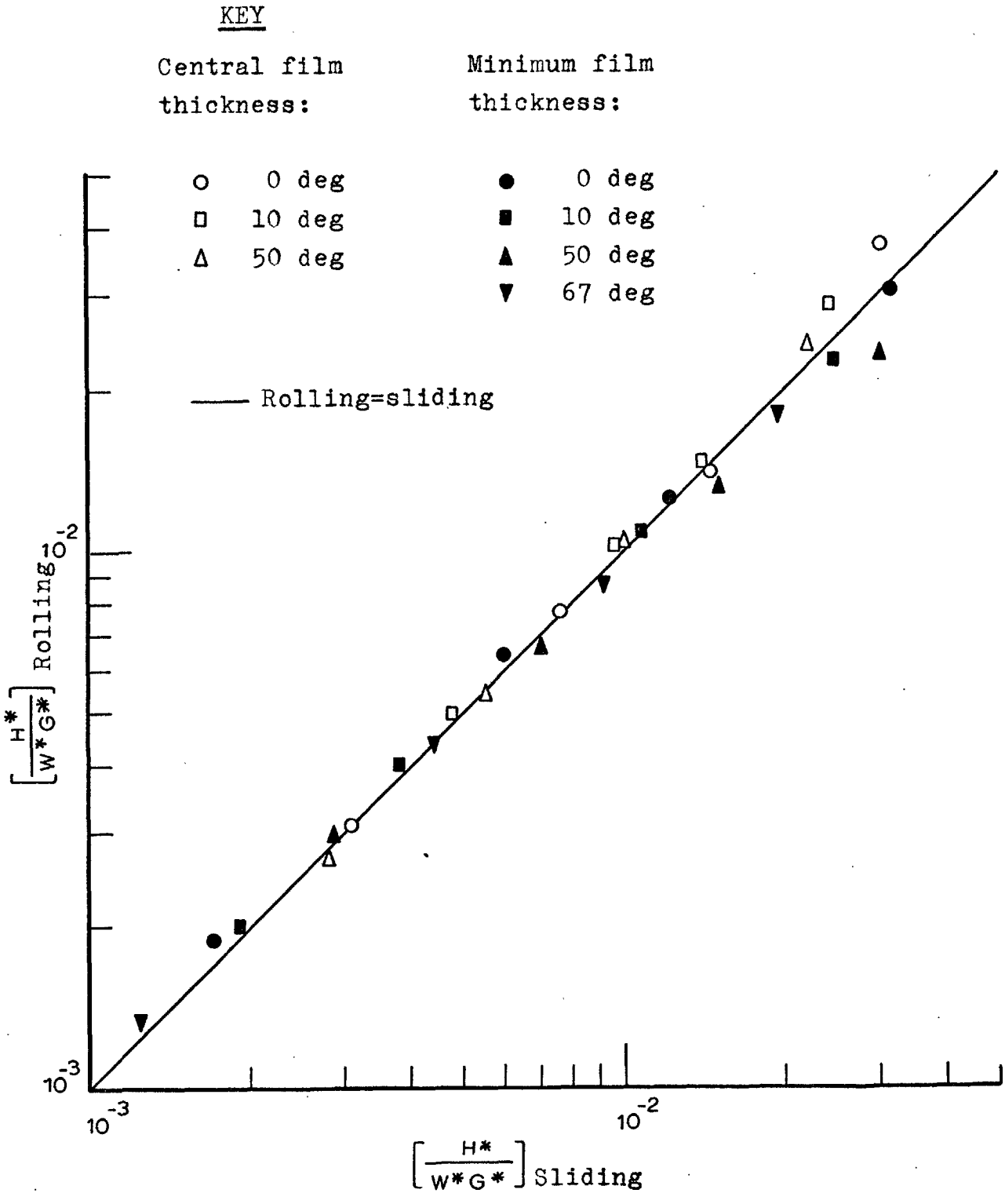


Fig. 5.45 Comparison of rolling & sliding ehd film thicknesses.

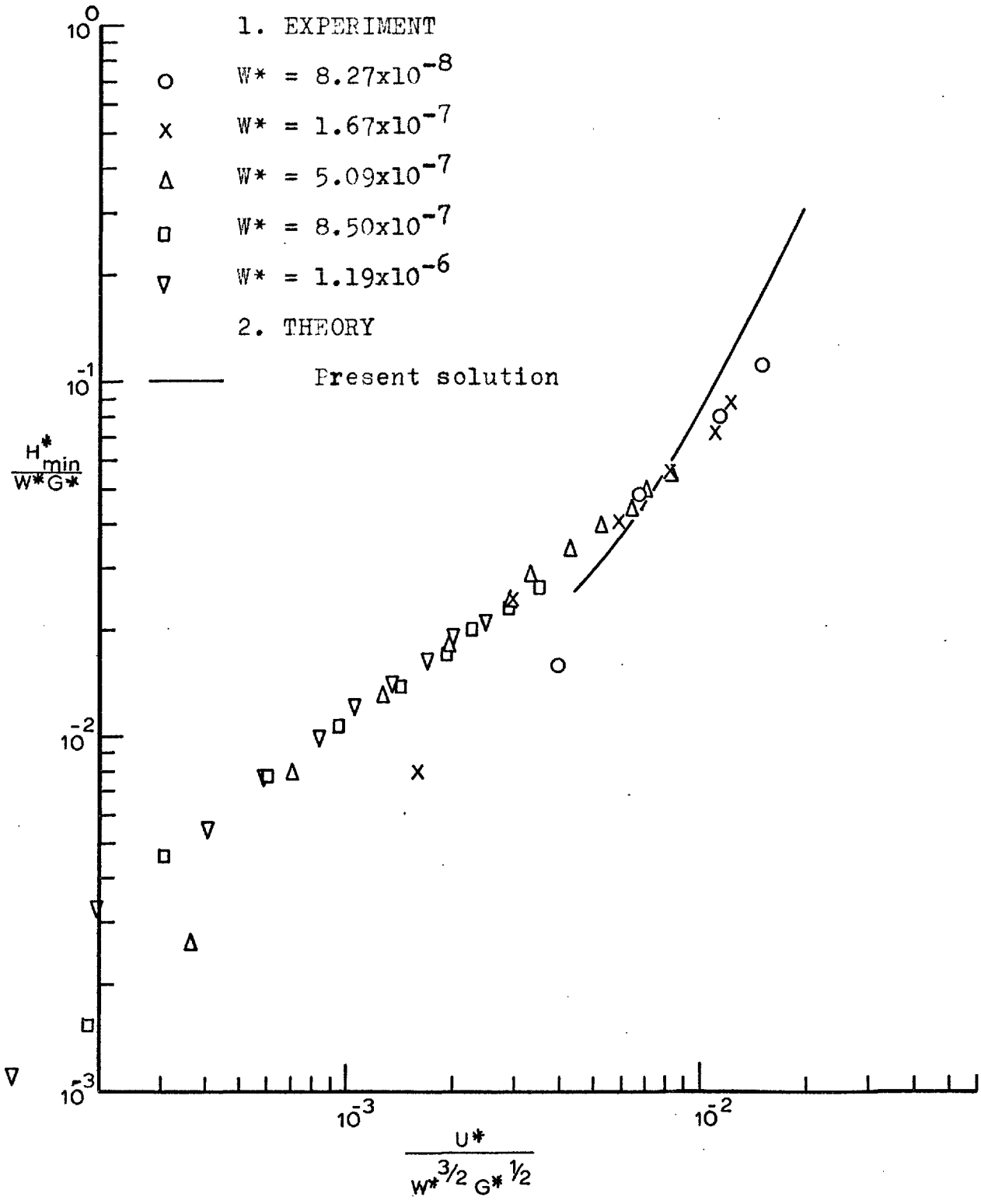


Fig. 5.46 Minimum film thickness group vs. speed group for drive angle of 0 deg. (Rolling contact)

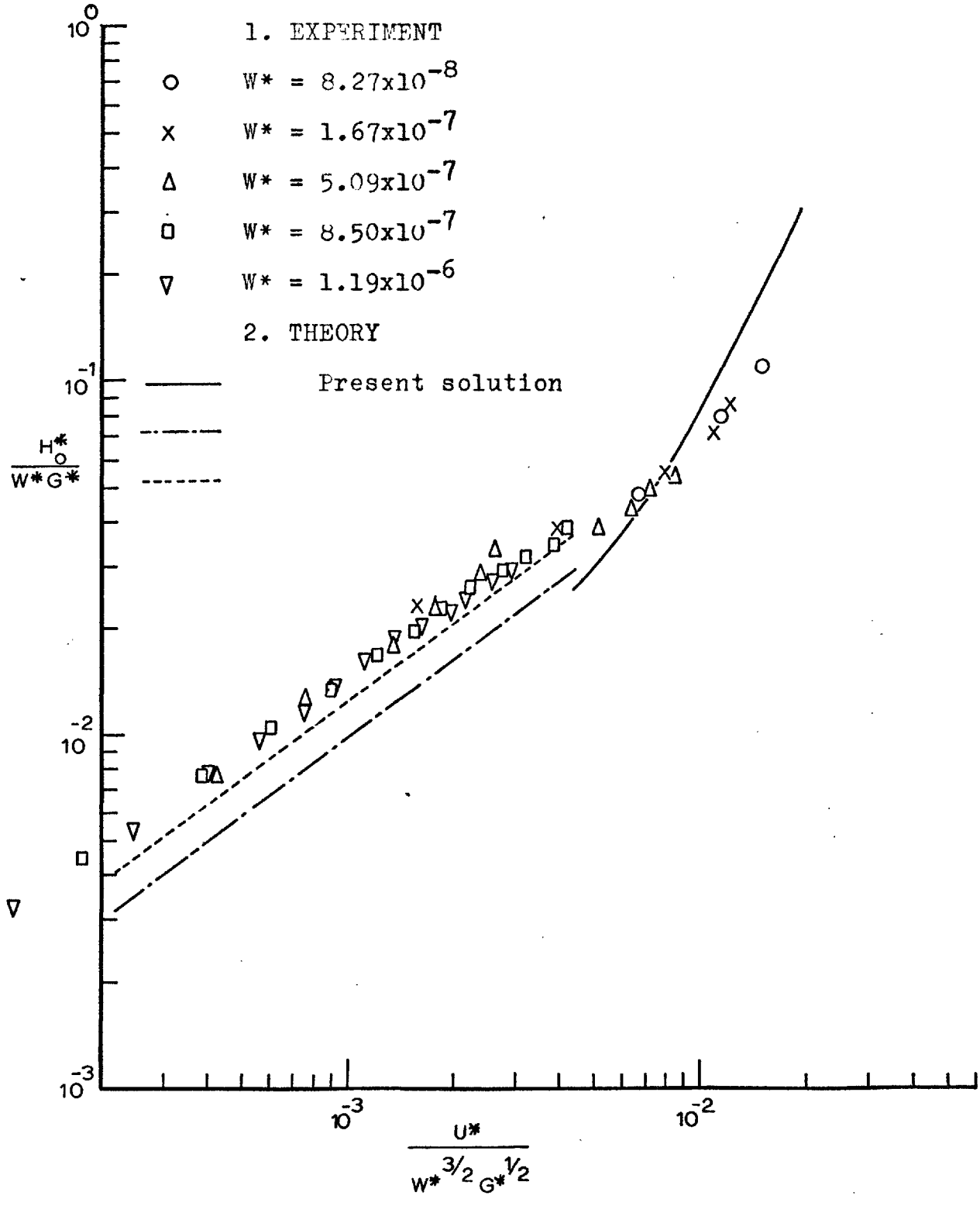


Fig. 5.47 Central film thickness group vs. speed group for drive angle of 0 deg. (Rolling contact)

at all angles in the EHL range of experiments. There is no noticeable difference between rolling and sliding film thicknesses. Foord (2), however, found that film thicknesses in sliding, for the same dimensionless speed parameters were considerably lower than rolling values. He concluded that this was almost certainly due to viscous heating in the inlet sweep. As the conditions in the elliptical contact experiments were less severe than in Foord's point contact experiments, such heating is reduced and differences between rolling and sliding would be expected to be less, as is indeed the case.

The speed used when plotting figures 5.35 to 5.44 was calculated from equation 5.24. Thus, when slip occured, the plotted values of $U^*/(W^{*3/2} G^{*1/2})$ was too large causing an apparent drop in film thickness for a given speed, particularly noticeable in the minimum film thickness plots. Figures 5.46 and 5.47 show the minimum and central film thicknesses for rolling along the groove ($\theta = 0^\circ$) but with slip measured and U^* corrected accordingly. The theories of Archard andCowking, Cheng and section 5.2 are shown for comparison. Since the results are the same as in sliding, conclusions made earlier also apply here.

Slip corrections have been restricted to the 0° case because at any other angle they become meaningless, as equation 5.25 demonstrates. As slide/roll ratio varies, so too does the effective drive angle. Thus, except at 0°, a slip corrected graph would no longer be for a constant effective drive angle. In the EHL region, however, where slip is negligible, the results are still valid and the conclusions of section 5.3.5 still stand.

One other topic of interest on all the film thickness

graphs presented is the appearance of points well below the majority - especially noticeable on minimum film thickness plots. These all represent the first black fringe and consequently a film thickness of about 1 - 2 μin. Three possible explanations can be offered.

a) There may be an error in measurement because the observations are at the limit of the simple optical technique employed.If so, it is very consistent, which tends to suggest that some other reason should be sought.

b) Some non-hydrodynamic mechanism, such as surface chemistry, may be acting. Wymer (16), who observed a similar effect in line contacts, found that it depended on the lubricant composition.

c) Since the oil film thickness is the same order as the surface roughness, it could be that asperity contact may be playing an important role. However, if an appreciable portion of the load were being taken by the asperities, one would expect the film to be thicker than that produced by EHD action alone.

No definite conclusions can be drawn without further investigations using a refined optical technique such as that of Westlake (2).

References for Chapter 5

1. Foord C.A., Hammann W.C. and Cameron A. 'Evaluation of lubricants using optical elastohydrodynamics' ASLE trans. Vol. 11, 1968, pp.31-43.
2. Foord C.A., Wedeven L.D., Westlake F.J. and Cameron A. 'Optical elastohydrodynamics' Proc. I.Mech.E. Vol. 184 Pt.1.
3. Gohar R., 'Oil film thickness and rolling friction in elastohydrodynamic point contact' ASME Paper no. 70-Lub-2 Lubrication Conference 1970.
4. Kapitza P.L., 'Hydrodynamic theory of lubrication during rolling' Zhurn. Tekh. Fiz., Vol. 25, No. 4, 1955, pp.747-62.
5. Archard J.F., and Cowking E.W., 'Elastohydrodynamic lubrication at point contacts' Proc. I.Mech.E. Vol.180 Pt. 3B 1965-1966, pp. 47-56.
6. Cheng H.S., 'A numerical solution of the elastohydrodynamic film thickness in an elliptical contact' Journal of Lubrication Technology, Trans. ASME, Series F,Vol. 92, No.1, Jan. 1970, pp.155-162.
7. Cameron A., 'Principles of lubrication' Longmans, London 1966.
8. Wedeven L.D., Evans D. and Cameron A., 'Optical analysis of ball bearing starvation' ASME Paper no. 70-Lub-19, Lubrication Conference, Oct. 1970.
9. Hertz H., 'On the contact of elastic solids' and 'On the contact of rigid elastic solids and on hardness' reprinted in 'Miscellaneous Papers' translated by Jones D.E. and Schott G.A. Macmillan Co. Ltd., London 1896, pp. 146-162, 163-183.
10. Snidle R.W. and Archard J.F. 'Lubrication at elliptical contacts' I.Mech.E. Tribology Convention 1969, Paper 17 pp.140-148.

11.'Investigation of scientific and industrial research', Central Scientific Research Institute for Technology and Mechanical Engineering, Moscow, Book no.30, 1949 pp.115-116.

12.Dowson D., Higginson G.R. and Whitaker A.V., 'Elasohydrodynamic lubrication: A survey of isothermal solutions', Journal of Mechanical Engineering Science, Vol. 4, 1962 p.121

13.Taylor G.I., 'Cavitation in hydrodynamic lubrication' 'Cavitation in real liquids' pp.81-101, Ed. Davies R., Elsevier 1964.

14.Gohar R., 'Oil films under elastohydrodynamic conditions', Ph.D. thesis, 1965 University of London.

15.Ranger A., Private communication, Imperial College.

16.Wymer D.G., 'Elastohydrodynamic lubrication of a rolling line contact', Ph.D. thesis, 1972 University of London.

Chapter 6 SLIDING FRICTION IN ELASTOHYDRODYNAMIC CONTACTS

6.1 Review

Some recent research in elastohydrodynamic lubrication has been on the traction characteristics of the contact. This has important applications in rolling element bearings, gears and friction drives. The theoretical model has usually been one of nominal line contact, where the slip to roll ratio of the rolling elements can be varied. This model has the advantage of relative simplicity coupled with the fact that considerable information has been amassed from computer solutions giving details of film shape and pressure distribution (1). Both these are important in the determination of traction forces. By assuming that the load between steel discs was sufficient to cause an elliptical pressure distribution, Crook (2), found how the traction varied with slip-roll ratio. Using a simple Newtonian model for the oil, which was piezo-viscous, he showed that the heat generated by viscous shearing depended on the local viscosity and temperature in the nip. These were shown to be little affected by the presence either of isothermal bounding surfaces or of surfaces whose temperatures increased due to heating. When he compared his theoretical results with those he had found experimentally from a 2-disc machine, theoretical traction was too high, although the general shape of the traction speed curve was the same, the traction rising from zero to a maximum and then falling with increase in sliding speed. The rise and fall he attributed to the gradual increase of heating in the oil film.

More recently, investigators have turned their attention to the possible causes of the difference between theory and

experiment. One approach has been to assume that experimental results are correct and use these in the theory to determine the oil pressure-viscosity properties under shear (3). Another has been to try various oil pressure-temperature-viscosity relationships until a good fit between theory and experiment is obtained (4). Under these circumstances the results cannot fail to be successful and have indeed provided a major breakthrough in our knowledge of oil traction properties.

Some traction studies have also been carried out using nominal point contact geometry. Although it is experimentally easier to measure film thickness (by interferometry), an accurate theory, with a minimum of assumptions, is more difficult to obtain. However, Grubin-type approximations have yielded accurate film thickness predictions (ref:5) and rolling friction has been determined both theoretically and experimentally (ref:6) Smith (7) has investigated sliding friction between a spherical and a cylindrical steel roller and interpreted his results on the hypothesis that the frictional force represents the shearing of a film of essentially solidified lubricant at a shear plane of molecular dimensions. More recently, Gentle (8) used a ball and plate machine to examine non-Newtonian effects in the oil film. He used an analogy of the granular behaviour of solids to describe the effects theoretically.

There is still, however, a need to compare theory with experiment for point contacts using established properties of the oil and straight-forward elastohydrodynamic theory. This is done in the work presented below. The theory, for the most part, uses Crook's analytical approach but numerical solutions which enable the use of more realistic temperature boundary conditions are also presented. Theoretical frictions calculated

using isothermal assumptions, are provided as a basis for comparison. The predictions are compared with friction measurements for three different material combinations, with reduced moduli from 0.89×10^6 lbf/in^2 to 65.4×10^6 lbf/in^2. By this means the ranges of application of various theories and assumptions were investigated.

All experiments were restricted to pure sliding, that is, with a slide/roll ratio of unity. This was simpler experimentally and had the advantage that the rolling friction could be ignored in all theoretical predictions, being negligible with respect to the sliding friction (6). Also, all experimental work was performed using a circular point geometry, this being necessitated by the need for varying the material combination, since flat discs of Perspex, glass and sapphire were readily available. In addition, it was easier to reach higher Hertz pressures than with grooved plates. However, although the integrals become more involved, the theory may be readily extended to the geometry of an elliptical contact and the conclusions are completely general.

6.2 Theory

6.2.1 Introduction

All predictions of elastohydrodynamic sliding friction presented here involve the assumption that the region of friction is Hertzian in shape (figure 6.1) of radius 'a', where 'a' is given by:-

$$a^3 = \frac{3}{2}\frac{RW}{E'} \qquad -6.1$$

and that the pressure p, at radius r is given by:

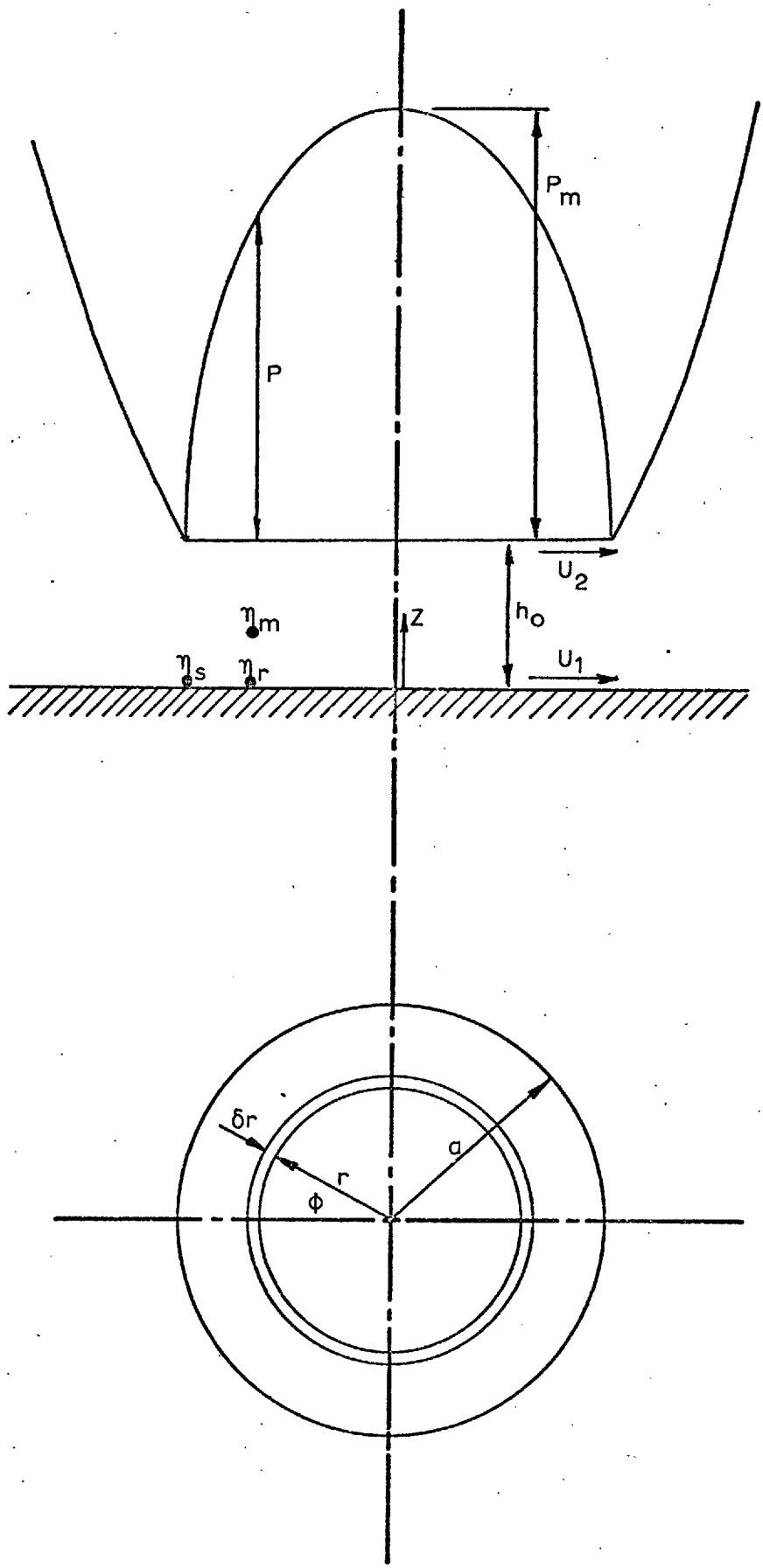


Fig.6.1 Diagram of the contact with co-ordinate system.

$$p = p_m \left(1 - \left(\frac{r}{a}\right)^2\right)^{\frac{1}{2}} \qquad -6.2$$

where $$p_m = \frac{3W}{2\pi a^2} \qquad -6.3$$

and if $r > a$ then $p = 0$.

This is not exactly true, as the pressure on the entry side starts to become finite at a considerable distance from the centre of the contact. However, it only becomes large when $r < a$ so the viscosity outside the contact is low and as h increases sharply for $r > a$ friction for $r > a$ is small also. Hence the limitation on the area is accurate enough.

When there is a difference in the velocities of the two surfaces bounding the lubricating oil film, then the oil is subject to shear forces. Therefore, assuming Newtonian behaviour, the shear stress in the x direction (τ) on a small element is:-

$$\tau = \eta \frac{\partial u}{\partial z} \qquad -6.4$$

where, in general, η is a function of pressure and temperature. The friction force due to sliding, F_s, is obtained by integrating $\tau \, dx \, dy$ over the area of friction.

6.2.2 Isothermal sliding friction

Assuming that η is constant across the film and that pressure gradients can be neglected, the velocity gradient $\partial u / \partial z$ may be written $(U_2 - U_1)/h_o$. Hence the coefficient of friction μ (defined as F_s/W) may be obtained from:-

$$\mu = 2.\pi \frac{(U_2 - U_1)}{W h_o} \int_o^a \eta \, r \, dr \qquad -6.5$$

If η is constant with pressure and temperature, then this becomes

$$\mu = 4.12 \left[\frac{\delta^* U^*}{W^{*\frac{1}{3}} H_o^*} \right] \qquad -6.6$$

As has been mentioned above, accurate film thickness predictions are available from computer solutions. Evans (9) gives:-

$$H_o^* = 1.055 \, (G^* U^*)^{5/7} \, (W^*)^{-1/21} \qquad -6.7$$

Substituting 6.7 in 6.6 gives:-

$$\mu\left(\frac{W^*}{U^*}\right) = 3.9 \, \delta^* \left(\frac{U^* G^*}{W^*}\right)^{-5/7} \qquad -6.8$$

If we assume that viscosity is exponentially dependent upon pressure, then 6.5 becomes:-

$$\mu = \frac{2\pi (U_2 - U_1)\eta_o}{W h_o} \int_o^a \exp\left\{\alpha p_m \sqrt{1 - \left(\frac{r}{a}\right)^2}\right\} r \, dr \qquad -6.9$$

Integrating between the specified limits and choosing dimensionless groups as before, 6.9 becomes:-

$$\mu\left(\frac{W^*}{U^*}\right) = 7.8 \, \delta^* \left(\frac{U^* G^*}{W^*}\right)^{-5/7} \left[\frac{e^{\bar{p}_m} (\bar{p}_m - 1) + 1}{\bar{p}_m^{\,2}} \right] \qquad -6.10$$

Where $\bar{p}_m$, the non-dimensional peak pressure, may be obtained from:-

$$\bar{p}_m = 0.366 \, W^{*\frac{1}{3}} \, G^* \qquad -6.11$$

Assuming that viscosity depends on pressure, as discussed in section 4.4, then equation 6.5 becomes:-

$$\mu = \frac{2\pi (U_2 - U_1)\eta_o}{W h_o} \int_o^a \exp\left[\frac{K_o p}{1 + K_1 p}\right] r \, dr \qquad -6.12$$

where p is given by equation 6.2.

This expression cannot be integrated analytically except to give a series solution. The results were therefore obtained using a simple numerical integration, giving an answer of the

form:-

$$\mu\left(\frac{W^*}{U^*}\right) = 7.8\ \delta^*\left(\frac{U^*\ G^*}{W^*}\right)^{-5/7}\int_0^1 \phi_2(p)\ \bar{r}\ d\bar{r} \qquad -6.13$$

That no errors were introduced by using this numerical procedure was verified by integrating 6.9 similarly and comparing with the analytical solution.

It should be noted that equations 6.8 and 6.13 contain an anomaly since they are derived using values of h_o given by 6.7 and this equation was itself derived assuming exponential pressure viscosity dependence. However, provided that the predictions (especially from 6.8) are regarded as the result of applying the assumptions at a given film thickness, this being the real film thickness, they are of value.

As would be expected from the assumptions, the scope of the isothermal predictions of equations 6.8, 6.10 and 6.13 are severely limited. However, there are applications to soft EHD contacts since the pressures in them are low and hence viscosities and viscous heating are low too. Under other, more severe, conditions the frictions predicted by all, except the isoviscous case of equation 8, are far higher than those experienced. The error lies in the viscosity term being too great and only by considering the reduction of viscosity across the film, resulting from shear heating, can more realistic friction predictions be made.

6.2.3 Sliding friction with heating (analytical)

The temperature rise in the oil film depends on the balance between the generation and the dissipation of the heat resulting from the shearing of the oil. Dissipation takes place by conduction through the oil to the disc surfaces and by convection in the oil flowing through the contact. Crook (2)

has shown that, except in regions far from the contact, heat dissipation by convection is negligble compared to conduction. With this assumption and ignoring compressibility, the energy equation for the heat balance may be written as:-

$$\eta\left(\frac{\partial u}{\partial z}\right)^2 = -K\,\frac{d^2\theta}{dz^2} \qquad -6.14$$

where θ is the temperature and K the thermal conductivity of the oil.

From the simplified Navier-Stokes equation:-

$$\left.\begin{aligned}\frac{\partial p}{\partial x} &= \frac{\partial}{\partial z}\left(\eta\,\frac{\partial u}{\partial z}\right)\\ \frac{\partial p}{\partial y} &= \frac{\partial}{\partial z}\left(\eta\,\frac{\partial v}{\partial z}\right)\end{aligned}\right\} \qquad -6.15$$

If rolling friction is ignored, it can be shown that (ref:2) 6.15 becomes:-

$$\frac{\partial u}{\partial z} = \frac{-\eta_m^2}{\eta}\cdot\frac{(U_2 - U_1)^2}{h^2} \qquad -6.16$$

Combining 6.14 and 6.16

$$K\,\frac{\partial^2\theta}{\partial z^2} = -\frac{\eta_m^2}{\eta}\cdot\frac{(U_2 - U_1)^2}{h^2} \qquad -6.17$$

If the viscosity varies with temperature as postulated in equation 4.7, then

$$\eta = \eta_r\, e^{-\beta\theta} \qquad -6.18$$

where $\eta_r = \eta_o \int \phi_3(p)$

Substituting 6.18 in 6.17 and integrating gives:-

$$\frac{\partial\theta}{\partial z} = \pm\left[2\omega\left(1 - \frac{A}{\omega\beta}\, e^{\beta\theta}\right)\right]^{\frac{1}{2}} \qquad -6.19$$

where ω is an integration constant and

$$A = \frac{\eta_m^2 (U_2 - U_1)^2}{K h^2 . \eta_r}$$

Equation 6.19 suggests slope symmetry about the median plane. Thus, if we assume that the surface temperatures are both the same, being that of the oil at inlet, (θ_s), the temperature rise at both surfaces is zero, and ω may be determined from the boundary conditions:

$$\theta = 0 \text{ when } z = 0 \quad \text{and} \quad \theta = 0 \text{ when } z = h$$

ω is found to be given by:-

$$\omega = \frac{8 \eta_m^2}{\eta_r^2 h^2 \beta^2} . \varphi (\varphi + 1) \qquad -6.20$$

where $$\varphi = \frac{(U_2 - U_1)^2 \eta_r \beta}{8 K} \qquad -6.21$$

From 6.19 it can be seen that θ is at a maximum (θ_c) when $z = h/2$. This occurs when $\partial\theta/\partial z = 0$, that is when

$$A e^{\beta\theta_c} = \omega \beta \qquad -6.22$$

Hence from 6.20 and 6.22 the maximum temperature rise can be found:-

$$\theta_c = \frac{1}{\beta} \ln \left[\frac{\eta_r \beta (U_2 - U_1)^2}{8 K} + 1 \right] \qquad -6.23$$

In general, the temperature at $z = h/m$ differs from θ_c. However, by integrating equation 6.19 and using the boundary conditions that when $z = 0$ $\theta = 0$ and when $z = h/2$ $\theta = \theta_c$ an expression for ω and hence, from equation 6.20 η_m / η_r may be found:

$$\frac{\eta_m}{\eta_r} = \frac{1}{\sqrt{\varphi}\ \sqrt{\varphi+1}} \ln\left(\sqrt{\varphi+1} + \sqrt{\varphi}\right) \qquad -6.24$$

If $\bar{\eta}_m = \frac{\eta_m}{\eta_o}$ and $K^* = \frac{K \eta_o \alpha^2}{\beta R^2}$, then assuming an exponential pressure viscosity law, equations 6.21 and 6.24 can be written as:-

$$\varphi = \frac{\delta^{*2} U^{*2} G^{*2}}{8 K^*} \exp\left[0.365\ G^*\ W^{*\frac{1}{3}}\ (1 - \bar{r}^2)^{\frac{1}{2}}\right] \qquad -6.25$$

$$\bar{\eta}_m = \exp\left[0.365\ G^*\ W^{*\frac{1}{3}}\ (1 - \bar{r}^2)^{\frac{1}{2}}\right] \cdot \frac{\ln\left(\sqrt{\varphi+1} + \sqrt{\varphi}\right)}{\sqrt{\varphi}\ .\ \sqrt{\varphi+1}} \qquad -6.26$$

Since the rolling friction has been neglected, the shear stress through the film is constant at

$$\tau_{zr} = \frac{\eta_m (U_2 - U_1)}{h_o}$$

Therefore for a circular contact, the sliding friction coefficient is:-

$$\mu = \frac{2\pi (U_2 - U_1)}{W h_o} \int_o^a \eta_m\ r\ dr \qquad -6.27$$

Substituting H^* from equation 6.7 and expressing the results non-dimensionally:-

$$\mu\left(\frac{W^*}{U^*}\right) = 7.8\ \delta^* \left(\frac{U^* G^*}{W^*}\right)^{-5/7} \int_o^1 \bar{\eta}_m\ \bar{r}\ d\bar{r} \qquad -6.28$$

The friction was obtained by integrating equation 6.27 numerically in a similar manner to equation 6.12 and the result was expressed in the form of equation 6.28.

The procedure was repeated and the friction predictions obtained using the alternative pressure viscosity law of equation 4.3. The only changes necessary were to the exponent

terms in equations 6.25 and 6.26. As mentioned before, there exists an anomaly between the law used to derive film thickness and the law used to predict friction. The error in this instance was considered to be negligible, however, since the inclusion of equation 4.3 in the film thickness prediction would have very little effect on the result.

The maximum temperature rise in the oil film was also predicted in both cases using equation 6.23.

An additional assumption implicit in the prediction of sliding friction is concerned with the temperature boundary conditions. There was some doubt as to the realism of those used in the previous analysis, namely that both surfaces were at the same temperature throughout the contact. However, since the resulting symmetry was necessary to the solution of the equations, alternative boundary conditions did not lead to an analytical solution.

It seems more logical that, in the experimental situation where the plate is stationary, θ should be the temperature rise from the ball which remains at a constant temperature close to that at the inlet. If speeds are high then there will be insufficient time for a steady state temperature distribution to be established in the ball. It will thus continuously present the contact with a cool surface and hence will absorb most of the heat. The stationary plate, however, will become heated up until it reaches equilibrium and will absorb very little heat. If speeds are low, then steady state conditions may be obtained in both bodies. Both surfaces may then be considered to be at a mean temperature given by flash theory (10) with heat flows inversely proportional to their thermal conductivities. However, since all plate materials used in the experiments were poor

conductors of heat, the ratio of the heat flows to the ball and plate repectively was large ($\simeq 40$) and so the ball still absorbed most of the heat.

In the limit, therefore, realistic boundary conditions will be an isothermal ball and an adiabatic plate. To enable these and, if necessary, other boundary conditions to be employed, a numerical solution for the temperature, velocity and viscosity profiles within the contact was attempted.

6.2.4 Sliding friction with heating (numerical)

The disadvantage of any full numerical solution is the resulting complexity, which makes the use of a computer a necessity for performing the calculations. The gains in accuracy from such a procedure are often doubtful, but in the present case, as has been indicated, it appears that the boundary conditions used analytically are far from realistic and so the gains from a full solution could well be worthwhile.

Since one result of the solution was a viscosity profile, the use of the viscosity η_m was not necessary and so the equations solved were the energy equation as before (equation 6.17 and the Navier-Stokes equation (6.15) with $\partial p/\partial x = \partial p/\partial y = 0$; that is with no pressure gradients and hence no rolling friction. All flow was thus assumed to be in the x-direction with the shear stress still constant across the film.

At each radius the procedure was as follows:

1. Guess initial solutions for the distribution of velocity, viscosity and temperature rise across the film.
2. Calculate a new velocity profile using the Navier-Stokes equation and the old viscosity profile.
3. Calculate a new temperature profile from the energy equation and the new velocity and old viscosity profiles.

4. Calculate a new viscosity profile from the new temperature profile using a temperature viscosity relationship.
5. Return to step 2 and repeat the procedure until there is no change in the calculated profiles.

Having determined the distributions at each station, the shear stress was found from the product of the velocity gradient and viscosity at any one point in the film. The friction was then obtained by integrating over the whole contact, as before.

Details of the program with the finite difference equations and listings are given in appendix 4.

6.2.5 Non-dimensional groups

In general terms, with $\delta^* = 1$, equation 6.28 can be written as:-

$$\mu\left(\frac{W^*}{U^*}\right) = \Phi_4\left[\left(\frac{U^*}{W^{*3/2}\ G^{*1/2}}\right),\ (G^{*3}\ W^*),\ (G^{*6}\ K^*)\right] \qquad -6.29$$

for thermal conditions.

If φ approaches zero, isothermal conditions prevail throughout the film. Equation 6.28 can then be integrated analytically and becomes the same as equation 6.10. Non-dimensionally this can be written as:-

$$\mu\left(\frac{W^*}{U^*}\right) = \Phi_5\left[\left(\frac{U^*}{W^{*3/2}\ G^{*1/2}}\right),\ (G^{*3}\ W^*)\right] \qquad -6.30$$

for isothermal conditions. Note that one group is suppressed when the conditions become isothermal. If, in addition, elasticity is not important, but viscosity still increases with pressure, equation 6.30 becomes:-

$$\mu\left(\frac{W^*}{U^*}\right) = \Phi_6\left[\left(\frac{U^*}{W^{*3/2}\ G^{*1/2}}\right)\right] \qquad -6.31$$

Finally, with no dependence of viscosity upon pressure,

$$\mu\left(\frac{W^*}{U^*}\right) = \text{constant} \qquad -6.32$$

This is the correct form of expression for undistorted sliding point contact friction under isoviscous conditions.

It is interesting to note that, in addition, the rolling friction can be expressed as:-

$$\mu_R\left(\frac{W^*}{U^*}\right) = 8.6 \left(\frac{U^*}{W^{*3/2}\, G^{*1/2}} \right)^{-0.2} \left(W^*\, G^{*3} \right)^{-0.033} \qquad -6.33$$

where equation 6.33 has been obtained from reference 6. It was shown there that $\mu_R \ll \mu$ at all but very low values of slip.

The results of the prediction and of the experiments were plotted in the manner suggested by equation 6.29 and 6.30, that is, with $U^*/(W^{*3/2}\, G^{*1/2})$ as abscissae and $\mu\,(W^*/U^*)$ as ordinates. For a given material combination, K^* and G^* remained constant, whilst W^* and U^* were varied. Since the two plotted groups do not contain E', they therefore apply to an undistorted contact. A similar form of plot is used for film thickness in chapter 5.

6.3 Experiment

6.3.1 Low modulus materials (Perspex)

The plots of figures 6.2 and 6.3 show the experimentally determined frictions for a tungsten carbide ball sliding against a Perspex plate. The experimental points are for a range of loads and the band of theory represents the predicted spread with the same load range.

Figure 6.2 shows the isothermal theories of equations 6.8, 6.10 and 6.13 superimposed for comparison on the experimental

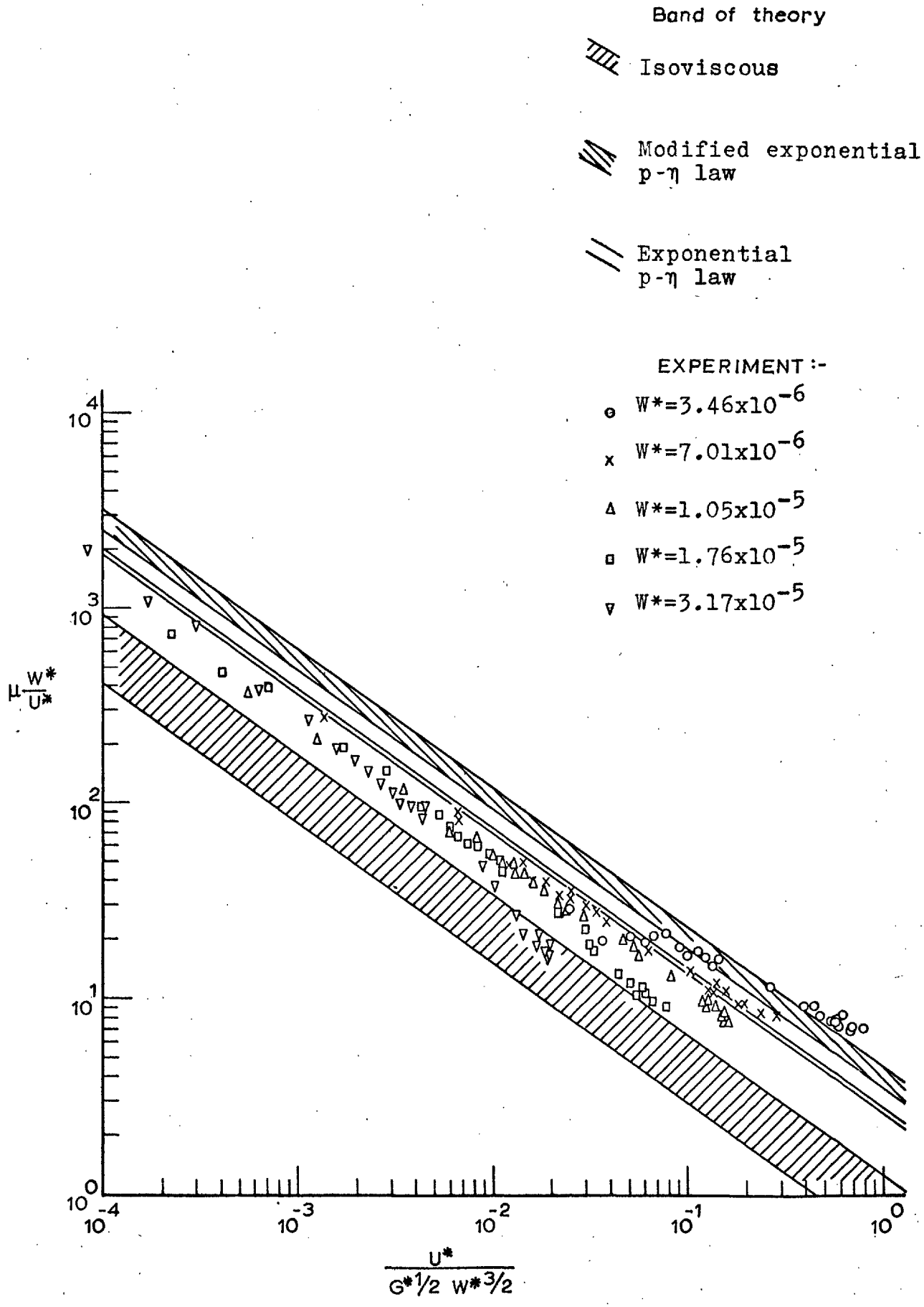


Fig.6.2 Sliding friction on perspex : experiment & isothermal theories.

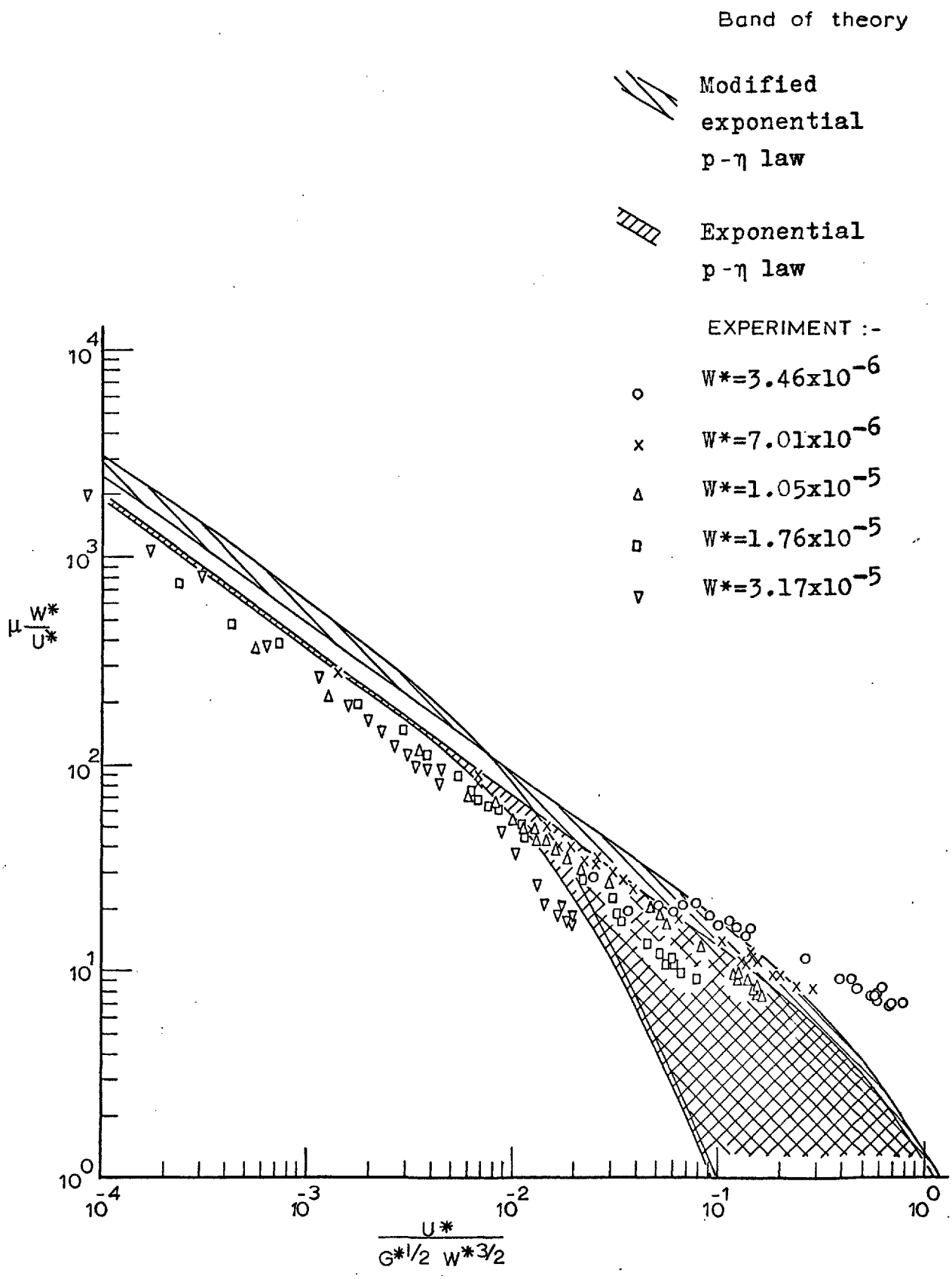


Fig.6.3 Sliding friction on perspex : experiment & thermal theories

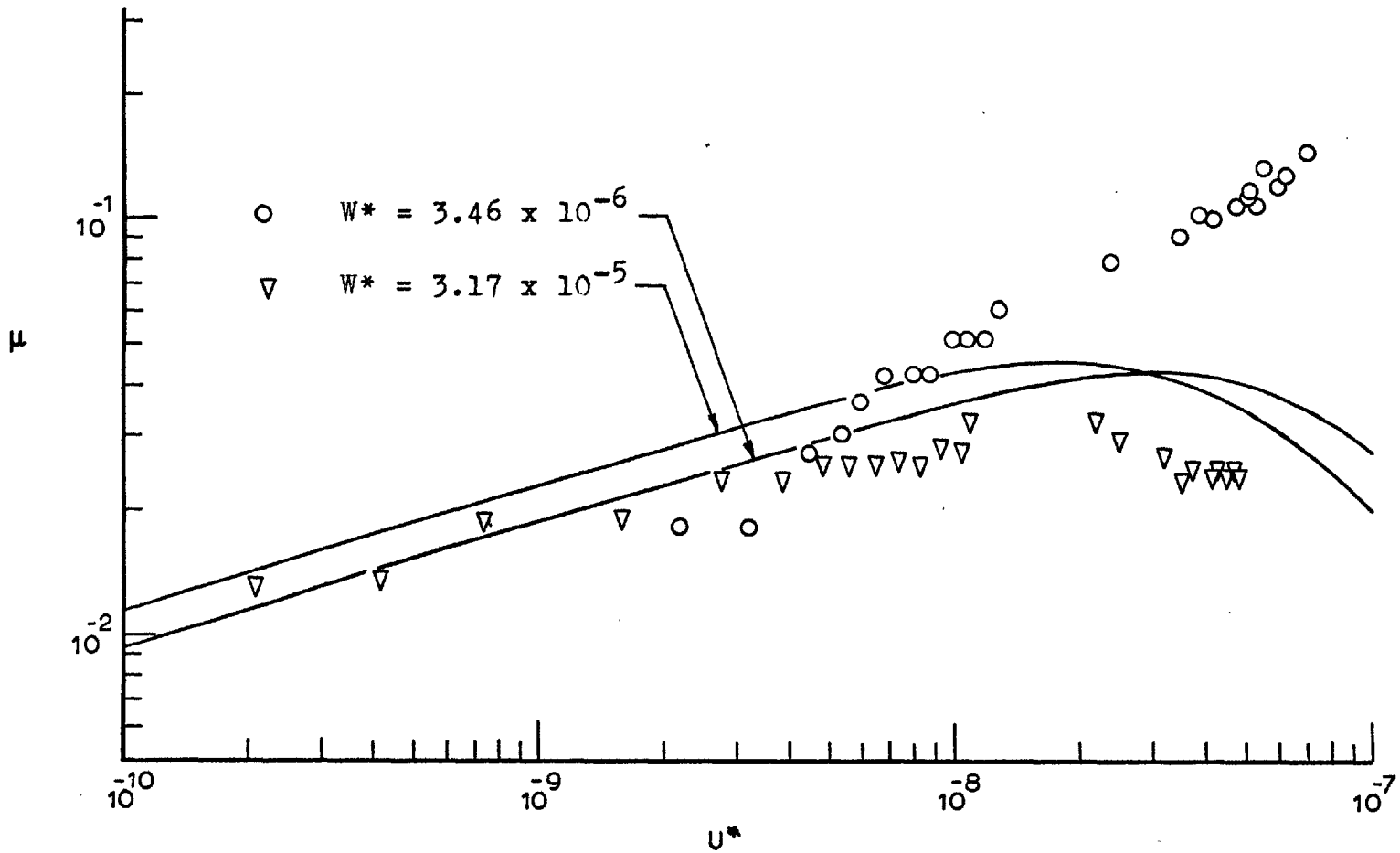


Fig.6.4 Perspex: sliding friction coefficient versus non-dimensional speed

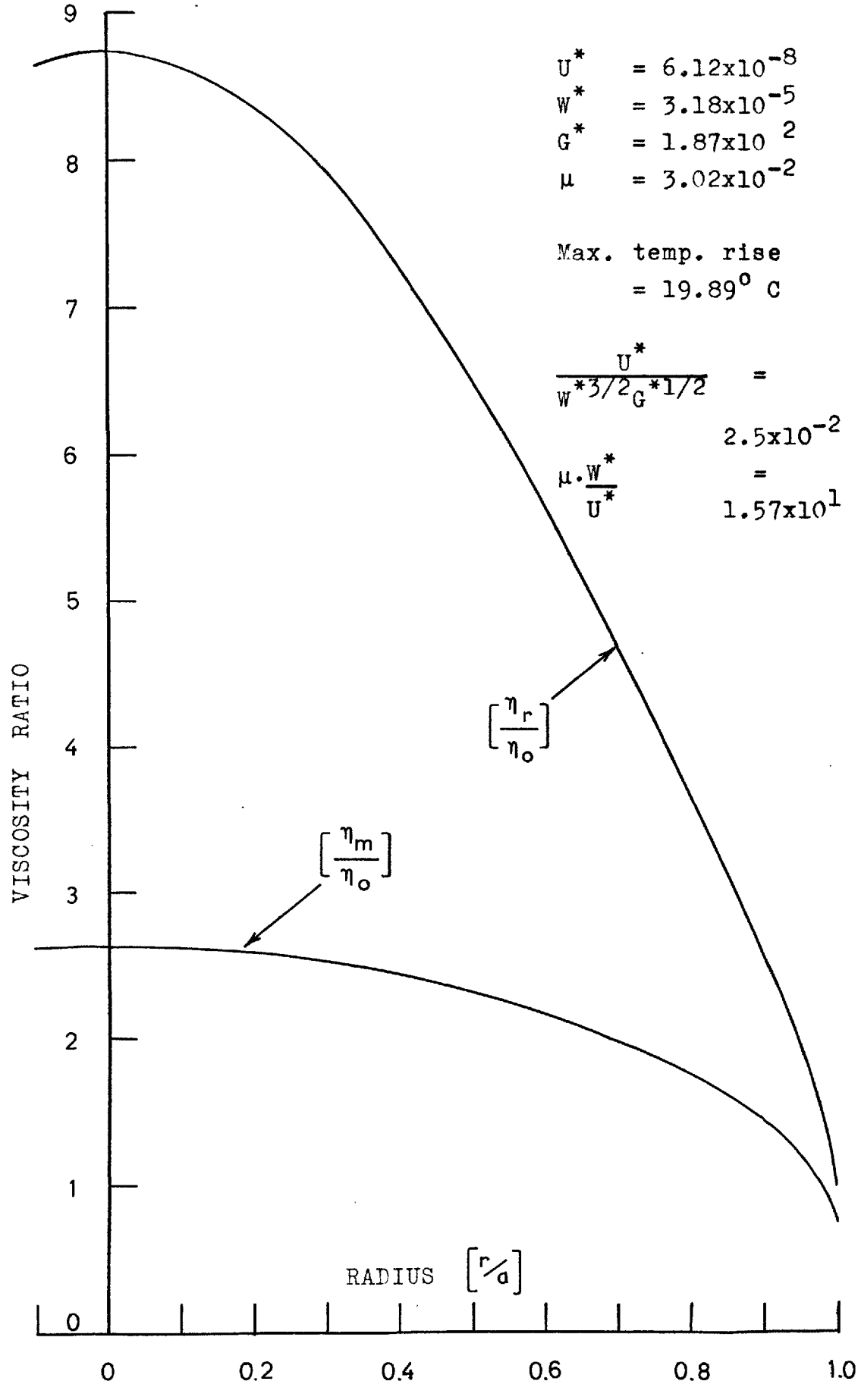


Fig.6.5 Reduction of viscosity by heating in a perspex contact

results. The theory of equation 6.8 predicts friction below experiment because of the absence of any increase in viscosity with pressure. Inclusion of this effect raises the theory to above the experiment, the exponential preesure viscosity law giving closer predictions than the modified law. Remembering the fit of these laws to the experimentally determined viscosities (figure 4.5) the opposite would be expected. However, since the material combination was so soft ($E' = 0.89 \times 10^6$ lbf/in^2), the peak pressures were very low (< 10,300 psi), hence the α -value used in equation 6.10 was the value at atmospheric pressure which, for this special case, gives a better prediction of viscosity than the modified law whose constants were chosen to give the best fit over the whole range.

The piezo-viscous theories and the experiments both have a small spread, showing the weak effect of the load group $W^* G^{*3}$. At higher speeds, the experimental results spread out, the same effect being noticed when the thermal theories are plotted as in figure 6.3. The spread can be attributed to the increased significance of the additional group $G^{*6} K^*$.

At even higher speeds, experiment tends to level off to a constant $\mu W^*/U^*$. This trend is suggested by equation 6.32. The speed has become so high that the surfaces are regaining their undeformed shapes and conditions are becoming isoviscous. The thermal theory is, by this stage, no longer valid since the assumption of a Hertzian region of friction no longer applies. Although careful use of dimensionless groups can explain experimental results with a minimum of plotting, the significance of individual parameters (such as μ) can become obscured. Thus, figure 6.4 shows μ plotted against U^* for the largest and smallest of the five experimental loads, the others being

omitted for clarity.Also shown are the predictions of equation 6.27 (with heating and an exponential pressure viscosity law), for the extremes of load used.

Over the lower part of the speed range, for all loads, friction increases as predicted, that is, $\mu \propto U^{*0.286}$. At higher speeds for the heaviest load, the Hertzian assumption still applies and there is a reduction in friction with increase of speed due to viscous heating. The effect that this heating has in reducing the working viscosity is demonstrated in figure 6.5. As can be seen, the working viscosity (η_m) in the centre of the contact is about three times smaller than the isothermally predicted viscosity η_r. At these higher speeds, for light loads there is a change in pressure distribution and consequent relaxation of the surfaces which leads to isoviscous undistorted conditions. μ should then increase in direct proportion to U^*. This tendency is already seen to be starting with the lowest value of W^* plotted on figure 6.4.

6.3.2 Medium modulus materials (glass)

The results presented in this section were obtained with a material combination having a reduced modulus of 19×10^6 lbf/in^2 provided by a tungsten carbide ball sliding against a lead glass plate.As before, the experimentally determined frictions are shown for a range of loads together with the band of theory representing the same load range.

Figure 6.6 shows the experimental results together with the isoviscous, the isothermal and the thermal theories, these last two employing the exponential pressure viscosity law. The pressure viscosity coefficient was taken as the dynamic value of 1.58×10^{-4} in^2/lbf determined by the method described in section 4.3.2. Figure 6.7 again shows experiment and isoviscous

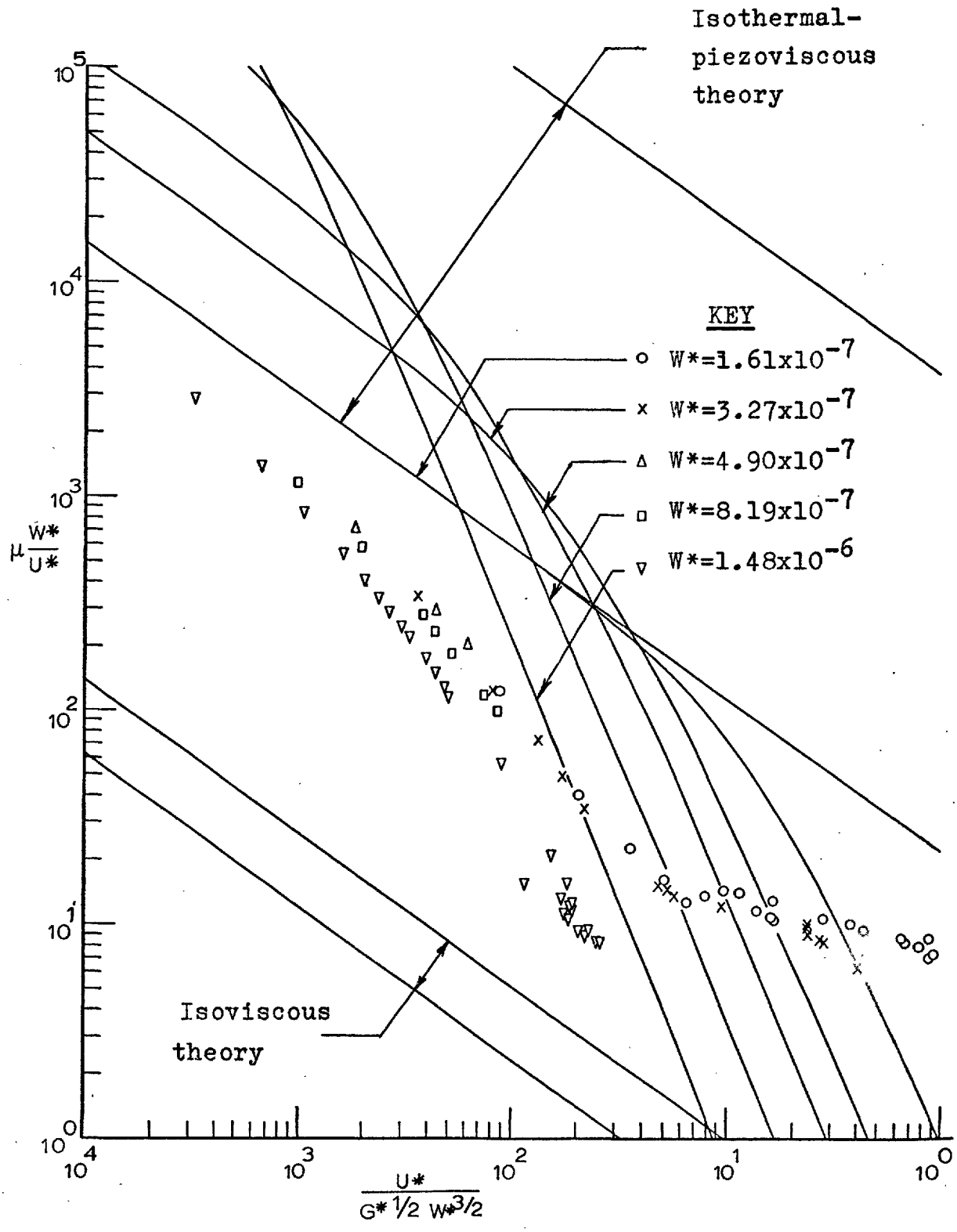


Fig.6.6 Sliding friction on glass : experiment & theory with exponential p-η law.

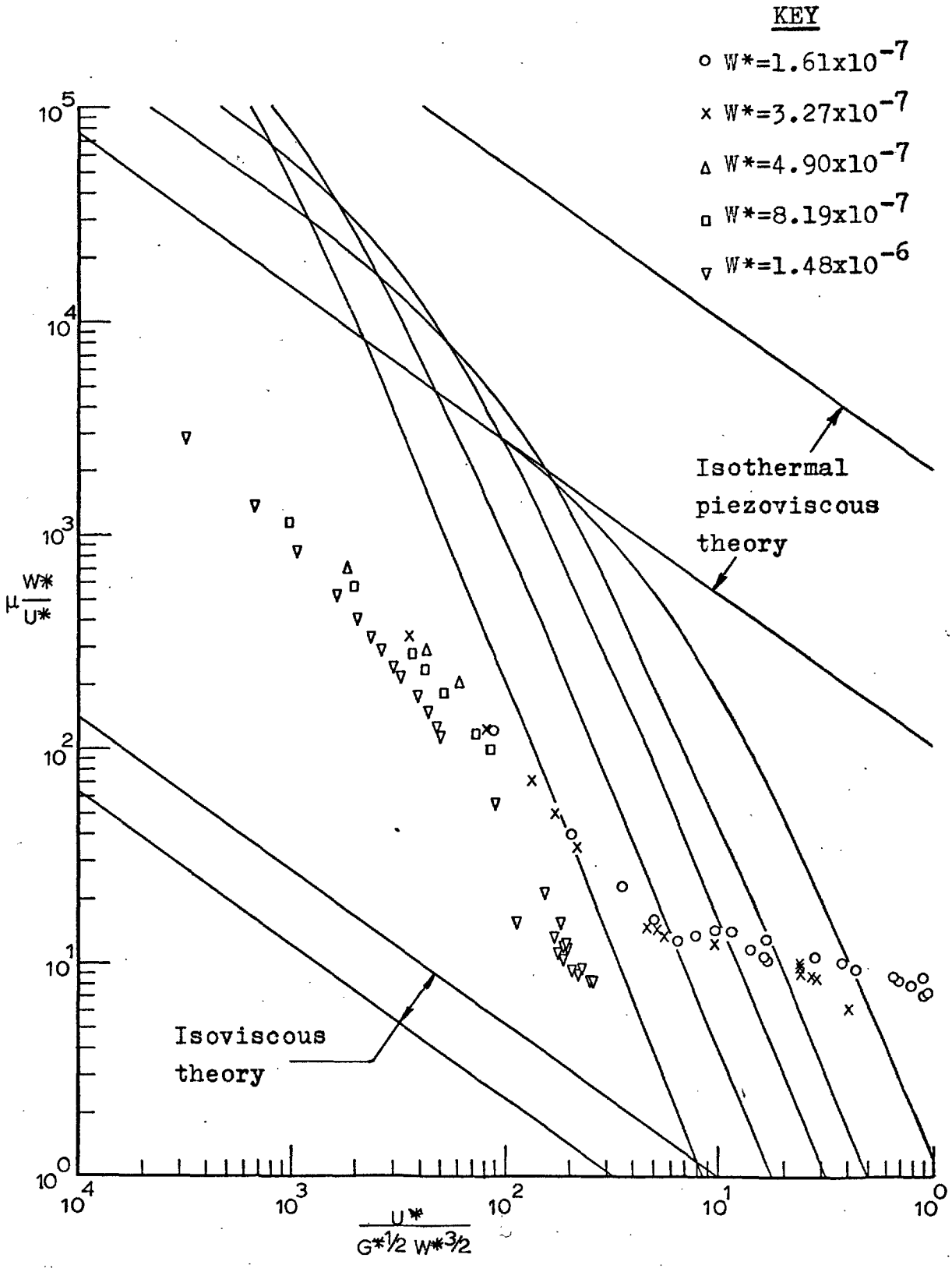


Fig.6.7 Sliding friction on glass : experiment & theory with modified exponential p-η law.

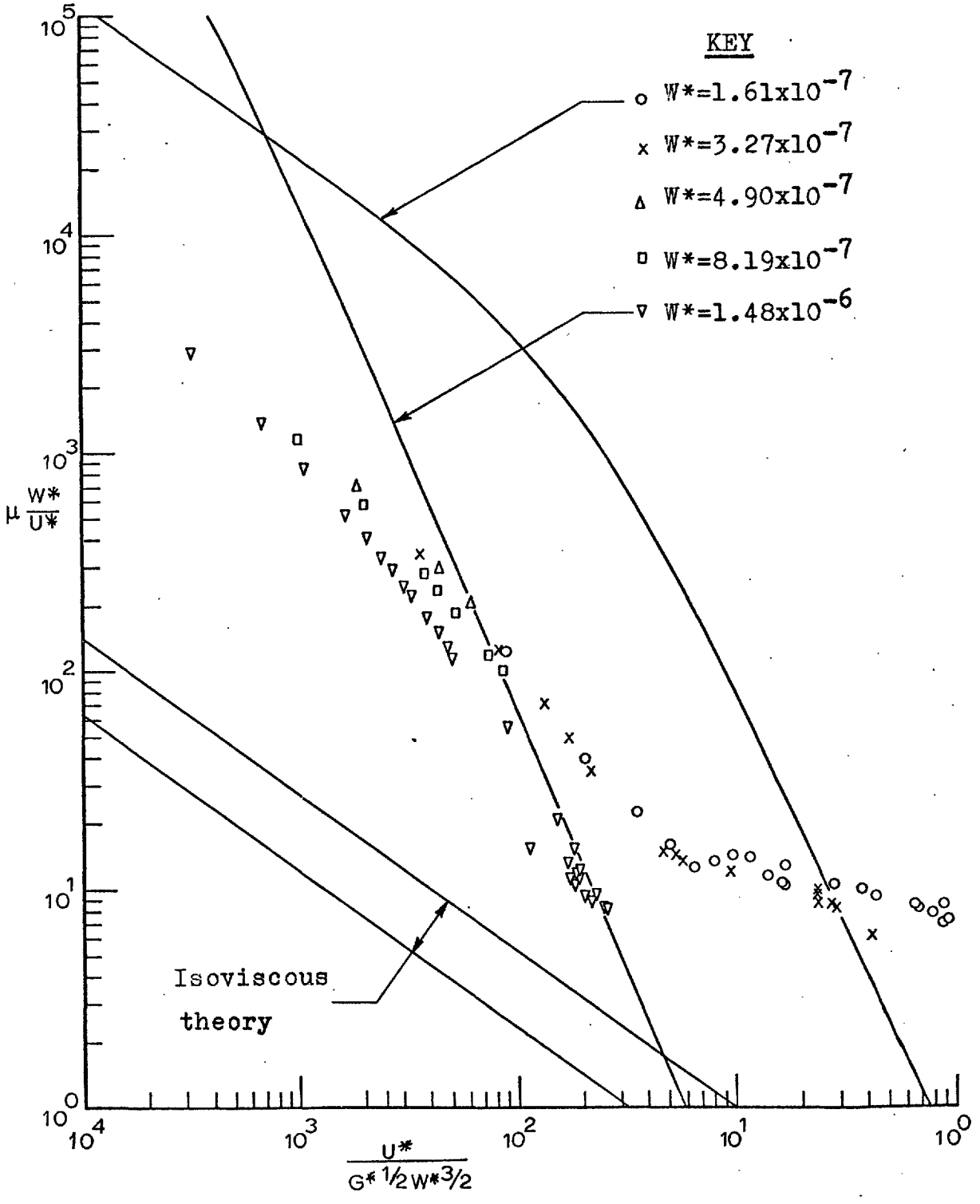


Fig.6.8 Sliding friction on glass : experiment & thermal theory - numerical solution.

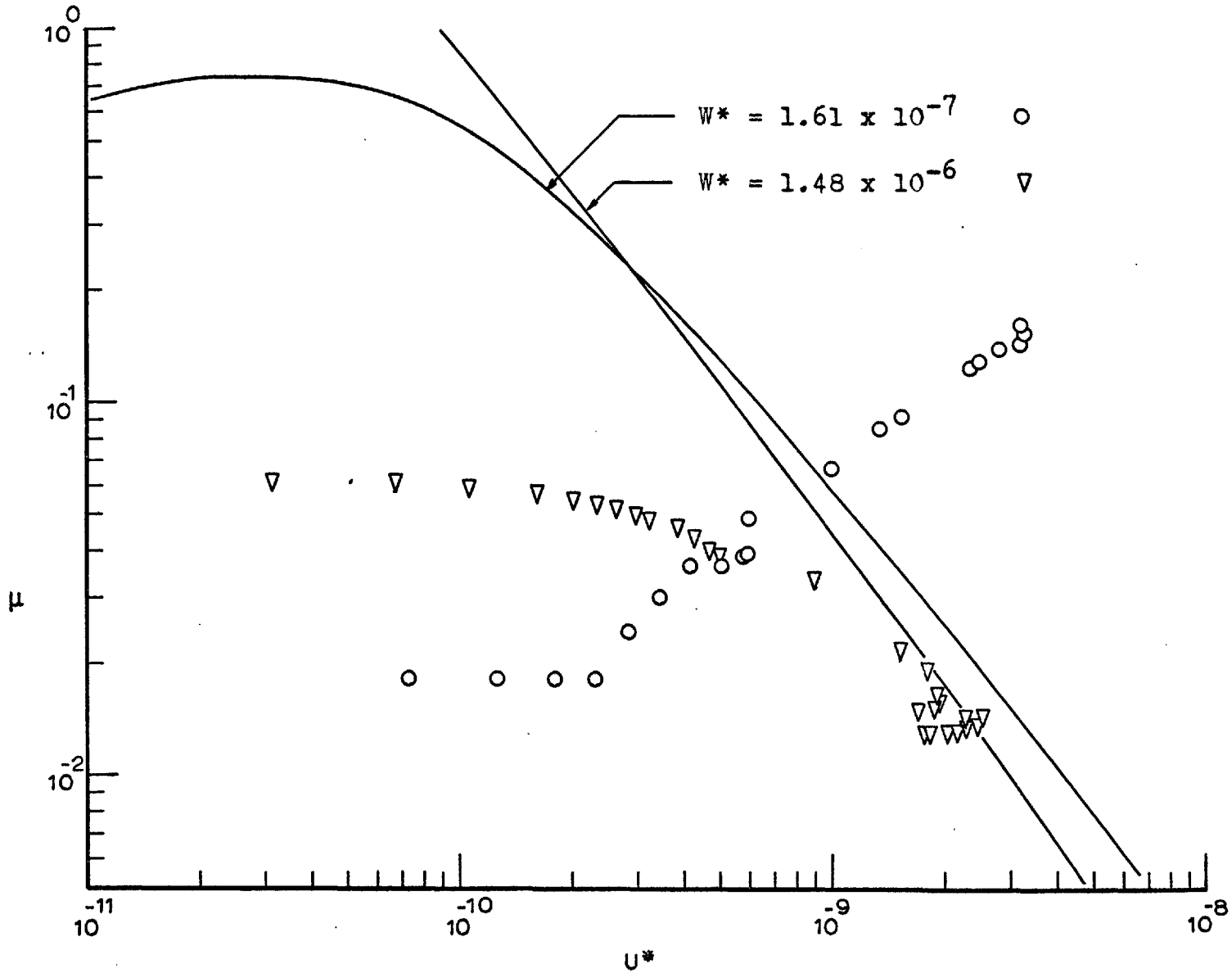


Fig.6.9 Glass: sliding friction coefficient versus non-dimensional speed

theories but here the isothermal and thermal theories employ the modified pressure viscosity law of equation 4.3.

Again, the isoviscous equation 6.8, predicts frictions well below the experiment for the same reasons as described in the last section. However, for this harder material combination, the isothermal theories of equations 6.10 and 6.13 both predict unrealistically high frictions. Clearly, then, it is no longer adequate to assume isothermal conditions and thermal theory has to be invoked to obtain closer friction predictions.

However, although much closer to the experiment, the thermal friction predictions, with either pressure viscosity law, are still too large. Noteworthy, when comparing the theories with each other, is that, in the isothermal region the use of the modified exponential pressure viscosity law decreases the dependence of friction on load, as would be expected. However, when conditions have become fully thermal, this is not the case and the change in pressure viscosity law from the purely exponential has very little effect. In this region, therefore, it follows that the temperature viscosity law is far more significant and swamps differences resulting from a change in the pressure viscosity law.

This overwhelming effect of temperature indicated that the temperature viscosity law should be as accurate as possible. To permit an analytical approach to the friction predictions, the approximate exponential temperature viscosity relationship had to be assumed with an average coefficient. In order to incorporate a more sophisticated law the numerical solution procedure described in section 6.2.4 had to be adopted. There was however, the added advantage that the more realistic temperature boundary conditions could be adopted at the same time.

In the first instance the B.P. equation (equation 4.5) was used to predict the viscosities at the calculated preesure and temperature. However, it soon became evident that, although it had the advantage of being a temperature-pressure-viscosity relationship, the pressure viscosity part was not sufficiently accurate. The modified exponential pressure viscosity law was therefore adopted in conjunction with the Vogel temperature viscosity law modified to take into account pressure changes as described in section 4.6. The resulting calculation procedure therefore, incorporated the thermal theory with realistic boundary conditions, an accurate pressure viscosity law and an accurate temperature viscosity law.

Figure 6.8 shows the results of this procedure for the highest and lowest loads, with the experimental results, yet again,for comparison. The increased sophistication of the model has improved the predictions at the highest load, but has not noticeably improved those at the lowest load.

Considering first the lightly loaded case, for values of the speed group greater than about 5×10^{-2}, conditions are no longer Hertzian, as indicated by the change in the gradient of the experimental points. In this region, therefore, the theory cannot be expected to apply. For values less than about 10^{-2}, the film thicknesses predicted by equation 6.7 are of the order of the surface roughnesses of the raceway elements and so EHD conditions do not properly prevail and the theory once again cannot be expected to apply. The inapplicability of the theory becomes obvious when compared with experiment in figure 6.9 which is a plot of μ against U^*, theory and experiment having gradients of opposite sign!

In the highly loaded case, at high speeds, the Hertzian

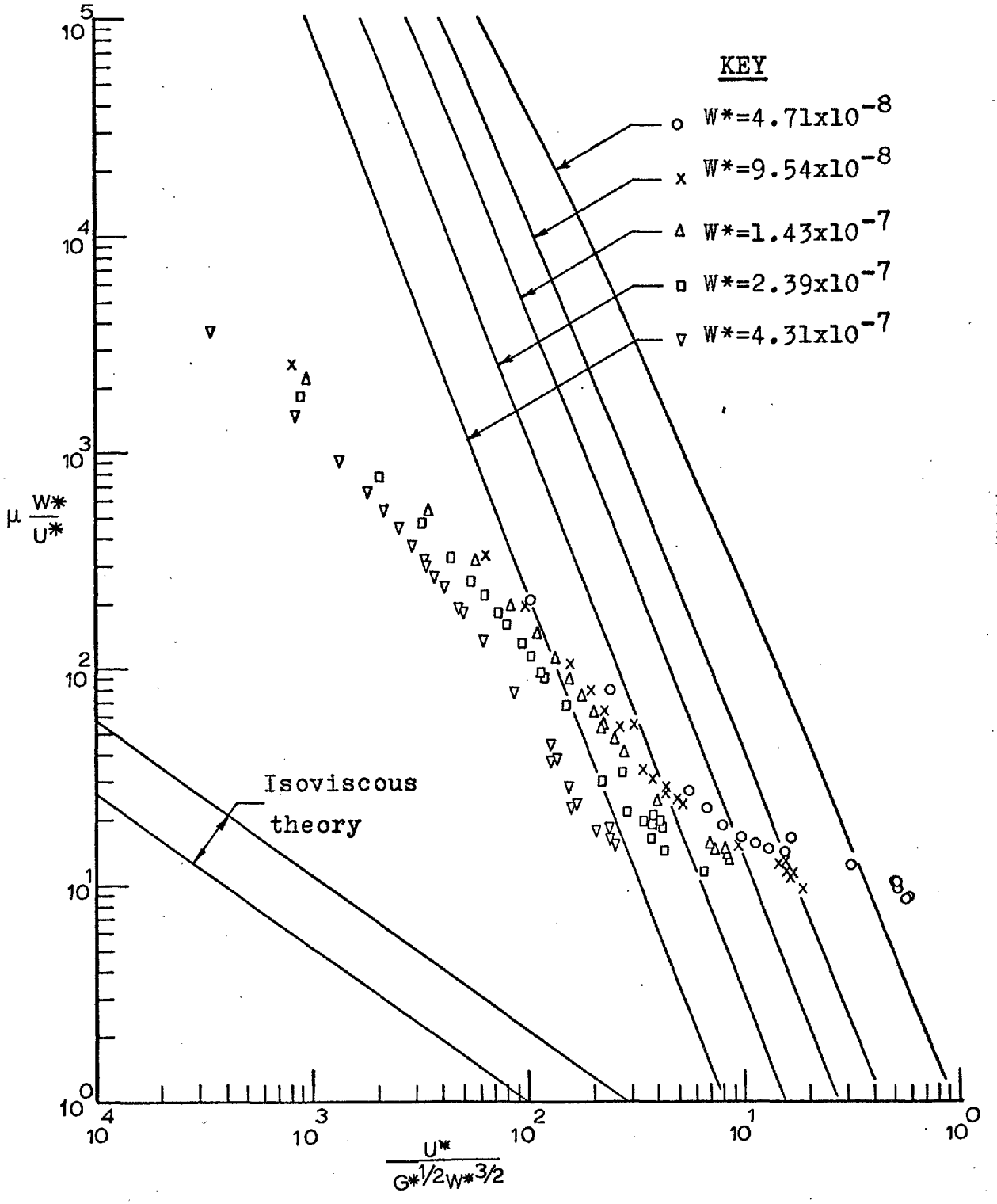


Fig.6.10 Sliding friction on sapphire : experiment & thermal theory with exponential p-η law.

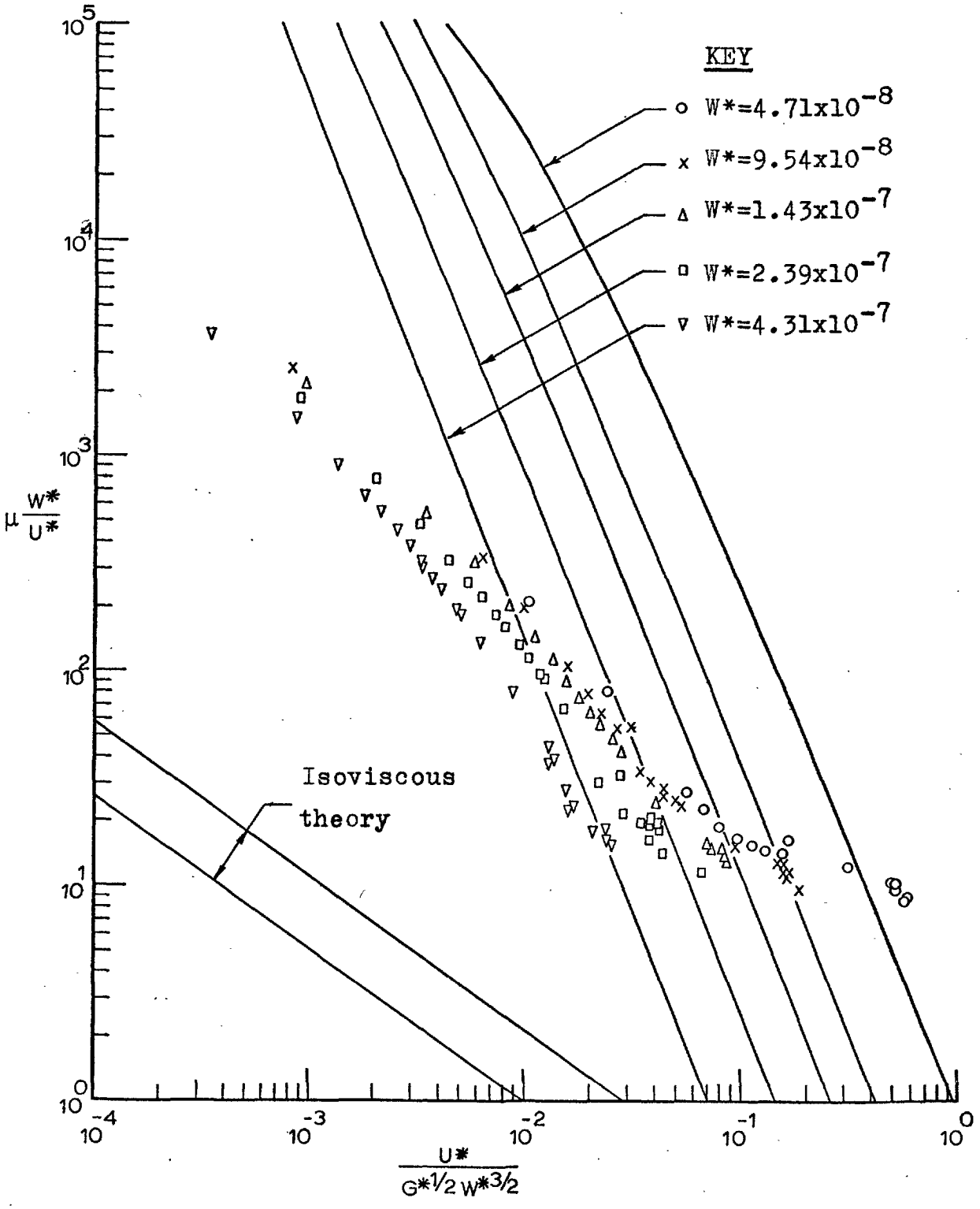


Fig.6.11 Sliding friction on sapphire : experiment & thermal theory with modified exponential p- η law.

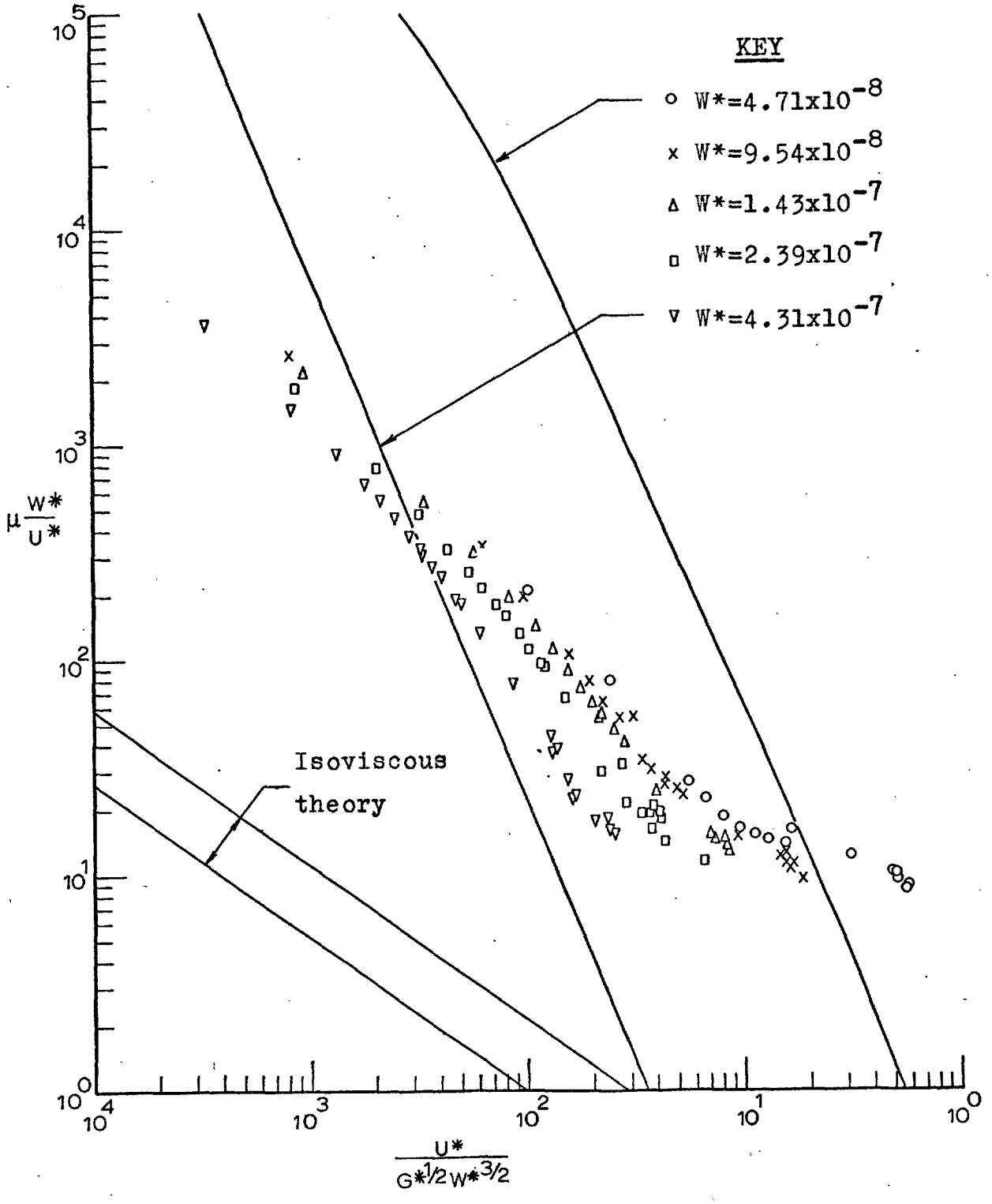


Fig.6.12 Sliding friction on sapphire : experiment & thermal theory - numerical solution.

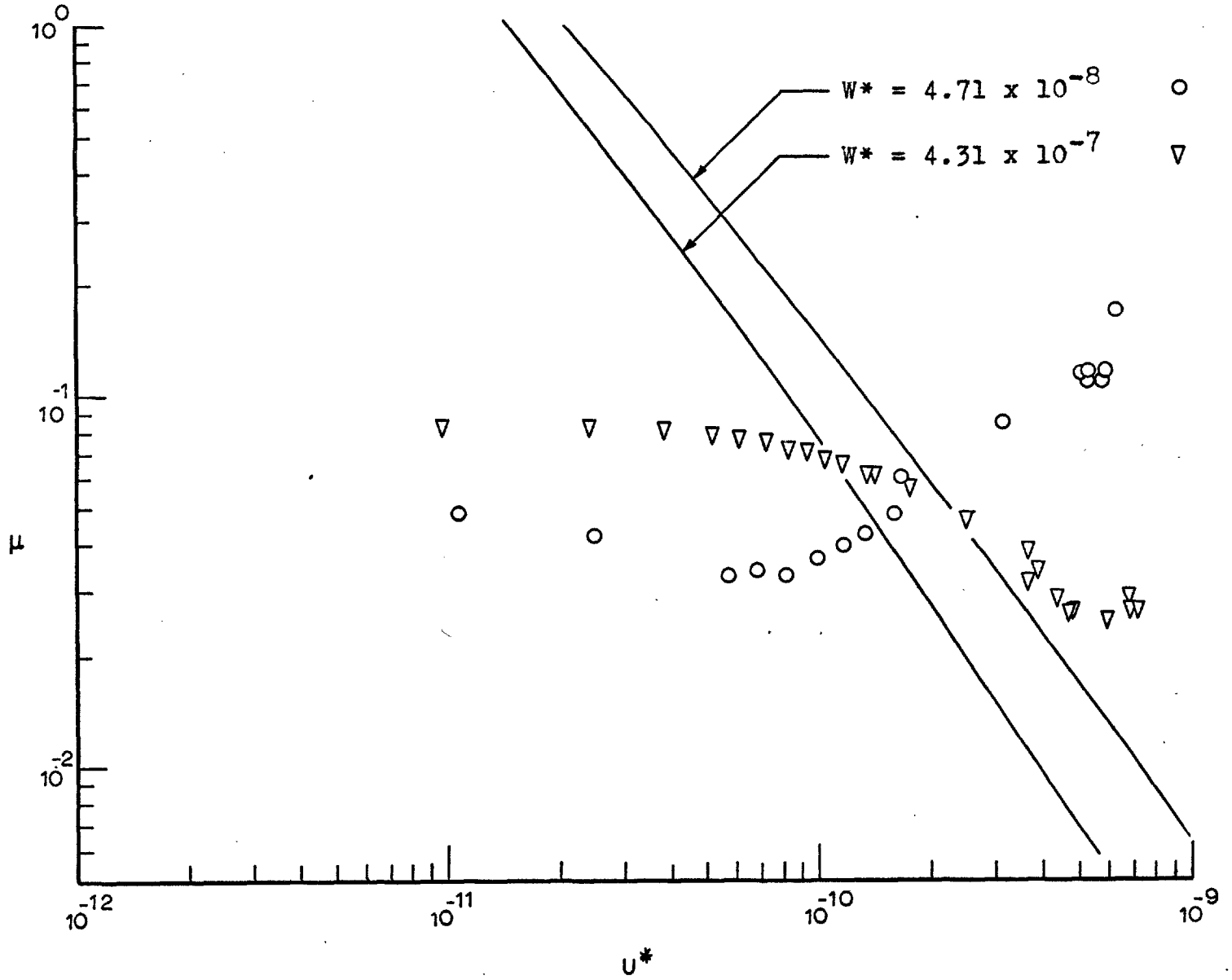


Fig.6.13 Sapphire: sliding friction coefficient versus non-dimensional speed

assumption again does not apply. For lower speeds the predictions are quite reasonable until the speed group of figure 6.8 drops below 6×10^{-3}. At values less than this the frictions predicted are much greater than those measured.

6.3.3 High modulus materials (sapphire)

The range of material constants was extended to $E' = 65.4 \times 10^6 lbf/in^2$ by employing a sapphire plate with the tungsten carbide ball. Friction measurements were made as before and the results are shown, plotted as combinations of groups, in figures 6.10, 6.11 and 6.12, and as μ versus U^* in figure 6.12. Theoretical predictions are given for comparison. Figure 6.10 shows experiment, isoviscous theory and thermal theory employing the exponential viscosity relationship (with $\alpha = 1.58 \times 10^{-4}$ in^2/lbf). Figure 6.11 shows the effect of changing to the modified exponential pressure viscosity law and figure 6.12 shows the predictions of the full numerical solution. A plot of coefficient of friction against non-dimensional speed is shown in figure 6.13.

Most of the comments made in the previous section for the 'glass' friction also apply to the'sapphire' friction. However, for this very hard material combination, the isothermal predictions of equations 6.10 and 6.13 were so unrealistic, that they are not presented.

6.4 Discussion of friction results

The differences between theory and experiment as presented, may be due to several effects. It has already been pointed out that in some regions the film thickness equation gives predictions of the order of the surface roughnesses and so cannot be expected to apply. However, also in the high load, high

speed cases Grubin-type solutions give inadequate film thickness predictions. This fact has been demonstrated by Kannel et al (reported in reference 11) for line contacts. Their data, obtained using the X-ray technique show that the dependence of the minimum film thickness upon load in these conditions is far higher than that predicted by Dowson-Higginson theory.

Several explanations have been suggested by Cheng (11) as to the possible cause of this discrepancy. These are:

1. the heating effect in the inlet region,
2. a time lag in the increase of viscosity with pressure,
3. loss of viscosity as a result of shear thinning.

He pointed out that a thermal analysis in the inlet region can account for a major part of the loss of film generating capacity at high speeds although it cannot account for the high load dependence observed by Kannel.

The latter two effects on their own could account for the errors in the friction predictions, even assuming film thickness to be correctly calculated.

The inability of the lubricant viscosity to follow the rise in pressure would result, effectively, in a reduced pressure viscosity coefficient which, in its turn, would reduce the values of predicted frictions. If the lubricant suffered from shear thinning then the assumption of a Newtonian fluid implicit in equation 6.4 no longer holds true and the whole analysis becomes invalid. However, the oil being used, being a mineral oil, was shear stable and unlikely to suffer from this phenomenon (see chapter 4, section 4.3.2).

However, quite apart from these effects, serious discrepancies exist in the theory itself. Crook (2) considered the assumption that $\partial p / \partial x$ is zero as being equivalent to disregarding the

rolling component of frictional traction. However, if the Hertzian pressure distribution is assumed, $\partial p/\partial x$ is only zero at the contact centre. As the edge of the contact is approached, $\partial p/\partial x$ increases until at the Hertz radius it becomes infinite. Thus over the outer parts of the contact $\partial p/\partial x$ should not be neglected. It follows that in these regions the shear stress is no longer constant throughout the film thickness and also that the contact can no longer be considered axi-symmetric. The errors resulting from the assumption of zero pressure gradient everywhere are mitigated somewhat by the fact that in practice, pressure builds up slowly and, although it can decay rapidly, its gradient can never become infinite.

A more serious discrepancy is that the solutions given by the numerical procedure do not satisfy the fundamental equation of continuity. This is a consequence of simplifying the treatment of what, even with the assumption of no side leakage, is a two dimensional situation, by employing a one dimensional analysis. A condition for a one dimensional situation is that $\partial^2 p/\partial x^2 = 0$. Both theoretically and experimentally, this condition is not satisfied since, assuming a Hertzian pressure distribution, $\partial p/\partial x$ varies from plus to minus infinity over the width of the contact.

The same criticism can be made of the analysis performed by Crook. However, since he restricted himself to a perfectly symmetrical situation, the velocity distributions which he presents (see figure 6.14) do satisfy continuity. Had he endeavoured to take into account pressure gradients or used boundary conditions which were anything other than symmetrical then his results too would violate continuity.

It must be questioned, therefore, whether or not the analysis has any value at all. Since any correct solution would need to be fully two-dimensional, any simplification, however approximate must be welcomed. A full solution to the problem is not justified because of the possible inadequacy of the available pressure-temperature- viscosity relationships and because of the uncertain lubricant behaviour in the contact.

The analytical solutions, following the lines laid by Crook, are hampered by being restricted to the simplest pressure and temperature viscosity laws. The numerical procedure outlined overcomes this restriction and also provides the opportunity to alter boundary conditions. If symmetrical boundary conditions are employed the calculated velocity profiles are of the form shown in figure 6.14 taken from Crook's paper (2). Since the variations from the linear profile are anti-symmetrical about the centre of the film, overall continuity is preserved no matter how large the variations. Changing to the more realistic boundary conditions, of one adiabatic and one isothermal bounding surface results in calculated velocity profiles shown in figure 6.15 (together with the corresponding temperature distributions). As a consequence the mass flow varies with changes in velocity profile. However, as can be seen from the plot of mass flow rate,

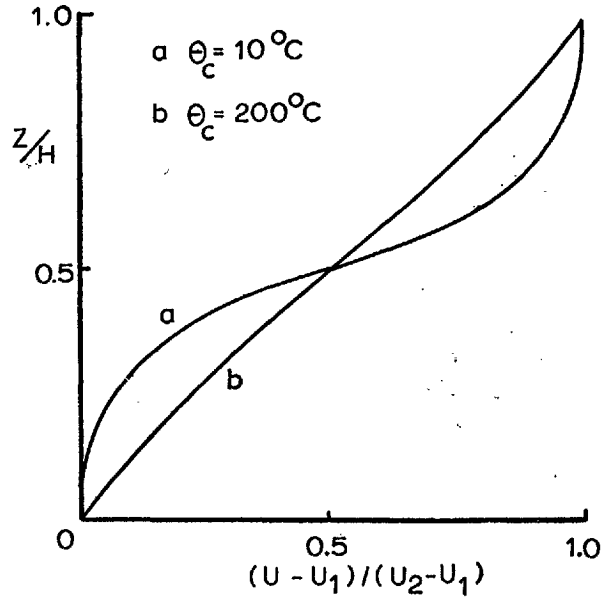
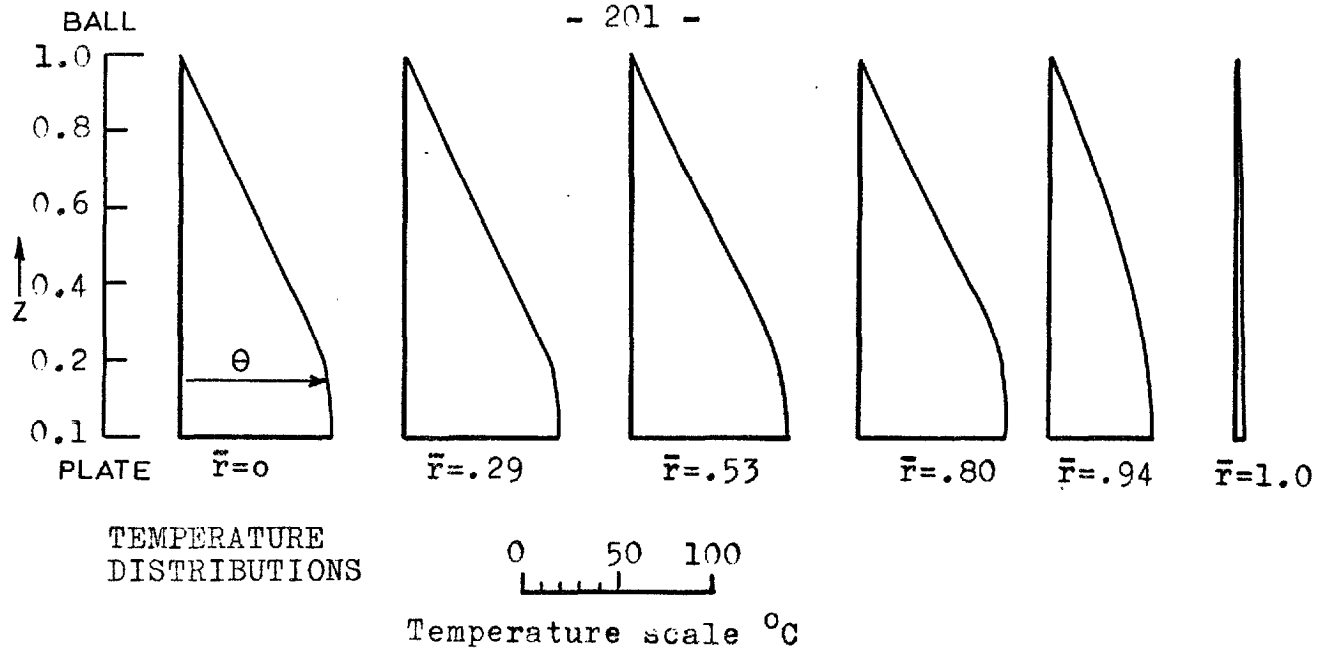
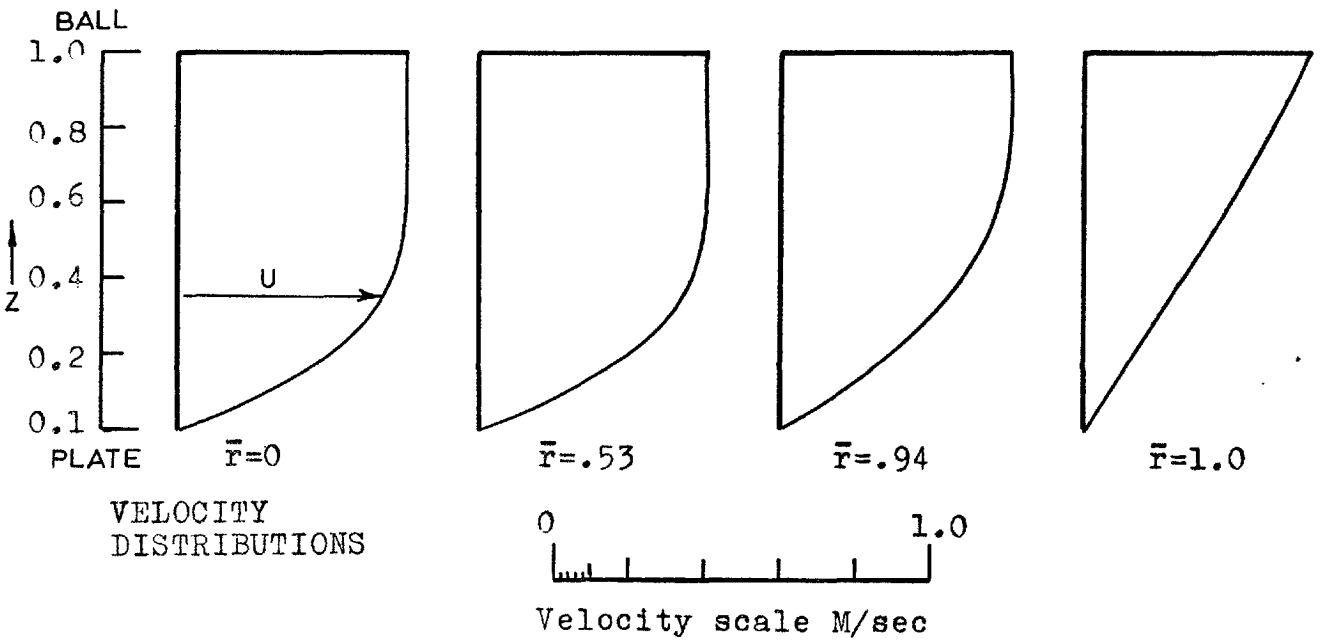


Fig.6.14 Velocity profiles after Crook (reference 2).





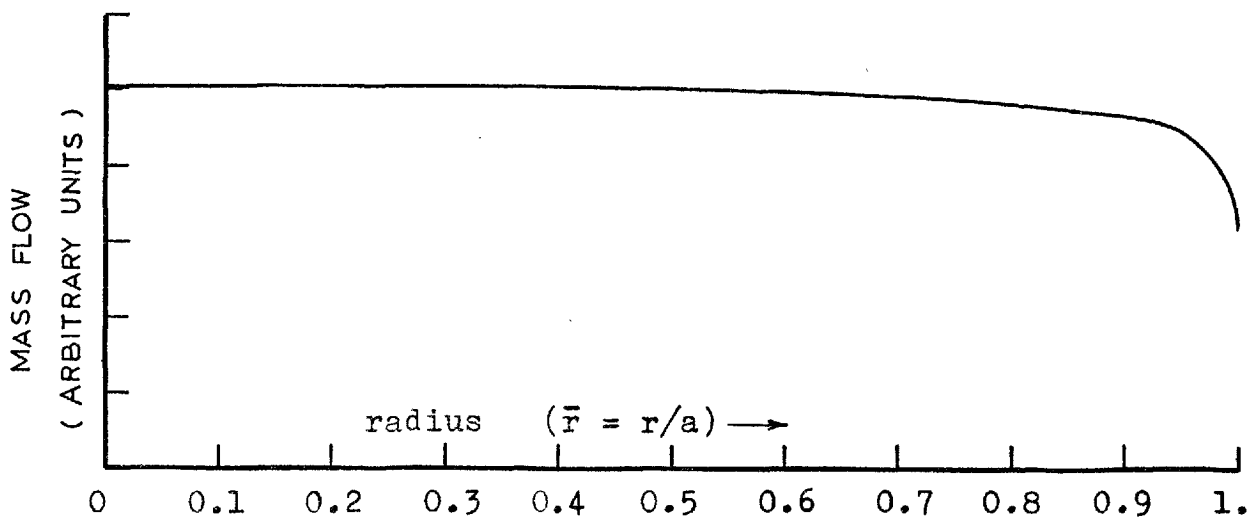


Fig. 6.15 Property distributions across a typical contact
($G^* = 3.016 \times 10^{3}$, $W^* = 1.48 \times 10^{-6}$, $U^* = 1.27 \times 10^{-9}$)

also on figure 6.15, over 80% of the contact the flow is constant to within 5%. It does, however, drop considerably over the outermost part where the assumption of negligible pressure gradient is totally unrealistic.

The contribution to the total friction of this outermost part is less than 10% and the error in the friction will be much less than this. Thus it may be concluded that the overall predictions of the numerical procedure are meaningful - a fact which is borne out by comparison with experimental measurements.

6.5 Viscometry

It was stated at the begining of this chapter that one way to approach the traction problem is to take experimental results as being correct and to use them to derive oil pressure viscosity data.

Johnson and Cameron (3) used this technique at low sliding velocities and then predicted friction at high sliding velocities using the results in Crook's analysis (2). These predictions were, in general, far too high. The authors then showed that the hypothesis of a critical shear stress was more consistent with the data, although they could not say whether temperature or shear rate governed the critical stress.

More recently a similar approach has been made by Allen et al (12). They, however, used point contact spinning friction measurements to determine the constants in a composite pressure viscosity law having the general shape shown in figure 6.16.

The friction results presented earlier were used as the basis for similar viscosity derivations. Calculations were restricted to the measurements made with the Perspex plate since

there the assumptions of the theory were most valid. The expression for the friction (equation 6.10) was rearranged and, knowing μ and the external variables, was solved iteratively for the pressure viscosity coefficient, α (see appendix 5). Typical results for one of the loads are presented in figure 6.17. As can be seen, in the region where the theory applies, there is no variation of α with speed indicating the shear stability of the oil. Correspondin α -values were obtained for the other loads and, using these, the pressure viscosity curve of figure 6.18 was constructed. The B.P. pressure viscosity data is shown for comparison.

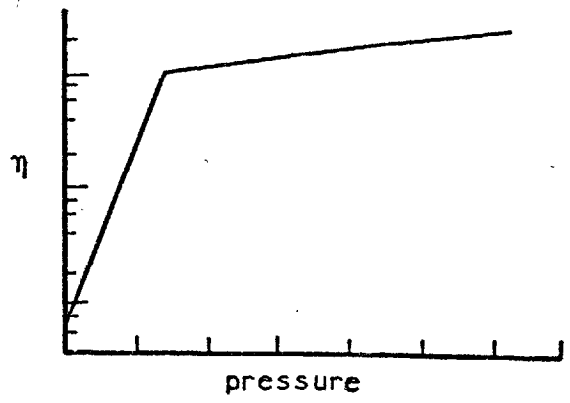


Fig.6.16 Viscosity model used by Allen et al. (12).

Unexpectedly, viscosity and hence traction coefficient appear to be almost independent of pressure. A similar effect was noticed by Johnson and Cameron but at much higher pressures (≈ 200,000 psi) which they noted were of the same order as the yield stress of their steel. They did not report, however, any plastic flow of their discs, although this has been observed by other workers (13).

In the present work there was evidence of plastic flow of the Perspex plate (as distinct from Brinelling). Although it is not strictly correct to talk of a yield stress for a material such as Perspex, it is relevant to note that the ultimate tensile stress lies in the range 7-10,000 psi. Since this is the same as the pressures used in the experiments, it is tempting to try to explain the limiting traction

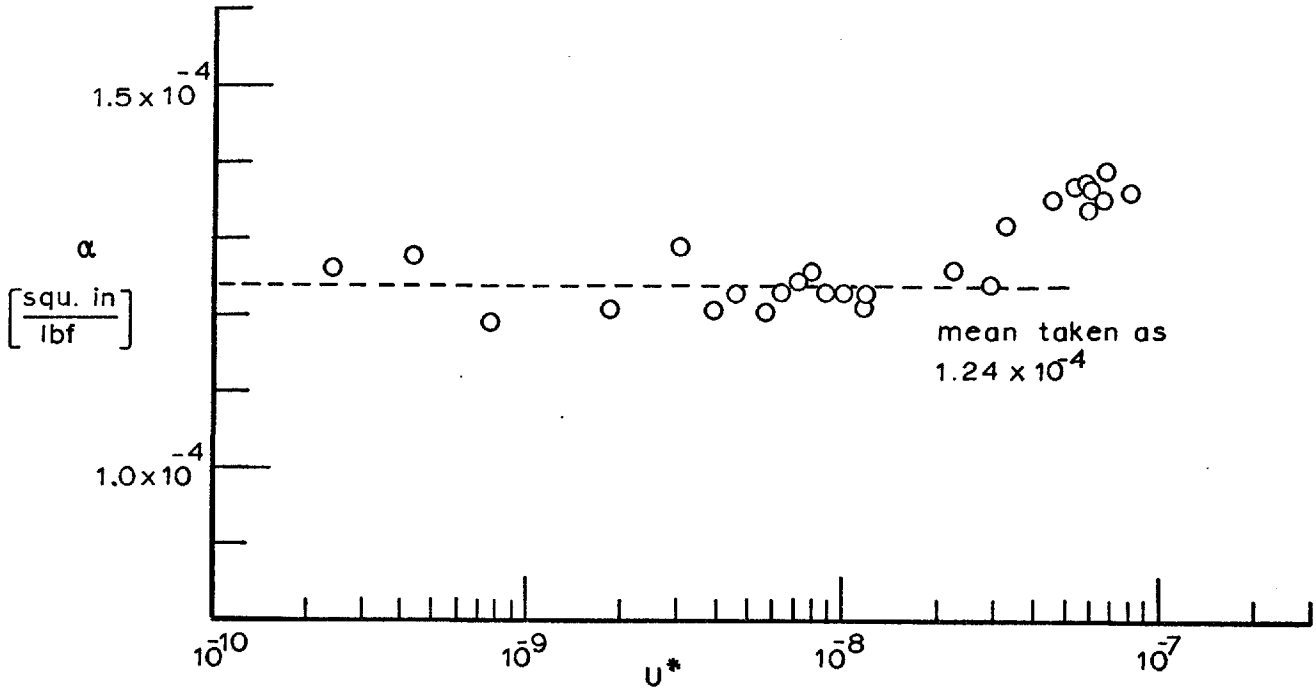


Fig.6.17 Pressure viscosity coefficient vs. speed ($W^*=1.76\times10^{-5}$)

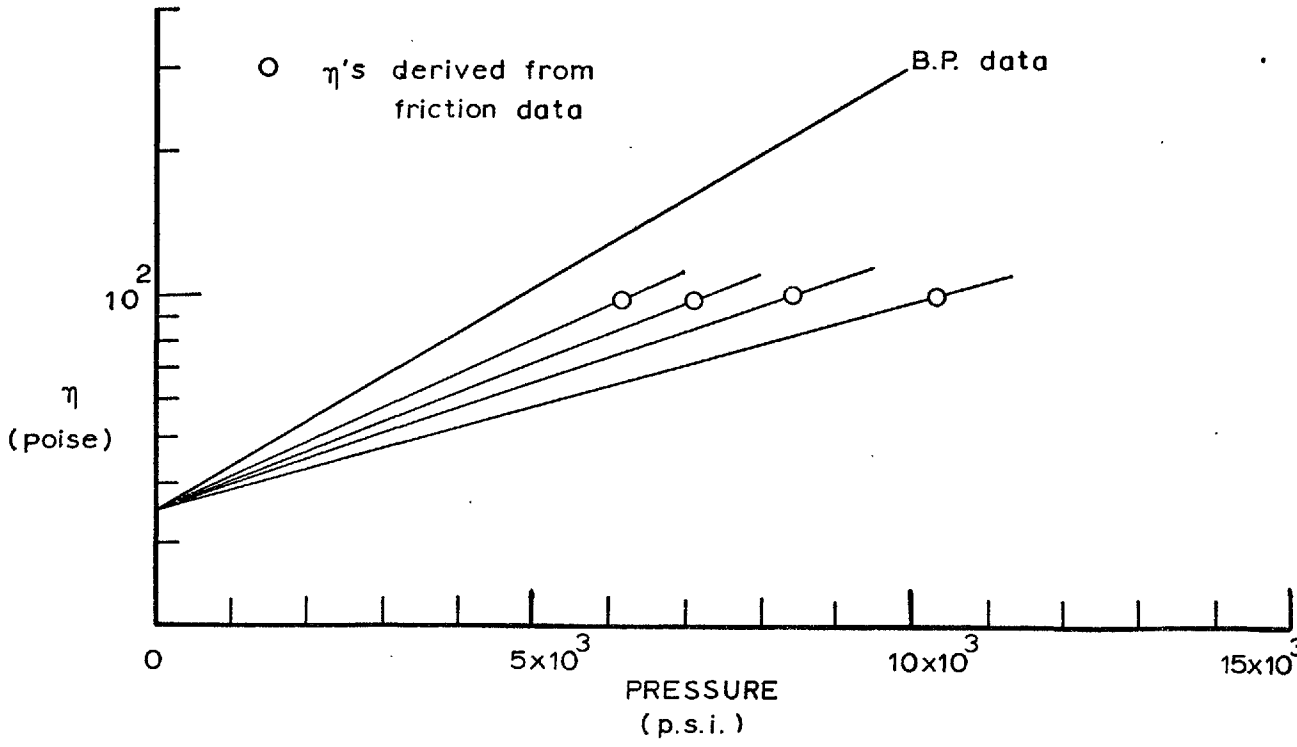


Fig.6.18 Friction derived pressure viscosity data

evidenced in figure 6.18 in terms of yield of the plate material. The mechanism by which this may happen is not clear and deserves further investigation.

6.6 Conclusions

The experiments have demonstrated how friction varies in sliding point contacts. Conventional elastohydrodynamic theory has been shown to be adequate to predict friction in low modulus sliding contacts providing oil property data is known. Predictions at the higher pressures experienced in high modulus contacts are reasonable only over part of the speed and load ranges (provided thermal effects are taken into account) but in general leave considerable room for improvement. The improvements which resulted from the application of more accurate pressure viscosity and temperature viscosity laws indicate that errors in the predictions are the result of the lack of accurate data on the lubricant behaviour at these high pressures. It is concluded, therefore, that for mineral oils similar to that used, it is not always necessary to take into consideration possible non-Newtonian behaviour of the lubricant to predict tractions. A similar conclusion was reached by Ten Napel et al (14) for line contacts.

As predicted by equation 6.31 measured frictions for all materials merge at high speeds where distortions are reduced. In these high speed, low load regions, therefore, a different approach is needed to the friction predictions. The next chapter is a description of such an approach.

References for Chapter 6

1. Dowson D. & Whitaker A.V. 'A numerical procedure for the solution of the elastohydrodynamic problem of rolling and sliding contacts lubricated by a Newtonian fluid' Proc. I.Mech.E., 1965-66, Vol.180 Pt.3B, pp 57-71.
2. Crook A.W. 'The lubrication of rollers. III A theoretical discussion of friction and the temperatures in the oil film' Phil. Trans. Roy. Soc., Series A, Vol.254, p 237.
3. Johnson K.L. & Cameron R. 'Shear behaviour of elastohydrodynamic oil films at high rolling contact pressures' Proc. I.Mech.E., 1967-68, Vol.182 Pt.1 no.14, pp 307-319.
4. Kannel J.W. & Walowit J.A. 'Simplified analysis for tractions between rolling-sliding elastohydrodynamic contacts' Trans. ASME, Series F, Jour. Lub. Tech., 1971, Vol.93 no.1, pp 39-46.
5. Grubin A.N. 'Investigation of Scientific and Industrial Research' Central Scientific Research Institute for Technology and Mechanical Engineering, Moscow, Book no.30, 1949, pp 115-116.
6. Gohar R. 'Oil film thickness and rolling friction in elastohydrodynamic point contact' Trans. ASME, Series F, Jour. Lub. Tech., 1971, Vol.93 no.3, pp 371-382.
7. Smith F.W. 'The effect of temperature in concentrated contact lubrication' Trans. ASLE, Vol.5, 1962, pp 142-148.
8. Gentle C.R. 'Optical interferometry study of film formation in lubrication of sliding or rolling contacts' NASA Report CR - 120842 (to be published 1972).
9. Wedeven L.D., Evans D. & Cameron A. 'Optical analysis of ball bearing starvation' Trans. ASME, Series F, Jour. Lub. Tech., 1971, Vol.93 no. 3, pp 349-363.

10. Archard J.F. 'The temperature of rubbing surfaces' Wear, Vol.2, 1957-59, pp 438-455.

11. Cheng H.S. 'Isothermal elastohydrodynamic theory for the full range of pressure-viscosity coefficient' Trans. ASME, Series F, Jour.Lub. Tech. 1972, Vol.94 no.1, pp 35-43.

12. Allen C.W., Townsend D.P. & Zaretsky E.V. 'Comparison of conventional and microasperity elastohydrodynamic lubrication of a ball spinning in a non-conforming groove' NASA Technical Note TN D-6761, April 1972.

13. Hirano F., Yamashita N. & Kamitani T. 'Effect of surface roughness on work-hardening and rolling fatigue in relation to elastohydrodynamic lubrication' I.Mech.E., Tribology Convention 1971, Paper no. C85/71, pp 151-163.

14. Ten Napel W.E., Moes H. & Bosma R. 'Traction in elasto-hydrodynamic lubrication at low sliding speeds' I.Mech.E., Tribology convention 1971, Paper no. C82/71, pp 142-150.

Chapter 7 FRICTION IN UNDISTORTED CONTACTS

7.1 Review of previous work

Some early predictions of friction in rigid point contacts were aimed at gaining an understanding of the lubrication of four-ball machines. For instance, Howlett (1) in 1946 investigated the transition from hydrodynamic friction to boundary friction in such an apparatus. He presented a solution which assumed that the balls were undistorted. However, Korovchinskii (2), has pointed out that Howlett's results for load carrying capacity are in error by a factor of $2\sqrt{2}$ and that his expression for the moment of friction is entirely wrong. Another serious defect in Howlett's solution is the assumption of an isoviscous lubricant, whereas, as is now well known, viscosity increases rapidly with pressure.

Both Kapitza (3) and Korovchinskii (2) introduced exponentially pressure dependent viscosities into their solutions and consequently predicted a limiting film thickness. However, when calculating load carrying capacity and power loss (related to friction), Kapitza ignored this relationship and presented equations only for the isoviscous case. Korovchinskii went one step further and retained pressure dependence of viscosity. The equations he produced for friction were consequently extremely involved, although he also produced tables of friction for various pressure viscosity coefficients. Korovchinskii's solutions, as well as those of Kapitza and Howlett, assumed half- Sommerfeld boundary conditions.

A recent solution to the problem is by Niemann and Geupel (4). The equations they present are the general solution of the differential equation as well as the particular integral

proposed by Kapitza. They obtained these results by comparison of line and point contact solutions, but their experimental verifications were only partially successful because the pressure probe they used modified the pressure profile being measured. The equations were derived for half-Sommerfeld boundary conditions and an 'average' viscosity (i.e. isoviscous conditions).

Another recent solution to the problem has been by Dalmaz and Godet (5). They used, as a basis for their friction predictions, a numerical solution for the pressure distribution in an undistorted concentrated contact and were thus able to apply Reynold's boundary conditions. A rectangular mesh was used for the computations and only circular contacts were investigated. Satisfactory quantitative agreement between theory and experiment was demonstrated. However, the experimental traction force which they measured was higher than that calculated. They suggested that this could be due to errors in choosing a suitable boundary for integration of the shear forces (see section 7.5).

A similar approach is made in this chapter for elliptical contacts. A theory for the friction is first presented using as a basis the pressure distributions from the analysis of chapter 5. Experimentally determined frictions for elliptical contacts are then given and compared with the theory. Finally the results are discussed in the light of the comparisons.

7.2 Theory

7.2.1 Introduction

Newton's shear law, which gives the shear stress (τ) on any element, may be written as:

$$\tau = \eta \frac{\partial u}{\partial z} \qquad -7.1$$

The simplified Navier-Stokes equation as presented earlier (section 6.2.3) is, for a constant viscosity:-

$$\frac{\partial p}{\partial x} = \eta \frac{\partial^2 u}{\partial z^2} \quad ; \qquad \frac{\partial p}{\partial y} = \eta \frac{\partial^2 v}{\partial z^2} \qquad -7.2$$

Considering the x-direction only and integrating 7.2 once gives:-

$$\eta \frac{\partial u}{\partial z} = z \frac{\partial p}{\partial x} + C \qquad -7.3$$

Using boundary conditions (see figure 7.1)

$u = V$ when $z = h$

$u = 0$ when $z = 0$,

$$C = \frac{\eta V}{h} - \frac{\partial p}{\partial x}\frac{h}{2} \qquad -7.4$$

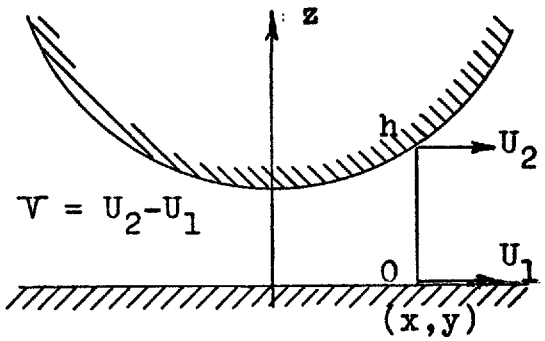


Fig. 7.1 Boundary conditions

Hence the shear stress on the plate (i.e. at $z = 0$) is given from equations 7.4, 7.3 and 7.1:-

$$\tau_x = -\frac{h}{2}\frac{\partial p}{\partial x} + \frac{\eta V}{h} \qquad -7.5$$

7.2.2 Rolling friction

The first term on the right hand side of equation 7.5 is due to pressure only; when integrated it gives the rolling friction, F_R. Thus:-

$$F_{R_x} = -\int\int \frac{h}{2}\cdot\frac{\partial p}{\partial x}\, dx.\, dy \qquad -7.6$$

The integration of equation 7.6 is carried out over the whole region of positive pressures. However, in the cavitated region, pressures and pressure gradients are zero and hence there is

no rolling friction. It is thus permissible to integrate over the whole of the region of friction, should it be more convenient.

To utilise the pressure distributions obtained by the numerical procedure described in chapter 5, equation 7.6 must first be non-dimensionalised and expressed in polar form. As before, (section 5.2.1), let

$$\bar{p} = \alpha p; \quad \bar{h} = h/h_o; \quad \bar{x} = x/a; \quad \bar{y} = y/b.$$

Hence, 7.6 becomes:-

$$F_{R_x} = - \frac{b.h_o}{2\alpha} \int\int \left(\frac{\partial \bar{p}}{\partial \bar{x}} . \bar{h} \right) d\bar{x} . d\bar{y} \qquad -7.7$$

In polar form, with $\bar{x} = \bar{r} \cos\phi \quad \bar{y} = \bar{r} \sin\phi$

$$F_{R_x} = - \frac{b.h_o}{2\alpha} \int\int \left(\cos\phi \frac{\partial \bar{p}}{\partial \bar{r}} - \frac{\sin\phi}{\bar{r}} \frac{\partial \bar{p}}{\partial \phi} \right) \bar{h} . \bar{r} . d\bar{r} . d\phi \qquad -7.8$$

If $\bar{r}_B$ is the limit of the grid in the radial direction, then integrating equation 7.8 by parts within the limits $0 \leqslant \bar{r} \leqslant \bar{r}_B$ and $0 \leqslant \phi \leqslant 2\pi$ gives:-

$$\frac{2 F_{R_x} \alpha}{h_o b} = - \int_0^{2\pi} \left(\left[\cos\phi . \bar{h} . \bar{r} . \bar{p} \right]_0^{\bar{r}_B} - \int_0^{\bar{r}_B} \left[\bar{p} \cos\phi \frac{\partial \bar{h}\bar{r}}{\partial \bar{r}} d\bar{r} \right] \right) d\phi$$
$$+ \int_0^{\bar{r}_B} \left(\left[\bar{h} \sin\phi \, \bar{p} \right]_0^{2\pi} - \int_0^{2\pi} \left[\bar{p} \frac{\partial (\bar{h} \sin\phi)}{\partial \phi} d\phi \right] \right) d\bar{r} \qquad -7.9$$

The first and third terms on the right hand side of equation 7.9 are zero because at $\bar{r} = \bar{r}_B$ the boundary condition is that $\bar{p} = 0$ for all ϕ.

Integrating equation 7.9 again, it is found that two terms cancel leaving the comparatively simple expression:

$$\frac{2\,F_{R_x}\,\alpha}{h_o\,b} = \int_0^{2\pi}\int_0^{\bar{r}_B} \bar{p}\left(\cos\phi\,\frac{\partial\bar{h}}{\partial\bar{r}} - \frac{\sin\phi}{\bar{r}}\,\frac{\partial\bar{h}}{\partial\phi}\right)\bar{r}\,d\bar{r}\,d\phi \qquad -7.10$$

The term in the bracket represents $\partial\bar{h}/\partial\bar{x}$ and hence may be written simply as $2\bar{r}\cos\phi$. The equation thus becomes:-

$$\frac{F_{R_x}\,\alpha}{h_o\,b} = \int_0^{2\pi}\int_0^{\bar{r}_B} \bar{p}\,\bar{r}^2\cos\phi\,d\bar{r}\,d\phi \qquad -7.11$$

Rearranging the terms in equation 7.11 and introducing non-dimensional groups as in section 5.2.4 gives:-

$$\mu_{R_x}\,\frac{W^*}{U^*} = 12.\left(\frac{b}{a}\right)\left(\frac{h_o^{3/2}\,A^{1/2}}{6\,\eta_o\bar{V}\,\alpha}\right)\int_0^{2\pi}\int_0^{\bar{r}_B}\bar{p}\,\bar{r}^2\cos\phi\,d\bar{r}\,d\phi \qquad -7.12$$

but $(6\,\eta_o\bar{V}\alpha)/(h_o^{3/2}\,A^{1/2})$ is the main independent variable used in the calculation of the pressure field. Denoting this group by ξ we can therefore write

$$\mu_{R_x}\,\frac{W^*}{U^*} = \frac{12}{\xi}\left(\frac{b}{a}\right)\int_0^{2\pi}\int_0^{\bar{r}_B}\bar{p}\,\bar{r}^2\cos\phi\,d\bar{r}\,d\phi \qquad -7.13$$

Although there can be no bodily movement of the ball in the y-direction, because of the constraint imposed by the groove, angling will cause both rolling and sliding components of surface motion. It follows that, in general, there will also be components of rolling and sliding friction in the y-direction. A similar expression to equation 7.13 can therefore be derived to express the rolling friction in the y-direction, using a similar analysis to that just presented. The expression is found to be:-

$$\mu_{R_y}\,\frac{W^*}{U^*} = \frac{12.}{\xi}\,\frac{B}{A}\left(\frac{b}{a}\right)^2\int_0^{2\pi}\int_0^{\bar{r}_B}\bar{p}.\bar{r}^2\sin\phi\,d\bar{r}\,d\phi \qquad -7.14$$

The total rolling friction in the direction of sliding was obtained by adding the resolved components of the x and y-direction rolling frictions. Thus:-

$$\mu_R \frac{W^*}{U^*} = \left(\mu_{R_x} \frac{W^*}{U^*}\right)\cos\Theta + \left(\mu_{R_y} \frac{W^*}{U^*}\right)\sin\Theta \qquad -7.15$$

7.2.3 Sliding friction

The second term in equation 7.5 is due to viscous shear forces; when integrated it gives the sliding friction F_s. Thus

$$F_s = \iint_{A_p} \frac{\eta V}{h}\, dx\, dy \qquad -7.16$$

where A_p is the area of integration. Normalising and expressing the result in polar form gives:-

$$F_s = \frac{1}{A}\cdot\left(\frac{b}{a}\right)\iint_{A_p} \frac{\eta V}{\bar{h}}\, \bar{r}\, d\bar{r}\, d\phi \qquad -7.17$$

If we assume an exponential dependence of pressure on viscosity, then

$$\eta = \eta_o e^{\bar{p}} = \frac{\eta_o}{(1 - \bar{q})} \qquad -7.18$$

Thus equation 7.17 becomes

$$\frac{F_s A}{\eta_o V} = \left(\frac{b}{a}\right)\iint_{A_p} \frac{\bar{r}\, d\bar{r}\, d\phi}{\bar{h}\,(1 - \bar{q})} \qquad -7.19$$

Expressed in terms of the usual non-dimensional groups, equation 7.19 becomes:-

$$\mu_s \frac{W^*}{U^*} = 2\left(\frac{b}{a}\right)\iint_{A_p} \frac{\bar{r}\, d\bar{r}\, d\phi}{\bar{h}\,(1 - \bar{q})} \qquad -7.20$$

The region of integration (A_p) is, as with the rolling friction, that area where there are positive pressures. When integrating equation 7.8 for rolling friction, the integration covered

the whole finite difference grid because, in the region of film rupture, the pressures and pressure gradients were zero everywhere and hence the expression being integrated was zero also. When integrating equation 7.20, however, the area of film rupture must be expressly excluded from the calculations. The determination of the sliding friction in this region is the subject of the next section.

7.2.4 Sliding friction in the cavitated region

Beyond the finish of the pressure zone, there is insufficient oil to fill the gap. Thus, the gap must run less than full (i.e. cavitated) and, as has been found experimentally, the oil breaks up into streamers aligned with the velocity vector.

At each point on the cavitation boundary the oil available just fills the gap and is equal to $(\nabla h_c)/2$ where h_c is the local film thickness. At a point in the cavitated region further down the same streamline, the oil required to fill the gap is $(\nabla h)/2$ where h is again the local film thickness. Thus the ratio of the available flow to the necessary flow is h_c/h. If we assume that all the oil is found in the streamers which completely fill the gap between the surfaces, then the total friction drag of these streamers, F_c, is given by:-

$$F_c = \iint_{A_c} \frac{h_c}{h} \frac{\eta}{h} \nabla \, dx \, dy \qquad -7.21$$

which, as before, can be written as:-

$$\mu_c \frac{W^*}{U^*} = 2 \left(\frac{b}{a}\right) \iint_{A_c} \frac{\bar{h}_c}{\bar{h}^2} \, d\bar{x} \, d\bar{y} \qquad -7.22$$

A_c, the region of integration, is the whole of the cavitated part of the grid. Its extent downstream of the rupture boundary will be discussed further in section 7.5.

7.2.5 Direction of friction forces

The sliding friction is such that it will always oppose the motion. However, this is not always the case with rolling friction as reference to figure 7.2 demonstrates. In region 'a' $\bar{p}$ is positive and $\partial\bar{h}/\partial\bar{x}$ negative; F_R as predicted by equation 7.13 is therefore negative and consequently acts in the opposite direction to the sliding friction (F_s). In the region 'b', both $\bar{p}$ and $\partial\bar{h}/\partial\bar{x}$ are positive. F_R is thus also positive and reinforces F_s. In region 'c' $\bar{p}$ is zero and hence there is no contribution to the rolling friction. Part 'a' comprises the majority of the pressure region and so dominates the rolling friction term. It follows, therefore, that the total rolling friction acts to oppose the sliding friction.

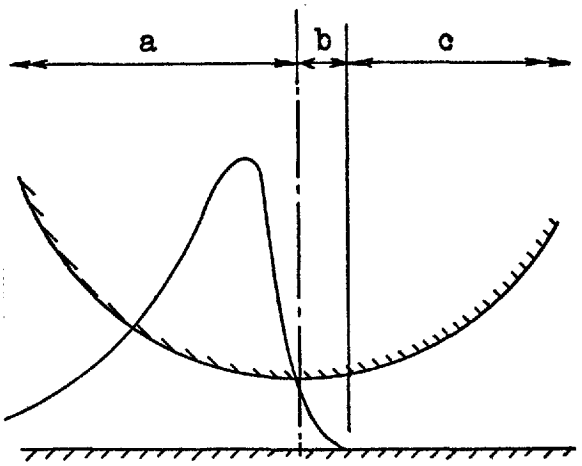


Fig. 7.2 Friction regions

7.3 Approximate analytic solutions

7.3.1 Introduction

If there is no angling (i.e. $\Theta = 0^{\circ}$) approximate solutions with simplified boundary conditions may be calculated for the three component parts of the total friction. They provide an order of magnitude check on the numerical results and, more important, give some physical insight into the importance of the various parameters involved.

7.3.2 Sliding friction in the cavitated region

Equation 7.22 derived earlier gives an expression for the cavitation component of friction in terms of the film thickness at the point of rupture ($\bar{h}_c$) and the local film thickness ($\bar{h}$).

If we assume half-Sommerfeld boundary conditions, then $\bar{h}_c$ is the film thickness at x = 0 and hence is given by

$$\bar{h}_c = 1 + G\bar{y}^2 \qquad -7.23$$

where G is the geometry group

$$G = \frac{B}{A}\left(\frac{b}{a}\right)^2$$

$\bar{h}$ is given by equation 5.5 and may be written as:-

$$\bar{h} = 1 + \bar{x}^2 + G\bar{y}^2 \qquad -7.24$$

Thus equation 7.22 may be rewritten as:-

$$\mu_c \frac{W^*}{U^*} = 2\left(\frac{b}{a}\right)\iint_{A_c} \frac{1 + G\bar{y}^2}{(1 + \bar{x}^2 + G\bar{y}^2)^2}\, d\bar{x}\, d\bar{y} \qquad -7.25$$

Integrating with respect to $\bar{x}$ between the limits $\bar{x} = 0$ and $\bar{x} = \infty$ gives:-

$$\mu_c \frac{W^*}{U^*} = 2\left(\frac{b}{a}\right)\frac{\pi}{4}\int \frac{d\bar{y}}{(1 + G\bar{y}^2)^{\frac{1}{2}}} \qquad -7.26$$

Integrating with respect to $\bar{y}$ between the limits $\pm\bar{y} = \bar{y}_B$ gives:-

$$\mu_c \frac{W^*}{U^*} = \left(\frac{A}{B}\right)^{\frac{1}{2}} \pi \left\{ \ln\left[\bar{y}_B + \left(\bar{y}^2_B + \frac{1}{G}\right)^{\frac{1}{2}}\right] - \ln\left[\left(\frac{1}{G}\right)^{\frac{1}{2}}\right]\right\} \qquad -7.27$$

7.3.3 Rolling friction

An approximate expression for the rolling friction is not easy to obtain because of the complexity of the function to be integrated. However, an estimate can be made if the reduced pressure solution of Kapitza is integrated using the half-Sommerfeld boundary conditions.

In the present normalised nomenclature, Kapitza's pressure distribution may be written as:-

$$\bar{q} = \left(\frac{6\,\eta_o V \alpha}{h_o^{3/2} A^{1/2}}\right)\left(\frac{A}{2B + 3A}\right)\frac{\bar{x}}{\bar{h}^2} \qquad -7.28$$

Changing equation 7.12 into Cartesian form, and substituting equation 7.28 and 7.24 gives:-

$$\mu_{R_x}\frac{W^*}{U^*} = 12\left(\frac{b}{a}\right)\left(\frac{A}{2B + 3A}\right)\iint_{A_p}\frac{\bar{x}^2\,d\bar{x}\,d\bar{y}}{(1 + \bar{x}^2 + G\bar{y}^2)^2} \qquad -7.29$$

Integrating with respect to $\bar{x}$ between the limits 0 and $-\infty$ gives:-

$$\mu_{R_x}\frac{W^*}{U^*} = 12\left(\frac{b}{a}\right)\left(\frac{A}{2B + 3A}\right)\frac{\pi}{4}\int\frac{d\bar{y}}{(1 + G\bar{y}^2)^{\frac{1}{2}}} \qquad -7.30$$

Comparison of equations 7.26 and 7.30 shows surprisingly that the dependence on $\bar{y}$ is the same for both rolling and cavitated sliding frictions, the former being greater by a factor of $6A/(2B + 3A)$, that is by 1.20 for a circular point contact and 1.87 for the experimental geometry.

7.3.4 Sliding friction

To obtain an approximate equation for the sliding friction it is necessary to assume that the viscosity is constant. Attempts to include pressure dependence of viscosity and a Kapitza pressure distribution, have led to functions which have not been possible to integrate analytically. The expression to be derived in this section, therefore, is the least satisfactory of the three component frictions.

The function to be integrated is equation 7.20 expressed in Cartesian co-ordinates, with $\bar{q} = 0$, that is:-

$$\mu_s\frac{W^*}{U^*} = 2\left(\frac{b}{a}\right)\iint_{A_p}\frac{d\bar{x}\;d\bar{y}}{(1 + \bar{x}^2 + G\bar{y}^2)} \qquad -7.31$$

Integrating with respect to $\bar{x}$ between the limits $\bar{x} = 0$ and $\bar{x} = -\infty$ gives:-

$$\mu_s \frac{W^*}{U^*} = 2\left(\frac{b}{a}\right) \frac{\pi}{2} \int \frac{d\bar{y}}{(1 + G\bar{y}^2)^{\frac{3}{2}}} \qquad -7.32$$

Comparison with equations 7.30 and 7.26 shows that the dependence of the sliding friction on $\bar{y}$ is the same as in the previous two cases. Also the isoviscous sliding friction for all contact geometries is exactly twice the cavitated sliding friction, and 1.66 and 1.07 times the rolling friction for circular and elliptical point contact geometries.

Figure 7.3 shows, for the experimental geometry ($G = 2.05$), the variation of the approximate expressions for the three component frictions as $\bar{y}_B$ changes.

Although changes with $\bar{y}_B$ are most rapid close to the contact centre, the tendency to reach a limiting value of friction is not as pronounced as with load and pressure (cf. figure 5.3). It follows, therefore, that the choice of boundary is of greater importance when predicting friction.

7.4 Numerical solutions

7.4.1 Calculation procedure

The pressure distributions obtained from the theory of chapter 5 formed the basis of numerical predictions of friction in rigid contacts. The technique used to calculate the friction integrals in the pressure region was a straight-forward double trapezoidal rule, the only modification being to avoid integration in the region of film rupture. An almost identical procedure was used earlier to calculate the load from the pressure integral and is described briefly in appendix 2.

The integration for the sliding friction in the cavitated

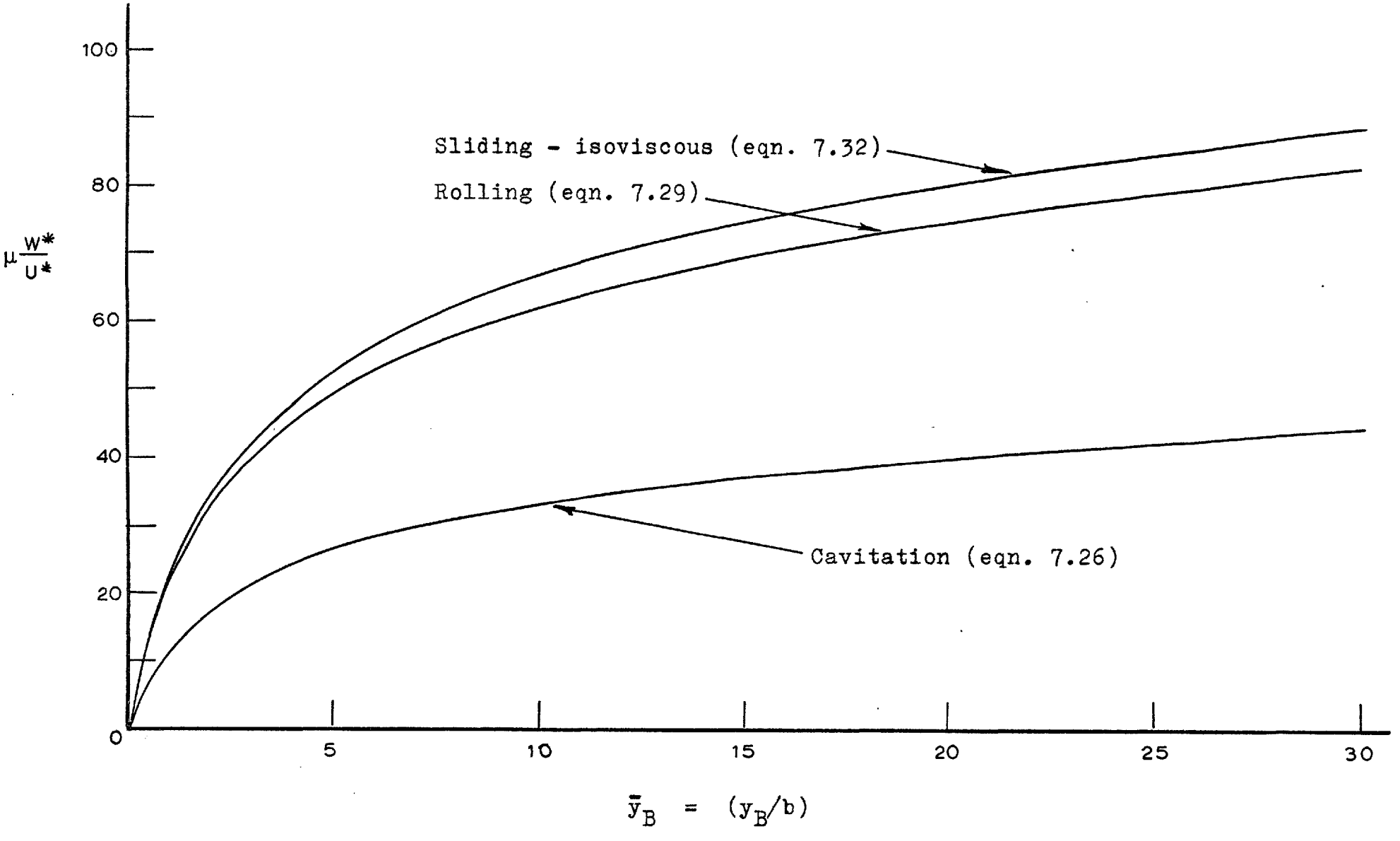


Fig. 7.3 Effect of integration boundary on approximate friction expressions

part is more complex, however. The difficulties arise because of the need to integrate along the streamlines, using in the equation the local value of the film thickness at the point of rupture (h_B). Fortunately, as was discussed in section 5.4.4 the streamlines in this region are straight and parallel, and thus ideally suited to integration in Cartesian co-odinates. Integration was first performed along the flowlines (i.e in the x-direction) and then in the y-direction. When the flow was not along the groove, but at some angle Θ, the axes were rotated to permit the integration to proceed.

To be able to calculate the film thickness at rupture, the position of the cavitation boundary has first to be found. A pressure contour was therefore calculated with a value slightly above zero and the co-ordinates on this contour were taken as being on the boundary. If zero were taken as the boundary value, no unique line would ensue since all pressures in the cavitation region were zero. The procedure followed for determining the contour's Cartesian co-ordinates($\bar{x}'$ and $\bar{y}'$) was the same as that in the calcomp routine described in appendix 2, except that account was taken of angling by using the transform:-

$$\bar{x}' = (\sin\phi \sin\Theta - \cos\phi \cos\Theta)\,\bar{r}$$

$$\bar{y}' = (\sin\phi \cos\Theta + \cos\phi \sin\Theta)\,\bar{r}$$

The points on the rupture boundary, although obtained systematically from the polar grid, were not in any useful order for calculation on the rectangular grid; it was therefore necessary to sort into some convenient sequence. This was performed using the Harwell Program Library subroutine KBO 3A to give the points on the boundary in ascending values of $\bar{y}'$. The subroutine gives the re-arranged array Y(K) and also an

array INDEX (K) which contains the original values of K for each Y element. It was thus possible to maintain correspondence between the X(K) and Y(K) arrays.

One short-coming of the procedure was that it could not tackle re-entrant curves. As it was just possible that a re-entrant boundary might occur at some drive angles, the sorted Y(K) and corresponding X(K) were printed out to enable a manual check to be made. Fortunately, none have been experienced so it would appear that fears were groundless.

The limits of the integration are discussed in section7.5 and further details of the friction subroutines are given in appendix 6.

7.4.2 Velocity correction

In the region near the point of minimum film thickness, changes in the velocity resulting from the curvature of the ball are small and may be neglected. However, far out from the centre, these changes can no longer be assumed to be negligible and a correction must be applied to allow for them.

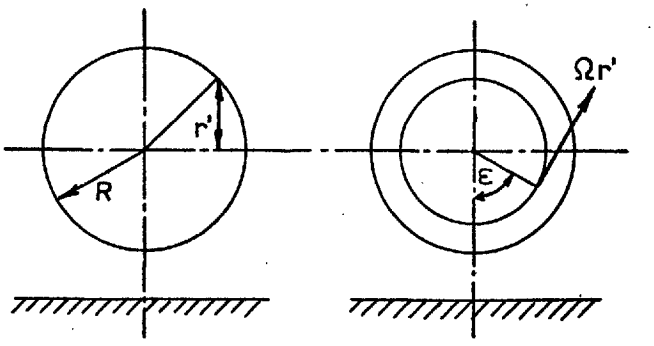


Fig. 7.4 Velocity correction

Referring to figure7.4 and taking the angular velocity of the ball as Ω, the local surface speed at the point (x,y) is $\Omega r'$ and the component in the x-direction is $\Omega r' \cos\varepsilon$. But:-

$$r'^2 = R^2 - y^2 \qquad -7.33$$

and

$$\cos\varepsilon = \left[\frac{R^2 - y^2 - x^2}{R^2 - y^2}\right]^{\frac{1}{2}} \qquad -7.34$$

The speed at the point of minimum film thickness ($\overline{V}$), usually assumed to be uniform, is ΩR. Thus, to correct for speed variation resulting from curvature, $\overline{V}$ becomes ($\overline{V}$ (a cosε)/R). The multiplier may be written more fully as:-

$$M = \frac{(R^2 - y^2 - x^2)^{\frac{1}{2}}}{R} \qquad -7.35$$

Substituting the normalised terms $\bar{x} = x/a$ and $\bar{y} = y/b$, and remembering that $a^2/2\ R\ h_o$ has been chosen to be unity, we obtain:-

$$M = \left[1 - 2H^* \left(\bar{x}^2 + \bar{y}^2 \left(\frac{b}{a}\right)^2 \right) \right]^{\frac{1}{2}} \qquad -7.36$$

M, of course, must be real and so we require that:-

$$2H^* \left(\bar{x}^2 + \bar{y}^2 \left(\frac{b}{a}\right)^2 \right) < 1 \qquad -7.37$$

Physically, equation 7.37 may be interpreted as the limitation placed on the friction field by the size of the ball. Obviously the field can be no wider than the ball and is always very much less. Even if this limit is approached, the correction will have little value, because the assumption of a parabolic film shape will by that time have become grossly inaccurate. However, in the intervening region, equation 7.36 will remove the errors resulting from curvature, whilst those resulting from the wrong film shape have to be tolerated for the sake of computational expediency.

7.5 Region of friction

7.5.1 Experimental measurement

In chapter 5, when calculating pressure distributions, the extent of the calculation grid in the radial direction was chosen so as to be effectively infinite. Because pressures

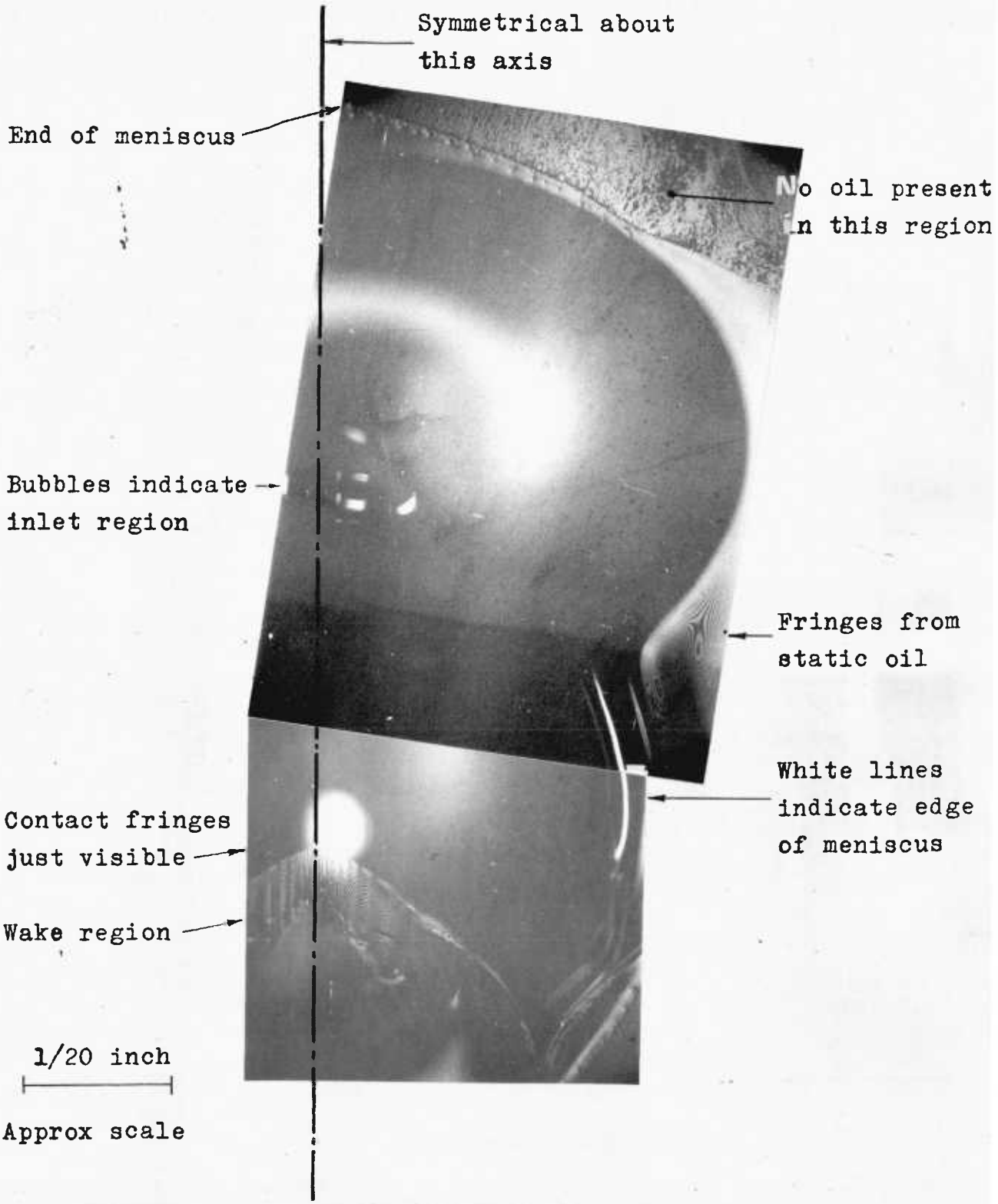


Fig. 7.5 Oil meniscus around a point contact.

at very large radii are nearly zero, further increase in size had a negligible effect on the load. However, as has been demonstrated above, the choice of boundary is more critical when considering friction. Some criterion for determining the boundary has, therefore, to be found.

To obtain an idea of the real boundary, the contact was viewed using a very low power microscope. Unfortunately, for the reasons explained in section 3.5, investigations had to be restricted to circular point contacts. Figure 7.5 shows a photograph of a contact at low magnification. Because the lenses available were not properly suited to the task, the field of view was rather small and hence figure 7.5 has had to be compounded from two prints. The white lines on the right have provided the means whereby the two were correlated. The figure is largely self-explanatory, but of particular interest are the bubbles on the symmetry axis near the centre of the photograph.

It is assumed that these bubbles indicate the beginning of the inlet region. In general an excess of oil will be carried up on the ball surface to the contact region. Oil will collect in front of the inlet until the meniscus is large enough for the excess to spill around the contact and steady flow conditions are reached. There will still be an excess of oil ahead of the contact, however, and within this excess recirculation will occur (see Fig. 7.6). It is hypothesised that the recirculating oil entrains air which results in the bubbles

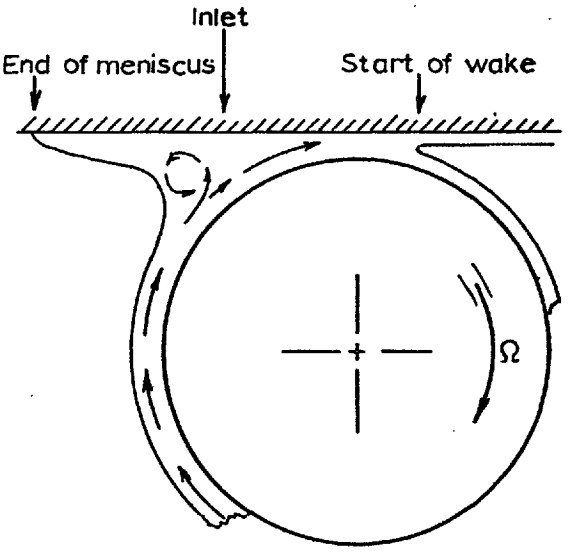


Fig. 7.6 Contact meniscus

of figure 7.5. When pressure build-up starts, they will be forced into solution and will no longer be visible. The pressure region should therefore start just downstream of the bubbles. If this is so then the pressure region in figure 7.5 is approximately circular with the centre of the circle at the contact centre.

Measurements of the radius of this circle have shown it to be approximately equal to 0.12ins. when using a 1 inch diameter ball. The size of region was not found to vary noticeable with either speed or load. If the further assumption is made that the region of pressure for an elliptical contact is elliptical with the minor semi-axis again equal to 0.12ins., then the measurement may be used as a criterion for the limit of the numerical integrations.

7.5.2 Dimensional analysis

To apply a fixed physical boundary (x_B) to the calculation procedure entails introducing a new dimensionless group.

From the equations for the film shape (equation 5.5), the load (equation 5.8) and the sliding friction (equation7.19) we can collect the dimensionless groups relevant to the problem:-

$$\frac{a^2}{2 R h_o}, \quad \frac{2 \nabla \eta_o R}{h_o \mu W}, \quad \frac{a^2}{\alpha W} \quad \text{and} \quad \frac{b}{a}.$$

In addition we have the geometry group due to the boundary $\bar{x}_B = x_B/a$. Hence for an invariant geometry we may write:-

$$\frac{2 \nabla \eta_o R}{h_o \mu W} = \phi_7 \left[\frac{a^2}{2 R h_o}, \frac{a^2}{\alpha W}, \frac{x_B}{a} \right] \qquad -7.38$$

As before, we can choose 'a', the arbitrary scaling factor, such that

$$a^2 = 2 R h_o \qquad -7.39$$

Substituting equation 7.39 into 7.38 and re-arranging to form the usual non-dimensional groups gives:-

$$\mu\left(\frac{W^*}{U^*}\right) = \phi_8\left[\frac{H_o^*}{W^* G^*}, \quad \frac{x_B^*}{H_o^{*\frac{1}{2}}}\right] \qquad -7.40$$

where $x_B^* = x_B/R$.

This may equally well be written:-

$$\mu\left(\frac{W^*}{U^*}\right) = \phi_9\left[\frac{H_o^*}{W^* G^*}, \quad \frac{x_B^*}{(W^* G^*)^{1/2}}\right] \qquad -7.41$$

but from equation 5.10

$$\frac{H_o^*}{W^* G^*} = \phi_1\left[\frac{U^*}{W^{*3/2} G^{*1/2}}\right]$$

hence equation 7.41 becomes:-

$$\mu\left(\frac{W^*}{U^*}\right) = \phi_{10}\left[\frac{U^*}{W^{*3/2} G^{*1/2}}, \quad \frac{x_B^*}{(W^* G^*)^{1/2}}\right] \qquad -7.42$$

The theoretical predictions may thus be plotted on the same axes as used in chapter 6 for a constant $x_B^*/(W^* G^*)^{\frac{1}{2}}$. x_B^* has been measured to be constant at 0.24 and, therefore, the effect of the new group is a dependence of the solution upon the load group (W^*) for a given G^*.

7.6 Experimental and theoretical results

7.6.1 Experimental frictions

Figures 7.7 to 7.11 show the experimentally determined frictions for a ball in a groove at various drive angles. All measurements were taken at a slide/roll ratio of 1.0 using the small glass raceway. The friction measured was the component of the total friction acting along the groove axis; in a real bearing it is this component which governs the bearing torque.

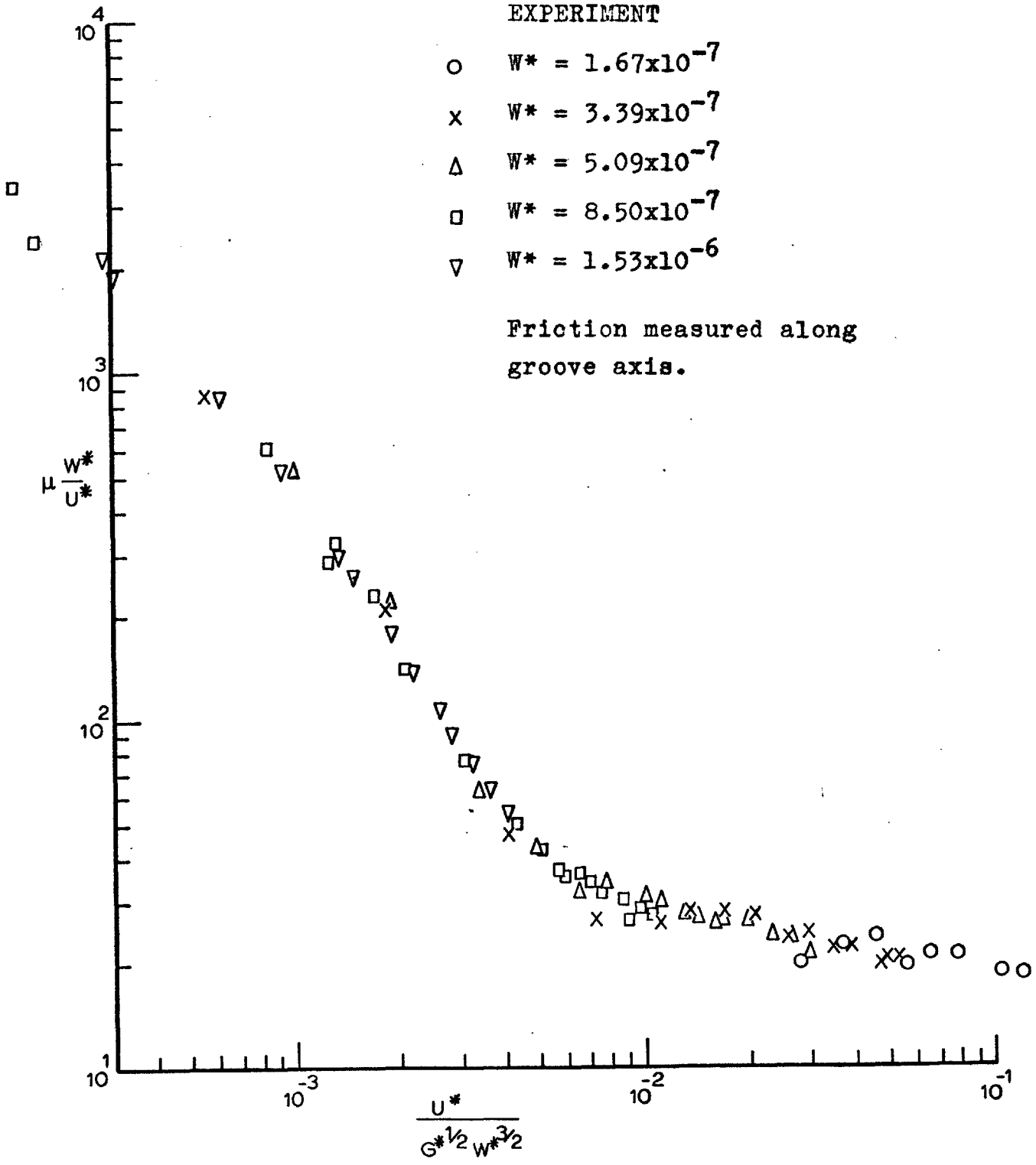


Fig. 7.7 Friction group vs speed group for drive angle of 0 deg. (Sliding elliptical contact)

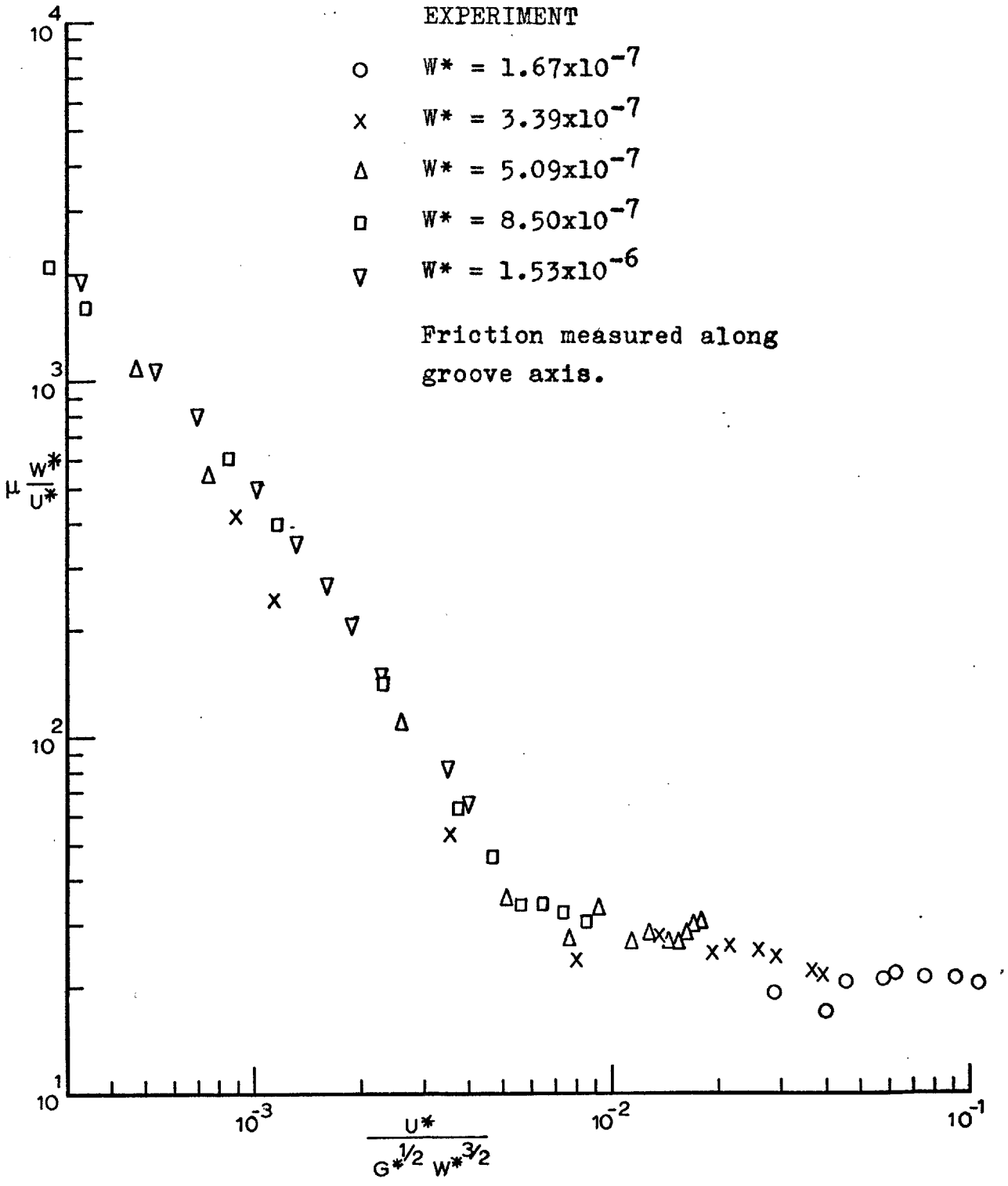


Fig. 7.8 Friction group vs speed group for drive angle of 10 deg. (Sliding elliptical contact)

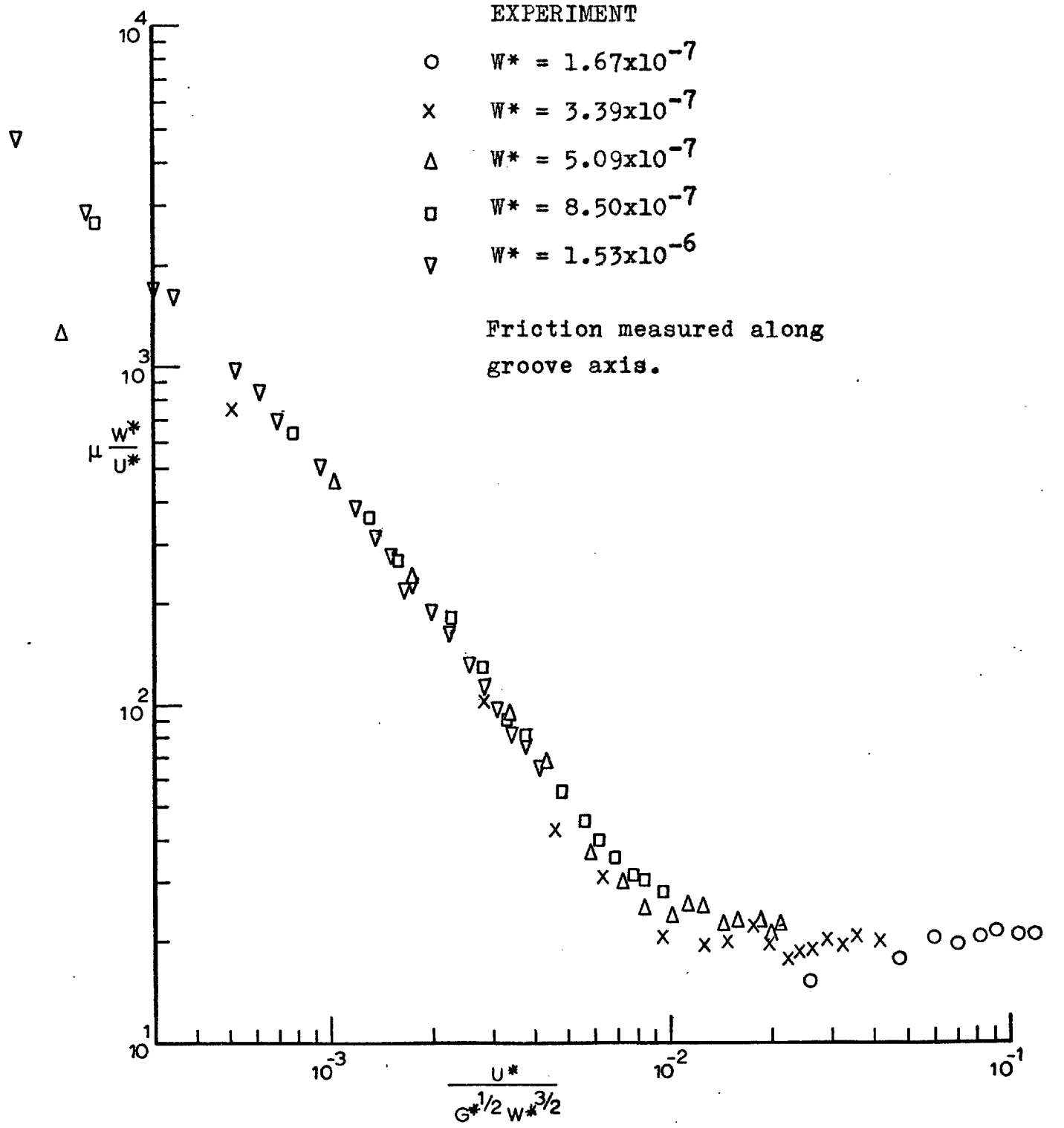


Fig. 7.9 Friction group vs speed group for drive angle of 50 deg. (Sliding elliptical contact)

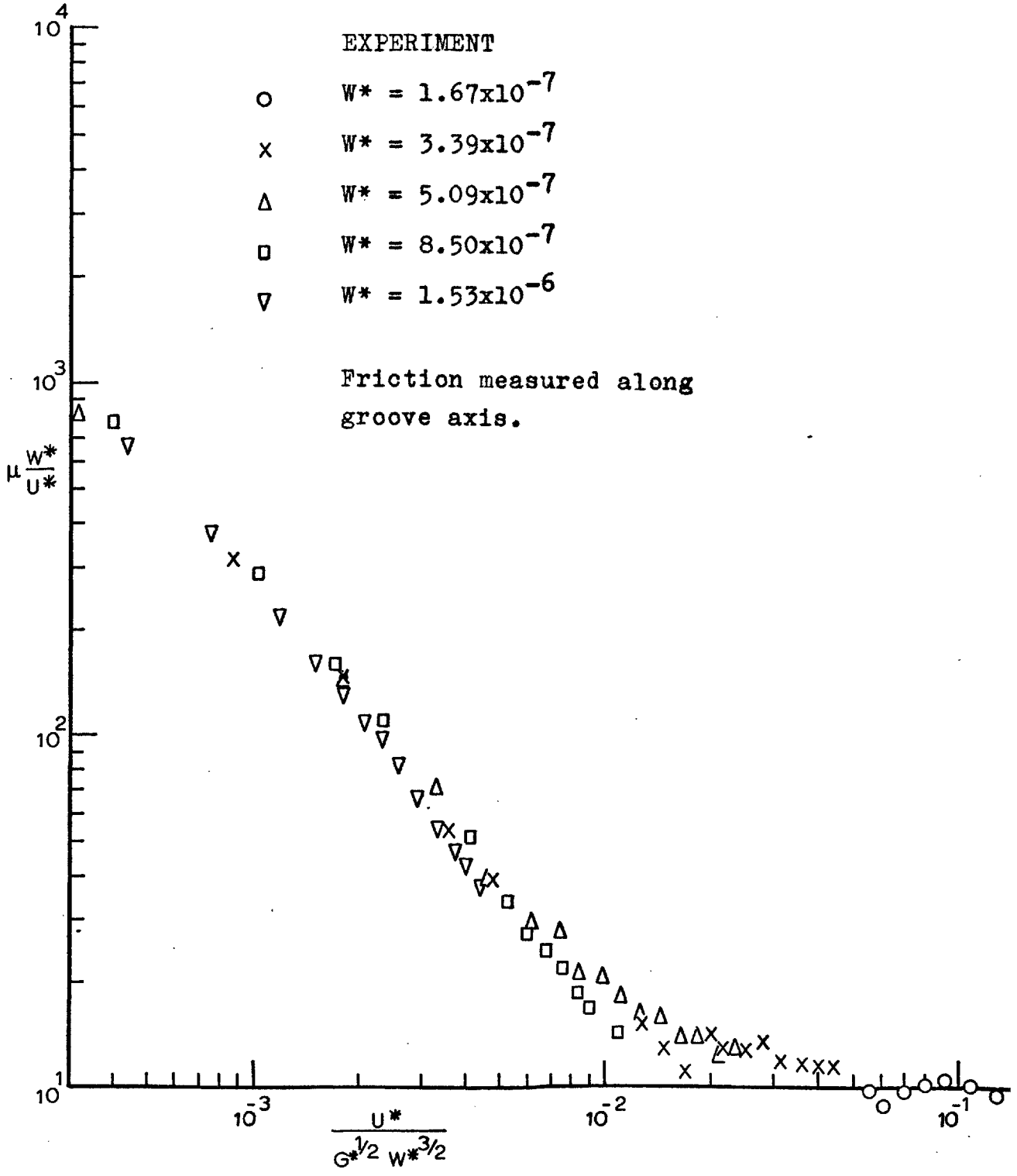


Fig. 7.10 Friction group vs speed group for drive angle of 67 deg. (Sliding elliptical contact)

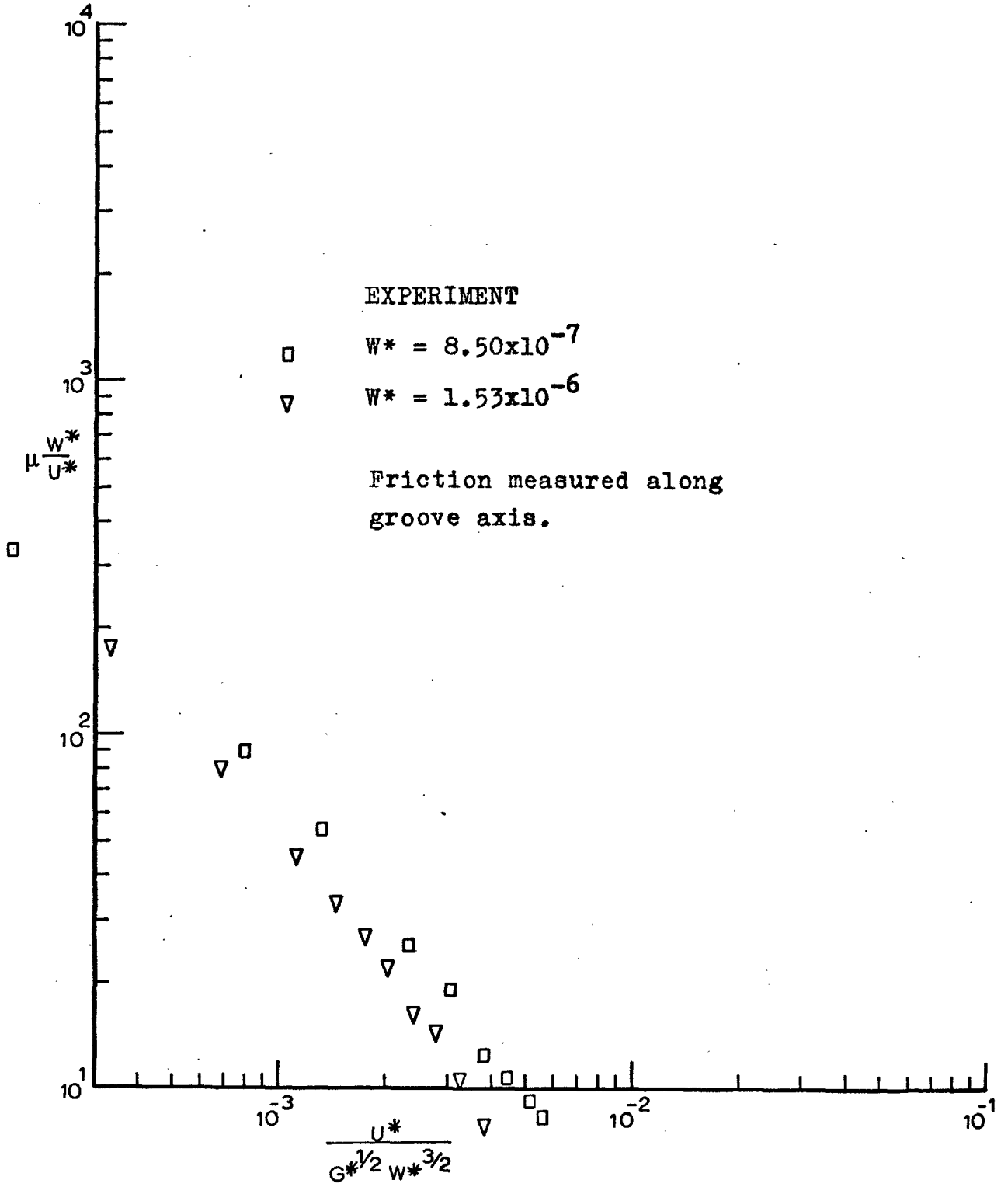


Fig. 7.11 Friction group vs speed group for drive angle of 82 deg. (Sliding elliptical contact)

The results shown are for a range of load but, because they are plotted using the groups discussed in section 6.2.5, a single curve has been obtained.

Comparison between the graphs shows that friction along the groove is not noticeably dependent on drive angle up to 50°, but thereafter falls rapidly with further increases up to 90° when it must, of necessity, be zero. Thus the graph at 82° shows points only for the heaviest loads because at lower values the friction had dropped to a level below the sensitivity of the simple apparatus used.

As with the film thickness plots, the transition into the rigid piezo-viscous regime shows itself in a change of gradient of the curve. Eventually, as predicted by equation 6.32, the curve will become a horizontal line with $\mu\ (W^{*}/U^{*})$ equal to a constant.

7.6.2 Theoretical frictions (elliptical contacts)

As already mentioned, the results to be presented in this section use the pressure distributions obtained from the theory of chapter 5. These were calculated with the boundary condition $\bar{q} = 0$ applied at a non-dimensional radius of 23.25. However, the friction integrals, as discussed in section 7.5, extend only to the value $\bar{r}_B$ which, in general, is less than 23.25. It is implicit, therefore, that $\bar{q}$ will not be zero around the edge of the 'friction grid'. The pressure distributions calculated earlier were available on punched cards and because of the computer time involved, it was not practicable to re-calculate the distribution every time $\bar{r}_B$ differed from 23.25. The errors introduced by this approximation are likely to be very small until $\bar{r}_B$ is reduced to 2.5 or less. For instance, even when the pressures are at their greatest and

$\bar{q}_{max} = 1$, $\bar{q}$ drops to 10% of the peak value when $\bar{r}$ has reached 2.0. When $\bar{r}_B$ was required to be greater than 23.25 it was necessary to set it equal to 23.25, because it was not possible to extend the range of the grid without re-calculating the pressure distribution.

Figures 7.12 and 7.13 show respectively the friction and its component parts for the maximum and minimum values of $x_B^*/(W^* G^*)^{\frac{1}{2}}$ encountered experimentally. The experimental results are also shown for comparison. Note that the ordinates are plotted on a linear scale to permit a realistic comparison to be made. It can be seen that there is poor correlation between theory and experiment, the theory being, in general, too high. Furthermore,the extra non-dimensional group has caused a significant load dependence which is not evident experimentally.

The most serious contradiction with the experiment is that there is no tendency for $\mu(W^*/U^*)$ to become constant. The criterion of a fixed value of $x_B^*/(W^* G^*)^{\frac{1}{2}}$ for the range of friction must therefore be examined. It results in an ever-decreasing non-dimensional boundary, thus on the graphs presented at large value of the speed group, $\bar{r}_B$ has become much less than the suggested minimum of 2.5 with a consequently large discontinuity in pressure at the boundary of the area of integration. At the lower end of the speed range, on figure 7.12, the boundary has reached the maximum limit of the grid and a discontinuity has been caused in the predictions.

Strictly, the predicted load dependence should be slightly less than that shown because results with the highest load used experimentally do not extend into the rigid piezo-viscous regime. However, there is no reason to suppose that, if they

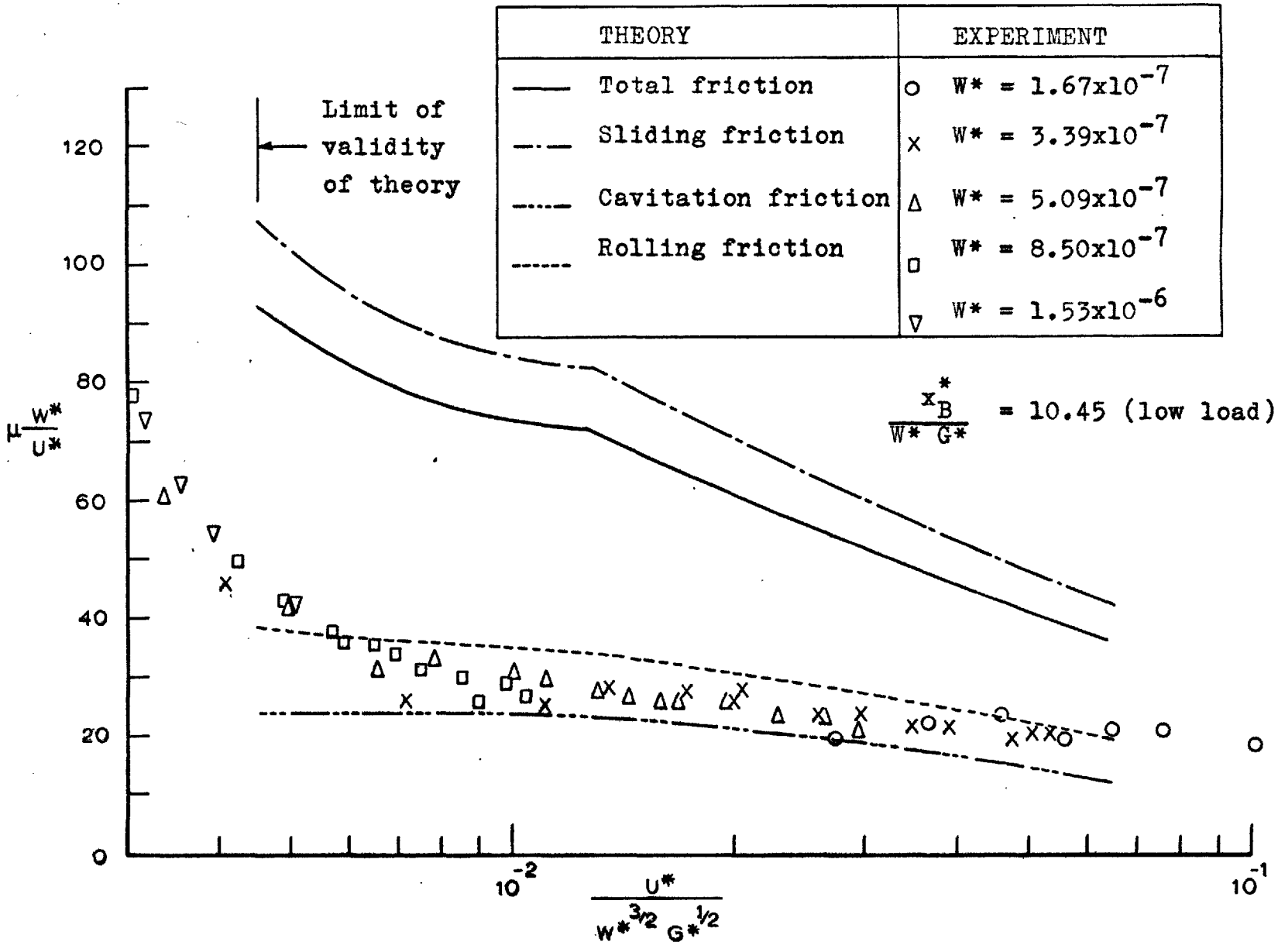


Fig. 7.12 Friction group vs speed group for drive angle of 0 deg. (Sliding elliptical contact)

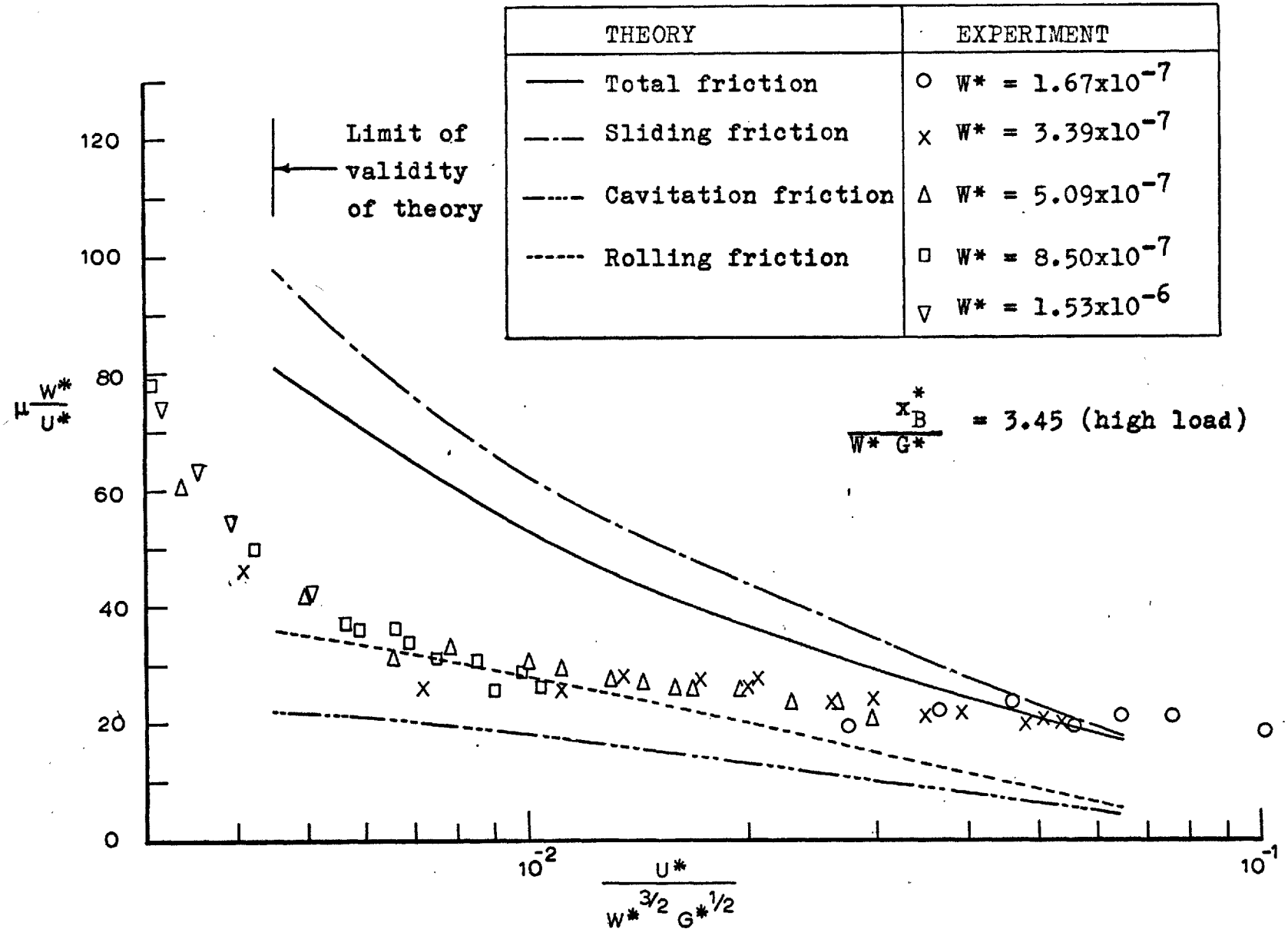


Fig. 7.13 Friction group vs speed group for drive angle of 0 deg. (Sliding elliptical contact)

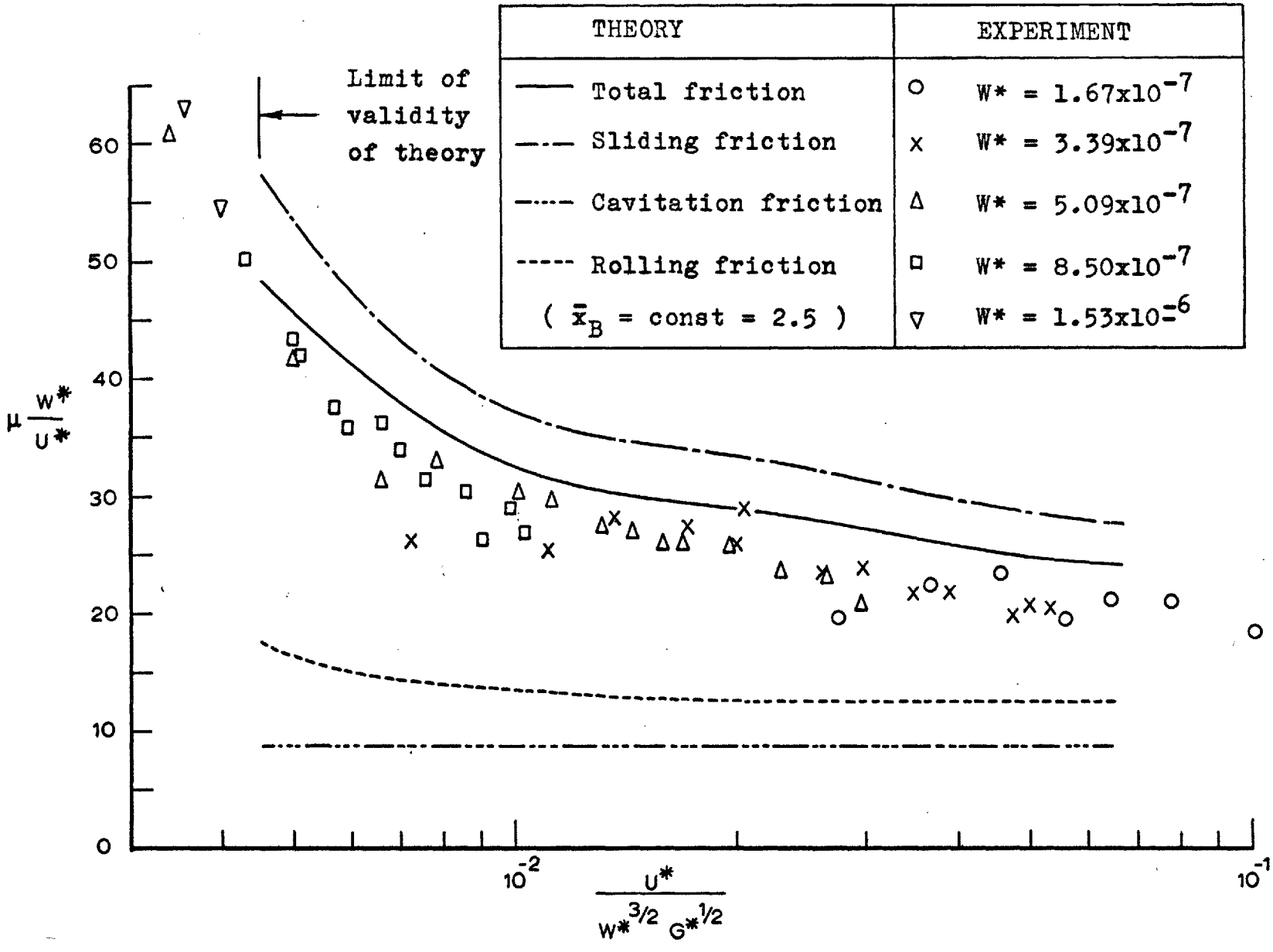


Fig. 7.14 Friction group vs speed group for drive angle of 0 deg (Sliding elliptical contact)

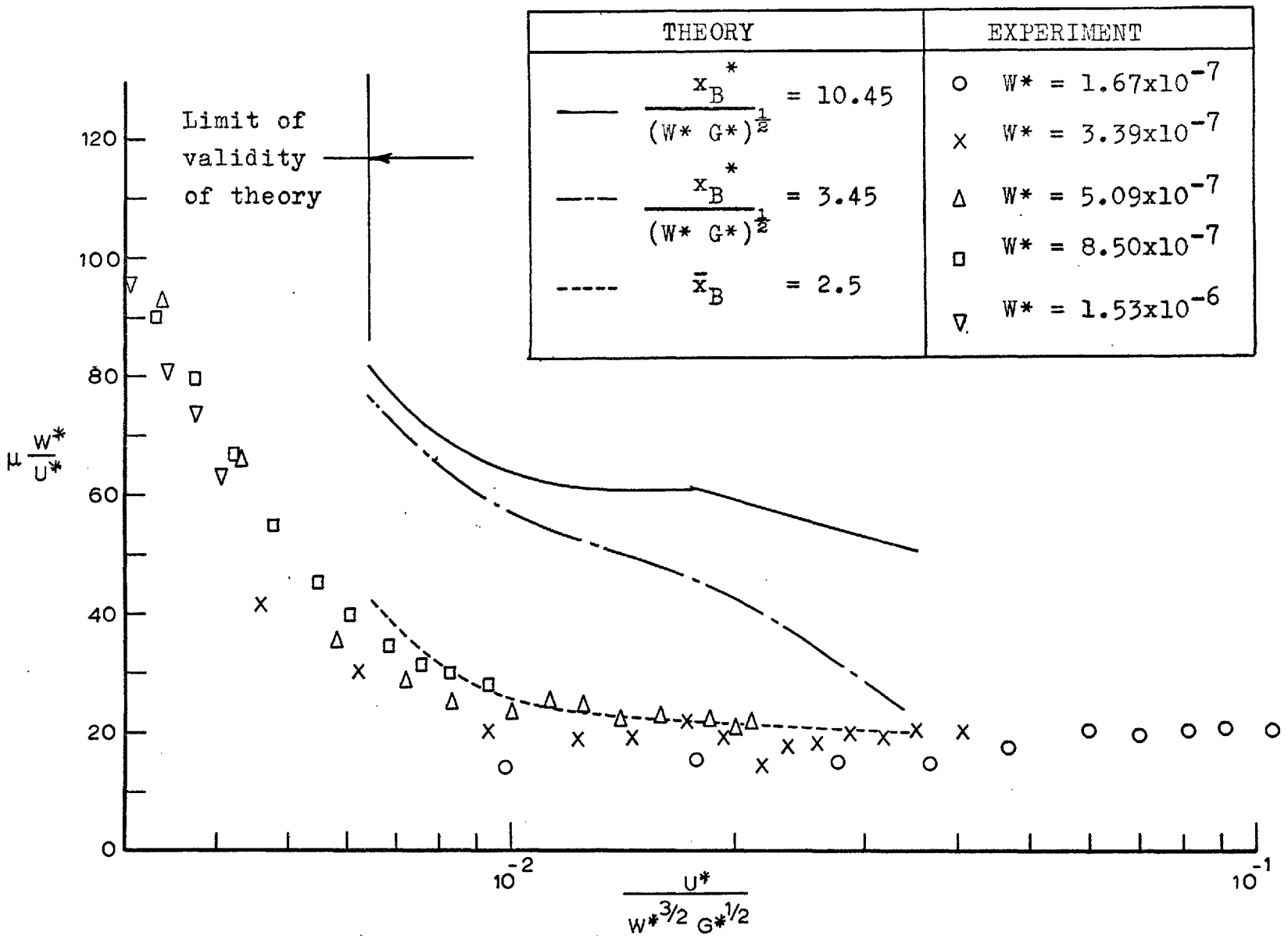


Fig. 7.15 Elliptical contact (50 deg drive angle) : experiment & numerical theory (rigid surfaces)

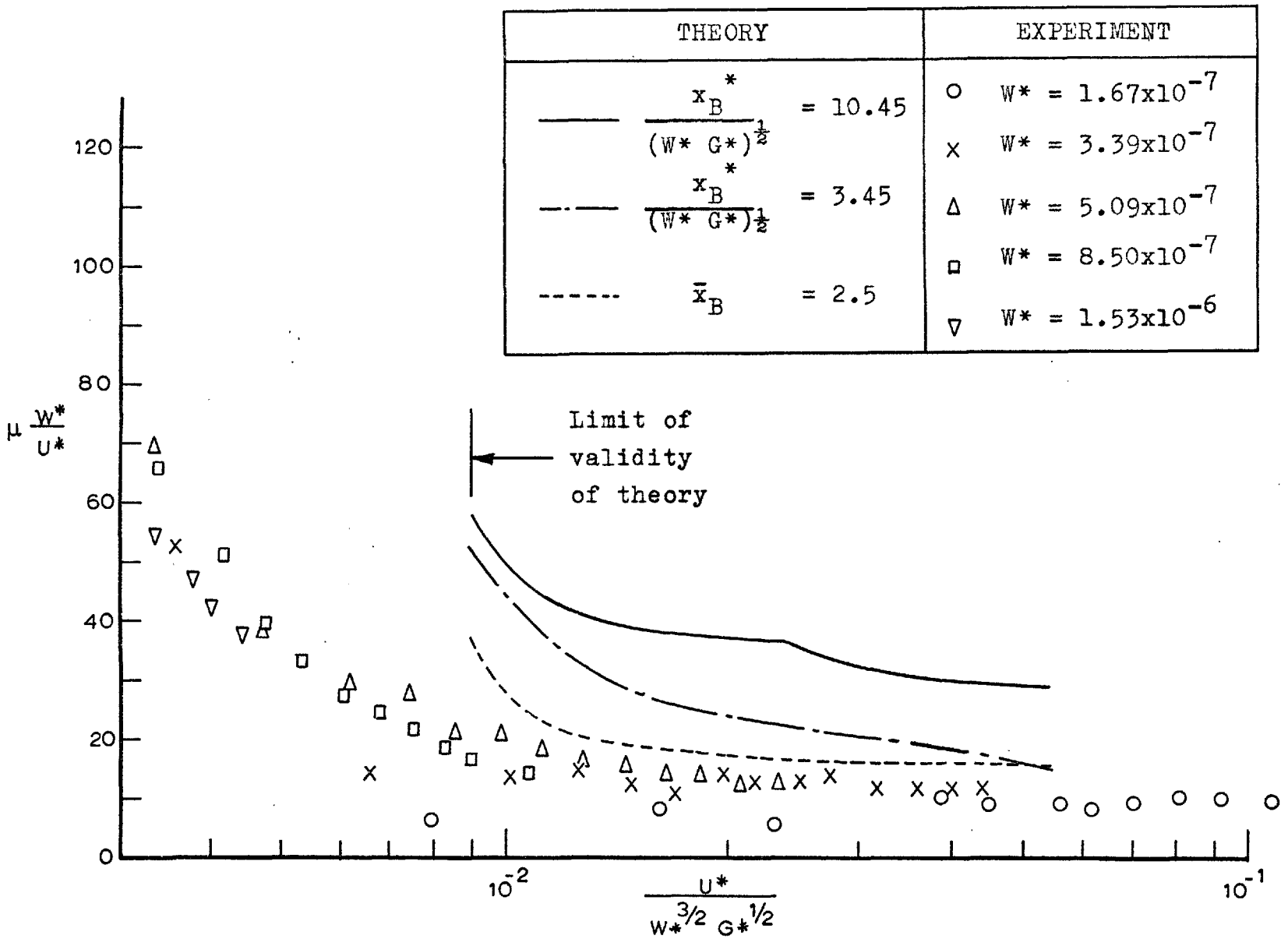


Fig. 7.16 Elliptical contact (67 deg drive angle) : experiment & numerical theory (rigid surfaces)

did, there would be any greater experimental spread than already present. It is possible, however, to preclude spread due to load by using a fixed non-dimensional boundary. Figure 7.14, therefore, shows further predictions with this as the criterion for the range of friction. $\bar{x}_B$ was chosen intuitively to be 2.5, being the smallest value for which the use of the available pressure distributions could be justified. As can be seen, this last set of predictions is remarkably close to experiment, being on average too large by 4 which represents about 12% over the range investigated.

Figures 7.15 and 7.16 show corresponding predictions for drive angles of 50° and 67° respectively. Only total frictions are shown, but for both boundary criteria. Comparison with experiment shows the same results as in the 0° case, a fixed value of $\bar{x}_B$ resulting in better correlation.

7.6.3 Theoretical friction (circular contacts)

The experimental measurements presented in chapter 6 extended into the piezo-viscous regime. Predictions for circular contacts were therefore made to compare with these measurements.

Figures 7.17 to 7.19 show only the total friction for the two boundary criteria and the experimental results for Perspex, glass and sapphire respectively. One advantage of comparing with these circular contact experiments is that the boundary measurements reported in section 7.5.1 will apply without any further assumptions.

The boundary criterion based on a constant $x^*_B/(W^* G^*)^{\frac{1}{2}}$ results in much better agreement with these results than with the elliptical contact data presented above. Also, except for the measurements with the glass disc, it appears to give better predictions than does the second criterion which is based on

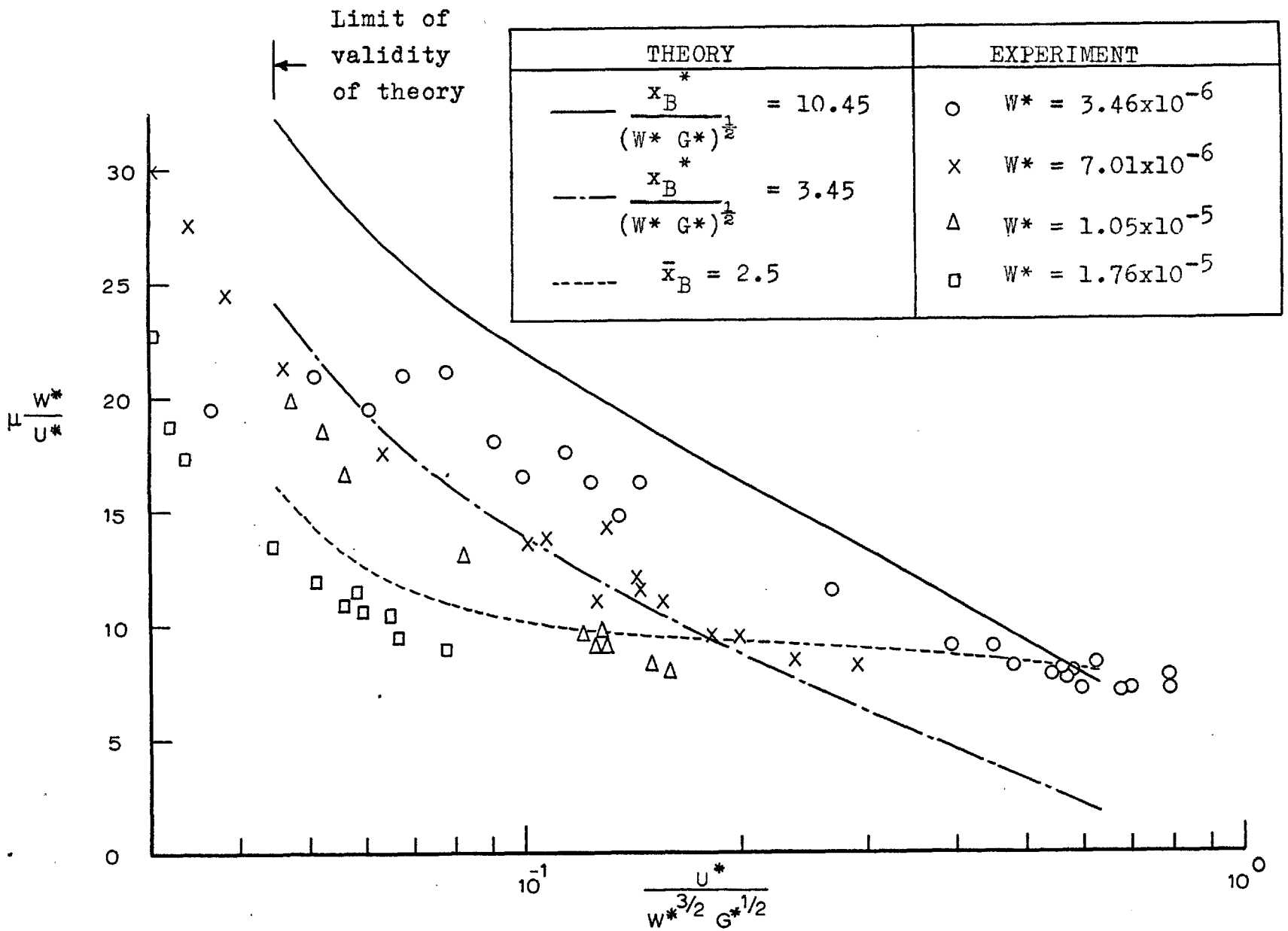


Fig. 7.17 Sliding friction on Perspex : experiment & numerical predictions (rigid surfaces)

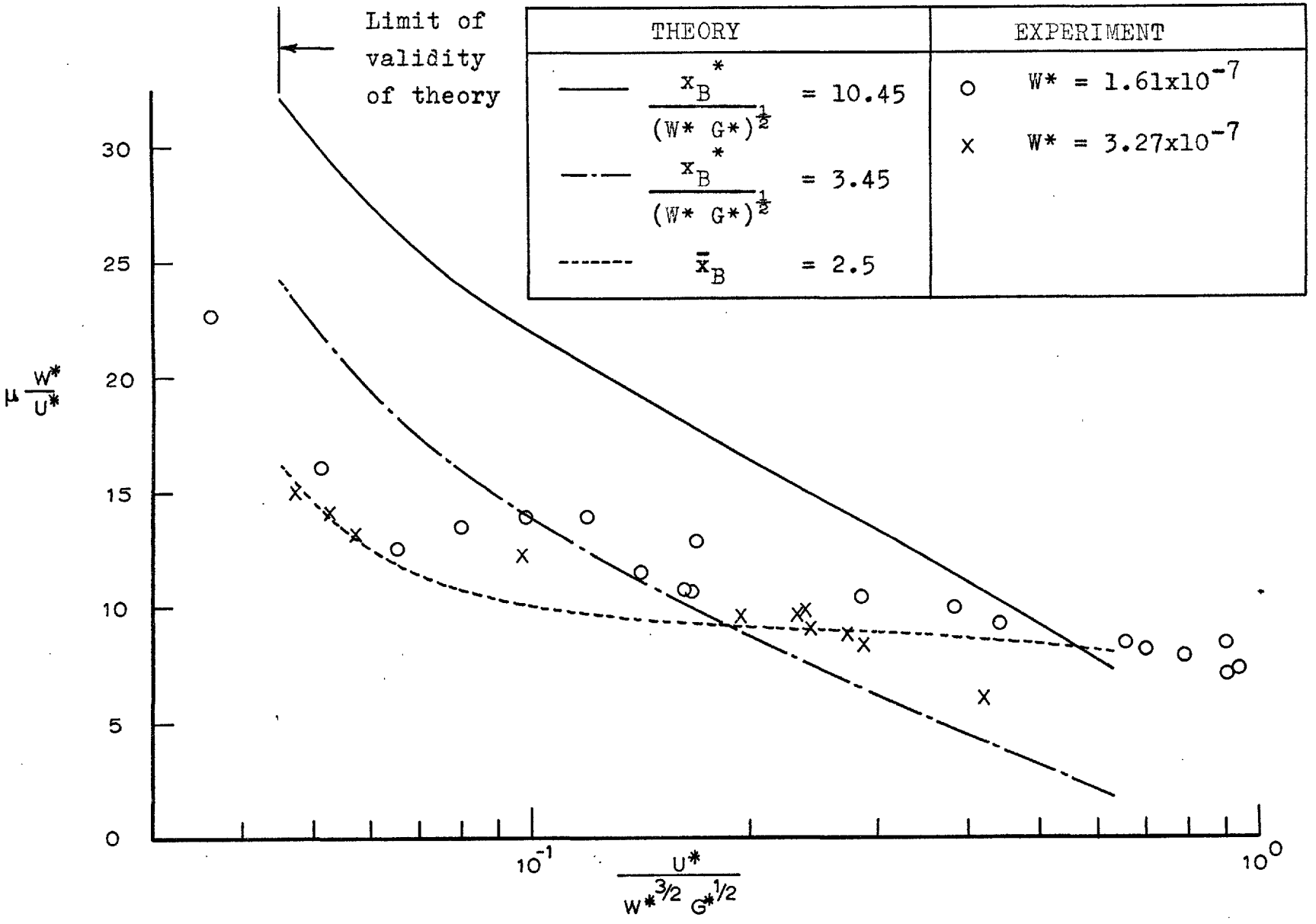


Fig. 7.18 Sliding friction on glass : experiment & numerical predictions (rigid surfaces)

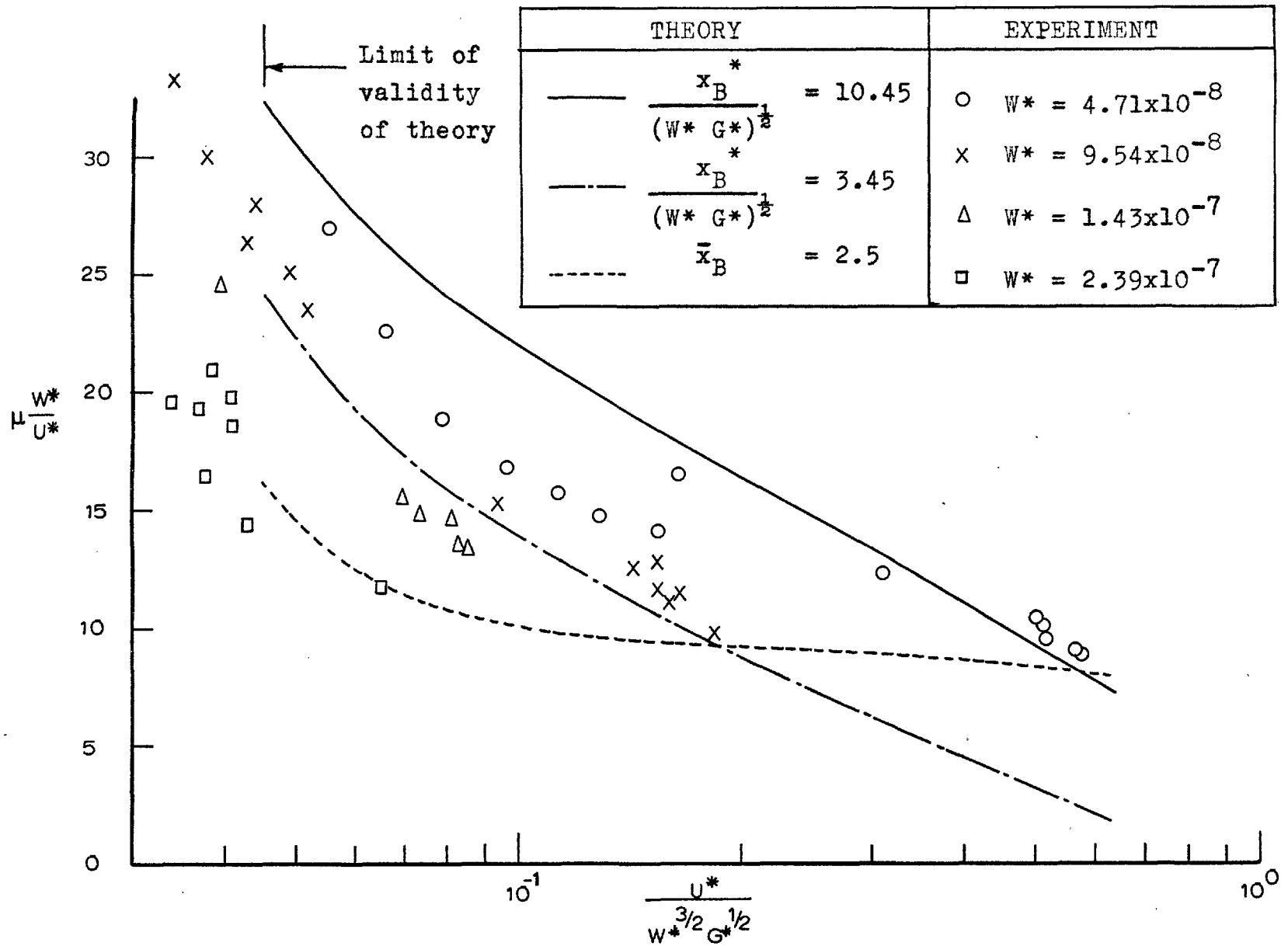


Fig. 7.19 Sliding friction on sapphire : experiment & numerical theory (rigid surfaces)

a fixed value of $\bar{r}_B$. Gradients are closer to experiment, and the spread with load variation is reproduced.

At high values of the speed group, the experiment tends to level off to a constant $\mu(W^*/U^*)$. This is the same value for all the material combinations because, when distortion is absent, the modulus of elasticity naturally has no effect. The numerical predictions based on the first criterion, however, continue to drop, but divergence between theory and experiment is significant only when $\bar{r}_B$ has been reduced below the suggested minimum of 2.5, that is, when the predictions are below those based on the second criterion.

7.7 Discussion of results

Before the comparisons just described can be evaluated properly, the physical meaning of the two boundary criteria used in the calculations must be examined.

a) Fixed inlet boundary

A fixed value of the group $x_B^*/(W^* G^*)^{\frac{1}{2}}$ represents a fixed physical inlet distance x_B. Considering only the x-axis, the film thickness at x_B is given by:-

$$h_B = h_o + \frac{x_B^2}{2R} \qquad -7.43$$

In general, $x_B \gg h_o$ and so h_o may be neglected and equation 7.43 rewritten as:-

$$h_B = \frac{x_B^2}{2R} \qquad -7.44$$

Thus this first inlet boundary criterion represents a fixed inlet film thickness and hence a fixed lubricant supply condition.

b) Floating inlet boundary

The criterion of a constant $\bar{r}_B$ results in a constant $\bar{x}_B$ ($= x_B/\sqrt{2\ R\ h_o}$) which represents a floating physical inlet boundary distance. The greater the central film thickness, the larger is the inlet boundary, x_B. However, if the film thickness is large, the pressure build-up will be very gradual and may need to start at an inlet distance greater than x_B. Thus this criterion represents a fixed lubrication condition which, unless the pressure curve starts within the boundary x_B, will be one of starvation.

In actual bearings and certainly in these experiments, criterion (a) would appear to be the more realistic. Indeed, granted the assumption that the bubbles in figure 7.5 show the start of the inlet region, it is the condition observed. It appears paradoxical,then,that criterion (b) should give better agreement when there is elliptical contact. However, as the fixed inlet boundary criterion (a) gives results close to experiment with point contacts, the implication is that the assumption that the region of friction is elliptical, in the elliptical contact case, might not be justified. A consideration of the distances involved confirms this. If $x_B \simeq 0.1$ ins. and the ellipse ratio $\simeq 4.5$, the total length of the meniscus in the y-direction must be $\simeq 0.9$ins. The groove is only about 0.5 ins. wide, hence the contact is truncated in the y-direction. Examination of the approximate solutions for the component parts of friction (equation 7.26, 7.30 and 7.32) shows that the choice of boundary in the y-direction is more important than that in the x-direction. Integration to infinity with respect to x results in a factor of $\pi/2$ or $\pi/4$ depending which friction component is being considered. Integration

with respect to y, however, (equation 7.27) gives (to a first approximation) friction as proportional to $\ln(y_B)$.

It may be concluded, therefore, that although a fixed $x_B^*/(W^* G^*)^{\frac{1}{2}}$ is the correct inlet boundary criterion to apply when computing frictions in the rigid piezo-viscous regime, premature starvation can be caused by physical restriction on the maximum width of the oil meniscus. In the circular point contact case, it was possible to measure the meniscus in the y-direction and hence justify the use of a circular mesh for computation. Unfortunately, in the elliptical case, it was not possible to compute on anything other than an elliptical mesh without completely rewriting the computer program. However, by reducing the less important boundary in the x-direction, as well as in the y-direction, criterion (b) could be applied and, as demonstrated in figures 7.14 to 7.16, better predictions obtained.

At high values of the speed group criterion (a) appears to be inadequate because predictions are too low, these low values being caused by the reduction of the non-dimensional boundary below the minimum of 2.5. Thus the part of the curve in this region is invalid and to obtain theoretical predictions using (a), it would be necessary to recalculate the pressure distributions. Reference to figure 5.3 shows that if the non-dimensional inlet radius is as low as 2.5 the load capacity has dropped appreciably. It follows, then, that if the load is kept constant, film thickness will drop instead.

Wedeven (6) has proposed a starvation parameter for EHL contacts in terms of the effect on central film thickness. He found that the effect was noticeable only when the inlet distance was of the order of the Hertz contact diameter. In

the EHL regime, pressures are large only over a very small area and so the inlet boundary must be very small if it is to cause starvation. In the rigid surface regime, however, pressure build-up is more gradual and so a contact will starve much more easily than under EHL conditions. It is therefore suggested that starvation in this regime will occur at values of $\bar{r}_B$ less than 2.5.

If this be the case, then should the non-dimensional inlet boundary be reduced to 2.5, the contact will be starved and the governing criterion will change from (a) to (b); for speed group values larger than that at the changeover point, (b) will be the more appropriate. As speed increases, so too does film thickness and also, for a given lubricant supply, the degree of starvation. However, a constant $\bar{x}_B$ represents fixed starvation conditions. In the rigid surface regimes film thickness is significantly dependent upon load and in the limit is proportional to W^{-2}. As starvation increases, load capacity will drop. If the load is to be constant, the film thickness must therefore drop to reduce starvation and hence support the load. It is unlikely that experimentally constant starvation will occur, but theoretical predictions based on a constant $\bar{x}_B$ will be more accurate than those based on a constant $x_B^*/(W^* G^*)^{\frac{1}{2}}$.

The differences between the theory and experiment can therefore be explained and, by basing prediction on a combination of the two boundary criteria, largely removed. Figure 7.20 shows the predictions using the combined boundary criteria. The axes are both logarithmic to permit the full range of experimental results to be shown. These are those obtained with the Perspex plate for which the conventional EHL friction

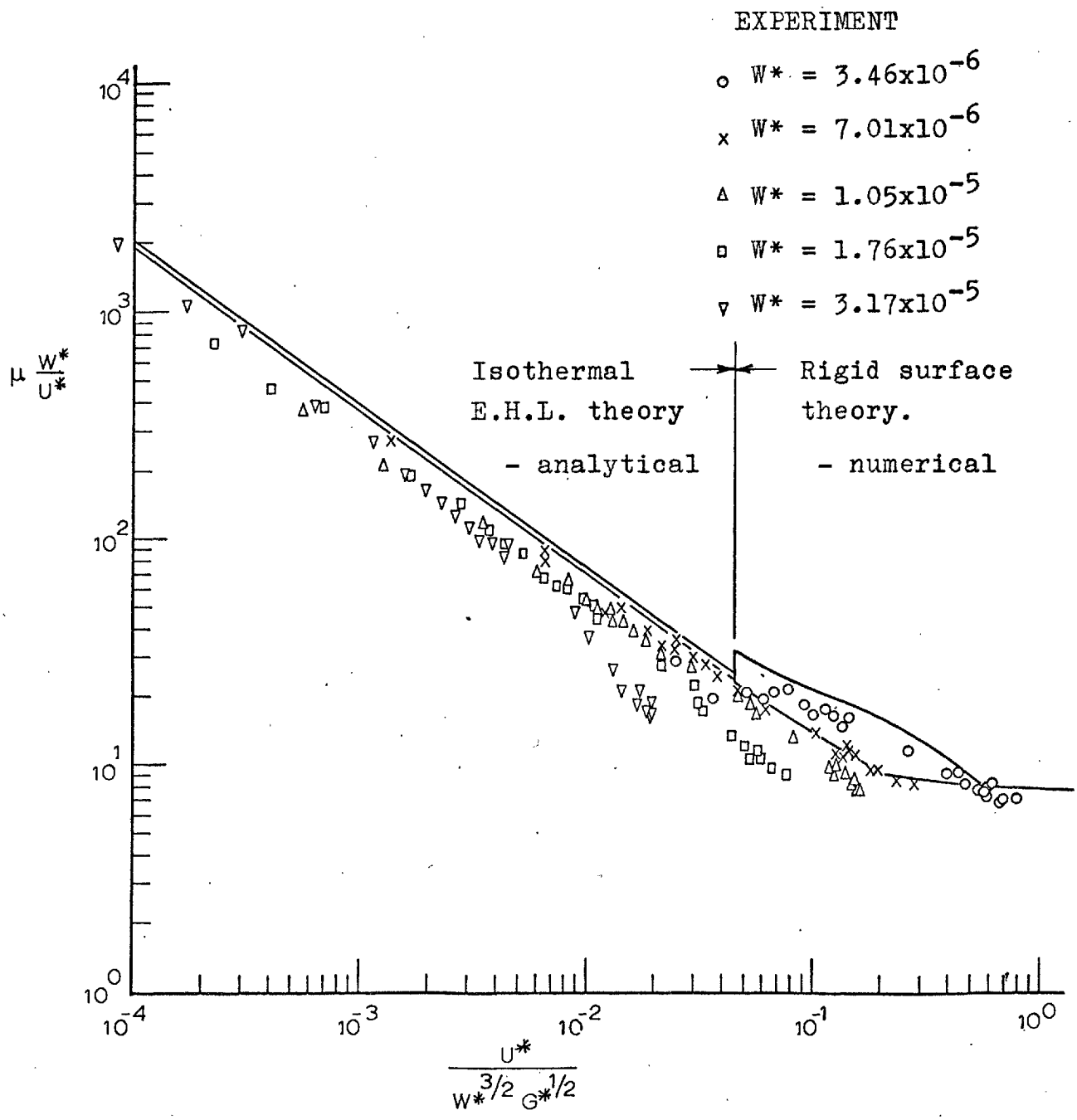


Fig. 7.20 Sliding friction on Perspex : experiment and various theories.

predictions of chapter 6, also shown, were most accurate. The graph demonstrates how the two entirely different friction theories merge, the rigid surface theory continuing to give reasonable predictions when the EHL theory has become invalid.

References for Chapter 7

1. Howlett J. 'Film lubrication between spherical surfaces with an application to the theory of four-ball lubricant testing instrument' Jour. Appl. Phys., 1946, Vol. 17, p 137.
2. Korovchinskii M.V. 'Possible limiting conditions of hydrodynamic friction in a four-ball testing machine' Trenie i Iznos v Mashinax, Akad. Nauk., Moscow, Vol.12, p233, (1958).
3. Kapitza P.L. 'Hydrodynamic theory of lubrication during rolling' Zhurn. Tekh. Fiz., 1955, Vol. 25, No.4, pp 747-762.
4. Niemann G. & Geupel H. 'Fluid friction in point contact' Konstruktion, Vol. 21 (1969), No. 11, pp 428 - 35.
5. Dalmaz G. & Godet M. 'L'hydrodynamique du contact sphere plan. Premiere partie: solution theoretique numerique exacte en regime equi et piezovisqueux' Revue du GAMI, 'Mecanique Materiaux Electricite', April 1972, No. 268 pp 32 - 41.
6. Wedeven L.D., Evans D. & Cameron A., 'Optical analysis of ball bearing starvation' Trans. ASME, 1971, Series F, Jour. Lub. Tech., Vol. 93, No. 3, p 349.

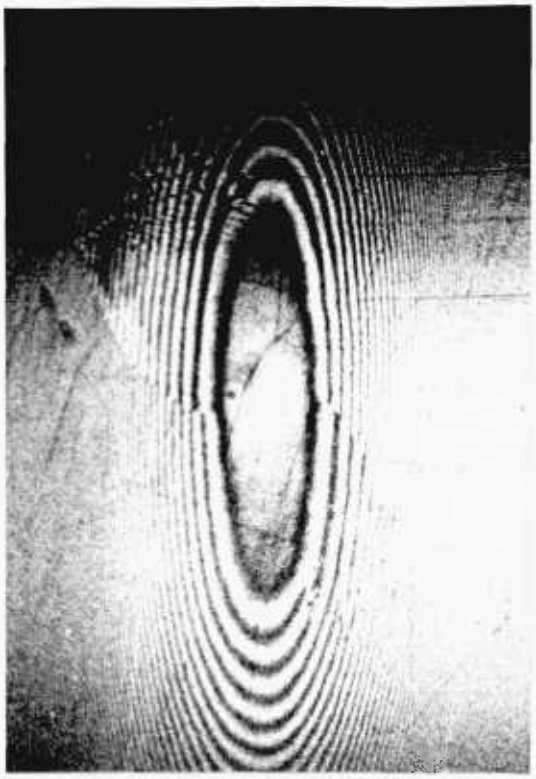
Chapter 8 FURTHER FILM THICKNESS INVESTIGATIONS

8.1 Film thicknesses under pure spinning

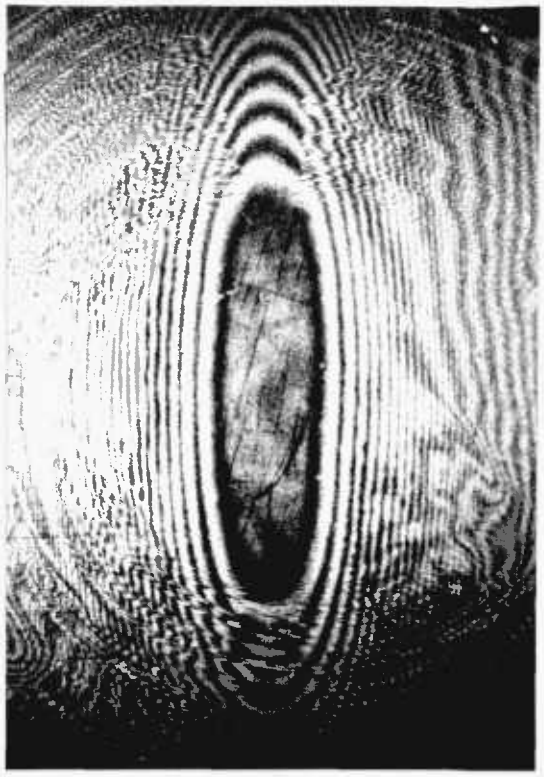
A brief investigation was undertaken of the film formation under the action of pure spinning; that is, with the ball rotating about an axis normal to the groove. Such a motion gives rise to film thicknesses very much smaller than those generated under rolling or sliding action. To date, in spite of considerable interest in the topic (see section 1.4) no attempts to measure these films have been reported. The present work, therefore, examines the feasibility of applying optical interferometry to spinning contacts.

Because the arrangement used to obtain an elliptical contact was closely akin to a real bearing, with a ball in a partially conforming groove, rather than an equivalent geometry, a spinning contact could be readily achieved using the modified apparatus described in section 2.5. Figure 8.1 shows four interference fringe photographs obtained in this way. It is immediately obvious that no details of the shape can be seen in these fringes, the film thickness being so small. However, some qualitative information may be deduced by examination of these photographs.

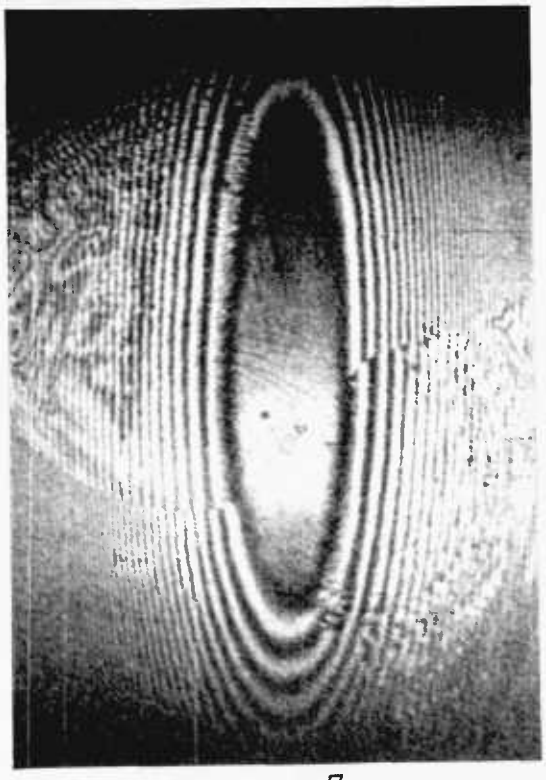
Figure 8.1(b) shows a typical spinning contact. There is some pressure generated, the distribution of which can be inferred from the wake pattern. Assuming the ball is viewed from above, its rotation is anticlockwise. There has been a pressure build-up on the top of the contact between the wake patterns, because the oil is entrained with a radial motion into a narrowing wedge. Beyond the minimum film centre line (along the ellipse major axis) the oil sees a diverging wedge



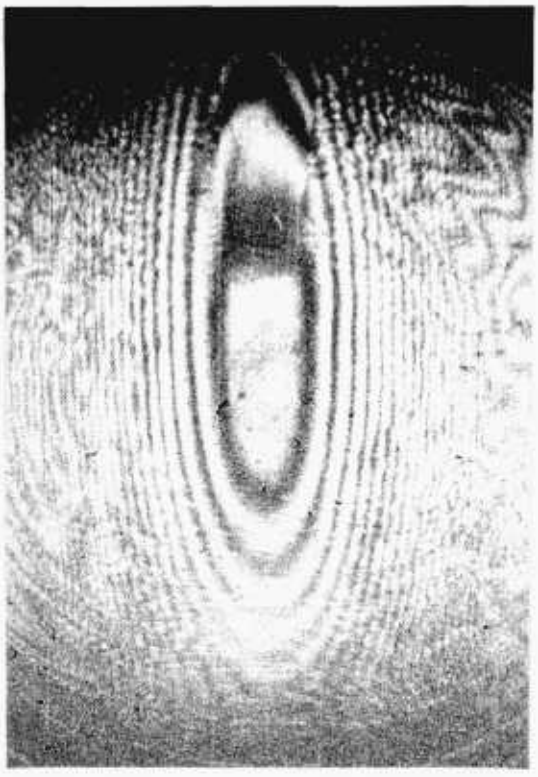
(a) $W^* = 2.4 \times 10^{-7}$ $\Omega = 1$ rpm



(b) $W^* = 2.4 \times 10^{-7}$ $\Omega = 198$ rpm



(c) $W^* = 5.5 \times 10^{-7}$ $\Omega = 19$ rpm



(d) $W^* = 6.5 \times 10^{-8}$ $\Omega = 208$ rpm

MAGNIFICATION X 85

Fig. 8.1 Film shapes under pure spinning. (Ω is anti-clockwise)

and eventually separates or cavitates. It remains so until there is another pressure build-up in the lower part of the figure. Note that the non-cavitated parts are not displaced symmetrically about the ellipse major axis because one boundary is determined by film rupture and one by film reformation. The oil film thickness in figure (b) appears to be uniform over the whole of the contact. There has been a slight darkening in the central region, which statically is grey, indicating that a thin oil film does exist although it is less than the height represented by the first dark fringe ($\simeq 2\ \mu$in.).

The contact of figure (a), which is at a very much lower speed, has remained grey suggesting no film generation. However, the film thickness appears to have reached the first dark fringe at the top and to be approaching it at the bottom. Film generation under EHL spinning conditions will be greatest at the ends of the contact ellipse because the entrainment velocity is greater there, being proportional to the distance from the axis of spin. Experimentally it was difficult to ensure that the spin axis coincided with the centre of the contact ellipse which accounts for the asymmetry of figure (a). It is interesting to note that at this very low rotational speed, the cavitated region is contained within the lubricant meniscus surrounding the contact region and consists of a single bubble in the lower part of the picture, and a few bubbles in the upper part where the film is more developed. Similar wake patterns have been observed by Archard and Kirk (1) and by Wedeven (2) in the sliding and rolling point contacts respectively. Because of the glare the boundary of the cavitated region in the lower part of figure (a) is not easily seen; however, the extent of the region may readily be inferred from

the change in spacing of the interference fringes. A wider spacing indicates a reduction in density of the oil and hence the extent of the wake.

Figure (c) shows a spinning contact at a higher load and lower speed than figure (b). However, the film thickness over the majority of the contact is thicker than in (b), although a thinner film might well be anticipated. Snidle and Archard (3) have pointed out that at large radii from the spin axis, the approach of the two surfaces resulting from deformations should improve the ability of the motion to generate a hydrodynamic pressure, because the minimum film thickness along any arc of constant radius is reduced. They also predict that, under high loads, it would be more difficult to generate a hydrodynamic film in the region close to the axis of rotation than suggested by their theory. When the radius is less than the contact ellipse semi-axis, there is no converging wedge to generate hydrodynamic pressure. Their theoretical analysis, however, was for an undistorted contact. The film thickness near the axis in figure (c), that is, just below the centre of the contact ellipse, appears to be negligible, confirming this prediction. Note that, although the wake extends well beyond the central area, the oil film reforms considerably earlier than in figure (b). This may be attributed partly to the reduced rotational speed which gives the streamers more time to merge and also to the fact that there is probably more lubricant available than in the example shown in (b). In the lower part of (b) the wake streamers cross the pressure region which indicates the onset of starvation.

Figure (d) shows a spinning contact where the starvation is much more severe. Once again, the axis of rotation is

slightly off-centre causing the lower half of the contact to starve first. The film has dropped to zero over the majority of the contact ellipse although at the uppermost part, where starvation is least, it is still up to the height of the first dark fringe.

Although not discernable on the photographs, observations were made of a region near the minor axis just outside the contact ellipse which had not cavitated and was therefore at, or slightly above, atmospheric pressure. The presence of such a region may be explained by reference to figure 8.2. If the

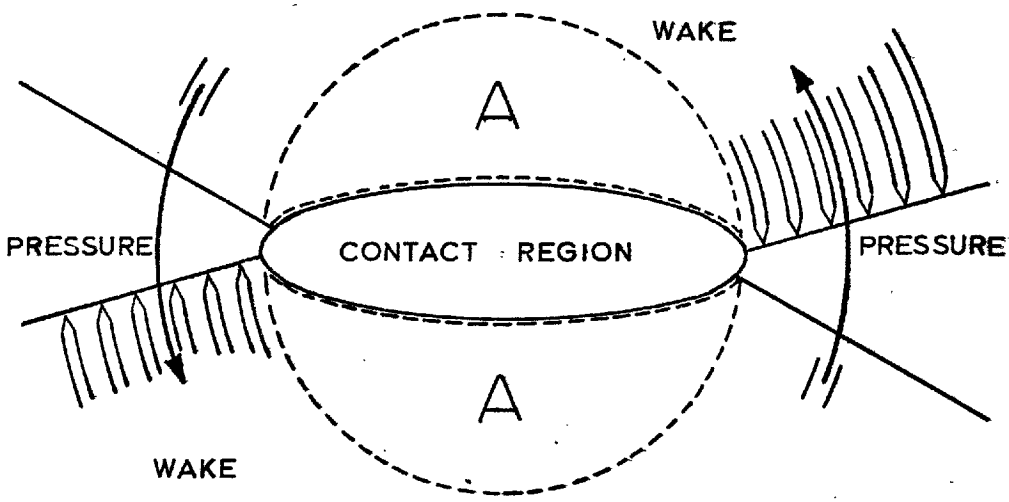


Figure 8.2 Diagram of a spinning contact.

film thickness in the contact region is zero or nearly zero then the fluid in the two regions marked 'A' will not be able to follow the main flow pattern and thus will probably form a low velocity eddy and tend not to cavitate. However, this region will gradually be starved of oil as it will be drawn into the cavitated part which must be slightly below atmospheric pressure. An oil film, if any, must therefore

depend solely on the two pressure nests descibed earlier, as any contribution to the load capacity from the pressure in regions 'A' is only transient.

Snidle and Archard (3) have produced an expression for the limiting film thickness for a ball spinning in a groove. They made the assumptions of rigid surfaces, exponentially pressure dependent viscosity and half-Sommerfeld boundary conditions. In the present nomenclature this expression may be written as:-

$$h_L = 0.5\,\Omega\,\eta_o\,\alpha\,R\left(\frac{A}{B}\right)^{\frac{1}{2}}\left[\frac{\left(\frac{A}{B}-1\right)}{\left(\frac{A}{B}+1\right)}\right] \qquad -8.1$$

where Ω is the angular velocity of spin.

The maximum non-dimensional load ($\hat{W}^*$) for which this expression applies is given by:-

$$\hat{W}^* = \frac{\Omega\,\eta_o}{E'}\;\frac{4\left(\frac{A}{B}\right)\left(\frac{A}{B}-1\right)}{\left(\frac{A}{B}+1\right)}\left\{\ln\left[\frac{\left(\frac{A}{B}+1\right)}{\Omega\,\eta_o\,\alpha\left(\frac{A}{B}\right)^{\frac{1}{2}}\left(\frac{A}{B}-1\right)}\right] - \frac{\frac{A}{B}}{\left(\frac{A}{B}-1\right)}\ln\left(\frac{A}{B}\right)\right\} \qquad -8.2$$

At <u>very</u> high values of Ω , the validity of equation 8.2 must be questioned because $\hat{W}^*$ is predicted to be negative. For the experimental conditions this occurs if Ω is greater than 3×10^6 r.p.m. which is well outside the speed range employed.

For the experimental geometry, equations 8.1 and 8.2 reduce to 8.3 and 8.4 respectively:-

$$h_L = 0.652\,\Omega\,\eta_o\,\alpha \qquad -8.3$$

$$\hat{W}^* = 33.5 \frac{\Omega \eta_o}{E} \left\{ \ln \left[\frac{0.382}{\Omega . \eta_o . \alpha} \right] - 2.57 \right\} \quad -8.4$$

If the pressure viscosity coefficient, α , is taken as being the value at atmospheric pressure, $\hat{W}^*$ and h_L may be calculated for the four cases presented in figure 8.1:-

a) $\hat{W}^* = 1.23 \times 10^{-9}$ $\quad h_L = 6.24 \times 10^{-9}$ ins.

b) $\hat{W}^* = 1.59 \times 10^{-7}$ $\quad h_L = 1.24 \times 10^{-6}$ ins.

c) $\hat{W}^* = 1.89 \times 10^{-8}$ $\quad h_L = 1.19 \times 10^{-7}$ ins.

d) $\hat{W}^* = 1.64 \times 10^{-7}$ $\quad h_L = 1.30 \times 10^{-6}$ ins.

It can be seen that in all cases the predicted values of h_L are less than the height of the first dark fringe, and that the theory is only applicable to case (d). In the other three cases, the experimental load exceeds the maximum permissible if the theory is to apply, although case (b) is close to the dividing line.

The theory of Allen et al (4) deals with higher loads than does that of Snidle and Archard (3) but the authors were primarily interested in friction rather than film thickness. They assumed a near Hertzian shape and considered the generation of hydrodynamic pressures in elemental strips. By neglecting side leakage they were able to apply the theory of Dowson and Higginson to each strip and hence obtain the film thickness at any point in the contact. The validity of these assumptions is discussed in detail in reference 3.

The interference fringes obtained experimentally are not detailed enough to reveal the film shape with any accuracy, thus precluding any quantitative comparisons with theory. However, they do indicate that a film does exist and that,

provided a more refined technique is employed such as that of Westlake (5), optical interferometry may be adapted readily to the study of spinning contacts.

8.2 Film thickness in a high modulus point contact

The sapphire disc used in the friction measurements reported in section 6.3.3 was coated with a semi-reflecting chromium layer, to enable film thicknesses to be measured. Figures 8.3 and 8.4 show the results of measurements obtained using this disc in conjunction with a tungsten carbide ball; the combination has a reduced modulus of 65.4×10^6 lbf/in^2 giving $G^* = 10{,}300$.

The graphs are for minimum and central film thickness respectively and both are plotted using the groups suggested by the analysis of section 5.2.4. Figure 8.4 also shows the theory of Wedeven, Evans and Cameron (2) for an average W^* equal to 2×10^{-7}. In terms of the groups used, their equation may be written as:-

$$\frac{H_o^*}{W^* G^*} = 1.055 \left(\frac{U^*}{W^{*3/2} G^{*1/2}} \right)^{5/7} \left(W^* G^{*3} \right)^{1/42} \quad -8.5$$

Both figures also show the theory of chapter 5 modified to treat a circular contact.

Gohar (6) has already presented film thickness plots for this material combination under rolling conditions. However, his results do not reach the high values of the group $U^*/(W^{*3/2} G^{*1/2})$ at which the transition from the EHL regime to the rigid-piezoviscous regime occurs. As can be seen from the graphs, this transition, both experimentally and theoretically is far less pronounced than for elliptical contacts (cf. figure 5.22 , page 130).

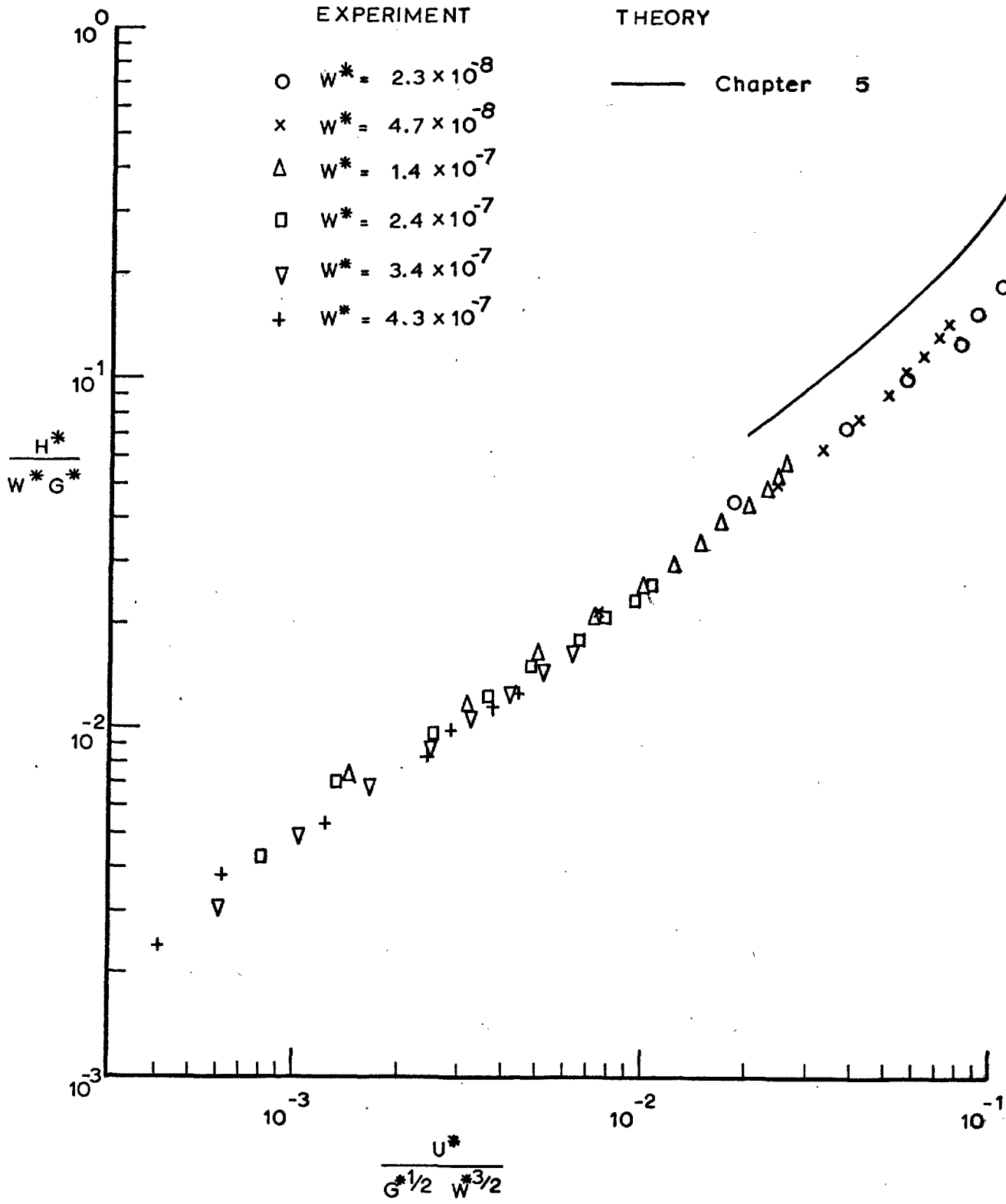


Fig. 8.3 Minimum film thickness group vs. speed group for high modulus circular point contact (sliding).

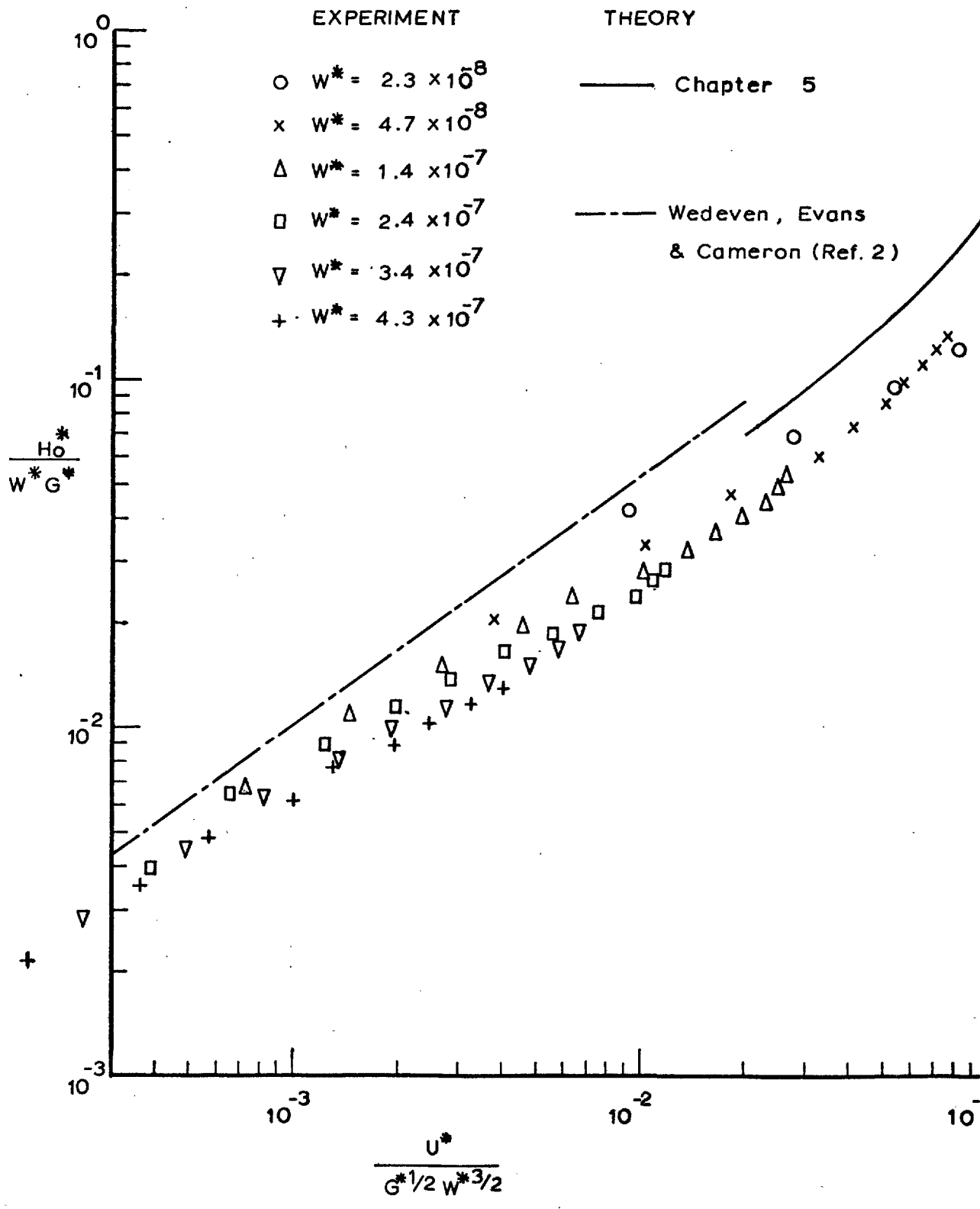
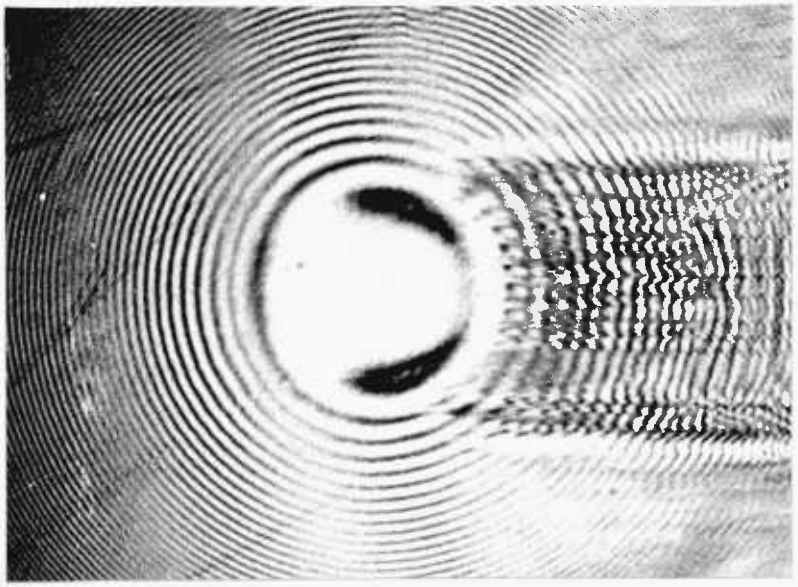


Fig. 8.4 Central film thickness group vs. speed group for high modulus circular point contact (sliding).

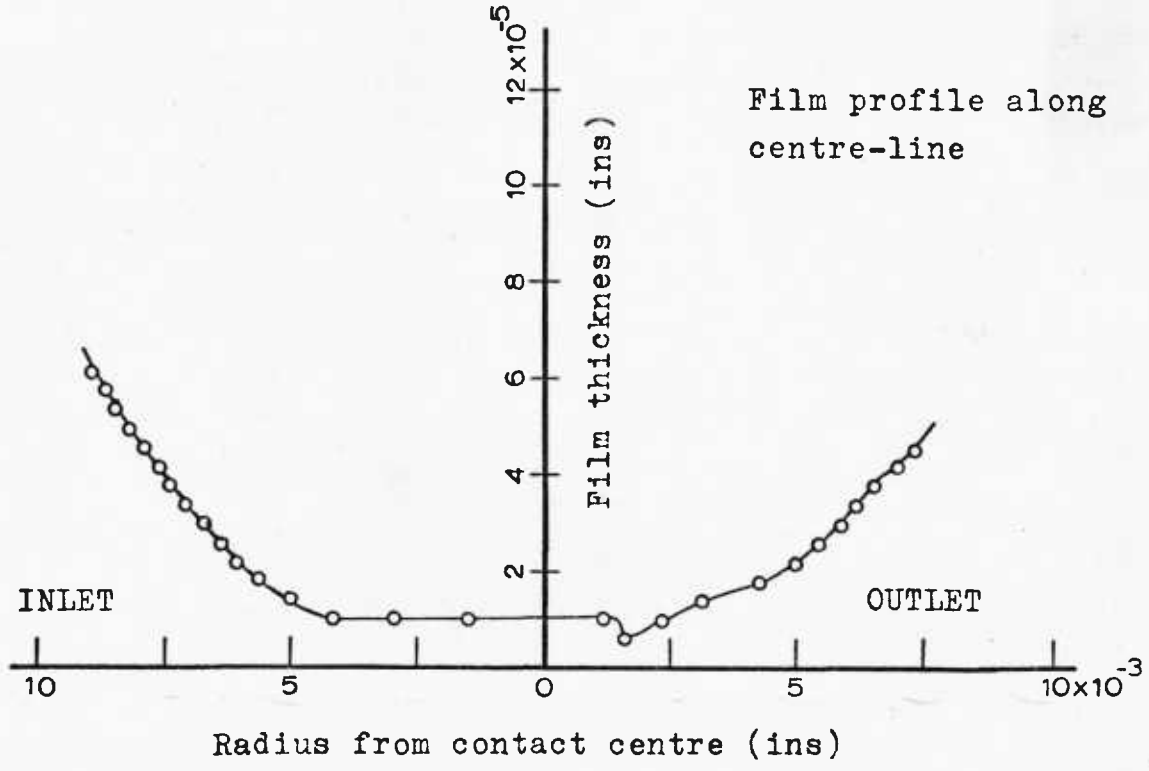
What is more interesting is that although the gradients of the experimental lines in the EHL regime are much as expected (0.72 for minimum film thickness and approximately 0.64 for central film thicknesses), the values of the group $H_o^*/(W^*G^*)$ fall below those predicted. The same is true in the rigid-piezoviscous regime. The explanation for this effect may well lie in the assumption of a Hertzian shape implicit in equation 8.5. The points plotted on figure 8.4 show scatter with load over most of the range, but there is a tendency for this scatter to reduce and also for theory and experiment to merge at low at low values of the speed group. Gohar(6) also found good agreement between theory and experiment at these lower values. It is suggested that all this indicates that the film thickness measured, which was that at the centre of the contact, is not in this instance, the most appropriate to compare with the theory.

At high load or low speeds, the sapphire/tungsten carbide contact exhibits typical side closures similar to those observed in glass/steel contacts and has a nominally flat central region (see figure 8.5). Under these conditions the central film thickness may reasonably be assumed to be comparible with the film thickness predicted by a Grubin-type solution.

Note that the lack of clarity on the fringe photograph, especially in the cavitation region, is a result of using the sodium light source rather than the xenon flash as in the work presented previously. The narrow bandwidth results in excellent fringe definition, but long exposures ($\simeq$ 1sec.) are required with resultant blurring of any moving object, such as the wake. The bright hazy bands running nearly vertically across the print are caused by variations in the structure of the sapphire and recur at regular intervals of approximately 3.7×10^{-3}inches.

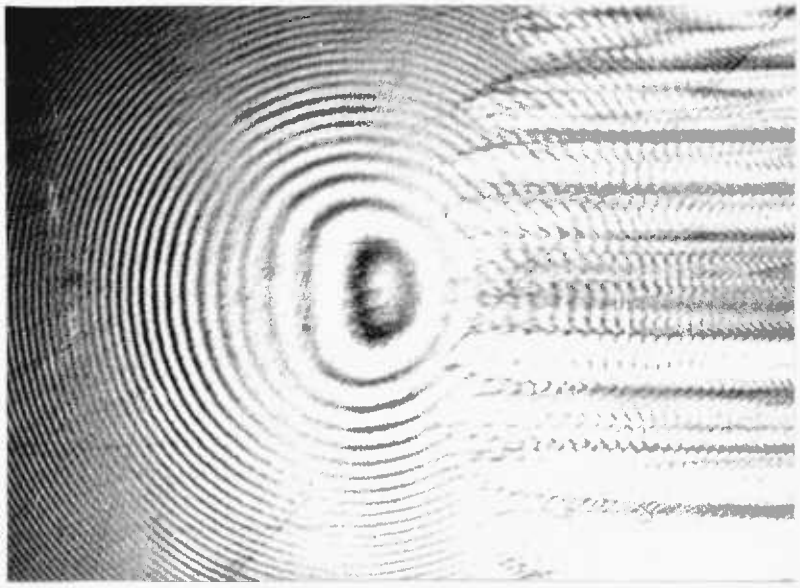


MAGNIFICATION X 130

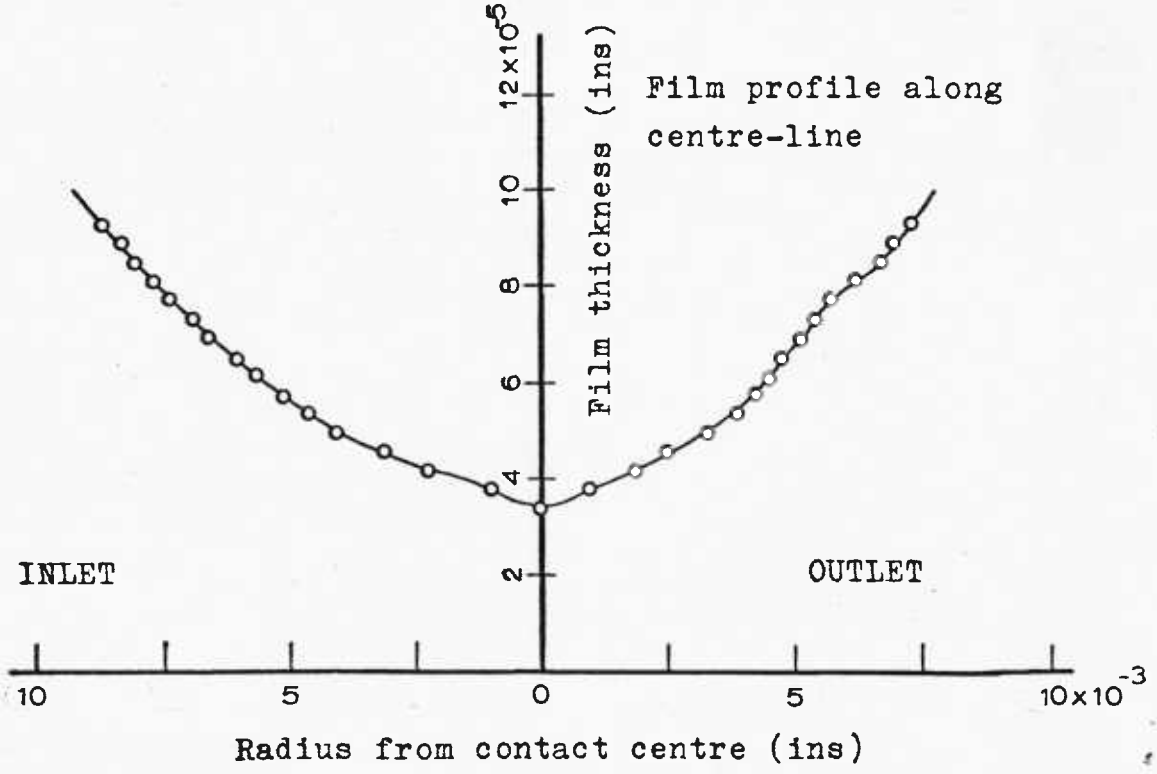


$$\frac{H_o^*}{W^* G^*} = 3.99\times10^{-3} \qquad \frac{U^*}{W^{*3/2} G^{*1/2}} = 3.82\times10^{-4} \qquad W^* = 4.31\times10^{-7}$$

Fig. 8.5 Film shape for a contact in the EHL regime.

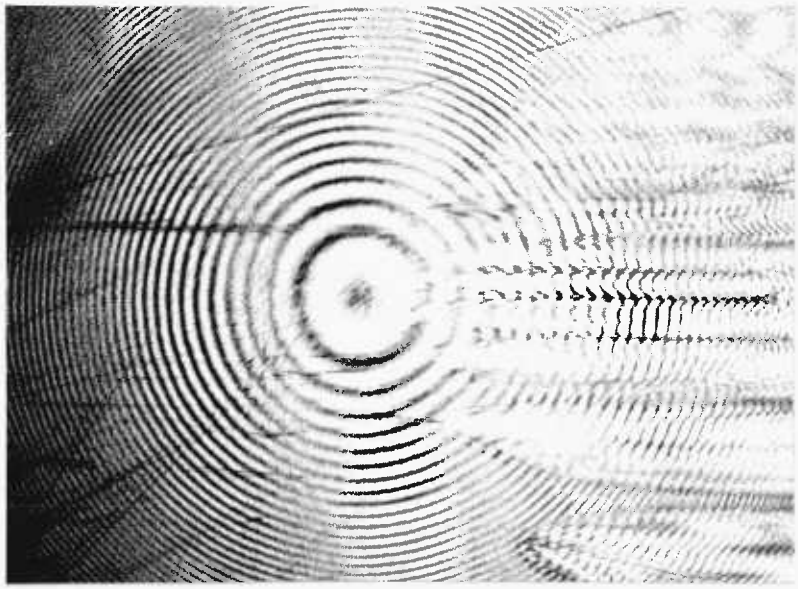


MAGNIFICATION X 130

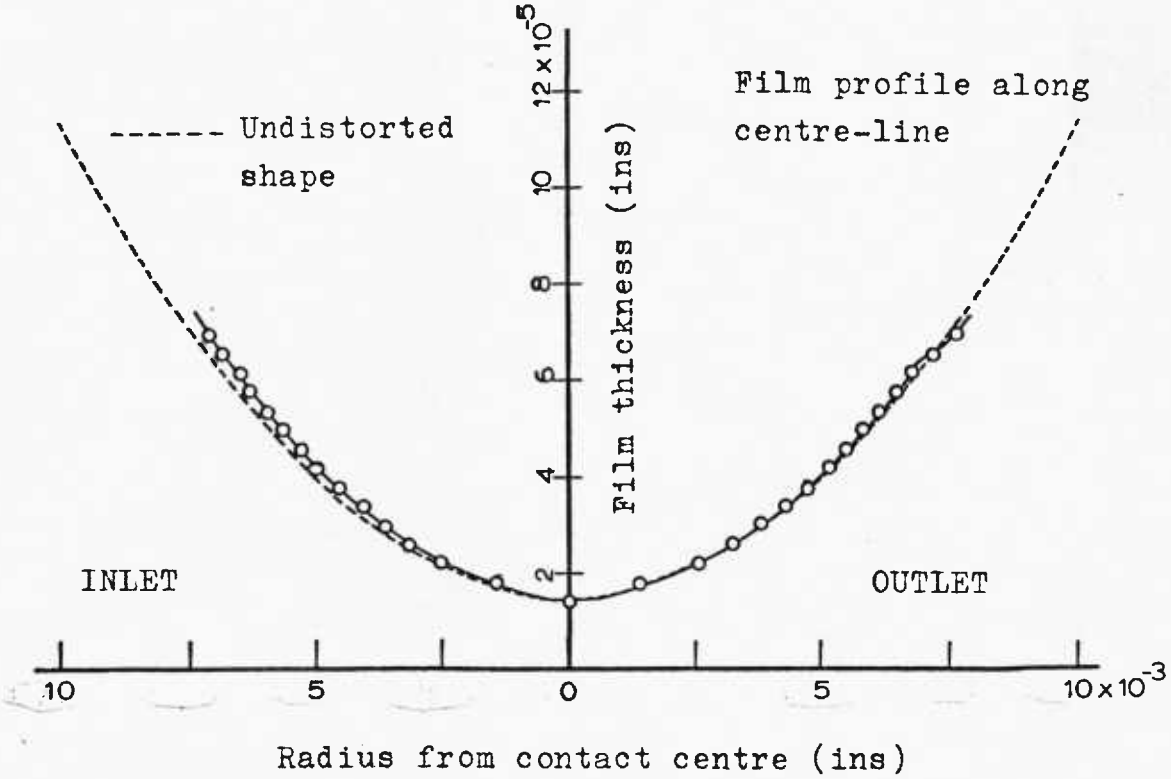


$$\frac{H^*}{W^* G^*} = 4.14\times10^{-2} \qquad \frac{U^*}{W^{*3/2} G^{*1/2}} = 1.96\times10^{-2} \qquad W^* = 1.9\times10^{-7}$$

Fig. 8.6 Film shape for a contact in the transition region.



MAGNIFICATION X 130



$$\frac{H^*}{W^* G^*} = 1.14\times10^{-1} \qquad \frac{U^*}{W^{*3/2} G^{*1/2}} = 6.16\times10^{-2} \qquad W^* \; 2.32\times10^{-8}$$

Fig. 8.7 Film shape for a contact in the rigid-piezoviscous region.

At higher speeds and lighter loads than those of figure 8.5, the hard materials tend to their undeformed shapes more readily than do soft materials. Figure 8.6 shows a typical fringe pattern for a contact in this transition region. It is clear that there are no side closures and that the central region is far from flat. In the inlet region, the fringes are not concentric circles but have become almost straight parallel lines. The film shape is therefore similar to that of an inclined pad slider bearing. For such conditions comparison with predictions based on a Grubin-type solution cannot be justified. However, it is equally difficult to justify the use of a theory based on an undistorted contact shape. A meaningful comparison in this intermediate regime is therefore not possible.

The differences between theory and experiment in the rigid-piezoviscous region are more difficult to explain. In figure 8.7 the interference fringes have become concentric circles and the profile of the contact indicates that distortion has disappeared almost completely. It is unlikely, therefore, that the errors are a result of the assumption of rigid surfaces. One possible explanation is that heating resulting from the high sliding speed has caused the viscosity to drop and may even have affected the pressure viscosity coefficient. As the theory does not take into account either of these effects, they may be the source of the discrepancies.

References for Chapter 8

1. Archard J.F. & Kirk M.T. 'Influence of elastic modulus on the lubrication of point contacts' I.Mech.E., Lubrication and Wear Convention 1963, Paper 15, pp 181 -189.
2. Wedeven L.D. Evans D. & Cameron A. 'Optical analysis of ball bearing starvation' Trans. ASME, 1971, Series F Jour. Lub. Tech., Vol. 93, No. 3, p 349.
3. Snidle R.W. & Archard J.F. 'Theory of hydrodynamic lubrication for a spinning sphere' Proc. I.Mech. E., 1969 - 70, Vol. 184, Pt. 1, pp 839 -848.
4. Allen C.W., Townsend D.P. & Zaretsky E.V. 'Elastohydrodynamic lubrication of a spinning ball in a non-conforming groove' Trans. ASME 1970, Series F, Jour. Lub. Tech., Vol. 92, pp 89 - 96.
5. Westlake F.J. & Cameron A. 'A study of ultra-thin lubricant films using an optical technique' Proc. I. Mech. E., 1967 -68, Vol. 182, Pt. 3G, pp 75 - 78.
6. Gohar R. 'Oil film thickness and rolling friction in elastohydrodynamic point contact' Trans. ASME 1971, Series F, Jour. Lub. Tech., Vol. 93, No. 3.

Chapter 9 CONCLUSIONS AND SUGGESTIONS FOR FUTURE WORK

9.1 Summary of main conclusions

Optical interferometry has been applied to the investigation of the elliptical contact existing between a ball and a grooved raceway; by angling the ball shaft, gyroscopic sliding has been simulated. Measurements of oil film thickness and shape have shown that the most favourable condition for a thick oil film occurs when angling is absent. The change from the EHL regime to the rigid piezo-viscous regime is evident from a change in gradient of the film thickness vs. speed graphs. A numerical solution to the relevant equations has been developed for this latter regime and gives good agreement with experiment. In the EHL regime, existing elliptical contact theories have been shown to be adequate for predicting film thicknesses under most conditions.

Friction was measured in circular point contacts under conditions of pure sliding. Conventional elastohydrodynamic theory has been adequate in predicting friction in low modulus contacts, providing oil property data is known. However, at the high pressures present in harder contacts, this theory is adequate only over part of the speed and load range. The improvements which resulted from prediction using more accurate temperature and pressure viscosity laws indicate that non-Newtonian behaviour does have some effect, but does not fully explain discrepancies between theory and experiment.

At high speeds, measured frictions were found to merge for all material combinations, indicating the transition from the EHL regime into the rigid surface regime. Advantage was taken of the low contact stresses existing in elliptical contacts

to obtain further experimental data under these conditions. The pressure distributions calculated for the rigid piezo-viscous regime were then used as a basis for friction predictions to compare with these data.

Solutions were found to be highly dependent on the choice of the limits for the region of integration. A limit representing a fixed physical boundary (decided experimentally) was shown to be the best criterion to give good agreement with the measurements from circular contacts. However, in elliptical contacts at all speeds, and in circular contacts at very high speeds, a floating physical boundary representing a fixed degree of starvation gave better agreement. It was concluded, therefore, that these contacts were starved and that, in the rigid surface regime, starvation could occur far more readily than in the EHL regime.

Investigations of the film formed by pure spinning showed that only very thin films are generated under light loads. However, the deformations resulting from increased load improve the film generating capacity and can cause a greater thickness in spite of the higher load.

9.2 A new thrust bearing rig.

9.2.1 General description

As a basis for future work, a new apparatus has been designed with which it is intended to overcome the limitations of the equipment used during the present work (discussed in chapter 2). At the time of writing, the new rig has been manufactured and is in the process of being commissioned. A half-section assembly drawing is shown in figure 9.1.

The apparatus is composed of two raceways separated by a

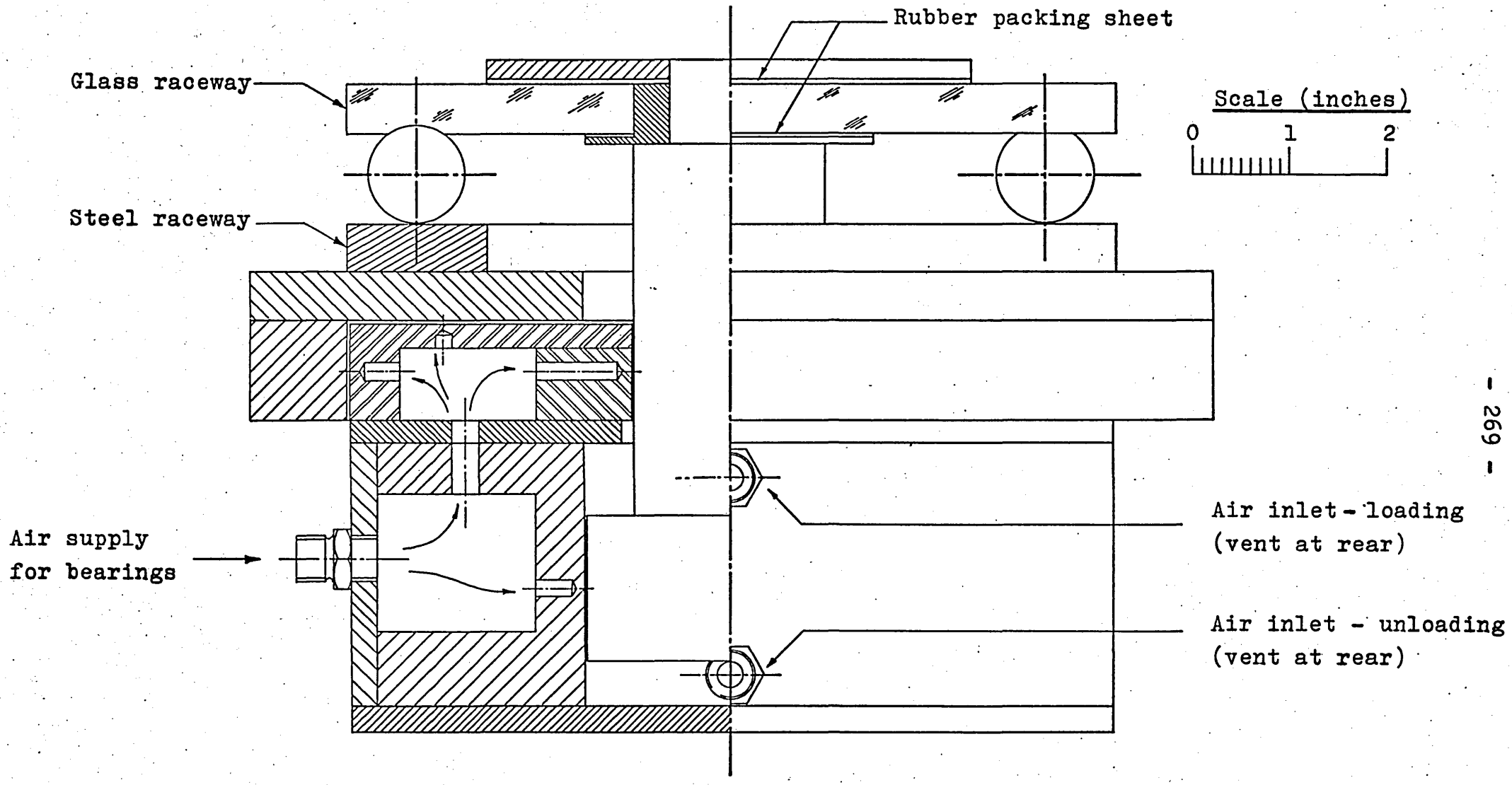


Fig. 9.1 Half-section assembly view of new thrust bearing rig. (Nuts, bolts, etc., omitted for clarity)

minimum of three balls. The lower race is supported on a large aerostatic thrust bearing capable of carrying over 600 lb load. The steel ring around the outside of the thrust plate acts as a flywheel to help maintain constant speed and also serves to locate the plate radially by acting as the rotor of an aerostatic journal bearing. The lower raceway proper is clamped to the thrust plate. Initially it is to be of flat ground steel, but it is anticipated that it may later be replaced by a commercial thrust bearing race. The glass disc is supported by balls running on the lower race and is located radially by the shaft upon which it is mounted. The apparatus has been designed to use 1in. diameter balls, but it is capable of using any in the range 0.75in. to 1.25in. They are located by means of a cage (not shown) which can be fixed in space to cause the races to counter-rotate. When running in this mode, drive is supplied by a shaft mounted ball. However, should it be necessary to drive the races directly, rubber friction wheels may be employed, the various support bearings being designed to carry the resulting radial loads.

Load is applied pneumatically to the contacts via the shaft on which the upper race is mounted. This shaft is stepped and doubles as a loading piston. Provision has been made for upward 'loading' as well as downward. By this means the self-weight of the race and its mounting can be counteracted and lightly loaded contacts investigated. The shaft runs in two separate single row aerostatic journal bearings. These two bearings, the thrust bearing and the lower race locating bearing, were all designed using the procedure outlined in reference 1. The results of the design calculations are summarised in appendix 7.

9.2.2 Ball torque dynamometer

A separate dynamometer subassembly has been designed and manufactured to enable ball torque to be measured. Measurements may be made at different slide/roll ratios by applying braking to the ball shaft by means of an eddy current device. This consists of an aluminium disc rotating between the poles of two electromagnets as shown in the assembly drawing of figure 9.2.

A brake of this type was selected, in preference to a more simple band brake, because it is stable over the whole of the torque speed curve. A band brake gives a constant braking torque irrespective of speed and thus is only stable if torque rises with slip speed. Under other conditions stalling will result. An eddy current brake, however, gives a braking torque proportional to speed and is stable under all circumstances. A clear discussion of these phenomena is given in reference 2 and so will not be repeated here.

The subassembly consists of two shafts running in identical air bearings. That on the right-hand side of the drawing carries the ball shaft at one end and the brake disc at the other. Its axial position is maintained to well within 0.002 in. each way by a semi-annular double thrust air bearing. The design data for all bearings are again summarised in appendix 7. The other shaft carries the electromagnets on one side of the bearing pillar and a flywheel which serves as a counterbalance on the other side. Reaction torque is provided by a torsion spring and its deflection is measured optically by a light beam and mirror, an arrangement which has the advantage of simplicity and low cost.

The electromagnets are supplied from a variable d.c.

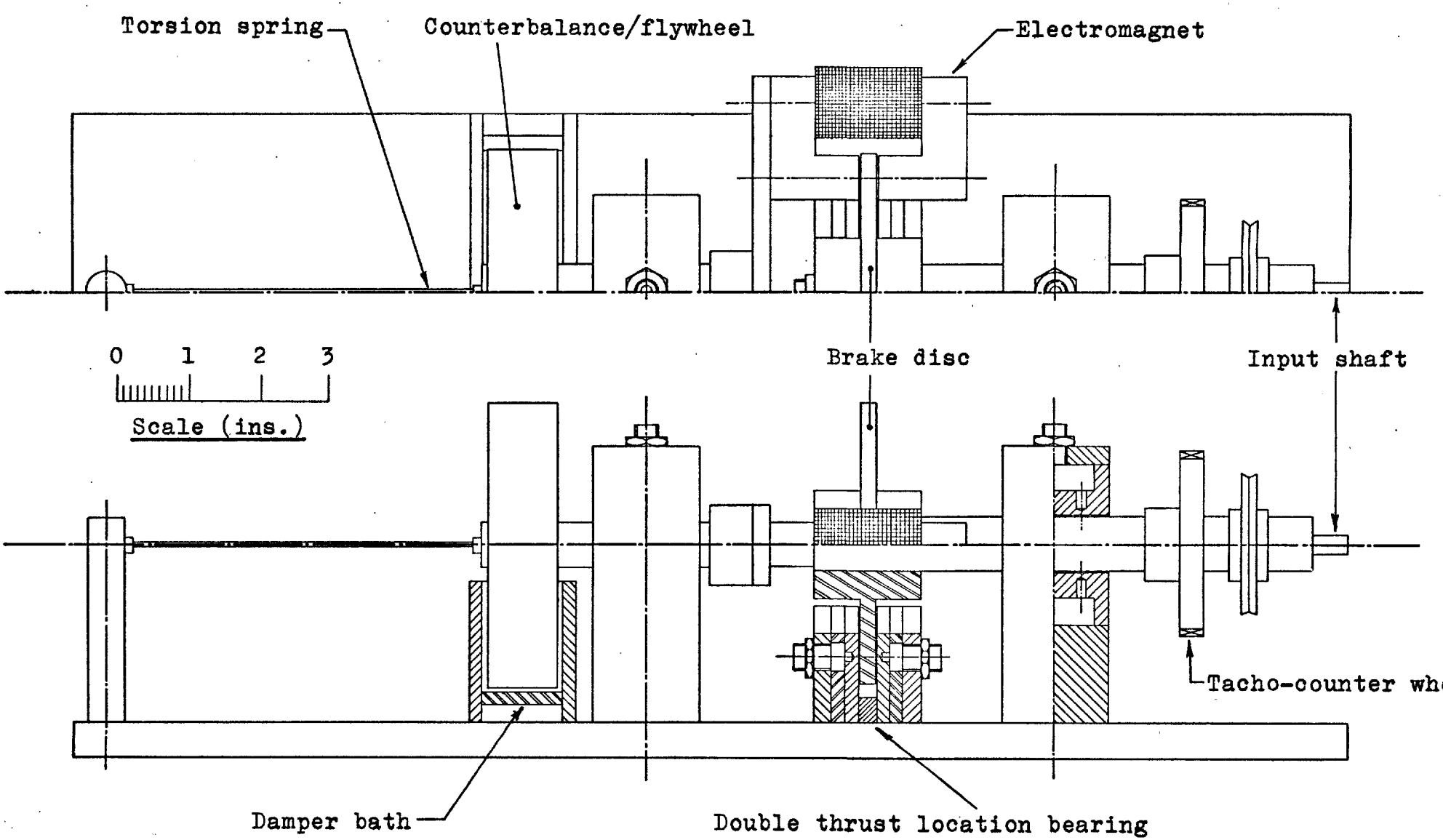


Fig. 9.2 Ball torque dynamometer assembly - Half plan and sectional elevation (1st angle)

supply and braking torque may be adjusted by varying the current flowing in the coils. The dynamometer has been designed to give a maximim braking torque of $4.7\,\omega$ gmf. cm. where ω is the speed of the input shaft in radians/sec. The design calculations are given in appendix 8.

9.3 Suggestions for future work

a) Using the apparatus described above,the range of loads and speeds can be extended beyond those covered in the present work.

b) By changing the size of the balls, the effect of varying conformity on film thickness and friction could be determined.

c) An investigation of the effect of various cage designs on the contact oil film thickness and ball friction would provide useful knowledge on a neglected topic. Various cage concepts could be employed, includung machined brass, pressed steel and rolling element cages. Criteria for a good design would be low friction and good lubricant supply to the ball/race contact.

d) By fitting a window to a cage, or by making a completely transparent cage segment, the cage/ball contact may be examined. The sliding work presented in this thesis is directly applicable to such a situation. The direction of the resultant velocity vector can be determined from the wake pattern and hence the ball dynamics derived.

e) If a dynamometer is attached to the upper race, the effect of spin torque can be determined. The space diagram of figure 9.3 shows the forces acting on the ball. At each ball/race contact there is a spin torque, T, and a force F. If the ball is shaft mounted and the races counter-rotated, the ball torque dynamometer will measure $R(F_1 + F_2)$, where R is the ball radius

The dynamometer on the top plate will measure $(F_2R_t + T_2)$ where R_t is the track radius and T_2 the spin torque at the top plate/ball contact.

If the upper race contact is elliptical and the lower race contact circular, then the spin torque at the lower contact (T_1) will be very small compared with the upper contact spin torque (T_2). Thus, neglecting T_1, F_1 may be found using a ball and plate machine such as that of Gentle (3). F_2 and hence T_2 may then be obtained. It is anticipated that the value of T_2 will be very small except at high conformities.

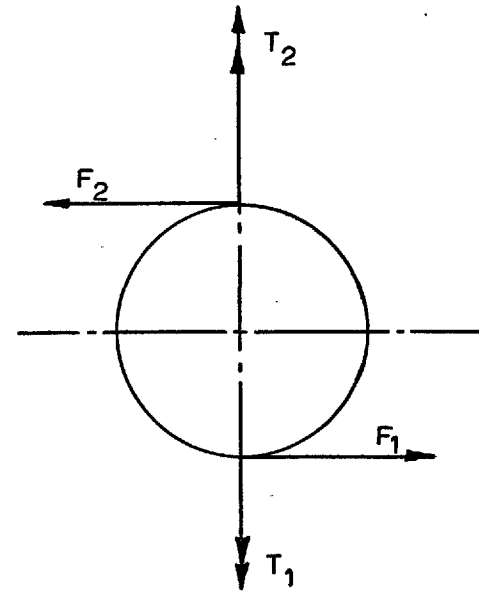


Fig. 9.3 Side elevation of ball showing forces acting.

f) Theoretically, the work presented in this thesis could be extended to include non-Newtonian effects. The theoretical model must first be examined to determine whether or not such extra complications are justified.

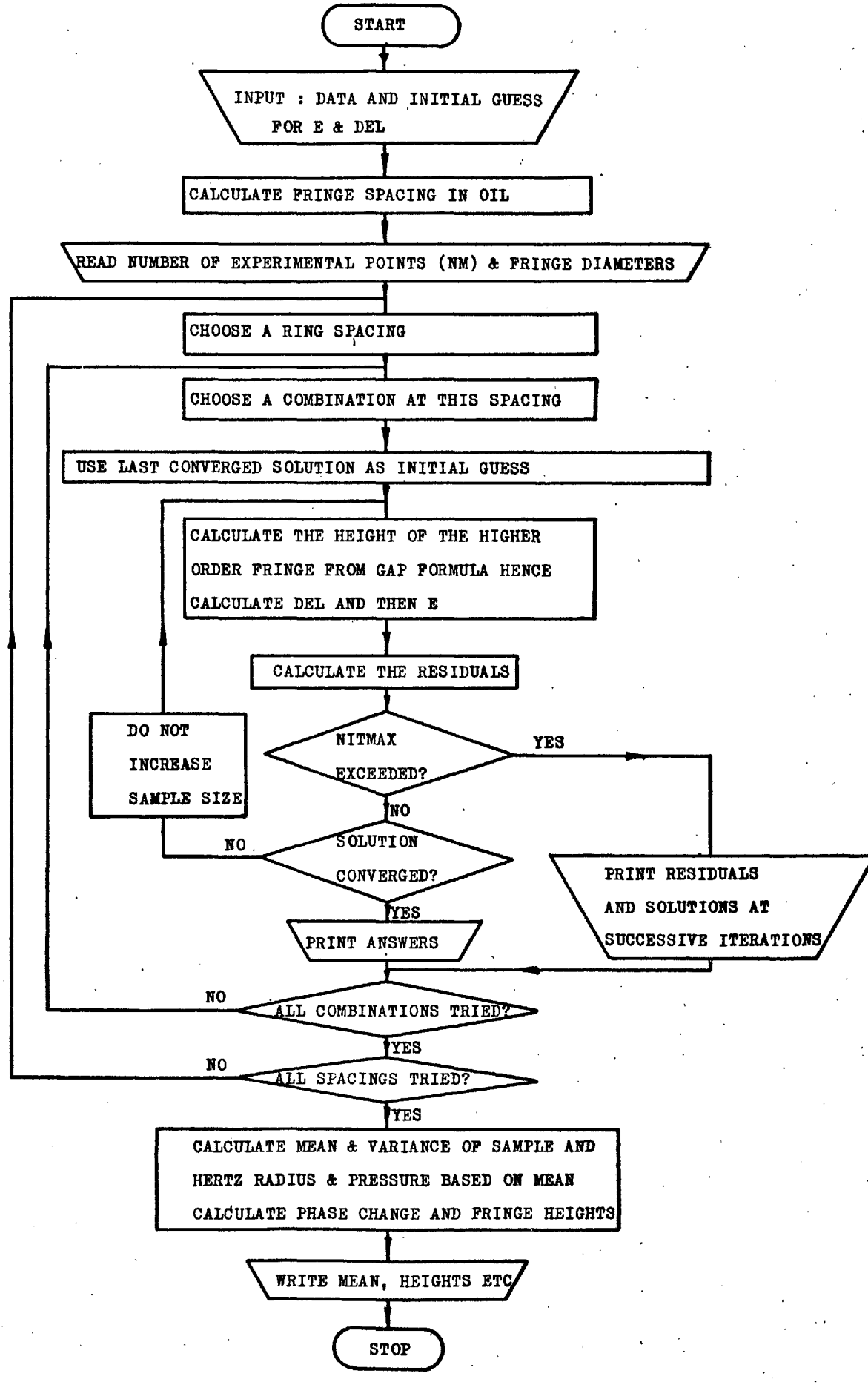
g) Finally, it is suggested that there is a need to investigate rolling/sliding/spinning contacts, since angular contact bearings have components of all these motions. Spin has very little direct effect on film thickness, but when combined with rolling or sliding its effect is not known. A completely new apparatus would be required for these investigations.

References for Chapter 9.

1. Mechanical Technology Inc., 'M.T.I. gas bearing design manual' Gas bearing design course (1969), University of Southampton.
2. Jefferis M.A. & Johnson K.L. 'Sliding friction between lubricated rollers' Proc. I.Mech. E. 1967 -68, Vol. 182 Pt.1, No.14.
3. Gentle C.R. 'Traction in elastohydrodynamic point contacts' Ph.D. Thesis, 1971, University of London.

APPENDICES

Appendix 1. A PROGRAM TO CALCULATE REDUCED MODULUS & PHASE CHANGE



```
C     ****************************************************************
C     PROGRAM E-CAL TO DETERMINE REDUCED MODULUS AND CALIBRATION
C     ****************************************************************
      DIMENSION AE(500),ADEL(500)
      COMMON/CONE/D(50),R(50),A
      DATA  CC/0.00001/
      DATA  NITMAX/400/
      DATA  E/20.0E6/
      DATA  WAVLEN/5893.0/
      DATA  REFIND/1.506/
      DATA  W/1.8/
      DATA  DIA/1.0/
      W=1.8*2.205
C     LOAD IS NOW IN POUNDS
      INC=0
C     DELH IS THE DISTANCE BETWEEN ADJACENT BLACK FRINGES IN INCHES
      DELH=(WAVLEN/REFIND)*1.0E-8/(2.0*2.54)
      WRITE(6,102)DELH
      SAV2=E
      SAVV2=DELH
C     NM IS THE NUMBER OF RINGS MEASURED  NM TO BE LESS THAN 50
      READ(5,100)NM
      NLL=NM-3
      DO10 N=1,NM
C     THE RING DIAMETER IS IN MILLIMETRES
      READ(5,101)D(N)
      R(N)=D(N)/(2.0*25.4)
      WRITE(6,200)R(N),D(N)
   10 CONTINUE
      WRITE(6,104)
      DO40 M=1,NLL
      WRITE(6,106)
      ISPACE=NM-M
      DO40 N=1,M
      NN=N+ISPACE
      E=SAV2
      DEL=SAVV2
      KOUNT=0
      HH=DEL+DELH*FLOAT(ISPACE+N-1)
   20 CONTINUE
      KOUNT=KOUNT+1
      A=0.721*(W*DIA*2.0/E)**(1.0/3.0)
      IF(A.GT.R(1))A=2.0*R(1)-R(2)
      PMAX=(1.5*W)/(A**2*3.14159265)
      SAVV=HH
      HH=ABS((A*PMAX/E)*G(NN))
      H=HH-DELH*FLOAT(ISPACE)
      SAV=E
      DEL=H-DELH*FLOAT(N-1)
      E=ABS((A*PMAX/H)*G(N))
      E=SAV+0.25*(E-SAV)
      RES1=(SAVV-HH)/HH
      RES2=(SAV-E)/E
      RES=RES1
      IF(ABS(RES2).GT.ABS(RES1))RES=RES2
      IF(ABS(RES).LT.CC)GOTO30
      IF(KOUNT.GT.(NITMAX-1 ))WRITE(6,111)E,DEL,A,PMAX,KOUNT,N,NN,RES1,
     1RES2
      IF(KOUNT.GT.NITMAX)WRITE(6,105)
      IF(KOUNT.GT.NITMAX)GOTO40
      GOTO20
   30 CONTINUE
      IF(DEL.LT.0.0)GOTO35
      SAV2=E
      SAVV2=DEL
      INC=INC+1
      AE(INC)=E
      ADEL(INC)=DEL
      IF(INC.EQ.500)GOTO60
   35 WRITE(6,103)E,DEL,A,PMAX,KOUNT,N,NN
   40 CONTINUE
      GOTO 60
   50 CONTINUE
   60 CONTINUE
      WRITE(6,110)INC
C     CALCULATE THE MEAN AND VARIANCE OF THE SAMPLE
      SUM=0.0
      SUMM=0.0
      SSUM=0.0
      SSUMM=0.0
      DO70 I=1,INC
      SUM=SUM+AE(I)
      SUMM=SUMM+ADEL(I)
   70 CONTINUE
```

```
      EMEAN=SUM/FLOAT(INC)
      DELMEN=SUMM/FLOAT(INC)
      DO80 I=1,INC
      SSUM=SSUM+(AE(I)-EMEAN)**2
      SSUMM=SSUMM+(ADEL(I)-DELMEN)**2
   80 CONTINUE
      ESIG=SQRT(SSUM/FLOAT(INC-1))
      DELSIG=SQRT(SSUMM/FLOAT(INC-1))
      WRITE(6,107)EMEAN,ESIG
      WRITE(6,108)DELMEN,DELSIG
C     CALCULATE HERTZ RADIUS AND PEAK STRESS BASED ON MEAN VALUES
      A=0.721*(W*DIA*2.0/EMEAN)**(1.0/3.0)
      PMAX=(1.5*W)/(A**2*3.14159265)
      WRITE(6,109)A,PMAX
C     CALCULATE PHASE CHANGES AND FRINGE HEIGHTS
      PHICO=-4.0*DELMEN*REFIND*2.54E8/WAVLEN
      FRACT=DELMEN/(2.0*DELH)
      WRITE(6,112)PHICO,FRACT
      DO99 M=1,2
      IF(M.EQ.1)GOTO 90
      WRITE(6,116)
      DELH=(5893.0/REFIND)*1.0E-8/(2.0*2.54)
      DEL=FRACT*2.0*DELH
      GOTO 95
   90 WRITE(6,117)
      DELH=(5461.0/REFIND)*1.0E-8/(2.0*2.54)
      DEL=FRACT*2.0*DELH
   95 CONTINUE
      WRITE(6,113)
      DO99 N=1,15
      FHB=DEL+FLOAT(N-1)*DELH
      FHW=FHB+DELH/2.0
      WRITE(6,114)N,FHB
      WRITE(6,115)N,FHW
   99 CONTINUE
  100 FORMAT(I2)
  101 FORMAT(F6.4)
  102 FORMAT(1H1,5X,42HDISTANCE BETWEEN ADJACENT BLACK FRINGES - ,
     1 1PE12.4,5H  INS.//)
  103 FORMAT(4(1PE16.4),3(I10))
  104 FORMAT(//,8X,6HYOUNGS,9X,9HHEIGHT OF,9X,5HHERTZ,8X,10HPEAK HERTZ,
     1 4X,9HNUMBER OF,2X,18HFRINGE ORDERS USED,/,8X,7HMODULUS,7X,
     2 11HFIRST BLACK,7X,6HRADIUS,9X,8HPRESSURE,4X,10HITERATIONS,3X,
     3 15HIN CALCULATIONS,//,6X,10HLBF/SQ.IN.,10X,3HINS,13X,3HINS,9X,
     4 10HLBF/SQ.IN.,//)
  105 FORMAT(//5X,47HNUMBER OF ITERATIONS EXCEEDED MAXIMUM PERMITTED)
  106 FORMAT(5X,/)
  107 FORMAT(//5X,58HMEAN AND VARIANCE OF MODULUS DISTRIBUTION ARE RESPE
     1CTIVELY,2(1PE16.4))
  108 FORMAT(//5X,57HMEAN AND VARIANCE OF HEIGHT DISTRIBUTION ARE RESPEC
     1TIVELY,2(1PE16.4))
  109 FORMAT(//5X,59HHERTZ RADIUS AND PEAK STRESS BASED ON MEAN ARE RESP
     1ECTIVELY,2(1PE16.4))
  110 FORMAT(//5X,18HSIZE OF SAMPLE IS ,I10)
  111 FORMAT(4(1PE16.4),3(I10),2(1PE16.4))
  112 FORMAT(//5X,45HPHASE CHANGE AT THE SEMI-REFLECTING LAYER IS ,
     1 1PE16.4,5H X PI,5X,18HHEIGHT IS LAMDA X ,1PE16.4)
  113 FORMAT(//5X,13HFRINGE  ORDER,10X,20HFRINGE  HEIGHT (INS),//)
  114 FORMAT(7X,I2,2X,5HBLACK,17X,1PE16.4)
  115 FORMAT(7X,I2,2X,5HWHITE,17X,1PE16.4)
  116 FORMAT(//,5X,65HHEIGHTS FOR SODIUM LIGHT (5893A) IN OIL OF REFRACT
     1IVE INDEX 1.506)
  117 FORMAT(//,5X,66HHEIGHTS FOR MERCURY LIGHT (5461A) IN OIL OF REFRAC
     1TIVE INDEX 1.506)
  200 FORMAT(2(1PE16.4))
      STOP
      END
```

```
      FUNCTION G(N)
      COMMON/CONE/D(50),R(50),A
      TANGENT=(SQRT(R(N)**2-A**2))/A
      G=-(2.0-(R(N)/A)**2)*ATAN(TANGENT)
     1  +SQRT((R(N)/A)**2-1.0)
      RETURN
      END
```

Appendix 2. COMPUTER PREDICTION OF PRESSURE IN A PIEZO - VISCOUS ELLIPTICAL CONTACT

After early, unsatisfactory, attempts to solve the problem using rectangular grids with various transforms to allow treatment of the ellipse, a circular grid was decided upon. The equations solved were the polar Reynold's equation (5.3) and the film shape equation (5.4) as developed in section 5.2.1. Both these equations included a transform to permit calculations to be performed over a circular rather than elliptical grid.

Equation 5.3 may be rewritten more briefly as:-

$$D_4 \frac{\partial p}{\partial r} + D_5 \frac{\partial p}{\partial \phi} + D_6 \frac{\partial^2 p}{\partial r^2} + D_7 \frac{\partial^2 p}{\partial r \partial \phi} + D_8 \frac{\partial^2 p}{\partial \phi^2} = \text{R.H.S.}$$

where D_4 to D_8 are coefficients involving the film gradients $\partial h/\partial r$, $\partial h/\partial \phi$, the film thickness h, h^2 etc., and the geometric groups D_1 to D_3, where

$$D_1 = \cos^2\phi + \left(\frac{a^2}{b^2}\right) \sin^2 \phi$$

$$D_2 = \sin^2\phi + \left(\frac{a^2}{b^2}\right) \cos^2 \phi$$

$$D_3 = \sin \phi \cos \phi \left[1 - \frac{a^2}{b^2} \right]$$

The pressure gradient terms were expressed in finite difference form using central differences. These are standard results and will not be reproduced here. They may be found in most text books on numerical programming, for instance Smith[1]. The equation was then rearranged to express the pressure at a

1. Smith G.D. 'Numerical solution of partial differential equations' Oxford University Press, London 1965.

node in terms of the pressures at the surrounding nodes.

The resulting matrix was then inverted, two different procedures being tried. Initially a direct iterative procedure was employed solving point by point. This is a commonly used technique and was known to be applicable to this situation. As mentioned in section 5.2.3 it gives rise to a singularity at the grid centre because $\bar{r}$ is zero. The iterative boundary condition thus required at this point was obtained by interpolation:

The Taylor series of the function f(x) with centre at a is

$$f(x) = f(a) + f'(a)(x - a) + f''(a)\frac{(x - a)^2}{2!} \ldots\ldots$$

$$\ldots + f^n(a)\frac{(x - a)^n}{n!} \ldots\ldots$$

This formula can be extended to finite differences instead of derivatives. Considering directly the problem of the singularity at $r(1) = 0$, we can expand the function (f) about this point. In finite difference form

$$f'(2) = \frac{f(3) - f(1)}{R_{(3)} - R_{(1)}}$$

$$f''(2) = \frac{\dfrac{f(3) - f(2)}{R_{(3)} - R_{(2)}} - \dfrac{f(2) - f(1)}{R_{(2)} - R_{(1)}}}{\left[R_{(3)} - R_{(1)}\right]/2}$$

If we take the first three terms of the series and expand the function about point 2 (i.e. a = 2) and extrapolate to point 0 (i.e. x = 0) we get

$$f(0) = f(2) + f'(2)(-R_{(2)}) + \frac{f''(2)(-R_{(2)})^2}{2}$$

This has a similar form to the Gregory-Newton interpolation formula[2].

To apply interpolation in practice, the procedure was to calculate the function in the grid centre, f(0), by extrapolation along each radius in turn. A mean of all the f(0)'s so obtained was then taken as the value at the centre node.

An iterative solution, however, has the disadvantage of being relatively inefficient. In an attempt to improve efficiency a line by line solution was tried in the form of a tri-diagonal algorithm (TDMA):

The equations for a single radius may be written very generally as

$$
\begin{aligned}
p_1 - A_1 p_2 &= C_1 \\
-B_2 p_1 + p_2 - A_2 p_3 &= C_2 \\
&\cdots\cdots\cdots\cdots \\
-B_i p_{i-1} + p_i - A_i p_{i+1} &= C_i \\
&\cdots\cdots\cdots\cdots \\
-B_{m-1} p_{m-2} + p_{m-1} - A_{m-1} p_m &= C_{m-1} \\
-B_m p_{m-1} + p_m &= C_m
\end{aligned}
\qquad \text{-A2.1}
$$

where the A's, B's and C's are known.

The first equation may be used to eliminate p_1 from the second, the new second equation used to eliminate p_2 from the third and so on , until finally the new last but two equation can be used to eliminate p_{m-2} from the last but one equation, giving one equation with only one unknown p_{m-1}. (p_m is a known boundary condition).

2. Lanczos 'Applied analysis' Pitman, 1957.

Thus part-way through we reach the stage where we have as our equations:-

$$p_{i-1} - A'_{i-1}p_i = C'_{i-1}$$

that is

$$p_{i-1} = A'_{i-1}p_i + C'_{i-1} \qquad \text{-A2.2}$$

and the next in order as

$$p_i = A_i p_{i+1} + B_i p_{i-1} + C_i \qquad \text{-A2.3}$$

Substituting A2.2 in A2.3 gives, after re-arrangement,

$$p_i = \frac{A_i p_{i+1} + B_i C'_{i-1} + C_i}{1 - B_i A'_{i-1}} \qquad \text{-A2.4}$$

Equation A2.2 is general and so can be expressed as

$$p_i = A'_i p_{i+1} + C'_i \qquad \text{-A2.5}$$

Comparing A2.4 and A2.5, we deduce that

$$A'_i = \frac{A_i}{1 - B_i A'_{i-1}} \quad \text{and} \quad C'_i = \frac{B_i C'_{i-1} + C_i}{1 - B_i A'_{i-1}} \qquad \text{-A2.6}$$

Special treatment is required at the first point since there

$$p_1 = A_1 p_2 + C_1 \qquad \text{-A2.7}$$

From A2.7 we deduce that

$$A'_1 = A_1 \qquad C'_1 = C_1 \qquad \text{-A2.8}$$

Also, at the last point we have, from A2.2

$$p_{m-1} = A'_{m-1}p_m + C'_{m-1} \qquad \text{-A2.9}$$

but at this point we also have

$$p_m = B_m p_{m-1} + C_m \qquad \text{-A2.10}$$

Substituting equation A2.9 in A2.10 and re-arranging:-

$$p_m = \frac{B_m C'_{m-1} + C_m}{1 - B_m A'_{m-1}}$$

that is

$$A'_m = 0 \qquad \text{-A2.11}$$

The procedure followed can thus be summarised. For each radial line, first all A'_i and C'_i were calculated from equations A2.6, A2.8 and A2.11, then all the p_i's from equation A2.5. The equations to be solved are of the form:

$$p_p = C_E p_E + C_W p_W + C_N p_N + C_S p_S + D$$

In order to apply the TDMA, we simply take either the E,W or the N,S terms to be known and solve for the others.

In practice the TDMA was disappointing. Iteration time was indeed saved by up to 40% (see figure A2.1). However, the calculations were more involved and consequently the overall saving in the real criterion, computer time, was almost nil. There were also doubts as to the effect of the 'marching' cavitation boundary on the validity of the solutions. No evidence was found in the present work to support these doubts, but to avoid them most computations employed the direct iterative solution to the equations. Every attempt was

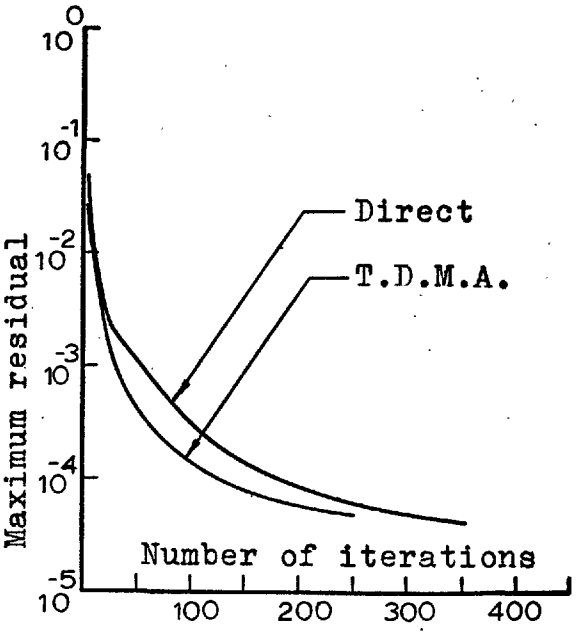


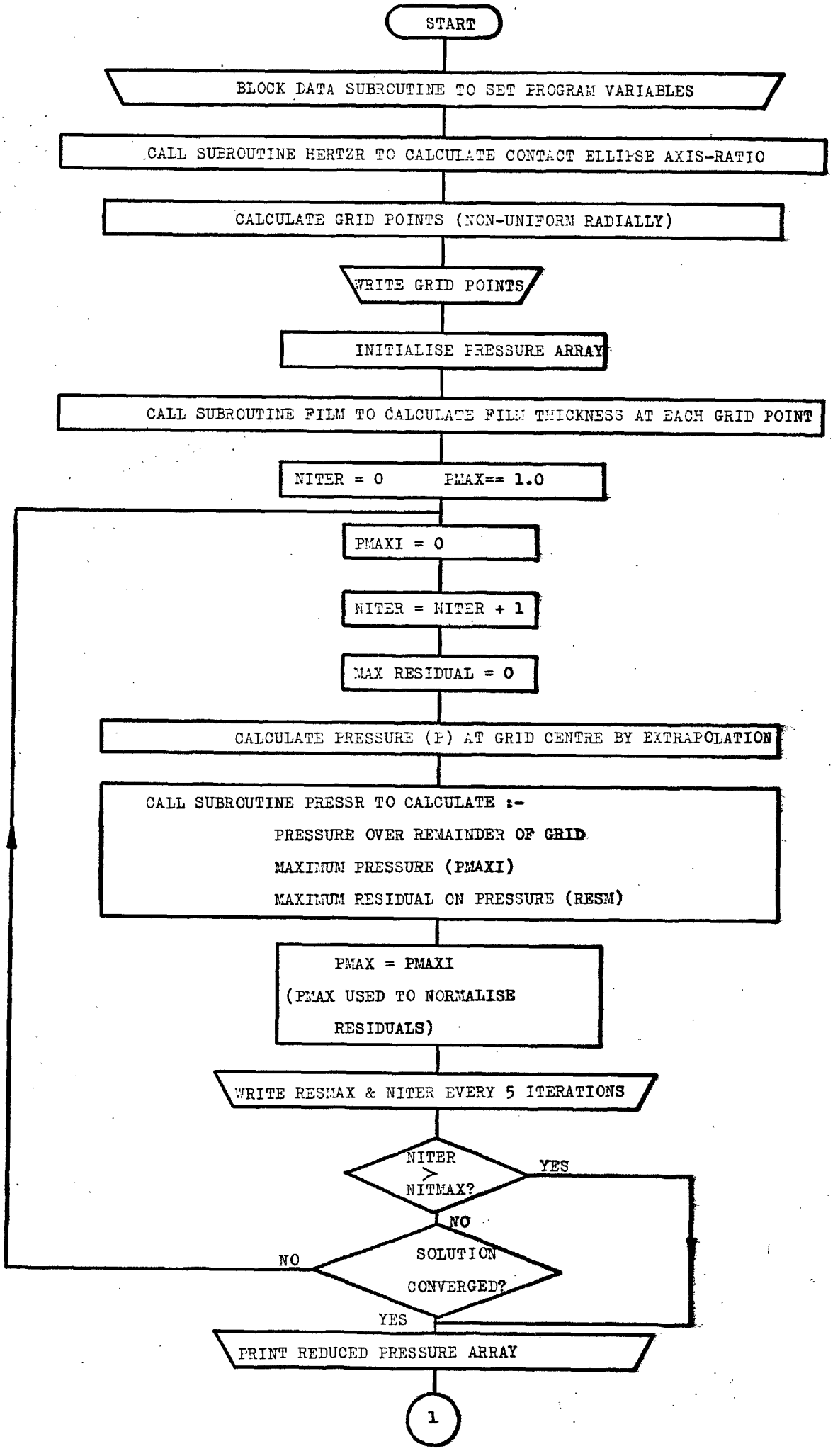
Fig. A.2.1 Comparison of the two solution procedures.

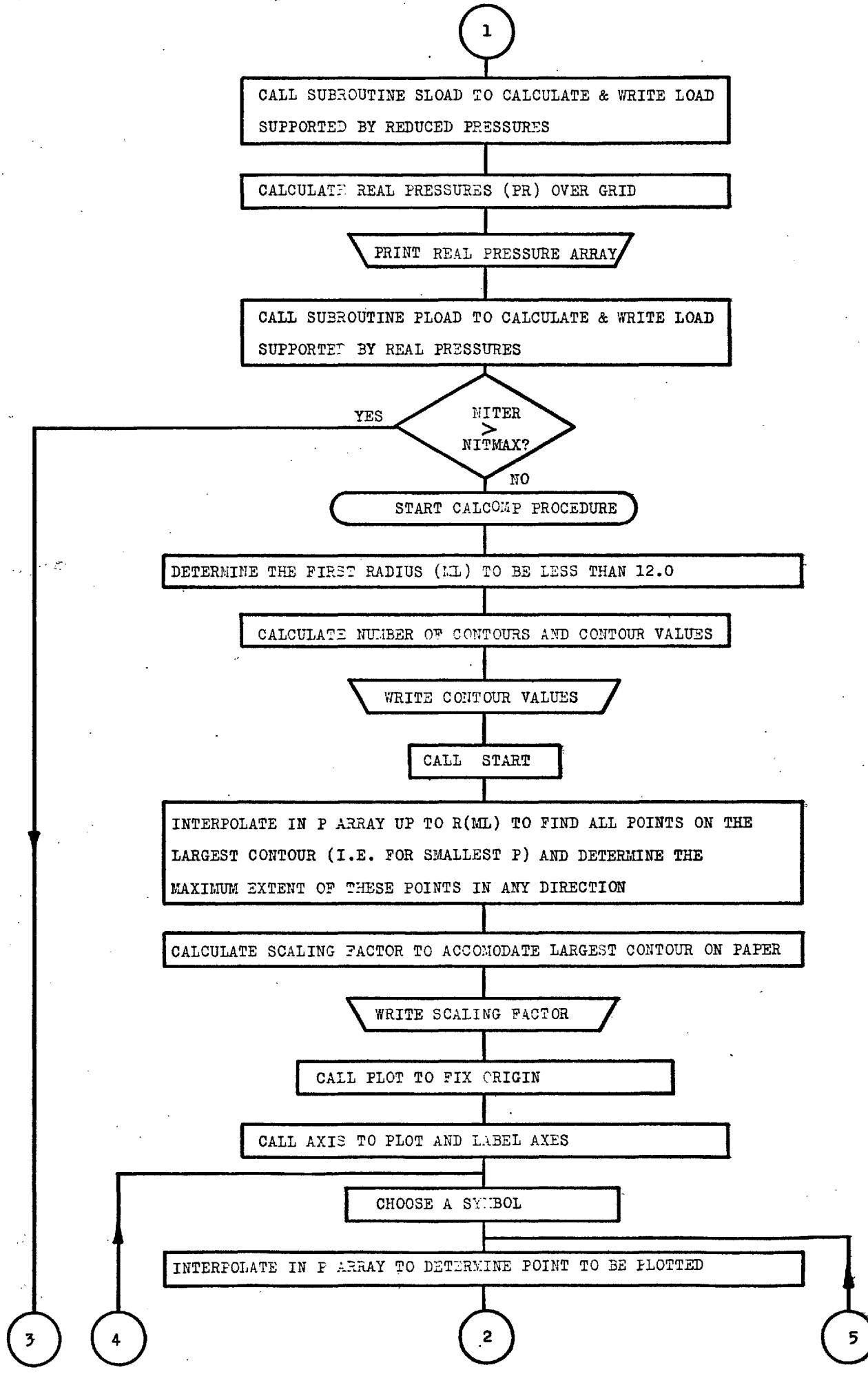
made to make the sub-routine which performed the iteration (PRESSR) as efficient as possible.

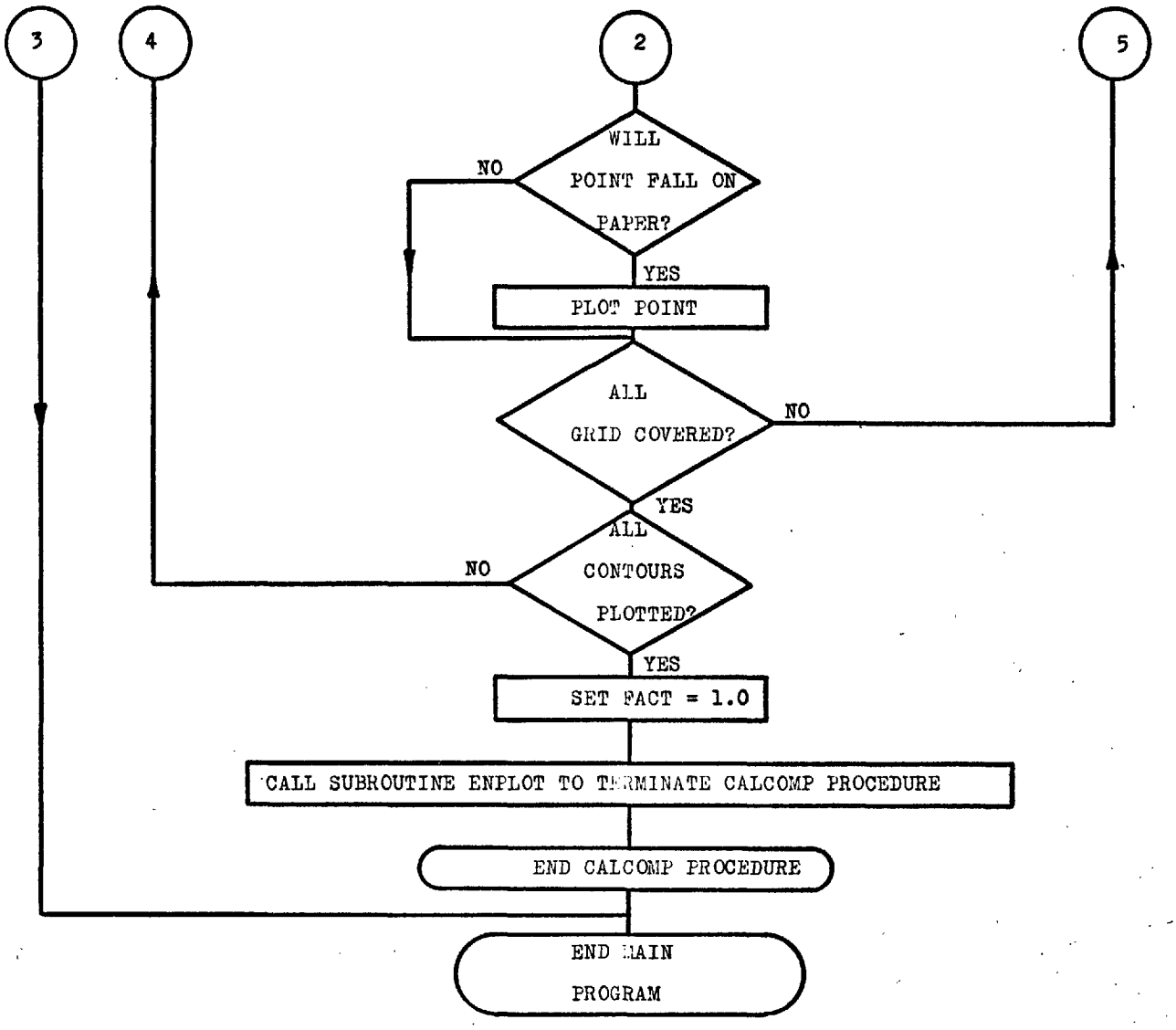
The majority of computer time was used by this routine and it was found that by taking into account the comparative execution times of different operations, considerable time-savings could be made. The sub-routine HERTZR calculated the ratio a/b from elasticity theory by interpolation in the tables provided by Hertz. A direct calculation involves elliptic integrals and was not feasible.

Load was calculated (in sub-routines PLOAD and SLOAD) by integrating pressure using the trapezoidal rule. Integrations were performed first round each circle and the radially to give the total over the whole contact.

A simplified flow chart and listing of the program in its iterative form are given on the following pages.


START
BLOCK DATA SUBROUTINE TO SET PROGRAM VARIABLES
CALL SUBROUTINE HERTZR TO CALCULATE CONTACT ELLIPSE AXIS-RATIO
CALCULATE GRID POINTS (NON-UNIFORM RADIALLY)
WRITE GRID POINTS
INITIALISE PRESSURE ARRAY
CALL SUBROUTINE FILM TO CALCULATE FILM THICKNESS AT EACH GRID POINT
NITER = 0 PMAX== 1.0
PMAXI = 0
NITER = NITER + 1
MAX RESIDUAL = 0
CALCULATE PRESSURE (P) AT GRID CENTRE BY EXTRAPOLATION
CALL SUBROUTINE PRESSR TO CALCULATE :-
PRESSURE OVER REMAINDER OF GRID
MAXIMUM PRESSURE (PMAXI)
MAXIMUM RESIDUAL ON PRESSURE (RESM)
PMAX = PMAXI
(PMAX USED TO NORMALISE
RESIDUALS)
WRITE RESMAX & NITER EVERY 5 ITERATIONS
NITER > NITMAX?
YES
NO
SOLUTION CONVERGED?
NO
YES
PRINT REDUCED PRESSURE ARRAY
1


1
CALL SUBROUTINE SLOAD TO CALCULATE & WRITE LOAD SUPPORTED BY REDUCED PRESSURES
CALCULATE REAL PRESSURES (PR) OVER GRID
PRINT REAL PRESSURE ARRAY
CALL SUBROUTINE PLOAD TO CALCULATE & WRITE LOAD SUPPORTED BY REAL PRESSURES
NITER > NITMAX?
YES
NO
START CALCOMP PROCEDURE
DETERMINE THE FIRST RADIUS (ML) TO BE LESS THAN 12.0
CALCULATE NUMBER OF CONTOURS AND CONTOUR VALUES
WRITE CONTOUR VALUES
CALL START
INTERPOLATE IN P ARRAY UP TO R(ML) TO FIND ALL POINTS ON THE LARGEST CONTOUR (I.E. FOR SMALLEST P) AND DETERMINE THE MAXIMUM EXTENT OF THESE POINTS IN ANY DIRECTION
CALCULATE SCALING FACTOR TO ACCOMODATE LARGEST CONTOUR ON PAPER
WRITE SCALING FACTOR
CALL PLOT TO FIX ORIGIN
CALL AXIS TO PLOT AND LABEL AXES
CHOOSE A SYMBOL
INTERPOLATE IN P ARRAY TO DETERMINE POINT TO BE PLOTTED
3
4
2
5


3
4
2
5
WILL POINT FALL ON PAPER?
NO
YES
PLOT POINT
ALL GRID COVERED?
NO
YES
ALL CONTOURS PLOTTED?
NO
YES
SET FACT = 1.0
CALL SUBROUTINE ENPLOT TO TERMINATE CALCOMP PROCEDURE
END CALCOMP PROCEDURE
END MAIN PROGRAM

```
      BLOCK DATA
C*****************************************************************
C     INPUT OF PROGRAM VARIABLES
C*****************************************************************
      COMMON/CONE/P(51,51),H(51,51),R(51),PHI(51),THETA,PYE3
      COMMON/CTWO/M,N
      COMMON/CFIVE/RATIO
      COMMON/CSEV/PYE2
      COMMON/CEIGHT/CC,GRID
      COMMON/CNINE/NL,W(20),ML,CI
      DATA  CI/0.10/
      DATA  RATIO/0.099099/
      DATA  THETA/82.0/
      DATA  N/36/
      DATA  M/31/
      DATA  PYE2/1.0/
      DATA  PYE3/19.0/
      DATA  CC/5.0E-4/
      DATA  GRID/1.80/
      END




C*****************************************************************
C     MAIN PROGRAM TO CALCULATE THE PRESSURES IN THE CONTACT
C*****************************************************************
      DIMENSION AR(51)
      COMMON/CONE/P(51,51),H(51,51),R(51),PHI(51),THETA,PYE3
      COMMON/CTWO/M,N
      COMMON/CTHREE/I,J
      COMMON/CFOUR/ELLR,ELLMD,ELLND
      COMMON/CFIVE/RATIO
      COMMON/CSIX/PR(51,51)
      COMMON/CSEV/PYE2
      COMMON/CEIGHT/CC,GRID
      COMMON/CNINE/NL,W(20),ML,CI
      COMMON/CTEN/PMAX,PMAXI,RESM
      COMMON/CELEV/NITER
      THETA=THETA*3.14159265/180.0
      MM=M-1
      NN=N-1
      WRITE(6,901)
      CALL HERTZR
C
C     CALCULATE AND PRINT THE R VALUES FOR NON-UNIFORM GRID
      Z=0.05/(1.0-GRID)
      DO10 I=1,10
      K=11-I
   10 R(I)=1.0+Z*(1.0-GRID**K)
      DO20 I=11,31
      K=31-I
   20 R(I)=0.05*FLOAT(K)
      DO30 I=1,M
   30 AR(I)=R(M-I+1)
      DO40 I=1,M
      R(I)=AR(I)
   40 WRITE(6,902)I,R(I)
C
C     CALCULATE AND PRINT THE PHI VALUES
C
      Z=360.0/FLOAT(N)
      DO50 J=1,N
      PHI(J)=FLOAT(J1*Z
      WRITE(6,903)J,PHI(J)
      PHI(J)=PHI(J)*3.14159265/180.0
C
C     SET ARRAY TO INITIAL VALUES
C
      P(M,J)=0.0
      DO50 I=1,MM
   50 P(I,J)=0.6
      CALL FILM
C
C     SET UP ITERATION COUNT (NITER)
C
      NITER=0
      PMAX=1.0
   60 CONTINUE
      PMAXI=0.0
      NITER=NITER+1
C
C     SET MAXIMUM RESIDUAL (RESM) TO ZERO
```

```
C
      RESM=0
C
C     CALCULATE P(I,J) AT THE CENTRE OF THE GRID
C
      TOTAL=0.0
      DO70 J=1,N
      P(1,J)=P(3,J)+((P(4,J)-P(2,J))/(R(4)-R(2)))*(-R(3))+
     1((((P(4,J)-P(3,J))/(R(4)-R(3)))-((P(3,J)-P(2,J))/
     2(R(3)-R(2))))/(R(4)-R(2)))*(R(3)**2)
   70 TOTAL=TOTAL+P(1,J)
      DO80 J=1,N
   80 P(1,J)=TOTAL/FLOAT(N)
      CALL PRESSR
      PMAX=PMAXI
C
C     WRITE OUT THE RESIDUAL VALUE AND THE ITERATION NUMBER
C
      IF(((NITER+4)/5).NE.(NITER/5))GOTO90
      WRITE(6,904)NITER, RESM
   90 CONTINUE
      IF(NITER.EQ.500)GOTO100
      IF(ABS(RESM).GT.CC)GOTO60
      IF(NITER.LT.350)GOTO60
  100 CALL PRINTB(51,51,P,M,N)
      CALL SLOAD
      DO110 I=1,M
      DO110 J=I,N
      IF(P(I,J).GT.1.0)P(I,J)=0.0
  110 PR(I,J)=-ALOG(ABS(1.0-P(I,J)))
      CALL PRINTA(51,51,PR,M,N)
      CALL PLOAD
      IF(NITER.EQ.500)GOTO300
      DO120 I=1,M
  120 IF((R(I)-12.0).GT.0.0)GOTO130
      I=M+1
  130 ML=I-1
      NL=PMAX/CI+2
      IF(NL.GT.14)NL=14
      WRITE(6,905)NL
      W(1)=-0.0012
      W(2)=0.0
      DO140 L=1,2
  140 WRITE(6,906)L,W(L)
      DO150 L=3,NL
      W(L)=CI*FLOAT(L-2)
  150 WRITE(6,906) L,W(L)
      CALL START
      CALL CONTOR
      CALL ENPLOT(12.5)
  300 CONTINUE
  901 FORMAT(1H1)
  902 FORMAT(5H    I=,I6,9H    R(I)= ,F16.7)
  903 FORMAT(5H    J=,I6,9H PHI(J)= ,F16.7)
  904 FORMAT(5X,I5,6(1PE15.3))
  905 FORMAT(20X,I2,22H  VALUES TO BE PLOTTED//)
  906 FORMAT(25X,I5,1PE11.3)
      STOP
      END



      SUBROUTINE PRESSR
C*****************************************************************
C     SUBROUTINE TO CALCULATE PRESSURE OVER WHOLE GRID EXCEPTING
C     CENTRE AND OUTER BOUNDARY
C*****************************************************************
      COMMON/CONE/P(40,40),H(40,40),R(40),PHI(40),THETA,PYE3
      COMMON/CTWO/M,N
      COMMON/CTHREE/I,J
      COMMON/CFOUR/ELLR,ELLMD,ELLND
      COMMON/CTEN/PMAX,PMAX1,RESM,IKEEP,JKEEP
      COMMON/CELEV/NITER
      COMMON/CTWEL/PCAV,PCAVB
      PHI(N+1)=PHI(N)+PHI(1)
      CTH=COS(THETA)
      STH=SIN(THETA)
      MM=M-1
      DO40 J=1,N
      CPJ=COS(PHI(J))
      SPJ=SIN(PHI(J))
      JP=J+1
      JM=J-1
      IF(J.NE.1.AND.J.NE.N)GOTO20
      IF(J.NE.1)GOTO10
      JM=N
      PHI(JM)=0.0
```

```
      GOTO20
   10 JP=1
   20 CONTINUE
      B1=1.0/(PHI(J+1)-PHI(JM))
      B2=1.0/(PHI(J+1)-PHI(J))
      B3=1.0/(PHI(J)-PHI(JM))
      B4=B1*B2
      B5=B1*B3
      D1=CPJ**2+(SPJ/ELLR)**2
      D2=SPJ**2+(CPJ/ELLR)**2
      D3=(1.0-1.0/ELLR**2)*SPJ*CPJ
      RHS1=(STH*CPJ)/ELLR-CTH*SPJ
      RHS2=CTH*CPJ+(STH*SPJ)/ELLR
      DO30 I=2,MM
      SAVE=P(I,J)
      IP=I+1
      IM=I-1
      H2=H(I,J)**2
      H3=H(I,J)**3
      R1=1.0/R(I)
      R2=R1*R1
      A1=1.0/(R(IP)-R(IM))
      A2=1.0/(R(IP)-R(I))
      A3=1.0/(R(I)-R(IM))
      A4=A1*A2
      A5=A1*A3
      DHDR=(H(IP,J)-H(IM,J))*A1
      DHDPHI=(H(I,JP)-H(I,JM))*B1
      DPDRDI=(P(IP,JP)-P(IM,JP)-P(IP,JM)+P(IM,JM))*A1*B1
      RHS=PYE3*(DHDR*RHS2+(DHDPHI*RHS1)*R1)
      D4=3.0*H2*(DHDR*D1-DHDPHI*D3*R1)+H3*D2*R1
      D5=3.0*H2*(DHDPHI*D2*R2-DHDR*D3*R1)+2.0*H3*D3*R2
      D6=H3*D1
      D8=H3*D2*R2
      D9=-2.0*H3*D3*R1*DPDRDI
      CA=2.0*(D6*(A4+A5)+D8*(B4+B5))
      C1=1.0/CA
      CN=(D4*A1+2.0*D6*A4)*C1
      CS=(-D4*A1+2.0*D6*A5)*C1
      CE=(D5*B1+2.0*D8*B4)*C1
      CW=(-D5*B1+2.0*D8*B5)*C1
      D=(D9-RHS)*C1
      P(I,J)=CN*P(IP,J)+CS*P(IM,J)+CE*P(I,JP)+CW*P(I,JM)+D
      IF(P(I,J).LT.PCAV)P(I,J)=PCAV
      IF(ABS(P(I,J)).GT.ABS(PMAX1))PMAX1=P(I,J)
      RES=(P(I,J)-SAVE)/PMAX
      IF(ABS(RES).LE.ABS(RESM))GOTO30
      RESM=RES
      IKEEP=I
      JKEEP=J
   30 CONTINUE
      PHI(N)=6.2831853
   40 CONTINUE
      RETURN
      END
```

```
      SUBROUTINE   HERTZR
C*****************************************************************
C     SUBROUTINE TO CALCULATE THE HERTZ CONTACT AXIS-RATIO
C*****************************************************************
      COMMON/CFOUR/ELLR,ELLMD,ELLND
      COMMON/CFIVE/RATIO
      DIMENSION TEETA(20),ELLM(20),ELLN(20)
      DATA TEETA(1),ELLM(1),ELLN(1)/10.0,6.612,0.319/
      DATA TEETA(2),ELLM(2),ELLN(2)/20.0,3.778,0.408/
      DATA TEETA(3),ELLM(3),ELLN(3)/30.0,2.731,0.493/
      DATA TEETA(4),ELLM(4),ELLN(4)/35.0,2.397,0.530/
      DATA TEETA(5),ELLM(5),ELLN(5)/40.0,2.136,0.567/
      DATA TEETA(6),ELLM(6),ELLN(6)/45.0,1.926,0.604/
      DATA TEETA(7),ELLM(7),ELLN(7)/50.0,1.754,0.641/
      DATA TEETA(8),ELLM(8),ELLN(8)/55.0,1.611,0.678/
      DATA TEETA(9),ELLM(9),ELLN(9)/60.0,1.486,0.717/
      DATA TEETA(10),ELLM(10),ELLN(10)/65.0,1.378,0.759/
      DATA TEETA(11),ELLM(11),ELLN(11)/70.0,1.284,0.802/
      DATA TEETA(12),ELLM(12),ELLN(12)/75.0,1.202,0.846/
      DATA TEETA(13),ELLM(13),ELLN(13)/80.0,1.128,0.893/
      DATA TEETA(14),ELLM(14),ELLN(14)/85.0,1.061,0.944/
      DATA TEETA(15),ELLM(15),ELLN(15)/90.0,1.000,1.000/
      IF(ABS(RATIO).EQ.1.0)GOTO 200
      COSS=(1.0-RATIO)/(1.0+RATIO)
      TEETAD=ATAN(ABS(((1.0-COSS**2)**0.5)/COSS))
      TEETAD=TEETAD*180.0/3.14159265
      L=0
```

```
  201 L=L+1
      IF(TEETAD-TEETA(L).GE.TEETA(L+1)-TEETA(L))GOTO201
      IF(TEETAD.EQ.TEETA(L))ELLMD=ELLM(L)
      IF(TEETAD.EQ.TEETA(L))ELLND=ELLN(L)
      IF(TEETAD.EQ.TEETA(L))GOTO202
      ELLMD=ELLM(L)+(ELLM(L+1)-ELLM(L))*(TEETAD-TEETA(L))/
     1       (TEETA(L+1)-TEETA(L))
      ELLND=ELLN(L)+(ELLN(L+1)-ELLN(L))*(TEETAD-TEETA(L))/
     1       (TEETA(L+1)-TEETA(L))
  202 CONTINUE
  200 IF(ABS(RATIO).EQ.1.0)TEETAD=90.0
      IF(ABS(RATIO).EQ.1.0)ELLMD=1.0
      IF(ABS(RATIO).EQ.1.0)ELLND=1.0
      ELLR=ELLMD/ELLND
      IF(ABS(RATIO).GT.1.0)ELLR=1.0/ELLR
      WRITE( 6,203 )TEETAD,ELLMD,ELLND,ELLR
  203 FORMAT(9H    THETA=,F7.3,9H    ELLMD=,F7.3,9H    ELLND=,F7.3,
     1       9H    ELLR=,F7.3)
      RETURN
      END
```

```
      SUBROUTINE  FILM
C*****************************************************************************
C     SUBROUTINE TO CALCULATE FILM THICKNESSES
C*****************************************************************************
      COMMON/CONE/P(51,51),H(51,51),R(51),PHI(51),THETA,PYE3
      COMMON/CTWO/M,N
      COMMON/CFOUR/ELLR,ELLMD,ELLND
      COMMON/CFIVE/RATIO
      COMMON/CSEV/PYE2
      DO1 J=1,N
      SPJ=SIN(PHI(J))
      CPJ=COS(PHI(J))
      DO1 I=1,M
    1 H(I,J)=1.0+PYE2*((R(I)*CPJ)**2+RATIO*(ELLR*R(I)*SPJ)**2) -
      RETURN
      END
```

```
      SUBROUTINE  PRINTA(N1,N2,PR,M,N)
C*****************************************************************************
C     OUTPUT SUBROUTINE FOR THE REAL PRESSURE FIELD
C*****************************************************************************
      DIMENSION  PR(N1,N2)
      WRITE(6,100)
      DO2 L=1,N
      J=N+1-L
    2 WRITE(6,101)(PR(I,J),I=1,11),J
      WRITE(6,102)(I,I=1,11)
      DO3 L=1,N
      J=N+1-L
    3 WRITE(6,101)(PR(I,J),I=12,22),J
      WRITE(6,102)(I,I=12,22)
      DO4 L=1,N
      J=N+1-L
    4 WRITE(6,103)(PR(I,J),I=23,31),J
      WRITE(6,104)(I,I=23,31)
  100 FORMAT(//5X18HDISTRIBUTION OF PR/5X,18(1H-)/129X,1HJ)
  101 FORMAT(1H ,3X,11(1PE11.3),3X,I2)
  102 FORMAT(1H0,3H   I,4X,10(I2,9X),I2/)
  103 FORMAT(1H ,3X,9(1PE11.3),25X,I2)
  104 FORMAT(1H0,3H   I,4X,9(I2,9X)//)
      RETURN
      END
```

```
      SUBROUTINE PRINTB(N1,N2,P,M,N)
C*****************************************************************
C     OUTPUT SUBROUTINE FOR THE REDUCED PRESSURE FIELD
C*****************************************************************
      DIMENSION P(N1,N2)
      WRITE (6,100)
      DO2 L=1,N
      J=N+1-L
    2 WRITE(6,101)(P(I,J),I=1,11),J
      WRITE(6,102)(I,I=1,11)
      DO3 L=1,N
      J=N+1-L
    3 WRITE(6,101)(P(I,J),I=12,22),J
      WRITE(6,102)(I,I=12,22)
      DO4 L=1,N
      J=N+1-L
    4 WRITE(6,103)(P(I,J),I=23,31),J
      WRITE(6,104)(I,I=23,31)
  100 FORMAT(//5X,17HDISTRIBUTION OF P/5X,17(1H-)/129X,1HJ)
  101 FORMAT(1H ,3X,11(1PE11.3),3X,I2)
  102 FORMAT(1H0,3H  I,4X,10(I2,9X),I2/)
  103 FORMAT(1H ,3X,9(1PE11.3),25X,I2)
  104 FORMAT(1H0,3H  I,4X,9(I2,9X)//)
      RETURN
      END
```

```
      SUBROUTINE SLOAD
C*****************************************************************
C     SUBROUTINE TO INTEGRATE THE REDUCED PRESSURES OVER THE FIELD
C*****************************************************************
      DIMENSION SUM(51)
      COMMON/CONE/P(51,51),H(51,51),R(51),PHI(51),THETA,PYE3
      COMMON/CTWO/M,N
      COMMON/CFOUR/ELLR,ELLMO,ELLNO
      NA=N-1
      DO1 I=1,M
      SUM(I)=0.5*R(I)*PHI(I)*(P(I,N)+P(I,1))
      DO1 J=1,NA
    1 SUM(I)=SUM(I)+0.5*R(I)*(PHI(J+1)-PHI(J))*(P(I,J)+P(I,J+1))
      MA=M-1
      ALOAD=0.0
      DO2 I=1,MA
    2 ALOAO=ALOAO+0.5*(SUM(I)+SUM(I+1))*(R(I+1)-R(I))
      WRITE(6,3)ALOAD
    3 FORMAT(39H   LOAD GIVEN BY INTEGRATED PRESSURE = ,1PE11.3)
      G1=1.0/(ALOAO*ELLR*2.0)
      G2=G1**1.5*PYE3/(6.0*SQRT(2.0))
      WRITE(6,20)G1,G2
   20 FORMAT(28X,11HH*/W*,G* = ,1PE11.3,/,27X,3H3/2,3X,3H1/2,/,
     122X,17HU*/W*    ,G*     = ,1PE11.3/)
      RETURN
      END
```

```
      SUBROUTINE PLOAD
C*****************************************************************
C     SUBROUTINE TO INTEGRATE THE REAL PRESSURES OVER THE FIELD
C*****************************************************************
      DIMENSION SUM(51)
      COMMON/CONE/P(51,51),H(51,51),R(51),PHI(51),THETA,PYE3
      COMMON/CTWO/M,N
      COMMON/CFOUR/ELLR,ELLMD,ELLNO
      COMMON/CSIX/PR(51,51)
      DO10 I=1,M
      DO 10 J=I,N
   10 IF(PR(I,J).LT.0.0)PR(I,J)=0.0
      NA=N-1
      DO1 I=1,M
      SUM(I)=0.5*R(I)*PHI(1)*(PR(I,N)+PR(I,1))
      DO1 J=1,NA
    1 SUM(I)=SUM(I)+0.5*R(I)*(PHI(J+1)-PHI(J))*(PR(I,J)+PR(I,J+1))
      MA=M-1
      ALOAD=0.0
```

```
      DO2 I=1,MA
    2 ALOAD=ALOAD+0.5*(SUM(I)+SUM(I+1))*(R(I+1)-R(I))
      WRITE(6,3)ALOAD
    3 FORMAT(39H   LOAD GIVEN BY INTEGRATED PRESSURE = ,1PE11.3)
      G1=1.0/(ALOAD*ELLR*2.0)
      G2=G1**1.5*PYE3/(6.0*SQRT(2.0))
      WRITE(6,20)G1,G2
   20 FORMAT(28X,11HH*/W*,G* = ,1PE11.3,/,27X,3H3/2,3X,3H1/2,/,
     122X,17HU*/W*    ,G*    = ,1PE11.3/)
      RETURN
      END
```

```
      SUBROUTINE CONTOR
C*************************************************************************
C     CALCOMP SUBROUTINE TO INTERPOLATE, SCALE, AND PLOT POINTS
C*************************************************************************
      DIMENSION X(300),Y(300)
      COMMON/CONE/P(51,51),H(51,51),R(51),PHI(51),THETA,PYE3
      COMMON/CTWO/M,N
      COMMON/CFOUR/ELLR,ELLMD,ELLND
      COMMON/CNINE/NL,W(20),ML,CI
      L=3
      K=0
      DO100 J=1,N
      DO100 I=2,ML
      IF(.NOT.((P(I-1,J).LT.W(L).AND.P(I,J).GE.W(L)).OR.(P(I-1,J).GT.W(L
     1).AND.P(I,J).LE.W(L))))GOTO100
      DELR=(W(L)-P(I-1,J))/(P(I,J)-P(I-1,J))*(R(I)-R(I-1))
      K=K+1
      X(K)=(R(I-1)+DELR)*COS(PHI(J))/ELLR
      Y(K)=(R(I-1)+DELR)*SIN(PHI(J))
  100 CONTINUE
      DO150 I=2,ML
      DO150 J=1,N
      JK=J+1
      JL=J-1
      IF(J.EQ.1)JL=N
      IF(J.EQ.1)PHI(JL)=0.0
      IF(.NOT.((P(I,JL).LT.W(L).AND.P(I,J).GE.W(L)).OR.(P(I,JL).GT.W(L).
     1AND.P(I,J).LE.W(L))))GOTO150
      DELPHI=(W(L)-P(I,JL))/(P(I,J)-P(I,JL))*(PHI(J)-PHI(JL))
      K=K+1
      X(K)=(R(I)/ELLR)*COS(PHI(JL)+DELPHI)
      Y(K)=R(I)*SIN(PHI(JL)+DELPHI)
  150 PHI(N)=2.0*3.14159265
      KM=K
      MX=1
      MXX=1
      MY=1
      MYY=1
      DO200 K=2,KM
      IF((X(K)-X(MX)).GT.0.0)MX=K
      IF((X(MXX)-X(K)).GT.0.0)MXX=K
      IF((Y(K)-Y(MY)).GT.0.0)MY=K
  200 IF((Y(MYY)-Y(K)).GT.0.0)MYY=K
      YM=ABS(Y(MY))
      IF(ABS(Y(MYY)).GT.ABS(Y(MY)))YM=ABS(Y(MYY))
      XM=ABS(X(MX))
      IF(ABS(X(MXX)).GT.ABS(X(MX)))XM=ABS(X(MXX))
      SCAL=XM
      IF(YM.GT.XM)SCAL=YM
      MSCAL=IFIX(SCAL)
      MSCAL=MSCAL+1
      SCAL=FLOAT(MSCAL)
      FACT=1.0
      WRITE(6,901)KM,X(MX),X(MXX),Y(MY),Y(MYY),FACT,MSCAL
      IF(MSCAL.EQ.1)FACT=10.0
      IF(MSCAL.EQ.2)FACT=5.0
      IF(MSCAL.EQ.3)FACT=3.0
      IF(MSCAL.EQ.4.OR.MSCAL.EQ.5)FACT=2.0
      WRITE(6,902)FACT
```

```
      FACT=5.0
      CALL PLOT(12.0,14.5,-3)
      CALL AXIS(0.0,-10.0,1H ,1,20.0,90.0,-10.0/FACT,1.0/FACT)
      CALL AXIS(-10.0,0.0,0.0,1H ,1,20.0,0.0,-10.0/FACT,1.0/FACT)
      CALL FACTOR(FACT)
      DO400 L=1,NL
      IF(P(1,1).NE.W(L))GOT250
      CALL SYMBOL(0.0,0.0,0.07,L,0.0,-1)
      GOTO 400
  250 DO300 J=1,N
      DO300 I=2,ML
      IF(.NOT.((P(I-1,J).LT.W(L).AND.P(I,J).GE.W(L)).OR.(P(I-1,J).GT.W(L
     1).AND.P(I,J).LE.W(L))))GOTO300
      DELR=(W(L)-P(I-1,J))/(P(I,J)-P(I-1,J))*(R(I)-R(I-1))
      XR=(R(I-1)+DELR)*COS(PHI(J))/ELLR
      YR=(R(I-1)+DELR)*SIN(PHI(J))
      IF(ABS(YR*FACT).GT.12.0.OR.ABS(XR*FACT).GT.12.0)GOTO300
      CALL SYMBOL(XR,YR,0.07/FACT,L,0.0,-1)
  300 CONTINUE
      DO400 I=2,ML
      DO400 J=1,N
      JK=J+1
      JL=J-1
      IF(J.EQ.1)JL=N
      IF(J.EQ.1)PHI(JL)=0.0
      IF(.NOT.((P(I,JL).LT.W(L).AND.P(I,J).GE.W(L)).OR.(P(I,JL).GT.W(L).
     1AND.P(I,J).LE.W(L))))GOTO400
      DELPHI=(W(L)-P(I,JL))/(P(I,J)-P(I,JL))*(PHI(J)-PHI(JL))
      XR=(R(I)/ELLR)*COS(PHI(JL)+DELPHI)
      YR=R(I)*SIN(PHI(JL)+DELPHI)
      IF(ABS(YR*FACT).GT.12.0.OR.ABS(XR*FACT).GT.12.0)GOTO350
      CALL SYMBOL(XR,YR,0.07/FACT,L,0.0,-1)
  350 CONTINUE
      PHI(N)=2.0*3.14159265
  400 CONTINUE
      CALL FACTOR(1.0)
  901 FORMAT(I10,5(1PE11.4),I10)
  902 FORMAT(/29X,7HFACT = ,F5.1)
      RETURN
      END
```

Appendix 3. ADAPTATION OF EXISTING ELLIPTICAL CONTACT THEORIES TO THE PLOTTED GROUPS

In order to compare with experimental results, Cheng's solution for an elliptical elastohydrodynamic contact (ref.6 chapter 5) can be modified in the following manner. He obtained the equation:-

$$\left(\frac{h_o}{R_x}\right)^{2-n} = 12C\left(\frac{\eta_o \alpha U}{2R_x}\right)\left(\frac{c}{R_x}\right)\left(\frac{3W}{2\pi E' d R_x}\right)^{-n} \qquad \text{-A3.1}$$

Equation A3.1 uses the present notation. C and n are constants for a specified geometry. Using Hertz theory as described by Cheng and rearranging, equation A3.1 can be rewritten as:-

$$H_o^* = \left(U^*\right)^{\frac{1}{2-n}}\left(G^*\right)^{\frac{1}{2-n}}\left(W^*\right)^{\frac{1-2n}{6-3n}}\cdot(12C)^{\frac{1}{2-n}}\cdot\left(\frac{3a}{b}\right)^{\frac{1-2n}{6-3n}} \times\left(\frac{1}{\pi}\right)^{\frac{1}{3}}\left(2\right)^{\frac{n-1}{2-n}}\left[\frac{m^2\,\pi^2}{\left(\frac{b}{a}\right)^2\left(1+\frac{B}{A}\right)}\right]^{\frac{n+1}{6-3n}} \qquad \text{-A3.2}$$

where $m = d\left[\frac{3}{2}\frac{W}{(A+B)E'}\right]^{-\frac{1}{3}}$

For the geometry used in these experiments, and with sliding along the raceway axis ($\theta = 0^o$), equation A3.2 reduces to

$$\frac{H_o^*}{W^*G^*} = 1.45\left(\frac{U^*}{G^{*1/2}W^{*3/2}}\right)^{0.738}(W^*\,G^*)^{0.036} \qquad \text{-A3.3}$$

Similarly, when sliding is across the raceway ($\theta = 90^o$), one obtains

$$\frac{H_o^*}{W^*G^*} = 0.462\left(\frac{U^*}{G^{*1/2}W^{*3/2}}\right)^{0.639}(W^*\,G^{*3})^{-0.014} \qquad \text{-A3.4}$$

Archard's analysis (ref.5 chapter5) results in the following

equation (using the present notation)

$$h_o = 2.04\left(\alpha \eta_o \frac{U}{2}\right)^{0.74} R^{0.407}\left(\frac{E'}{W}\right)^{0.074} \Phi^{0.74} \qquad \text{-A3.5}$$

where

$$\Phi = \left[1 + \frac{2}{3}\frac{R_x}{R_y}\right]^{-1} \qquad \text{-A3.6}$$

This may be rewritten as

$$H_o^* = 1.22\, \Phi^{0.74}\, U^{*0.74}\, G^{*0.74}\, W^{*-0.074} \qquad \text{-A3.7}$$

which, for the geometry used, and with $\theta = 0^o$, becomes

$$\frac{H_o^*}{G^* W^*} = 1.165\left(\frac{U^*}{G^{*1/2} W^{*3/2}}\right)^{0.74} (W^* G^{*3})^{0.037} \qquad \text{-A3.8}$$

with sliding across the raceway ($\theta = 90^o$), one gets

$$\frac{H_o^*}{G^* W^*} = 0.269\left(\frac{U^*}{G^{*1/2} W^{*3/2}}\right)^{0.74} (W^* G^{*3})^{0.037} \qquad \text{-A3.9}$$

Appendix 4. A PROGRAM TO GIVE A NUMERICAL SOLUTION FOR THE SLIDING FRICTION WITH HEATING

The equations to be solved are the Navier-Stokes equation with zero pressure gradient:-

$$\frac{\partial}{\partial z}\left(\eta \frac{\partial u}{\partial z}\right) = 0 \qquad \text{-A4.1}$$

and the energy equation:-

$$-K \frac{\partial^2 \theta}{\partial z^2} = \eta \left(\frac{\partial u}{\partial z}\right)^2 \qquad \text{-A4.2}$$

The film thickness was divided into a series of grid lines and the equations solved using finite difference techniques at each grid point. Central differences were used throughout and the quantity at point z_m expressed in terms of those at point z_{m+1} and z_{m-1} [1]. Expressing equation A4.1 in finite difference form and re-arranging, an expression for u_m was derived:-

$$u_m = \frac{u_{m+1}(\eta_{m+1}+\eta_m)(z_m-z_{m-1}) + u_{m-1}(\eta_m+\eta_{m-1})(z_{m+1}-z_m)}{(\eta_{m+1}+\eta_m)(z_m-z_{m-1}) + (\eta_m+\eta_{m-1})(z_{m+1}-z_m)} \qquad \text{-A4.3}$$

Similarly, equation A4.2 was expressed in finite difference form:-

$$\theta_m = \frac{\eta_m \cdot (u_{m+1}-u_{m-1})^2}{2K\,(z_{m+1}-z_{m-1})^2}(z_m-z_{m+1})(z_{m+1}-z_m) + \left(\frac{z_m-z_{m-1}}{z_{m+1}-z_{m-1}}\right)\theta_{m+1} + \left(\frac{z_{m+1}-z_m}{z_{m+1}-z_{m-1}}\right)\theta_{m-1} \qquad \text{-A4.4}$$

One of the boundary conditions on temperature was known to be

---

1. Smith G.D. 'Numerical solution of partial differential equations' Oxford University Press, London, 1965.

zero temperature gradient at the surface. To speed convergence this was made implicit as follows:

Equation A4.4 may be expressed as:-

$$\theta_m = D_m + C_m \theta_{m+1} + B_m \theta_{m-1} \qquad \text{-A4.5}$$

where D_m, C_m and B_m are respectively the coefficient in equation A4.4. At the near-wall point $\theta_{m-1} = \theta_m$, hence

$$\theta_m = \frac{C_m \theta_{m+1}}{1 - B_m} + \frac{D_m}{1 - B_m} \qquad \text{-A4.6}$$

Equation A4.6 was used to calculate θ at the near-wall point and θ at the boundary was then up-dated accordingly.

The equations were programmed in such a way that it was possible to over-relax each variable (θ, U, η) individually and thus speed convergence. However, no single set of over-relaxation factors was found to be satisfactory over the complete range of speeds and loads covered by the calculations. A large factor (= 1.7) speeded convergence when heating was large, but caused instabilities when it was small. The factors were therefore adjusted depending on the amount of heating anticipated.

Solutions were shown to be independent of initial guess to within 1% which was considered satisfactory. A convergence criterion of 0.0005 was found to be sufficient to ensure this independence.

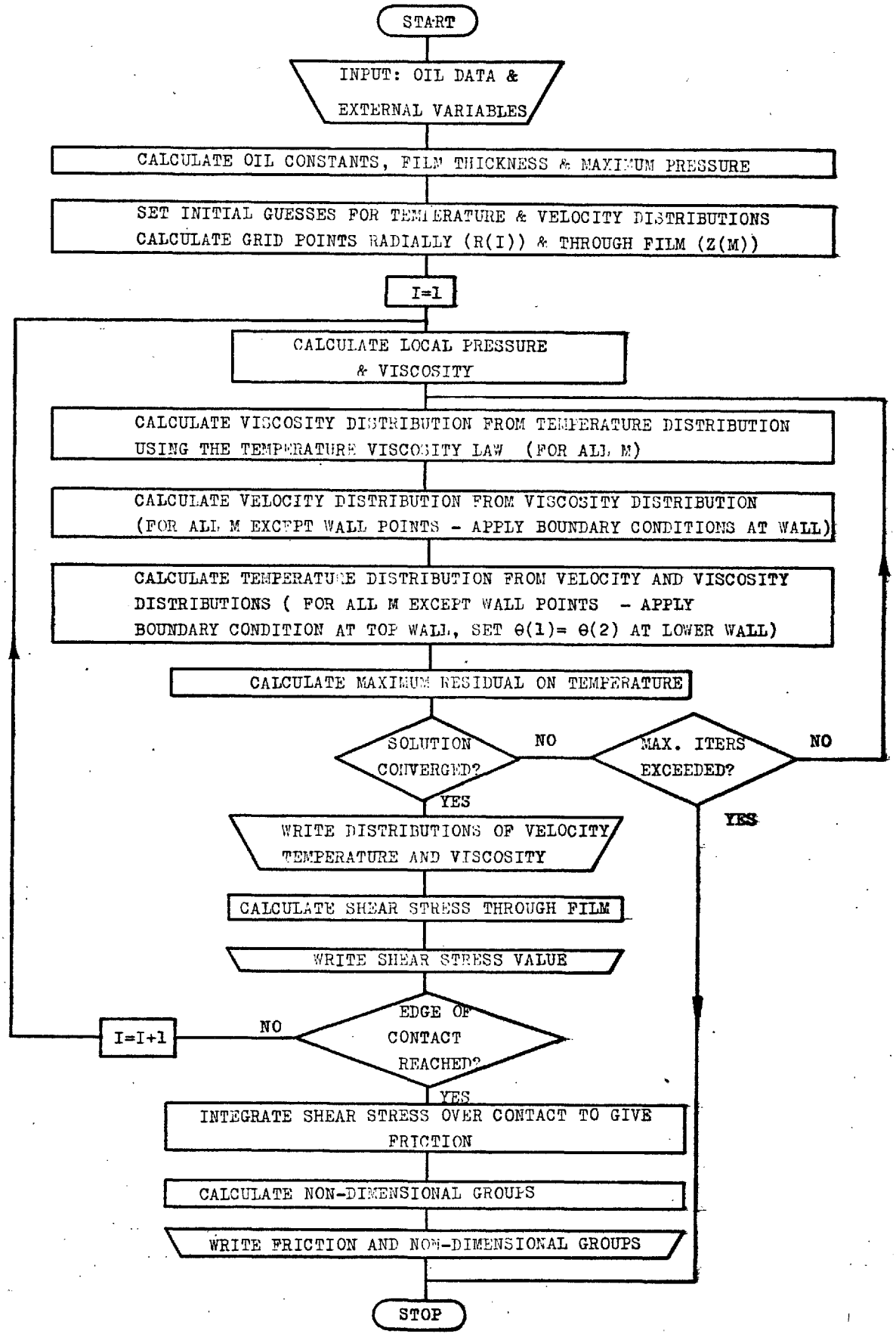
The number of grid lines in the z-direction (through the thickness of the film) was chosen to be as small as was possible whilst still having the solution remain grid independent. 15 grid lines were found to give independence to within 1%. An improvement inaccuracy for a given number of grid lines could have been made by storing the values of θ and η at the nodes

between the U's. However, in practice this was not found to be necessary, the accuracy being sufficient.

A check on the consistency of the solution with the assumption of constant shear stress through the film was obtained by calculating this quantity at each grid line. The maximum variation was about 1½%, which was considered sufficiently constant.

The total friction was obtained by integration over the contact area, a non-uniform grid being used in the radial direction to minimise the tendency for instabilities to be introduced by the rapid changes in pressure which occur as the Hertz radius is approached.

The iteration procedure outlined in section 6.2.4 is given in more detail in the flow chart overleaf and in the subsequent listing of the program.


START
INPUT: OIL DATA & EXTERNAL VARIABLES
CALCULATE OIL CONSTANTS, FILM THICKNESS & MAXIMUM PRESSURE
SET INITIAL GUESSES FOR TEMPERATURE & VELOCITY DISTRIBUTIONS
CALCULATE GRID POINTS RADIALLY (R(I)) & THROUGH FILM (Z(M))
I=1
CALCULATE LOCAL PRESSURE & VISCOSITY
CALCULATE VISCOSITY DISTRIBUTION FROM TEMPERATURE DISTRIBUTION USING THE TEMPERATURE VISCOSITY LAW (FOR ALL M)
CALCULATE VELOCITY DISTRIBUTION FROM VISCOSITY DISTRIBUTION (FOR ALL M EXCEPT WALL POINTS - APPLY BOUNDARY CONDITIONS AT WALL)
CALCULATE TEMPERATURE DISTRIBUTION FROM VELOCITY AND VISCOSITY DISTRIBUTIONS (FOR ALL M EXCEPT WALL POINTS - APPLY BOUNDARY CONDITION AT TOP WALL, SET θ(1)= θ(2) AT LOWER WALL)
CALCULATE MAXIMUM RESIDUAL ON TEMPERATURE
SOLUTION CONVERGED?
NO
MAX. ITERS EXCEEDED?
NO
YES
YES
WRITE DISTRIBUTIONS OF VELOCITY TEMPERATURE AND VISCOSITY
CALCULATE SHEAR STRESS THROUGH FILM
WRITE SHEAR STRESS VALUE
EDGE OF CONTACT REACHED?
NO
I=I+1
YES
INTEGRATE SHEAR STRESS OVER CONTACT TO GIVE FRICTION
CALCULATE NON-DIMENSIONAL GROUPS
WRITE FRICTION AND NON-DIMENSIONAL GROUPS
STOP

```
C*********************************************************************
C     PROGRAM TO CALCULATE THE FRICTION IN A CONTACT WITH SHEAR HEATING
C*********************************************************************
      DIMENSION Z(16),ETA(16),U(16),THETA(16),T(16),P(16)
      DIMENSION TAU(16)
      DIMENSION R(16)
      DATA  CON/0.0005/
      DATA  IM/11/
      DATA  MM/16/
      DATA  TGUESS/130.0/
      DATA  E,GSTAR/19.07E6,3.016E3/
      DATA  WSTAR/1.48E-6/
      DATA  RBALL/0.0127/
C     UNITS OF RADIUS ARE M (HALF INCH RADIUS BALL)
      DATA  RK/0.1352/
C     UNITS OF RK ARE N/(SEC.DEG C)
      DATA  USTAR/1.27E-9/
      DATA  AK0,AK1/3.02E-4,1.41E-5/
      DATA  T0,ETA0/23.0,3.5/
      DATA  T1,ETA1/37.8,1.081/
      DATA  T2,ETA2/98.9,0.045/
C     UNITS OF ETA ARE N.SEC/(M**2)
      DATA  UORF/1.0/
      DATA  EORF/1.0/
      DATA  TORF/1.0/
      T1=T1-T0
      T2=T2-T0
      THE=T1*T2*ALOG(ETA1/ETA2)/(T1*ALOG(ETA2/ETA0)-T2*ALOG(ETA1/ETA0))
      BEE=ALOG(ETA1/ETA2)*(T1+THE)*(T2+THE)/(T2-T1)
      TEMAX=1.0
      R(1)=0.0
      R(2)=1.0
      WRITE(6,101)
      WRITE(6,103)THE,BEE
      E=E*6895.0E-6
      UBALL=(USTAR*E*RBALL)/(ETA0*1.0E-6)
C     UNITS OF E ARE NOW MN/M**2
      PMAX=0.364*E*WSTAR**(1.0/3.0)
C     UNITS OF P ARE MN/(M**2)  (400 MN/(M**2)=APPROX 58,000PSI)
      HOSTAR=1.055*(GSTAR*USTAR)**(5.0/7.0)*WSTAR**(-1.0/21.0)
      SUM=0.0
      IL=IM-1
      M2=(MM+1)/2
      ML=MM-1
      DO5 M=1,MM
      Z(M)=FLOAT(M-1)/FLOAT(MM-1)
      U(M)=UBALL*FLOAT(M-1)/FLOAT(MM-1)
      THETA(M)=TGUESS*FLOAT(MM-M)/FLOAT(MM-1)
      ETA(M)=ETA0
5     CONTINUE
      DO6 I=3,IM
      R(I)=R(I-1)+0.9*(R(I-1)-R(I-2))
6     CONTINUE
      DO40 I=1,IM
      NITER=0
      R(I)=R(I)/R(IM)
      P(I)=PMAX*SQRT(1.0-R(I)**2)
      PIMP=P(I)/6895.0E-6
      ETAR=ETA0*EXP(AK0*PIMP/(1.0+AK1*PIMP))
10    CONTINUE
      NITER=NITER+1
      RESMAX=0.0
      THMAX=0.0
      DO15 M=1,MM
      EKEEP=ETA(M)
      PDEP=0.0015
      EXV=-BEE/(THE**2+THE*THETA(M))
      EXMOD=EXP(PDEP*P(I))
      EXVP=EXV*EXMOD
      EXT=THETA(M)*EXVP
      EDEL=ETAR*EXP(EXT)-EKEEP
      ETA(M)=EKEEP+EDEL*EORF
C     UNITS OF ETA ARE NOW N.SEC/(M**2)
15    CONTINUE
      DO20 M=2,ML
      UKEEP=U(M)
```

```
      A=ETA(M+1)+ETA(M)
      AA=ETA(M)+ETA(M-1)
      C=Z(M)-Z(M-1)
      CC=Z(M+1)-Z(M)
      UDEL=((U(M+1)*A*C+U(M-1)*AA*CC)/(A*C+AA*CC))-UKEEP
      U(M)=UKEEP+UDEL*UORF
20    CONTINUE
      DO25 M=2,ML
      SAVE=THETA(M)
      TKEEP=THETA(M)
      C=Z(M)-Z(M-1)
      CC=Z(M+1)-Z(M)
      CCC=Z(M+1)-Z(M-1)
      F=(C*CC/CCC)
      FF=(ETA(M)*(U(M+1)-U(M-1))**2)/(2.0*RK*CCC)
      IF(M.NE.2)GOTO21
      F4=1.0-CC/CCC
      TDEL=((FF*F/F4)+((C/CCC)*THETA(M+1))/F4)-TKEEP
      THETA(M)=ABS(TKEEP+TDEL*TORF)
      GOTO22
21    CONTINUE
      FFF=(THETA(M+1)*C+THETA(M-1)*CC)/(C*CC)
      TDEL=(F*(FF+FFF))-TKEEP
      THETA(M)=ABS(TKEEP+TDEL*TORF)
22    CONTINUE
      RES=(THETA(M)-SAVE)/TEMAX
      IF(ABS(RES).GT.ABS(RESMAX))RESMAX=RES
      IF(THETA(M).GT.THMAX)THMAX=THETA(M)
25    CONTINUE
      THETA(1)=THETA(2)
      TEMAX=THMAX
      IF(((NITER+19)/20).EQ.(NITER/20))PRINT 102,NITER,RESMAX,TEMAX
      IF(ABS(RESMAX).LT.ABS(CON))GOTO27
      IF(NITER.GT.400)GOTO60
      GOTO10
27    CONTINUE
      WRITE(6,106)
      WRITE(6,102)NITER,RESMAX,TEMAX
      WRITE(6,108)
      DO30 M=1,MM
      WRITE(6,103)Z(M),ETA(M),U(M),THETA(M)
30    CONTINUE
      VSUM=0.0
      DO35 M=1,ML
      VSUM=VSUM+((U(M)+U(M+1))/2.0)*(Z(M+1)-Z(M))
35    CONTINUE
      WRITE(6,103)VSUM
      TAU(I)=ETA(M2)*(U(M2+1)-U(M2-1))/(Z(M2+1)-Z(M2-1))
      WRITE(6,107)
      WRITE(6,102)I,R(I),TAU(I),P(I)
40    CONTINUE
      DO50 I=1,IL
      SUMBIT=(TAU(I)+TAU(I+1))*(R(I+1)-R(I))*R(I)
      WRITE(6,103)SUMBIT
      SUM=SUM+SUMBIT
50    CONTINUE
      SUM=SUM/(ETA0*UBALL)
      RMU=USTAR*WSTAR**(-1.0/3.0)*SUM*2.0*3.14159265*1.31/HOSTAR
      G1=RMU*WSTAR/USTAR
      G2=USTAR/SQRT(WSTAR**3*GSTAR)
      WRITE(6,104)
      WRITE(6,103)UBALL,PMAX,HOSTAR,SUM
      WRITE(6,105)
      WRITE(6,103)RMU,G1,G2
60    CONTINUE
101   FORMAT(1H1//)
102   FORMAT(I16,4(1PE16.4),///)
103   FORMAT(6(1PE16.4))
104   FORMAT(6X,6H UBALL,10X,6H PMAX ,10X,6HHOSTAR,10X,6H SUM  )
105   FORMAT(6X,6H RMU  ,10X,6HMU*W/U,10X,6HU/F(W*G))
106   FORMAT(6X,6H NITER,10X,6HRESMAX,10X,6H TEMAX)
107   FORMAT(6X,6H      I,10X,6H R(I) ,10X,6HTAU(I),10X,6H P(I) )
108   FORMAT(//6X,6H Z(M) ,10X,6HETA(M),10X,6H U(M) ,10X,8HTHETA(M)//)
      STOP
      END
```

Appendix 5. PROGRAM TO DERIVE α-VALUE FROM FRICTION MEASUREMENTS

Equation 6.10, the expression for μ in an isothermal distorted contact, may be written as:-

$$G^{*5/7} = N \left(\frac{e^{\bar{p}_m} (\bar{p}_m - 1) + 1}{\bar{p}_m^{\,2}} \right) \qquad \text{-A5.1}$$

where $N = \dfrac{7.8\ \delta^*\ U^{*2/7}\ W^{*-2/7}}{\mu}$

and $\bar{p}_m = 0.366\ W^{*1/3}\ G^*$ -A5.2

Using equation A5.2 and remembering that $G^* = \alpha E'$, an expression for α in terms of $\bar{p}_m$ may be obtained:-

$$\alpha = \left[Q \left(e^{\bar{p}_m} (\bar{p}_m - 1) + 1 \right) \right]^{7/19} \qquad \text{-A5.3}$$

where $Q = \dfrac{N}{0.366^2\ W^{*2/3}\ E'^{19/7}}$

Equation A5.3 may also be re-arranged with $\bar{p}_m$ as the subject:-

$$\bar{p}_m = \left(\frac{\alpha^{19/7}}{Q} - 1 \right) \Big/ \left(\alpha . 0.366\ W^{*1/3}\ E' \right) + 1 \qquad \text{-A5.4}$$

Equation A5.3 was found to be highly unstable when used alone to obtain α. A more sophisticated procedure was therefore employed using both equations A5.3 and A5.4. The details of the procedure are shown later on, in the flow chart and listing. It may, however, be demonstrated graphically as shown below.

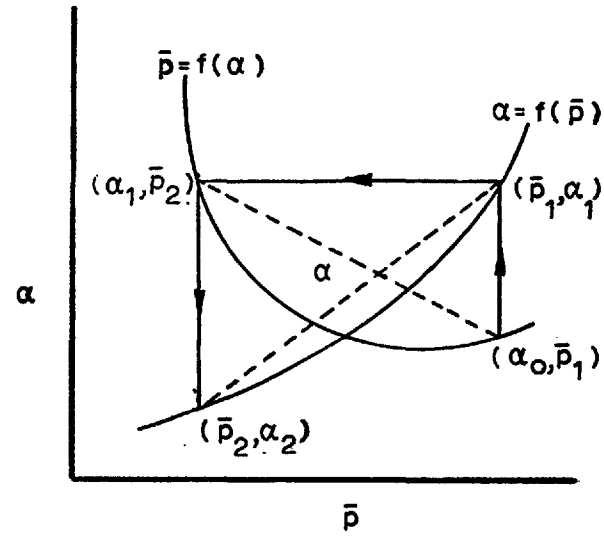
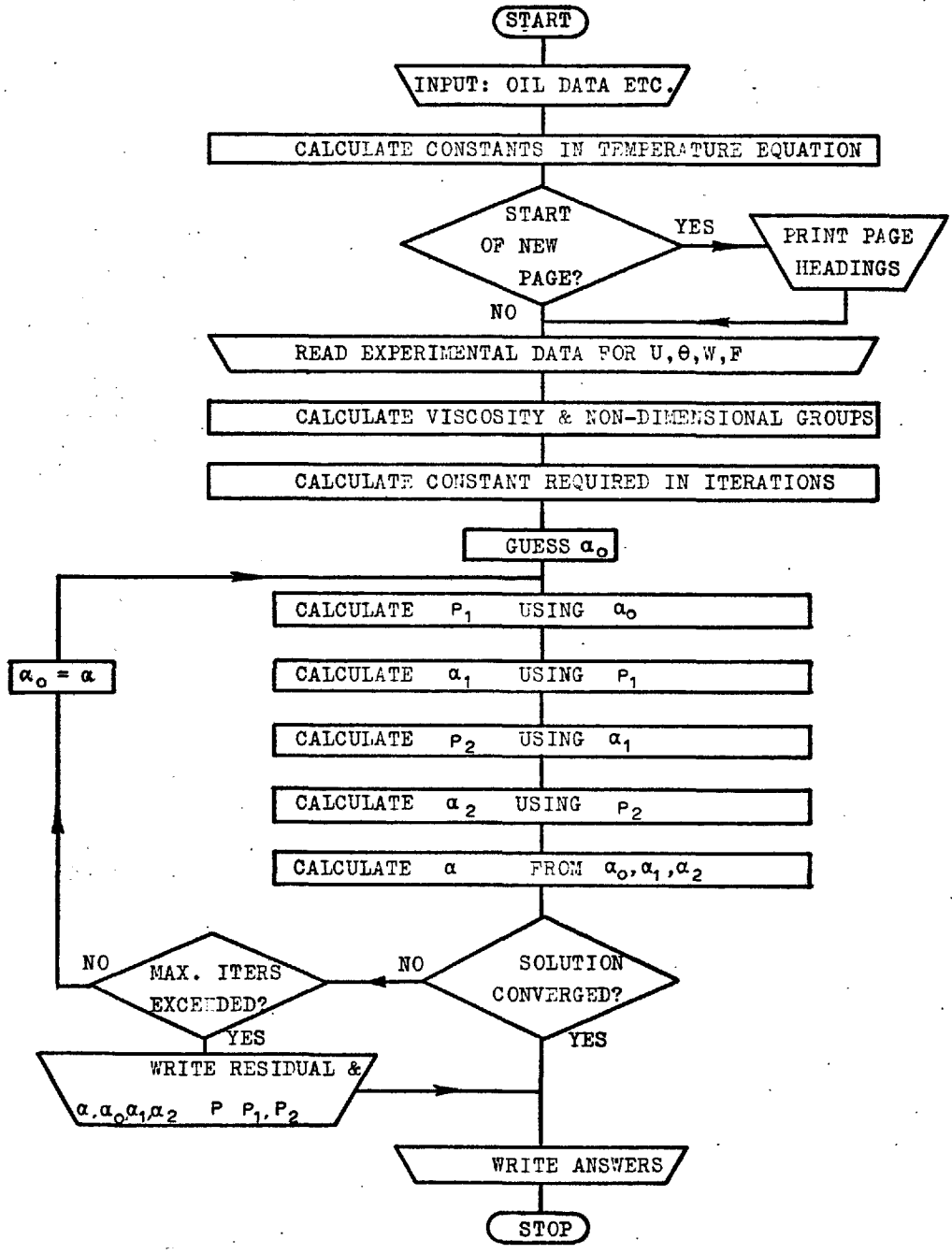


Fig.A.5.1Iteration procedure for program ALFRIC.

α_o is a guessed value and is used as a starting point for calculating α_1 and α_2. The equations are then approximated by straight lines and the intersection at α found from

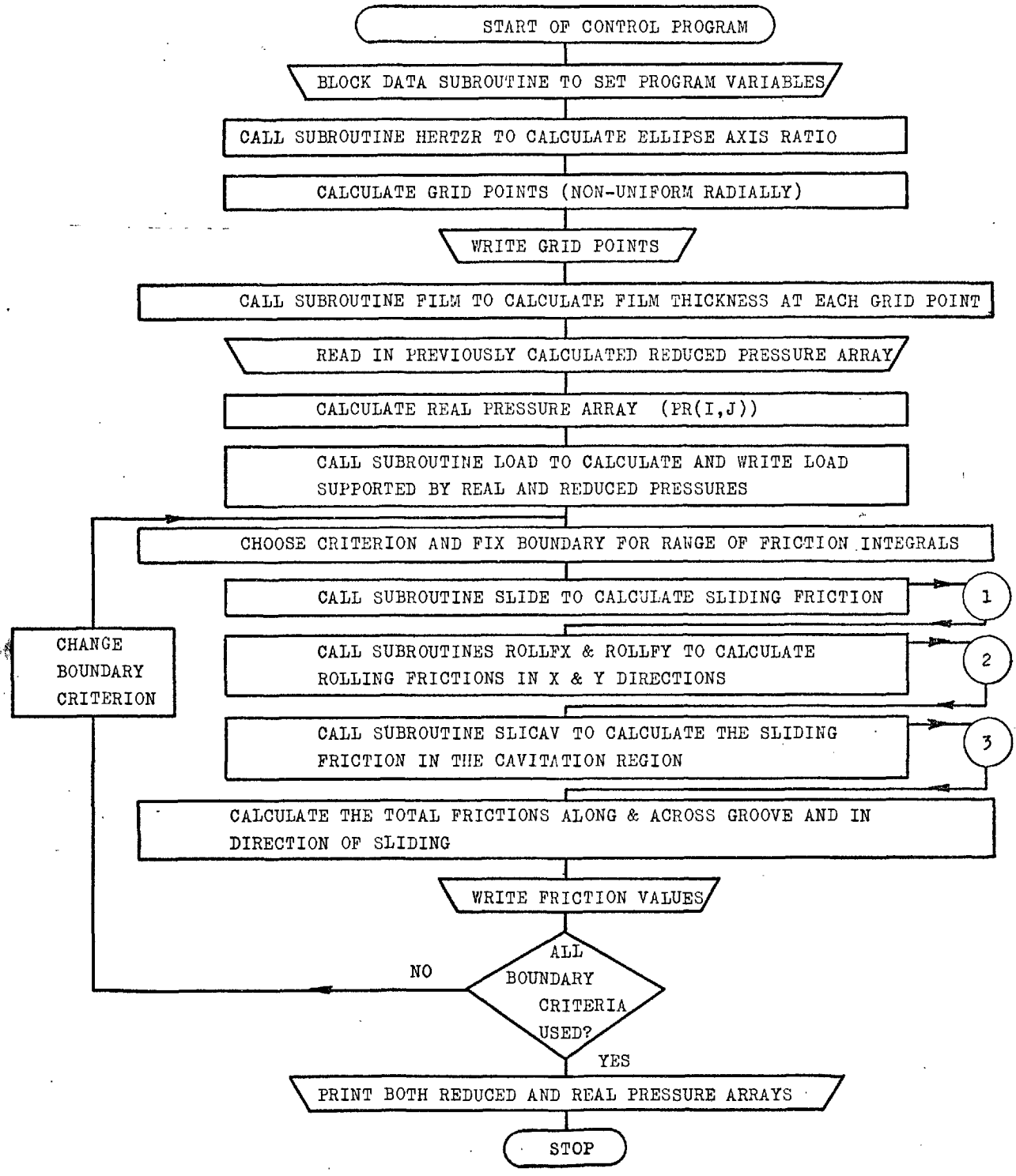
$$\alpha = \frac{\alpha_1^2 - \alpha_2\alpha_o}{2\alpha_1 - \alpha_o - \alpha_2} \qquad \text{-A5.5}$$

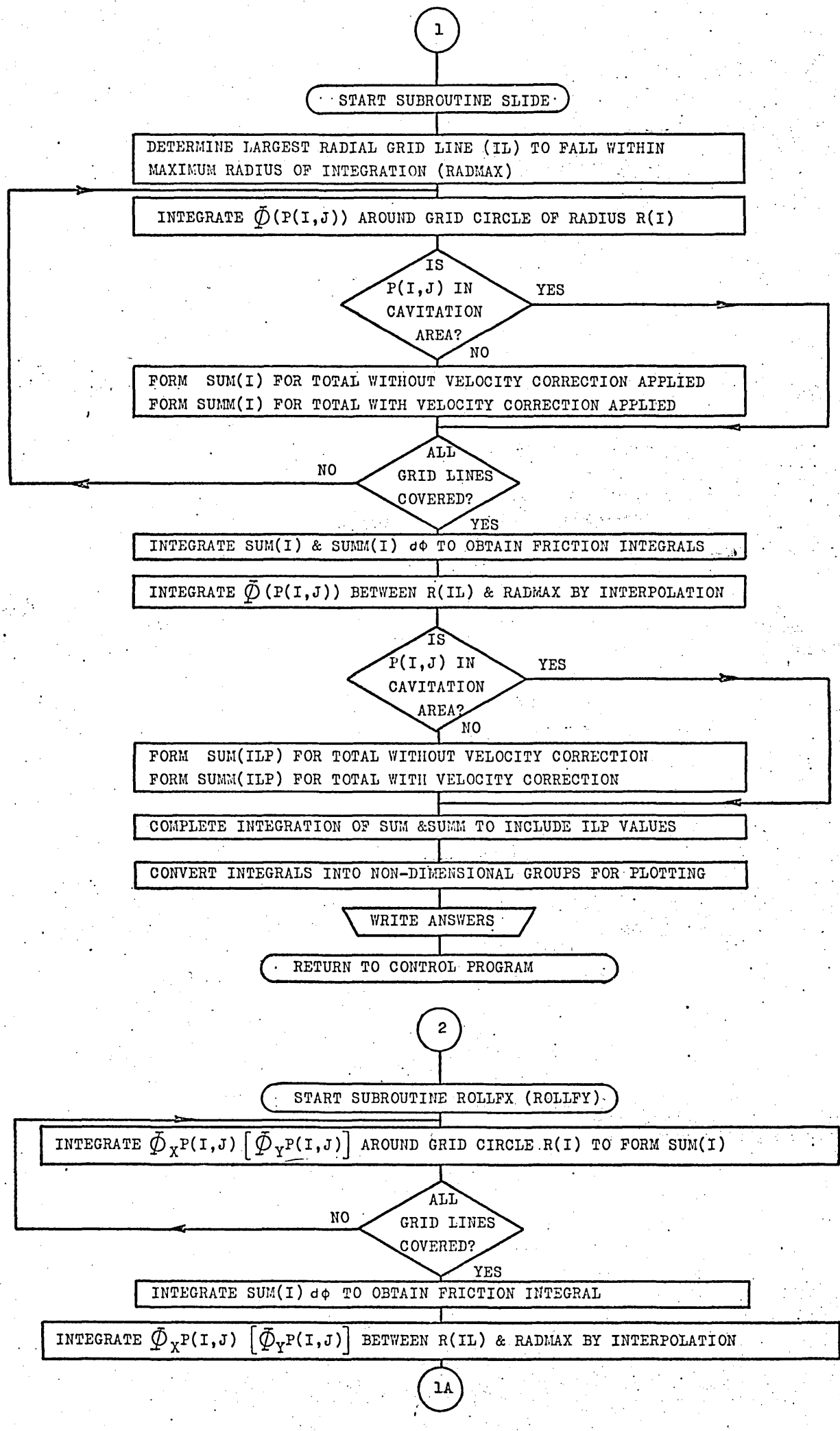
α is then used as the guess in the next calculation cycle.

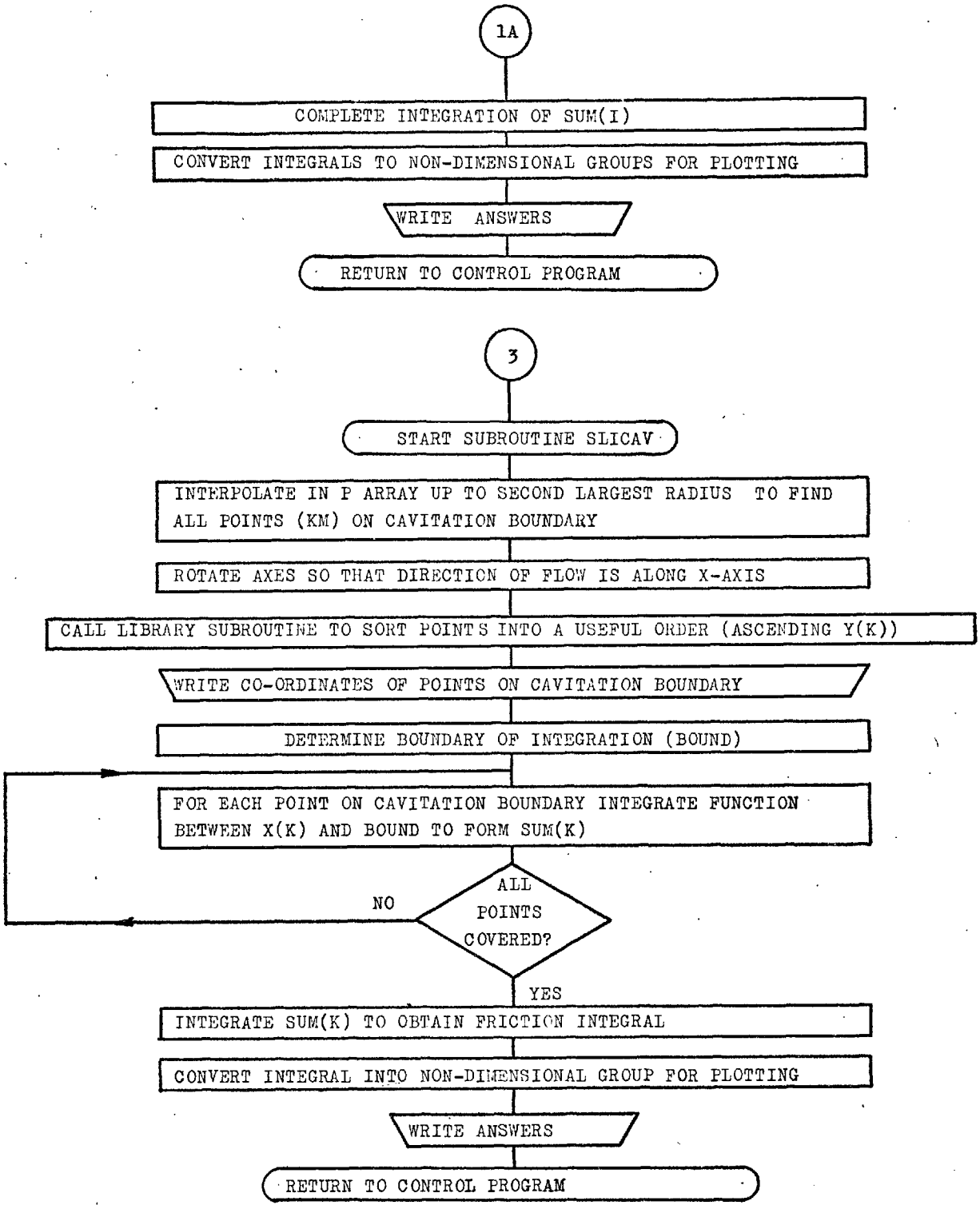

START
INPUT: OIL DATA ETC.
CALCULATE CONSTANTS IN TEMPERATURE EQUATION
START OF NEW PAGE?
YES
PRINT PAGE HEADINGS
NO
READ EXPERIMENTAL DATA FOR U,θ,W,F
CALCULATE VISCOSITY & NON-DIMENSIONAL GROUPS
CALCULATE CONSTANT REQUIRED IN ITERATIONS
GUESS α_o
CALCULATE P_1 USING α_o
$\alpha_o = \alpha$
CALCULATE α_1 USING P_1
CALCULATE P_2 USING α_1
CALCULATE α_2 USING P_2
CALCULATE α FROM $\alpha_o, \alpha_1, \alpha_2$
NO
MAX. ITERS EXCEEDED?
NO
SOLUTION CONVERGED?
YES
YES
WRITE RESIDUAL & $\alpha, \alpha_o, \alpha_1, \alpha_2$ P P_1, P_2
WRITE ANSWERS
STOP

```
C*********************************************************************
C     PROGRAM ALFRIC TO DERIVE ALPHA-VALUES FROM FRICTION DATA
C*********************************************************************
      DATA  ED/0.89E6/
      DATA RB,ELLR/0.5,4.532/
      DATA  GAMMA/1.8E-4/
      DATA  CC/0.001/
      DATA  NITMAX/50/
      DATA GEAR/7.2E4/
      DATA  T1,V1/37.78,1189.0/
      DATA  T2,V2/60.0,287.3/
      DATA RH03,T3/0.91,20.0/
      DATA RH04,T4/0.8985,37.78/
      DATA  ARM1,ARM2/1.0,3.375/
      KOUNT=40
CONVERT TEMPERATURES TO DEGREES ABSOLUTE
      T1=T1+273.0
      T2=T2+273.0
      T3=T3+273.0
      T4=T4+273.0
      GEAR=3.14159265/GEAR
      GEAR=GEAR*20.0
CALCULATE THE CONSTANTS IN THE WALTHER-ASTM EQUATION   (A AND B)
      X=ALOG(ALOG(V1+0.6))
      Y=ALOG(ALOG(V2+0.6))
      WW=ALOG(T1)
      Z=ALOG(T2)
      B=(X-Y)/(Z-WW)
      A=0.5*(X+Y+B*(WW+Z))
   50 CONTINUE
      ALPHA=GAMMA
      IF(KOUNT.NE.40)GOTO55
      WRITE(6,101)
      WRITE(6,103)ED
      WRITE(6,104)
      KOUNT=0
   55 CONTINUE
      KOUNT=KOUNT+1
      READ(5,100)UD,T,WD,FF
      IF(UD.LT.-1.0)KOUNT=40
      IF(UD.LT.-1.0)GOTO50
      IF(T.LT.-273.0)GOTO 200
      T=273.0+T
      U=UD*GEAR
CALCULATE ABSOLUTE VISCOSITY IN REYNS   (ETA)
      RHO=RH03+((T-T3)*(RH04-RH03))/(T4-T3)
      V=EXP(EXP(A-B*ALOG(T)))-0.6
      ETA=V*RHO
      ETAM=ETA
      ETA=ETA*1.4503E-7
CALCULATE NON-DIMENSIONAL VELOCITY   (UBAR)
      UBAR=(U*ETA)/(ED*RB)
CALCULATE NON-DIMENSIONAL LOAD (WBAR)
CALCULATE THE MAXIMUM HERTZ STRESS
      WBAR=WD/(ED*RB**2)
      AH=0.721*(WD*RB*4.0/ED)**(1.0/3.0)
      PMAX=(1.5*WD)/(AH**2*3.14159265)
CORRECT MEASURED FORCES FOR DIFFERING MOMENT ARMS
      FF=(FF*ARM1)/(ARM2*64.0)
CALCULATE FRICTION COEFFICIENT
      FMU=FF/WD
      ANUM=(7.8*(UBAR/WBAR)**(2.0/7.0))/FMU
      BNUM=((0.366)**2)*((WBAR)**(2.0/3.0))*((ED)**(19.0/7.0))
      AMULT=ANUM/BNUM
      TERM=0.366*ED*WBAR**(1.0/3.0)
      NITER=0
   60 CONTINUE
      AKEEP=ALPHA
      ALPHA0=ABS(ALPHA)
      PMBAR1=(((((ALPHA0**(19.0/7.0))/AMULT)-1.0)/EXP(TERM*ALPHA0))+1.0)
      ALPHA1=(AMULT*(EXP(PMBAR1)*(PMBAR1-1.0)+1.0))**(7.0/19.0)
      PMBAR2=(((((ALPHA1**(19.0/7.0))/AMULT)-1.0)/EXP(TERM*ALPHA1))+1.0)
      ALPHA2=(AMULT*(EXP(PMBAR2)*(PMBAR2-1.0)+1.0))**(7.0/19.0)
      ALPHA=(ALPHA1**2-ALPHA2*ALPHA0)/(2.0*ALPHA1-ALPHA0-ALPHA2)
      RES=(AKEEP-ALPHA)/ALPHA
      NITER=NITER+1
      IF(ABS(RES).LT.CC)GOTO65
      IF(NITER.LT.NITMAX)GOTO60
      WRITE(6,151)RES,ALPHA,NITER,ALPHA1,ALPHA2,PMBAR1,PMBAR2
   65 CONTINUE
      WRITE(6,150)UD,ETAM,U,WBAR,FMU,UBAR,PMAX,ALPHA
      GOTO50
  100 FORMAT(4(F10.2))
  101 FORMAT(1H1,//)
  103 FORMAT(46X,16HREDUCED MODULUS = ,1PE16.4,/)
  104 FORMAT(1HO,7X,5HTACHO,11X,8HABSOLUTE,8X,7HSURFACE,10X,
     12HW*,15X,2HMU,14X,2HU*,12X,5HPMAX ,10X,5HALPHA,/
     27X,7HREADING,10X,9HVISCOSITY,7X,8HVELOCITY,/,
     361X,1H2,/
     48X,3HTPM,15X,2HCP,12X,7HINS/SEC,9X,5HW/E.R,12X,4HFF/W,9X,
     510HETA0.U/E.R,6X,9HLBF/SQ.IN,7X,9HSQ.IN/LBF///)
  150 FORMAT(8(1PE16.4))
  151 FORMAT(2(1PE16.4),I10,6(1PE16.4))
  200 STOP
      END
```

Appendix 6. SUBROUTINES TO CALCULATE FRICTION IN UNDISTORTED CONTACTS




1
START SUBROUTINE SLIDE
DETERMINE LARGEST RADIAL GRID LINE (IL) TO FALL WITHIN MAXIMUM RADIUS OF INTEGRATION (RADMAX)
INTEGRATE $\bar{\Phi}$(P(I,J)) AROUND GRID CIRCLE OF RADIUS R(I)
IS P(I,J) IN CAVITATION AREA?
YES
NO
FORM SUM(I) FOR TOTAL WITHOUT VELOCITY CORRECTION APPLIED
FORM SUMM(I) FOR TOTAL WITH VELOCITY CORRECTION APPLIED
ALL GRID LINES COVERED?
NO
YES
INTEGRATE SUM(I) & SUMM(I) dΦ TO OBTAIN FRICTION INTEGRALS
INTEGRATE $\bar{\Phi}$(P(I,J)) BETWEEN R(IL) & RADMAX BY INTERPOLATION
IS P(I,J) IN CAVITATION AREA?
YES
NO
FORM SUM(ILP) FOR TOTAL WITHOUT VELOCITY CORRECTION
FORM SUMM(ILP) FOR TOTAL WITH VELOCITY CORRECTION
COMPLETE INTEGRATION OF SUM &SUMM TO INCLUDE ILP VALUES
CONVERT INTEGRALS INTO NON-DIMENSIONAL GROUPS FOR PLOTTING
WRITE ANSWERS
RETURN TO CONTROL PROGRAM
2
START SUBROUTINE ROLLFX (ROLLFY)
INTEGRATE $\bar{\Phi}_X P(I,J)\left[\bar{\Phi}_Y P(I,J)\right]$ AROUND GRID CIRCLE R(I) TO FORM SUM(I)
ALL GRID LINES COVERED?
NO
YES
INTEGRATE SUM(I) dΦ TO OBTAIN FRICTION INTEGRAL
INTEGRATE $\bar{\Phi}_X P(I,J)\left[\bar{\Phi}_Y P(I,J)\right]$ BETWEEN R(IL) & RADMAX BY INTERPOLATION
1A


1A
COMPLETE INTEGRATION OF SUM(I)
CONVERT INTEGRALS TO NON-DIMENSIONAL GROUPS FOR PLOTTING
WRITE ANSWERS
RETURN TO CONTROL PROGRAM
3
START SUBROUTINE SLICAV
INTERPOLATE IN P ARRAY UP TO SECOND LARGEST RADIUS TO FIND ALL POINTS (KM) ON CAVITATION BOUNDARY
ROTATE AXES SO THAT DIRECTION OF FLOW IS ALONG X-AXIS
CALL LIBRARY SUBROUTINE TO SORT POINTS INTO A USEFUL ORDER (ASCENDING Y(K))
WRITE CO-ORDINATES OF POINTS ON CAVITATION BOUNDARY
DETERMINE BOUNDARY OF INTEGRATION (BOUND)
FOR EACH POINT ON CAVITATION BOUNDARY INTEGRATE FUNCTION BETWEEN X(K) AND BOUND TO FORM SUM(K)
ALL POINTS COVERED?
NO
YES
INTEGRATE SUM(K) TO OBTAIN FRICTION INTEGRAL
CONVERT INTEGRAL INTO NON-DIMENSIONAL GROUP FOR PLOTTING
WRITE ANSWERS
RETURN TO CONTROL PROGRAM

```
      BLOCK DATA
C*********************************************************************
C     INPUT OF PRGRAM VARIABLES
C*********************************************************************
      COMMON/CONE/P(40,40),H(40,40),R(40),PHI(40),THETA,PYE3
      COMMON/CTWO/M,N
      COMMON/CFIVE/RATIO
      COMMON/CSEV/PYE2
      COMMON/CEIGHT/CC,GRID
      COMMON/CNINE/NL,W(20),ML,CI
      COMMON/CTWEL/PCAV,PCAVB
      COMMON/CFIFT/GSTAR,GKEEP,HSTAR
      DATA  PCAVB/1.0E-10/
      DATA  PCAV/0.0/
      DATA  CI/0.10/
      DATA  RATIO/0.099099/
      DATA  GSTAR/2.9056E3/
      DATA  THETA/67.0/
      DATA  N/36/
      DATA  M/31/
      DATA  PYE2/1.0/
      DATA  CC/5.0E-4/
      DATA  GRID/1.80/
      END



      PROGRAM RIGIDF(INPUT,OUTPUT,TAPE5=INPUT,TAPE6=OUTPUT)
C*********************************************************************
C     MAIN PRGRAM TO CALCULATE THE FRICTION IN AN UNDISTORTED CONTACT
C*********************************************************************
      DIMENSION ATITLE(6,3)
      DIMENSION ANAME(6,2)
      DIMENSION AR(40)
      COMMON/CONE/P(40,40),H(40,40),R(40),PHI(40),THETA,PYE3
      COMMON/CTWO/M,N
      COMMON/CTHREE/I,J
      COMMON/CFOUR/ELLR,ELLMD,ELLND
      COMMON/CFIVE/RATIO
      COMMON/CSIX/PR(40,40)
      COMMON/CSEV/PYE2
      COMMON/CEIGHT/CC,GRID
      COMMON/CNINE/NL,W(20),ML,CI
      COMMON/CTEN/PMAX,PMAXI,RESM,IKEEP,JKEEP
      COMMON/CELEV/NITER
      COMMON/CTWEL/PCAV,PCAVB
      COMMON/CFOREN/FROLLX,FROLLY,FRCAV1,FSFX,FSFLX
      COMMON/CFIFT/GSTAR,GKEEP,HSTAR
      COMMON/CSIXT/RADMAX,XBOUND,IL
      READ(5,108)ATITLE
      READ(5,108)ANAME
      THETA=THETA*3.14159265/180.0
      MM=M-1
      NN=N-1
      WRITE(6,100)
      CALL HERTZR
C
C     CALCULATE AND PRINT THE R VALUES FOR NON-UNIFORM GRID
      Z=0.05/(1.0-GRID)
      DO10 I=1,10
      K=11-I
   10 R(I)=1.0+Z*(1.0-GRID**K)
      DO20 I=11,31
      K=31-I
   20 R(I)=0.05*FLOAT(K)
      DO30 I=1,M
      II=M-I+1
   30 AR(I)=R(II)
      DO40 I=1,M
      R(I)=AR(I)
   40 WRITE(6,101)I,R(I)
C
C    CALCULATE AND PRINT THE PHI VALUES
C
      Z=360.0/FLOAT(N)
      DO50 J=1,N
      PHI(J)=FLOAT(J)*Z
      WRITE(6,102)J,PHI(J)
   50 PHI(J)=PHI(J)*3.14159265/180.0
      CALL FILM
C
C     READ IN THE PREVIOUSLY CALCULATED VALUES OF P(I,J)
C
      DO60 I=1,M
      DO60 J1=1,N,6
      J6=J1+5
```

```
   60 READ(5,103)(P(I,J),J=J1,J6)
      DO70 I=1,M
      DO70 J=1,N
      IF(P(I,J).GT.1.0.OR.P(I,J).LT.0.0)P(I,J)=0.0
   70 PR(I,J)=-ALOG(ABS(1.0-P(I,J)))
      CALL LOAD(40,40,P,M,N,1,ANAME)
      CALL LOAD(40,40,PR,M,N,2,ANAME)
      WRITE(6,104)
      DO80 L=1,3
      WSTAR=1.53E-6
      IF(L.EQ.1)WSTAR=1.67E-7
      XBOUND=0.23
      HSTAR=GKEEP*GSTAR*WSTAR
      RADMAX=XBOUND/SQRT(2.0*HSTAR)
      IF(L.EQ.3)RADMAX=2.5
      WRITE(6,106)RADMAX
      WRITE(6,107)XBOUND
      CALL SLIDE
      CALL ROLLFX
      CALL ROLLFY
      CALL SLICAV
      FROLL=FROLLX*COS(THETA)+FROLLY*SIN(THETA)
      TF=FROLL+FSFLX+FRCAV1
      TFX=TF*COS(THETA)
      TFY=TF*SIN(THETA)
      WRITE(6,105)TFX,TF,TFY
   80 CONTINUE
      CALL PRINTC(40,40,P,M,N,1,ATITLE)
      CALL PRINTC(40,40,PR,M,N,2,ATITLE)
  100 FORMAT(1H1)
  101 FORMAT(5H   I=,I6,9H   R(I)= ,F16.7)
  102 FORMAT(5H   J=,I6,9H PHI(J)= ,F16.7)
  103 FORMAT(6(1PE12.4))
  104 FORMAT(1H1,
     18X,59HFFFFFFF  RRRRRR   I   CCCCCC  TTTTTTT   I   000000   NN     N,
     2/,
     39X,59HF        R     R  I   C          T      I   0    0   N N    N,
     4/,
     59X,59HFFF      RRRRRR   I   C          T      I   0    0   N  N   N,
     6/,
     79X,59HF        R  R     I   C          T      I   0    0   N   N  N,
     8/,
     99X,59HF        R   R    I   CCCCCC     T      I   000000   N    NN)
  105 FORMAT(9X,32HTOTAL FRICTION ALONG GROOVE AXIS,////
     19X,2HW*,/,9X,8H--,MU = ,1PE11.3,/,9X,2HU*,////,
     29X,35HTOTAL FRICTION IN SLIDING DIRECTION,////,
     39X,2HW*,/,9X,8H--,MU = ,1PE11.3,/,9X,2HU*,////,
     49X,43HTOTAL FRICTION PERPENDICULAR TO GROOVE AXIS,////
     59X,2HW*,/,9X,8H--,MU = ,1PE11.3,/,9X,2HU*,////)
  106 FORMAT(/5X,9HRADMAX = ,1PE12.4)
  107 FORMAT(/5X,9HXBOUND = ,1PE12.4,/)
  108 FORMAT(6A6)
      STOP
      END
```

```
      SUBROUTINE SLIDE
C*****************************************************************
C     SUBROUTINE TO CALCULATE THE SLIDING FRICTION
C*****************************************************************
      DIMENSION SUM(40)
      DIMENSION SUMM(40)
      COMMON/CONE/P(40,40),H(40,40),R(40),PHI(40),THETA,PYE3
      COMMON/CTWO/M,N
      COMMON/CFOUR/ELLR,ELLMD,ELLND
      COMMON/CTWEL/PCAV,PCAVB
      COMMON/CFOREN/FROLLX,FROLLY,FRCAV1,FSFX,FSFLX
      COMMON/CFIFT/GSTAR,GKEEP,HSTAR
      COMMON/CSIXT/RADMAX,XBOUND,IL
C
C     CALCULATION OF THE FULL FILM SLIDING FRICTION
C     USING THE CORRECT VELOCITY EXPRESSION AT LARGE VALUES OF RADIUS
C
      IL=M
      IF(RADMAX.GE.R(M))GOTO40
      DO30 I=1,M
      IF(RADMAX-R(I).GT.0.0)GOTO30
      IL=I-1
      GOTO 40
   30 CONTINUE
   40 CONTINUE
      NM=N-1
      ILM=IL-1
      ILP=IL+1
```

```
      SUM(1)=0.0
      SUMM(1)=0.0
      DO50 I=2,IL
      SUM(I)=0.5*R(I)*PHI(1)*(SLIP1(I,N)+SLIP1(I,1))
      SUMM(I)=0.5*R(I)*PH1(I)*(SLIP2(I,N)+SLIP2(I,1))
      IF(P(I,1).LE.PCAV.AND.P(I,N).LE.PCAV)GOTO45
      GOTO 46
   45 CONTINUE
      SUM(1)=0.0
      SUMM(I)=0.0
   46 CONTINUE
      DO50 J=1,NM
      JP=J+1
      IF(P(I,J).LE.PCAV.AND.P(I,JP).LE.PCAV)GOTO50
      SUM(I)=SUM(I)+0.5*R(I)*(PHI(JP)-PHI(J))*(SLIP1(I,J)+SLIP1(I,JP))
      SUMM(I)=SUMM(I)+0.5*R(1)*(PHI(JP)-PHI(J))*(SLIP2(I,J)+SLIP2(I,JP))
   50 CONTINUE
      FSF=0.0
      FSFL=0.0
      DO53 I=1,ILM
      IP=I+1
      FSF=FSF+0.5*(SUM(I)+SUM(IP))*(R(IP)-R(I))
      FSFL=FSFL+0.5*(SUMM(I)+SUMM(IP))*(R(IP)-R(I))
   53 CONTINUE
      IF(RADMAX-R(M).GE.0.0)GOTO57
      SUM (ILP)=0.0
      SUMM(ILP)=0.0
      FRACT=(RADMAX-R(IL))/(R(ILP)-R(IL))
      IF(P(IL,1).LE.PCAV.AND.P(IL,N).LE.PCAV)GOTO55
      SUM (ILP)=0.5*RADMAX*PHI(1)*(
     1(SLIP1(IL,N)+(SLIP1(ILP,N)-SLIP1(IL,N))*FRACT)+
     2(SLIP1(IL,1)+(SLIP1(ILP,1)-SLIP1(IL,1))*FRACT))
      SUMM(ILP)=0.5*RADMAX*PHI(1)*(
     1(SLIP2(IL,N)+(SLIP2(ILP,N)-SLIP2(IL,N))*FRACT)+
     2(SLIP2(IL,1)+(SLIP2(ILP,1)-SLIP2(IL,1))*FRACT))
   55 CONTINUE
      DO56 J=1,NM
      JP=J+1
      IF(P(IL,J).LE.PCAV.AND.P(IL,JP).LE.PCAV)GOTO56
      SUM (ILP)=SUM (ILP)+0.5*RADMAX*(PHI(JP)-PHI(J))*(
     1(SLIP1(IL,J)+(SLIP1(ILP,J)-SLIP1(IL,J))*FRACT)+
     2(SLIP1(IL,JP)+(SLIP1(ILP,JP)-SLIP1(IL,JP))*FRACT))
      SUMM(ILP)=SUMM(ILP)+0.5*RADMAX*(PHI(JP)-PHI(J))*(
     1(SLIP2(IL,J)+(SLIP2(ILP,J)-SLIP2(IL,J))*FRACT)+
     2(SLIP2(IL,JP)+(SLIP2(ILP,JP)-SLIP2(IL,JP))*FRACT))
   56 CONTINUE
      FSF =FSF +0.5*(SUM (IL)+SUM (ILP))*(RADMAX-R(IL))
      FSFL=FSFL+0.5*(SUMM(IL)+SUMM(ILP))*(RADMAX-R(IL))
   57 CONTINUE
      FSFX=FSF*ELLR*2.0
      FSFLX=FSFL*ELLR*2.0
      FSFC=FSF-FSFL
      FSFCX=FSFX-FSFLX
      WRITE(6,1002)FSF,FSFX
      WRITE(6,1004)FSFL,FSFLX
      WRITE(6,1003)FSFC,FSFCX
      IF(FSFLX.GT.FSFX)FSFLX=FSFX
 1000 FORMAT(I10)
 1001 FORMAT(1PE12.4)
 1002 FORMAT(////,9X,40HFULL-FILM SLIDING FRICTION (APPROXIMATE),///
     19X,6X,2HFS,36X,2HW*,/
     29X,23H-------------,(A/B) = ,1PE11.3,10X,8H--,MU = ,1PE11.3,/
     39X,14H2R,ETA0(U2-U1),30X,2HU*,///)
 1003 FORMAT(////,9X,44HFULL-FILM SLIDING FRICTION (CORRECTION TERM),///
     19X,6X,2HFS,36X,2HW*,/
     29X,23H-------------,(A/B) = ,1PE11.3,10X,8H--,MU = ,1PE11.3,/
     39X,14H2R,ETA0(U2-U1),30X,2HU*,///)
 1004 FORMAT(////,9X,38HFULL-FILM SLIDING FRICTION (CORRECTED),///
     19X,6X,2HFS,36X,2HW*,/
     29X,23H-------------,(A/B) = ,1PE11.3,10X,8H--,MU = ,1PE11.3,/
     39X,14H2R,ETA0(U2-U1),30X,2HU*,///)
      RETURN
      END



      FUNCTION SLIP1(I,J)
      COMMON/CONE/P(40,40),H(40,40),R(40),PHI(40),THETA,PYE3
      SLIP1=1.0/(H(I,J)*(1.0-P(I,J)))
      RETURN
      END



      FUNCTION SLIP2(I,J)
      COMMON/CONE/P(40,40),H(40,40),R(40),PHI(40),THETA,PYE3
      COMMON/CFOUR/ELLR,ELLMD,ELLND
      COMMON/CF1FT/GSTAR,GKEEP,HSTAR
      SLIP2=(SQRT(ABS(1.0-2.0*HSTAR*((R(I)*COS(PHI(J)))**2+
     1(ELLR*R(I)*SIN(PHI(J)))**2))))/(H(I,J)*(1.0-P(I,J)))
      RETURN
      END
```

```
      SUBROUTINE ROLLFX
C*********************************************************************
C     SUBROUTINE TO CALCULATE THE X-DIRECTION ROLLING FRICTION
C*********************************************************************
      DIMENSION SUM(40)
      COMMON/CONE/P(40,40),H(40,40),R(40),PHI(40),THETA,PYE3
      COMMON/CTWO/M,N
      COMMON/CFOUR/ELLR,ELLMD,ELLND
      COMMON/CFOREN/FROLLX,FROLLY,FRCAV1,FSFX,FSFLX
      COMMON/CSIXT/RADMAX,XBOUND,IL
C
C     CALCULATION OF THE ROLLING FRICTION          (X-DIRECTION)
C
      ILL=IL-1
      ILP=IL+1
      NM=N-1
      MM=M-1
      SUM(1)=0.0
      SUM(M)=0.0
      DO20 I=2,MM
      SUM(I)=0.5*PHI(1)*(FRICTX(I,N)+FRICTX(I,1))
      DO20J=1,NM
      JP=J+1
   20 SUM(I)=SUM(I)+0.5*(PHI(JP)-PHI(J))*(FRICTX(I,J)+FRICTX(I,JP))
      FR=0.0
      DO30 I=1,ILL
      IP=I+1
   30 FR=FR+0.5*(SUM(I)+SUM(IP))*(R(IP)-R(I))
      IF(IL.EQ.M)GOTO35
      FR=FR+0.5*(2.0*SUM(IL)+(SUM(ILP)-SUM(IL))*(RADMAX-R(IL))/
     1(R(ILP)-R(IL)))*(RADMAX-R(IL))
   35 CONTINUE
      FRX=FR*ELLR
      FROLLX=12.0*FRX/PYE3
      WRITE(6,40)FROLLX
   40 FORMAT(///9X,30HROLLING FRICTION (X-DIRECTION),/
     1//,9X,2HW*,/,9X,8H--,MU = ,1PE11.3,/,9X,2HU*)
      RETURN
      END

      FUNCTION FRICTX(I,J)
      COMMON/CONE/P(40,40),H(40,40),R(40),PHI(40),THETA,PYE3
      COMMON/CSIX/PR(40,40)
      FRICTX=PR(I,J)*R(I)**2*COS(PHI(J))
      RETURN
      END


      SUBROUTINE ROLLFY
C*********************************************************************
C     SUBROUTINE TO CALCULATE THE Y-DIRECTION ROLLING FRICTION
C*********************************************************************
      DIMENSION SUM(40)
      COMMON/CONE/P(40,40),H(40,40),R(40),PHI(40),THETA,PYE3
      COMMON/CTWO/M,N
      COMMON/CFOUR/ELLR,ELLMD,ELLND
      COMMON/CFIVE/RATIO
      COMMON/CFOREN/FROLLX,FROLLY,FRCAV1,FSFX,FSFLX
      COMMON/CSIXT/RADMAX,XBOUND,IL
C
C     CALCULATION OF THE ROLLING FRICTION          (Y-DIRECTION)
C
      ILL=IL-1
      ILP=IL+1
      NM=N-1
      MM=M-1
      SUM(1)=0.0
      SUM(M)=0.0
      DO20 I=2,MM
      SUM(I)=0.5*R(1)*PHI(1)*(FRICTY(I,N)+FRICTY(I,1))
      DO20J=1,NM
      JP=J+1
   20 SUM(I)=SUM(I)+0.5*R(I)*(PHI(JP)-PHI(J))*(FRICTY(I,J)+FRICTY(I,JP))
      FR=0.0
      DO30 I=1,ILL
      IP=I+1
   30 FR=FR+0.5*(SUM(I)+SUM(IP))*(R(IP)-R(I))
      IF(IL.EQ.M)GOTO35
      FR=FR+0.5*(2.0*SUM(IL)+(SUM(ILP)-SUM(IL))*(RADMAX-R(IL))/
     1(R(ILP)-R(IL)))*(RADMAX-R(IL))
   35 CONTINUE
      FRY=FR*ELLR**2*RATIO
      FROLLY=12.0*FRY/PYE3
      WRITE(6,40)FROLLY
   40 FORMAT(///9X,30HROLLING FRICTION (Y-DIRECTION),/
     1//,9X,2HW*,/,9X,8H--,MU = ,1PE11.3,/,9X,2HU*)
      RETURN
      END

      FUNCTION FRICTY(I,J)
      COMMON/CONE/P(40,40),H(40,40),R(40),PHI(40),THETA,PYE3
      COMMON/CSIX/PR(40,40)
      FRICTY=PR(I,J)*R(I)**2*SIN(PHI(J))
      RETURN
      END
```

```
      SUBROUTINE SLICAV
C*****************************************************************
C     SUBROUTINE TO CALCULATE THE CAVITATION SLIDING FRICTION
C*****************************************************************
      DIMENSION SUM(300)
      COMMON/CONE/P(40,40),H(40,40),R(40),PHI(40),THETA,PYE3
      COMMON/CTWO/M,N
      COMMON/CFOUR/ELLR,ELLMD,ELLND
      COMMON/CFIVE/RATIO
      COMMON/CSEV/PYE2
      COMMON/CTWEL/PCAV,PCAVB
      COMMON/CTHIR/X(400),Y(400),INDEX(400),IWORK(400)
      COMMON/CFOREN/FROLLX,FROLLY,FRCAVI,FSFX,FSFLX
      COMMON/CSIXT/RADMAX,XBOUND,IL
      STH=SIN(THETA)
      CTH=COS(THETA)
      K=0
      ML=M-1
      DO100 J=1,N
      DO100 I=2,ML
      IL=I-1
      IF(.NOT.((P(IL,J).LT.PCAVB.AND.P(I,J).GE.PCAVB).OR.(P(IL,J).GT.
     1PCAVB.AND.P(I,J).LE.PCAVB)))GOTO100
      DELR=(PCAVB-P(IL,J))/(P(I,J)-P(IL,J))*(R(I)-R(IL))
      CPJ=COS(PHI(J))
      SPJ=SIN(PHI(J))
      K=K+1
      X(K)=(R(IL)+DELR)*(SPJ*STH-CPJ*CTH)
      Y(K)=(R(IL)+DELR)*(SPJ*CTH+CPJ*STH)
  100 CONTINUE
      DO150 I=2,ML
      DO150 J=1,N
      JL=J-1
      IF(J.EQ.1)JL=N
      IF(J.EQ.1)PHI(JL)=0.0
      IF(.NOT.((P(I,JL).LT.PCAVB.AND.P(I,J).GE.PCAVB).OR.(P(I,JL).GT.
     1PCAVB.AND.P(I,J).LE.PCAVB)))GOTO150
      DELPHI=(PCAVB-P(I,JL))/(P(I,J)-P(I,JL))*(PHI(J)-PHI(JL))
      CPDEL=COS(PHI(JL)+DELPHI)
      SPDEL=SIN(PHI(JL)+DELPHI)
      K=K+1
      X(K)=R(I)*(SPDEL*STH-CPDEL*CTH)
      Y(K)=R(I)*(SPDEL*CTH+CPDEL*STH)
  150 PHI(N)=2.0*3.14159265
      KM=K
      WRITE(6,502)KM
      CALL KB03A(Y,KM,KM,INDEX,IWORK)
CALCULATE THE INTEGRAL IN THE DIRECTION OF FLOW
      DO340 K=1,KM
      KK=INDEX(K)
      WRITE(6,500)K,Y(K),X(KK)
  340 CONTINUE
      RMAX=RADMAX
      DO350 K=1,KM
      IF(ABS(Y(K)).GE.ABS(RMAX))GOTO341
      GOTO342
  341 SUM(K)=0.0
      GOTO350
  342 CONTINUE
      L=0
      BOUND=SQRT(RMAX**2-Y(K)**2)
      BIT=RATIO*(ELLR*Y(K))**2
      SUM(K)=0.0
  346 L=L+1
      KK=INDEX(K)
      XX=-X(KK)+0.5*FLOAT(L-1)
      IF(ABS(XX).GT.ABS(BOUND))GOTO349
      XXX=XX+0.5
      IF(ABS(XXX).GT.ABS(BOUND))XXX=BOUND
      GAP1=1.0+PYE2*(XX**2+BIT)
      GAP2=1.0+PYE2*(XXX**2+BIT)
      SUM(K)=SUM(K)+0.5*(XXX-XX)*(1.0/GAP1**2+1.0/GAP2**2)
      GOTO346
  349 SUM(K)=SUM(K)*(1.0+PYE2*(X(KK)**2+BIT))
  350 CONTINUE
COMPLETE THE INTEGRATION  BY CONSIDERING THE Y-DIRECTION
      KML=KM-1
      FRCAV=0.0
      DO400 K=1,KML
      FRCAV=FRCAV+0.5*(SUM(K)+SUM(K+1))*(Y(K+1)-Y(K))
  400 CONTINUE
      FRCAV1=FRCAV*2.0*ELLR
      WRITE(6,501)FRCAV,FRCAV1
  440 CONTINUE
  500 FORMAT(I10,2(1PE16.4))
  501 FORMAT(////,9X,31HCAVITATED-FILM SLIDING FRICTION,////
     1 19X,6X,4HFCAV,34X,2HW*,/
     2 29X,23H--------------,(A/B) = ,1PE11.3,10X,8H--,MU = ,1PE11.3,/
     3 39X,14H2R,ETA0(U2-U1),30X,2HU*,///)
  502 FORMAT(9X,7HKMAX = ,I10)
      RETURN
      END
```

Appendix 7. SUMMARY OF AIR BEARING DATA

a) Glass raceway support shaft - upper bearing

Bearing type:- Single-plane admission, inherently compensated, admission plane on centre line

Special requirements:- Large radial clearance to minimise drag, operation from 60psig supply

Calculated bearing parameters:-

Length(nominal)	1.0 ins.
Diameter(nominal)	2.0 ins.
Clearance(radial)	0.001 ins.
Number of holes	18 equally spaced
Diameter of holes	0.014 ins.
Load capacity	24 lbf.
Stiffness	32,000 lbf/in.

b) Glass raceway support shaft - lower bearing

Bearing type:- Single plane admission, inherently compensated, admission plane on centre line

Special requirements:- Large radial clearance to minimise drag, operation from 60psig supply

Calculated bearing parameters:-

Length(nominal)	1.5 ins.
Diameter(nominal)	3.0 ins.
Clearance(radial)	0.0015 ins.
Number of holes	18 equally spaced
Diameter of holes	0.035 ins.
Load capacity	54 lbf.
Stiffness	48,000 lbf/in.

c) Lower raceway locating bearing

Bearing type:- Single plane admission, inherently compensated, admission plane on centre line

Special requirements:- Operation from 60psig supply

Calculated bearing parameters:-

Length(nominal)	1.0 ins.
Diameter(nominal)	8.0 ins.
Clearance(radial)	0.002 ins.
Number of holes	36 equally spaced
Diameter of holes	0.040 ins.
Load capacity	Length/diameter ratio outside range
Stiffness	of design chart.

d) Lower raceway thrust plate

Bearing type:- Plane thrust, inherently compensated single ring admission

Special requirements:- Maximum load capacity, operation from 60psig supply

Calculated bearing parameters:-

Inner radius	1.33 ins.
Outer radius	4.0 ins.
Feed hole p.c.d.	4.62 ins.
Number of holes	18 equally spaced
Diameter of holes	0.050 ins.
Load capacity	670 lbf.
Stiffness	3.56×10^{5} lb/in.
Resonant frequency	436 Hz.
Flow rate	1.25×10^{-2} lb/sec.
Film thickness(approx)	0.002 ins.

e) Ball dynamometer support bearings

Bearing type:-	Double-plane admission, inherently compensated, admission planes at 'quarter-stations'
Special requirements:-	Large radial clearance to minimise drag, operation from 60psig supply

Calculated bearing parameters:-

Length(nominal)	1.5 ins.
Diameter(nominal)	0.75 ins.
Clearance(radial)	0.001 ins.
Number of holes	12 equally spaced
Diameter of holes	0.30 ins.
Load capacity	17 lbf.
Stiffness	21,000 lbf/in.

f) Ball dynamometer brake disc locating bearing

Bearing type:-	Semi-annular, double thrust, inherently compensated, one thrust arc per side
Special requirements:-	Large axial clearance to minimise drag, operation from 60psig supply

Calculated bearing parameters:-

Inner radius	3.2 cm.
Outer radius	5.5 cm.
Feed hole pitch-circle radius	4 cm.
Length of arc	90°
Diameter of holes	0.040 ins.
Axial clearance	0.001 ins. each side
Stiffness, load etc.	No design procedures available.

Appendix 8. EDDY CURRENT DYNAMOMETER DESIGN

A8.1 Calculation of electromagnet coil data

The accompanying figure A8.1 shows the geometry of each of the electromagnets. The dimensions have largely been governed

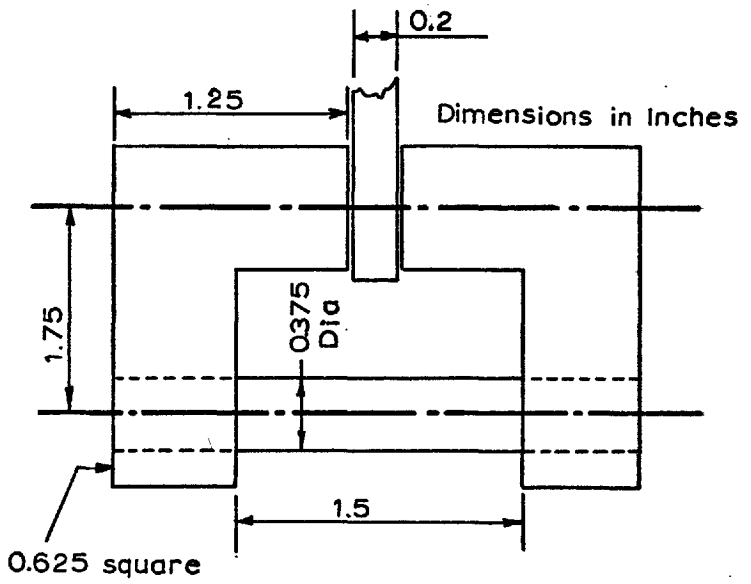


Figure A.8.1 Electromagnet

by space considerations and are summarised in the table below.

FLUX PATH	AREA (m^2)	LENGTH (m)
Core	0.712×10^{-4}	3.81×10^{-2}
Iron	2.52×10^{-4}	1.02×10^{-1}
Air (total)	2.52×10^{-4}	1.27×10^{-3}
Disc	2.52×10^{-4}	5.08×10^{-3}

Figure A8.2 shows a normal magnetisation (B - H) curve for 0.1% carbon mild steel; the data is taken from reference 1. Since the magnetic properties depend appreciably on heat treatment, mechanical working etc., the curve can only represent

---

1. Kaye and Laby 'Tables of physical and chemical constants' 13th. edition, Longmans, London.

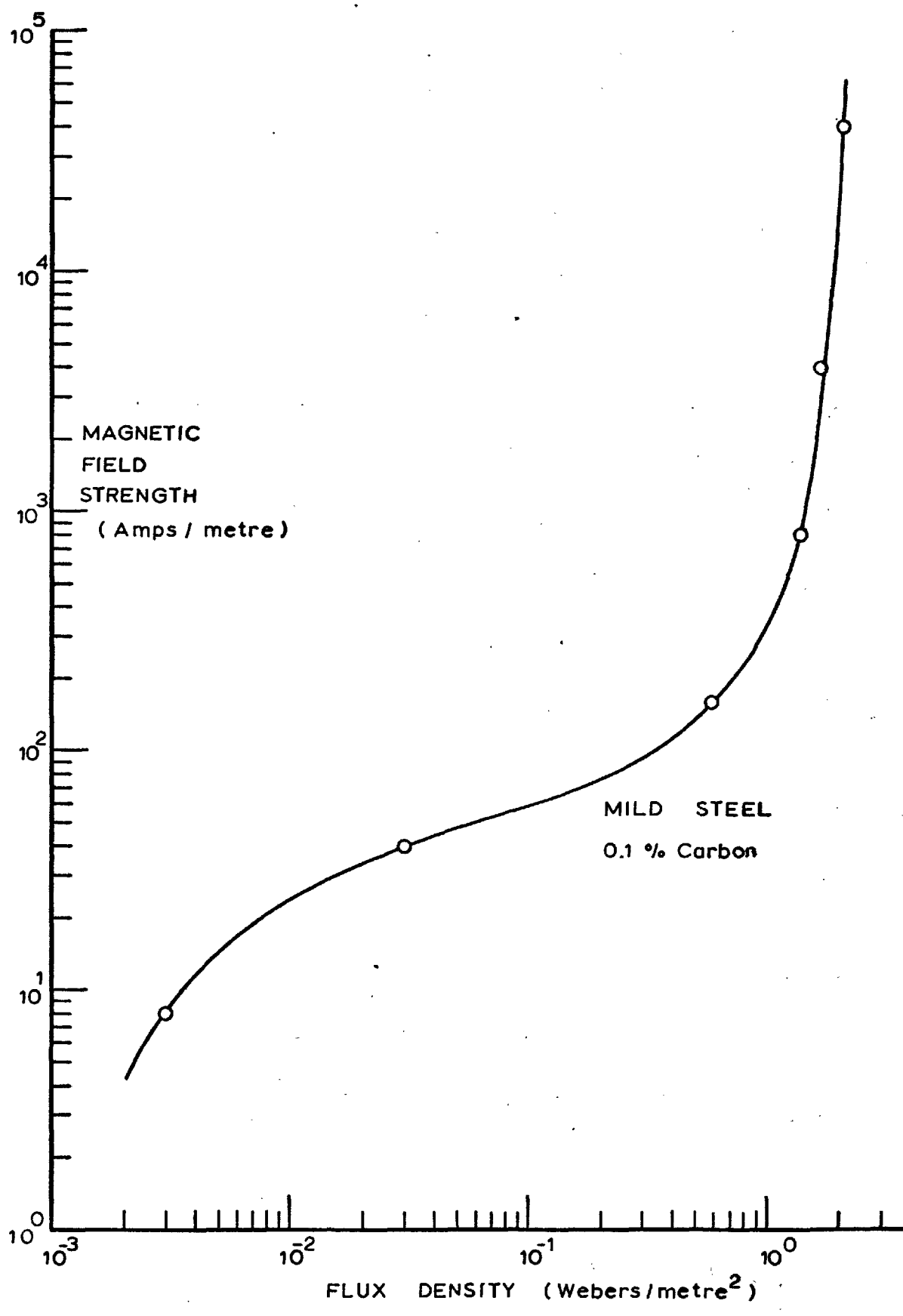


Figure A.8.2 Normal magnetisation curve for mild steel

the probable characteristics of the steel used and consequently high accuracy in the calculations is not justified.

The maximum magnetic flux in the circuit will be limited by the magnet core which will saturate (see figure A8.2) at a flux density of approximately 1 Wb/m^2 with a consequent total flux (B) of 0.71×10^{-4} Wb. Hence the flux density in the pole pieces will be 0.28 Wb/m^2. The necessary m.m.f's to produce these densities may be determined from figure A8.2 as 350A/m and 87A/m for the core and poles respectively.

Taking the permeability of free space (μ_o) as $4\pi \times 10^{-7}$ henry/m, the m.m.f. required to drive the flux across the air gap may be calculated from:-

$$H = \mu_o / B \qquad \text{-A8.1}$$
$$= 2.1 \times 10^5 \text{ A/m}$$

Within the accuracy of the calculations the permeability of aluminium (μ) may be taken as equal to μ_o and hence the m.m.f. required for the disc may also be calculated from A8.1 to be 2.1×10^5 A/m.

In these calculations flux leakage has been neglected as being small and no corrections have been made for fringing. Ignoring these corrections ensures a conservative design.

From the calculated m.m.f's and the lengths of the flux paths given in the table, an estimate of the number of ampere turns required may be obtained as 1450 amp. turns.

The maximum number of turns which it is possible to fit on the coil using 28s.w.g. varnish-insulated wire is apprximately 2000. For maximum braking effect a current of 0.7 amps is therefore necessary, giving a power dissipation of 14 watts, which is not excessive.

A8.2 Calculation of eddy current damping torque

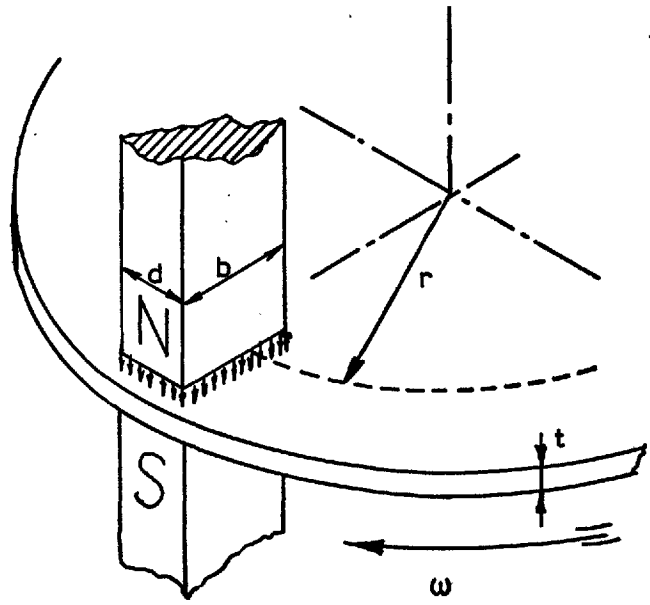


Figure A.8.3

If the flux density under the pole is B Wb/m^2, an emf

$$e = B\ b\ \omega\ r \text{ volts} \qquad \text{-A8.1}$$

will be induced in the portion of the disc which is, at any instant, in the interpolar gap. The radius r is measured from the centre of the disc to the centre of the pole faces. Considering only the portion of the disc which is immediately under the pole, the resistance of the eddy current path, R_e is

$$R_e = b.\ \rho / d.t$$

where b is the radial length of the pole (which is the length of the portion of the disc in which emf is generated)

d.t is the area of the disc which conducts the current

ρ is the resistivity of the material in ohm metres

The actual resistance of the total eddy current path depends upon the radial position of the pole and is somewhat greater than $b.\ \rho / d.t$. Denoting this resistance by $k.b.\ \rho / d.t$ where k is a constant (>1) for any given radial position of the poles, the eddy current is given by

$$i_e = B\,b\,\omega\,r.\ \frac{d.t}{k\,b\,\rho} \text{ amps}$$

The force, F, produced by reaction of this current on the field is

$$F = B.i_e.b \text{ newtons}$$

and the damping torque, T_D, is thus

$$T_D = \frac{B^2.b.d.t.r^2.\omega}{k.\rho} \text{ newton metres}$$

For the geometry used k has been found to be $\simeq 14$[2]. Taking ρ for aluminium as 2.67×10^{-8} Ωm at 20°C and remembering that the total flux between the poles, ϕ, is equal to B.d.b, T_D may be calculated, for the geometry used, as:

$$T_D = \phi^2\,\omega\ 9.1 \times 10^4 \text{ newton metres}$$

In section A8.1 the maximum flux was found to be 0.712×10^{-4} Wb, hence the maximum damping torque T_D is given by:

$$T_D = 4.7\,\omega \text{ gmf cm}$$

where ω is the rotational speed of the disc in rad/sec.

---

2. Drysdale and Jolley 'Electrical measuring instruments' Part 1, 2nd. edition, Chapman and Hall Ltd., 1952.

PUBLICATIONS

in U.S.A.

Paper No.
71-Lub-18

an ASME publication

The Society shall not be responsible for statements or opinions advanced in papers or in discussion at meetings of the Society or of its Divisions or Sections, or printed in its publications.

$3.00 PER COPY $1.00 TO ASME MEMBERS

N. THORP
R. GOHAR

Mechanical Engineering Department, Imperial College, London, England

Oil Film Thickness and Shape for a Ball Sliding in a Grooved Raceway

The behavior in the lubricated contact area of a driven ball sliding in a conforming glass groove, is studied. Interferometry is used to measure the oil film. Coupled ball surface velocity components are provided by angling the drive, while loads and speeds are varied in order to cover a range of conditions from undistorted surfaces to elastohydrodynamic lubrication. A general theory for lubrication with, no distortion and pressure-dependent viscosity, is developed and compared with experiment. Ball spin is found to have only a small effect on the oil film thickness.

Introduction

Over the past few years, there has been a considerable amount of experimental work devoted to the study of the oil films in elastohydrodynamic nominal point and line contact. Point contact has been achieved by using a ball loaded against a plate [1, 2, 3].[1] This arrangement has the advantage of simplicity, although it does not adequately simulate the geometry of a ball bearing. In order to do this, the experiments and theory described below use the arrangement of a ball sliding in a stationary straight conforming groove (Fig. 1). As previously [1, 2, 3], interferometry is used for measuring the oil film. Furthermore, advantage is taken of the quite low pressures that can be generated in such a contact. Thus, the oil film thickness and pressure distribution are found theoretically under "classical" conditions, that is, with the contiguous surfaces undistorted and only pressure-viscosity effects significant [4]. The effects of gyroscopic spin are also included and the results are compared with experiment. At higher loads, when elastohydrodynamic conditions obtain, experimental results are compared with the theories of Archard [5] and Cheng [6]. Finally, some results are given for the conditions of pure axial spin under low loads.

[1] Number in brackets designate References at end of paper.

Contributed by the Lubrication Division of The American Society of Mechanical Engineers for presentation at the ASLE-ASME Joint Lubrication Conference, Pittsburgh, Pa., October 5–7, 1971. Manuscript received by the Lubrication Division, March 24, 1971; revised manuscript received July 1, 1971. Paper No. 71-Lub-18.

Copies will be available until July, 1972.

Nomenclature

A = $1/(2R_x)$
B = $1/(2R_y)$
a, b = normalizing parameters
C = constant in equation (15)
c = semiaxis of the Hertzian contact ellipse in the x direction
d = semiaxis of the Hertzian contact ellipse in the y direction
E_1, E_2 = elastic modulii of materials
E = reduced modulus $\frac{1}{E} = \frac{1}{2}\left(\frac{1-\sigma_1^2}{E_1} + \frac{1-\sigma_2^2}{E_2}\right)$
EHL = abbreviation for elastohydrodynamic lubrication
G^* = αE = materials parameter
h = film thickness at x, y
h_{min} = minimum film thickness
h_0 = entry film thickness
$\bar{h}$ = h/h_{min} = nondimensional film thickness
H^* = h_{min}/R = minimum film thickness parameter
H_0^* = h_0/R = entry film thickness parameter
m = $d\left[\frac{3}{2}\frac{W}{(A+B)E}\right]^{-1/3}$
n = constant in equation (15)
p = pressure at x, y
$\bar{p}$ = nondimensional pressure
q = reduced pressure at x, y $q = \frac{1}{\alpha}(1 - e^{-\alpha p})$
$\bar{q}$ = αq = nondimensional reduced pressure $\bar{q} = (1 - e^{-\bar{p}})$
R = ball radius
Rg = groove radius
R_x = principal radius of curvature in the x direction
R_y = principal radius of curvature in the y direction
$\bar{r}$ = non dimensional polar coordinate
U = ball surface velocity at the contact in the x direction
U^* = $\frac{n_0 V}{RE}$ = speed parameter
V = ball surface velocity at the contact in the y direction
$\mathbf{V}$ = vector sum of U and V
V = modulus of $\mathbf{V}$
W = total load carried by contact
W^* = W/ER^2 = load parameter
$\bar{W}$ = nondimensional load
x = Cartesian coordinate along the groove

(Continued on next page)

Discussion on this paper will be accepted at ASME Headquarters until November 8, 1971



Fig. 1 Arrangement of ball and race as used in experiments

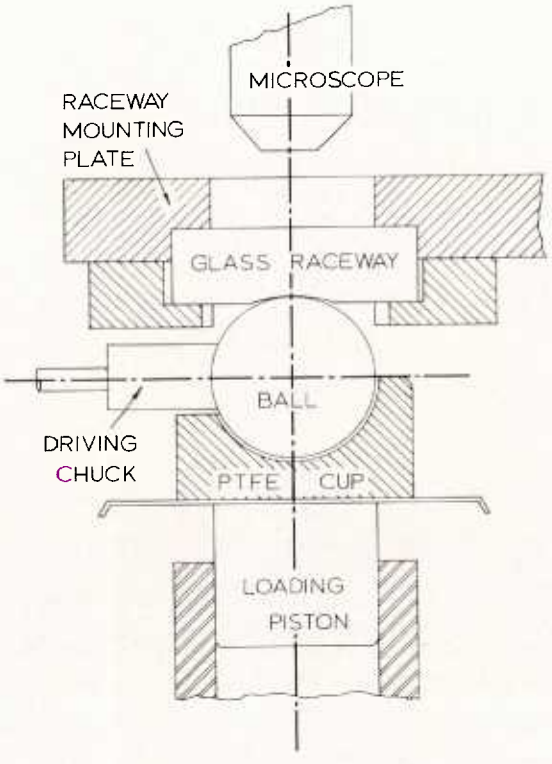


Fig. 2 Apparatus used in sliding experiments

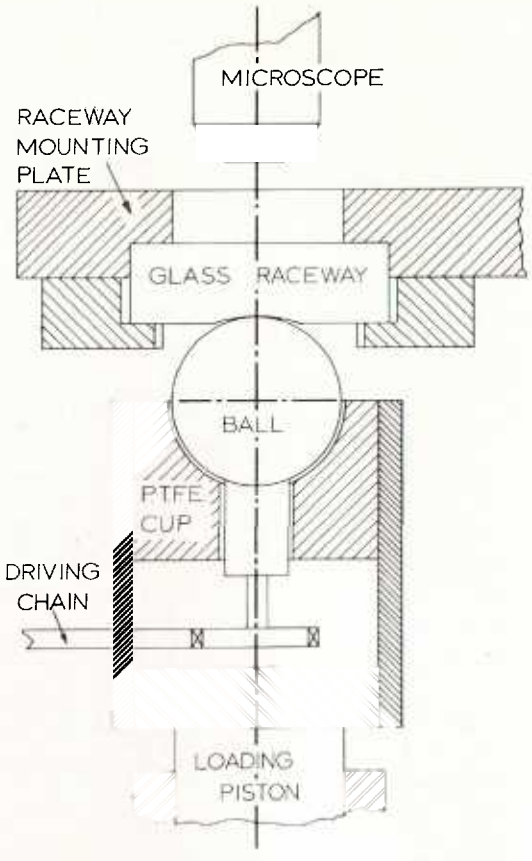


Fig. 3 Apparatus used in spinning experiments

Apparatus

The apparatus consisted of a 1-in-dia rotating ball, supported in a PTFE hemispherical cup, lubricated and loaded against the bottom of a glass raceway with a straight 0.555-in. radius groove machined in it (Figs. 1 and 2). The ball was glued to a steel chuck driven by a d-c shunt motor via a 20:1 reduction gearbox. The motor was fitted with a tacho-feedback speed control, and shaft speed was measured by an inductive transducer connected to a digital tachometer displaying to an accuracy of 0.003 percent.

Lubricant was supplied by gravity feed to the ball surface the oil then being carried up on the ball to the contact region. The cup was cut away in the meridian to reduce heating effects. In the inlet to the contact, a trailing thermocouple measured oil temperature. Readout of temperature was on a direct reading electronic thermometer. The whole cup assembly was mounted on an air piston and loaded pneumatically onto the glass raceway which was located rigidly above the ball. The ball drive could be angled in a horizontal plane between 0 and 90 deg. The contact region could be viewed through the glass race with a low power microscope and side illuminator above the objective. Monochromatic light was used to observe the interference pattern and thus measure the oil film thickness. The above method of measurement has been explained in detail in reference [2].

The apparatus could be modified in order to drive the ball in a spinning mode. In this arrangement, the ball was driven by a short shaft projecting through the base of the cup (Fig. 3). This shaft was driven from the motor by a light chain.

Experimental Results

In these experiments the independent variables were the ball surface speed, (V), the load, (W), and the drive angle (θ). The oil inlet viscosity (η_0) varied due to frictional heating at the sliding contact and in the P.T.F.E. cup. However, the value of the viscosity was known from a knowledge of the inlet temperature. This never increased by more than 3 deg C during each test. The materials reduced modulus, (E), oil pressure viscosity

Nomenclature

$\bar{x} = x/a$ = nondimensional Cartesian coordinate
y = Cartesian coordinate across the groove
$\bar{y} = y/b$ nondimensional Cartesian coordinate
α = pressure viscosity coefficient of the lubricant
η = viscosity at x, y
η_0 = isoviscous viscosity or entry viscosity
σ_1, σ_2 = Poisson's ratios of materials
θ = angle V makes with the x axis
ϕ = polar coordinate
$\Phi = \left[1 + \frac{2}{3}\frac{R_x}{R_y}\right]^{-1}$ = ellipticity factor

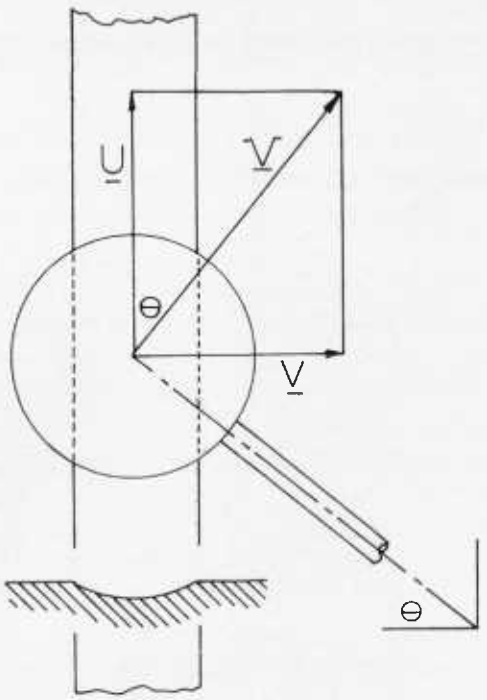


Fig. 4 Schematic layout of ball and groove

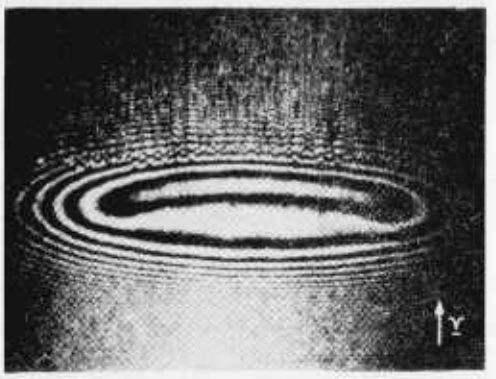


Fig. 5(a) $\theta = 0$ W = 2.49 kg $\frac{U^*}{W^{*1.5}G^{*0.5}} = 1.1 \times 10^{-3}$

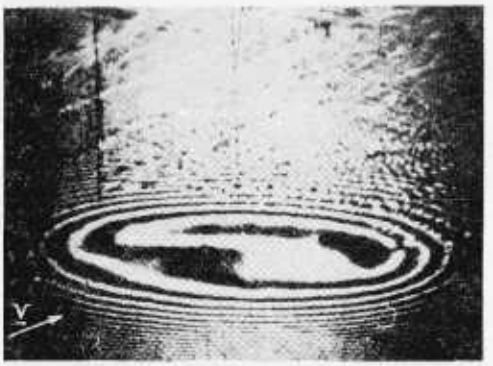


Fig. 5(b) $\theta = 67$ deg W = 2.49 kg $\frac{U^*}{W^{*1.5}G^{*0.5}} = 1.7 \times 10^{-3}$

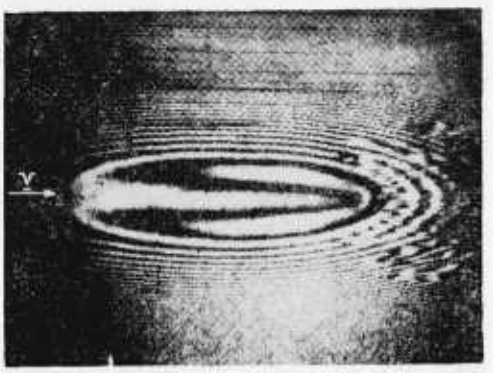


Fig. 5(c) $\theta = 90$ deg W = 2.49 kg $\frac{U^*}{W^{*1.5}G^{*0.5}} = 7.0 \times 10^{-4}$

Fig. 5 Effect of variation of drive angle (θ) on film shape at high loads

coefficient, (α) and the reduced radii (R_x, R_y) were constant. The dependent variable was the film shape, (h).

Angled Drive. For a series of drive angle (θ) varying between 0 and 90 deg in a horizontal plane, (Fig. 4) V was varied and the corresponding h was measured by interferometry [2]. For light loads, where distortion was not significant, h_{min} was noted. When distortion became important, the minimum film moved to one or both of the sides and the trailing edge of the contact, depending on the amount of angling. Fig. 5 shows this clearly, especially at $\theta = 90$ deg. In order to compare with current theories for elliptical distorted contact at $\theta = 0$ and 90 deg, the inlet region film thickness (h_0) was also recorded when the elastohydrodynamic conditions became apparent.

The oil used was of type BP 1065 and had a viscosity of 30 poise at 21.7 deg C (71 deg F). The pressure viscosity coefficient (α) had a value of $2.5 \times 10^{-8}\ m^2/N$ (1.74×10^{-4} in^2/lbf) (reference [7]). The surface speed of the ball ranged from zero to 0.276 m/sec and the load from 0.17 kg to 2.5 kg—this represents a range of peak Hertz stress from $1.1 \times 10^8\ N/m^2$ (15,000 lbf/in^2) to $2.8 \times 10^8\ N/m^2$ (40,000 lbf/in^2). This maximum load is low if one considers real bearings. Nevertheless, as the ball was sliding in the groove, low loads and reasonable speeds kept oil temperature down, thus enabling proper comparison with theory to be made. At some future date, the results of more involved investigations will appear. These will be for rolling contact under more severe conditions.

Spinning Drive. The object of these preliminary tests was to determine whether the presence of a vertical spin component of ball angular velocity affects the film thickness. The ball was first of all loaded lightly against the groove base, after having covered both surfaces with oil. It was then rotated in pure spin. The apparatus used is shown in Fig. 3.

In order to observe the wake pattern properly, a Xenon flash lamp and mercury green line filter were used, thus enabling exposure times for all photographs of interference fringes to be of the order of one millisecond. This effectively froze the wake.

Theory

Reynolds Equation. The Reynolds equation in two dimensions using cartesian coordinates and assuming a sliding contact and constant density, is:

$$\frac{\partial}{\partial x}\left(\frac{h^3}{6\eta}\frac{\partial p}{\partial x}\right) + \frac{\partial}{\partial y}\left(\frac{h^3}{6\eta}\frac{\partial p}{\partial y}\right) = \frac{\partial}{\partial x}(Uh) + \frac{\partial}{\partial y}(Vh) \quad (1)$$

If classical conditions obtain [4], then elastic distortion is absent, oil viscosity is constant, and U and V are considered constant in the vicinity of the contact. Thus, for a constant viscosity η_0 [4], let the pressure be denoted by a reduced pressure q. Equation (1) then reduces to

$$\frac{\partial}{\partial x}\left(h^3\frac{\partial q}{\partial x}\right) + \frac{\partial}{\partial y}\left(h^3\frac{\partial q}{\partial y}\right) = 6\eta_0\left[U\frac{\partial h}{\partial x} + V\frac{\partial h}{\partial y}\right] \quad (2)$$

Equation (2) may be normalized by substituting

$$\bar{q} = \alpha q \quad \bar{h} = h/h_{\min} \quad \bar{x} = x/a \quad \bar{y} = y/b$$

$$U = \mathrm{V}\cos\theta \quad V = \mathrm{V}\sin\theta$$

where a is an arbitrary scaling factor governing the distance of the inlet boundary from the contact center.

Let b be related to a by

$$b/a = d/c = \frac{\text{semiaxis of the Hertzian ellipse in the } y \text{ direction}}{\text{" " " " " " " } x \text{ "}}$$

The foregoing substitution transforms the region of calculation from an ellipse to a circle. In order to convert to polar coordinates, let

$$\bar{x} = \bar{r}\cos\phi$$

$$\bar{y} = \bar{r}\sin\phi$$

Equation (2) can now be written as

$$\left[\cos^2\phi + \sin^2\phi\left(\frac{a^2}{b^2}\right)\right]\left[3\bar{h}^2\frac{\partial\bar{h}}{\partial\bar{r}}\frac{\partial\bar{q}}{\partial\bar{r}} + \bar{h}^3\frac{\partial^2\bar{q}}{\partial\bar{r}^2}\right]$$
$$+\left[\sin^2\phi + \cos^2\phi\left(\frac{a^2}{b^2}\right)\right]\left[\frac{\bar{h}^3}{\bar{r}}\frac{\partial\bar{q}}{\partial\bar{r}} + \frac{\bar{h}^3}{\bar{r}^2}\frac{\partial^2\bar{q}}{\partial\phi^2} + \frac{3\bar{h}^2}{\bar{r}^2}\frac{\partial\bar{q}}{\partial\phi}\frac{\partial\bar{h}}{\partial\phi}\right]$$
$$-\left[\sin\phi\cos\phi\left(1 - \left(\frac{a^2}{b^2}\right)\right)\right]\left[\frac{2\bar{h}^3}{\bar{r}}\frac{\partial^2\bar{q}}{\partial\bar{r}\partial\phi} + \frac{3\bar{h}^2}{\bar{r}}\frac{\partial\bar{h}}{\partial\bar{r}}\frac{\partial\bar{q}}{\partial\phi}\right.$$
$$\left.+\frac{3\bar{h}^2}{\bar{r}}\frac{\partial\bar{q}}{\partial\bar{r}}\frac{\partial\bar{h}}{\partial\phi} - 2\frac{\bar{h}^3}{\bar{r}^2}\frac{\partial\bar{q}}{\partial\phi}\right] = \frac{6\eta_0\mathrm{V}a\alpha}{h_{\min^2}}\left[\frac{1}{\bar{r}}\frac{\partial\bar{h}}{\partial\phi}\left(\left(\frac{a}{b}\right)\right.\right.$$
$$\times\sin\theta\cos\phi - \cos\theta\sin\phi\Big) + \frac{\partial\bar{h}}{\partial\bar{r}}\left(\left(\frac{a}{b}\right)\sin\phi\sin\theta\right.$$
$$\left.\left.+\cos\phi\cos\theta\right)\right] \quad (3)$$

Film Shape. For no distortion of the contiguous surfaces, the film shape in the vicinity of the contact can be expressed as (4)

$$h = h_{\min} + Ax^2 + By^2 \quad (4)$$

where the geometry is shown in Fig. 6.

Normalizing and expressing it in polar form, gives equation (5).

$$\bar{h} = 1 + \frac{Aa^2}{h_{\min}}\left[(\bar{r}\cos\phi)^2 + \frac{B}{A}\left(\frac{b}{a}\right)^2(\bar{r}\sin\phi)^2\right] \quad (5)$$

Equations (3) and (5) were then solved for $\bar{q}$ over the whole region of contact using a finite difference method. Central differences were employed with a nonuniform grid in the radial direction with close spacing of the grid lines near the contact center. By this means, errors due to large gradients, in the region of high pressures, were minimized. The boundary conditions employed are discussed below.

Load Taken. The distribution of $\bar{q}$ obtained from equations (3) and (5) was then modified to take into account variation of viscosity with pressure. This was done by substituting $\bar{p} = -\ln(1 - \bar{q})$ to give the actual nondimensional pressure distribution. The resulting distribution was then integrated over the grid to give the nondimensional dependent load $\bar{W}$, where

$$\bar{W} = \iint \bar{p}d\bar{x}d\bar{y} \quad (6)$$

which can be written as

$$\left(\frac{a}{b}\right)\left(\frac{\alpha}{a^2}\right)\iint pdxdy \quad (7)$$

that is,

$$\bar{W} = \left(\frac{a}{b}\right)\left(\frac{W_\alpha}{a^2}\right) \quad (8)$$

Nondimensional Groups. The independent variables may be collected from equations (3) and (5) to form nondimensional groups

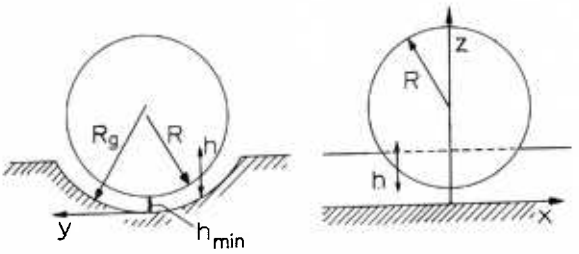


Fig. 6 Geometry of contact

$$\frac{B}{A'} \quad \frac{Aa^2}{h_{\min}}, \quad \frac{6\eta_0\mathrm{V}a\alpha}{h_{\min^2}}, \quad \theta$$

The ratio a/b is uniquely dependent on B/A [8]. Also, since a is arbitrary, it may be chosen to make one of the groups unity. Thus, let

$$a = (h_{\min}/A)^{1/2} \quad (9)$$

so the nondimensional groups are now

$$B/A, \quad \frac{6\eta_0\mathrm{V}\alpha}{A^{1/2}h_{\min^{3/2}}}, \quad \frac{W\alpha A}{h_{\min}}, \quad \theta$$

where $A = \dfrac{1}{2R_x} = \dfrac{1}{2R}$ for a ball in a straight groove.

If the parameters are put into the more familiar groups obtained for the point contact situation [3], namely

$$G^* = \alpha E$$

$$U^* = \frac{\eta_0\mathrm{V}}{RE}$$

$$W^* = \frac{W}{ER^2}$$

$$H^* = h_{\min}/R$$

after some manipulation, the following functional relationship is obtained

$$\frac{H^*}{W^*G^*} = f\left[\left(\frac{U^*}{W^{*3/2}G^{*1/2}}\right), \quad \left(\frac{B}{A}\right), \quad (\theta)\right] \quad (10)$$

for an undeformed contact.

As the geometry is invariable, B/A is constant and

$$\frac{H^*}{W^*G^*} \text{ may be plotted against } \frac{U^*}{W^{*3/2}G^{*1/2}}$$

for each value of θ. Now the pressure distributions $\bar{p}$, obtained from the expression $\bar{p} = -\ln(1 - \bar{q})$, no longer becomes valid when $\bar{q} = 1$, that is when $q = \dfrac{1}{\alpha}$. Kapitza [4] has called this the limiting pressure for pressure dependent viscosity. It seems reasonable to assume that by then deformation has become important. Inclusion of deformation should therefore add another group to equation (10).

Cheng [6] has obtained the entry film thickness for an elliptical contact by means of a Grubin approximation [9]. At present there is no complete numerical solution to elastohydrodynamic elliptical contacts. A Grubin approximation forces a Hertzian shape onto the inlet part of the oil film. This assumption makes the indices of U^* and W^* the same, whereas a full numerical solution might not. For example, in the numerical solution of the line contact problem, there is a difference between these indices [10], and in point contact experiments, the difference is quite significant [3]. However, Grubin type solutions have proved to be quite accurate at high loads and low speeds where

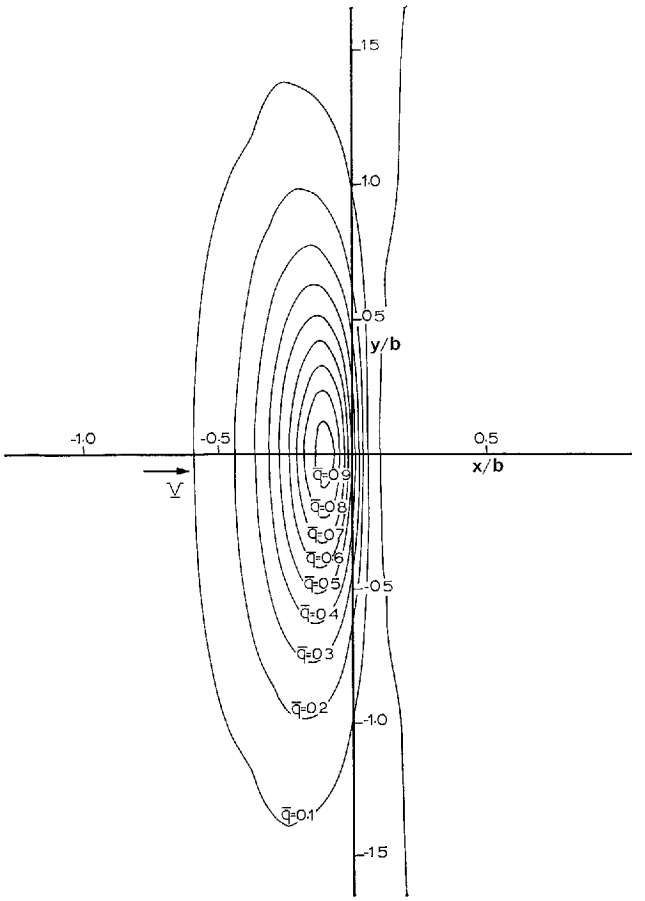


Fig. 7(a) $\theta = 0$ deg $H^*/W^*G^* = 3.1 \times 10^{-2}$ $\frac{U^*}{W^{*1.5}G^{*0.5}} = 5.0 \times 10^{-8}$

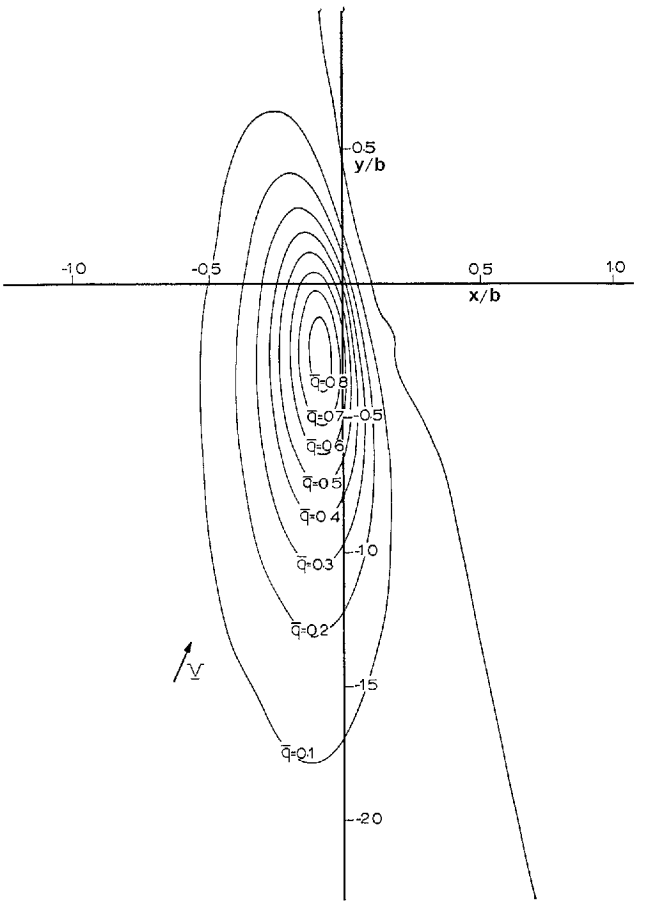


Fig. 7(b) $\theta = 67$ deg $H^*/W^*G^* = 3.5 \times 10^{-2}$ $\frac{U^*}{W^{*1.5}G^{*0.5}} = 1.1 \times 10^{-2}$

experiments have shown the film to be similar to the assumed shape [11]. Now in order to compare with experiments, which ranged from undistorted surfaces through to elastohydrodynamic conditions, Cheng's numerical solution can be adjusted to form the same groups as those of equation (10). Cheng's result (see Appendix) for an elliptical contact having the geometry used in the experiments, reduces to

$$\frac{H_0^*}{W^*G^*} = 1.45 \left(\frac{U^*}{G^{*1/2}W^{*3/2}}\right)^{0.738} (W^*G^{*3})^{0.036} \qquad (11)$$

for $\theta = 0$ deg,

and

$$\frac{H_0^*}{W^*G^*} = 0.462 \left(\frac{U^*}{G^{*1/2}W^{*3/2}}\right)^{0.639} (W^*G^{*3})^{-0.014} \qquad (12)$$

for $\theta = 90$ deg.

There is, therefore, an additional group (WG^3) caused by deformation effects. Note, however, that any solution is weakly dependent on this new group. For a one hundredfold change in W^*, the additional group only alters by a factor of 1.2 for $\theta = 0$ deg and 1.1 for $\theta = 90$ deg. Archard [5] has also obtained an approximate solution for an elliptical contact. He found the entry film thickness by considering only the axis of symmetry (x axis) of an elastohydrodynamic *point* contact. He then multiplied it by a function of a side leakage factor which was obtained from an undistorted contact given by a ball in a groove, assuming a half Sommerfeld pressure distribution.

Archard's solution (see Appendix) can be expressed as

$$\frac{H_0^*}{G^*W^*} = 1.165 \left(\frac{U^*}{G^{*1/2}W^{*3/2}}\right)^{0.74} (W^*G^{*3})^{0.037} \qquad (13)$$

for $\theta = 0$ deg

and

$$\frac{H_0^*}{G^*W^*} = 0.269 \left(\frac{U^*}{G^{*1/2}W^{*3/2}}\right)^{0.74} (W^*G^*)^{0.037} \qquad (14)$$

for $\theta = 90$ deg.

Boundary Conditions for Undistorted Surfaces. Assuming that cavitation causes rupture of the lubricating film on the exit side, then the Reynolds condition

$$q = \frac{\partial q}{\partial x} = \frac{\partial q}{\partial y} = 0$$

must be satisfied there [12]. These conditions are obtained by making $\bar{q}$ zero round the boundary of the finite difference grid, and also by making it zero wherever it goes negative. In this manner, the position and shape of the outlet boundary are determined.

The extent of the grid in the radial direction is ideally infinite. It is found however, that after a certain radius is reached, further increase does not have any significanct effect on the peak pressure or the load. This is the radius required to simulate fully flooded conditions, anything less being starved [11]. In practice, the inlet radius used is slightly larger than minimum, being given by $\bar{r} = 23.25$, that is at $x = 23.25\sqrt{h_{\min}/A}$.

An iterative boundary condition is required at the grid center because of a singularity caused by $\bar{r}$ being zero there. The singularity is avoided by ensuring continuity of pressure and pressure gradient at this point.

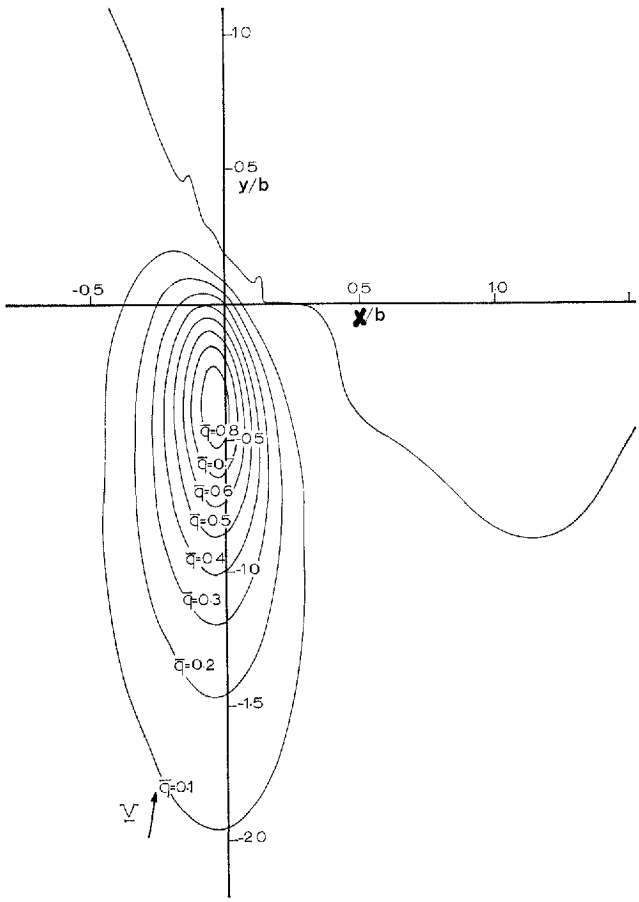


Fig. 7(c) $\theta = 82$ deg $H^*/W^*G^* = 3.5 \times 10^{-2}$ $\frac{U^*}{W^{*1.5}G^{*0.5}} = 1.4 \times 10^{-2}$

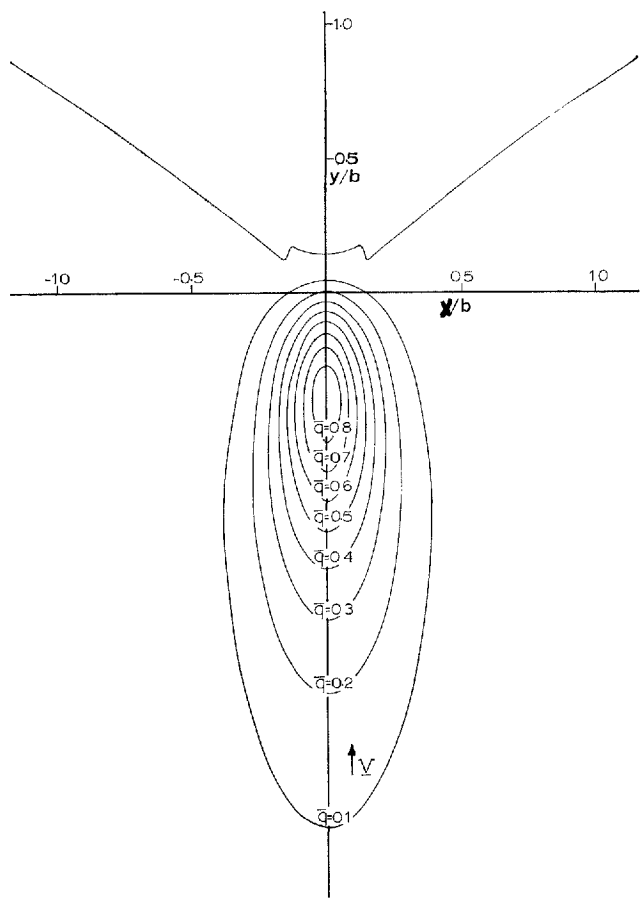


Fig. 7(d) $\theta = 90$ deg $H^*/W^*G^* = 3.5 \times 10^{-2}$ $\frac{U^*}{W^{*1.5}G^{*0.5}} = 1.5 \times 10^{-2}$

Fig. 7 Isobars obtained from solution of equations (3) and (5)

Discussion

Using the theory described above, nondimensional isobars have been produced for various drive angles (θ). These are shown in Fig. 7 for $\theta = 0$, 67, 80, and 90 deg. It is instructive to compare the isobars with fringe photos for the corresponding angles (Fig. 8). Observe that the film is practically undistorted, even in Fig. 8(*c*) where the load is high, but where there is also a high value of V. When θ is large, as in Figs. 8(*b*) and (*c*), the direction of **V** causes side leakage to reduce in the lower part of the region and increase in the upper part. Consequently, there is more oil available to fill the gap in the lower part and cavitation occurs later. The shape of the boundary, in the vicinity of the contact is similar in the corresponding fringe photos. Note that the pattern follows, quite faithfully, the direction of **V**. Fig. 9 shows the effect of speed on the cavitation boundary. θ is taken as zero. As the speed increases, the part of cavitation boundary close to the contact center moves out slightly. In this region, the film shape causes side leakage to be low, the position of the boundary being governed by the locus of the x direction local pressure maxima. Although not shown, these maxima move towards the inlet with increase of U ($V = 0$). Then, in accordance with flow continuity requirements, cavitation occurs later. As the figures show, the actual shape of the boundary is modified further out by side leakage. This causes the wake angle to decrease with speed increase.

Distorted Contact. A combination of the effects of load increase and speed decrease, modifies the pressure distribution sufficiently to cause elastic deformation of the bounding surfaces. The resultant film shape is shown in Fig. 5 for $\theta = 0$, 67, and 90 deg and differing values of U^*. Each of the film shapes is significant. The $\theta = 0$ deg example has a film with a long end closure and a limited localised side closure. Over most of the region the geometry is similar to that of a line contact. The shape suggests a pressure distribution which falls away quite gradually at the sides. On the other hand, when $\theta = 90$ deg, the minimum film wraps round the contact, and the oil is entrained through a narrow passage in the center. The pressure must climb up from a long inlet sweep, through a comparatively gradually changing geometry. At the sides, the fall away of pressure is more severe, causing the surfaces to spring out to form the characteristic side lobes seen in point contact (1). The film shape at an intermediate angle of $\theta = 67$ deg (Fig. 5*b*) has been distorted by the modified pressure distribution. The bottom left of Fig. 5(*b*) has become an inlet and there is a localised uniform film thickness occurring near the centre. Towards the outlet, in the top right part, end closure has occurred followed by the cavitation wake lined up to the velocity vector. Most of this film shape redistribution must be due to pressure rather than shear forces which are, at most, only 10 percent of the load under pure sliding [11].

Spinning Ball. The fringe photo in Fig. 10 is for the ball loaded against the groove base and driven about a vertical axis. The load is as low as possible (0.25 kg) and the speed is as high as would allow a proper photo to be taken (97 rpm). Archard [14] has developed a theory which gives the film thickness in pure spin for an undistorted contact assuming half Sommerfeld condi-

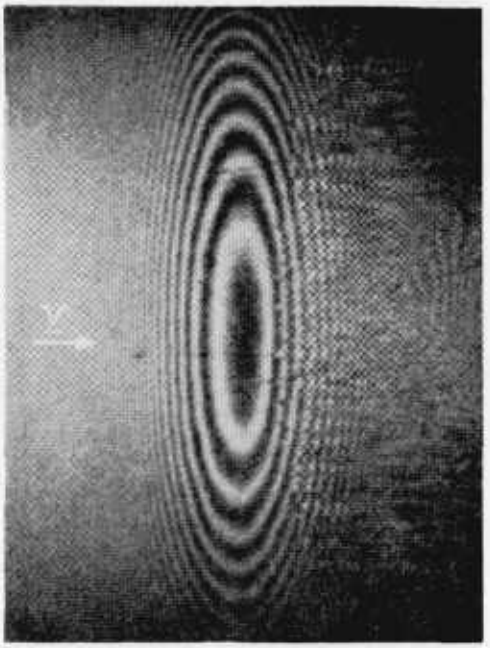


Fig. 8(a) $\theta = 0$ deg $W = 0.35$ kg $\frac{U^*}{W^{*1.5}G^{*0.5}} = 4.2 \times 10^{-3}$



Fig. 8(b) $\theta = 67$ deg $W = 1.06$ kg $\frac{U^*}{W^{*1.5}G^{*0.5}} = 8.0 \times 10^{-3}$

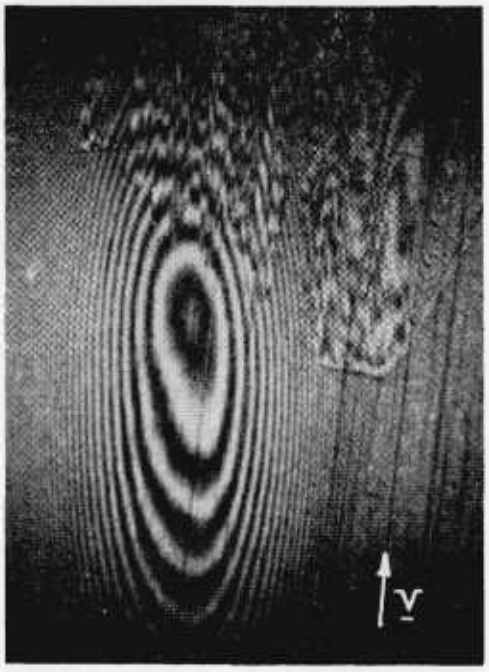


Fig. 8(c) $\theta = 82$ deg $W = 2.49$ kg $\frac{U^*}{W^{*1.5}G^{*0.5}} = 8.0 \times 10^{-3}$

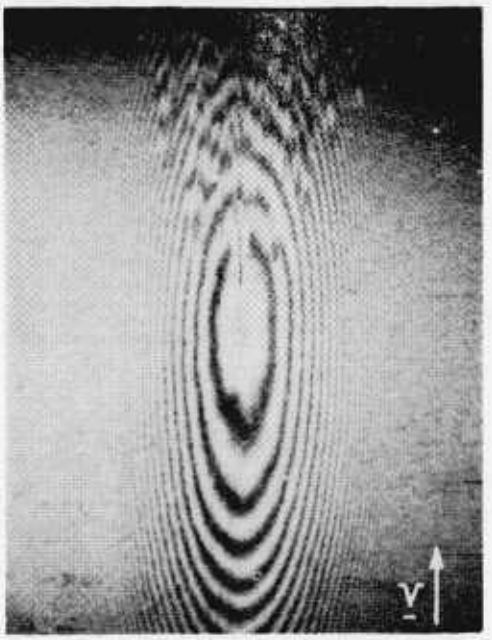


Fig. 8(d) $\theta = 90$ deg $W = 0.35$ kg $\frac{U^*}{W^{*1.5}G^{*0.5}} = 3.0 \times 10^{-2}$

Fig. 8 Effect of variation of drive angle (θ) on film shape at low loads or high speeds

tions. According to the expression he derives, the limiting film thickness in the example shown should come to 1.3×10^{-6} cm, which is effectively no film. Archard pointed out that EHL might improve the film thickness mechanism. In fact, because of the low surface speeds, there is some EHL and with it a trace of an oil film towards the edges of the central region, which would otherwise be flat. But, to all intents and purposes, at the centre, no oil film is present. (Statically, the centre is white because of a phase change of the light on reflection.)

However, there is some pressure generated in the contact. The distribution of this pressure can be inferred from the wake pattern. Assuming the ball is viewed from above, its rotation is anticlockwise. There has been a pressure build up on the right of the contact between the wake patterns because the oil is entrained in a radial motion into a narrowing wedge. Past the minimum film centre line (along the ellipse major axis) the oil sees a diverging wedge and eventually separates or cavitates. It remains so until there is another pressure build up in the top left part of the figure.

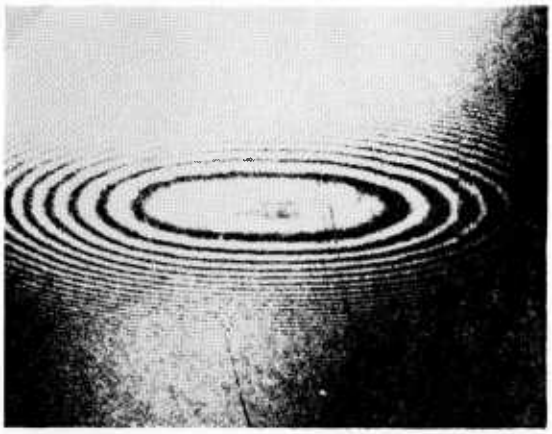


Fig. 9(a) $\theta = 0$ deg $W = 0.35$ kg static contact

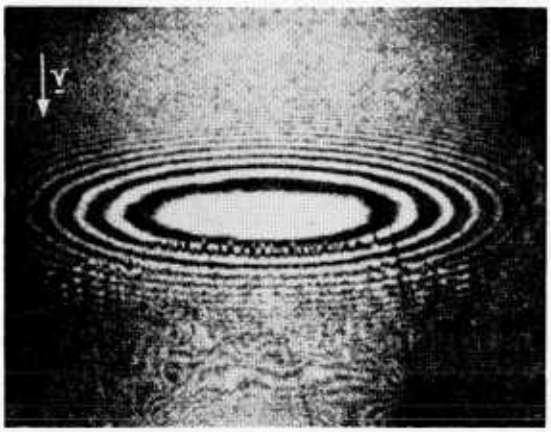


Fig. 9(b) $\theta = 0$ deg $W = 0.35$ kg $\dfrac{U^*}{W^{*1.5}G^{*0.5}} = 4.5 \times 10^{-4}$

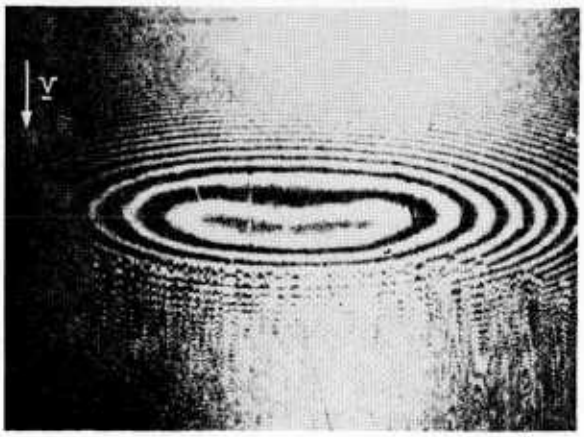


Fig. 9(c) $\theta = 0$ deg $W = 1.06$ kg $\dfrac{U^*}{W^{*1.5}G^{*0.5}} = 2.3 \times 10^{-3}$

Fig. 9 Effect of variation of speed on the position of the cavitation boundary

Note that the non cavitated parts are *not* displaced symmetrically about the ellipse major axis.

There appears to be, in addition, near the minor axis above and below the contact, a region which has not cavitated, and is therefore at or slightly above atmospheric pressure. Remembering that the central part has no proper oil film and rotation of the fluid is in concentric circles, then this region will gradually be

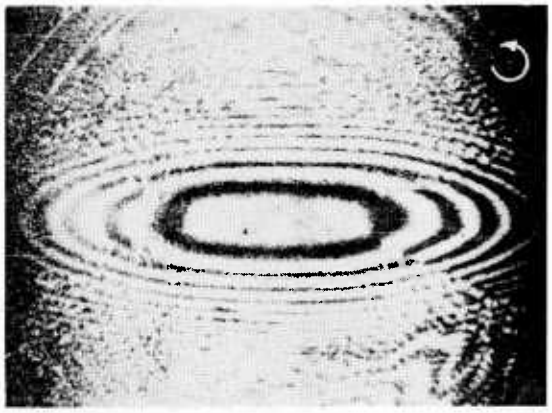


Fig. 10 Film shape under pure spinning. $W = 0.25$ kg speed = 97 rpm

starved of oil as it will be drawn into the cavitated part which must be slightly below atmospheric. An oil film, if any, must therefore eventually depend solely on the two pressure nests described above.

Film Thickness. In order to show how the oil film alters with change in the external parameters, graphs have been plotted between the appropriate non dimensional groups discussed in the theory. Figs. 11 to 14 show how the minimum film H^* varies with U^* and W^* for different θ, while Figs. 15 and 16 show how the entry film H_0^* varies. The following observations can be made.

1 For a given value of G^* (constant at 3578 in all experiments) only two groups are necessary, despite the range of conditions.

2 In Figs. 11 to 14, for H^*, the slope changes from about 1.75 for undistorted contact to about 0.78 when the conditions are full EHL.

3 In Figs. 15 and 16, for H_0^*, the slope changes from about 1.75 for undistorted contact, to 0.68 for $\theta = 0$ and 0.58 for $\theta = 90$ deg, when the conditions are EHL.

4 The lower the value of θ, the higher the film thickness under given external conditions. Also, the lower θ, the lower the value of $\dfrac{U^*}{W^{*2/3}G^{*1/2}}$ at which EHL commences.

The observations are now discussed:

The first has been noted by Gohar for point contact [3]. His experimental results can be expressed

$$\frac{H_0^*}{W^*G^*} \sim 1.28 \left(\frac{U^*}{W^{*2/3}G^{*1/2}}\right)^{0.7} (W^*G^{*3})^{-0.05}$$

Changes in the group (W^*G^{*3}) hardly affect $\left(\dfrac{H_0^*}{W^*G^*}\right)$.

In the second, note that a slope of 2 is obtained for undistorted isoviscous point contact assuming half Sommerfeld conditions [12]. Gohar [3] has obtained a slope of 0.78 for H^* in EHL point contact.

In the third, the low slope is a characteristic of sliding EHL contacts. Archard has obtained a value of 0.58 on a crossed cylinder machine [13]. Figs. 15 and 16 also show Cheng's [6] and Archard and Cowking's [5] theories for H_0^*. The agreement is quite good, except for Archard's $\theta = 90$ deg result. It is gratifying to see that Cheng's graphs also show a reduction in slope at $\theta = 90$ deg. The differences between theory and experiment must be in part due to the assumption that the main contact region at inlet is flat, whereas in fact it can be grossly distorted, especially when $\theta = 90$ deg (Fig. 5(*c*)). Fortunately, this condition is never realized in real bearings. A value of $\theta = 10$ deg seems more likely, component V being caused by gyroscopic spin.

It can be concluded from observation [4] that $\theta = 0$ deg is the most favorable condition, at least when fully flooded condi-

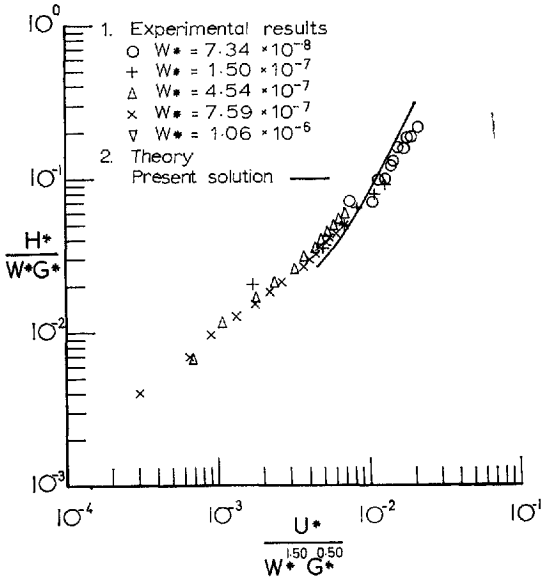


Fig. 11 Minimum film thickness group versus speed group for θ = 0 deg

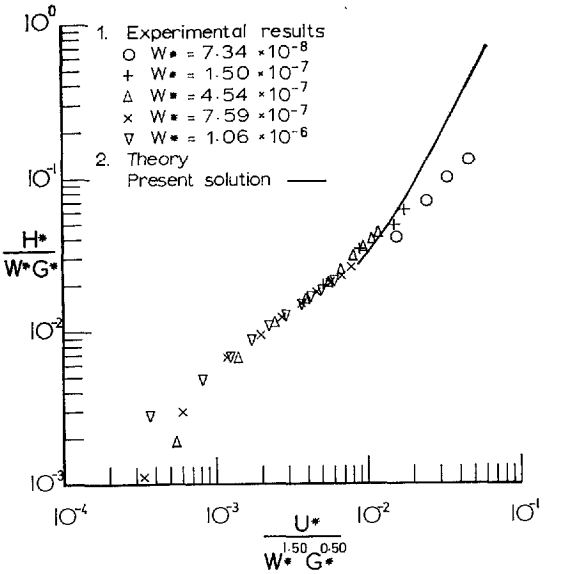


Fig. 12 Minimum film thickness group versus speed group for θ = 67 deg

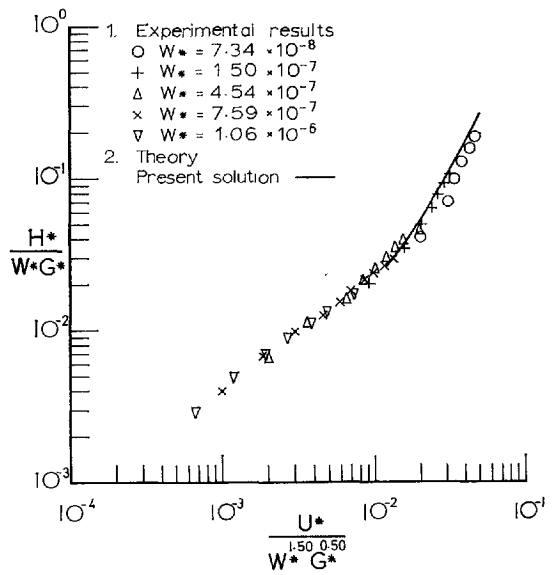


Fig. 13 Minimum film thickness group versus speed group for θ = 82 deg

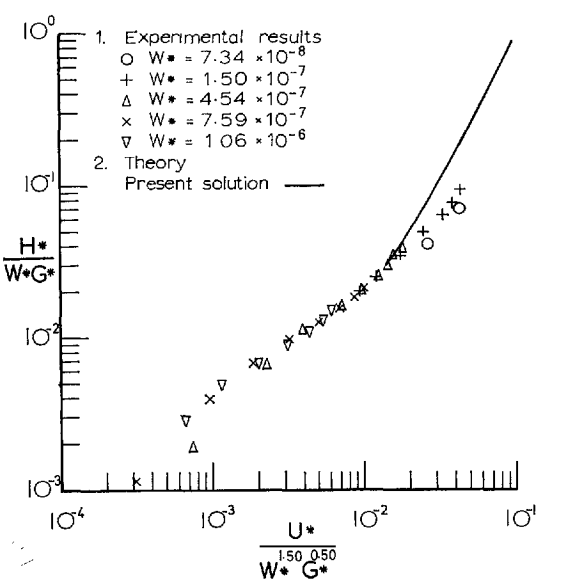


Fig. 14 Minimum film thickness group versus speed group for θ = 0 deg

tions obtain. However, there may be advantages derived from the other velocity component V caused by gyroscopic effects in a rolling bearing, namely the continual presentation of a fresh part of the ball surface to the groove. That EHL becomes important earlier at high values of θ, is explained by Fig. 5. Distortion is much more pronounced when θ is high.

Conclusion

The experiments have shown how the oil film shape and thickness vary when a ball slides in a conforming groove. The most favorable condition for a thick oil film, occurs when the sliding is along the groove axis. Pure spin appears to have only a minor effect on the film thickness.

Although the condition was one of pure sliding and loads and speeds were low, (loads less than 2.5 kg with corresponding peak Hertz stress 2.8 × 10^8 N/m^2 (40,000 lbf/in^2) and speeds less than 0.28 m/sec), the results do give some indication of the mechanism of lubrication in ball bearings.

Acknowledgments

The authors would like to thank the Science Research Council for the grant which is supporting this research project. They would also like to thank Mr. Bedley for taking the photograph in Fig. 1.

References

1 Foord, C. A., Hammann, W. C. and Cameron, A., "Evaluation of Lubricants Using Optical Elastohydrodynamics," *ASLE Trans.*, Vol. 11, 1968, pp. 31–43.

2 Foord, C. A., Wedeven, L. D., Westlake, F. J., and Cameron, A., "Optical Elastohydrodynamics," *Proceedings of the Institution of Mechanical Engineers*, Vol. 184, Part 1, 1969–1970.

3 Gohar, R., "Oil Film Thickness and Rolling Friction in Elastohydrodynamic Point Contact," ASME Paper No. 70-Lub-2. Lubrication Conference Oct. 1970.

4 Kapitza, P. L., "Hydrodynamic Theory of Lubrication During Rolling," *Zhurn. Tekh. Fiz.*, Vol. 25, No. 4, 1955, pp. 747–762.

5 Archard, J. F., and Cowking, E. W., "Elastohydrodynamic Lubrication at Point Contacts," *Proceedings of the Institution of Mechanical Engineers*, Vol. 180, Part 3B, 1965–1966, pp. 47–56.

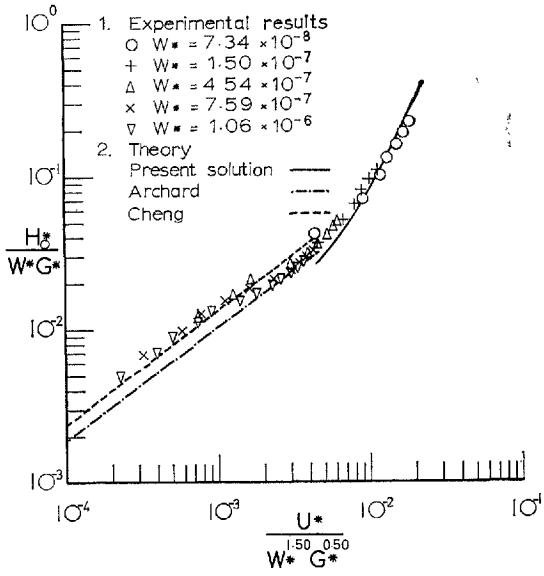


Fig. 15 Inlet film thickness group versus speed group for θ = 0 deg

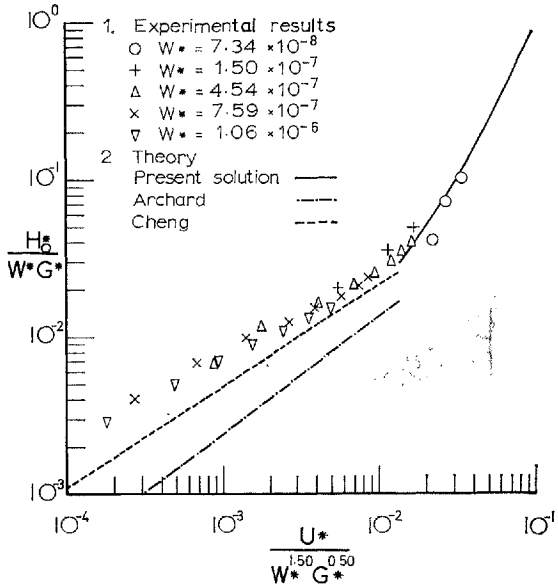


Fig. 16 Inlet film thickness group versus speed group for θ = 90 deg

6 Cheng, H. S., "A Numerical Solution of the Elastohydrodynamic Film Thickness in an Elliptical Contact," JOURNAL OF LUBRICATION TECHNOLOGY, TRANS. ASME, Series F, Vol. 92, No. 1, Jan. 1970, pp. 155–162.

7 Gohar, R., "Oil Films Under Elastohydrodynamic Conditions," PhD thesis, 1965, University of London.

8 Hertz, H., "On the Contact of Elastic Solids," and "On the Contact of Rigid Elastic Solids and on Hardness," reprinted in *Miscellaneous Papers*, translated by Jones, D. E., and Schott, G. A., Macmillan Co. Ltd., London, 1896, pp. 146–162, 163–183.

9 "Investigation of Scientific and Industrial Research," Central Scientific Research Institute for Technology and Mechanical Engineering, Moscow, Book, No. 30, 1949, pp. 115–116.

10 Dowson, D., Higginson, G. R., and Whitaker, A. V., "Elastohydrodynamic Lubrication: A Survey of Isothermal Solutions," *Journal of Mechanical Engineering Science*, Vol. 4, 1962, p. 121.

11 Wedeven, L. D., Evans, D., and Cameron, A., "Optical Analysis of Ball Bearing Starvation," ASME Paper No. 70-Lub-19. Lubrication Conference, Oct. 1970.

12 Cameron, A., *Principles of Lubrication*, Longmans, London, 1966.

13 Archard, J. F., and Kirk, M. T., "Lubrication at Point Contacts," *Proceedings of the Royal Society*, Series A, Vol. 261, 1961, p. 532.

14 Snidle, R. W., and Archard, J. F., "Theory of Hydrodynamic Lubrication for a Spinning Sphere," *Proceedings of the Institution of Mechanical Engineers*, Vol. 184, Part 1, 1969–1970.

APPENDIX

In order to compare with experimental results, Cheng's solution for an elliptical elastohydrodynamic contact (6) can be modified in the following manner. He obtained the equation

$$\left(\frac{h_0}{R_x}\right)^{-2n} = 12C\left(\frac{\eta_0\alpha U}{2R_x}\right)\left(\frac{c}{R_x}\right)\left(\frac{3W}{2\pi dR_x}\right)^{-n} \tag{15}$$

Equation (15) uses the present notation. C and n are constants for a specified geometry. Equation (15) can be rewritten as

$$H_0^* = U^{*\frac{1}{2-n}} \cdot G^{*\frac{1}{2-n}} \cdot W^{*\frac{1-2n}{6-3n}} \cdot (12C)^{\frac{1}{2-n}} \times \left(\frac{3a}{b}\right)^{\frac{1-2n}{6-3n}} \left(\frac{1}{\pi}\right)^{1/3} \left(2\right)^{\frac{n-1}{2-n}} \left[\frac{m^3\pi^2}{\left(\frac{b}{a}\right)^2\left(1+\frac{B}{A}\right)}\right]^{\frac{n+1}{6-3n}} \tag{16}$$

where

$$m = d\left[\frac{3}{2}\frac{W}{(A+B)E}\right]^{-1/3}$$

For the geometry used in these experiments, and with sliding along the raceway axis (θ = 0 deg), equation (16) reduces to

$$\frac{H_0^*}{W^*G^*} = 1.45\left(\frac{U^*}{G^{*1/2}W^{*3/2}}\right)^{0.738}(W^*G^{*3})^{0.036} \tag{17}$$

Similarly, when sliding is across the raceway (θ = 90 deg), one obtains

$$\frac{H_0^*}{W^*G^*} = 0.462\left(\frac{U^*}{G^{*1/2}W^{*3/2}}\right)^{0.639}(W^*G^{*3})^{-0.014} \tag{18}$$

Archard's analysis [5] results in the following equation (using the present notation)

$$h_0 = 2.04\left(\alpha\eta\frac{U}{2}\right)^{0.74}R^{0.74}\left(\frac{E}{W}\right)^{0.074}\Phi^{0.70} \tag{19}$$

where

$$\Phi = \left[1+\frac{2}{3}\frac{R_x}{R_y}\right]^{-1} \tag{20}$$

This may be rewritten as

$$H_0^* = 1.22\Phi^{0.74}U^{*0.74}G^{*0.74}W^{*-0.074} \tag{21}$$

which, for the geometry used, and with θ = 0 deg, becomes

$$\left(\frac{H_0^*}{G^*W^*}\right) = 1.165\left(\frac{U^*}{G^{*1/2}W^{*3/2}}\right)^{0.74}(W^*G^{*3})^{0.037} \tag{22}$$

with sliding across the raceway (θ = 90 deg), one gets

$$\left(\frac{H_0^*}{G^*W^*}\right) = 0.269\left(\frac{U^*}{G^{*1/2}W^{*3/2}}\right)^{0.74}(W^*G^{*3})^{0.037} \tag{23}$$

Printed in U. S. A.

DISCUSSION

A. Cameron[2]

The authors are to be congratulated on presenting results of film thickness using a geometry which approximates to that of a real ball bearing although there is the constraint of pure sliding. There is much to be said in tackling a research problem, such as elastohydrodynamics, by gradual evolution from an elementary ball on flat situation to a complete bearing. They have therefore, rightly, only presented results at quite low loads and speeds, which can be checked by existing theories. The authors, together with others working under Dr. Cameron, are now studying friction and film thickness under rolling/sliding conditions in elliptical contacts as well as spin effects, coupled with roll and slide, under elastohydrodynamic conditions. In this manner, the I.C. Lube Lab hopes, eventually, to present a complete picture of ball dynamics in high speed bearings.

He would like to ask what relevance they think this very lightly loaded case has to real life bearings.

G. Dalmaz,[3] D. Berthe,[3] and M. Godet[3]

The authors' paper is of very special interest as it is concerned with a contact geometry in which pure equiviscous or piezo-viscous conditions can be maintained even at reasonably high loads—which guarantees good stability—without entering the elastohydrodynamic conditions. This allows for good correlation between theoretical and experimental results.

We will not comment on the experimental results but limit our analysis to the authors' theoretical solution which can be applied equally to the sphere-plane contact for which we have recently obtained a general numerical solution for pressure distribution, load, and friction and which has been confirmed, as far as the load and the friction is concerned, by experiments run at light loads.[4] Fig. 17 gives our results using the authors' notation. Both solutions use the satisfactory Reynolds' condition at exit. The pressure distribution obtained in our analysis is identical to that given in Figs. 7(*a*) and (*d*). The general shape of the boundary between full and partial film is similar except for the rather sudden irregularities which occur not only in Fig. 7(*d*) but also in Fig. 7(*c*) and for which we cannot find a suitable explanation. Could the authors comment on this point?

The authors' insist quite correctly on the importance of the entry conditions which define the pressure zone in the contact. In fact two types of entry conditions may be chosen. In the first, the choice is based on purely numerical criteria and does not take into account oil film thickness at entrance. Here the pressure zone or domain varies with minimum film thickness, the pressure curves calculated for different film thicknesses will therefore intersect at entrance. This approach implies that the oil film thickness at entrance is larger than the minimum film thickness required to satisfy the oil flow conditions in the contact. This type of solution is used by the authors and was used in our first solution. In the second type of entry condition, which we have also used, the oil film thickness at entry is fixed and this in turn defines the boundary of the pressure domain at entrance independently of the minimum film thickness parameter. Here the pressure curves all start from the same point and thus never intersect, and restrictions on flow conditions can be included in the analysis. This last aspect is of particular importance in starvation problems such as those visualised in pure rolling by Wedeven, Evans, and Cameron,[5] and in pure sliding by ourselves. Our analysis further shows that the variation of the friction force with entrance condition, and thus with the size of the domain, is very much larger than that of the load, particularly in pure sliding.

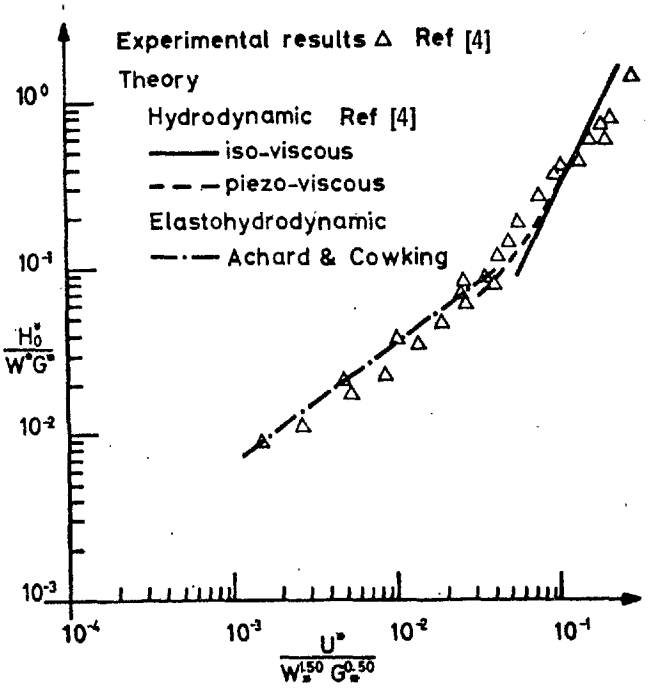


Fig. 17 Theoretical and experimental results of sphere-plane contact in pure sliding

In conclusion, we believe that the second type of entry condition is able to give a better representation of the real phenomenon than the first and we would like to have the authors' point of view on that problem.

J. M. McGrew[6]

The authors are to be congratulated on the preparation of an interesting and timely paper. The optical data that they have presented provides a valuable extension of previous work to a contact geometry more closely simulating that which occurs in a real bearing. Although the loads used by the authors are somewhat lower than those encountered in practical bearing operation, it is felt that the qualitative significance of their data is an important addition to optical elastohydrodynamic technology. This discussion is not intended to pose criticism toward the paper, but to put forth one minor observation that might be of interest regarding the elastic consistency of the data.

Elastohydrodynamic theory has shown that in a full elastohydrodynamic contact, the shape of the inlet zone will closely approximate that for dry Hertz contact. We have a computer program for computing the exterior Hertz profile in an elliptical elastic contact. The program provides as one of its outputs, values of x and y-coordinates at constant separation which would correspond to optical fringe patterns. For the authors' geometry, which corresponds to a 0.5 in. radius ball in a 0.555 in. radius groove, the ratio of the minor to major axes of the bands of constant separation in dry elastic contact, would vary from 0.221 to 0.314—the former being the ratio of the axes of the Hertz contact ellipse and the latter being the axis ratio of bands of constant separation far away from the contact ellipse.

---

[2] Department of Mechanical Engineering, Imperial College of Science and Technology, London, England.

[3] Institut National des Sciences Appliquées de Lyon, Villeurbanne, France.

[4] Dalmaz G. "L'hydrodynamique du contact sphère-plan," Thèse de Docteur-Ingénieur, Université de Lyon, May 1971.

[5] Wedeven L. D., Evans D., and Cameron A. "Optical Analysis of Ball Bearing Starvation," JOURNAL OF LUBRICATION TECHNOLOGY, TRANS. ASME, Series F, Vol. 93, No. 3, July 1971, p. 349.

[6] Mechanical Technology Inc., Latham, N. Y.

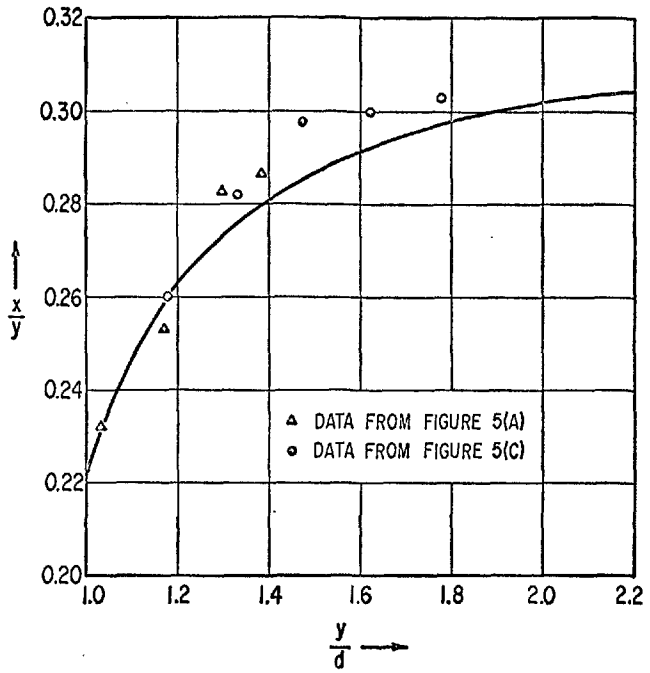


Fig. 18 Comparison of interference band geometry with Hertz contact theory

The axis ratio of bands of constant separation (x/y) predicted from Hertz contact theory is plotted as a function of y/d in Fig. 18. The curve depends only on geometry and is independent of load and elastic properties. The experimental points were obtained from Fig. 5. The ordinates were readily obtained by taking ratios of the band axes. The location of the Hertz contact ellipse could not be directly determined from the photographs, hence the axis ratio of the inner most "elliptical" band was matched with the curve to determine the scale for the abscissa, which is why the lower points obtained from Figs. 5(a) and 5(c) fall directly on the curve.

In light of the magnified scale used for Fig. 18, the agreement between theory and experiment appears to be relatively good, thereby providing another indication of consistency with existing elastohydrodynamic theory.

Authors' Closure

The authors would like to thank all the discussers for their interest and their comments. In reply to Dr. Cameron, this lightly loaded case is relevant over, for example, the greater part of a journal ball bearing, since here the loads are low and gross slip may occur with consequent heating of the lubricant. These conditions also prevail in the cage/ball contact where the condition is always one of pure sliding.

Drs. Dalmaz, Berthe, and Godet have raised some very pertinent points. We are unable to give any positive explaination for the irregularities in the boundaries of Figs. 7(c) and 7(d). They are probably due to interpolation errors in the calcomp plotting program since, as the computations are performed on a circular mesh, these errors are magnified when plotting elliptically. However, the irregularities were not evident in plots for the point contact case (as confirmed by the discussers) so it was decided to present the results without smoothing as this might not be justified.

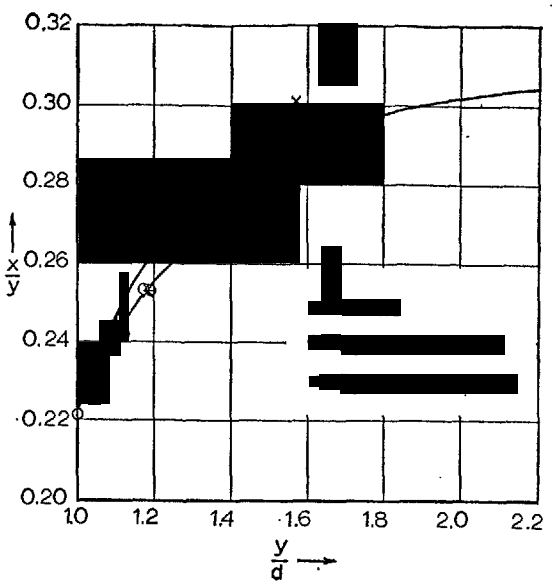


Fig. 19

It should be noticed that similar irregularities can be seen experimentally in Figs. 5(c) and 8(d) although they are masked in the latter by cavitation which has started early at a scratch on the glass raceway.

With regard to the question of entry conditions, it was convenient to use a fixed value of $\bar{r}$ since we were investigating only fully flooded contacts, for which film-thickness and load are not greatly dependent on the inlet boundary. That these conditions prevailed experimentally was confirmed by measurements of the size of the inlet meniscus. We are in complete agreement with the discussers that the second entry condition they mention is more realistic for starved conditions and is especially necessary when considering predictions of friction.

The curve presented by Dr. McGrew shows quite good agreement between theory and experiment, but it was felt that this would be better still if the difficulties inherent in measuring and scaling the photographs presented in the paper were removed.

To this end, Fig. 19 shows data obtained from two original photographs with identical magnifications. One was for static conditions and the other moving, with conditions similar to those of Fig. 5(a). As can be seen, the static curve differs from that predicted by Dr. McGrew. This must be due either to an inaccuracy of the Hertz theory or, more likely, an error in the quoted groove radius. This, however, was inferred from the Hertz contact axis-ratio, at which point the two curves agree.

The other points are for the axis ratio of bands of constant separation measured experimentally in the inlet and in the outlet regions. The former show excellent agreement with the measured Hertzian shape (about 1 percent at $y/d = 1.6$), whilst the latter has relatively poor agreement (about 9 percent at $y/d = 1.6$). This is in accord with present E. H. D. theory which assumes a Hertzian shape in the inlet region. The shape measured in the exit region is non-Hertzian probably because pressures have already fallen to low values and also because an inaccuracy creeps in. This is because in the exit region there is air in the oil which results in a change in refractive index and hence a change in the fringe radius for a given separation.

Elastohydrodynamic sliding friction in a low modulus point contact

by N. Thorp

R. Gohar

Imperial College

Manuscript accepted for publication by the Institution of Mechanical Engineers in the Journal of Mechanical Engineering Science

Contents:-

	Page
Abstract	1
Introduction	2
Experimental details	3
Theory	5
Discussion of results	9
Conclusions	10
Acknowledgements	11
References	12
List of Figures	14
Nomenclature	15

Abstract

The friction in a lubricated point contact between a driven tungsten carbide ball sliding against a flat perspex plate is studied. Loads and speeds are varied to cover a wide range of conditions. Predictions based on established properties of the oil and straightforward elastohydrodynamic theory are compared with experiments. The range of application of various theories is discussed.

Introduction

Some recent research in elastohydrodynamic lubrication has been on the traction characteristics of the contact. This has important applications in rolling element bearings, gears and friction drives. The theoretical model has usually been one of nominal line contact, where the slip to roll ratio of the rolling elements can be varied. This model has the advantage of relative simplicity coupled with the fact that considerable information has been amassed from computer solutions giving details of film shape and pressure distribution (1). Both these are important in the determination of traction forces. By assuming that the load between steel discs was sufficient to cause an elliptical pressure distribution, Crook,(2), found how the traction varied with slip-roll ratio. Using a simple Newtonian model for the oil, which was piezo-viscous, he showed that the heat generated by viscous shearing depended on the local viscosity and temperature in the nip. These were shown to be little affected by the presence either of isothermal bounding surfaces or of surfaces whose temperatures increased due to the heating. When he compared his theoretical results with those he had found experimentally from a 2-disc machine, theoretical traction was too high, although the general shape of the traction~speed curve was the same, the traction rising from zero to a maximum and then falling with increase in sliding speed. The rise and fall he attributed to the gradual increase of heating in the oil film.

More recently, investigators have turned their attention to the possible causes of the difference between theory and experiment. One approach has been to assume that experimental results are correct and use these in the theory to determine the oil pressure-viscosity properties under shear (3). Another has been to try various oil pressure-temperature-viscosity relationships until a good fit between theory and experiment is obtained (4). Under these circumstances the results

cannot fail to be successful and have indeed provided a major breakthrough in our knowledge of oil traction properties.

Some traction studies have also been carried out using nominal point contact geometry. Although it is experimentally easier to measure both film thickness (by interferometry) and traction, an accurate theory, with a minimum of assumptions is more difficult to obtain. However, Grubin type approximations have yielded accurate film thickness predictions (5), and rolling friction has been determined both theoretically and experimentally (6). Gentle (7) has also used a ball and plate machine to examine non-Newtonian effects in the oil film. He used an analogy of the granular behaviour of solids to describe them theoretically.

There is still, however, a need to compare theory with experiment using established properties of the oil and straightforward elastohydrodynamic theory. The work described below therefore uses Crook's theoretical approach but is confined to moderate speeds and pressures up to 10,000 lbf in^{-2} (6.9×10^7 Nm^{-2}) in a nominal point contact.

Experimental details

The apparatus used has been fully described in reference 8. Basically, it was composed of a tungsten carbide ball which was rotated and loaded against a stationary perspex plate. The reduced modulus (E) of the combination was 8.9×10^5 lbf/in^2 (6.14×10^8 Nm^{-2}).

The perspex plate was mounted on a bearing which was restrained by means of a small spring balance. Thus the friction force exerted on the plate by the shearing of the oil was registered on the balance, the size of the reading being magnified by different moment arms to increase accuracy of reading. All bearings in the system were aerostatic to give zero friction. Although the friction measuring arrangement was a

spring-mass system, theoretically prone to vibration, no damping was found to be necessary in practice, since instabilities did not occur.

A paraffinic mineral oil, (BP 1065) having an atmospheric viscosity (η_o) of about 35 poise was used. Its pressure viscosity coefficient (α) was considered to be constant under the low pressures and speeds employed in the experiment. Its value was determined from experimental data obtained by B.P. Ltd. (9) using a high pressure viscometer. The value of α came to 2.1×10^{-4} in^2/lbf (3.04×10^{-8} m^2/N) and G* was therefore 187. The temperature coefficient of viscosity (β) was also determined from B.P.'s results and had a value of 8.55×10^{-2} $^oC^{-1}$.

The kinematics of the arrangement were such that there was pure sliding (slide/roll ratio of unity). The range of speeds and loads was $U^* = 1.2 \times 10^{-10}$ to 7.84×10^{-8} and $W^* = 3.46 \times 10^{-6}$ to 3.17×10^{-5}. By employing perspex as one of the materials, optical interference methods could be used to determine oil film thickness. This was not measured in detail in the work described below having already been done, as reported in reference 6.

A typical shape of the contact is shown in fig 1. Note that most of the load bearing region is uniform. Such a shape can therefore be associated with a nearly ellipsoidal pressure distribution, typical of materials subjected to a high dimensionless load, (W*) and moving at low to moderate dimensionless speeds (U*). Experimental evidence of such a distribution for line contacts and a similar reduced modulus, (G*), is given in reference 10. Fig 2 is reproduced from this reference. The hydrodynamic pressure distribution is nearly an ellipse over most of the load bearing region.

The inlet oil temperature was measured with a trailing thermocouple resting on the ball surface ahead of the contact. The tempera-

ture measured remained approximately equal to that of the bulk oil because of the low sliding speeds and loads. A more detailed investigation of inlet temperature variation as the contact is approached is given in reference 11.

Theory

The assumptions of the theory for point contact are similar to those used by Crook (2) for his line contact analysis. These are:-

1. The region of friction is circular, of Hertzian radius and pressure distribution, friction in the non-parallel zone being negligible in comparison.
2. The heat generated is caused by viscous shearing of the oil due to slip.
3. The rolling component of friction is ignored. Hence it follows that the shear stress is constant through the thickness of the film.
4. In common with the usual hydrodynamic analysis, inertia and body forces are neglected and pressure is considered constant across the film.
5. There are equal heat flows to the bounding surfaces.
6. Both the moving and the fixed bounding surfaces are considered to be isothermal,having a temperature equal to that of the inlet.
7. Heating due to compression is negligible compared with that due to sliding.
8. Pressure and temperature coefficients of viscosity do not vary with temperature and pressure and any shear rate effects are ignored. This is a reasonable assumption when the contact is sub-

jected to low maximum pressures (less than 10,000 psi).

Referring to fig 3 and using assumptions 1-8, by Crook's analysis (2) we obtain an expression for the viscosity η_m of a point in the film, at radius r, at which $\partial u/\partial z = (U_2 - U_1)/h$, z being the co-ordinate across the film. This is:-

$$\eta_m = \eta_s \, e^{\alpha p} \, \frac{\ln (\sqrt{\psi+1} + \sqrt{\psi})}{\sqrt{\psi}.\sqrt{\psi+1}} \qquad (1)$$

where η_s is the viscosity at radius a (the start of the ellipsoidal pressure distribution - effectively the inlet viscosity) and

$$\psi = \frac{\eta_s \, e^{\alpha p} \, \beta \, U^2}{8K} \qquad (2)$$

If U is large, (1) can be simplified to

$$\eta_m = \frac{4K}{\beta.U^2} \left[\alpha p + \ln \left(\frac{\eta_s \, \beta \, U^2}{2K} \right) \right]$$

η_m is seen to depend on external variables and the pressure at each radius r.

As the pressure distribution is ellipsoidal (Hertzian theory assumption)

$$\alpha p = \alpha p_{max} \, (1 - r^2/a^2)^{\frac{1}{2}}$$

or $$\bar{p} = \bar{p}_{max} \, (1 - \bar{r}^2)^{\frac{1}{2}}$$

that is $$\bar{p} = .365 \, G^* \, (W^*)^{1/3} \, (1 - \bar{r}^2)^{\frac{1}{2}}$$

since $\bar{p}_{max} = .365\ G^*\ (W^*)^{1/3}$ by Hertzian theory.

If $\eta_m^* = \eta_m/\eta_s$ and $K^* = \dfrac{K\eta_s\alpha^2}{\beta R^2}$ then equations (2) and (1) can be written as

$$\psi = \frac{U^{*2}G^{*2}}{8K^*} \cdot \exp\ [.365\ G^*\ W^{*1/3}\ (1 - \bar{r}^2)^{\frac{1}{2}}]$$

$$\eta_m^* = \frac{\exp\ [.365\ G^*\ W^{*1/3}(1 - \bar{r}^2)^{\frac{1}{2}}] \cdot \ln\ (\sqrt{\psi+1} + \sqrt{\psi})}{\sqrt{\psi}.\sqrt{\psi+1}} \qquad (3)$$

Now $\tau_{zr} = \dfrac{\eta_m U}{h_o}$ is constant through the film (assumption 3).

Therefore, for a circular contact, the sliding friction is

$$F_s = \frac{2\pi U}{h_o} \int_o^a \eta_m\ r.dr \qquad (4)$$

h_o is known from existing e.h.l. theory (12) and, since the rolling speed equals the sliding speed, can be expressed as

$$H_o^* = 1.06\ (U^*G^*)^{.714}\ W^{*-.0476} \qquad (5)$$

Then if $\mu = F_s/W$ we have from (3), (4) and (5)

$$\mu = 7.8\ (\frac{U^*}{W^*})^{.286}\ G^{*-.714} \int_o^1 \eta_m^*\ r^*\ dr^*$$

or after rearrangement

$$\mu(\frac{W^*}{U^*}) = 7.8\ (\frac{U^*G^*}{W^*})^{-.714} \int_o^1 \eta_m^*\ r^*\ dr^* \qquad (6)$$

As $\psi \to 0$ we obtain isothermal conditions throughout the film. Equation (6) can then be integrated and becomes

$$\mu\left(\frac{W^*}{U^*}\right) = 7.8\ \left(\frac{U^*G^*}{W^*}\right)^{-.714} \left[\frac{e^{\bar{p}_{max}}\ (\bar{p}_{max} - 1) + 1}{\bar{p}_{max}^{\,2}}\right] \tag{7}$$

In general terms (6) can be written as

$$\mu\left(\frac{W^*}{U^*}\right) = \Phi_1\left[\frac{U^*}{W^{*\,3/2}\ G^{*\,1/2}}\ ,\ G^{*3}\ W^*,\ G^{*6}\ K^*\right] \tag{8}$$

for thermal conditions, and (7) can be written as

$$\mu\left(\frac{W^*}{U^*}\right) = \Phi_2\left[\frac{U^*}{W^{*\,3/2}\ G^{*\,1/2}}\ ,\ G^{*3}\ W^*\right] \tag{9}$$

for isothermal conditions. Note that one group has been suppressed when the conditions become isothermal. If, in addition, elasticity is not important, but viscosity still increases with pressure, then (9) becomes

$$\mu\left(\frac{W^*}{U^*}\right) = \Phi_3\left[\frac{U^*}{W^{*\,3/2}\ G^{*\,1/2}}\right]$$

Finally, with no dependence of viscosity upon pressure,

$$\mu\left(\frac{W^*}{U^*}\right) = \text{const} \tag{10}$$

This is the correct form of expression for undistorted sliding point contact friction under isoviscous conditions.

In addition, the rolling friction can be expressed as

$$\mu_r\left(\frac{W^*}{U^*}\right) = 8.6\left(\frac{U^*}{G^{*1/2}\,W^{*3/2}}\right)^{-.2}(W^*G^{*3})^{-.033} \qquad (11)$$

where (11) has been obtained from reference 6. It was shown there that $\mu_r << \mu$ at all but very low values of slip.

Equations (6) and (7) were solved numerically, but were plotted in the manner suggested by equations (8) and (9), that is, with $\left(\frac{U^*}{W^{*3/2}\,G^{*1/2}}\right)$ as abscissae and $\mu\left(\frac{W^*}{U^*}\right)$ as ordinates. K* and G* remained constant, whilst W* and U* were varied. Note that the two plotted groups do not contain E and therefore also apply to an undistorted contact. A similar form of plot was used for film thickness in reference 8.

Discussion

Figs 4 and 5 show the experimental results with predicted friction superimposed on them for comparison. The experimental points are for a range of loads and the band of theory represents the spread with the same load range.

Using the groups suggested by eqn (9), fig 4 shows isothermal theory superimposed on the experimental results. The theory is slightly above experiment and both have a small spread showing the weak effect of the load group W^*G^{*3}. At higher speeds, the experimental results spread out, the same effect being noticed when the thermal theory is plotted, as in fig 5. The spread can be attributed to the increased significance of the additional group $G^{*6}K^*$.

At even higher speeds, experiment tends to level off to a constant $\mu W^*/U^*$. This trend is suggested by eqn (10). The speed has become so

high, that the surfaces are regaining their undeformed shapes and conditions are becoming isoviscous. The thermal theory is, by this stage, no longer valid, since assumption (1) no longer applies.

Although careful use of dimensionless groups can explain experimental results with a minimum of plotting, especially when different materials are used, the physical significance of individual parameters (such as μ) can become obscured. Thus, fig 6 shows μ plotted against U^* for three of the five experimental loads, the others being omitted for clarity.

Over the lower part of the speed range, for all loads, friction increases as predicted by eqn (6), that is, $\mu \propto U^{*\cdot 286}$. At higher speeds for the heaviest load, assumption 1 is still valid and there is a reduction in friction with increase of speed due to viscous heating. At these higher speeds, for reduced loads, there is a change in pressure distribution and consequent relaxation of the surfaces which leads to isoviscous undistorted conditions. μ should then increase in direct proportion to U^*. This tendency is seen to be already starting with the lowest value of W^* plotted on fig 6.

Conclusion

The experiments have shown how the friction varies in low modulus sliding point contacts. Conventional elastohydrodynamic theory has been shown to be adequate to predict the friction under these low contact pressures, providing oil property data is available.

Acknowledgements

The authors would like to thank the Science Research Council for the grant which is supporting this research project. They would also like to thank B.P. Ltd., for supplying data on the oil used.

References

1. Dowson D. and Whitaker A.V. 'A numerical procedure for the solution of the elastohydrodynamic problem of rolling and sliding contacts lubricated by a Newtonian fluid' Proceedings of the Institution of Mechanical Engineers 1965-66 Vol 180 Part 3B pp 57-71

2. Crook A.W. 'The lubrication of rollers- part III' Philosophical Transactions of the Royal Society. Series A Vol 254 p 237

3. Jefferis J.A. and Johnson K.L. 'Sliding friction between lubricated rollers' Proceedings of the Institution of Mechanical Engineers 1967-68 Vol 182 Part 1 No 14 pp 281-291

4. Kannel J.W. and Walowit J.A. 'Simplified analysis for tractions between rolling-sliding elastohydrodynamic contacts' Transactions of the ASME. Series F. Journal of Lubrication Technology Jan 1971 Vol 93 No 1 pp 39-46

5. Grubin A.N. 'Investigation of Scientific and Industrial Research', Central Scientific Research Institute for Technology and Mechanical Engineering, Moscow, Book No 30, 1949, pp 115-116

6. Gohar R. 'Oil film thickness and rolling friction in elastohydrodynamic point contact' Transaction of the ASME Series F. Journal of Lubrication Technology July 1971 Vol 93 No 3 pp 371-382

7. Gentle C.R. 'Optical interferometry study of film formation in lubrication of sliding or rolling contacts' NASA Report CR-120842 (to be published 1972)

8. Thorp N. and Gohar R. 'Oil film thickness and shape for a ball sliding in a grooved raceway' ASME Paper No 71-Lub-18 Lubrication Conference Oct. 1971

9. Pywell R.F. 'Viscosities and densities of oils at high pressure and their dependence on hydrocarbon type' Internal Report 10, 155(S), 1970 B.P. Research Centre, Sunbury, Middx.

10. Cope D.L. and Haines D.J. 'Interferometric determination of elastohydrodynamic lubrication contact pressures' Proceedings of the Institution of Mechanical Engineers 1969-70, Vol 184 Part 1 No 35 pp 633-646

11. Gohar R. 'Oil films under elastohydrodynamic conditions' Ph.D. thesis 1965 University of London

12. Wedeven L.D., Evans D. and Cameron A. 'Optical analysis of ball bearing starvation' Transactions of the ASME Series F. Journal of Lubrication Technology July 1971 Vol 93 No 3 pp 349-363

List of Figures

Fig 1 Typical film shape for elastohydrodynamic perspex contact ($W^* = 1.95 \times 10^{-4}$ $U^* = 2.24 \times 10^{-9}$ $G^* = 187$)

Fig 2 Non-dimensional pressure distribution and equivalent Hertzian pressure ellipse (from ref 10)

Fig 3 Co-ordinate system

Fig 4 Friction group versus speed group - experimental and isothermal theory

Fig 5 Friction group versus speed group - experimental and thermal theory

Fig 6 Experimental friction versus non-dimensional speed

Nomenclature

a	=	radius of Hertzian contact
E	=	reduced modulus of elasticity
F_s	=	sliding frictional force
G^*	=	$\alpha.E$ = materials parameter
h	=	film thickness at r,θ
h_o	=	central film thickness
H_o^*	=	h_o/R = central film thickness parameter
K	=	thermal conductivity of the oil
K^*	=	$\frac{K\eta_s\alpha^2}{\beta R^2}$ = thermal heating parameter
p	=	pressure at r,θ
$\bar{p}$	=	αp = non-dimensional pressure
p_{max}	=	maximum Hertz pressure
$\bar{p}_{max}$	=	αp_{max} = non-dimensional maximum Hertz pressure
r	=	polar co-ordinate
$\bar{r}$	=	r/a = non-dimensional polar co-ordinate
R	=	ball radius
u	=	oil velocity at r,θ,z
U	=	$(U_2 - U_1)$ = sliding speed
U_2	=	ball surface velocity
U_1	=	plate surface velocity
U^*	=	$\frac{\eta_o U}{ER}$ = speed parameter
W	=	total load carried by contact
W^*	=	W/ER^2 = load parameter
z	=	co-ordinate through the film thickness
α	=	pressure viscosity coefficient of the lubricant

β = temperature viscosity coefficient of the lubricant

η_m = viscosity at a point in the film (see eqn (1))

η_o = oil viscosity at atmospheric pressure and temperature

η_s = η_o = oil viscosity at radius a

θ = polar co-ordinate

μ = coefficient of friction (sliding)

μ_r = coefficient of friction (rolling)

$\tau_{r,z}$ = shear stress at r,z

Φ = denotes a functional relationship

ψ = see equation (2)

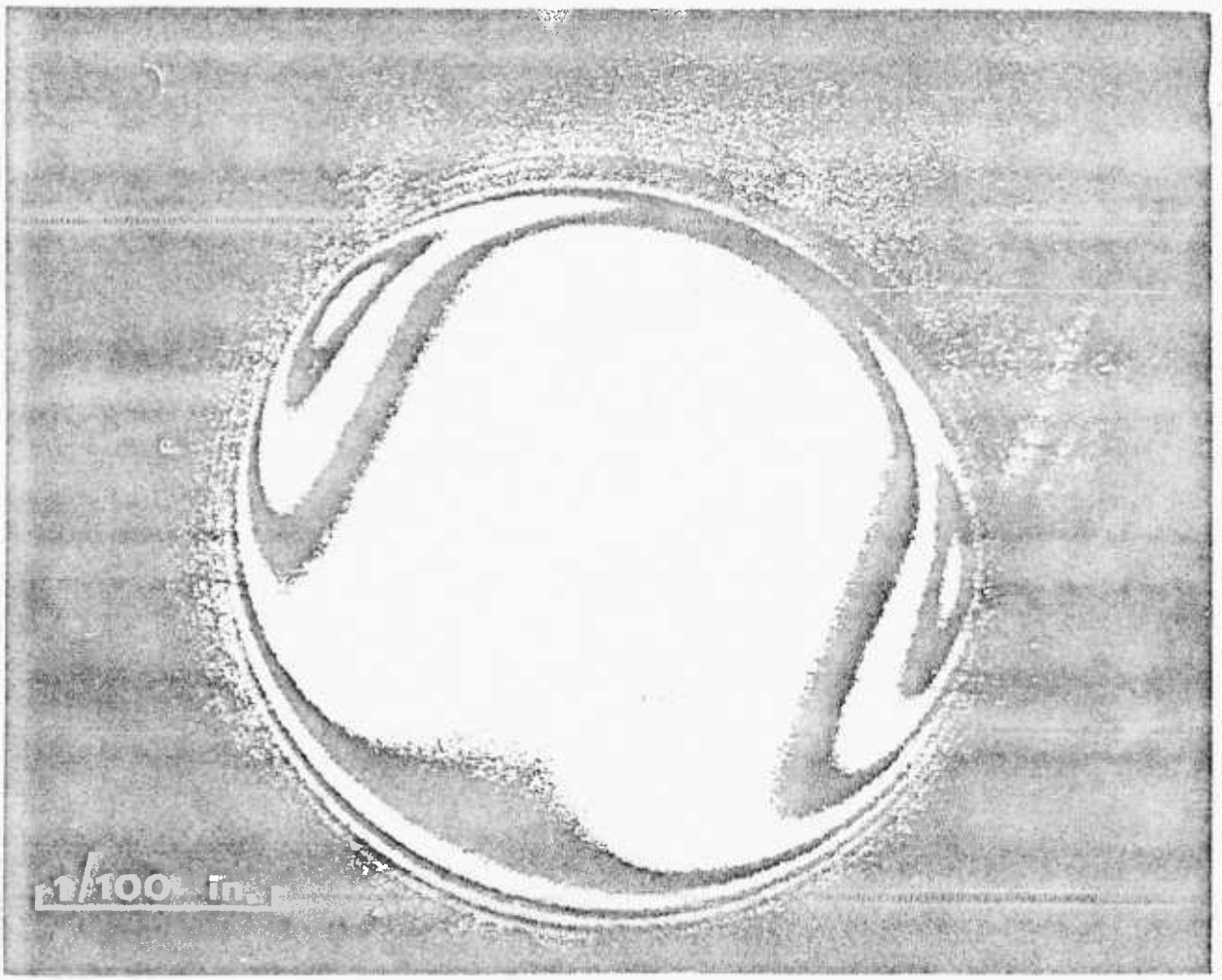
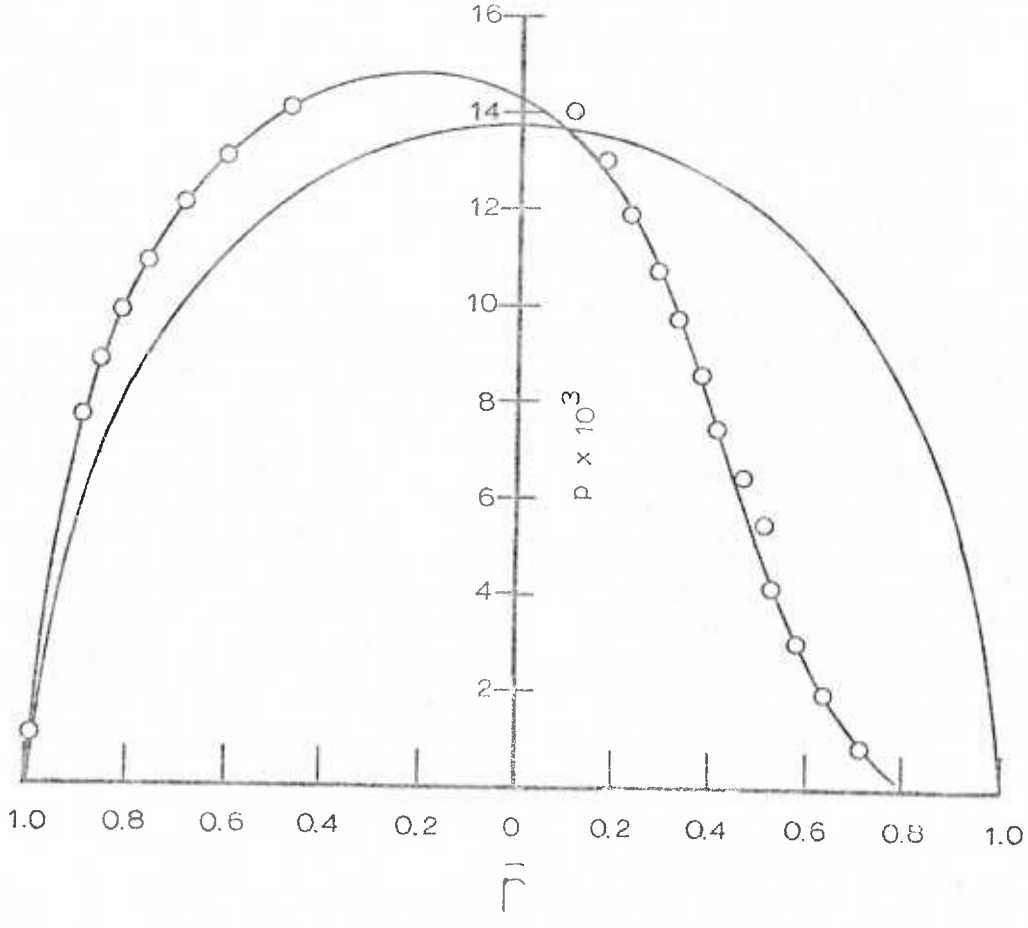


FIGURE 1



$W^* = 1.2 \times 10^{-3}$ $U^* = 6.3 \times 10^{-10}$ $G^* = 202$

FIGURE 2

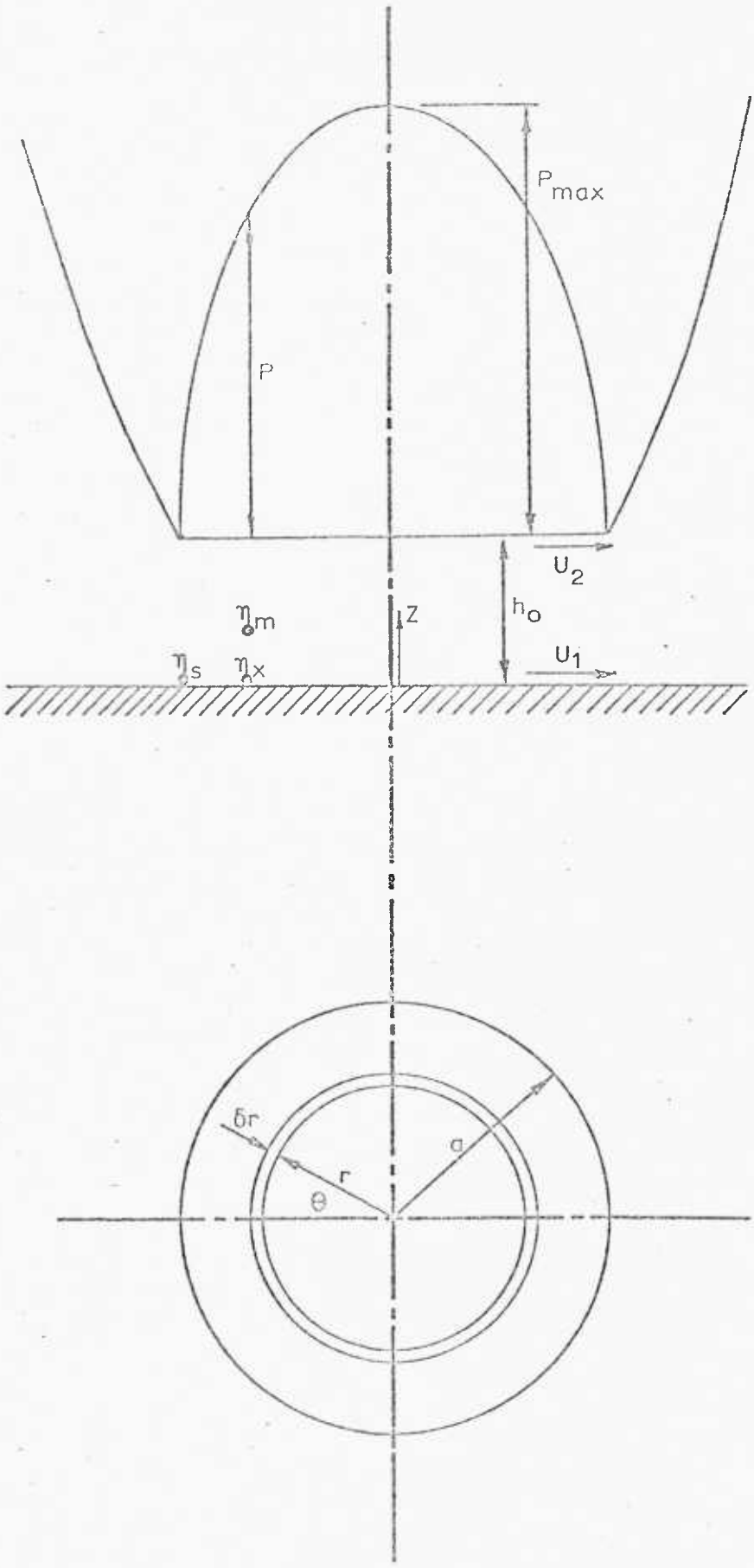


FIGURE 3

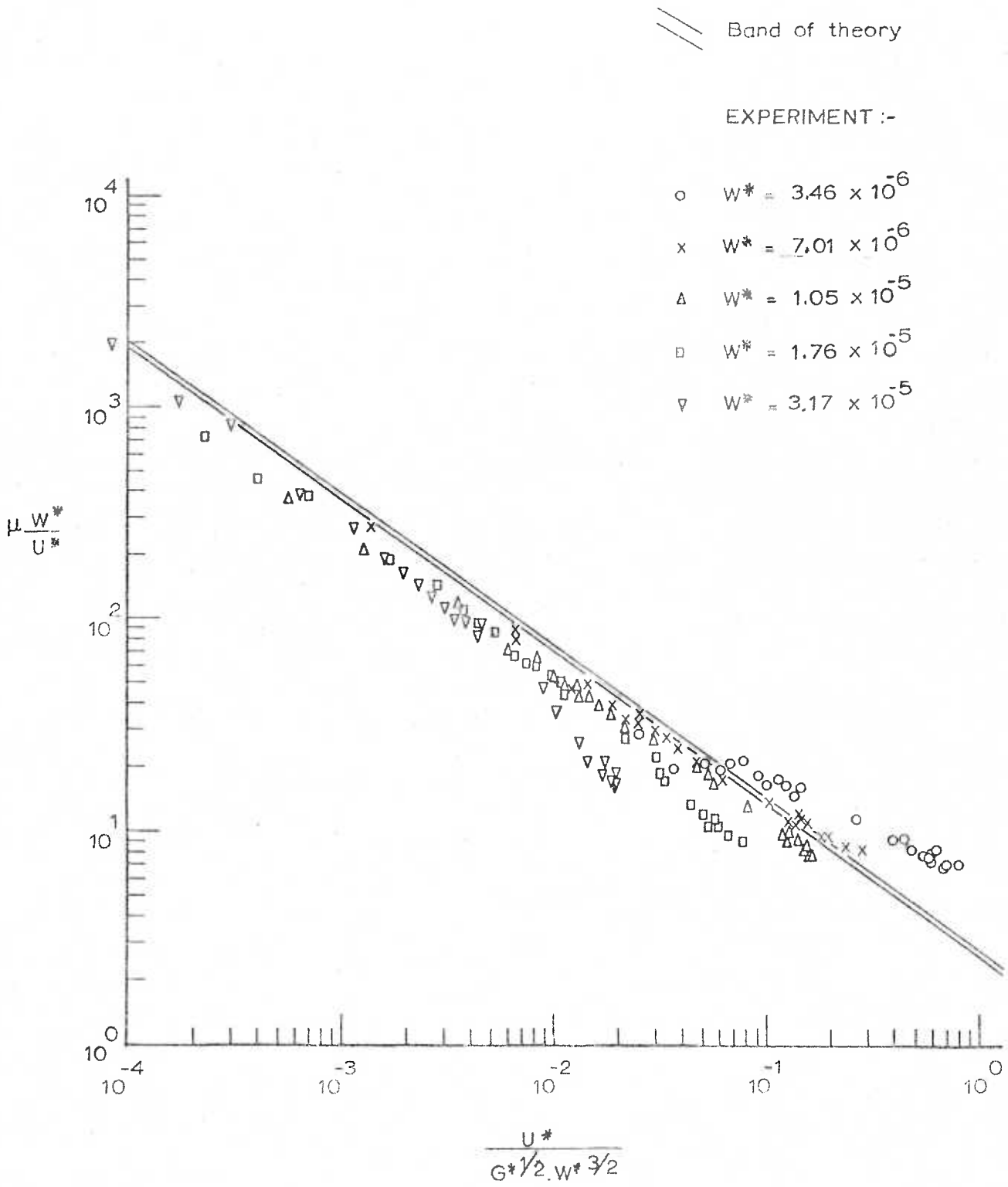

Band of theory
EXPERIMENT :-
o W* = 3.46 x 10^-6
x W* = 7.01 x 10^-6
Δ W* = 1.05 x 10^-5
□ W* = 1.76 x 10^-5
▽ W* = 3.17 x 10^-5
μ W*/U*
10^4
10^3
10^2
10^1
10^0
10^-4
10^-3
10^-2
10^-1
10^0
U*/G*^1/2 . W*^3/2

FIGURE 4

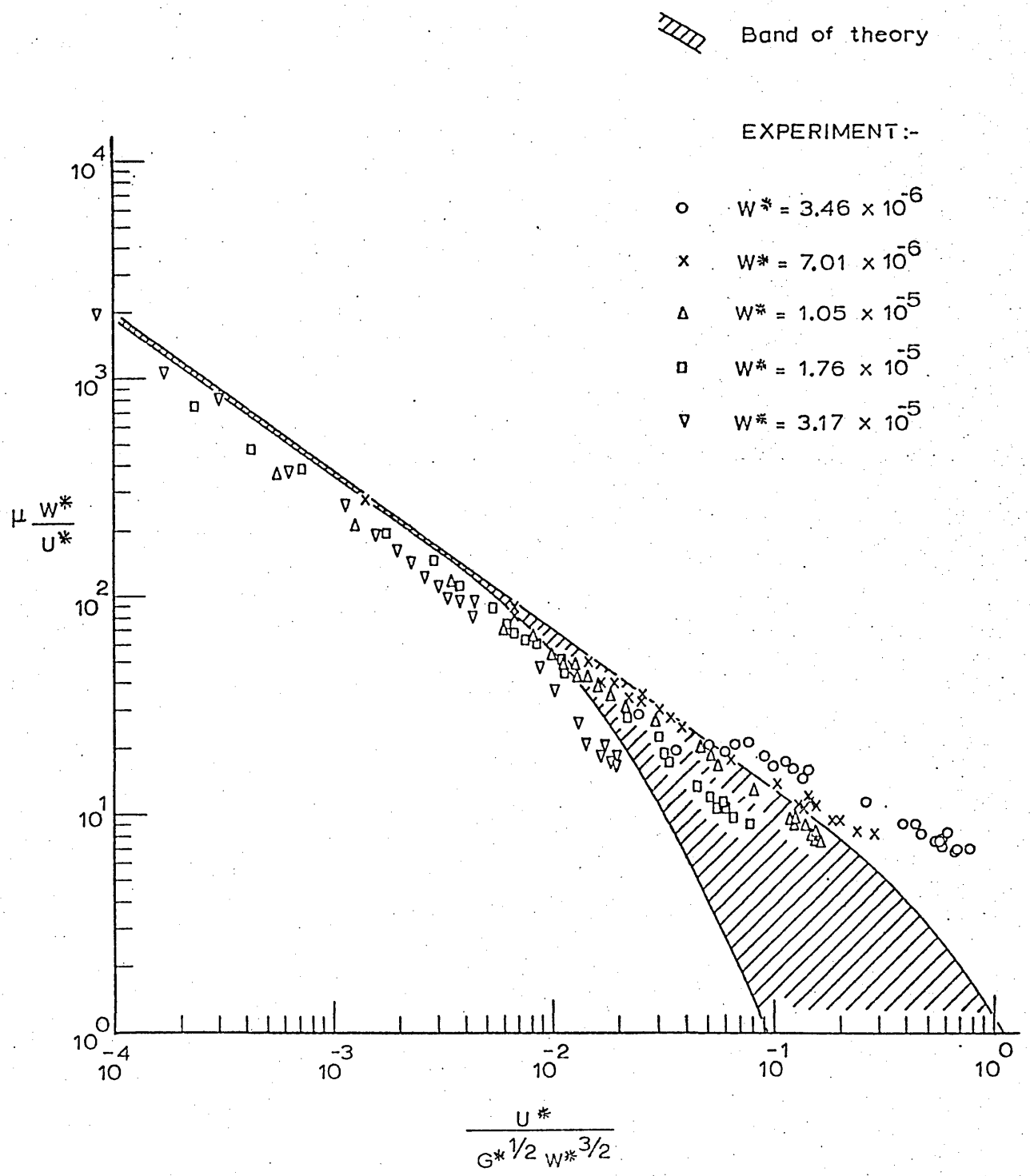

Band of theory
EXPERIMENT :-
o W* = 3.46 x 10^-6
x W* = 7.01 x 10^-6
Δ W* = 1.05 x 10^-5
□ W* = 1.76 x 10^-5
▽ W* = 3.17 x 10^-5
μ W*/U*
10^4
10^3
10^2
10^1
10^0
10^-4
10^-3
10^-2
10^-1
10^0
U*/G*^1/2 W*^3/2

FIGURE 5

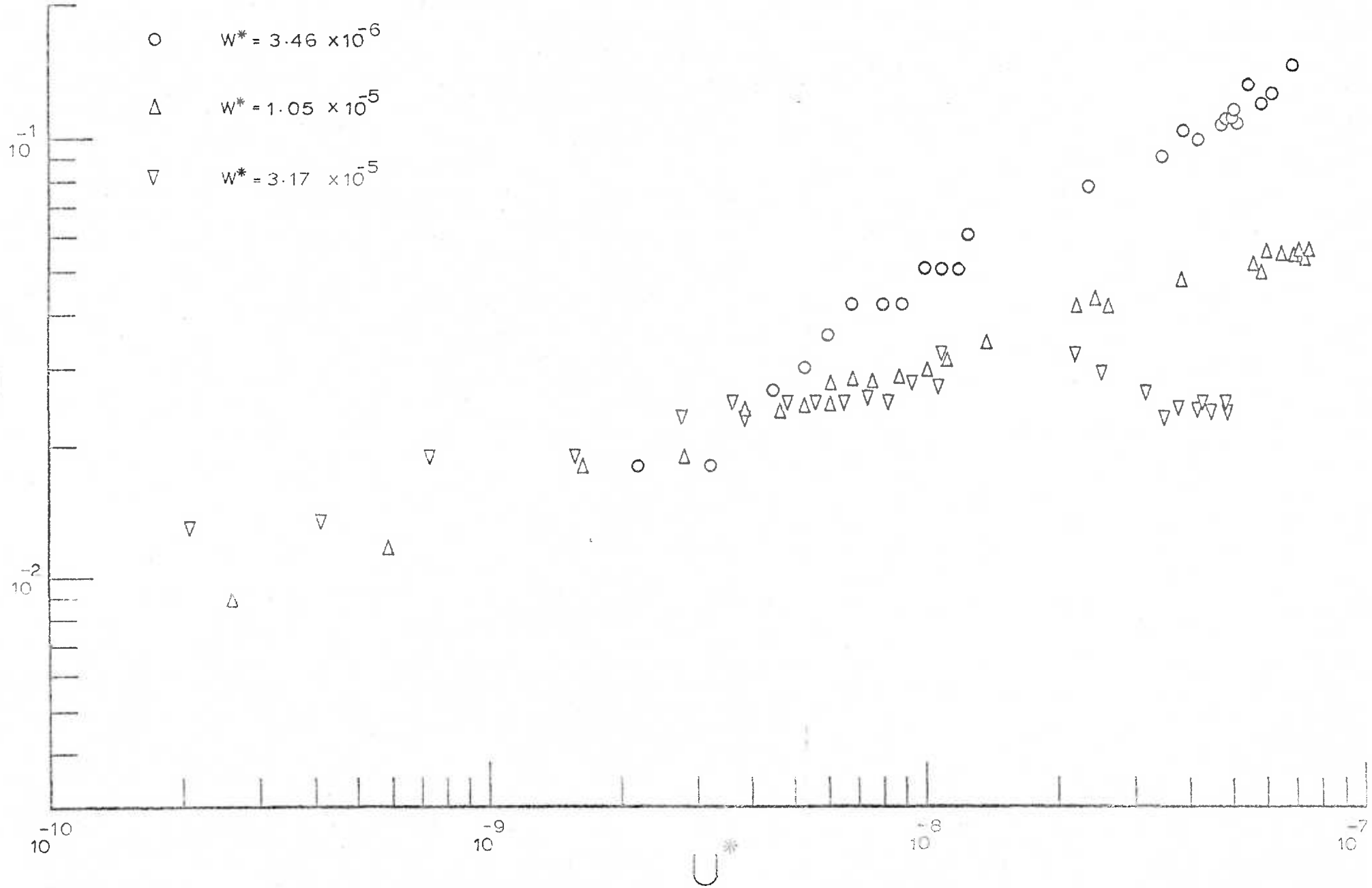


FIGURE 6